

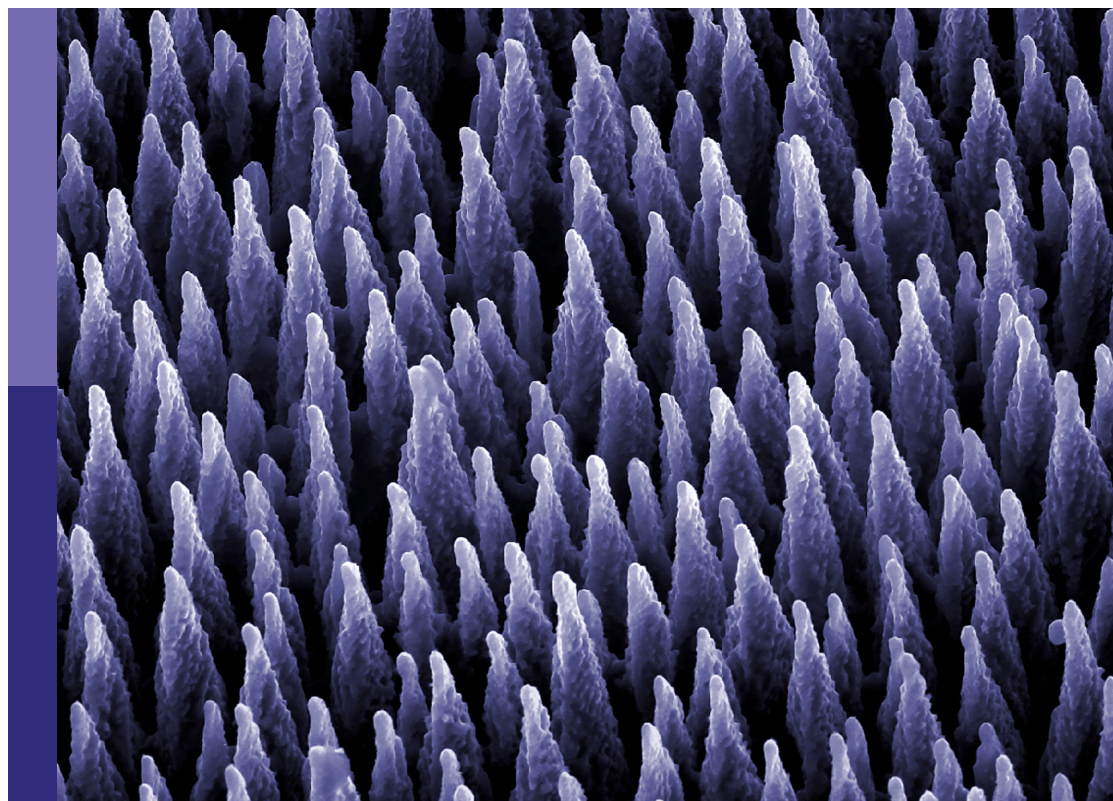
# ECCM Research Topic on advanced manufacturing of composites

**Edited by**

Veronique Michaud, Baris Caglar, Christophe Binetruy,  
Lode Daelemans and Clemens Dransfeld

**Published in**

Frontiers in Materials



## FRONTIERS EBOOK COPYRIGHT STATEMENT

The copyright in the text of individual articles in this ebook is the property of their respective authors or their respective institutions or funders. The copyright in graphics and images within each article may be subject to copyright of other parties. In both cases this is subject to a license granted to Frontiers.

The compilation of articles constituting this ebook is the property of Frontiers.

Each article within this ebook, and the ebook itself, are published under the most recent version of the Creative Commons CC-BY licence. The version current at the date of publication of this ebook is CC-BY 4.0. If the CC-BY licence is updated, the licence granted by Frontiers is automatically updated to the new version.

When exercising any right under the CC-BY licence, Frontiers must be attributed as the original publisher of the article or ebook, as applicable.

Authors have the responsibility of ensuring that any graphics or other materials which are the property of others may be included in the CC-BY licence, but this should be checked before relying on the CC-BY licence to reproduce those materials. Any copyright notices relating to those materials must be complied with.

Copyright and source acknowledgement notices may not be removed and must be displayed in any copy, derivative work or partial copy which includes the elements in question.

All copyright, and all rights therein, are protected by national and international copyright laws. The above represents a summary only. For further information please read Frontiers' Conditions for Website Use and Copyright Statement, and the applicable CC-BY licence.

ISSN 1664-8714  
ISBN 978-2-8325-3689-6  
DOI 10.3389/978-2-8325-3689-6

## About Frontiers

Frontiers is more than just an open access publisher of scholarly articles: it is a pioneering approach to the world of academia, radically improving the way scholarly research is managed. The grand vision of Frontiers is a world where all people have an equal opportunity to seek, share and generate knowledge. Frontiers provides immediate and permanent online open access to all its publications, but this alone is not enough to realize our grand goals.

## Frontiers journal series

The Frontiers journal series is a multi-tier and interdisciplinary set of open-access, online journals, promising a paradigm shift from the current review, selection and dissemination processes in academic publishing. All Frontiers journals are driven by researchers for researchers; therefore, they constitute a service to the scholarly community. At the same time, the *Frontiers journal series* operates on a revolutionary invention, the tiered publishing system, initially addressing specific communities of scholars, and gradually climbing up to broader public understanding, thus serving the interests of the lay society, too.

## Dedication to quality

Each Frontiers article is a landmark of the highest quality, thanks to genuinely collaborative interactions between authors and review editors, who include some of the world's best academicians. Research must be certified by peers before entering a stream of knowledge that may eventually reach the public - and shape society; therefore, Frontiers only applies the most rigorous and unbiased reviews. Frontiers revolutionizes research publishing by freely delivering the most outstanding research, evaluated with no bias from both the academic and social point of view. By applying the most advanced information technologies, Frontiers is catapulting scholarly publishing into a new generation.

## What are Frontiers Research Topics?

Frontiers Research Topics are very popular trademarks of the *Frontiers journals series*: they are collections of at least ten articles, all centered on a particular subject. With their unique mix of varied contributions from Original Research to Review Articles, Frontiers Research Topics unify the most influential researchers, the latest key findings and historical advances in a hot research area.

Find out more on how to host your own Frontiers Research Topic or contribute to one as an author by contacting the Frontiers editorial office: [frontiersin.org/about/contact](https://frontiersin.org/about/contact)



# ECCM Research Topic on advanced manufacturing of composites

## Topic editors

Veronique Michaud — Swiss Federal Institute of Technology Lausanne, Switzerland  
Baris Caglar — Delft University of Technology, Netherlands  
Christophe Binetruy — Ecole Centrale de Nantes, France  
Lode Daelemans — Ghent University, Belgium  
Clemens Dransfeld — Delft University of Technology, Netherlands

## Citation

Michaud, V., Caglar, B., Binetruy, C., Daelemans, L., Dransfeld, C., eds. (2023).  
*ECCM Research Topic on advanced manufacturing of composites*.  
Lausanne: Frontiers Media SA. doi: 10.3389/978-2-8325-3689-6

## Table of contents

- 05 **Editorial: ECCM Research Topic on advanced manufacturing of composites**  
Christophe Binetruy, Baris Caglar, Lode Daelemans, Clemens Dransfeld and Véronique Michaud
- 07 **Experimental and numerical analysis of the consolidation process for additive manufactured continuous carbon fiber-reinforced polyamide 12 composites**  
Igor Zhilyaev, Stefan Grieder, Marco Küng, Christian Brauner, Michael Akermann, Jonas Bosshard, Petra Inderkum, João Francisco and Martin Eichenhofer
- 29 **Carbon and cellulose based nanofillers reinforcement to strengthen carbon fiber-epoxy composites: Processing, characterizations, and applications**  
Pias Kumar Biswas, Oluwaseun Omole, Garrett Peterson, Eric Cumbo, Mangilal Agarwal and Hamid Dalir
- 53 **Influence of NCF architecture on the morphology of forming induced wrinkling**  
Claudia Jimenez Martin, Vincent K. Maes, Turlough McMahon and James Kratz
- 64 **Optical inspection of the braid formation zone during manufacturing of preforms from reinforcement fibers for defect detection purposes**  
Stephan Maidl, Maximilian Hilbck, Kalle Kind and Klaus Drechsler
- 76 **Zonally heated tooling for moulding complex and highly tapered composite parts**  
Vincent K. Maes, Arjun Radhakrishnan, Diego Lombetti and James Kratz
- 85 **On the relationship of morphology evolution and thermal conductivity of flax reinforced polypropylene laminates**  
Masoud Bodaghi, Doriane Delfrari, Margot Lucas, Noha-Lys Senoussaoui, Yao Koutsawa, Burcu Karaca Uğural and Henri Perrin
- 100 **Rapid and facile preparation of nanocomposite film heaters for composite manufacturing**  
Iman Naseri, Behnam Ashrafi, Michael Jakubinek, Yadienka Martinez-Rubi and Mostafa Yourdkhani
- 109 **Machine vision system for digital twin modeling of composite structures**  
Oliver Döbrich and Christian Brauner
- 119 **Numerical simulation of inductive heating in thermoplastic unidirectional cross-ply laminates**  
A. J. de Wit, N. van Hoorn, L. S. Straathof and W. J. Vankan

- 136 **Unified numerical process modeling of forming and consolidation for thermoplastic composites with prepreg patches**  
P. D. Mulye, L. Morañay, C. Binetruy, S. Comas-Cardona, A. Leygue and D. Guillon
- 158 **Development of flax/basalt/PA11 bio-composites: optimal formulation and modelling of the quasi-static behaviour**  
Wassim Guerfala, Patrick Rozycki and Christophe Binetruy
- 172 **Designing of carbon fiber-reinforced polymer (CFRP) composites for a second-life in the aeronautic industry: strategies towards a more sustainable future**  
Carolina Borges, A. Chicharo, A. Araújo, J. Silva and R. M. Santos
- 186 **Evaluation of draping simulations by means of 3D laser scans and robot supported fiber angle scans**  
Joachim Osterberger, Franz Maier, Sophia Keller and Roland Markus Hinterhölzl





## OPEN ACCESS

## EDITED AND REVIEWED BY

Robert Li,  
City University of Hong Kong, Hong Kong  
SAR, China

## \*CORRESPONDENCE

Véronique Michaud,  
✉ veronique.michaud@epfl.ch

RECEIVED 18 September 2023

ACCEPTED 19 September 2023

PUBLISHED 27 September 2023

## CITATION

Binetruy C, Caglar B, Daelemans L,  
Dransfeld C and Michaud V (2023),  
Editorial: ECCM Research Topic on  
advanced manufacturing of composites.  
*Front. Mater.* 10:1296247.  
doi: 10.3389/fmats.2023.1296247

## COPYRIGHT

© 2023 Binetruy, Caglar, Daelemans,  
Dransfeld and Michaud. This is an open-  
access article distributed under the terms  
of the [Creative Commons Attribution  
License \(CC BY\)](#). The use, distribution or  
reproduction in other forums is  
permitted, provided the original author(s)  
and the copyright owner(s) are credited  
and that the original publication in this  
journal is cited, in accordance with  
accepted academic practice. No use,  
distribution or reproduction is permitted  
which does not comply with these terms.

# Editorial: ECCM Research Topic on advanced manufacturing of composites

Christophe Binetruy<sup>1</sup>, Baris Caglar<sup>2</sup>, Lode Daelemans<sup>3</sup>,  
Clemens Dransfeld<sup>2</sup> and Véronique Michaud<sup>4\*</sup>

<sup>1</sup>Nantes University, Centrale Nantes, GeM, UMR CNRS 6183, Nantes, France, <sup>2</sup>Aerospace Structures and Materials Department, Faculty of Aerospace Engineering, Delft University of Technology, Delft, Netherlands, <sup>3</sup>Department of Materials, Textiles and Chemical Engineering (MaTCh), Ghent University, Ghent, Belgium, <sup>4</sup>Laboratory for Processing of Advanced Composites (LPAC), Institute of Materials (IMX), Ecole Polytechnique Fédérale de Lausanne (EPFL), Lausanne, Switzerland

## KEYWORDS

composite manufacturing, sustainability, energy efficiency, automation, digital twin

## Editorial on the Research Topic

### ECCM Research Topic on advanced manufacturing of composites

The 20th European Conference on Composite Materials (ECCM20) took place in Lausanne, Switzerland, June 26-30, 2022, organized by the Composite Construction Laboratory (CCLab) and the Laboratory for Processing of Advanced Composites (LPAC) of the Ecole Polytechnique Fédérale de Lausanne (EPFL). The Conference theme was “Composites meet Sustainability”. As a result, even if all fields of research related to composite processing, properties and applications were covered, sustainability aspects were highlighted with specific lectures, roundtables, and sessions on a range of topics, from bio-based composites to energy efficiency in materials production and use phases, as well as end-of-life scenarios and recycling.

Following the conference, we invited participants who focused on the field of advanced manufacturing methods and automation for composite materials, with a particular emphasis on sustainability aspects, to contribute a full paper to form a Research Topic, in the Polymer Composite section of *Frontiers in Materials*.

The resulting collection of articles in *Frontiers in Materials* highlights the diversity in approaches and methods used to address this Research Topic through composites manufacturing. We identified three main pathways of sustainable development: i) research related to the adaptation of more sustainable material classes, ii) research towards the improved modelling of manufacturing processes limiting materials waste, iii) research towards novel manufacturing and tooling methods reducing energy demand.

A first strategy explored the use of recycled or natural materials. [Borges et al.](#) approached the Research Topic by exploring second life of carbon fiber reinforced polymer (CFRP) scraps into PEEK carbon composites, using a twin-screw extruder. They found that this type of composite can lead to parts of industrial relevance, if the CF is sufficiently long, even at low fiber content. [Guerfala et al.](#) produced hybrid composites combining long flax and basalt fibers with a biosourced PA11 matrix, for semi-structural automotive applications, highlighting the potential of hybridization to enhance the composite properties with respect to pure flax fiber composites, while keeping all constituents naturally sourced. [Bodaghi et al.](#) also evaluated long flax fiber composites, with PP matrices, and proposed to

analyze their thermal conductivity as a method to evaluate the consolidation quality of the obtained parts. Biswas et al. evaluated the use of nanofillers to further enhance the mechanical properties of carbon fiber laminates, in addition to their physical properties such as electrical conductivity. Although these fillers may affect the manufacturing route, they can help in the quest to limit material resources.

A second strategy relied on improving the modelling methods to limit waste or poor-quality parts or improving part production. As an example, Mulye et al. developed a unified modelling approach to simulate the forming and consolidation of thermoplastic composites made from prepreg patches (Quilted Stratum Process). Through-thickness stress, final deformed shape of the plies including the squeeze flow effect and the changes in the orientation of fibers within the plies during and after the process were thus predicted. Manufacturers can thus design better tooling based on the outcomes of the numerical process simulation to achieve the desired product quality and final fiber orientation which results from the initial position of the patch, its forming and squeeze flow. Jan de Wit et al. proposed a numerical simulation of inductive heating for UD thermoplastic composites, combining electromagnetic and thermal effects. This led to improved design of UD laminates for easier induction welding during the assembly phase. Döbrich and Brauner developed a digital twin model, using a machine vision system based on a simple Microsoft Kinect camera to evaluate local fiber orientations after preform draping. This data can be compared to numerical simulations, enabling detection of deviations or unwanted defects. Similarly, Osterberger et al. evaluated experimental visual methods to analyze fiber orientations after part draping, as well as wrinkles or other potential defects, for comparison with numerical predictions. Results were more satisfactory for UD laminates than for cross-ply laminates which are more difficult to visually analyze. Jimenez Martin et al. analyzed wrinkling patterns in large draped NCF fabrics using 3D scans, highlighting the complexity of scaling-up the processes to large scale. Maidl et al. also made use of optical inspection to detect defects during the braiding of preforms. A single camera can track yarn curvature and angular spacing in real time using image analysis, to propose corrective actions as soon as these parameters deviate, thus enabling reduced scrap rates and improved preform reproducibility.

A third strategy investigated novel manufacturing and tooling concepts to lower energy demand and improve part processing kinetics and quality. Naseri et al. proposed an elegant way to produce nanocomposite film heaters for out-of-oven energy-efficient curing of thermoset composites. With these heating films, a composite based on a commercial prepreg was cured using 400 times less energy than in a conventional convection oven. Maes et al. introduced zonal heating of molds, to tailor the temperature profile to adapt it to part thickness variations. They showed that this approach can save up to 45% in energy

consumption as compared to convection heating. Finally, Zhilyaev et al. proposed to further improve the additive manufacturing of continuous fiber reinforced thermoplastics through a post-consolidation process to lower voids. An advanced finite element model allowed to evaluate potential process-induced deformations and simulate porosity reduction; this model was validated against experimental data from the manufacturing of an aerospace part.

In summary, the need to develop sustainable solutions in composites is driving innovation in many areas. Contributions focus on the bio-sourcing of materials, the reduction of waste and energy consumption in production, the optimal design of parts and production tools, and better control of manufacturing processes to reduce defects and production waste. The use of digital process twins and advanced monitoring techniques contributes to this overall objective. Undoubtedly, the sustainability of composites solutions will remain the focus of future research.

## Author contributions

CB: Writing–review and editing. BC: Writing–review and editing. LD: Writing–review and editing. CD: Writing–review and editing. VM: Writing–original draft, Writing–review and editing.

## Acknowledgments

We would like to thank all the contributors of this Research Topic, as well as the reviewers, for their valuable contributions to the ECCM 20 legacy.

## Conflict of interest

The authors declare that the research was conducted in the absence of any commercial or financial relationships that could be construed as a potential conflict of interest.

The author(s) declared that they were an editorial board member of Frontiers, at the time of submission. This had no impact on the peer review process and the final decision.

## Publisher's note

All claims expressed in this article are solely those of the authors and do not necessarily represent those of their affiliated organizations, or those of the publisher, the editors and the reviewers. Any product that may be evaluated in this article, or claim that may be made by its manufacturer, is not guaranteed or endorsed by the publisher.



## OPEN ACCESS

## EDITED BY

Lode Daelemans,  
Ghent University, Belgium

## REVIEWED BY

Zoltan Major,  
Johannes Kepler University of Linz,  
Austria  
Narinder Singh,  
University of Naples Parthenope, Italy

## \*CORRESPONDENCE

Igor Zhilyaev,  
zhilyaev@fhnw.ch

## SPECIALTY SECTION

This article was submitted to Polymeric  
and Composite Materials,  
a section of the journal  
Frontiers in Materials

RECEIVED 12 October 2022

ACCEPTED 23 November 2022

PUBLISHED 12 December 2022

## CITATION

Zhilyaev I, Grieder S, Küng M, Brauner C,  
Akermann M, Bosshard J, Inderkum P,  
Francisco J and Eichenhofer M (2022),  
Experimental and numerical analysis of  
the consolidation process for additive  
manufactured continuous carbon fiber-  
reinforced polyamide 12 composites.  
*Front. Mater.* 9:1068261.  
doi: 10.3389/fmats.2022.1068261

## COPYRIGHT

© 2022 Zhilyaev, Grieder, Küng,  
Brauner, Akermann, Bosshard,  
Inderkum, Francisco and Eichenhofer.  
This is an open-access article  
distributed under the terms of the  
[Creative Commons Attribution License](#)  
(CC BY). The use, distribution or  
reproduction in other forums is  
permitted, provided the original  
author(s) and the copyright owner(s) are  
credited and that the original  
publication in this journal is cited, in  
accordance with accepted academic  
practice. No use, distribution or  
reproduction is permitted which does  
not comply with these terms.

# Experimental and numerical analysis of the consolidation process for additive manufactured continuous carbon fiber-reinforced polyamide 12 composites

Igor Zhilyaev<sup>1\*</sup>, Stefan Grieder<sup>1</sup>, Marco Küng<sup>1</sup>,  
Christian Brauner<sup>1</sup>, Michael Akermann<sup>2</sup>, Jonas Bosshard<sup>2</sup>,  
Petra Inderkum<sup>2</sup>, João Francisco<sup>2</sup> and Martin Eichenhofer<sup>2</sup>

<sup>1</sup>Lightweight Design and Composite Technologies Group, Institute of Polymer Engineering, FHNW University of Applied Sciences and Arts Northwestern Switzerland, Windisch, Switzerland, <sup>2</sup>9T Labs, Zurich, Switzerland

Substitution of conventional metal structures with fiber-reinforced polymers is possible because of their sustainable performance. One of the primary disadvantages of these composite materials is their high cost due to labor-intensive manufacturing. Because the fiber path can be steered directly along the load path, structures can be manufactured in a near-net shape, and a high degree of reproducibility with low scrap rates can be achieved. Additive manufacturing of these composite structures could enable cost efficiency with a high degree of complexity. However, the high degree of porosity and high void content between the printed fiber filaments results in unacceptable structural performance. Following the printing process, a post-consolidation process (additive fusion) can be performed to improve the mechanical performance of the part and use fiber-reinforced polymers for load-bearing applications. Numerical simulation of the consolidation process enables the production of these complex parts without expensive prototyping iterations. Because of the rapid and local changes in material stiffness, the simulation of the consolidation process is combined with a set of numerical model convergence problems. An advanced finite-element numerical model for simulating the consolidation process of additive manufactured continuous fiber composite parts is presented in this paper. The additive fusion step simulation allows for the evaluation of process-induced deformations, final engineering constants, and porosity. The simulation workflow is demonstrated and validated using experimental data from the manufacturing process of a typical aerospace part, specifically a helicopter hinge element.



## KEYWORDS

additive manufacturing, fiber-reinforced composites, additive fusion, consolidation, process-induced deformations, porosity evaluation, consolidation simulation

## 1 Introduction

The enhanced properties of continuous carbon fiber-reinforced polymers, such as high stiffness, high strength, and a good stiffness-to-weight ratio, can be used in additive manufactured composite structures (Gebhardt et al., 2019). Various surveys and scientific publications on the performance of these highly optimized structures can be found based on the available printing technology from companies such as Markforged, Anisoprint, 2021, Arevo, 2021, and 9 T Labs to manufacture thermoplastic composite parts (Gregory and Gonzdz 2016; Blok et al., 2018; Goh et al., 2018; Iragi et al., 2019; Borowski et al., 2021).

These companies use a modified version of the FFF method, which combines polymer and pre-impregnated carbon fiber printing. Because of its low cost and ease of use, the FFF method is one of the most widely used processes in additive manufacturing. Pre-impregnated fiber-reinforced materials are used in continuous fiber additive manufacturing, similarly to conventional composite manufacturing methods such as automated fiber placement, automated tape laying, or custom fiber placement. The disadvantage of any additive manufacturing method is that, as the print speed increases, the level of porosity increases, and the requirements for a load-bearing part are no longer fulfilled. Therefore, a consolidation step was required. To address this problem, various approaches such as heat treatment during printing (Bhandari et al., 2019) and annealing or compaction during post-processing can be used (Meng et al., 2019; Zhang et al., 2020). Compaction is the subject of two developments. Using additional rollers to integrate a compaction unit into the printing process. This is the state-of-the-art automated tape-laying method. However, the part can be consolidated using a press and solid mold. The second approach also allows for the addition of more complexity to the part. Eguemann et al. (2013) combined several 3D printed preforms and metallic inserts into a single part using consolidation. The Airbus Helicopters former Eurocopter Germany GmbH application case is a machined steel hinge from rotorcraft model EC 135, weighing 135 g and mounted on a carbon fiber-reinforced polymer door structure. Eguemann et al. (2013) demonstrated the load case, and various composite-related manufacturing processes, such as injection molding, compression molding, and hand lamination, were evaluated and compared to the steel baseline.

This study demonstrates a novel method for simulating the additive fusion (consolidation) process of a complex-shaped composite part to investigate the dependence of the final mechanical properties and residual stresses on the process conditions. The method is presented by the authors as a

sequential thermo-mechanical coupled, transient implicit analysis in ANSYS R2022 based on user material subroutines (Grieder et al., 2022). The phase transition behavior of the polymer from solid to molten and back to solid was modeled. Temperature, fiber volume content, porosity, and crystallization all influence the engineering properties of composite materials. The validation of the model for process-induced deformations and porosity in an aerospace part, namely, the helicopter hinge and a bracket to assemble the helicopter door, is the focus of this study. Figure 1 depicts the composite parts under consideration and the manufacturing workflow.

## 2 State-of-the-art simulation methods for the consolidation process

Wijskamp (2005) presented a sequentially coupled thermo-mechanical transient simulation approach that couples relative crystallization with phase transitions from the molten to the solid phase. It is possible to accurately calculate process-induced deformations by making the stiffness during a mechanical simulation dependent on the phase change by using relative crystallization as a status variable. Wijskamp (2005) assumed that when a material's relative crystallization exceeds 50%, it starts to behave as a solid. This transition point is known as the solidification point, and it is critical for calculating process-induced deformations because after a material passes this point, thermal loads caused by the cooling process can cause deformations.

This approach has also been used in the literature by researchers such as Wijskamp (2005) and Brauner et al. (2014) to analyze process-induced deformation during the thermoforming process of composites. The Nakamura model is used in both models (Nakamura et al., 1972; Nakamura et al., 1973). The cooling phase crystallization kinetics are demonstrated by

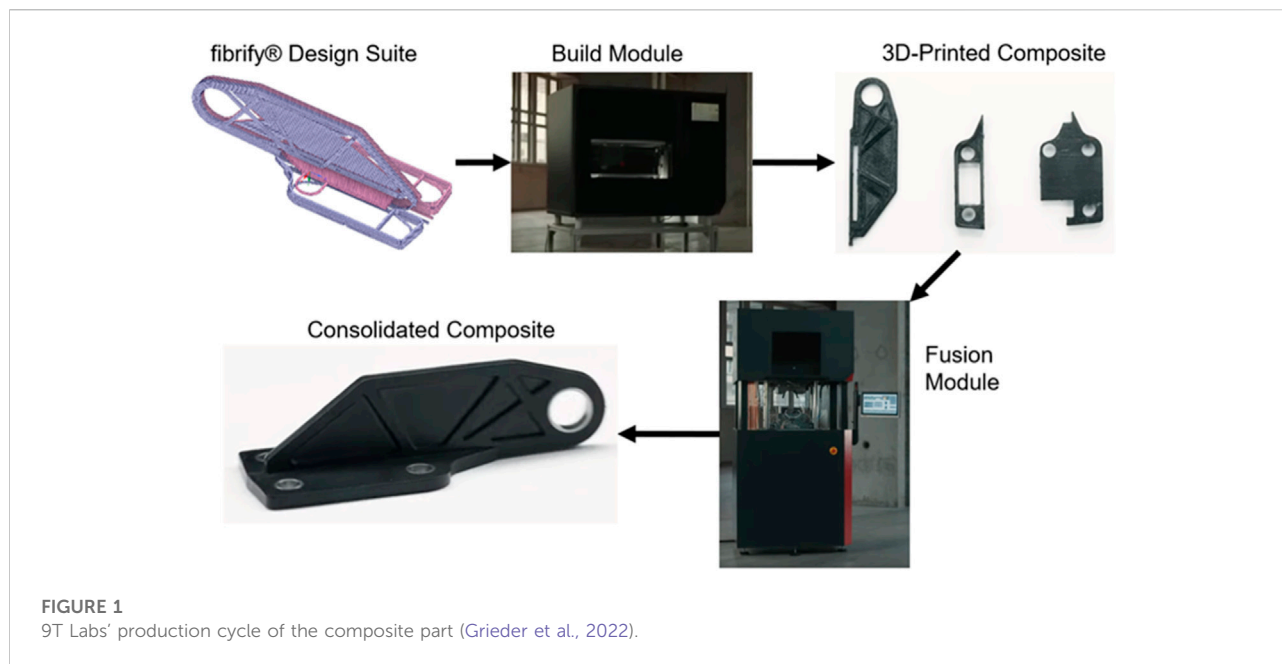
$$\frac{\partial \theta}{\partial t} = n \cdot K(T) \cdot (1 - \theta) [-\ln(1 - \theta)]^{\frac{n-1}{n}} \quad (1)$$

where  $T$ ,  $\theta$ , and  $K(T)$  represent the temperature, degree of crystallization, and Avrami coefficient, respectively.

$$K(T) = \left( \frac{\ln(2)}{t_{1/2}^n} \right)^{\frac{1}{n}} \quad (2)$$

where  $t_{1/2}$  represents the half-crystallization time:

$$t_{1/2} = a \cdot \left( \frac{\partial T}{\partial t} \right)^b + c \quad (3)$$



Based on the experimental data, the parameters  $n, a, b, c$  were defined by fitting the crystallization vs temperature dependencies for various cooling rates.

Similarly, melting behavior can be represented by a phase change from 1 (solid state) to 0 (molten state) according to Wijsskamp (2005), Greco and Maffezzoli (2003), Brenken et al. (2018).

$$\frac{\partial \theta}{\partial T} = k_{mb} \cdot e^{-k_{mb}(T-T_m)} \left[ 1 + (d-1)e^{-k_{mb}(T-T_m)} \right]^{\frac{d}{1-d}} \quad (4)$$

The values of the coefficients  $n, a, b, c$  from Eqs 1–3 and  $k_{mb}$  and  $d$  from Eq. 4 for this study are presented in the following section.

Using the relative crystallization and the definition of the solidification point, the Young's modulus of the polymer was discovered to be temperature dependent during the process. This approach is considered the standard for thermoset-related processes that use the degree of cure. The resin modulus can be linear or nonlinear in its dependence (Wijsskamp 2005; Brauner et al., 2011). The polymer modulus can also be used to determine the engineering properties of a unidirectional composite ply. Schürmann (2007) and Halpin and Kardos (1976) provided different homogenization approaches for composite materials, and Brauner (2013) provided an overview. The process-induced deformation and residual stress can be determined using this incremental elastic approach (Zobeiry 2006). These methods are capable of accurately simulating process-induced deformation stresses. However, residual stresses could be overestimated because stress relaxation was not considered. However, the effect of relaxation is irrelevant for thermoplastic composites that are

additively manufactured because Young's modulus is very low compared to that of a thermoset resin.

The transition between the solid and molten material states used in this study is nonstepwise and nonlinear, which improves numerical robustness. This transition was calculated in Grieder et al. (2022) using dynamic mechanical analysis (DMA) and rheometer measurements. This is illustrated in Supplementary Figure S1.

The transverse isotropic mechanical properties were evaluated in this study using the homogenization approach from Halpin-Tsai (Halpin and Kardos 1976; Schürmann 2007). The elastic modulus in the fiber direction  $E_1$  is defined as follows (Halpin and Kardos 1976):

$$E_1 = E_{f,1}\varphi + E_m(1 - \varphi) \quad (5)$$

The elastic moduli in the transverse and thickness directions are defined as (Schürmann 2007)

$$E_2 = E_3 = E_m \frac{1 + \zeta_1 \cdot \varphi (E_{f,2} - E_m) / (E_{f,2} + \zeta_1 \cdot E_m)}{1 - (E_{f,2} - E_m) / (E_{f,2} + \zeta_1 \cdot E_m) \varphi} \quad (6)$$

In this case,  $\zeta_1 = 3.3$  represents the model parameter fit to the experimental data for carbon fiber-reinforced polyamide 12 (PA12-CF) to provide a modulus value close to the measurement results in comparison to the present study (Grieder et al., 2022).

$$\nu_{12} = \nu_{13} = \nu_{23} = \nu_f \varphi + \nu_m(1 - \varphi) \quad (7)$$

Poisson's ratio is defined as (Grieder et al., 2022).

Shear moduli are defined as follows (Halpin and Kardos 1976; Schürmann 2007):

$$G_m = \frac{E_m}{2(1 + \nu_m)} \quad (8)$$

$$G_{12} = G_{13} = G_m \frac{1 + \zeta_2 \cdot \varphi \cdot \frac{G_{f,12} - G_m}{G_{f,12} + \zeta_2 G_m}}{1 - \varphi \cdot \frac{G_{f,12} - G_m}{G_{f,12} + \zeta_2 G_m}} \quad (9)$$

$$G_{23} = \frac{E_2}{2(1 + \nu_{23})} \quad (10)$$

In this case,  $\zeta_2 = 1.675$  represents the model parameter fitted to the experimental data for PA12-CF to obtain a modulus value that is close to the measurement results (Grieder et al., 2022).

In the solid state, the mixing rules (5–10) are applied to the PA12-CF filament, whereas in the molten state, the material is considered isotropic, with material properties corresponding to pure polyamide 12 (PA12).

The mixing rules for orthotropic coefficients of thermal expansion (CTE) and crystallization shrinkage could be introduced to the model. The coefficients of thermal expansion in the transverse and longitudinal directions are calculated using the following equations (Schürmann 2007):

$$\alpha_1 = S_1 \frac{\alpha_m \cdot E_m \cdot (1 - \varphi) + \alpha_{f,1} \cdot E_{f,1} \cdot \varphi}{E_m \cdot (1 - \varphi) + E_{f,1} \cdot \varphi} \quad (11)$$

$$\alpha_2 = S_2 (\varphi \cdot \alpha_{f,2} + (1 - \varphi) \cdot \alpha_m) \quad (12)$$

$$\alpha_3 = S_3 \alpha_2 \quad (13)$$

Here,  $\alpha_m$ ,  $\alpha_{f,1}$  and  $\alpha_{f,2}$  represent the longitudinal and transverse coefficients of thermal expansion for the matrix and the fiber, respectively. To account for possible changes in the CTE after reaching the glass transition temperature, the correction coefficients  $S_{1,2,3}$  are introduced into the model. The coefficient values used in this study are presented in the following section.

Shrinkage is a crucial consolidation process-induced effect that has a significant impact on the final warpage of a part. The shrinkage of the PA12 composite was shown to be temperature and printed lay-up dependent (Negi and Rajesh 2016; Li et al., 2020). The shrinkage of composite materials is defined *via* the following mixing rules (Wijskamp 2005; Schürmann 2007):

$$\beta_1 = (1 - \varphi) \cdot E_m \cdot \beta / (\varphi \cdot E_{f,1} + (1 - \varphi) E_m) \quad (14)$$

$$\begin{aligned} \beta_2 &= \beta_3 \\ &= (1 - \varphi) \cdot (1 + \nu_m) \cdot \beta - (\nu_{13} \cdot \varphi + \nu_m \cdot (1 - \varphi)) \\ &\quad \times \left( \frac{\beta \cdot (1 - \varphi) \cdot E_m}{\varphi \cdot E_{f,1} + (1 - \varphi) \cdot E_m} \right) \end{aligned} \quad (15)$$

where  $\beta$  represents the total volumetric shrinkage of PA12. Because the value of volumetric shrinkage was not measured within the scope of the present study, it was based on the average value of 3% (Benedetti et al., 2019; Li et al., 2020).

For the investigated additive-manufactured composite materials, porosity exhibits the greatest impact. Blok et al.

investigated porosity during FFF manufacturing for SFR and CFR (Blok et al., 2018). The void content exhibits a significant negative impact on the composite properties. A high void ratio reduces strength, durability, and fatigue resistance, increases moisture absorption, and causes composite properties to vary within one part (Cable 1991; Ghiorse 1993; Mahoor et al., 2018). Therefore, void content should be minimized in bear-loading applications.

Zingraff et al. (2005) and Zingraff (2004) addressed void-process-induced formation in the composite processing literature. Voids may form in autoclave processing when the resin shrinks during thermoplastic crystallization (Eom et al., 2001). Grieder et al. (2022) demonstrated that the level of porosity of additively manufactured composites can reach 20–30% for simple geometry. Letierrier and G'sell, (1994) demonstrated that free heating of the composite specimen could result in an increase of up to 60% in the initial void content. This indicates the need for a consolidation step, which must be incorporated into the process simulation method.

During solidification, specific pressure and temperature regimes can be used to avoid void formation (Long et al., 1995; Lundstrom and Gebart (1994). Eom et al. (2001) proposed process conditions that yield void-free composites while requiring a minimum amount of pressure (0.2 MPa). Specially designed molds can minimize void formation and process-induced deformation (Eguemann et al., 2013). In this study, a similar approach was developed and implemented in which an advanced mold design was provided to minimize part porosity and warpage.

Experimental and numerical studies on void formation mechanisms in mesostructures and the influence of pores on the mechanical properties of 3D-printed composites have been presented in the literature (Bellehumeur et al., 2004; Wang et al., 2016). Multiscale finite element modeling methods for studying the influence of micro- and mesoporosity and process parameters on the mechanical properties of composites are illustrated in Calneryte et al. (2018), Rodriguez et al. (2000), and Xue et al. (2019). The power law empirical relationship can express stiffness-porosity dependence (Jaroslav 1999).

$$E = E_0 \cdot \left( 1 - \frac{\phi}{\phi_c} \right)^s \quad (16)$$

Here,  $E$  represents the effective Young's modulus of the porous medium,  $\phi$  represents the porosity,  $E_0$  represents Young's modulus of the fully consolidated solid material, and  $\phi_c$  represents the porosity at which the effective Young's modulus becomes zero. The model parameter  $S$  is determined *via* the porous material structure, pore geometry, and other structural properties. For each material and structure, the value of parameter  $S$  must be defined (Wagh et al., 1991; Jaroslav 1999; Grieder et al., 2022).



The power-law porosity dependence (18) was successfully implemented in the finite element model for non-polymer materials with a relatively low initial porosity (Hardin and Beckermann 2007; Morrissey and Nakhla 2018). However, this definition necessitates experimental measurements to tune the stiffness of the porosity function. Moreover, most of the presented approaches only allow for robust numerical simulation for a small range of void content change, failing in the case of rapid porosity evolution from 20 to 30% to almost zero void content.

In this study, a similar approach is presented in which the stiffness is determined using the local porosity content *via* a power law. Temperature, crystallization degree, and porosity all affect the matrix elastic modulus  $E_m$ . Therefore, the following empirical dependence was developed (Grieder et al., 2022):

$$E_m = E_{m,s} \cdot (\theta)^K \cdot (1 - \phi)^S + E_{m,b} \cdot (1 - \theta)^K \cdot (1 - \phi)^M \quad (17)$$

Here,  $E_{m,b}$  represents the molten polymer bulk modulus measured with a pressure evaluation study (Grieder et al., 2022), and  $E_{m,s}(T)$  represents the temperature-dependent elastic modulus in the solid phase measured with DMA (Grieder et al., 2022);  $K$ ,  $S$ , and  $M$  represent model design parameters that must be fitted to the experimental data depending on the material and composite layout. The values of these parameters relevant to this study are presented in Supplementary Table S1;  $\phi$  represents the void content, which considers the influence of mechanical deformations and air diffusion into the PA12 matrix on porosity.

Composite material properties are defined according to the mixing rules (5)–(15), which determine the proportion of pure fiber to pure matrix properties based on the fiber volume ratio  $\varphi$ : CTE (11)–(13), crystallization shrinkage (14)–(15), and stiffness (17). The relationship between the fiber volume ratio and porosity is not well covered in the literature. However, assuming that the fiber volume ratio is proportional to the void content, Grieder et al. (2022) proposed the simplest linear dependence on porosity:

$$\varphi = \varphi_0 (1 - \phi) \quad (18)$$

where  $\varphi_0$  represents the measured fiber volume ratio corresponding to a fully consolidated material with no void content.

Many phenomena occur concurrently during consolidation, including bulk compaction, intimate contact between adjacent plies, interlaminar adhesion, fiber deformation, movement, and molecular diffusion (Koerdt et al., 2022). These phenomena interact in complex ways and are influenced by process parameters such as time, temperature, and pressure. The resin pressure must be evaluated to model void formation. This can be accomplished by simplifications or Darcy's law when modeling a flow problem. Grieder et al. (2022) developed a simplified porosity model based on the approach of Barari et al. (2020).

In the model, porosity  $\phi$  is represented as a dimensionless variable with a value between 0 and 1, where 0 indicates that the material is fully consolidated and one indicates that the volume of the entire considered finite element is empty. The initial porosity value is determined using the material and printing configuration.

According to Barari et al. (2020), the hydrostatic pressure,  $p_h$  is calculated as follows:

$$p_h = \begin{cases} P_0 \cdot \frac{\phi_0}{\phi} \frac{T}{T_0} (1 - V_d), & \phi > \phi_{min} \\ 0, & \phi \leq \phi_{min} \end{cases} \quad (19)$$

where  $P_0$  represents the initial (atmospheric) pressure,  $T_0$  represents the initial (room) temperature,  $\phi_0$  represents the initial porosity,  $\phi_{min} = 0.001$  represents the minimum considered porosity, and  $V_d$  represents the relative volume of dissolved air.

The volume of dissolved air is a dimensionless variable with values in the range of 0–1, with 0 indicating that the air occupies 100% of its initial volume and one indicating that the air is completely dissolved in the surrounding matrix. Because it is assumed that air traps have spherical shapes, the volume can be defined as

$$V_d = 1 - R_b^3 \quad (20)$$

$R_b$  represents a dimensionless variable that represents the air bubble radius and exhibits values in the range of 0–1, with 0 indicating that the air bubble is completely dissolved in the resin and one indicating that the bubble radius has returned to 100% of its initial value. Therefore,  $R_0 = 1$ . Eq. 20 is a semi-analytical approach based on dimensionless dissolved volume and bubble radius definitions (Grieder et al., 2022).

The fundamental mechanisms of air bubble formation and reduction in thermoplastic composites remain unknown. Early models incorporated diffusion into the isothermal growth of spherical gas bubbles in a viscous fluid (Moris and Costel 1984). Further studies expanded the model to include many bubbles in highly viscous fluids (Arefmanesh et al., 1990; Arefmanesh 1991). These models were then applied to thermoplastic composites for structural applications (Roychowdhury 1995; Roychowdhury et al., 2001; Johann et al., 2008; Jin et al., 2020).

Gas diffusion into molten polymer was considered in the literature (Wood and Bader 1994; Zingraff 2004; Zingraff et al., 2005), where the diffusion coefficient for the polymer material was measured. However, the dimensionless diffusion coefficient in the present approach represents not only the diffusion and dissolution processes but also the air evacuation through the void channels along the filament's printing path. Therefore, the diffusion coefficient  $D$  is a model design parameter that cannot be directly measured but must be adjusted for each new material, composite structure, and printing condition (Grieder et al., 2022).

TABLE 1 Material properties at room temperature (Grieder et al., 2022).

Material	Property	Identifier and value	Unit
PA12	Young's modulus	$E_m = 1,372$	MPa
PA12	Poisson's ratio	$\nu_m = 0.43$	-
PA12	Glass transition temperature	$T_g = 94$	°C
PA12	Melting temperature	$T_m = 179$	°C
PA12	Crystallization shrinkage	$\beta = 3.0$	%
Fiber	Young's modulus in the fiber direction	$E_{f,1} = 231,000$	MPa
Fiber	Young's modulus transverse to the fiber direction	$E_{f,2} = 28,000$	MPa
Fiber	Shear modulus	$G_{f,12} = 28,600$	MPa
Fiber	Poisson's ratio	$\nu_f = 0.23$	-
PA12-CF	Young's modulus in the fiber direction	$E_1 = 132,632$	MPa
PA12-CF	Young's modulus transverse to the fiber direction	$E_2 = 6,568$	MPa
PA12-CF	Shear modulus	$G_{12} = 2035$	MPa
PA12-CF	Poisson's ratio	$\nu_{12} = 0.298$	-
PA12-CF	Fiber volume content (fully consolidated)	$\phi_0 = 0.573$	-

In Grieder et al. (2022), it was assumed that every finite element contains an air bubble that evolves independently of the surrounding medium and other bubbles. The relative bubble radius was calculated as follows (Wood and Bader 1994; Advani and Sozer 2010):

$$R_b = (R_0 - D \cdot (p_h - p_{h,0}) \cdot t)^{0.5} \quad (21)$$

where  $D$  represents a dimensionless diffusion model parameter and  $p_{h,0}$  represents the hydrostatic pressures when melting occurs.

A general description of hydrodynamics is required for polymer melts (Joel et al., 1997). This description considers viscoelasticity, die swelling, and shear thinning. These properties necessitate nontrivial modifications to the hydrodynamic formulation of the fluid, resulting in advanced constitutive equations that significantly increase the complexity of the problem and computational effort. Because of the limitations of the finite-element software ANSYS and the aforementioned issue, this study considers a simplified model of the squeeze flow.

The simplified orthotropic squeeze pressure  $p_{sq}$  was only considered in the liquid state and was evaluated using the method demonstrated by Barari et al. (2020):

$$p_{sq,i} = \begin{cases} \frac{\eta(T)}{12 \cdot K_i} \cdot \Lambda_i^2 \cdot \frac{\partial \varepsilon_{m,i}}{\partial t}, & \phi > \phi_{min}, \quad i = \{2, 3\} \\ 0, & \phi \leq \phi_{min} \text{ or } i = 1 \end{cases} \quad (22)$$

where  $\eta(T)$  represents the viscosity of the molten matrix and  $\Lambda_i$  represents the directional distance to the nearest void (defined by the printing setup). The voids are represented as channels in the printing direction due to the composite

manufacturing method. Therefore, the distance in the printing direction  $\Lambda_1$  to the closest void is assumed to be zero, implying that there is no squeeze flow in the printing direction.  $\varepsilon_{m1}, \varepsilon_{m2}, \varepsilon_{m3}$  are the strains of the matrix material inside the fiber filament are evaluated using Schürmann (2007):

$$\varepsilon_{m,i} = \frac{\varepsilon_i}{l_m/l_0 + E_m/E_{f,i} \cdot (1 - l_m/l_0)}, \quad i = \{1, 2, 3\} \quad (23)$$

where  $\varepsilon_1, \varepsilon_2, \varepsilon_3$  represent the longitudinal, transverse, and thickness strains, respectively;  $E_m$  represents the matrix elastic modulus;  $E_{f,i}, i = \{1, 2, 3\}$  are the longitudinal, transverse, and thickness elastic moduli of the fiber ( $E_{f,2} = E_{f,3}$ ), and  $l_m/l_0$  is defined as (Schürmann 2007)

$$l_m/l_0 = 1 - \left(\frac{4}{\pi} \phi\right)^{0.5} \quad (24)$$

where  $\phi$  represents the fiber volume ratio. The permeability in the transverse and thickness directions can be defined by simplifying the interlayer region into a rectangular duct as (Zingraff 2004; Advani and Sozer 2010)

$$K_2 = \frac{a^2}{12} \left[ 1 - \frac{192 \cdot a}{w \cdot \pi^5} \sum_{i=1,3,5,\dots}^9 \frac{\tanh\left(\frac{i \cdot \pi \cdot w}{2 \cdot a}\right)}{i^5} \right] \quad (25)$$

$$K_3 = \frac{w^2}{12} \left[ 1 - \frac{192 \cdot w}{a \cdot \pi^5} \sum_{i=1,3,5,\dots}^9 \frac{\tanh\left(\frac{i \cdot \pi \cdot a}{2 \cdot w}\right)}{i^5} \right] \quad (26)$$

where  $a$  and  $w$  represent the height and width of the rectangular duct, respectively, evaluated according to the following:

$$w = w_0 \cdot (1 + \varepsilon_2) \quad (27)$$

$$a = a_0 \cdot (1 + \varepsilon_3) \quad (28)$$

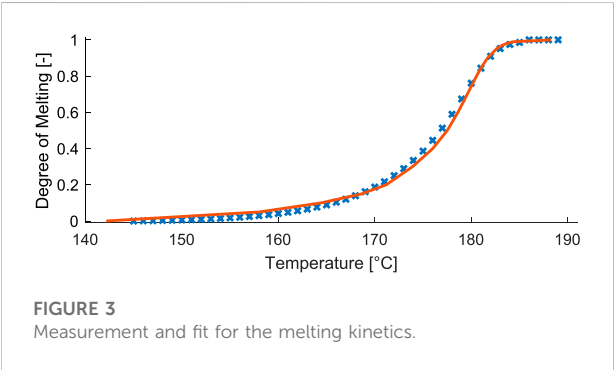
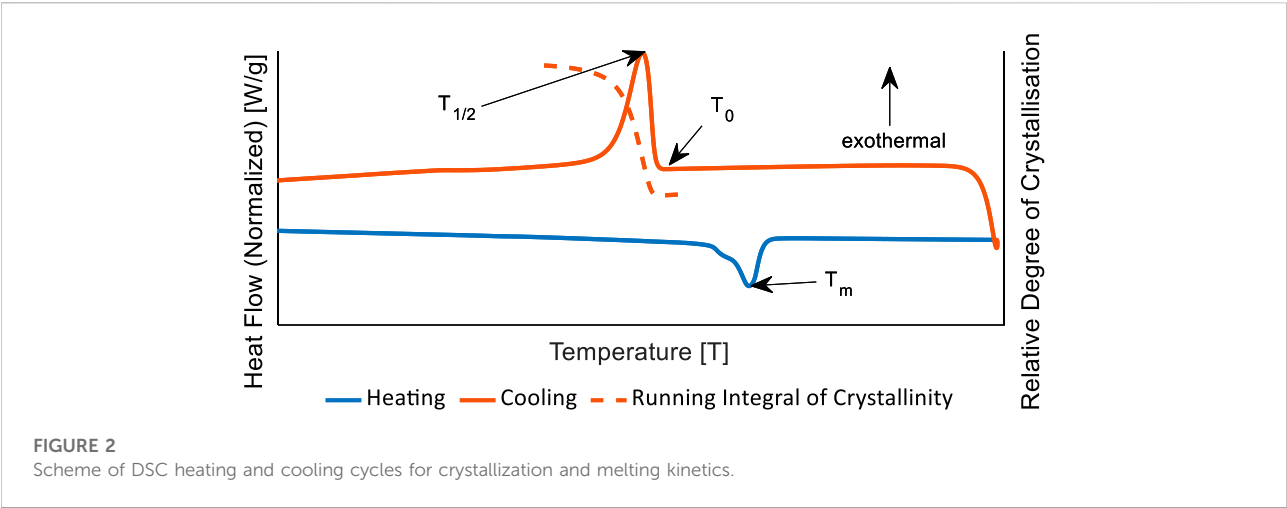


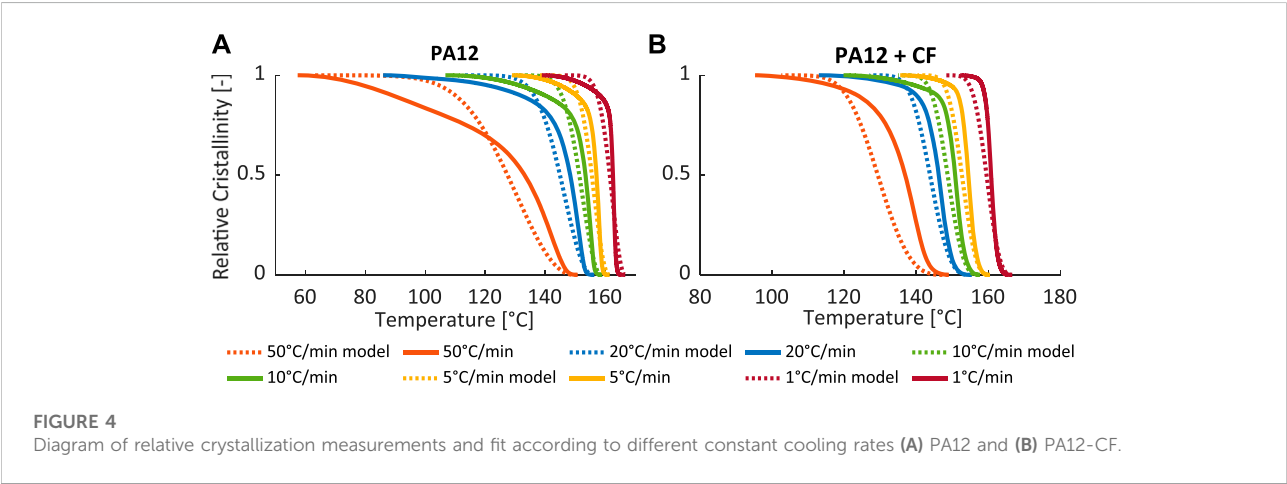
TABLE 3 Parameters for the crystallization kinetics equations.

Material	Identifier and value	Unit
PA12	$a = 3.63$	-
	$b = -1.31$	-
	$c = 0.37$	-
	$n = 2.00$	-
PA12-CF	$a = 5.50$	-
	$b = -1.02$	-
	$c = 0.18$	-
	$n = 2.85$	-

TABLE 2 Parameters for the melting kinetics equations.

Material	Identifier and value	Unit
PA12 &	$k_{mb} = 0.85$	-
PA12-CF	$d = 7.00$	-

where  $w_0$  and  $a_0$  represent the width and height of the printed filament, respectively. The values of these parameters relative to the current study are presented in [Grieder et al. \(2022\)](#).





As a function of the bulk strain  $\varepsilon_{bulk}$ , porosity was calculated as follows (Barari et al., 2020):

$$\phi = (\phi_0 + \varepsilon_{bulk}) \cdot (1 - D \cdot (p_h - p_{h,0}) \cdot t)^{0.5} \quad (29)$$

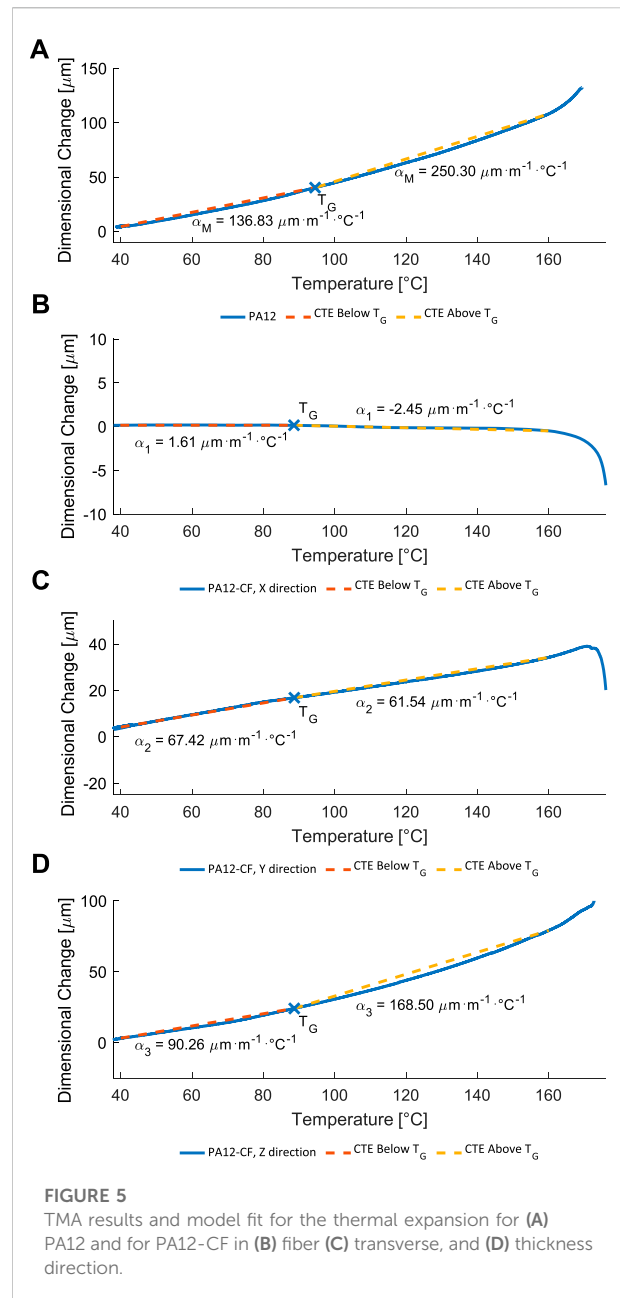
$$\varepsilon_{bulk} = (1 + \varepsilon_1) \cdot (1 + \varepsilon_2) \cdot (1 + \varepsilon_3) - 1 \quad (30)$$

where  $\phi_0$  represents the initial porosity,  $\varepsilon_{bulk}$  represents the bulk strain,  $p_h$  represents the hydrostatic void pressure, and  $p_{h,0}$  represents the hydrostatic pressure when melting occurs.  $D$  represents a dimensionless diffusion model parameter that considers air dissolution and air evacuation using open-air channels Grieder et al. (2022). The authors' developed porosity approach is based on (Wood and Bader 1994; Zingraff 2004; Barari et al., 2020) and is described in detail in Grieder et al. (2022). Depending on the internal void hydrostatic pressure, amount of diffused volume, and squeeze flow, void reduction is assumed to occur only in the molten and transitional material states.

The physics of rapid bubble collapse and its impact on the surrounding viscous medium have been discussed in terms of fluid mechanics for liquid media (Flynn 1975; Brujan and Vogel 2006). The bubble collapse process was studied for the solid or molten material state in Jin et al. (2020), where it was demonstrated that violent bubble collapse causes significant changes in material properties. When a porous material is subjected to large deformation, the failure threshold is predicted not directly by the total stress applied but by a certain difference between the total compressive stress and pore pressure. Skempton (1960) investigated the effective stress for volumetric deformation. The pore pressure should be considered in the constitutive equations (Skempton 1960; Barari et al., 2020), but a simple calculation of the pore stress using the ideal gas law results in rapid growth of the internal void pressure during fast void collapse (Grieder et al., 2022), which causes convergence problems when using the finite element method. For a more accurate description of bubble collapse in polymer melt, advanced viscoelastic models are required (Gaudron et al., 2015). Because of the simplicity of the proposed hydrodynamic model, the evaluated void pressure was not considered in the constitutive equations in the current study. However, the pressure indirectly influences the process-induced stresses *via* stiffness, which is a function of porosity (17) and changes owing to the compaction degree and air diffusion. The stiffness-porosity relationship is controlled by the model design parameters  $S$  and  $M$ . Therefore, the model can be tuned to compensate for the influence of internal void pressure on the surrounding resin medium (Grieder et al., 2022).

### 3 Materials, methods, and characterization

This section introduces the material and provides detailed characterizations. The following experimental characterizations were used: differential scanning calorimetry (DSC) was used to



determine the crystallization/melting behavior, and thermomechanical analysis (TMA) was used to measure the coefficient of thermal expansion. The computer was used to determine the final shape and the porosity content of the consolidated composite part.

#### 3.1 Material and sample preparation

Carbon fiber-reinforced material with a PA12 matrix, high tensile fibers with a fiber volume content of 57%, and a

PA12 material provided by 9 T Labs were used in this study. Table 1 summarizes the engineering properties of the composite, which were previously presented by the authors (Grieder et al., 2022).

The hinge subparts used in the study were printed separately (Figure 1) using the 9T Labs Build Module. The list of the printing parameters is presented in Supplementary Table S2. The composite design tool was used to determine the location and orientation of the reinforcing plies (Figure 1). The free space in the part volume where there are no fibers is filled with pure PA12. The build module has two nozzles: one for the unreinforced material, similar to the nozzle of another Fused Deposition Modeling (FDM), and a more complex nozzle for fibers, which has a patented cutting unit that allows for the printing of complex fiber paths.

Following printing, the hinge parts are assembled in the fusion module and consolidated. In this study, two different process conditions were used for model validation (samples A and B). An average temperature of 240°C was used as the baseline for the sample, resulting in an average heat rate of 8 °C/min. The temperature baseline for sample B was set at 184°C, resulting in a heating rate of 2 °C/min. Because the initial temperature of the mold pre-heating in both cases was 80°C. The part was actively cooled to 80°C and then demolded after approximately 4 min of consolidation at the maximum applied temperature and pressure.

A consolidation force of 30 kN was applied to both samples. After the final temperature was reached, the force was then increased to 45 kN. By applying pressure from the bottom, the hinge's base plate consolidated. The force was transferred to the sides of the vertical plate for consolidation using a sliding system. The consolidation force application and process conditions are presented in Supplementary Figure S2.

### 3.2 Characterization of the crystallization and melting behavior

Temperature-dependent changes in materials, such as melting or crystallization, can be detected using DSC. The endothermic heat flow in the case of melting and exothermic heat flow in the case of crystallization can be measured and interpreted using this method, with the assumption that the measured heat flow is proportional to the change in crystallization. The relative crystallization  $\theta_{rel}(t)$  is a conversion factor that ranges from 0 (no crystallization network) to 1 (maximum relative degree of crystallization). Melting or crystallization kinetics can be derived from DSC measurements to predict the formation and growth of the relative crystallization parameter as a function of time and temperature under various experimental conditions.

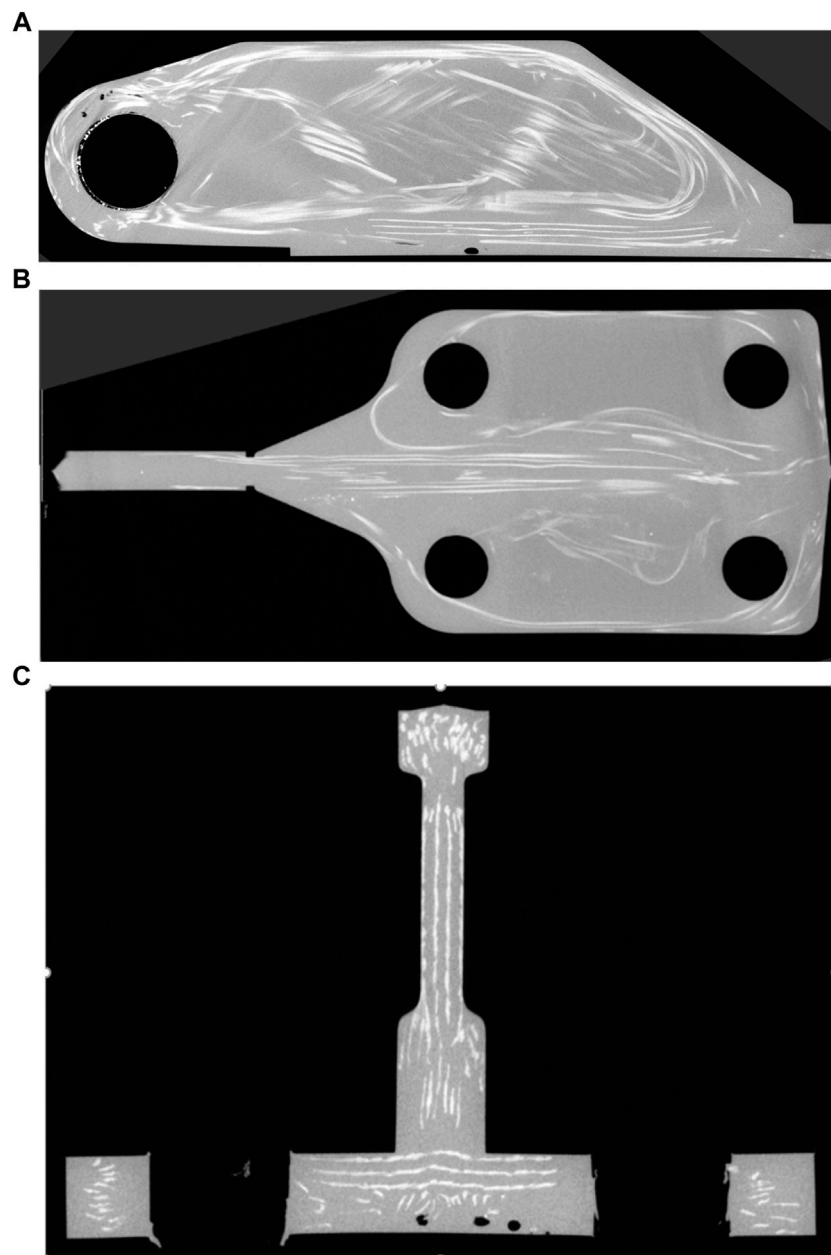
DSC experiments were performed using a DSC 25 instrument (TA Instruments, New Castle, DE

TABLE 4 Measured values of the CTE.

Material	Property, identifier, unit	Value	
		Below $T_g$	Above $T_g$
PA12	Coefficient of thermal expansion (CTE), $\alpha_m$ , $K^{-1}$	$136.83 \times 10^{-6}$	$250.3 \times 10^{-6}$
PA12-CF	CTE in the fiber direction, $\alpha_1$ , $K^{-1}$	$1.609 \times 10^{-6}$	$-2.45 \times 10^{-6}$
PA12-CF	CTE transverse to fiber direction, $\alpha_2$ , $K^{-1}$	$67.417 \times 10^{-6}$	$61.543 \times 10^{-6}$
PA12-CF	CTE in out of the plane direction, $\alpha_3$ , $K^{-1}$	$90.257 \times 10^{-6}$	$168.5 \times 10^{-6}$

TABLE 5 Process setup and results of the CT analysis.

Sample	A	B	U
Average peak consolidation temperature, °C	242	184	-
Initial (maximum) consolidation force, KN	30 (45)	30 (45)	-
Initial average (range) thickness of the base plate's assembly, mm	6.15 (6.11–6.18)	6.25 (6.09–6.40)	-
Initial average (range) thickness of the vertical plate's assembly, mm	6.23 (6.11–6.31)	6.11 (6.07–6.15)	-
Weight before (after) consolidation, g	26.6 (24.85)	26.55 (25.7)	-
Initial average porosity, %	-	-	3.5
Final average porosity, %	0.17	3.78	-



**FIGURE 6**  
Sample (A) CT material density analysis results (A) side view cross-section (B) plane view cross-section, and (C) front view cross-section.

United States). A small probe (approximately 13 mg) was extracted from the composite material and the neat polymer. The fibers serve as the initial nuclei during crystallization, influencing the formation of the crystalline network. Therefore, the composite material was directly used as the sample material, and the mass correction was performed with only the matrix component. The material was heated in the DSC oven to  $70^{\circ}\text{C}$  above melting temperature ( $T_m = 180^{\circ}\text{C}$ ), resulting in a final temperature of  $T_{\text{max}} = 250^{\circ}\text{C}$  at a heating rate of 10 K/

min. The sample was kept at isothermal temperatures for 5 min to ensure that it was completely molten. The sample was then cooled at various rates: 1, 5, 10, 20, and 50 K/min. Each measurement was performed three times, and the average results are presented. Figure 2 demonstrates the scheme of DSC measurement.

The melting kinetics were determined by integrating the endothermal heat flow over a sigmoidal baseline in the temperature range between  $145^{\circ}\text{C}$  and  $190^{\circ}\text{C}$  to determine the

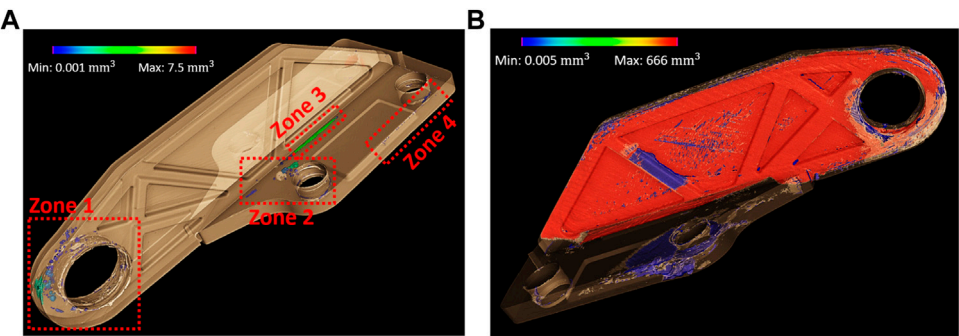


FIGURE 7  
CT porosity analysis (A) Sample A and (B) Sample (B)

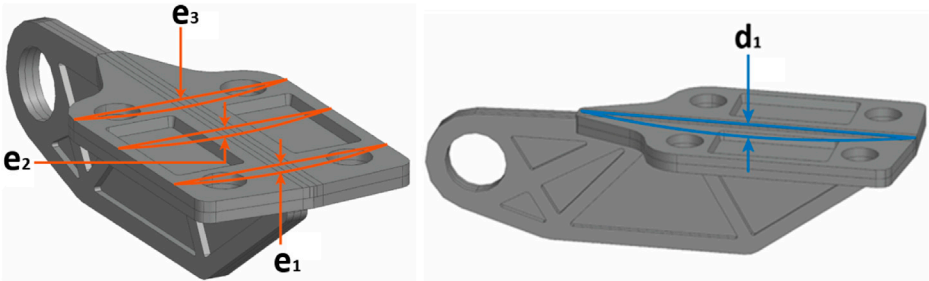


FIGURE 8  
Process-induced deformations measurement scheme.

TABLE 6 Measured and simulated the final deformation of the consolidated hinge.

Representative scalars	Sample A		Sample B	
	Experiment	Model	Experiment	Model
$d_1$ , mm	0.33	0.40	0.15	0.25
$e_1$ , mm	-0.53	-0.47	0.21	0.09
$e_2$ , mm	0.21	0.61	0.38	0.24
$e_3$ , mm	0.44	0.66	0.60	0.18
Average compaction of the base plate, mm	1.36	1.31	1.10	1.13
Average compaction of vertical plate, mm	0.95	0.97	0.51	0.24

degree of melting between 0 (solid-state) and 1 (molten state). The model parameters  $k_{mb}$  and  $d$  of Eq. 4 were fitted to the experimental data (Figure 3). Table 2 shows that the same melting model parameters were valid for the PA12 and PA12-CF materials.

To determine crystallization kinetics, the exothermal heat flow peak that occurs during the cooling process can be

integrated over a sigmoidal baseline. The parameters for Nakamura Equations 1–3 were determined using a fitting procedure for PA12 and PA12-CF materials, they are presented in Table 3. Figure 4 depicts a comparison of the developed kinetic model predictions with the measured relative crystallinity for various cooling rates.

### 3.3 Measurement of thermal expansion based on thermomechanical analysis

TMA can be used to determine the coefficient of thermal expansion of a material. The thermal expansion was directly measured in a small oven with a small tip on the surface of the specimen using this method. The coefficient of thermal expansion can be calculated using TMA measurements to predict expansion as a function of temperature.

TMA experiments were performed on a Q400 TMA instrument (TA Instruments). A small cubic specimen (approximately 5 mm in edge length) was taken from the consolidated composite material and neat polymer. The cube was positioned in the TMA oven and heated to 15°C below melting temperature ( $T_m = 180^\circ\text{C}$ ), resulting in a final temperature of  $T_{\max} = 165^\circ\text{C}$  at a heating rate of  $2^\circ\text{C}/\text{min}$ . Each measurement was repeated three times. The average measured data and the model fit are shown in Figure 5.

In the scope of this study, the CTEs of the fiber in the printing and transverse to the printing directions were not measured. Schürmann (2007) provided a range of possible values for various fiber types. Therefore, from the range of possible values,  $\alpha_{f,1} = -2.23 \times 10^{-6}$  and  $\alpha_{f,2} = 1.57 \times 10^{-5}$  were defined by substituting the measured CTEs from Table 4 into formulas (11)–(13) for room temperature (app.  $22^\circ\text{C}$ ).

According to the TMA measurements, the CTE of PA12  $\alpha_m$  was increased above  $T_g$  (Table 4). Based on the results of the analysis, the following correction coefficients for CTE mixing rules were assigned (11)–(13):

$$\begin{aligned} S_1 &= \begin{cases} 1, T < T_g \\ 1.16, T \geq T_g \end{cases}; & S_2 &= \begin{cases} 1, T < T_g \\ 2.74, T \geq T_g \end{cases}; \\ S_3 &= \begin{cases} 1.34, T < T_g \\ 2.74, T \geq T_g \end{cases} \end{aligned} \quad (31)$$

The material model incorporates the correction coefficients  $S_{1,2,3}$  based on the measured difference between the expansion of the composite in the transverse and thickness directions and the observed increase in the CTE of the composite above  $T_g$ . In the molten material state, all CTE coefficients (11)–(13) are assumed to be zero.

### 3.4 CT analysis

The authors previously presented the methodology for the computed tomography (CT) measurements (Grieder et al., 2022). The hinges were analyzed by Maxerial (2022). A Waygate v|tome|x M300 X-ray computed tomography system with a long-life X-ray source, a high-flux target, and a dynamic 41|200 Csl scintillation detector was used. The scan parameters were: 60  $\mu\text{m}$  voxel size, 150 kV acceleration voltage, 500  $\mu\text{A}$  tube current, and 75 W power.

The CT analysis was performed on three hinges in total. Two of the hinges (Samples A and B) were consolidated using two different heating parameter sets, whereas the third (Sample U) was not consolidated and therefore consisted of four individual 3D-printed sub-parts (two subparts from the so-called base plate and two others from the vertical plate of the hinge. Sample A was consolidated according to the established 9 T Labs workflow, while Sample B was consolidated at a lower temperature to investigate the void evolution process and the developed model's ability to detect improper part consolidation. Table 5 contains information regarding the consolidation setup, initial and final thicknesses of the vertical and base plates, and weight.

The general porosity identification algorithm does not capture open porosity (porosity that is not enclosed in the material) and does not properly estimate the void ratio correctly for elongated void channels, which are the most common ones in additive manufacturing. Therefore, the CT analysis of the unconsolidated specimen yielded an unreliably low porosity value (Table 5). Therefore, the initial porosities assigned to the PA12 and PA12-CF materials in the developed numerical model are 15% and 35%, respectively. The initial porosity values assumed were based on previous estimates for simple unidirectional samples (Grieder et al., 2022).

Figure 6 shows 3D overviews of the CT scan results for all three samples. The primary focus of this research is on Sample A, while Sample B is of less interest due to the low consolidation level resulting in poor part quality. 3D overviews of CT scans for Sample B and C are presented in (Supplementary Figures S3,S4).

The final void contents of samples A and B are illustrated in Table 5. Figure 7 depicts an overview of the porosity analysis of these samples. The four zones in sample A are denoted by using red rectangles. The CT algorithm detects most of the final porosity in these zones.

The GD&T flatness method was used to calculate the process-induced deformations of the hinges, where the flatness tolerance refers to two parallel planes that define the zone where the entire reference surface must lie (GD&T, 2022). Figure 8 depicts four pairs of parallel planes that are defined on the base plate. Table 6 compares the CT warpage analysis results to the simulation results in the following model application and validation section.

## 4 Model application and validation

The developed numerical approach was implemented using a user material subroutine in the commercial finite-element software ANSYS (v. 2022 R1). The layup was created using the SpaceClaim plugin Fibrify® and then mapped to 3D finite elements. Data exchange with the using hierarchical data format five ACP.

The results of the developed numerical approach for samples A and B are presented in this section, as

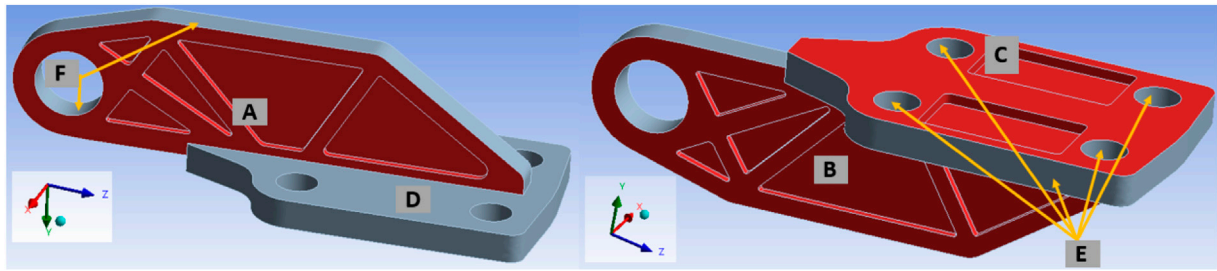


FIGURE 9

Boundary conditions for the mechanical problem: Pressure is applied to the sets of surfaces (A–C) (marked in red). Surface (E) has free displacement only in the y-direction, and Surfaces (D,F) have free displacement only in the x-direction.

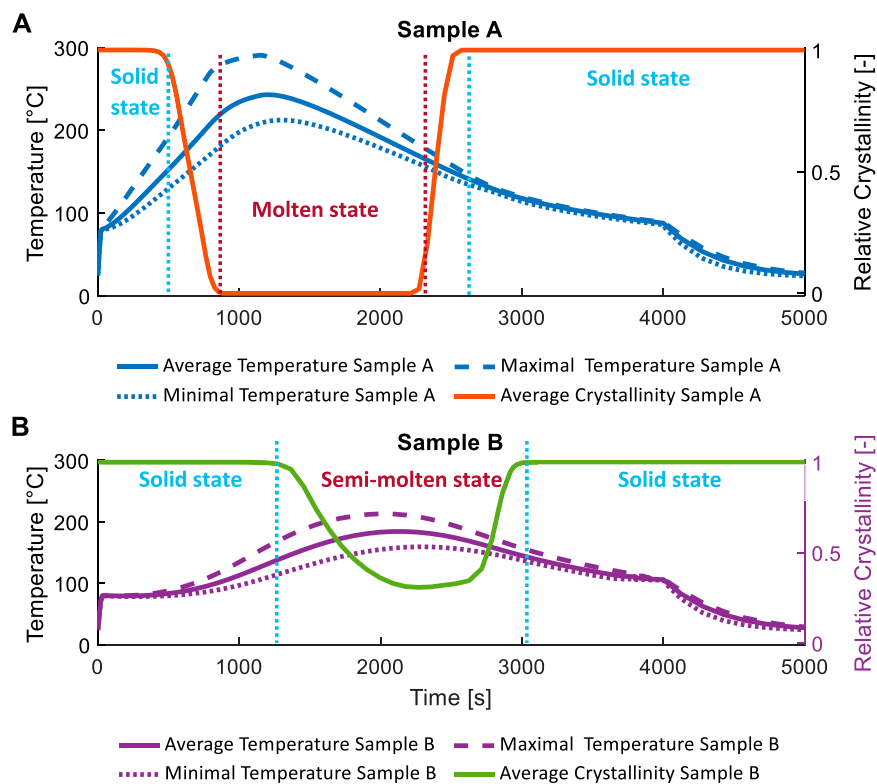


FIGURE 10

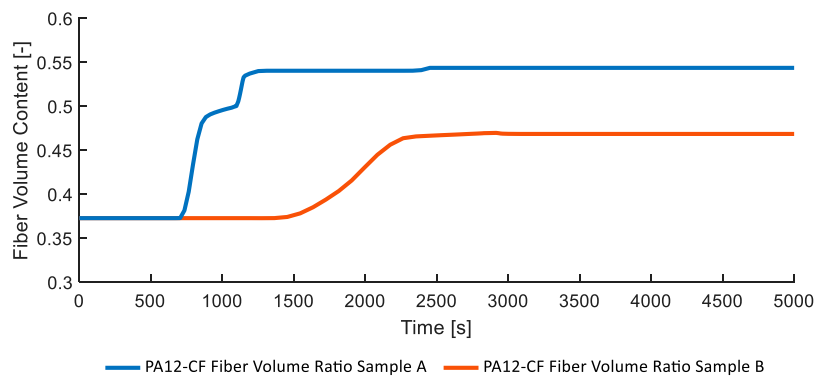
Average in domain temperature and crystallization degree (A) Sample A and (B) Sample B.

demonstrated in the previous section. The crystallization, process-induced deformations, residual stresses, porosity, and squeeze pressure results of the sequentially coupled thermal and mechanical solutions are presented. The model was validated using CT porosity and process-induced deformation analysis results.

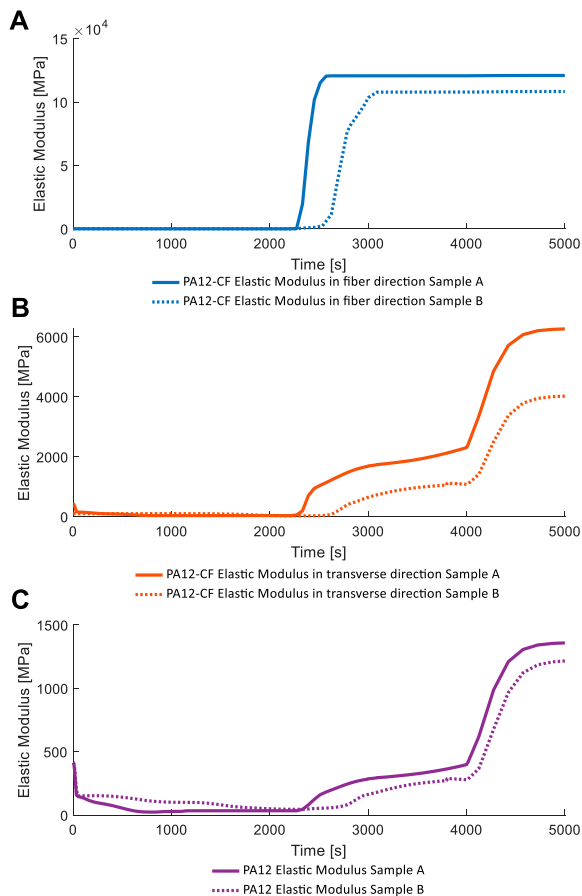
## 4.1 Application and FEM model description

The finite-element thermal model considers all three phases of the consolidation: heating, melting, and cooling. The proportional–integral–derivative controllers attached to the heating and cooling channels in the mold provided a





**FIGURE 11**  
PA12-CF fiber volume ratio for Samples (A) and (B)



**FIGURE 12**  
Elastic moduli for Samples A and B in (A) fiber direction (B) transverse direction, and (C) for a neat PA12 matrix.

temperature regime corresponding to the experimental setup. After 4,000 s, the free convection of the hinge with air was simulated. The boundary conditions for the thermal model

are the convection of all the outer mold surfaces with the surrounding air and the radiosity of the outer walls.

The mechanical model only solves this problem for the composite part. The proposed approach involves performing a sequentially coupled thermal-stress analysis in which the temperature field is independent of the stress field. Figure 9 shows the boundary conditions. The release from the mold was simulated by removing all applied forces (after 3,000 s) and displacement constraints (after 4,000 s) and providing a 3-point fixation of the hinge, which allowed simulation of free shrinkage during cooling.

The entire tool was modeled in the thermal model using 2'686'092 tetrahedral elements. Only the composite part in the mechanical part was modeled with 84'389 hexahedral elements. The solution is calculated in approximately 24 h and 6 h for the thermal model and the mechanical model, respectively, using four Intel Xeon Gold 2.7 GHz processors and 64 GB of RAM on a 64-bit operating system. The relatively long calculation time of the thermal problem is due to the use of four proportional–integral–derivative thermal controllers using the Ansys Parametric Design language. These controllers could be replaced with the heating flow BC fitted to the experimental data without a significant loss in solution accuracy, resulting in approximately 2 h of calculation.

## 4.2 Results of the thermal analysis

Figure 10 shows the temperature and crystallization solution. The maximum temperature variation for samples A and B was approximately 90°C and 60°C, respectively. In contrast to Sample A, where all the finite elements reached a fully molten state, Sample B did not reach a fully molten state (the average crystallization degree for all elements was 0.3 at the moment of maximum melting). Because the material state does not change stepwise, the semi-molten state can be considered (Wijskamp 2005; Brauner et al., 2014); it evolves according to the proposed melting kinetics 4)

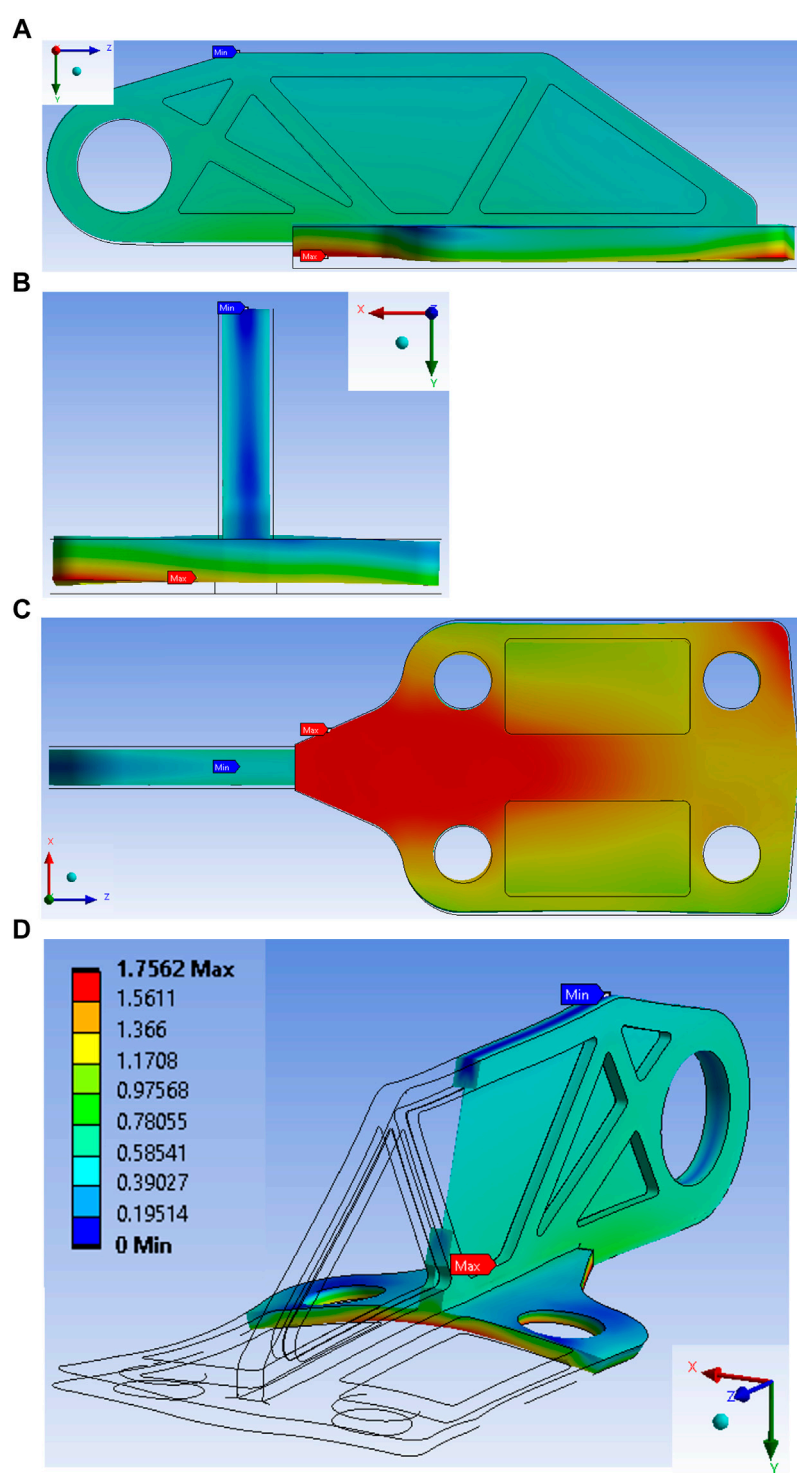
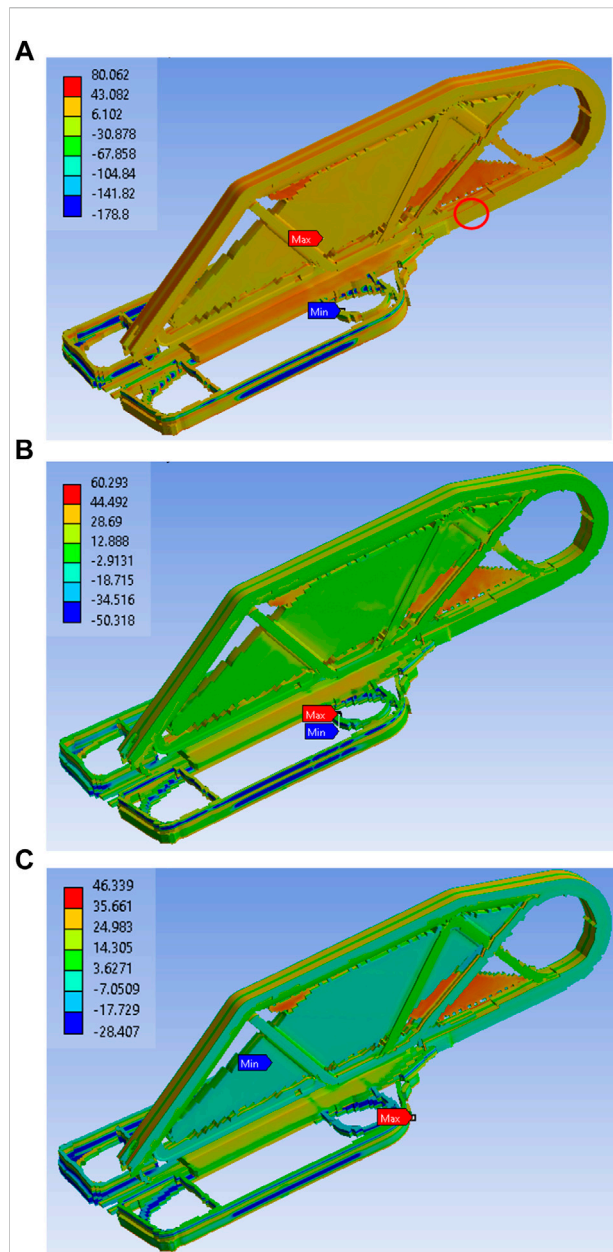


FIGURE 13

Sample (A) Simulated final process-induced deformations in mm (color legend is the same for all the figures) (A) (B) (C) plane views (D) isometric cross-section, the deformation is scaled 3.5 times, the black contour represents the deformed shape of the hidden domain.



**FIGURE 14**  
Final stress distribution in Sample A in (A) fiber (B) transverse, and (C) thickness direction.

(Grieder et al., 2022). This allowed us to calculate the porosity evolution in the transitional phase, whereas the porosity was assumed to be constant in the solid state.

The base plates of the hinge were subjected to a higher temperature than the vertical plates due to the mold construction. This was true of both samples. In Sample A, however, the melting temperature was reached for all subparts, whereas in Sample B, the vertical plates were not completely molten. The temperature distribution in samples A

and B at the maximum temperature is presented in (Supplementary Figures S5,S6).

### 4.3 Results of the mechanical analysis

The evolution of the average fiber volume content ratio in the PA12-CF layup is shown in Figure 11. Both samples started with the same fiber volume ratio because they exhibited the same initial degree of porosity. The final application should have a fiber volume ratio of 0.573, which corresponds to a fully consolidated fiber filament. Sample A achieved this, whereas Sample B was only partially consolidated, resulting in an average fiber volume content of 0.47.

Figure 12 depicts the process-dependent elastic moduli of the composite in the fiber and transverse directions, as well as the elastic modulus of the pure resin matrix. The initial and final stiffnesses also changed during the process as the fiber volume content changed. According to the proposed mixing rules (5)–(10), porosity influences the final stiffness depending on the fiber volume ratio 18) (Wijskamp 2005; Schürmann 2007; Brauner et al., 2014; Grieder et al., 2022).

Sample B has not been completely consolidated. It exhibits large gaps between the assembled and nonconsolidated subparts. Therefore, the developed finite-element model fails to accurately predict process-induced deformations because it lacks gaps. Therefore, the following plots only show the results for Sample A. Nonetheless, Table 6 provides a summary of the simulated compaction and warpage for Sample B.

Figure 13 depicts the final deformation of sample A. The original hinge shape is depicted using black contour lines (except for the scaled deformation in Figure 13D). The largest deformation occurred in the base plate based on the printed lay-up and consolidation process conditions. Because of the non-uniform and non-symmetrical temperature distribution during the cooling phase and the non-symmetrical initial assembly of the sub-parts, these deformations are not symmetrical relative to the yz-plane.

Table 6 compares process-induced deformations simulated and experimentally observed at representative points on the base plate (Figure 8). The developed model predicted the average final compaction for the base and vertical plates accurately (the error relative to the initial plate thickness is less than 1% for Sample A and less than 5% for Sample B). The simulated process-induced deformation follows the same trend as the measured deformation:  $e_2$  and  $e_3$  are bent symmetrically in the middle (Figure 13D), whereas  $e_1$  is bent in a more complex manner, with the middle of the representative scalar deformed by less than one of the outer points, resulting in a negative value of  $e_1$  (Figure 13C, where the negative sign represents the bending direction).

Table 6 shows that in the case of the fully consolidated hinge, the model provides more accurate predictions. It is explained by the uncertainty in material properties in the semi-molten state, which cannot be measured. Therefore, they were interpolated using the measured values for the solid and

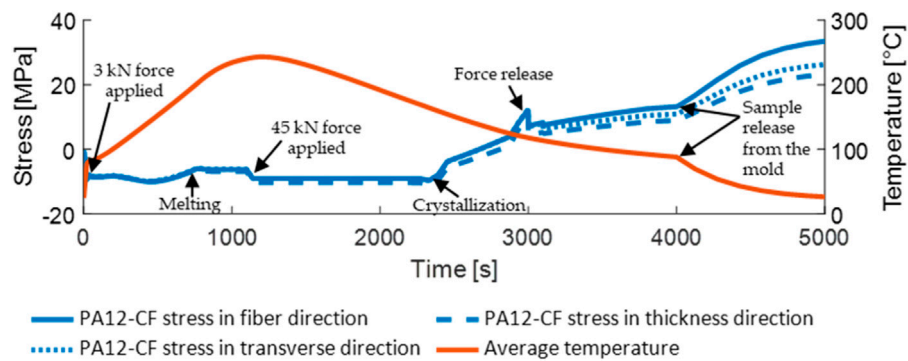


FIGURE 15

Process-induced stress in fiber, transverse, and thickness direction for the vertical plate's PA12-CF element in Sample A.

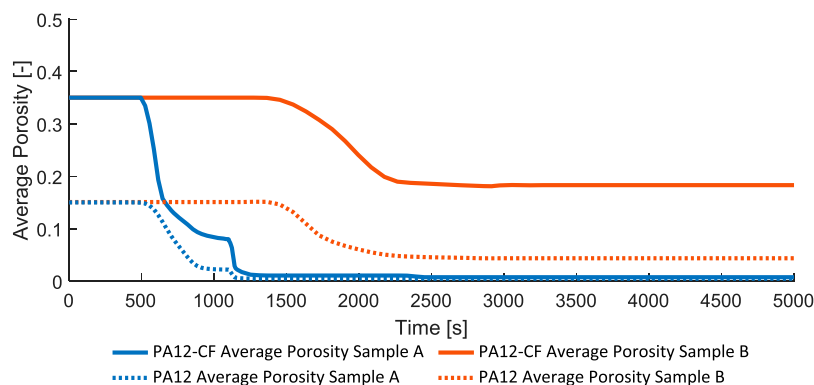


FIGURE 16

Average porosity in PA12 and PA12-CF finite elements for Samples (A) and (B)

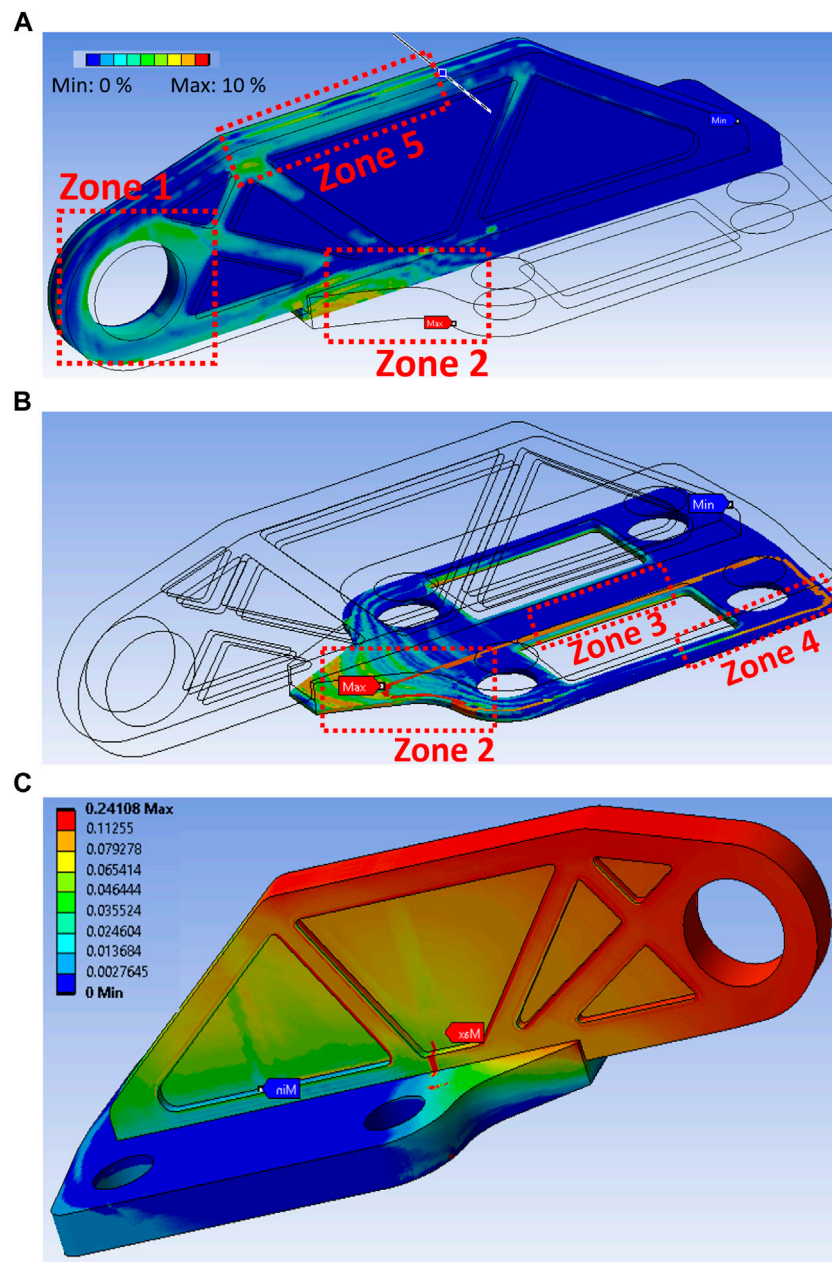
molten states and the developed stiffness function 17) (Grieder et al., 2022). Other possible causes of the inaccuracy of the process-induced deformation simulation can be summarized as follows:

- The developed approach has limitations such as the implementation of the elastic model; no pressure gradient is considered in the part due to the simplified porosity approach; insufficient quality of the finite element mesh; and/or relatively large time steps (the average model time step is 15 s). Consideration of advanced viscoelastic models in conjunction with the full Darcy equations and further investigation of the dependence of the model sensitivity on the mesh could improve the model predictions.
- Inaccurate measurement and consideration of the initial thickness and porosity of the hinge parts: the thicknesses of the base and vertical plates varied slightly in the experiment, whereas the model assumed they were uniform.

Furthermore, the model assumes zero initial warpage and stresses, whereas the printed hinge sub-parts have process-induced local deformations due to manufacturing. Some important features (such as air gaps between the subparts) were overlooked, which could be critical for predicting the final warpage.

Figure 14 depicts the directional stresses in the PA12-CF layup. The provided finite-element mesh resolution was insufficient for mapping the composite layup without sharp edges and breaks in the fiber path. Therefore, the maximum and minimum observable stresses are discovered at the finite-element singularity points, which do not accurately represent the final stress states at these locations.

Figure 15 depicts the directional stresses in the PA12-CF element (the element is marked with a red circle in Figure 14A). Because the considered fiber filament element is where hinge



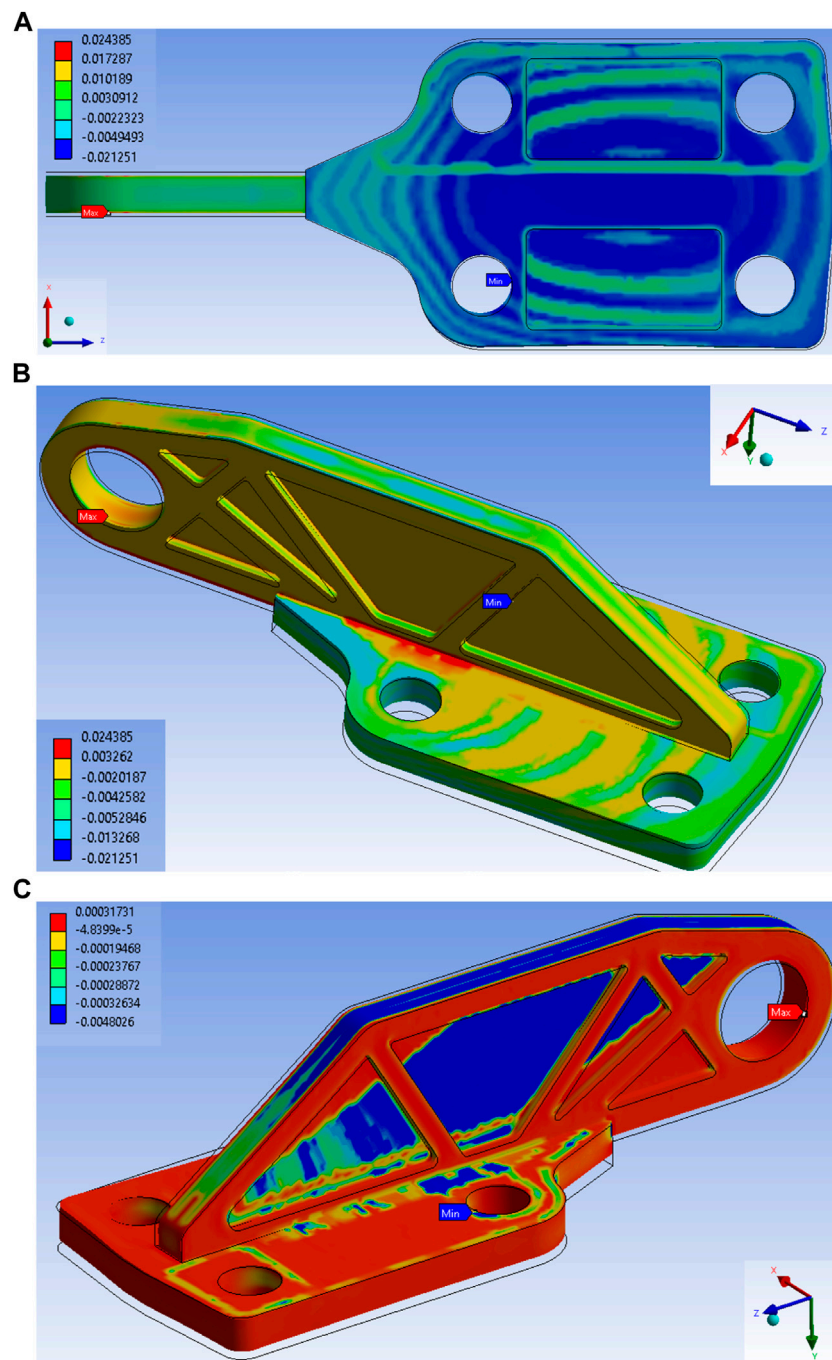
**FIGURE 17**  
Porosity distribution (A) Sample A vertical plate cross-section (B) Sample A base plate cross-section and (C) Sample (B)

failure starts during mechanical tests, residual stresses in this location are critical for hinge performance.

The developed model predicts local process-induced void reduction using Eqs 19–30. Figure 16 depicts the average porosity evolution for Samples A and B. In both cases, the void change occurs only after melting. However, before the additional pressure was applied, Sample A exhibited a decrease in porosity (with 30 kN pressure applied, before 1–100 s). The

porosity decreased below 0.1% after the additional pressure (up to 45 kN, after 1–100 s). In contrast, sample B exhibited a lower porosity reduction. Therefore, a two-step pressure application did not influence the porosity reduction because no melting state was reached before the application of 45 kN. The final simulated average void content was 0.43% for sample A and 4.3% for sample B, which are close to CT values of 0.17% and 3.78%, respectively (Table 5).





**FIGURE 18**  
Squeeze pressure Sample A: (A) (B) in transverse direction (C) in thickness direction.

Figure 17A B depicts cross-sections of Sample A, with zone 1–5 markers indicating the local final porosity. Because there was only porosity in the internal elements of Sample A, cross-sections are

shown. Therefore, the porosity was not visible on the surface of the hinge (which fits the CT data, Figure 7A). Five zones were defined based on the cross-sectional analysis to represent the parts of the



hinge where the void content reached maximum values (or did not fully reach the consolidated state). For zones 1–4, the simulation results showed the same local void content distribution as the CT scans. However, the model predicts nonzero porosity for zone five, although the CT scan is fully consolidated.

In contrast to Sample A, the porosity evolution in Sample B resulted in a non-zero void content throughout the vertical plate and in specific locations throughout the base plate. The porosity distribution on the outer surface of Sample B is depicted in Figure 17C. Such local void formation is caused by the observed low temperature in the vertical plate and corresponds to the porosity determined using CT analysis (Figure 7B).

The approach presented here does not allow for the simulation of material redistribution and fiber movement in the molten state. However, directional squeeze flows can be numerically analyzed. The results of this analysis can be compared to the fiber movement visualized using CT. Figure 18 shows the calculated directional squeeze pressures for the entire domain of Sample A.

The simulation results agree well with the CT-analysis presented above.

- Figure 20A shows that the minimum negative values of the transverse squeeze pressure in the direction were reached at the center of the base plate. This indicates that a significant amount of material flows to this region, resulting in a strong fiber outflow. Figure 6B depicts this, with the fiber movement of the base plate visible.
- Figure 20B shows the maximum positive squeeze flow between the two round inserts in the center of the base plate. This causes material to flow out of this area (zone 2). Therefore, this area exhibits a relatively high void content. (Figure 7A).
- Figure 20C shows that the majority of the squeeze pressure was achieved in the vertical plate lay-up and in zones 2, 3, and 4, which exhibited the highest degree of porosity.

Detailed analysis of squeeze pressure distribution in selected layouts is given in (Supplementary Figure S9). Such an analysis allows prediction of the fiber flow, which is essential for structural performance of consolidated composites.

## 5 Conclusion

In this study, the composite consolidation process was investigated experimentally and numerically. The initial and final porosities, CTEs, and crystallization and melting kinetics of the pure PA12 and composite PA12-CF materials were determined experimentally. On the basis of these findings, a mathematical model for the consolidation process was developed and numerically solved using the finite element method. By considering the orthotropic composite properties, the proposed finite-element model predicts the final process-induced deformations of the consolidated part. Temperature, crystallization, and porosity all influence these deformations. The proposed model can

predict the final composition of a part with high accuracy. The predicted warpage followed the same trend as the observed warpage. However, their absolute values differed. This difference could be caused by various factors, including inaccuracy of the thermal simulation, limitations in the simplified porosity model, defined homogenization mixing rules, imprecision in the initial data provided to the model, and inaccuracy in the CT measurements. The developed approach includes a set of design variables that must be adjusted for each material and composite structure. Furthermore, due to the ACP fiber filament mapping method, the model is extremely sensitive to the finite element mesh. Nonetheless, the developed approach enables rapid simulation of the consolidation process considering multiple physical and structural effects. The final residual stresses and porosity are predicted by the model. This is an important step toward achieving “first time right” composite production. The proposed approach provides a digital model of the consolidation process, which reduces the number of expensive prototyping iterations. The combination of highly accurate 3D-printing and post-printing consolidation, as well as the ANSYS finite-element model and fiber filament layup design, allows for the transition to serial production of additively manufactured continuous fiber composite parts.

The authors intend to use a local initial porosity distribution that depends on the printing process parameters and layup in a future study. Furthermore, novel measurement techniques to investigate porosity and crystallization are required.

## Data availability statement

The original contributions presented in the study are included in the article/Supplementary Material, further inquiries can be directed to the corresponding author.

## Author contributions

CB conceptualization, writing—review and editing, supervision, and project administration. MA conceptualization, methodology, software, writing—editing, project administration. SG and IZ methodology, software, investigation, formal analysis, writing—original draft, writing—review and editing, and visualization. MK methodology. JB, PI, and JF methodology, software, writing—editing. ME conceptualization and supervision. All the authors have read and agreed to the published version of the manuscript.

## Funding

This research was supported by the national funded project AddFu (Grant Number 38729.1 IP-ENG), which was supported by Innosuisse, Swiss Innovation Promotion Agency.

## Acknowledgments

The CT-analysis of the material distribution, the local porosity, and process-induced warpage was performed by the maXerial company. The authors thank maXerial for accurate analysis, attention to detail, and consideration of the authors' requests.

## Conflict of interest

The authors declare that the research was conducted in the absence of any commercial or financial relationships that could be construed as a potential conflict of interest.

## References

- Advani, S., and Sozer, E. (2010). *Process modelling in composites manufacturing*. 2nd ed. Abingdon, UK: CRC Press.
- Anisoprint (2021). Stop metal thinking! Start anisoprinting. Available online: <https://anisoprint.com/solutions> (accessed on March 25, 2021).
- Arefmanesh, A., Advani, S. G., and Michaelides, E. E. (1990). A numerical study of bubble growth during low-pressure structural foam molding process. *Polym. Eng. Sci.* 30, 1330–1337. doi:10.1002/pen.760302011
- Arefmanesh, A. (1991). *Numerical and experimental study of bubble growth in highly viscous fluids*. Delaware: University of Delaware ProQuest Dissertations Publishing.
- Arevo (2021). *Making the world lighter*. <https://arevoinc.com/products?lang=en> (accessed on March 25, 2021).
- Author Anunous (2022). Your all-in-one solution for digital composite production. <https://www.9tlabs.com> (accessed on August 29, 2022).
- Barari, B., Simacek, P., Yarlaga, S., Crane, R., and Advani, S. G. (2020). Prediction of process-induced void formation in anisotropic fiber-reinforced autoclave composite parts. *Int. J. Mat. Form.* 13, 143–158. doi:10.1007/s12289-019-01477-4
- Bellehumeur, C., Li, L., Sun, Q., and Gu, P. (2004). Modeling of bond formation between polymer filaments in the fused deposition modeling process. *J. Manuf. Process.* 6, 170–178. doi:10.1016/S1526-6125(04)70071-7
- Benedetti, L., Brulé, B., Decreamer, N., Evans, K. E., and Ghita, O. (2019). Shrinkage behaviour of semi-crystalline polymers in laser sintering: PEKK and PA12. *Mat. Des.* 181, 107906. doi:10.1016/j.matdes.2019.107906
- Bhandari, S., Lopez-Anido, R. A., and Gardner, D. J. (2019). Enhancing the interlayer tensile strength of 3D printed short carbon fiber reinforced PETG and PLA composites via annealing. *Addit. Manuf.* 30, 100922. doi:10.1016/j.addma.2019.100922
- Blok, L. G., Longana, M. L., Yu, H., and Woods, B. K. S. (2018). An investigation into 3D printing of fibre reinforced thermoplastic composites. *Addit. Manuf.* 22, 176–186. doi:10.1016/j.addma.2018.04.039
- Borowski, A., Vogel, C., Behnisch, T., Geske, V., Gude, M., and Modler, N. (2021). Additive manufacturing-based *in situ* consolidation of continuous carbon fibre-reinforced polycarbonate. *Materials* 14, 2450. doi:10.3390/ma14092450
- Brauner, C. (2013). *Analysis of process-induced distortions and residual stresses of composite structures*. Berlin, Germany: Logos Verlag Berlin GmbH.
- Brauner, C., Block, T. B., and Herrmann, A. S. (2011). Meso-level manufacturing process simulation of sandwich structures to analyze viscoelastic-dependent residual stresses. *J. Compos. Mat.* 46 (7), 783–799. doi:10.1177/0021998311410498
- Brauner, C., Peters, C., Brandwein, F., and Herrmann, A. (2014). Analysis of process-induced deformations in thermoplastic composite materials. *J. Compos. Mat.* 48, 2779–2791. doi:10.1177/0021998313502101
- Brenken, B., Barocio, E., Favaloro, A., Kunc, V., and Pipes, R. (2018). Development and validation of extrusion deposition additive manufacturing process simulations. *Addit. Manuf.* 25, 218–226. doi:10.1016/j.addma.2018.10.041
- Brujan, E. A., and Vogel, A. (2006). Stress wave emission and cavitation bubble dynamics by nanosecond optical breakdown in a tissue phantom. *J. Fluid Mech.* 558, 281–308. doi:10.1017/S00222112006000115
- Cable, C. W. (1991). The effect of defects in glass-reinforced plastic (GRP). *Mar. Technol. SNAME News* 28 (2), 91–98. doi:10.5957/mt.1991.28.2.91
- Calneryte, D., Barauskas, R., Milasienė, D., Maskeliūnas, R., Neciunas, A., Ostreika, A., et al. (2018). Multi-scale finite element modeling of 3D printed structures subjected to mechanical loads. *Rapid Prototyp. J.* 24 (1), 177–187. doi:10.1108/RPJ-05-2016-0074
- Eguemann, N., Giger, L., Roux, M., Dransfeld, C., Thiebaud, F., and Perreux, D. (2013). “Compression moulding of complex parts for aerospace with discontinuous novel and recycled thermoplastic composite materials,” in 19th International conference on composite materials, Paris, France, January 23 – 24, 2017, 1–11.
- Eom, Y., Boogh, L., Michaud, V., and Manson, J.-A. (2001). A structure and property-based process window for void-free thermoset composites. *Polym. Compos.* 22 (1), 22–31. doi:10.1002/pc.10512
- Flynn, H. G. (1975). Cavitation dynamics. I. A mathematical formulation. *J. Acoust. Soc. Am.* 57, 1379–1396. doi:10.1121/1.380624
- Gaudron, R., Warnez, M. T., and Johnsen, E. (2015). Bubble dynamics in a viscoelastic medium with nonlinear elasticity. *J. Fluid Mech.* 766, 54–75. doi:10.1017/jfm.2015.7
- GD&T (2022). Flatness method. <https://www.gdandtbasics.com/flatness> (accessed on August 29, 2022).
- Gebhardt, A., Kessler, J., and Thurn, L. (2019). *3D printing: Understanding additive manufacturing*. 2nd ed. Munich, Germany: Carl Hanser Verlag.
- Ghiorse, S. R. (1993). Effect of void contents on the mechanical properties of carbon/epoxy laminates. *SAMPE Q.* 24 (2), 54–59.
- Goh, G. D., Dikshit, V., Nagalingam, A. P., Goh, G. L., Agarwala, S., Sing, S. L., et al. (2018). Characterization of mechanical properties and fracture mode of additively manufactured carbon fiber and glass fiber reinforced thermoplastics. *Mat. Des.* 137, 79–89. doi:10.1016/j.matdes.2017.10.021
- Greco, A., and Maffezzoli, A. (2003). Statistical and kinetic approaches for linear low-density polyethylene melting modeling. *J. Appl. Polym. Sci.* 89, 289–295. doi:10.1002/app.12079
- Gregory, T. M., and Gonzdz, A. S. (2016). Methods for composite filament fabrication in three dimensional printing. US20160346998A1,
- Grieder, S., Zhilyaev, I., Küng, M., Brauner, C., Akermann, M., Bosshard, J., et al. (2022). Consolidation of additive manufactured continuous carbon fiber reinforced polyamide 12 composites and the development of process-related numerical simulation methods. *Polymers* 14, 3429. doi:10.3390/polym14163429
- Halpin, J. C., and Kardos, J. L. (1976). The halpin-tsai equations: A review. *Polym. Eng. Sci.* 16, 344–352. doi:10.1002/pen.760160512
- Hardin, R. A., and Beckermann, C. (2007). Effect of porosity on the stiffness of cast steel. *Metall. Mat. Trans. A* 38, 2992–3006. doi:10.1007/s11661-007-9390-4
- Iragi, M., Pascual-González, C., Esnaola, A., Lopes, C. S., and Aretxabala, L. (2019). Ply and interlaminar behaviors of 3D printed continuous carbon fiber-reinforced thermoplastic laminates; effects of processing conditions and microstructure. *Addit. Manuf.* 30, 100884. [CrossRef].

## Publisher's note

All claims expressed in this article are solely those of the authors and do not necessarily represent those of their affiliated organizations, or those of the publisher, the editors and the reviewers. Any product that may be evaluated in this article, or claim that may be made by its manufacturer, is not guaranteed or endorsed by the publisher.

## Supplementary material

The Supplementary Material for this article can be found online at: <https://www.frontiersin.org/articles/10.3389/fmats.2022.1068261/full#supplementary-material>

- Jaroslav, K. (1999). Correlation between Young's modulus and porosity in porous materials. *J. Mat. Sci. Lett.* 18 (13), 1007–1010. doi:10.1023/A:1006669914946
- Jin, Y., Harry, C. C., and Christian, F. (2020). Extracting non-linear viscoelastic material properties from violently-collapsing cavitation bubbles. *Extreme Mech. Lett.* 39, 100839. doi:10.1016/j.eml.2020.100839
- Joel, D. S., David, R., Luc, P., Celeste, S., and Martin, G. (1997). *Flow of polymer melts*. Montreal, QC: Physics in Canada.
- Koerdt, M., Koerdt, M., Grobrüg, T., Skowronek, M., and Herrmann, A. S. (2022). Modelling and analysis of the thermal characteristic of thermoplastic composites from hybrid textiles during compression moulding. *J. Thermoplast. Compos. Mater.* 35, 127–146. doi:10.1177/0892705719875204
- Leterrier, Y., and G'sell, C. (1994). Formation and elimination of voids during the processing of thermoplastic of matrix composites. *Polym. Compos.* 15, 101–105. doi:10.1002/pc.750150203
- Li, J., Yuan, S., Zhu, J., Li, S., and Zhang, W. (2020). Numerical model and experimental validation for laser sinterable semi-crystalline polymer: Shrinkage and warping. *Polymers* 12, 1373. doi:10.3390/polym12061373
- Long, S. D., Dawood, I., Coates, P. D., and Johnson, A. F. (1995). Influence of reaction injection moulding (RIM) processing variables on the mechanical properties of a commercial linear segmented polyamide. *Plast. Rubber Compos. Process Appl.* 23 (3), 161–174.
- Lundstrom, T. S., and Gebart, B. R. (1994). Influence from process parameters on void formation in resin transfer molding. *Polym. Compos.* 15 (1), 25–33. doi:10.1002/pc.750150105
- Mahoor, M., Larissa, G., Ignaas, V., and Stepan, V. L. (2018). Voids in fiber-reinforced polymer composites: A review on their formation, characteristics, and effects on mechanical performance. *J. Compos. Mat.* 53, 1579–1669. doi:10.1177/0021998318772152
- Maxerial (2022). <https://www.maxerial.io/> (accessed on August 29, 2022).
- Meng, L., Xiaoyong, T., Junfan, S., Weijun, Z., Dichen, L., and Yingjie, Q. (2019). Impregnation, and interlayer bonding behaviours of 3D-printed continuous carbon-fiber-reinforced poly-ether-ether-ketone composites. *Compos. Part A Appl. Sci. Manuf.* 121, 130–138. doi:10.1016/j.compositesa.2019.03.020
- Moris, A., and Costel, D. D. (1984). A study of the dynamics of foam growth: Analysis of the growth of closely spaced spherical bubbles. *Polym. Eng. Sci.* 24, 1026–1034. doi:10.1002/pen.760241306
- Morrissey, L. S., and Nakhla, S. (2018). A finite element model to predict the effect of porosity on elastic modulus in low-porosity materials. *Metall. Mat. Trans. A* 49, 2622–2630. doi:10.1007/s11661-018-4623-2
- Nakamura, K., Katayama, K., and Amano, T. (1973). Some aspects of nonisothermal crystallization of polymers II - consideration of the isokinetic condition. *J. Appl. Polym. Sci.* 17, 1031–1041. doi:10.1002/app.1973.070170404
- Nakamura, K., Watanabe, T., Katayama, K., and Amano, T. (1972). Some aspects of nonisothermal crystallization of polymers I - relationship between crystallization temperature, crystallinity, and cooling conditions. *J. Appl. Polym. Sci.* 16, 1077–1091. doi:10.1002/app.1972.070160503
- Negi, S., and Rajesh, S. (2016). Study on shrinkage behaviour of laser sintered PA 3200GF specimens using RSM and ANN. *Rapid Prototyp. J.* 22, 645–659. doi:10.1108/rpj-08-2014-0090
- Rodriguez, J. F., Thomas, J. P., and Renaud, J. E. (2000). Characterization of the mesostructure of fused-deposition acrylonitrile-butadiene-styrene materials. *Rapid Prototyp. J.* 6 (3), 175–186. doi:10.1108/13552540010337056
- Roychowdhury, S., Gillespie, J. W., Jr., and Advani, S. G. (2001). Volatile-induced void formation in amorphous thermoplastic polymeric materials: I. Modeling and parametric studies. *J. Compos. Mat.* 35, 340–366. doi:10.1177/002199801772662208
- Roychowdhury, S. (1995). *Void formation and growth in amorphous thermoplastic polymeric materials*. Delaware: University of Delaware ProQuest Dissertations Publishing.
- Schürmann, H. (2007). *Konstruieren mit Faser-Kunststoff-Verbunden 2. Auflage*. Berlin, Germany: Springer-Verlag.
- Skempton, A. W. (1960). "Terzaghi's discovery of effective stress," in *From theory to practice in soil mechanics*. Editors L. Bjerrum, A. Casagrande, R. B. Peck, and A. W. Skempton (New York: Wiley), 42–53.
- Wagh, A. S., Poeppel, R. B., and Singh, J. P. (1991). Open pore description of mechanical properties of ceramics. *J. Mat. Sci.* 26, 3862–3868. doi:10.1007/BF01184983
- Wang, J., Xie, H., Weng, Z., Senthil, T., and Wu, L. (2016). A novel approach to improve mechanical properties of parts fabricated by fused deposition modeling. *Mat. Des.* 105, 152–159. doi:10.1016/j.matdes.2016.05.078
- Wijskamp, S. (2005). "Shape distortion in composite forming." [PhD thesis] ([Enschede, Netherlands]: University of Twente).
- Wood, J. R., and Bader, M. G. (1994). Void control for polymer-matrix composites (1): Theoretical and experimental methods for determining the growth and collapse of gas bubbles. *Compos. Manuf.* 5, 139–147. doi:10.1016/0956-7143(94)90023-X
- Xue, W., Liping, Z., Jerry, Y. H. F., and Heow, P. L. (2019). Effect of porosity on mechanical properties of 3D printed polymers: Experiments and micromechanical modeling based on X-ray computed tomography analysis. *Polymers* 11 (7), 1154. doi:10.3390/polym11071154
- Yohann, L., Robert, P., Fabrice, S., Laurent, M., and Gérard, B. (2008). "Modeling of void growth mechanisms during the manufacturing of composite laminates," in 9th International Conference on Flow Processes in Composite Materials - FPCM-9, Montréal, Canada, 1–9.
- Zhang, J., Zhou, Z., Zhang, F., Tan, Y., Tu, Y., and Yang, B. (2020). Performance of 3D-printed continuous-carbon-fiber-reinforced plastics with pressure. *Materials* 13, 471. doi:10.3390/ma13020471
- Zingraff, L., Michaud, V., Bourban, P.-E., and Manson, J.-A. E. (2005). Resin transfer moulding of anionically polymerised polyamide 12. *Compos. Part A Appl. Sci. Manuf.* 36, 1675–1686. doi:10.1016/j.compositesa.2005.03.023
- Zingraff, L. (2004). "Void formation and transport during liquid composite molding and forming of reactive thermoplastic composites." [PhD Thesis] (Lausanne, Switzerland: EPFL).
- Zobeiry, N. (2006). "Viscoelastic constitutive models for evaluation of residual stress in thermoset composite during cure." [PhD thesis] ([Vancouver, Canada]: University of British Columbia).



## OPEN ACCESS

EDITED BY  
Christophe Binetruy,  
Ecole Centrale de Nantes, France

REVIEWED BY  
Marco Monti,  
Proplast Consortium for the Promotion  
of the Plastic Culture, Italy  
Wang Xiaoqiang,  
Shenyang Aerospace University, China

\*CORRESPONDENCE  
Mangilal Agarwal,  
✉ agarwal@iupui.edu  
Hamid Dalir,  
✉ hdalir@aiu.edu

SPECIALTY SECTION  
This article was submitted to  
Polymeric and Composite Materials,  
a section of the journal  
Frontiers in Materials

RECEIVED 04 November 2022  
ACCEPTED 28 November 2022  
PUBLISHED 10 January 2023

CITATION  
Biswas PK, Omole O, Peterson G,  
Cumbo E, Agarwal M and Dalir H (2023),  
Carbon and cellulose based nanofillers  
reinforcement to strengthen carbon  
fiber-epoxy composites: Processing,  
characterizations, and applications.  
*Front. Mater.* 9:1089996.  
doi: 10.3389/fmats.2022.1089996

COPYRIGHT  
© 2023 Biswas, Omole, Peterson,  
Cumbo, Agarwal and Dalir. This is an  
open-access article distributed under  
the terms of the [Creative Commons  
Attribution License \(CC BY\)](#). The use,  
distribution or reproduction in other  
forums is permitted, provided the  
original author(s) and the copyright  
owner(s) are credited and that the  
original publication in this journal is  
cited, in accordance with accepted  
academic practice. No use, distribution  
or reproduction is permitted which does  
not comply with these terms.

# Carbon and cellulose based nanofillers reinforcement to strengthen carbon fiber-epoxy composites: Processing, characterizations, and applications

Pias Kumar Biswas<sup>1,2</sup>, Oluwaseun Omole<sup>1</sup>, Garrett Peterson<sup>1</sup>,  
Eric Cumbo<sup>1</sup>, Mangilal Agarwal<sup>1\*</sup> and Hamid Dalir<sup>1\*</sup>

<sup>1</sup>Integrated Nanosystems Development Institute, IUPUI, Indianapolis, IN, United States, <sup>2</sup>School of Mechanical Engineering, Purdue University, West Lafayette, IN, United States

Since the inception of carbon fiber reinforced polymer (CFRP) composites, different nanofillers have been investigated to strengthen their mechanical and physical properties. To date, the majority of research has focused on enhancing fiber/matrix interface characteristics and/or optimizing nanofiller dispersion within the matrix, both of which improve the performance of carbon fiber-epoxy composite structures. Nanofillers can be dispersed into the polymer matrix by different techniques or nanofillers are chemically bonded to fiber, polymer, or both via multiple reaction steps. However, a few studies were conducted showing the effects of different nanofillers on the performance of carbon fiber-epoxy composites. Here a critical study has been done to explore different carbon and cellulose-based nanofillers which are used to enhance the mechanical and physical properties of carbon fiber-epoxy composites. After giving a short history of carbon fiber production, the synthesis of carbon nanotubes (CNTs), graphene, cellulose-based nanofillers (cellulose nanocrystals and nanofibers), their dispersion in the polymer matrix, and chemical/physical bonding with the fiber or polymer have been extensively described here along with their processing techniques, characterizations, and applications in various fields.

## KEYWORDS

polymer, matrix, CRFP, nanofillers, composite materials, epoxy composite

## Introduction

Sir Joseph Wilson Swan has been coined as the father of the carbon fiber industry after he invented new incandescent light bulbs with carbonized paper as the newly used filament (Keyte et al., 2019). The American chemical inventor and businessman Thomas A. Edison commercialized the use of carbon filaments in his light bulbs. The use of carbon



filaments allowed his bulbs to last for over 1200 h in his patent Electric-Lamp (U.S.P. Office, 1880). Minor discoveries in the use of carbon fiber were uncovered in the early 1900 s, but the next major milestone for carbon fiber was with Roger Bacon's discovery of graphite whiskers, in the later 1950 s. These thin cylindrical-like layers of graphene laid the foundation of what we know today as carbon fibers, as Bacon discovered that when graphite was heated to arc temperatures, they form incredibly strong and flexible filaments (Bacon, 1960). In later years, Bacon also uncovered further discoveries with the microstructure of graphite (Bacon and Tang, 1964), further aiding to our current knowledge of carbon fibers. One of such discoveries Bacon and Wesley Schalamon patented was the use of creating carbon fiber by heating rayon and implementing a new method of stretching these fibers at temperatures as high as 2800°C, which resulted in greater young's modulus (Schalamon et al., 1970). On the other side of the globe, researchers were uncovering the intricacies of carbon in tandem to Bacon. Polyacrylonitrile (PAN) acquired by Dr. Akio Shindo was researched in 1959 and it was discovered that it produced the greatest increase in mechanical properties. Shindo delved deeper in order to compare oxidized PAN fibers to non-oxidized PAN fibers which helped uncover that the oxidized fibers were better when simultaneously carbonizing a vast array of carbon fiber batches (Tanaka et al., 2018). After this discovery, William Watt and William Johnson, under the Royal Aircraft Establishment (RAE), spearheaded the commercial use of high-strength carbon fibers in 1963. It was discovered that heating the

PAN fibers to 2500°C nearly tripled its stiffness and restricting the PAN fibers during oxidation allowed full production lines to be implemented by 1966 (Johnson and Figueiredo, 1990). These discoveries pushed PAN-based fibers into being the primary method of forming carbon fibers even currently forming 90% of all commercially used carbon fibers (Frank et al., 2017).

Rayon was first used to create high-strength carbon fibers back in the 1960 s, however, these produced low tensile strength and Young's modulus relative to the other materials. Rayon is a cellulose-based carbon fiber, that is, known for having defects such as large void contents and interfilament bonding (Peng et al., 2003). However, a better method of creating usable carbon fiber was through another material called Pitch, which is derived from petroleum asphalt, coal tar or polyvinyl chloride. Pitch-based carbon fibers can be formed into either isotropic-pitch-based or mesophase-pitch-based carbon fibers (Inagaki and Inagaki, 2000). However, only mesophase pitches are commercially used to create carbon fiber. Pitch is typically used to create high-modulus fibers that many critical military operations need, while PAN allows for high-strength fibers. Currently, about 90% of the carbon fiber used is PAN-based. These three materials have led to a key shift in the use of carbon fiber as a material in popularity similar to aluminum, primarily due to material's lightweight and strength properties. Despite its humble beginnings, the use of carbon fibers in structural applications has transformed this material into a multi-billion dollar industry (Mohee et al., 2016). Due to its increase in



popularity, the PAN-based CF industry has been estimated to grow by 10% per year (Tanaka et al., 2018). Increasing its global market from \$3.7 billion in 2020 to \$8.9 billion in 2031 (Gogoi et al., 2022). This percentage increases within the construction industry, where estimates of its global usage increases by 12% (Roberts, 2009). However, due to the recent COVID-19 pandemic, the production of most composite businesses was halted with decreased production, increased costs and material and labor shortages.

Let's discuss present day carbon fiber uses and how their versatility is displayed around the world. In recent years, (carbon) fiber-reinforced plastics usage within concrete has been investigated globally (Hollaway, 2003; Van Den Einde et al., 2003; Sadeghian et al., 2010; Mehdi and Resatoglu, 2022). In Asia, tests have been conducted on the effects of carbon fiber on their structures to replace steel (Ueda and Sato, 2002; Wu et al., 2014). The automotive industry also recognizes the application of composites, like carbon fiber, for introducing light weight structures (Alves et al., 2010; Koronis et al., 2013). As the price of CFRPs decreases yearly, composite usage is becoming more and more cost-effective. The main drawback of CFRPs is their ability to meet the needs of high-volume manufacturability or low downtime production. Still CFRPs are desired for their superior mechanical and structural properties relative to traditional materials (Ravishankar et al., 2019). In fact, when three Korean manufacturing companies joined together to create a CF battery pack module carrier, they experienced a 26% weight reduction, better recyclability, and cost reductions relative to a standard steel carrier (Koniuszewska and Kaczmar, 2016). Carbon fiber composites have also found their way into the sporting industry, once their price decreased to 100 Euro/kg (Perner et al., 2016). Super lightweight bicycle frames, tennis rackets and kayaks have been formed with carbon fiber prepreg. Even sensors and detection systems have been researched, with the aim of creating sensors that detect deformations within composite structures. The aviation and space industry are also looking at the key advantages that CFRPs have, especially Boeing and Airbus. In fact, 50 wt% of their newer airplanes, such as the Boeing 787 and Airbus 350, are composed of composites, which they have been using since the start of 1980s (Maria, 2013; Gerard, 2015). Aerospace manufacturers claimed that the use of these composite materials would help lower operating costs by 20% and lower greenhouse gas emissions by 25% (Marsh, 2007). Even other classes of airplanes, specifically privatized aircraft, have responded to this dramatic change from aluminum to composites. Airplanes can take advantage of carbon fiber's high heat capacity and low density to create brake disks that are 40% lighter and lasts twice as long compared to traditional steel brakes (Windhorst and Blount, 1997). The defense and space industry has invested major stakes into CFRPs and their high strength to weight ratio. The British Aerospace Defense has spent the last 50 years developing and implementing carbon fiber composites within their war fighting planes, all to bluster their

defenses and air superiority (Lewis, 1994). The Moscow based company AeroComposit is a company focused on researching and applying stronger components like carbon fiber within Russian aircraft for next-generation, single-aisle aircraft (Koniuszewska and Kaczmar, 2016). Due to stipulations put forth by the FAA, increasing thickness or radically changing aircraft internal features in favor of increased strength and mechanical properties incurs costly impacts on composites, while maintaining a factor of safety. These issues are of key importance to the aerospace and defense industry (Mason et al., 2004).

One way carbon fiber can increase strength without increasing thickness is through its fiber orientation. Carbon fiber has four main orientations: uni-directional, bi-directional, quasi-isotropic and randomly oriented. When a load is placed onto a carbon fiber composite, the load must be distributed in the direction of the fibers, as opposed to the weak resin, else delamination occurs, and the component fails. A uni-directionally oriented composite has fibers along only one axis (vertically, horizontally, or diagonally), bi-directional has fibers aligned onto two axes, typically vertically and horizontally. Most applications have quasi-isotropic carbon fibers, due to its ability to apply loads in any direction which is done with different stackups. Most stackups use a variety of uni and bi-directional fibers assorted in different orientations.

A more recent approach to increasing the strength of these carbon composites has been the application of adding nanofillers between the epoxy matrix—nanoscopic materials that have the ability to increase the mechanical and electrical properties of composites. The word nanotechnology has been in use since the 1970s and was coined to distinguish the difference between microscale and nanoscale materials (Njuguna and Pielichowski, 2004a). Due to the large area of conventional fillers, it's only natural that buds and voids can occur randomly, which causes reductions in the laminate's strength. Nanoparticles such as multi-walled carbon nanotubes (MWCNTs) and single-walled carbon nanotubes (SWCNTs) have gained much popularity and are being studied globally as an answer to composite reinforcement (Njuguna and Pielichowski, 2004b). CNTs are cylindrical hollow structures of pure graphite sheets. CNT structures are 100 times stronger than steel, while being six times less dense (Mittal et al., 2018). SWCNTs tend to have greater electrical properties than their multi-walled counterparts, which allows them to be used in electrical applications. Cellulose nanocrystals (CNC) are cellulose extracted from plant cell walls or other biological sources, with length and diameter within the nano scale (Xu et al., 2013). The properties of CNCs are greatly subject to change and can vary based on size, structure, and surface charge (Liu et al., 2011). These changes can occur due to their extraction method, but as a result of this versatility, CNCs and CNTs have been used in optical and chemical sensors (Consales et al., 2006; Cusano et al., 2006; Huang et al., 2015).



Graphene is another nanomaterial that has been regarded as a wonder material, when referring to its electrical properties. Graphene is a monolayer of carbon atoms, which form a two-dimensional lattice, *versus* the one-dimensional graphite (Geim and Novoselov, 2007). Graphene and CNC have shown promising results as a superconductor with high power and energy density (Yang et al., 2019). It has also been studied within the nuclear industry for its uranium absorption (Liu and Mao, 2021). However, its high cost tends to make others shy from using this. To produce graphene with the greatest surface area and nearly defect-free an expensive bottom-up technique such as chemical vapor deposition, total organic synthesis or epitaxial growth is needed to synthesize graphene (Lee et al., 2019). Three innovative routes for low-cost graphene bulk manufacturing have been created, using graphite oxide, liquid-phase exfoliation and an electrochemical route (Zhong et al., 2015). This paper aims to review the current innovative uses of these nanomaterials as carbon composite reinforcements. These nano-reinforcements offer to strengthen the mechanical and physical properties of CFRPs composites. The paper also seeks an in-depth analysis of the material synthesis process and processing strategies utilizing polymer composites along with their applications.

## Types of failure and strengthening of carbon fiber reinforced polymer composites

In the advanced composites sector, continuous fiber-reinforced composites play a larger role than nanocomposites when it comes to mechanical qualities. The CFRP manufacturing process has multiple varying elements, of both chemical and physical inputs, which can affect things like surface quality due to coefficient of thermal expansion, wetting, *etc.* These defects can also contribute to various flaws in the composite laminate. Moreover, the failure modes found in composites are considerably more complex. It depends on the types of loads, physical qualities, and element microstructures. (Talreja, 1994). Typically, the failure mechanism of polymer composites is a fully random process, with damage dispersed throughout the composites (Dzenis, 1996). Before the final catastrophic breakdown, damage accumulates and combines to form macroscopic cracking. Moreover, the types of failure in composite materials differ significantly from those of metals. Here, the failure was governed by the propagation and expansion of a single crack until catastrophic failure occurred. As depicted in Figure 1, FRP composites typically experience multiple types of failure over their lifetime, including fiber/matrix debonding, interlaminar delamination, fiber breaking, and matrix cracking (Dzenis and Qian, 2001).

Matrix cracking theoretically occurs when the polymer tensile stress exceeds the matrix's ultimate tensile strength.

Fiber rupture occurs when the normal stress exceeds the ultimate tensile strength of the fiber. Moreover, fiber/matrix debonding depends on interfacial bonding or strength parameters. Due to the fact that fiber reinforcement is a two-dimensional architecture, the out-of-plane mechanical properties (interlayer fracture toughness and shear strength) of typical laminated composites are significantly lower than the in-plane properties. Interlaminar fracture has thus been identified as the most catastrophic and severe failure mechanism in composite materials. Due to these limitations, considerable effort has been devoted to identifying the failure modes of FRP composites for applications that are superior and more plausible. In addition, recent advances in nanotechnology have provided a promising avenue for improving the chemical, thermal, electrical, and mechanical properties of CFRP composites. Mechanical parameters such as shear and flexural strength and interlaminar fracture toughness can be enhanced by incorporating nanomaterials into laminated composites. In practice, nanostructured materials can either replace the resins used to produce composites or integrate within the interlayers of resin sandwiching the composite plies. Nanoscale materials such as nanoclay, nanofilaments, and carbon nanotubes (CNTs) have been investigated for the reinforcement of composite materials (Dzenis and Qian, 2001; Wu, 2003; Wu, 2009). Among a variety of nanomaterials, electrospinning-produced continuous nanofilaments have garnered considerable interest over the past decade. ENFs offer distinct advantages over other nanostructured materials, such as carbon nanotubes and clay nanoparticles, including low-cost production, continuity, flexible material characteristics, and fiber diameter. In addition, an overview of nanofiber production through electrospinning and other techniques is presented in this article.

Standard one-dimensional nanostructure materials include organic and inorganic nanoparticles, nanorods, carbon nanotubes, polymer, and Carbon nanofibers. The division of these varying types of organic and inorganic nanofillers can be shown in Figure 2. Among the aforementioned nanomaterials, carbon nanotubes are the most studied for increasing the mechanical properties of engineering materials. Nonetheless, due to the many factors such as agglomeration and poor dispersion properties, increasing experimental data have projected growing uncertainties regarding the CNTs' impact on the reinforcement of structural materials. In addition, the expensive cost of CNTs inhibits their widespread application in large structural components such as aviation or aerospace components. Clay nanoparticles are widely considered an evolution in terms of the reinforcing phase when it comes to innovative polymer nanocomposites. These nanoparticles can improve the stiffness, fracture toughness, and tensile strength of a wide variety of polymers (Subramaniyan and Sun, 2007). Since the first research in Toyota Inc., Japan, clay-reinforced polymer

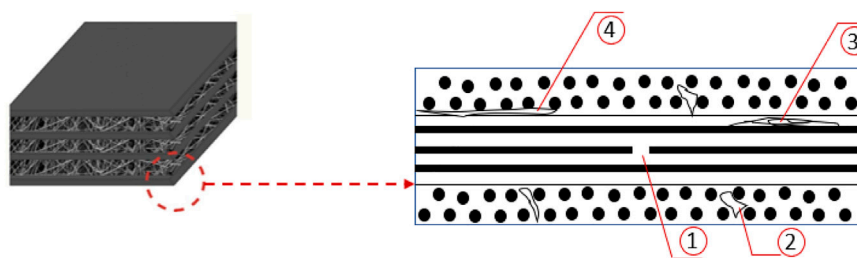


FIGURE 1

Common modes of damage in a cross-layer composite include (1) fiber breakage, (2) matrix cracking, (3) matrix/fiber debonding, and (4) delamination.

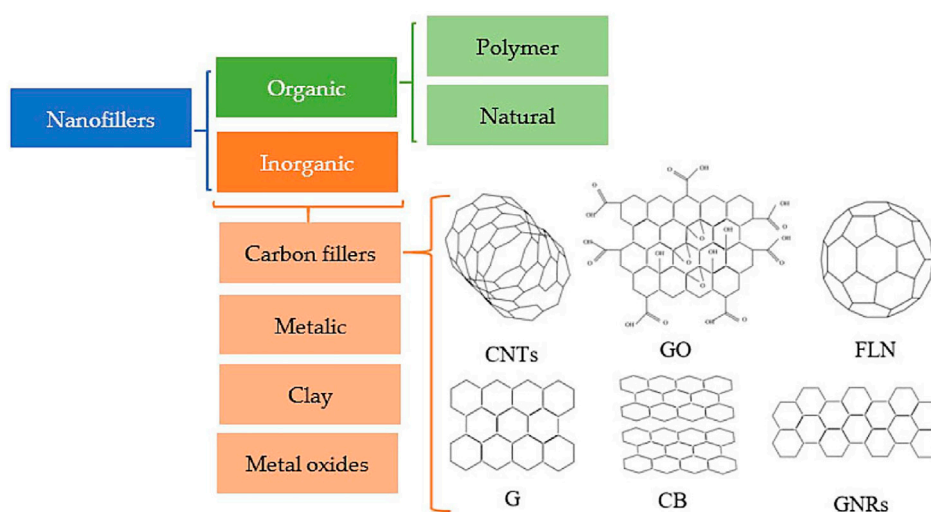


FIGURE 2

Different types of nanofillers (Ehsani et al., 2021).

nanoparticles have found uses in numerous industries, including automobile components. However, an experimental study on fiber-reinforced polymer composites found that nanoparticles of clay have a limited effect on interlaminar fracture toughness because clay platelets are equivalent to strengthening fibers (Subramaniyan and Sun, 2008). Recent research has demonstrated that functionalized carbon nanotubes strengthen the interlaminar characteristics of FRP composites (Sager et al., 2011) and electrospun polymer nanofibers (Wu, 2009) can be utilized. There has been no prior study on the interfacial toughening/strengthening of woven fabrics/epoxy structures made using electrospun thermoset CNT/epoxy nanofibers. As a result, we are very interested in employing the low-cost continuous nanofibers electrospinning technology to improve the mechanical characteristics of FRP composites.

## Carbon nanotube integrated polymer composites

Carbon is an incredibly versatile and resourceful chemical that can be used in most scientific situations and applications. Carbon can diverge into many different allotropes with varying properties and configurations (Zhang and Jiang, 2018). One allotropes that has been garnering much attention are carbon nanotubes (CNTs). In fact, many researchers have explored the potential of integrating CNTs into carbon fiber. A comprehensive table displaying many of their results can be shown in Table 1. It is well known that the base chemical structure of carbon consists of a one-dimensional (1D) layer of graphite, and when these layers are oriented in such a way that they “roll” onto each other, they form a cylindrical tube-like structure. When only one layer

**TABLE 1 Summary of mechanical properties improvement of carbon fiber-epoxy composite by carbon nanotubes.**

Material	wt %	Flexural strength increment (%)	Flexural modulus increment (%)	Tensile strength increment (%)	ILSS/IFSS increment (%)	References
MWNT/PEI	5.5%	—	—	—	ILSS: 170%	Kamae and Drzal, (2012)
CNT	1%	—	—	—	ILSS: 12%	Dong et al. (2014)
CNT-COOH	0.5%	59.2%	54.3%	—	27.2%	Zhang and Jiang, (2018)
MWCNT-T300	0.1%	15.1%	3.1%	17.6%	12.6%	Xiao et al. (2018)
CNTs	—	—	—	—	94%	An et al. (2012)
MWCNT	2.0%	—	<5%	<5%	—	Tehrani et al
Silanized CNT	—	55	11	—	—	Kim et al. (2020)
CNT (Functionalized/non-F)	0.1%	7/11	3.3/–1	7/–3.8	ILSS: 7.7/5.6%	Sánchez et al
MMWCT (avg)	—	—	—	7.53	ILSS: 6.2%	Zhang et al. (2019a)
CNT/PI-BDA	0.5%	—	—	—	ILSS: 102.9%	Wang et al. (2017a)
CNT	—	—	—	16	IFSS: 68.8%	Guo et al
CNT	0.5%	—	—	3.8	PFT (by CC): 24.1%	Kermansaravi et al
MWCNTs/GO-CF/E (Mode I)	0.25%	—	—	—	ILSS: 4.7% G <sub>IC</sub> :16.7%	Rodríguez-González et al. (2018)

of graphite is rolled, it is called a single-walled carbon nanotube (SWCNT), and multiple layers of graphite form multi-walled carbon nanotubes (MWCNTs) (Ahmad, 1999). The diameters of these cylindrical tubes typically range within the nanometer range, more than a billionth of a meter, and several microns in length. Research has shown that these tubes can reach diameters as narrow as 4 Å, the lowest it can theoretically be, while remaining energetically stable (Qin et al., 2000), and these small diameters have elevated CNTs into a prominent role within the composite industry. However, relative to graphite powders and soot products, the manufacturing costs of these nanomaterials remain a hindrance for its usage within the manufacturing industry (Hammel et al., 2004). Despite this, the outstanding properties that CNTs offer, branches the gulf of price and usability. Kamae and Drzal (2012) showed the development of carbon nanotube coated carbon fibers and the evaluation of their adhesion. A carbon fiber bundle was dipped into the solution, then squeezed and dried, obtaining MWNT/polyelectrolyte coated CF, which was then evaluated. As a result, the use of repulsive forces between the polyelectrolyte-treated MWNTs achieved a good dispersion of the MWNTs in water. Using the charge differential between the MWNTs and CF resulted in a uniform coating of MWNTs to the CF, also resin sizing and the MWNT coating combined resulted in good adhesion to the epoxy matrix. Incorporating MWNTs at the

CF/matrix interface resulted in improved mechanical properties, such as shear modulus and strength, increasing stress transfer, and subsequently IFSS. Also, using PEI as a cationic polymer caused high interfacial shear strength (IFSS), given the strong interaction between its amine groups and epoxy groups. The novelty of the experiment and research in this paper is to be able to coat CFs with CNTs by a process in which the CF is dipped into a water/CNT suspension.

In another study of manufacturing and characterization of carbon fiber/epoxy composite prepregs containing carbon nanotubes, it was shown that Epoxy was added to the CNT/acetone solution, mixed by ultrasonication, and degassed in a vacuum oven to remove acetone completely (Siddiqui et al., 2011) as shown in Figure 3B. To further disperse the CNT, a shear speed mixer was used. To select the optimal matrix material and prepreg parameters, four types of resin blends were studied, 0 wt%, 0.5 wt%, 0.7 wt%, and 1.0 wt% CNT. The viscosity changes were measured, and the effects of shear mixing speed, type of epoxy, and CNT functionalization were evaluated. Also evaluated were the effects of CNT on curing during the prepreg process. The study concluded that increasing the CNT content in the epoxy resin increased its viscosity. Such viscosity was lowered by using high-speed shear mixing and functionalization of the CNT. It was also concluded that the adverse effects of the higher viscosity could be mitigated by increasing resin temperature,

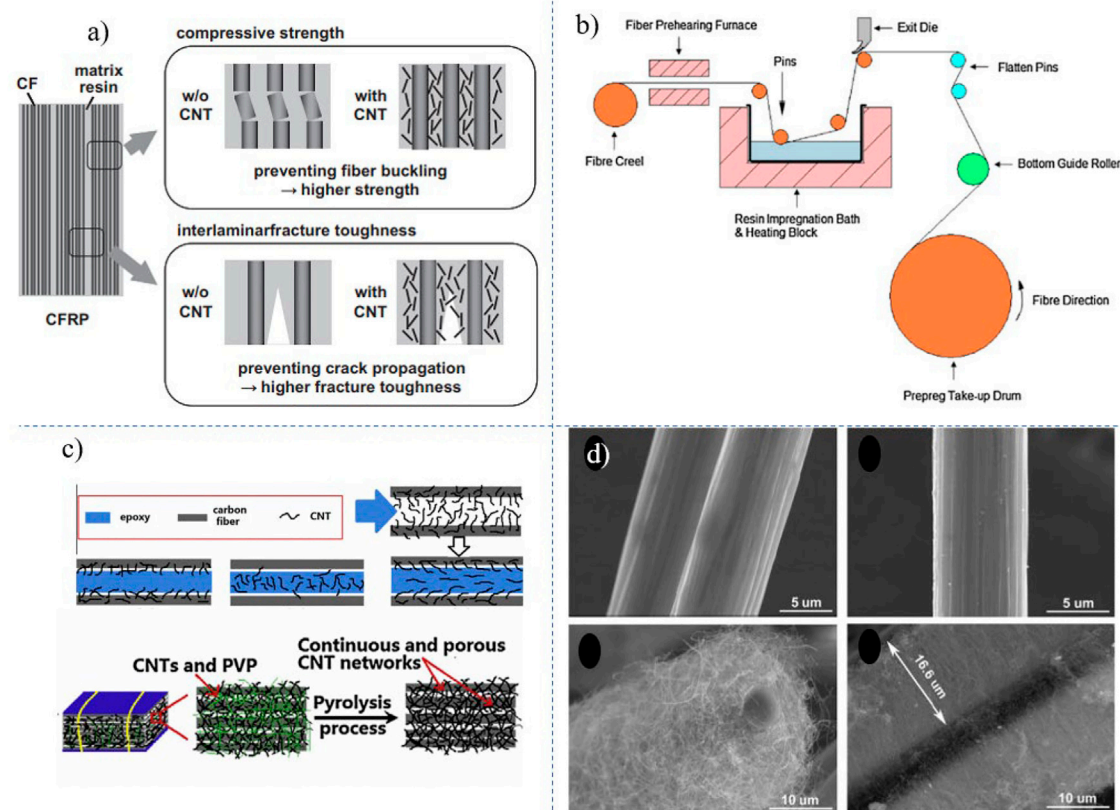


FIGURE 3

(A) Examples of anticipated property enhancements of CFRP due to CNT incorporation; (B) schematic of prepregger (Siddiqui et al., 2011), (C) Dispersion state of carbon nanotubes in fiber/epoxy composites: primarily in interface and matrix, demonstrating CNT morphology between fibers before (upper) and after (lower) epoxy was introduced into fabric (Dong et al., 2014). SEM images of unsized carbon fibers, displayed on top, and unaligned vs aligned MWCNTs displayed on the bottom respectively (De Greef et al., 2011).

fiber tension, and the exit dies gap of the prepreg. Also, the catalytic activity of surfactant treated CNT only became prominent at a CNT content of 1.0 wt%. The novelty of this study was to analyze how resin type and CNT content would affect various parameters in the whole prepreg process. The preparation of continuous carbon nanotube networks in carbon fiber/epoxy composite was shown in another work (Dong et al., 2014) as shown in Figures 3C, D. The materials used were polyacrylonitrile-based carbon fiber, plain cloth woven in a 0°/90° satin-weave. A CNT paste was used, with a CNT, water, polyvinyl pyrrolidone dispersant, weight ratio of 5:95:1, and CNT diameter between 10 and 30 nm and length between 1 and 5 μm. A glycidyl epoxy resin was used with a methylnadic anhydride curing agent. The mix ratio of curing agent to epoxy was 135 to 100 g. The CNT paste was diluted using deionized water, with concentrations of 1 wt% to 2 wt%. The CF fabric, fixed by glass slides, was immersed into this solution under a vacuum, then dried by freeze-drying, followed by heat-treatment under an argon atmosphere. Liquid epoxy resin was introduced

into three types of CF and cured. The process resulted in a significant increase in the electrical conductivity of the composite. It is also stated that an appropriate CNT network could increase the interlaminar shear strength of the composite. The study assesses that the process in question is expected to provide a new method to optimize the CNT dispersion rate in fiber fabrics and composites. The novelty of this study is the use of the freeze-drying method in the preparation of continuous CNT networks, and how feasible the process would be.

The effect of carbon nanotubes on the damage development in carbon fiber/epoxy composites was shown in another work (De Greef et al., 2011). The materials used in this study were a balanced carbon twin 2/2 fabric, with an areal density of 300 g/m<sup>2</sup>, woven from 6 K yarns of AS4C GP carbon fiber. A CNT modified resin was used, based on liquid Bisphenol-A epoxy resin, with a high concentration of NC 700 multi-walled carbon nanotubes. The CNTs have an average diameter of 9.5 nm. The no-CNT composites utilized Epikote 828LVEL epoxy and 1,2-diaminocyclohexane Dytex DCH-99 hardener. The experimental

methodology utilized consisted of three steps. The first step consisted of tensile static tests and acoustic emissions registration. The second step focused on identifying characteristic thresholds of damage from the first step. The third step investigated the damage patterns by using X-ray and SEM. The results of the study showed no improvement of the young's modulus in the fiber direction, but a slight improvement in strength (3.1%) and strain-to-failure (4.6%). An improvement in the three damage development thresholds ( $\epsilon_{\min}$ ,  $\epsilon_1$ ,  $\epsilon_2$ ) 30%, 42%, and 56% were observed, as well as a reduced number of medium energy events and an increase in low energy events in non-engineered fiber reinforced composites (nFRC). A reduced density of transverse cracks was also observed (15.7%–10%), but isolated debonded fibers were found. The novelty of this study was the use of acoustic emissions as a method to investigate the effects of CNTs on transverse cracking in nFRCs.

One study found that controlling the orientation and length of carbon nanotubes grown on carbon fibers increased the interfacial strength of carbon fiber/epoxy composites (Lv et al., 2011). The materials used were carbon fiber based on polyacrylonitrile with a high modulus and an average diameter of 7.5  $\mu\text{m}$ . Thermal treatment at 800°C in the presence of argon yields CFs without dimensions. A matrix of bisphenol-A epoxy resin was utilized. ICVD in a reactor corundum tube furnace was the method for the growth of MWCNTs on CFs. To align the MWCNTs on CFs, the surface of the CNTs was treated by immersing them in toluene containing 5% tetraethoxy silane and 5% silicon tetrachloride. The CFs were coated with a solid SiO<sub>2</sub> layer after hydrolysis and pyrolysis. The chemical composition before and after the treatment was characterized using X-ray photoelectron spectroscopy. SEM and TEM were used to analyze the properties of the MWCNTs and surface-modified CFs. The surface characteristics of unsized CFs and MWCNT-CF hybrids were determined by nitrogen absorption, and the wettability of such hybrids with epoxy resin was measured in a drop-on-fiber system using the generalized drop length-height method. The tensile strength of each fiber was measured using a WDW-50/100 Microcomputer-Control Electronic universal Testing Machine to determine the effect of CNT growth on axial properties. In addition, single fiber fragmentation tests were conducted to evaluate the fiber/matrix interface. The MWCNT-CF hybrid increased the specific surface area by two orders of magnitude, according to the study's findings. The contact angle test demonstrated excellent wettability. Depending on the orientation and length of the MWCNT arrays, the IFSS improvement between the MWCNT-CF and the epoxy resin varied. With MWCNT arrays measuring 47.2  $\mu\text{m}$  in length, the IFSS was enhanced by as much as 175 percent. The novelty of this study was the analysis of IFSS in MWCNT-CF hybrids based on the orientation and length of the CNTs, as well as the analysis of the hybrid's physical properties.

The interfacial enhancement of carbon fiber/epoxy composites has been investigated utilizing a simple approach for depositing commercially functionalized carbon nanotubes on the fibers (Li et al., 2013) as shown in Figure 4A. The materials used for this study were two types of carbon fiber, T700SC yarns of 1200 filament count (7  $\mu\text{m}$  diameter, circular cross-section), and T300B yarns of 3000 filament count (7  $\mu\text{m}$  diameter, irregular circular, or elliptical cross-section). Both have a sizing content of 1 wt%. Two types of MWCNTs were used, MWCNTs functionalized with carboxylic acid (COOH-CNT) and functionalized with hydroxyl groups (OH-CNT), with lengths varying from 0.2 to 2  $\mu\text{m}$ , and diameters between 20 and 40  $\mu\text{m}$ . For the matrix, a diglycidylether of bisphenol A based epoxy resin (YD-128) was used, as well as a polyether amine-based hardener (EC301). The preparation process began with the CNTs being dispersed in de-ionized water, obtaining a concentration of 0.05 wt%. After, the CF bundles were immersed in a bath with the CNT suspension, then dried at two different temperatures. The CNTs in suspension had their structures examined by a TEM. Another suspension was prepared to contain a non-ionic surfactant polyoxyethylene octyl phenyl ether to increase CNT content. TEM and FTIR were used to observe the dimensions of functionalized CNTs and to confirm the functional groups on the surface respectively. With the CNT-depositing completed, the bundles were examined by an SEM, to evaluate the adherence of CNT onto the fiber surface. Surface roughness was determined by an AFM. To test the dynamic contact angle and determine wettability, the modified Wilhelmy plate method was used. FTIR was also used to confirm if the functionalized CNTs can react with the industrial sizing of CF. Single fiber-composite fragmentation was used to assess the influence of CNTs on the interfacial bonding by testing its IFSS. The results of the study show that the CNT deposition process improved the interfacial shear strength of the composite. It also showed that the increased interfacial bonding between the CNT-hybridized carbon fiber and epoxy matrix is due to the interfacial friction, chemical bonding, and resin toughening near the interphase. There were also improvements in the tensile strength and interlaminar shear strength of the composite.

The novelty of the study is the use of evaluation methods such as investigating IFSS, focusing on the interfacial reinforcing mechanism, effects of CNT depositing on fiber surface morphology, wettability of epoxy on fiber, chemical bonding, and fracture pattern to improve the interfacial strength between CNT-deposited CF and epoxy matrix. Improving interfacial and mechanical properties of nanotube-sized carbon fiber/epoxy composites as studied (Zhang et al., 2019a) in Figure 4C. The study utilized materials that were unsized, commercial JH-T800 carbon fiber, with an average 5  $\mu\text{m}$  diameter and sizing content of approximately 1 wt%. Multiwalled carboxyl-functionalized CNT (MWCNT-COOH) with 10–30  $\mu\text{m}$  diameter and MWCNT-NH<sub>2</sub> CNTs were used. For the matrix, a diglycidyl ester of aliphatic cyclo tri-functional epoxy, with 4,4'-diaminodiphenylmethane



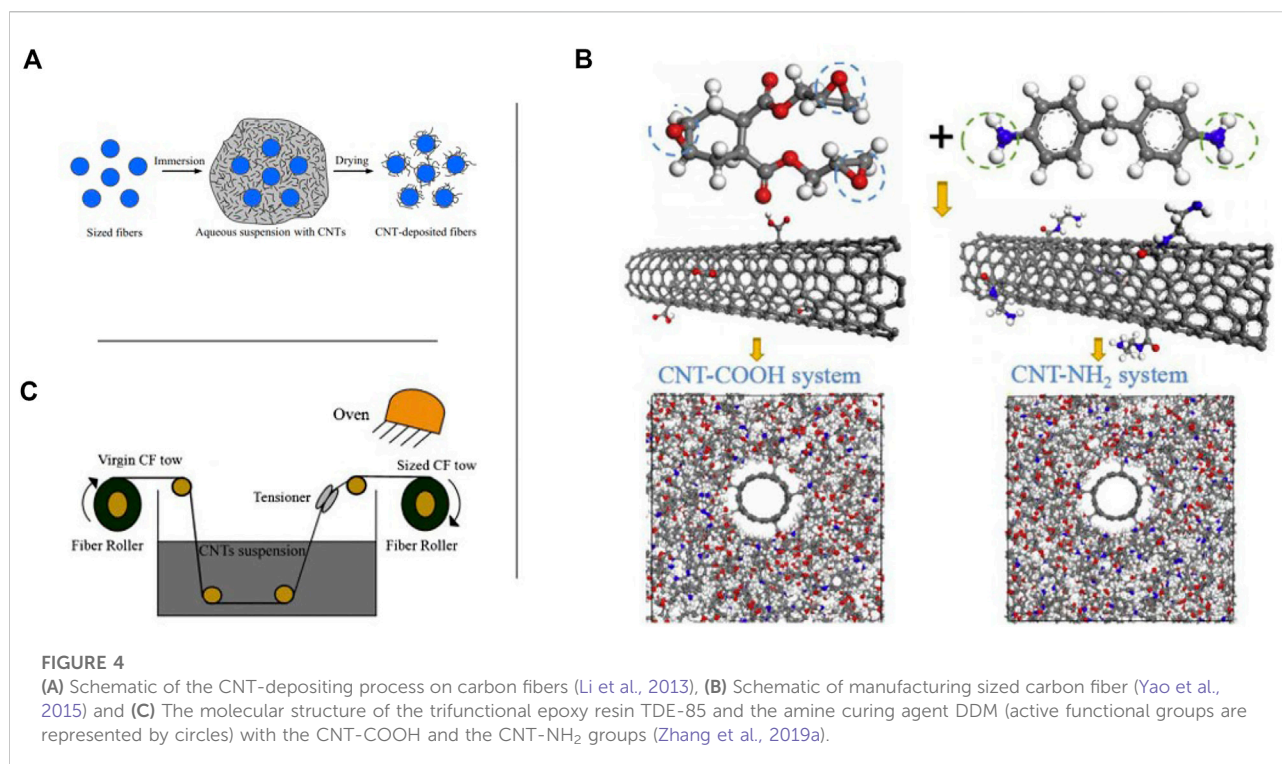


FIGURE 4

(A) Schematic of the CNT-depositing process on carbon fibers (Li et al., 2013), (B) Schematic of manufacturing sized carbon fiber (Yao et al., 2015) and (C) The molecular structure of the trifunctional epoxy resin TDE-85 and the amine curing agent DDM (active functional groups are represented by circles) with the CNT-COOH and the CNT-NH<sub>2</sub> groups (Zhang et al., 2019a).

curing agent was used. The samples were prepared by dispersing both MWCNTs in the sizing agent at 0.5 wt%, then immersing the CFs in the solution for a set time, followed by drying it. Both single fiber and unidirectional composite samples were created (average volume fraction of CF of 60%). Dimensions and chemical composition of functionalized CNTs were observed by a TEM and XPS respectively. Fracture morphology and CF surface were analyzed *via* SEM, and surface roughness was determined by an AFM. To evaluate the IFSS of single fiber composites, single fiber fragmentation tests were performed under shear loading. For unidirectional composites, interlaminar shear strength (ILSS) and flexural properties were tested by a universal testing machine. A model was created to investigate the relationship between components, structures, properties of the system, and the effects of functionalized CNTs in the sizing agent. The MD simulations were conducted using Material Studio 6.0 Software. The interaction and interfacial bonding energy, mean-squared displacement, radial distribution function, and relative concentration were calculated using different equations. The results of this study showed that CNT-COOH-sized CFs had a significant performance improvement of 10%, 27%, and 59% in the IFSS, ILSS, and flexural strength respectively when compared to commercial CF. CNT-NH<sub>2</sub>-sized CF showed adverse effects on IFSS and ILSS and a smaller improvement in flexural strength when compared to CNT-COOH-sized CF. The interfacial bonding between fiber and matrix still needs to be clarified. The novelty of the study is the use of experiments

and simulations to investigate and detail the mechanisms of different functionalized CNT-reinforced composites on the surface of CFs, and their effects on the molecular structure of the matrix and the properties of the composites.

Another study was conducted on interfacial and mechanical improvement of carbon fiber/epoxy composites by depositing multi-walled carbon nanotubes on fibers (Xiao et al., 2018). The materials used in the study were a monodirectional carbon fiber fabric, S-MWNT-1020, with a 0.5–2  $\mu\text{m}$  length, 10–20 nm diameter, and a purity greater than 97%. E-44 epoxy resin (0.44 mol/100 g epoxy value), and a D-230 polyether amine curing agent were used. The MWCNTs were dispersed in de-ionized water by ultrasonication to obtain a CNT suspension of 0.1 wt% concentration. CF fabric was immersed in the suspension, for a set time, then dried at two different temperatures. The sample laminates were prepared by compression molding. After deposition, the CF fabric was torn apart and examined by a SEM to evaluate CNT/fiber adhesion. Tensile strength and modulus were measured by the electronic universal machine, as well as a three-point bending test. ILSS was also tested. The test specimens had their mechanical properties tested after being placed in sealed plastic bags with distilled water at a certain temperature for 24 h and dried. The heat resistance was measured by DSC, and the micromorphology of the fracture surface was examined by SEM. The results of the study showed an improvement in the interfacial interaction and interfacial bond strength between MWCNTs-T300 and EP, and a reduction in the contact angle



(40.3°). The interfacial energy and adhesion work were increased by 49.5% and 4.7% respectively, compared to original T300 fiber. The mechanical properties of MWCNT-T300/EP laminated composite also improved. Flexural strength, tensile strength, and interlaminar shear strength increased by 15.1%, 17.6%, and 12.6% respectively. After CNT deposition, the (MWCNT-T300/EP) composite interfacial strength is improved. The novelty of the study was using an aqueous suspension deposition method to coat CF with MWCNTs to improve interfacial and mechanical properties, evaluating surface morphology, wettability, and interfacial properties, as well as testing mechanical properties.

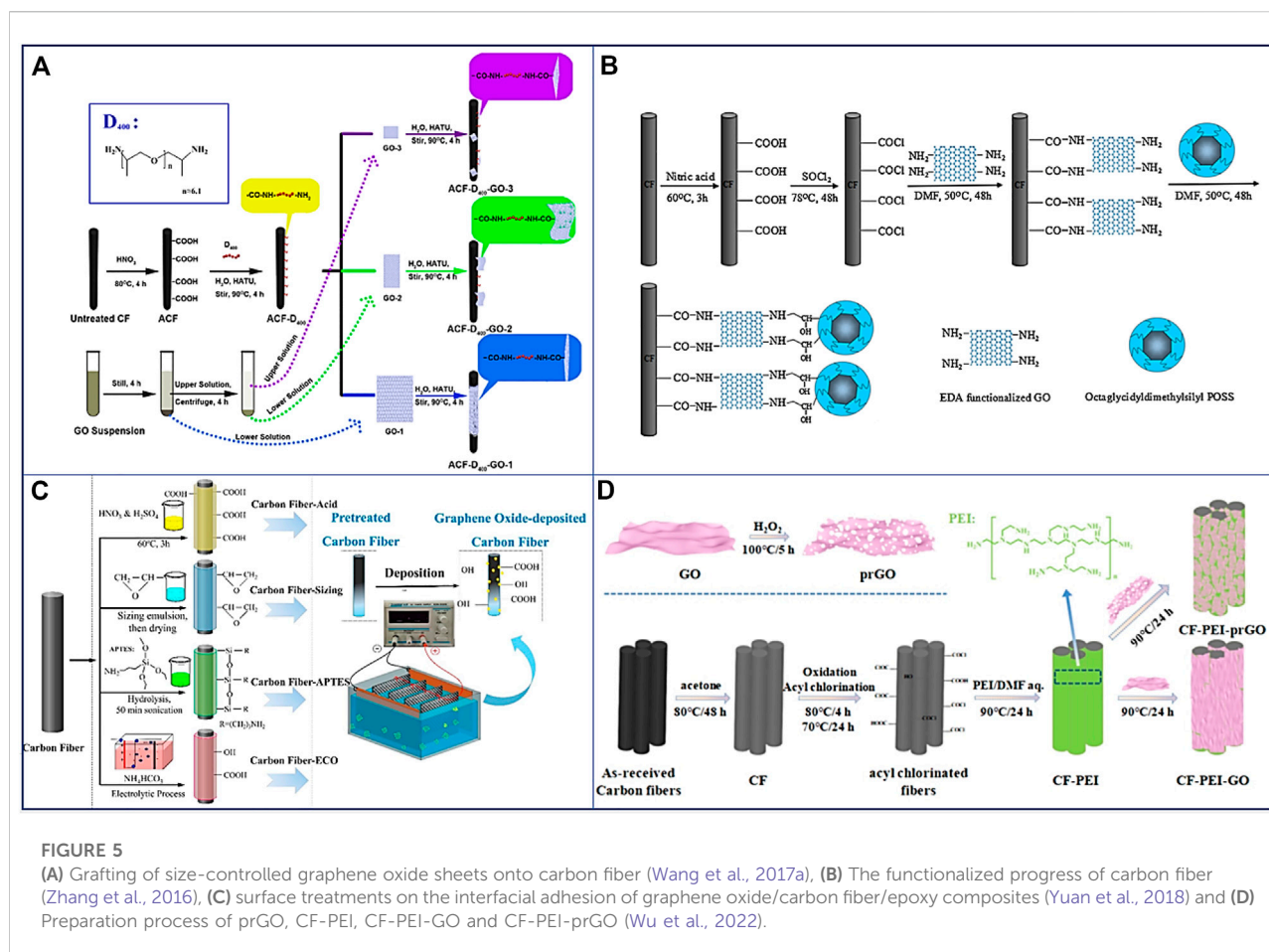
Preparation and characterization of carbon nanotube-hybridized carbon fiber to reinforce epoxy composite has been explored (An et al., 2012). The materials used in the study were an unsized polyacrylonitrile-based carbon fiber, analytical grade reagents of ferrocene and acetone, E-51 epoxy resin consisting of diglycidyl ether of bisphenol-A, and phthalic anhydride and benzyl dimethylamine as curing agents. The preparation of the CNT-hybridized CF happened in a single zone horizontal quartz tube furnace, using acetylene (carbon source), ferrocene and a  $H_2/N_2$  carrier gas mix. CFs were placed at the center, and a pure nitrogen atmosphere was created. At 700°C, Ferrocene-acetone introduced, and an aerosol is formed, ferrocene is decomposed into catalyst, depositing onto CFs. At 750°C,  $C_2H_2$  is introduced, and CNT growth starts. After a set time, carbon source stops being fed, and power is turned off to allow for cool down. Both a monofilament of CNT/CF hybrid composite and multifilament unidirectional CNT/CF hybrid composite were created. SEM and high-resolution transmission electron microscopy were used to characterize the morphology and microstructure of the CNT/CF hybrid. BET method and an absorption instrument were used to calculate the specific surface area of CF and CNT/CF hybrid. Single fiber tensile tests were conducted using a tensile testing machine, with an optical microscope being used to measure each specimen's diameter. To calculate IFSS, single fiber pull-out tests were conducted using an interfacial micro-bond evaluation instrument. Using a universal testing machine, the tension fracture for the cured epoxy composites was performed, and the morphology and structure of the fractured section were evaluated by a SEM. The results of the study show that grafting of CNTs on the CF surface resulted in a near threefold increase in BET surface area. The CF's tensile modulus remained similar while tensile strength had an approximately 10% decrease. Interfacial shear strength increased by 94%. The presence of CNTs resulted in different fracture morphology of the composite. There was an increase in fiber surface area, providing a stronger interfacial bonding between the fibers and matrix. The novelty of the study is the use of a newly developed aerosol-assisted chemical vapor deposition method to create CNT/CF hybrid composites by

using several methodologies and instruments to evaluate the material.

Optimization was done for interfacial microstructure and mechanical properties of carbon fiber/epoxy composites *via* carbon nanotube sizing (Yao et al., 2015). The materials used in the study were short hydroxyl MWCNT of 95% purity, length of 0.5–2  $\mu m$ , and -OH content of 1.76%, T700S carbon fibers, JC-02A modified epoxy, JH-0511 modified 2-ethyl-4-methylimidazole accelerant, and a tetrahydro phthalic anhydride curing agent. To remove the commercial sizing and help CNTs obtain a dispersion in the small inter-fiber-spaces of CF bundles, CFs were refluxed by acetone. The CNTs were dispersed in ethyl alcohol and sonicated for 2 h forming a suspension. The CF is then sized with a self-made device, passed through the sizing agent suspension, wound up on a roller and dried. The content of CNT on fiber surface was controlled by number of sizing treatment. Unidirectional CF composites with volume fraction of 45% were made. A SEM was used to detect CF surface topography and the fracture surface of composite specimens. A universal testing machine performed a short beam shear test and a flexural test to assess the influence of the sizing process on interfacial properties. Composite interfacial microstructures were investigated using EDS-equipped SEM and f-AFM. SEM for the distribution of carbon elements in the interference layer of composites and f-AFM for the distribution of modulus. The results of this study indicate that the sizing deposition method is a simple and continuous technique for producing CF/CNTs/epoxy composites on an industrial scale. In addition, a gradient transition interphase was discovered, allowing for the possibility of uniform stress transfer. In addition, it was discovered that a uniform CNT distribution on a CF surface caused the interface thickness of the composite's gradient structure and mechanical properties to increase gradually as the sizing treatment time increased. Interlaminar shear strength and flexure strength increased by 13.45% and 20.31%, respectively, in a quintuple-sized CF with a wider gradient interphase. However, excessive sizing will result in diminished mechanical properties. This study investigates the novel aspects of incorporating CNTs *via* a multi-sizing process into the interfacial microstructure and its relationship to composite performance.

## Incorporation of graphene in carbon composites

Graphene has often times been added to CF/epoxy composite materials to improve their mechanical and electrical properties (Hadden et al., 2015). This is possible due to it being a single-layered two-dimensional allotrope of carbon, which grants it greater properties than flax fibers like CNCs. Graphene, outside of its pristine form, has two main derivatives within the composites industry, graphene oxide (GO) and reduced



graphene oxide (rGO). Other form of graphene that have been researched are graphene nanoribbons (GNR) and graphene oxide nanoribbons (GONR) (Chien et al., 2015). Graphene fibers have also been explored as a potential substitute for carbon fiber, due to their large lateral crystal size. This allows it to potentially have greater mechanical, electrical, and thermal performance (Xu and Gao, 2015; Xu et al., 2016).

The use of graphene as a nanofiller, specifically graphene oxide (GO) has caught the attention of many researchers throughout the world. Researchers like Aduk et al. investigated the effects of the mechanical properties of carbon fiber with incorporated GO (Adak et al., 2018). To create the GO, graphite flakes were dispersed in THF at concentrations of 0.05 wt%, 0.1 wt%, 0.2 wt%, and 0.4 wt%. The GO/carbon fiber composites were created using the VARTM process. Through testing, a maximum of 0.4 wt% GO was used, but the best results were found at 0.2 wt% GO. Tensile testing results show an increase of 33.8% in tensile strength, a 19.7% increase in Young's modulus, and an 83.1% increase in toughness. While both the flexural strength and modulus testing showed increases of 35.7% and increases of 31.3% for flexural modulus. This is similar to the results found by Wang et al. where desized carbon

fibers and GO were made using carbon fibers and natural graphite flakes to increase the overall strength of the carbon fibers (Wang et al., 2017a). D400, concentrated nitric acid, a coupling agent (HATU), and deionized water was also used to create the GO mixtures. To facilitate separation, the GO suspension was placed in a burette. The solution at the bottom was labeled GO-1. The remaining solution was separated, centrifuged, then divided into GO-2 and GO-3 subgroups. The preparation of these materials can be visually shown in Figure 5A. SEM, TEM, and AFM were utilized to determine the structure, roughness, and thickness of the GO sheets. XPS analysis revealed a greater concentration of oxygen functional groups. The FTIR analysis revealed that amino groups were incorporated into the carbon fibers and that GO was covalently bonded to them. Dynamic contact angle tests performed to determine wettability revealed an increase in the surface free energy. Tensile strength tests revealed an increase in tensile strength from 4.72 GPa to 5.02 GPa when compared to GO-2 sheets. IFSS testing revealed an improvement in compressive strength from 46.8 MPa for untreated carbon fibers to 82.2 MPa for GO-2 sheets. This group developed a method for grafting GO onto carbon fibers that was simpler and

more environmentally friendly than previous methods. Their methodology made use of fewer resources and chemicals. Additionally, the separation of the GO solutions is time-consuming and results in lower quantities of each solution. In a study by [Altin et al. \(2020\)](#) an advanced Hummers technique was used to rectify this issue.

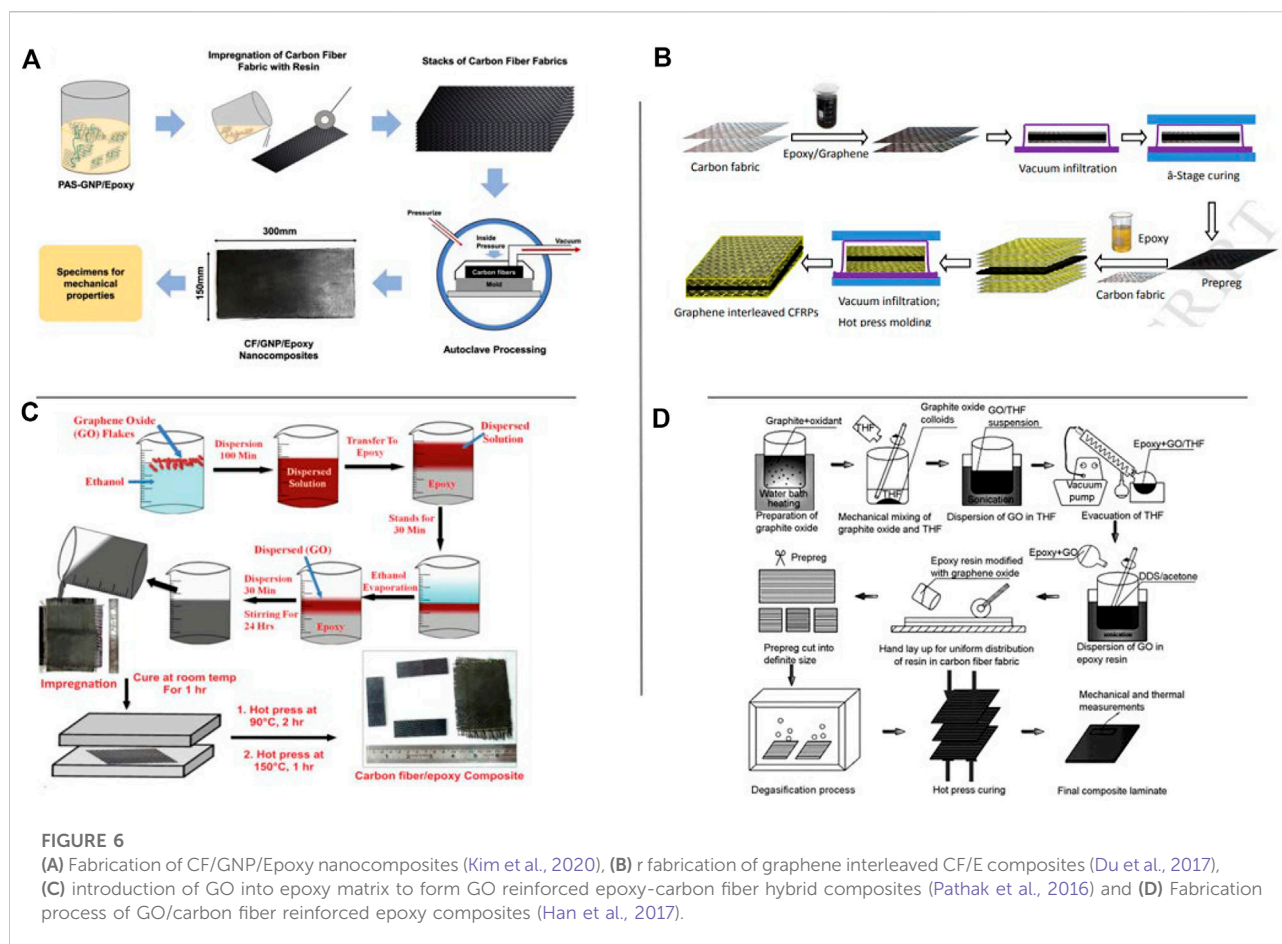
In this study, the production of GO was accomplished using this enhanced Hummers technique, where spraying 5, 10, and 20 ml of GO onto three samples produced 0.5 wt% GO/CF, 1 wt% GO/CF, and 2 wt% GO/CF, respectively. The FTIR study demonstrated that graphite was successfully oxidized by Hummers' technique and that oxygen functional groups were grafted. In mechanical tests, the 2 wt% group had the greatest gains in young's modulus and tensile strength at 23.5% and 54.1%, respectively. Calculations using TGA revealed that the thermal stability of the samples reduced as the amount of GO increased. This modification process of spraying GO has shown to be efficient and cost-effective as this process was successful in coating carbon fibers with GO and improving mechanical properties. When researching GO, the use of diamines has been scarcely explored, but [Ashori et al. \(2015\)](#) researched ways to enhance the properties of carbon fiber and GO through functionalization with three diamines. In his investigation, GO was functionalized in three ways: first with ethylenediamine (EDA), then with 4,4'-diaminodiphenyl sulfone (DDS), and finally with p-phenylenediamine (PPD). The graphene oxide was made with, 1 g graphite powder, combined with 18 ml H<sub>2</sub>SO<sub>4</sub>, 9 ml HNO<sub>3</sub>, and 11 g KClO<sub>3</sub>. GO and functionalized GO/CF (FGO/CF) were added at concentrations of 0.1 wt%, 0.3 wt%, and 0.5 wt%. This combination was oxidized, washed, and then dried in a vacuum. The fibers were orientated at 0°, 90°, and 0° angles *via* hand lay-up. FTIR analysis revealed that GO contains oxygenated functional groups as well as functional groups containing EDA, DDS, and PPD. Tensile testing revealed increases in tensile strength with 0.3 wt% of each concentration showing the greatest rise, specifically PPD-FGO showing the highest increase of 22.5%, while flexural strength increased by the greatest amount, 76% when 0.5 wt% PPD-FGO was used. While GO has been used to improve the mechanical qualities of CF, the use of three differing diamines is a unique solution to increasing CF properties, but once again the long preparation time hinders its usage.

In another study, [Yuan et al. \(2018\)](#) reviewed the results of GO engaging in oxidative pretreatment and non-oxidative pretreatment before electrophoretic deposition (EPD) to enhance CF properties. As shown in [Figure 5C](#), CF went through surface modifications of acid treatment oxidation, sizing treatment, APTES coupling agent treatment, and electrochemical oxidation. The EPD was completed using CF as the working electrode and a graphite plate as the counter electrode. Four samples were produced as GO/CF-Acid, GO/CF-Sizing, GO/CF-APTES, and GO/CF-ECO. Composite laminates

were then combined with each sample and produced using VARTM method. SEM and AFM analysis showed overall increased surface roughness and added topography, but the APTES group showed a lower Ra value than untreated CF. Interfacial shear strength testing showed the highest increase of 50% by the GO/CF-ECO sample. The goal of [Yuan et al. \(2018\)](#) was to show the effects of surface pretreatments of CF when combined with EPD of GO, and overall, this process was successful.

Another successful and novel process was completed by [Han et al., 2017](#) who for the first time, used GO combined with the organic solvent THF to boost the ILSS of CFRP. A modified version of the Hummer process was employed to create GO, which was then ultrasonically treated. The GO was then disseminated in the epoxy resin with the aid of. 0.05 wt%, 0.1 wt%, 0.2 wt%, and 0.4 wt% THF, after which, the cured resins were then painted on carbon fiber textiles. The FTIR and XPS analyses confirm that GO contains a wide range of functional oxygen groups. AFM image reveals a GO sheet thickness of 2–4 nm. When GO levels were low, TEM pictures revealed good dispersion of GO within the matrix, however substantial aggregation of GO layers was observed when GO content increased. After mechanical testing, the ILSS rose by 8.05% at 0.10 wt%, relative to epoxy samples without modifiers. Researching the use of GO and THF increased the ILSS of CFRP successfully while creating sheets that were thin and evenly spread when the weight percent was low, despite the novelty of this solution. Additional research aimed to do the same increase the mechanical properties of carbon fiber through GO ([Pathak et al., 2016](#)). Here, GO is added into the matrix using a wet transfer procedure to increase ILSS and bending strength by varying GO weights. The GO was produced using the Hummer's technique, and then washed in 5% HCl. The cleansed solution was then dried in an oven to generate GO flakes. Seven concentrations of CO content were created ranging from 0.0% to 0.6 wt% GO and tested. The creation of said concentrations can be seen in [Figure 6C](#). The greatest increases were observed at 0.3 wt%, after which, increases were affected at higher GO concentrations due to agglomeration. ILSS in samples containing 0.3wt% was found to have increased by 25%, with the flexural strength and modulus improved by 66 and 70 percent, respectively. Despite using conventional methods like the wet transfer method, increases in the mechanical characteristics of the material were achieved.

The same can be said in another attempt to raise the IFSS of carbon fiber by [Jiang et al. \(2017\)](#) in which, GO was disseminated into sizing agents at concentrations of 0, 0.2, 0.5, 1, and 2 wt%. After preparing a sizing agent with a GO concentration of 2 wt%, the mixture was combined and placed onto the carbon fibers. The SEM images of the CF samples revealed that the amount of GO sheets increased as the GO level rose, but as the wt% reached 2%, agglomerates were observed. Single fiber pull-out experiments were conducted to determine the IFSS of each concentration,



with the highest value found at 1% GO at 110.3 MPa, an 37.2% increase in strength. When determining impact resistance, this concentration also gave the highest increase at 79.16 kJ/m<sup>2</sup>, an increase of 45%. At 1 wt%, results were maximized, demonstrating the potential for enhancing IFSS by modifying GO sizing agents. Due to the great importance delamination can cause studies were also conducted to increase failure mode resistances (Du et al., 2017). GO was produced from graphite powder using a modified version of Hummer's procedure. Figure 6B visualizes the creation of CF composites, where graphene powder was disseminated in acetone and epoxy was subsequently added. Single-edge notched bend (SENB) tests were used to quantify fracture toughness. The sample with the biggest gain, 74%, was the 1.0 wt% sample as mode one interlaminar fracture energy was enhanced by 145% with this percentage. The same could be said concerning the samples' thermal characteristics, as samples containing 1.0 wt% exhibited a 30% drop in thermal expansion coefficient. In this investigation, the thermal reduction method of creating GO proved effective. The mechanical properties increased the most and the thermal coefficient decreased the most at a concentration of 1.0 wt%. It is also of utmost importance that the properties of carbon fiber

with GO are known in most environments. Qu et al. (2020) at 77 K, studied the cryogenic flexural characteristics of CFRP by augmenting the material with different percentages of graphene oxide. Graphite granules were oxidized with acid to produce GO at concentrations ranging from 0 to 0.5 wt%. The graphite was disseminated in deionized water, subjected to sonification, dried, dispersed in acetone, and subjected to sonification once again, to finally be incorporated into epoxy matrices and carbon fiber. AFM images determined the thickness of GO nanosheets to be between 0.5 and 1 nm, with XRD examinations reaffirming that GO effectively formed layered sheets. FTIR revealed the functional groups responsible for GO's effective dispersion in the matrix. Three-point bending tests were executed and 0.2% GO was the best-performing sample, with gains in flexural strength, flexural modulus, and ILSS of 6.4%, 9.6%, and 17.6%, respectively, at room temperature. At 77 K, these increases were 4.9%, 7.1%, and 8.7% respectively. While the biggest property enhancements were observed in samples at ambient temperature, the 77 K sample increases were significant and demonstrate evident application benefits in cryogenic environments. Despite determining the mechanical properties of carbon fiber at extreme temperatures, other



methods shown in this paper have demonstrated greater increases in room temperature, and this study could benefit from employing these approaches.

Other forms of graphene have been explored and used as nanofillers as researchers looked at additional ways to stretch our knowledge of graphene's effect on carbon fiber. Graphene nanoplatelets (GNP) are one of such forms. A study by Hawkins and Haque (2014) investigated the fracture resistance of carbon fiber-reinforced epoxy when reinforced with GNP. Before testing, G-Ep and C-G-Ep were manufactured using 0.1 wt% graphene, in which G-Ep was formed by mixing graphene nanopowder and acetone, followed by combining it with epoxy resin, heating it, and curing it. Other G-Ep samples with differing graphene concentrations were created without the use of acetone or high shear mixing, creating three samples: Carbon-epoxy (C-Ep), graphene-epoxy (G-Ep), and carbon-graphene-epoxy (C-G-Ep). Using SEM, the roughness of the fiber surfaces in G-Ep was found to be greater than in neat epoxy. This suggests increased fracture resistance. Three-point bending was used and verified that the fracture toughness of G-Ep rose by 128% relative to carbon fiber epoxy itself. As shown in this study, incorporating 0.1% graphene nanoplatelets significantly increased fracture toughness, which could be further improved. One improvement, suggested by the authors, was to improve the method of graphene dispersion to reduce graphene aggregation and enhance its mechanical characteristics. Another reason for GNP usage is its ability to be functionalized. Hence the usage of Poly (4-aminostyrene) (PAS) to non-covalently functionalize GNPs, was utilized by Kim et al. (2020) to boost fracture toughness and ILSS in CF composites. For the preparation of functionalized GNPs, PAS was dissolved in DMF, and GNPs were then added. These GNPs were subsequently dissolved in acetone and epoxy resin was applied for curing on CF. SEM imaging revealed that PAS-GNPs were uniformly dispersed inside the epoxy matrix, whereas GNPs without PAS exhibited aggregation. As a result, PAS-GNPs were able to further boost mechanical characteristics. This was verified when the ILSS of 4 wt% PAS-GNPs was raised by 252% and fracture toughness was increased by 142%. The use of functionalized GNPs and the application of PAS, permitted a more uniform dispersion in the matrix at high wt%. This resulted in a significant enhancement of mechanical characteristics.

In fact, Qin et al. (2015) allowed CFs to be coated with GNPs utilizing a continuous coating technique to evaluate 90° and 0° flexural strength as well as ILSS. SEM imaging revealed a homogeneous coating with additional roughness on the fibers. The flexural strength of GNP-coated CFs was 82% greater than that of uncoated CFs when tested at 90°. 0° testing revealed a 7% increase. Compared to uncoated CFs, the ILSS increased by 19%. GNPs have also been researched and their properties explored virtually (Hadden et al., 2015). The GNP molecules were modeled using molecular dynamics (MD) and micromechanical modeling. This studies the mechanical impact of adding graphene nanoplatelets (GNP) to carbon

fiber and epoxy composites. The molecular structure of GNP layers was modeled, and their mass density was analyzed. To validate their findings, experimental tests were conducted. Neat epoxy used 100 g of EPON 862 with 26.4 g of EPIKURE, the curing agent. GNP/epoxy used an "appropriate amount" of GNP mixed with EPIKURE and was incorporated into carbon fiber *via* a winding process. This GNP/epoxy/carbon fiber composite was cut into sheets and then cured. Mechanical testing was then completed to determine the tensile strength, elastic modulus, and normalized modulus for this material. This analysis outlined the potential for computational multiscale modeling of GNP/epoxy composites to predict elastic properties. Overall, it can be concluded that the method developed is accurate and can provide insight into mechanical behaviors, despite some discrepancies between the model and experimental data.

Other alternatives to graphene oxide are porous graphene oxide (prGO), silanized graphene oxide (SGO), and reduced graphene oxide (RGO), with each showing similar increases in carbon fiber properties relative to GO, if not more. Chemical grafting and prGO were utilized by Wu et al. to increase the interfacial adhesion of CFRPs, in which the GO and prGO were grafted onto CFRP by means of a chemical process (Wu et al., 2022). After the prGO and GO solutions were prepared, SEM pictures were captured to investigate the new structure of the changed fibers. Due to the grafting of GO and prGO, the fibers exhibited ridges and enhanced roughness. XPS analysis revealed greater O/C ratios in prGO samples compared to GO samples, indicating that prGO includes more oxygen groups. According to contact angle studies, the surface energy of the modified fibers increased as the contact angles decreased. All these factors contributed to a 78.64% increase in the interfacial shear strength of fibers containing prGO, while GO demonstrated a gain of 48.54%. The innovation was the utilization of prGO to enhance the CFRP characteristics. As this modifier had never been done previously, the overall improvement was successful and substantial. SGO also displayed similar success, when it was formed in order to increase GO dispersion and adherence to epoxy (Chen et al., 2014). Here, graphene oxide was functionalized with silane coupling agents to form silanized graphene oxide (SGO). After soaking unmodified carbon fibers into modified epoxy mixtures, samples with carbon nanoparticle concentrations of 0.2 wt%, 0.5 wt%, and 1 wt% were obtained. AFM measurements revealed that GO and SGO have similar thicknesses, with SGO having a greater thickness on the fibers and the XPS study verified that the functionalization of GO to SGO was effective. The 0.5 wt% sample demonstrated greater gains in IFSS, ILSS, flexural strength, and flexural modulus during mechanical testing than the other sample groups, at increases of 60%, 19%, 15%, and 16%, respectively. Chen et al. were able to successfully functionalize GO with silane and increase carbon fibers' mechanical characteristics, nevertheless, due to SGO's lengthy curing time, this technique is not the most effective.

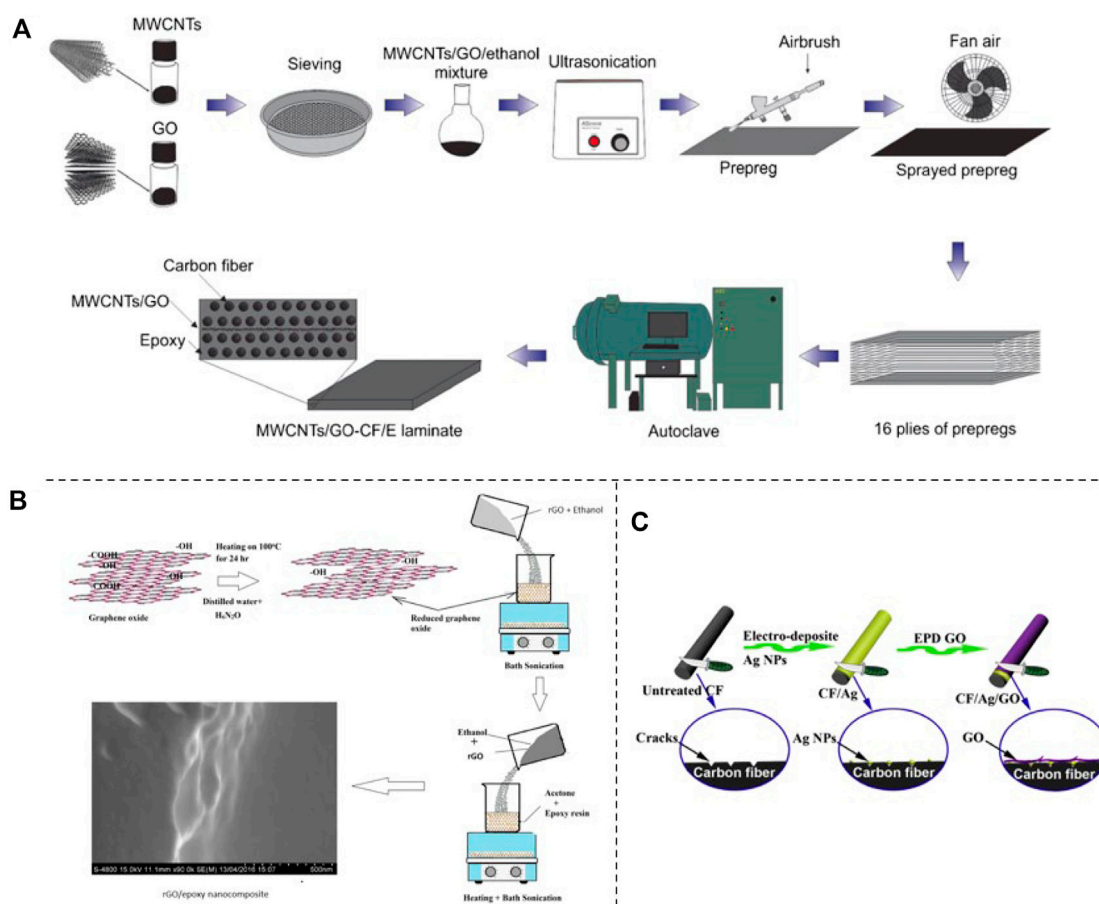


FIGURE 7

(A) Fabrication process of CF/E composite laminate with MWCNTs/GO hybrid (Rodríguez-González et al., 2018), (B) graphene oxide to rGO and epoxy/rGO composite (Jenkins et al., 2019) and (C) procedure for the fabrication of CF/Ag/GO (Wang et al., 2017b).

RGO offers potential as Jenkins et al. (2019) surveyed its enhancement of CFRP's mechanical properties. Graphene oxide was manufactured using a modified and enhanced version of Hummer's technique. A mixture of H<sub>2</sub>SO<sub>4</sub> and H<sub>3</sub>PO<sub>4</sub> was added to graphite powder and KMnO<sub>4</sub>, followed by 12 h of heated mixing. The cooled, rinsed, centrifuged, and then filtered mixture was then filtered into CFRP samples containing 0.1, 0.2, and 0.3 wt% RGO for testing, as shown in Figure 7B. The SEM images of RGO specimens revealed uneven, folding structures, which gave the composite stability, with TEM morphology confirming this. Flexural testing was conducted at -10°C, 23°C, and 40°C. The sample with the best performance was the 0.3 wt% set increasing the flexural strength by 62% and the flexural modulus by 44%. Overall, the objective of enhancing the CFRP's shear and flexural characteristics, with RGO, was achieved between -10°C and 23°C. There were noticeable slight strength decreases at 40°C.

Another RGO study explored creating hierarchical composites for greater mechanical and electrical effectiveness

(Li et al., 2016). In this case, RGO with help of tetrahydrofuran (THF), was dispersed into an epoxy resin and deposited into the CF interface. A modified Hummer's method was utilized to produce GO. This was then reduced, washed, and dried to form RGO resin, which was deposited into the CF. Through mechanical testing, 0.1 wt% was determined to be the highest-performing sample. ILSS improved by about 10% in RGO compared to non-modified CF. IFSS was increased by 21% in RGO. Reconfirming that RGO does successfully improve the mechanical properties of carbon fiber. Finally, laser-induced graphene (LIG) was used to enhance the fracture toughness of CF (Nasser et al., 2021). By using a 40 W CO<sub>2</sub> laser, LIG arrays with vertical alignment were generated on polyimide substrates, and the LIG was then transferred manually to CF prepreg. Short beam strength tests revealed a 300% increase in toughness. Additionally, mode I and mode II fracture toughness increased by 41% and 69%, respectively. Through the study, there was an increase in shear strength, fracture toughness, and both crack initiation and propagation resistance increased.



Crossbreeding of graphene with other nanomaterials were also explored to identify their effects on carbon fiber. Rodríguez-González et al. (2018) did so by using mode one and mode two interlaminar fracture toughness and interlaminar shear strength measurements to study the effects of MWCNTs and GO combinations. Using unidirectional carbon fiber/epoxy prepregs, three distinct samples of MWCNTs, graphene oxide, and MWCNTs/GO were sprayed onto carbon fiber at a concentration of 0.25 wt% relative to pristine carbon fiber, then cured for testing. A double cantilever beam test was used to determine the mode I interlaminar fracture toughness, and an end notched flexure testing was performed on pre-cracked and uncracked samples for mode II fracture toughness. Short beam shear tests were used to determine the interlaminar shear strength. SEM images were used to further assess the results following testing. Using double cantilever beam testing mode one toughness rose by 11.5%, 8.1%, and 16.7% for MWCNTs, GO, and MWCNTs/GO respectively. The same can be said with Mode two non-pre-cracked MWCNTs increasing by 14%, 8.1%, and 17.6% along with ILSS was increasing by 3.5%, 3.0%, and 4.7% respectively. In this article, although the total increase in ILSS was not as large as in other research, improvements were observed.

Similar to Gonzalez, Kwon et al. (2017) also used GO combined with carbon nanotubes (CNTs) to enhance the mechanical and electrical properties within CFRPs. In this case, GO sheets were produced from graphite flakes. 0.01 wt% of multi-walled CNTs were mixed into distilled water with 0.0003 wt% GO sheets. EPD was then utilized to allow the new GO/CNT hybrid to be deposited on the carbon fabric. After sample fabrication, weight percentages of 0.01, 0.37, 0.61, and 0.65 of GO/CNT were reported. Mechanical results from short beam strength showed a decrease from 62 MPa to 55 MPa due to excessive coating between carbon fibers. Crack pattern analysis showed that the applied load was transferred to the fibers instead of the epoxy. Electrical studies showed an increase of about 1400% in through-thickness electrical conductivity. Overall, the paper saw successful results in the main category they were striving for. The electrical properties were greatly enhanced with the obvious decrease in mechanical properties tested.

Another test that garnered improvements used silver nanoparticles (AgNPs), where through efficient electrodeposition and electrophoretic deposition, AgNPs and GO were deposited onto the surface of CF sheets to enhance the interfacial shear strength and tensile strength of the carbon fiber (Wang et al., 2017b). The process started by desizing CF in refluxed acetone. AgNPs were prepared for electrodeposition with CF as the cathode, stainless steel as the anode, and a mixture of  $\text{AgNO}_3$  and PVP as the electrolyte. This deposition was completed through electrophoretic deposition at times of 10, 30, 60, and 90 s. The samples CF/AG/GO-10, CF/AG/GO-30, CF/AG/GO-60, and CF/AG/GO-90 were named with respect to their deposition times. SEM and TEM images confirmed that AG NPs and GO were successfully deposited onto the CF sheets.

After this confirmation, tensile testing showed an increase of 36.8% in CF/AG/GO-60 compared to untreated CF. Interfacial shear strength was increased by 86.1% in CF/AG/GO-60 compared to untreated CF. This article verified that the use of nanoparticles and GO together was able to successfully fill in surface cracks of CF, increase wettability, and overall reinforce the composite. Other metals, like iron oxide ( $\text{Fe}_3\text{O}_4$ ) and their effects on the micro-crack behavior of CFs were also studied (He et al., 2018). To prepare these fillers, solid GO was obtained after filtration and freeze drying, with the  $\text{Fe}_3\text{O}_4$ /GO being magnetically separated and washed. The two mixes were created by adding either GO or  $\text{Fe}_3\text{O}_4$ /GO to epoxy in a 0.5:75 ratio and curing with D-230 in a 1:3 ratio. Through vacuum-assisted resin transfer molding, an epoxy laminate was strengthened with carbon fiber. In comparison to pure GO,  $\text{Fe}_3\text{O}_4$ /GO exhibited a significant reduction in the adsorption peaks of oxygen functional groups, *via* FTIR. XRD readings revealed the formation of a  $\text{Fe}_3\text{O}_4$ /GO particle during decomposition. SEM and TEM pictures revealed that the majority of GO coated with magnetite microspheres was reasonably uniform and that their distribution was uneven in shape and exhibited some aggregation. Tensile testing at room temperature and 77 K revealed an increase in tensile strength for GO and  $\text{Fe}_3\text{O}_4$ /GO composites. GO increased tensile strength by 6.9 percent at room temperature and  $\text{Fe}_3\text{O}_4$ /GO raised it by 14.1 percent. At 77K, GO increased tensile strength by 12.1% and  $\text{Fe}_3\text{O}_4$ /GO by 18.1%, and both Young's modulus and the percentage of failure strain increased as well.  $\text{Fe}_3\text{O}_4$ /GO also boosted fracture toughness and impact strength at 77K by 75% and 21.1%, respectively, as well as reducing the coefficient of thermal expansion by 51.6%. This research provides unique results by testing at different temperatures and this procedure was proven successful despite a lengthy and complicated process.

Zhang et al. (2016) also ran a lengthy experiment as this group investigated the impact of adding polyhedral oligomeric silsesquioxane (POSS) to multi-scale carbon fiber *via* graphene oxide (GO). Both the carbon fiber and GO were functionalized and prepared for use. Later, SEM images of carbon fiber were produced before and after the addition of GO, followed by GO-POSS. This showed the clear structural changes between unfunctionalized and GO-functionalized carbon fibers. This was confirmed with an atomic force microscopy (AFM), which was used to examine the topography and roughness of the carbon fiber. Additionally, X-ray photoelectron spectroscopy, thermogravimetric analysis, and dynamic contact angle testing were performed to detect chemical and contact angle differences between GO and POSS in order to ensure successful grafting. Mechanical testing was then used to determine increases in shear strength, and a considerable increase of up to 53.05% in the ILSS was demonstrated. The study is innovative in that it makes use of both GO and POSS concurrently. However, with a total processing time of 112.83 h for functionalizing the carbon fiber and preparing GO and POSS, the fundamental limitation

**TABLE 2 Summary of mechanical properties improvement of carbon fiber-epoxy composite by graphene/graphene oxide.**

Material	wt%	Flexural strength increment (%)	Flexural modulus increment (%)	Tensile strength increment (%)	ILSS/IFSS increment (%)	References
GO/oCF	2.0 g	—	—	—	ILSS: 59.4%	Jianjun et al
ACF-D <sub>400</sub> -GO-2	—	—	—	6.1%	IFSS: 59.3%	Wang et al. (2017)
Fe <sub>3</sub> O <sub>4</sub> /GO/epoxy (77K - RT)	0.5%	—	31%–58%	18%–14%	K <sub>IC</sub> : 75%–57%	He et al. (2018)
MWCNTs/GO-CF/E (Mode I)	0.25%	—	—	—	ILSS: 4.7% G <sub>IC</sub> :16.7%	Rodríguez-González et al. (2018)
GO	0.2%	55.5%	19.7%	23.9%	—	Adak et al. (2018)
GO-POSS	0.2 g	—	—	53.05%	—	Zhang et al. (2016)
CF/AG-60	3.36%			28%	IFSS: 86.1%	Wang et al. (2017c)
EDA	0.1, 0.3, 0.5%	−3.8, 12, 6.2%	6.7, 10, 8%	7.3, 19.7, 16%	—	Ashori et al. (2015)
CF-PEI-prGO	—	—	—	—	IFSS: 78.64%	Wu et al. (2003)
SGO	0.2%	13.5%	15.5	—	ILSS: 18.6% IFSS: 60.8%	Chen et al. (2014)
GO-CFC	2%	—	23.5%	53.9%	—	Altin et al. (2020)
GNP	0.4%	20.8%	20.5%	—	—	Srivastava et al
GO (RT/77K)	0.2%	6.4/4.9%	9.6/7.1%	—	ILSS: 17.6/8.7%	Qu et al. (2020)
rGO (−10°C)	0.3%	62%	44%	—	—	Jenkins et al. (2019)
GO	0.1%	—	—	—	ILSS: 8%	Han et al. (2017)
GO	1%	—	—	—	IFSS: 37.2%	Jiang et al. (2017)
GO	0.3%	66%	72%	—	ILSS: 25%	Pathak et al. (2016)
Graphene	1.0%	—	—	—	G <sub>IC</sub> : 145%	Du et al. (2017)
PAS-GNP	4.0%	—	—	—	ILSS: 252%	Kim et al. (2020)
LIG			−3%	−3%	ILSS: 3%	Nasser et al. (2021)
GnP	4.0%	7%	3%	—	ILSS: 19%	Qin et al. (2000)
GO	—	—	—	—	IFSS: 32%	Li et al. (2016)
GnP	0.1%	21%	7%	—	—	Tareq et al. (2019)

of this work is its time impracticality. Finally, Tareq et al. (2019) examined the effects of introducing montmorillonites nanoclay (MMT), GNPs, and a hybrid MMT and GNP to CFs. To disperse MMT, a 2% nanoclay was dried and then mixed with epoxy resin. GNP dispersion occurred from various ultrasonication and mixing with epoxy resin. These two processes came together to form the hybrid composite. After material preparation, 0.1 wt % GNP samples showed the best results of increasing flexural strength while 2% MMT increased flexural modulus the most with increases of 21% and 28% respectively. Overall interfacial bonding was improved in all modified sample types and was confirmed by SEM. Although both GNP and MMT samples

performed highest in different areas, the hybrid of the two, however, decreased flexural modulus by 5%. Table 2 below displays a culmination of the results discussed in this section. Showing graphene oxide used for carbon fiber optimization but with differing methods and results.

## Cellulose nanofibers and cellulose nanocrystals

Many studies aimed at increasing the interlaminar or interfacial fracture toughness of carbon fiber composites, specifically CFRPs

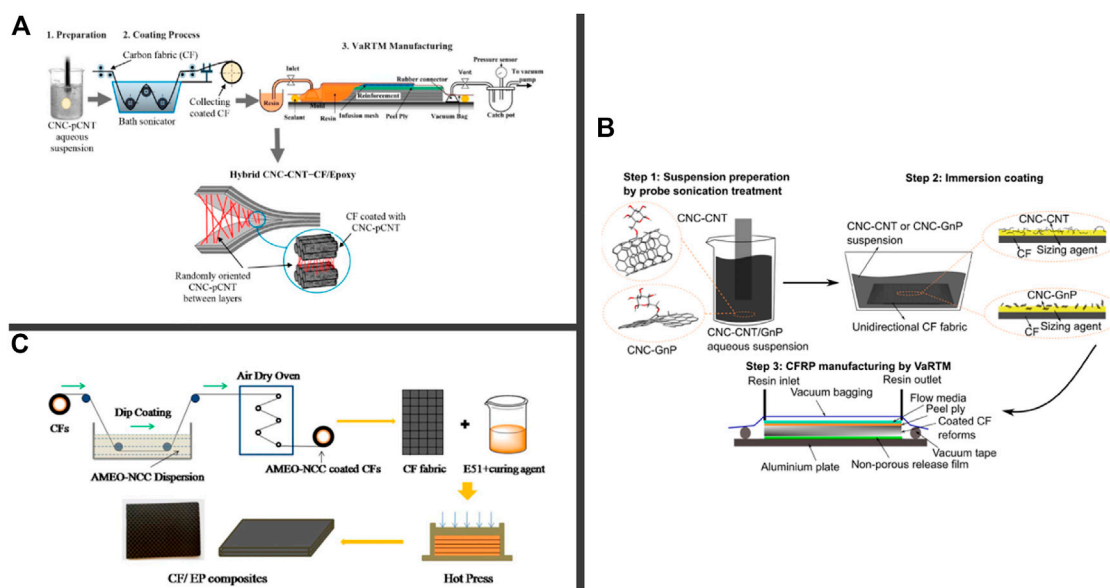


FIGURE 8

(A) Preparation of aqueous suspension of CNC-pCNT using probe sonication (Shariatnia et al., 2020), (B) Preparation of Homogeneous CNC-CNT and CNC-GnP Suspensions by Probe Sonication Treatment, (2) Immersion Coating of CFs to Integrate CNC-CNT and CNC-GnP on CF Surface (Kaynan et al., 2022), (C) the schematic of manufacturing AMEO-NCC coated CF and composites (Zhang et al., 2019b).

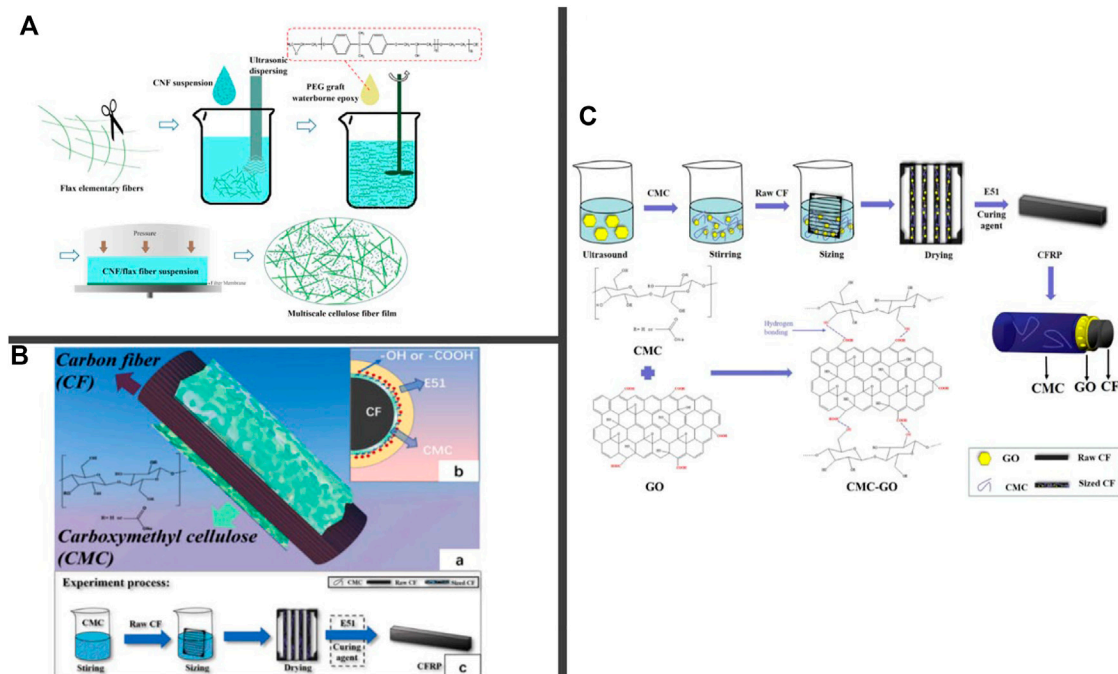


FIGURE 9

(A) preparation process of multiscale cellulose interlayer (Zhang et al., 2021), (B) Illustration of the preparation of modified CFRPs and reaction mechanism (Qiu et al., 2020), (C) Illustration of the preparation of modified CFs, the preparation structure of CFRPs, illustration of the experimental process of modified CFRPs. (Qiu et al., 2021).

with various nanomaterials. However, the high manufacturing and operating costs of using some of these nanomaterials have led researchers to study other cost-effective methods of creating stronger and more optimized composites. This has led to the creation of hybrid nanofillers, a fusion of two or more nanofillers that take on the properties of their constituents. A near-infinite number of these hybrid forms and concentrations can be created to construct stronger and more affordable components. In this section, some of these hybrids will be explored.

A key property that carbon fiber manufacturers aim to increase is the fracture toughness of these composites, to prevent delamination and ultimately, failure. Gabr et al. aimed to create tougher polymer matrix composites with epoxy resin, varying amounts of the nanomaterials bacterial cellulose, BC, (0, 0.5, and 1 wt%) and Carboxyl-Terminated Liquid Butadiene—Acrylonitrile (0, 10 and 20 wt%) or CTBN as enhancers for these composites (Gabr et al., 2010a). Initially, a decrease in young's modulus and tensile strength was found for all eight combinations, relative to pristine carbon fiber with only 1% BC/10%CTBN having higher tensile strength. Non-significant increases in flexural strength and modulus were discovered. However, the initial and propagation experienced a significant increase of 84% and 72% counteracting the decreases in other mechanical properties. Gabr et al. also studied the effects of 0%, 0.5wt%, 1wt%, and 2wt% of microfibrillated cellulose (MFCs) as the reinforcement of an epoxy polymer matrix and plain-woven carbon fiber. Using the JIS K7073 and K7086 standards 2wt% MFC experienced the greatest increase in mode one interlaminar fracture toughness, crack initiation force, and glass transition temperature with increases of 44%, 80%, and 12°C respectively.

Researchers at Doshisha University conducted a comparative study also using BC and MFCs against CNFs to research their effects on fatigue life (Shao et al., 2015). The weight fractions of both BC and MFC were separated into 0, 0.3, and 0.8 wt% of the epoxy matrix and once the carbon fiber was laminated and cut, both mechanical and fatigue tests were analyzed via ASTM D3039-08 and ASTM D3479 standards for two million cycles. The high cycle fatigue life increased greatly for 0.8 wt% MFC and BC, by nearly 10–30 times for 0.3 wt% MFC. The effects of the nanofillers with the carbon fiber and epoxy adhesion were also realized due to a 76.9% increase in the interfacial shear strength. There was also an increased delamination resistance as the energy release ratio increased by 1.6 times. These results exemplify the use of nanofillers to produce significant increases in carbon fiber fatigue life and are scarcely found throughout the composite industry.

These same researchers also researched hybridizing 0, 0.5, and 1 wt% MFCs and 0, 10 and 20 wt% CTBN (Gabr et al., 2010b). In this study, the hybrid nanofillers incurred slight decreases in the young's modulus, flexural and tensile strength, relative to pristine carbon fiber in all but one concentration. However, the mode one fracture toughness increased by 96% and 127% in both initial and propagation fracture toughness. These papers show the novelty of

using other cellulose microfibrils like MFC and BC to create increases in fracture toughness, with little to no effects, on a carbon fiber composite's mechanical structure. Another alternative cellulose that was explored is nanocrystalline cellulose (NCC) silanized by 3-aminopropyltriethoxysilane (AMEO) (Zhang et al., 2019b). Continuous coating was a method proposed by Zhang et al. as an inexpensive way to increase the interfacial properties of carbon fibers, in which concentrations of 0, 0.1, 0.3, 0.5 wt% AMEO-NCC was dip-coated onto eight layers of carbon fiber, cured, and cut for testing. This is accurately displayed under Figure 8C. The greatest mechanical increases of these hybrid concentrations were incurred by 0.3wt%, where interfacial shear strength, flexural modulus, and flexural strength increased by 91%, 23.24%, and 18.21%. Although continuous coating has been highly utilized, it has not been adequately studied for NCCs, hence the novelty of this experiment.

Another novel cellulose that has scarcely been utilized with carbon fiber is carboxymethyl cellulose (CMC). Qiu et al. (2021) studied the possibility of avoiding stress concentrations by introducing polar functional groups with 0, 0.025, 0.05, 0.075, and 1 g of CMC. The methodology of creating CMC-modified CFRPs can be visually shown within Figure 9C. After testing their modified carbon fiber samples, tests unveiled that the contact angle of modified samples decreased as CMC increased, proving greater wettability as CMC increases. The ILSS of modified CFs were tested using ASTM D2344 and increased with all amounts of CMC, most noticeably with an increase of 18% with CF/0.075 g CMC. Cellulose Nanocrystals (CNC) in combination with thermoplastic polysulfone (PSF) were used by Cai et al. (2019). To toughen the epoxy resin with the aim of creating stronger carbon fiber composites. A 16-layered carbon fiber composite was prepared using the hand-layup method with different CNC, PSF, and epoxy concentrations. CNC/Epoxy bulk composites were divided into 0.1%, 0.3%, 0.5%, 0.75% and 1%CNC/EP, with supplementary bulk composites comprised of: 10%PSF/EP, 20%PSF/EP, 10%PSF/0.5%CNC/EP and 20%PSF/0.5%CNC/EP. After each concentration was applied onto the composite, it was then evacuated for 30 min, cured for 16 h at 120°C under a 250 kPa load, and cut for the following ASTM tests: ASTM D3039, D7264, D5045, D5528, and D7905. These tests verified that 0.5%CNC/EP garnered the greatest increase in strength relative to other CNC/Epoxy bulk composites, increasing the tensile strength and modulus by 13% and 18%, as well as the critical stress intensity factor ( $K_{Ic}$ ) by 33%. Although these increases in strength are apparent, when it comes to the increases in fracture toughness, the PSF/EP and PSF/CNC/EP composites display much larger increases. These bulk composites increased the mode I and II fracture properties of critical strain energy release rate ( $G_{Ic}$ ) and  $K_{Ic}$  upwards of 126% and 109% respectively. However, the flexural and tensile strengths of these composites decrease significantly, limiting their use. Despite this, the use of PSF for increasing mode I and II fracture toughness, through electrospinning has been rarely explored. More researchers also modified carbon fiber

**TABLE 3 Summary of mechanical properties improvement of carbon fiber-epoxy composite by organic nanofillers (CNC/CNF).**

Material	wt%	Flexural strength increment (%)	Flexural modulus increment (%)	Tensile strength increment (%)	ILSS/IFSS increment (%)	References
BC0.5/CTBN0	0.5%/0%	−0.87	−4.4	−10.8	IF: 84% PF: 72%	Gabr et al. (2010a)
BC	0.8%	—	—	9	76.9%	Shao et al. (2015)
CNF	1.0%	—	—	—	104%	Umeki et al. (2016)
CF/GO/CMC	0.003 g/.05 g	—	—	—	IFSS: 58.93%	Qiu et al. (2021)
					ILSS: 50%	
CNC	0.5%	8.3	9.5	13.1	—	Cai et al. (2019)
CNC-pCNT	0.2–0.2%	34	15	−2.5	34.7%	Shariatnia et al. (2020)
CNC-GnP	4:1	13	—	13	ILSS: 28%	Kaynan et al. (2022)
					IFSS: 45%	
CNC-CNT	10:1	55	—	15	ILSS: 46%	Kaynan et al. (2022)
					IFSS: 100%	
MFC	2%	—	—	4	G <sub>IC</sub> : 79, 75, 66	Gabr et al. (2010b)
					G <sub>ICP</sub> : 14, 24, 52	
MFC/CBTN	1%/10%	−5	−2.6	−1.4	IFT: 96%	Gabr et al. (2010a)
					PFT: 127%	
AMEO-NCC	0.5%	15	12.9	0.9	IFSS: 94.22%	Zhang et al. (2019b)
CMC	0.075 g	—	—	8	ILSS: 18.09%	Qiu et al. (2021)
APTES-CNC (12 k/individual)	1%	—	—	—	IFSS: 77/81%	Batista et al.
CNF/FF-film (Without WE)	—	—	—	—	100%	Zhang et al. (2021)

with CNC through functionalizing cellulose nanocrystals with 3-aminopropyltriethoxysilane (APTES) (Reale Batista and Drzal, 2018).

The APTES-CNC solution concentrations were set at 0.6%, 1%, and 2 wt% for two varying sizing methods. The first was immersing 12 k CF tow into the solution for 20 s, then slowly raising CFs. The second sequence places the CFs in the solution at a sequence of 5 min with stir/3 min without stir for about 32 min. Respectively, these sequences produce 12 k tow-sized and individually sized carbon fibers. After ILSS testing was conducted 1.0 wt% APTES-CNC gave the largest growth at 77% and 81% increase for 12 k tow-sized CF and individually sized CF, respectively. Work done by Qiu et al. (2020) explored increasing the interfacial performance of carbon fiber through a sizing process with Carboxymethyl cellulose (CMC) and graphene oxide (GO) as the sizing agents. This research aimed to avoid mechanical damage but to also complete this

task in an environmentally friendly manner. Graphene oxide sheets were synthesized, and four test beakers were created containing, 100% CF, 0.003 g of GO, 0.05 g CMC and 0.003 g GO with 0.05 g CMC which were named CF, GO/CF, CMC/CF and CF/GO/CMC respectively. FTIR spectrometry, SEM imaging and Raman spectrometry were conducted and verified that hydrogen bonds were formed in this process, which increases the composites' energy absorption. This was verified through an interlaminar shear strength of the GO/CF, CMC/CF and CF/GO/CMC increased by 13.2%, 28%, and 50% respectively. With the rising concern of a product's environmental impact, increasing CFs in an environmentally friendly way like this article attempts to has been rarely explored.

Another way to test and optimize carbon fiber composites, in an environmentally friendly way is to do so virtually. Ahmad and Bajpai (2018) conducted an experiment electronically simulating the structural applications of jute fiber woven mats by using



simulation software such as Simulia Abaqus and Siemens PLM NX. Varying types of composite sheets were created and simulated, such as unidirectional jute fiber, Bi-directional woven jute mat and random oriented short jute fibers; all with jute amounts ranging from 0% to 100% jute. The tensile tests were conducted experimentally, under ASM D3039 standards, and through a simulation, in which the modeled data was slightly higher than the experimental findings. Additional parameters were chosen and studied, including ply orientation, varying jute fiber reinforcement and differing weft fiber angles. The methodology as to how the virtual carbon fibers were composed was extensive but very little is known about the physical CFs that were tested. Shariatnia et al. explored the use of producing hybrid composites without chemical functionalization or inserting surfactants into the manufacturing process, which can lead to a more cost-effective composite. Kaynan et al. (2022) also tried a new approach to create stronger CFRPs by using hybrid nanomaterials.

Kaynan aimed to insert CNT and graphene nanoplates (GnPs) *via* dip coating with CNCs to stabilize these nanomaterials within CFRPs. These nanomaterials were categorized *via* the mass ratio CNC to CNT/GnP and separated as CNC-CNT 4:1, 6:1, 8:1, 10:1, and 12:1 with CNC-GnP 1:1, 2:1, 4:1, and 6:1, all to be measure and tested (Kaynan et al., 2022). The combinations of CNC, CNC-CNT, and CNC-GnP accounted for 0.2 wt% of the epoxy matrix, in which the coating and immersion of unidirectional CF fabrics were applied for 20 min and cured at 120°C for 24 h. These CF fabrics were stacked in an  $[0_2, 90_2, 0_2]_s$  sequence using a VaRTM process and separated by nanomaterial for testing. The results showed that 10:1 CNC-CNT and 4:1 CNC-GnP had the greatest interfacial shear strength increases of 200% and 145% respectively, with morphology images showing that polar oxygen groups increase the adhesion of interfacial properties. It was also determined that flexural and tensile strengths increased as well. Although the process to create these results are not unique, as many have integrated nanomaterials onto CFRPs *via* dip coating, the results garnered are impactful, relevant, and offer minor disadvantages. Another plant fiber that has attained greater attention is chopped flax fibers (FFs). This is due to their microstructure enhancing the toughness of composites, which is what researchers at Tongji university aimed to do (Shariatnia et al., 2020). In their research, these researchers combined pristine carbon nanotubes (pCNT) and assisting FFs, such as CNC, on functionalized CNT (fCNTs) to aid in pCNT dispersion onto a CFRP polymer. Two coating processes were used for this project: Immersion (I-coating) and Simultaneous Immersion (IS-coating), for an eight-layered CF composite. After the layers have been oriented, they undergo a VaRTM process, then encased and vacuumed to permit resin infusion afterward, where the vent was operational for 24 h To promote curing. After said curing, the sample was cut *via* a water jet for various testing and analysis. Implanting CNC-pCNT onto CF produced increases in flexural

strength, flexural modulus and interlaminar shear strength by 33%, 15% and 35% respectively. The use of processing-manufacturing methods for creating CFRPs is not typical for structural applications but can be an appropriate method to do so, as this project produces noticeable results in mechanical and thermal properties, despite its novelty.

Wang et al. (2017c) utilized chemical vapor deposition in an experiment determining the effects of hybridizing polyimide-graft-bisphenol A diglyceryl acrylate (PI-BDA) and SWCNT concentrations to increase the ILSS of the carbon fiber matrix. The carbon fiber tows were prepared in two different ways, desize *via* Soxhlet extraction and the CVD method and separated into four concentrations of 0.2%, 0.5%, 1.0%, and 2.0% SWNT/PI-BDA. These concentrations were characterized under FESEM imaging, Raman spectrum analysis and atomic force microscopy (AFM). It was hypothesized the coatings allow for an increase within the carbon fiber and matrix contact area. After testing, the ILSS analysis showed significant increases in strength for all concentrations, with 0.5 wt% increasing the ILSS by 103%, relative to control CF/Epoxy composites. Zhang et al. (2021) also considered the use of plant fibers comprising of FFs and CNFs for interlaminar toughening. CNF/FF-film was created when flax fibers were dissolved into water with a CNF suspension and waterborne epoxy added. These were then separated into three interlayers: neat FF mat, CNF-network film and CNF-film for testing. The Mode II Interlaminar fracture toughness was analyzed using ASTM D7905 standards and it was discovered that the fracture toughness of each interlayer, barring CNF-networks without WE, increased relative to the control. The greatest increases were in CFRPs that contained WE and were found to be 38.7%, 69.4%, and 112% increases in mode II toughness.

Lastly, Umeki et al. (2016) expands on previous research to create a macro-thin composite which was made from plain woven fabrics and an extremely thin CNFs as combinations of regular N (120  $\mu$ m) and spread (40  $\mu$ m) carbon fiber tow. Umeki classified thick prepreg as a combination of 16 layers of regular CF tow and both epoxy resin with thin prepreg consisting of 48 layers of spread CF tow with both epoxy resin, creating four classes of testable laminates. These laminates were then subject to mechanical and fatigue life testing, in which minor increases in tensile strength and modulus were achieved, relative to the unmodified epoxy/regular tow. The modified epoxy/spread tow reached the greatest fatigue life, even exceeding the number of cycles to failure. A condensed culmination of all of these results can be shown below in Table 3.

## Future challenges and conclusion

The use of nanofillers within carbon fiber has been studied and proven to be successful when incorporated into epoxy and carbon fiber laminates. This paper has explored four main nanomaterials that have been gaining popularity, with the aim of providing up-to-date information on the novel studies

researchers have been conducting. This paper identified the current uses of pure graphene, CNT, CNC and CNF. Incorporating the cellulose based nanoreinforcements offered the greatest potential in increasing mechanical properties and was shown to increase interfacial interaction and roughness. The incorporation of graphene as nanoreinforcement was able to do so as well, irrespective of testing temperature, as well as increase CF electrical properties such as through-thickness conductivity. Hybrid combinations varying nanomaterials were shown to increase ILSS and IFSS. However, most reports showed that hybridization showed little, none or even negative effects on other parameters. Overall, the covalent interactions of the nanofillers with carbon fiber and its matrix led to the enhancement of its mechanical and even thermal and electrical properties. All while adding little to the weight and thickness of carbon fiber. Due to the unique composition of these nanomaterials, it has been shown that the mechanical properties of carbon fiber tend to increase with minimal weight percentages. Despite this, one challenge that was observed was the preparation time. In many processes to increase the strength of carbon fiber, long and complicated material preparation were recorded, which hinders the practicality of these methods. Hence, if timing is important, a compromise will have to be reached. To conclude, this comprehensive study on the preparation, testing and applications of these nanofillers demonstrate the immaturity of our knowledge, as unique processes are uncovered continuously. More research is required within this field to realize the full potential of these nanomaterials.

## References

- Adak, N. C., Chhetri, S., Kim, N. H., Murmu, N. C., Samanta, P., and Kuila, T. (2018). Static and dynamic mechanical properties of graphene oxide-incorporated woven carbon fiber/epoxy composite. *J. Mat. Eng. Perform.* 27 (3), 1138–1147. doi:10.1007/s11665-018-3201-5
- Ahmad, F., and Bajpai, P. K. (2018). Evaluation of stiffness in a cellulose fiber reinforced epoxy laminates for structural applications: Experimental and finite element analysis. *Def. Technol.* 14 (4), 278–286. doi:10.1016/j.dt.2018.05.006
- Ahmad, S. (1999). Carbon nanostructures fullerenes and carbon nanotubes. *IETE Tech. Rev.* 16 (3–4), 297–310. doi:10.1080/02564602.1999.11416845
- Altin, Y., Yilmaz, H., Unsal, O. F., and Bedeloglu, A. C. (2020). Graphene oxide modified carbon fiber reinforced epoxy composites. *J. Polym. Eng.* 40 (5), 415–420. doi:10.1515/polyeng-2019-0247
- Alves, C., Ferrao, P., Silva, A., Reis, L., Freitas, M., Rodrigues, L., et al. (2010). Ecodesign of automotive components making use of natural jute fiber composites. *J. Clean. Prod.* 18 (4), 313–327. doi:10.1016/j.jclepro.2009.10.022
- An, F., Lu, C., Li, Y., Guo, J., Lu, X., Lu, H., et al. (2012). Preparation and characterization of carbon nanotube-hybridized carbon fiber to reinforce epoxy composite. *Mater. Des.* 33, 197–202. doi:10.1016/j.matdes.2011.07.027
- Ashori, A., Rahmani, H., and Bahrami, R. (2015). Preparation and characterization of functionalized graphene oxide/carbon fiber/epoxy nanocomposites. *Polym. Test.* 48, 82–88. doi:10.1016/j.polymertesting.2015.09.010
- Bacon, R. (1960). Growth, structure, and properties of graphite whiskers. *J. Appl. Phys.* 31 (2), 283–290. doi:10.1063/1.1735559
- Bacon, R., and Tang, M. M. (1964). Carbonization of cellulose fibers—II. Physical property study. *Carbon* 2 (3), 221–225. doi:10.1016/0008-6223(64)90036-3
- Cai, S., Li, Y., Liu, H. Y., and Mai, Y. W. (2019). Effect of electrospun polysulfone/cellulose nanocrystals interleaves on the interlaminar fracture toughness of carbon fiber/epoxy composites. *Compos. Sci. Technol.* 181, 107673. doi:10.1016/j.compscitech.2019.05.030
- Chen, L., Jin, H., Xu, Z., Shan, M., Tian, X., Yang, C., et al. (2014). A design of gradient interphase reinforced by silanized graphene oxide and its effect on carbon fiber/epoxy interface. *Mater. Chem. Phys.* 145 (1), 186–196. doi:10.1016/j.matchemphys.2014.02.001
- Chien, A.-T., Liu, H. C., Newcomb, B. A., Xiang, C., Tour, J. M., and Kumar, S. (2015). Polyacrylonitrile fibers containing graphene oxide nanoribbons. *ACS Appl. Mat. Interfaces* 7 (9), 5281–5288. doi:10.1021/am508594p
- Consales, M., Cutolo, A., Cusano, A., Penza, M., Aversa, P., Giordano, M., et al. (2006). “Optical fiber sensors coated with carbon nanotubes, Tin dioxide and nanoporous polymers for cryogenic detection of hydrogen,” in *Sensors* (Jersey, United States: IEEE).
- Cusano, A., Pisco, M., Consales, M., Cutolo, A., Giordano, M., Penza, M., et al. (2006). Novel optochemical sensors based on hollow fibers and single walled carbon nanotubes. *IEEE Photonics Technol. Lett.* 18 (22), 2431–2433. doi:10.1109/lpt.2006.885618
- De Greef, N., Gorbatikh, L., Godara, A., Mezzo, L., Lomov, S. V., and Verpoest, I. (2011). The effect of carbon nanotubes on the damage development in carbon fiber/epoxy composites. *Carbon* 49, 4650–4664. doi:10.1016/j.carbon.2011.06.047
- Dong, L., Hou, F., Li, Y., Wang, L., Gao, H., and Tang, Y. (2014). Preparation of continuous carbon nanotube networks in carbon fiber/epoxy composite. *Compos. Part A Appl. Sci. Manuf.* 56, 248–255. doi:10.1016/j.compositesa.2013.10.016
- Du, X., Zhou, H., Sun, W., Liu, H. Y., Zhou, G., Zhou, H., et al. (2017). Graphene/epoxy interleaves for delamination toughening and monitoring of crack damage in carbon fibre/epoxy composite laminates. *Compos. Sci. Technol.* 140, 123–133. doi:10.1016/j.compscitech.2016.12.028
- Dzenis, Y. A., and Qian, J. (2001). Analysis of microdamage evolution histories in composites. *Int. J. Solids Struct.* 38 (10–13), 1831–1854. doi:10.1016/s0020-7683(00)00138-4

## Author contributions

PB and OO: Conceptualization, methodology, investigation, resources, and writing; GP and EC: Literature review, proofreading the manuscript; HD and MA: Supervision and project administration, funding acquisition.

## Conflict of interest

The authors declare a potential financial conflict of interest. Multiscale Integrated Technology Solutions LLC (MITS), which has been awarded the National Science Foundation (NSF) Small Business Technology Transfer (STTR) (#2036490) grant to conduct research and development (R&D) work on enhancing the strength of carbon fiber reinforced polymer composites, has potential commercial interest in the research presented in this paper.

## Publisher's note

All claims expressed in this article are solely those of the authors and do not necessarily represent those of their affiliated organizations, or those of the publisher, the editors and the reviewers. Any product that may be evaluated in this article, or claim that may be made by its manufacturer, is not guaranteed or endorsed by the publisher.

- Dzenis, Y. A. (1996). Stochastic damage evolution modeling in laminates. *J. Thermoplast. Compos. Mater.* 9 (1), 21–34. doi:10.1177/089270579600900103
- Ehsani, M., Rahimi, P., and Joseph, Y. (2021). Structure–function relationships of nanocarbon/polymer composites for chemiresistive sensing: A review. *Sensors* 21 (9), 3291. doi:10.3390/s21093291
- Frank, E., Ingildeev, D., and Buchmeiser, M. R. (2017). “2 - high-performance PAN-based carbon fibers and their performance requirements,” in *Structure and properties of high-performance fibers*. Editor G. Bhat (Oxford: Woodhead Publishing), 7–30.
- Gabr, M. H., Elrahman, M. A., Okubo, K., and Fujii, T. (2010). Interfacial adhesion improvement of plain woven carbon fiber reinforced epoxy filled with micro-fibrillated cellulose by addition liquid rubber. *J. Mat. Sci.* 45 (14), 3841–3850. doi:10.1007/s10853-010-4439-y
- Gabr, M. H., Elrahman, M. A., Okubo, K., and Fujii, T. (2010a). A study on mechanical properties of bacterial cellulose/epoxy reinforced by plain woven carbon fiber modified with liquid rubber. *Compos. Part A Appl. Sci. Manuf.* 41 (9), 1263–1271.
- Geim, A. K., and Novoselov, K. S. (2007). The rise of graphene. *Nat. Mat.* 6 (3), 183–191. doi:10.1038/nmat1849
- Gerard, H. G. (2015). “Boeing and the 787 dreamliner,” in *Decisions: An engineering and management perspective* (Jersey, United States: IEEE), 187–218.
- Gogoi, R., Maurya, A. K., and Manik, G. (2022). A review on recent development in carbon fiber reinforced polyolefin composites. *Compos. Part C. Open Access* 8, 100279. doi:10.1016/j.jcomc.2022.100279
- Hadden, C. M., Klimek-McDonald, D., Pineda, E., King, J., Reichanadter, A., Miskioğlu, I., et al. (2015). Mechanical properties of graphene nanoplatelet/carbon fiber/epoxy hybrid composites: Multiscale modeling and experiments. *Carbon* 95, 100–112. doi:10.1016/j.carbon.2015.08.026
- Hammel, E., Tang, X., Trampert, M., Schmitt, T., Mauthner, K., Eder, A., et al. (2004). Carbon nanofibers for composite applications. *Carbon* 42 (5), 1153–1158. doi:10.1016/j.carbon.2003.12.043
- Han, X., Zhao, Y., Sun, J. m., Li, Y., Zhang, J. d., and Hao, Y. (2017). Effect of graphene oxide addition on the interlaminar shear property of carbon fiber-reinforced epoxy composites. *Carbon N. Y.* 32 (1), 489–555. doi:10.1016/j.carbon.2017.02.077
- Hawkins, D. A., and Haque, A. (2014). Fracture toughness of carbon-graphene/epoxy hybrid nanocomposites. *Procedia Eng.* 90, 176–181. doi:10.1016/j.proeng.2014.11.833
- He, Y., Chen, Q., Yang, S., Lu, C., Feng, M., Jiang, Y., et al. (2018). Micro-crack behavior of carbon fiber reinforced Fe<sub>3</sub>O<sub>4</sub>/graphene oxide modified epoxy composites for cryogenic application. *Compos. Part A Appl. Sci. Manuf.* 108, 12–22. doi:10.1016/j.compositesa.2018.02.014
- Hollaway, L. C. (2003). The evolution of and the way forward for advanced polymer composites in the civil infrastructure. *Constr. Build. Mater.* 17 (6), 365–378. doi:10.1016/s0950-0618(03)00038-2
- Huang, J. Y., Tan, Y. C., and Chow, K. K. (2015). “Carbon-nanotube-deposited multi-mode fiber cavity for refractive index sensing applications,” in 2015 10th International Conference on Information, Communications and Signal Processing (ICICIS), Singapore, 02–04 December 2015.
- Inagaki, M. (2000). “Chapter 4 - carbon fibers,” in *New carbons - control of structure and functions*. Editor M. Inagaki (Oxford: Elsevier Science), 82–123.
- Jenkins, P., Siddique, S., Khan, S., Usman, A., Starost, K., MacPherson, A., et al. (2019). Influence of reduced graphene oxide on epoxy/carbon fiber-reinforced hybrid composite: Flexural and shear properties under varying temperature conditions. *Adv. Eng. Mat.* 21 (6), 1800614. doi:10.1002/adem.201800614
- Jiang, D., Liu, L., Wu, G., Zhang, Q., Long, J., Wu, Z., et al. (2017). Mechanical properties of carbon fiber composites modified with graphene oxide in the interphase. *Polym. Compos.* 38 (11), 2425–2432. doi:10.1002/pc.23828
- Johnson, D. J. (1990). “Structure and properties of carbon fibres,” in *Carbon fibers filaments and composites*. Editor J. L. Figueiredo (Dordrecht: Springer Netherlands), 119–146.
- Kamae, T., and Drzal, L. T. (2012). Carbon fiber/epoxy composite property enhancement through incorporation of carbon nanotubes at the fiber–matrix interphase – Part I: The development of carbon nanotube coated carbon fibers and the evaluation of their adhesion. *Compos. Part A Appl. Sci. Manuf.* 43 (9), 1569–1577. doi:10.1016/j.compositesa.2012.02.016
- Kaynan, O., Pérez, L. M., and Asadi, A. (2022). Cellulose nanocrystal-enabled Tailoring of the interface in carbon nanotube- and graphene nanoplatelet-carbon fiber polymer composites: Implications for structural applications. *ACS Appl. Nano Mat.* 5 (1), 1284–1295. doi:10.1021/acsnm.1c03860
- Keyte, J., Pancholi, K., and Njuguna, J. (2019). Recent developments in graphene oxide/epoxy carbon fiber-reinforced composites. *Front. Mat.* 6. doi:10.3389/fmats.2019.00224
- Kim, J., Cha, J., Chung, B., Ryu, S., and Hong, S. H. (2020). Fabrication and mechanical properties of carbon fiber/epoxy nanocomposites containing high loadings of noncovalently functionalized graphene nanoplatelets. *Compos. Sci. Technol.* 192, 108101. doi:10.1016/j.compscitech.2020.108101
- Koniuszewska, A. G., and Kaczmar, J. W. (2016). Application of polymer based composite materials in Transportation. *Prog. Rubber, Plastics Recycl. Technol.* 32 (1), 1–24. doi:10.1177/147776061603200101
- Koronis, G., Silva, A., and Fontul, M. (2013). Green composites: A review of adequate materials for automotive applications. *Compos. Part B Eng.* 44 (1), 120–127. doi:10.1016/j.compositesb.2012.07.004
- Kwon, Y. J., Kim, Y., Jeon, H., Cho, S., Lee, W., and Lee, J. U. (2017). Graphene/carbon nanotube hybrid as a multi-functional interfacial reinforcement for carbon fiber-reinforced composites. *Compos. Part B Eng.* 122, 23–30. doi:10.1016/j.compositesb.2017.04.005
- Lee, X. J., Hiew, B. Y. Z., Lai, K. C., Lee, L. Y., Gan, S., Thangalazhy-Gopakumar, S., et al. (2019). Review on graphene and its derivatives: Synthesis methods and potential industrial implementation. *J. Taiwan Inst. Chem. Eng.* 98, 163–180. doi:10.1016/j.jtice.2018.10.028
- Lewis, S. J. (1994). The use of carbon fibre composites on military aircraft. *Compos. Manuf.* 5 (2), 95–103. doi:10.1016/0956-7143(94)90060-4
- Li, M., Gu, Y., Liu, Y., Li, Y., and Zhang, Z. (2013). Interfacial improvement of carbon fiber/epoxy composites using a simple process for depositing commercially functionalized carbon nanotubes on the fibers. *Carbon* 52, 109–121. doi:10.1016/j.carbon.2012.09.011
- Li, Y., Zhao, Y., Sun, J., Hao, Y., Zhang, J., and Han, X. (2016). Mechanical and electromagnetic interference shielding properties of carbon fiber/graphene nanosheets/epoxy composite. *Polym. Compos.* 37 (8), 2494–2502. doi:10.1002/pc.23436
- Liu, D., Chen, X., Yue, Y., Chen, M., and Wu, Q. (2011). Structure and rheology of nanocrystalline cellulose. *Carbohydr. Polym.* 84 (1), 316–322. doi:10.1016/j.carbpol.2010.11.039
- Liu, H., and Mao, Y. (2021). Graphene oxide-based nanomaterials for uranium adsorptive uptake. *ES Mat. Manuf.* 13, 3–22. doi:10.30919/esmm5f453
- Lv, P., Feng, Y. y., Zhang, P., Chen, H. m., Zhao, N., and Feng, W. (2011). Increasing the interfacial strength in carbon fiber/epoxy composites by controlling the orientation and length of carbon nanotubes grown on the fibers. *Carbon* 49 (14), 4665–4673. doi:10.1016/j.carbon.2011.06.064
- Maria, M. (2013). Advanced composite materials of the future in aerospace industry. *INCAS Bull.* 5, 139–150. doi:10.13111/2066-8201.2013.5.3.14
- Marsh, G. (2007). Airbus takes on Boeing with reinforced plastic A350 XWB. *Reinf. Plast.* 51 (11), 26–29. doi:10.1016/s0034-3617(07)70383-1
- Mason, R. B., Gintert, L. A., Singleton, M. F., and Skelton, D. (2004). Composites for military equipment. *Adv. Mater. Process.* 162, 37.
- Mehdi, H., and Resatoglu, R. (2022). Confinement of concrete columns using CFRP and expanded grout. *J. Struct. Integr. Maintenance* 7 (2), 128–135. doi:10.1080/24705314.2021.2018841
- Mittal, G., Rhee, K. Y., Miskovic-Stankovic, V., and Hui, D. (2018). Reinforcements in multi-scale polymer composites: Processing, properties, and applications. *Compos. Part B Eng.* 138, 122–139. doi:10.1016/j.compositesb.2017.11.028
- Mohee, F. M., Al-Mayah, A., and Plumtree, A. (2016). Anchors for CFRP plates: State-of-the-art review and future potential. *Compos. Part B Eng.* 90, 432–442. doi:10.1016/j.compositesb.2016.01.011
- Nasser, J., Zhang, L., and Sodano, H. (2021). Laser induced graphene interlaminar reinforcement for tough carbon fiber/epoxy composites. *Compos. Sci. Technol.* 201, 108493. doi:10.1016/j.compscitech.2020.108493
- Njuguna, J., and Pielichowski, K. (2004). Polymer nanocomposites for aerospace applications: Characterization. *Adv. Eng. Mat.* 6 (4), 204–210. doi:10.1002/adem.200305110
- Njuguna, J., and Pielichowski, K. (2004). Polymer nanocomposites for aerospace applications: Fabrication. *Adv. Eng. Mat.* 6 (4), 193–203. doi:10.1002/adem.200305111
- Pathak, A. K., Borah, M., Gupta, A., Yokozeki, T., and Dhakate, S. R. (2016). Improved mechanical properties of carbon fiber/graphene oxide-epoxy hybrid composites. *Compos. Sci. Technol.* 135, 28–38. doi:10.1016/j.compscitech.2016.09.007
- Peng, S., Shao, H., and Hu, X. (2003). Lyocell fibers as the precursor of carbon fibers. *J. Appl. Polym. Sci.* 90 (7), 1941–1947. doi:10.1002/app.12879
- Perner, M., Algermissen, S., Keimer, R., and Monner, H. (2016). Avoiding defects in manufacturing processes: A review for automated CFRP production. *Robotics Computer-Integrated Manuf.* 38, 82–92. doi:10.1016/j.rcim.2015.10.008
- Qin, L.-C., Zhao, X., Hirahara, K., Miyamoto, Y., Ando, Y., and Iijima, S. (2000). The smallest carbon nanotube. *Nature* 408 (6808), 50. doi:10.1038/35040699
- Qin, W., Vautard, F., Drzal, L. T., and Yu, J. (2015). Mechanical and electrical properties of carbon fiber composites with incorporation of graphene nanoplatelets at the fiber–matrix interphase. *Compos. Part B Eng.* 69, 335–341. doi:10.1016/j.compositesb.2014.10.014

- Qiu, B., Li, M., Zhang, X., Chen, Y., Zhou, S., Liang, M., et al. (2021). Carboxymethyl cellulose sizing repairs carbon fiber surface defects in epoxy composites. *Mater. Chem. Phys.* 258, 123677. doi:10.1016/j.matchemphys.2020.123677
- Qiu, B., Sun, T., Li, M., Chen, Y., Zhou, S., Liang, M., et al. (2020). High micromechanical interlocking graphene oxide/carboxymethyl cellulose composite architectures for enhancing the interface adhesion between carbon fiber and epoxy. *Compos. Part A Appl. Sci. Manuf.* 139, 106092. doi:10.1016/j.compositesa.2020.106092
- Qu, C.-B., Huang, Y., Li, F., Xiao, H. M., Liu, Y., Feng, Q. P., et al. (2020). Enhanced cryogenic mechanical properties of carbon fiber reinforced epoxy composites by introducing graphene oxide. *Compos. Commun.* 22, 100480. doi:10.1016/j.coco.2020.100480
- Ravishanker, B., Nayak, S. K., and Kader, M. A. (2019). Hybrid composites for automotive applications – a review. *J. Reinf. Plastics Compos.* 38 (18), 835–845. doi:10.1177/0731684419849708
- Reale Batista, M. D., and Drzal, L. T. (2018). Carbon fiber/epoxy matrix composite interphases modified with cellulose nanocrystals. *Compos. Sci. Technol.* 164, 274–281. doi:10.1016/j.compscitech.2018.05.010
- Roberts, A. (2009). The carbon fibre industry worldwide 2008–2014. *Innovation Text.* 4.
- Rodríguez-González, J. A., Rubio-Gonzalez, C., Jimenez-Mora, M., Ramos-Galicia, L., and Velasco-Santos, C. (2018). Influence of the hybrid combination of multiwalled carbon nanotubes and graphene oxide on interlaminar mechanical properties of carbon fiber/epoxy laminates. *Appl. Compos. Mat. (Dordr.)* 25 (5), 1115–1131. doi:10.1007/s10443-017-9656-y
- Sadeghian, P., Rahai, A. R., and Ehsani, M. R. (2010). Effect of fiber orientation on compressive behavior of CFRP-confined concrete columns. *J. Reinf. Plastics Compos.* 29 (9), 1335–1346. doi:10.1177/0731684409102985
- Sager, R. J., Klein, P. J., Davis, D. C., Lagoudas, D. C., Warren, G. L., and Sue, H. J. (2011). Interlaminar fracture toughness of woven fabric composite laminates with carbon nanotube/epoxy interleaf films. *J. Appl. Polym. Sci.* 121 (4), 2394–2405. doi:10.1002/app.33479
- Schalamon, W., and Bacon, R. (1970). in *Process for producing carbon fibers having a high YOUNG'S modulus of elast city*. Editor U. S. Patent (United States: Union Carbide Corporation), 4.
- Shao, Y., Yashiro, T., Okubo, K., and Fujii, T. (2015). Effect of cellulose nano fiber (CNF) on fatigue performance of carbon fiber fabric composites. *Compos. Part A Appl. Sci. Manuf.* 76, 244–254. doi:10.1016/j.compositesa.2015.05.033
- Shariatnia, S., Kumar, A. V., Kaynan, O., and Asadi, A. (2020). Hybrid cellulose nanocrystal-bonded carbon nanotubes/carbon fiber polymer composites for structural applications. *ACS Appl. Nano Mat.* 3 (6), 5421–5436. doi:10.1021/acsnm.0c00785
- Siddiqui, N. A., Khan, S. U., Ma, P. C., Li, C. Y., and Kim, J. K. (2011). Manufacturing and characterization of carbon fiber/epoxy composite prepreps containing carbon nanotubes. *Compos. Part A Appl. Sci. Manuf.* 42 (10), 1412–1420. doi:10.1016/j.compositesa.2011.06.005
- Subramaniyan, A. K., and Sun, C. (2008). Interlaminar fracture behavior of nanoclay reinforced glass fiber composites. *J. Compos. Mater.* 42 (20), 2111–2122. doi:10.1177/0021998308094550
- Subramaniyan, A. K., and Sun, C. (2007). Toughening polymeric composites using nanoclay: Crack tip scale effects on fracture toughness. *Compos. Part A Appl. Sci. Manuf.* 38 (1), 34–43. doi:10.1016/j.compositesa.2006.01.021
- Talreja, R. (1994). *Damage mechanics of composite materials*. Amsterdam, Netherlands: Elsevier Science.
- Tanaka, F., and Okabe, T. (2018). “1.4 historical review of processing, microstructures, and mechanical properties of PAN-based carbon fibers,” in *Comprehensive composite materials II*. Editors P. W. R. Beaumont and C. H. Zweben (Oxford: Elsevier), 66–85.
- Tareq, M. S., Zainuddin, S., Woodside, E., and Syed, F. (2019). Investigation of the flexural and thermomechanical properties of nanoclay/graphene reinforced carbon fiber epoxy composites. *J. Mat. Res.* 34 (21), 3678–3687. doi:10.1557/jmr.2019.302
- Ueda, T., and Sato, Y. (2002). New approach for usage of continuous fiber as non-metallic reinforcement of concrete. *Struct. Eng. Int.* 12 (2), 111–116. doi:10.2749/101686602777965478
- Umeki, R., Tanaka, A., Okubo, K., Fujii, T., Kawabe, K., Kondo, K., et al. (2016). A new unidirectional carbon fiber prepreg using physically modified epoxy matrix with cellulose nano fibers and spread tows. *Compos. Part A Appl. Sci. Manuf.* 90, 400–409. doi:10.1016/j.compositesa.2016.06.011
- U.S.P. Office (1880). *Thomas edison and the electric lamp*. United States of America: U.S.P. Office.
- Van Den Einde, L., Zhao, L., and Seible, F. (2003). Use of FRP composites in civil structural applications. *Constr. Build. Mater.* 17 (6), 389–403. doi:10.1016/s0950-0618(03)00040-0
- Wang, C., Li, J., Yu, J., Sun, S., Li, X., Xie, F., et al. (2017). Grafting of size-controlled graphene oxide sheets onto carbon fiber for reinforcement of carbon fiber/epoxy composite interfacial strength. *Compos. Part A Appl. Sci. Manuf.* 101, 511–520. doi:10.1016/j.compositesa.2017.07.015
- Wang, C., Zhao, M., Li, J., Yu, J., Sun, S., Ge, S., et al. (2017). Silver nanoparticles/graphene oxide decorated carbon fiber synergistic reinforcement in epoxy-based composites. *Polymer* 131, 263–271. doi:10.1016/j.polymer.2017.10.049
- Wang, Y., Raman Pillai, S. K., Che, J., and Chan-Park, M. B. (2017). High interlaminar shear strength enhancement of carbon fiber/epoxy composite through fiber- and matrix-anchored carbon nanotube networks. *ACS Appl. Mat. Interfaces* 9 (10), 8960–8966. doi:10.1021/acsmi.6b13197
- Windhorst, T., and Blount, G. (1997). Carbon-carbon composites: A summary of recent developments and applications. *Mater. Des.* 18 (1), 11–15. doi:10.1016/s0261-3069(97)00024-1
- Wu, Q., Yang, X., He, J., Ye, Z., Liu, Q., Bai, H., et al. (2022). Improved interfacial adhesion of epoxy composites by grafting porous graphene oxide on carbon fiber. *Appl. Surf. Sci.* 573, 151605. doi:10.1016/j.apsusc.2021.151605
- Wu, X.-F. (2003). *Fracture of advanced polymer composites with nanofiber reinforced interfaces*. Lincoln, United States: University of Nebraska - Lincoln.
- Wu, X. (2009). *Fracture of advanced composites with nanofiber reinforced interfaces: Fabrication, characterization and modeling*. Werdohl, Germany: VDM Publishing.
- Wu, Z., Wang, X., Zhao, X., and Noori, M. (2014) State-of-the-art review of FRP composites for major construction with high performance and longevity 1(3): p. 201–231. doi:10.1504/ijssms.2014.062757
- Xiao, C., Tan, Y., Wang, X., Gao, L., Wang, L., and Qi, Z. (2018). Study on interfacial and mechanical improvement of carbon fiber/epoxy composites by depositing multi-walled carbon nanotubes on fibers. *Chem. Phys. Lett.* 703, 8–16. doi:10.1016/j.cplett.2018.05.012
- Xu, X., Liu, F., Jiang, L., Zhu, J. Y., Haagenson, D., and Wiesenborn, D. P. (2013). Cellulose nanocrystals vs. Cellulose nanofibrils: A comparative study on their microstructures and effects as polymer reinforcing agents. *ACS Appl. Mat. Interfaces* 5 (8), 2999–3009. doi:10.1021/am302624t
- Xu, Z., and Gao, C. (2015). Graphene fiber: A new trend in carbon fibers. *Mater. Today* 18 (9), 480–492. doi:10.1016/j.mattod.2015.06.009
- Xu, Z., Liu, Y., Zhao, X., Peng, L., Sun, H., Xu, Y., et al. (2016). Ultrastiff and strong graphene fibers via full-scale synergetic defect engineering. *Adv. Mat.* 28 (30), 6449–6456. doi:10.1002/adma.201506426
- Yang, Z., Tian, J., Yin, Z., Cui, C., Qian, W., and Wei, F. (2019). Carbon nanotube- and graphene-based nanomaterials and applications in high-voltage supercapacitor: A review. *Carbon* 141, 467–480. doi:10.1016/j.carbon.2018.10.010
- Yao, H., Sui, X., Zhao, Z., Xu, Z., Chen, L., Deng, H., et al. (2015). Optimization of interfacial microstructure and mechanical properties of carbon fiber/epoxy composites via carbon nanotube sizing. *Appl. Surf. Sci.* 347, 583–590. doi:10.1016/j.apsusc.2015.04.146
- Yuan, X., Zhu, B., Cai, X., Qiao, K., Zhao, S., and Yu, J. (2018). Influence of different surface treatments on the interfacial adhesion of graphene oxide/carbon fiber/epoxy composites. *Appl. Surf. Sci.* 458, 996–1005. doi:10.1016/j.apsusc.2018.06.161
- Zhang, M., Li, M., Liu, L., Fu, J., Jin, L., Shang, L., et al. (2019). Directly coating silanized nanocrystalline cellulose on carbon fiber for enhancing the interfacial adhesion of carbon fiber/epoxy resin composites. *Polym. Compos.* 40 (S1), E744–E752. doi:10.1002/pc.24983
- Zhang, R.-S., and Jiang, J.-W. (2018). The art of designing carbon allotropes. *Front. Phys. (Beijing)* 14 (1), 13401. doi:10.1007/s11467-018-0836-5
- Zhang, R. L., Gao, B., Du, W., Zhang, J., Cui, H., Liu, L., et al. (2016). Enhanced mechanical properties of multiscale carbon fiber/epoxy composites by fiber surface treatment with graphene oxide/polyhedral oligomeric silsesquioxane. *Compos. Part A Appl. Sci. Manuf.* 84, 455–463. doi:10.1016/j.compositesa.2016.02.021
- Zhang, W., Deng, X., Sui, G., and Yang, X. (2019). Improving interfacial and mechanical properties of carbon nanotube-sized carbon fiber/epoxy composites. *Carbon* 145, 629–639. doi:10.1016/j.carbon.2019.01.063
- Zhang, Z., Fu, K., and Li, Y. (2021). Improved interlaminar fracture toughness of carbon fiber/epoxy composites with a multiscale cellulose fiber interlayer. *Compos. Commun.* 27, 100898. doi:10.1016/j.coco.2021.100898
- Zhong, Y. L., Tian, Z., Simon, G. P., and Li, D. (2015). Scalable production of graphene via wet chemistry: Progress and challenges. *Mater. Today* 18 (2), 73–78. doi:10.1016/j.mattod.2014.08.019





## OPEN ACCESS

## EDITED BY

Veronique Michaud,  
Swiss Federal Institute of Technology  
Lausanne, Switzerland

## REVIEWED BY

Naim Naouar,  
Institut National des Sciences Appliquées  
de Lyon (INSA Lyon), France  
Malin Åkermo,  
Royal Institute of Technology, Sweden  
Philip Harrison,  
University of Glasgow, United Kingdom

## \*CORRESPONDENCE

James Kratz,  
✉ james.kratz@bristol.ac.uk

## SPECIALTY SECTION

This article was submitted to Polymeric  
and Composite Materials,  
a section of the journal  
Frontiers in Materials

RECEIVED 18 December 2022

ACCEPTED 31 January 2023

PUBLISHED 17 February 2023

## CITATION

Jimenez Martin C, Maes VK, McMahon T  
and Kratz J (2023), Influence of NCF  
architecture on the morphology of  
forming induced wrinkling.  
*Front. Mater.* 10:1126933.  
doi: 10.3389/fmats.2023.1126933

## COPYRIGHT

© 2023 Jimenez Martin, Maes, McMahon  
and Kratz. This is an open-access article  
distributed under the terms of the  
[Creative Commons Attribution License](https://creativecommons.org/licenses/by/4.0/)  
(CC BY). The use, distribution or  
reproduction in other forums is  
permitted, provided the original author(s)  
and the copyright owner(s) are credited  
and that the original publication in this  
journal is cited, in accordance with  
accepted academic practice. No use,  
distribution or reproduction is permitted  
which does not comply with these terms.

# Influence of NCF architecture on the morphology of forming induced wrinkling

Claudia Jimenez Martin<sup>1,2</sup>, Vincent K. Maes<sup>1</sup>, Turlough McMahon<sup>2</sup>  
and James Kratz<sup>1\*</sup>

<sup>1</sup>Bristol Composites Institute, University of Bristol, Bristol, United Kingdom, <sup>2</sup>Airbus UK, Bristol, United Kingdom

Biaxial Non-Crimp Fabrics (NCFs) offer the high deposition rates needed to meet the increased production rate targets of the aerospace industry, but formability remains an issue for complex parts. In this study a large scale, complex geometry with a span of 2 m is used to study wrinkle patterns in NCF preforms and how they are influenced by several key NCF parameters. Wrinkle dimensions are captured in 3D scans and used as a proxy metric for “formability”. Results show that whereas location and shape of the wrinkling are driven by geometry, wrinkle size and its metrics (amplitude, wavelength, aspect ratio) are driven by the NCF architecture. In addition, conflicting trends on wrinkle size observed show the complexity of forming as a process. The results presented show the importance of using several characterisation methods and not reducing wrinkling characterisation to a single data point or set.

## KEYWORDS

non-crimp fabric, forming, dry fibre process, wrinkles, characterisation

## 1 Introduction

Biaxial Non-Crimp Fabrics (NCFs) offer the high deposition rates needed to meet the increased production rate targets of the aerospace industry. A key step following deposition, is the forming of the reinforcement material into the final preform geometry (Turk et al., 2019). During forming, in-plane shear is the dominant deformation mechanism (Lomov, 2016), resulting in large rotations in the fibre direction and a change in the net shape of the material (Thompson et al., 2018). While most forming technologies are applied to woven fabric, non-crimp fabrics (NCFs) are often preferred by designers because of their higher mechanical properties (Lomov, 2016), as the fibres are stitched instead of woven. NCF's are often tailored to their application, for example through the addition of binder or veil for toughening properties or the combination of different fibre orientations for an optimised layup. Design for manufacture requires close examination into the effect of these parameters on the formability of the NCF.

Studies into formability of dry fibre textiles highlight the challenges in characterising the resultant preform quality. Benchtop geometries are often used to ensure as reliable and repeatable test specimens as possible, for example the hemisphere punch test (Nosrat et al., 2016; Bardl et al., 2018; Guzman-Maldonado et al., 2019; Viisainen and Sutcliffe, 2021) which takes advantage of a symmetric shape and the application of tension to the fabric. The dry fibre preforms are often characterised through the resultant features: out-of-plane wrinkling and in-plane shear. Some studies, use wrinkling as a discrete parameter (number of wrinkles) to show the relation of this



to material properties. Boisse et al. (Boisse et al., 2011) for example showed the direct effect of bending stiffness on number of wrinkles: a higher bending stiffness led to less wrinkles and hence more shearing in the material. In the case of the hemisphere, the final formed shape was used to show how the fabric compensates for the excess length caused by the 3D geometry. This was the case for example, in Chen et al.'s study (Chen et al., 2021) into the effect of NCF stitching on asymmetry of the resultant preform. Through the removal of the stitching from a biaxial NCF sample, it was shown wrinkling in the preform is successfully decreased. As NCF's require a weft stitch to maintain stability of the various layers, understanding of the influence of this on the fabric's formability is key. Other studies (Martin et al., 2022a) into NCF stitching use bias extension test set ups to show the difference in force extension behaviour for samples varying in stitch type, length and tension. The stabilising role of the stitch was highlighted in these studies through samples showing stitch breakage and subsequent tow dislocation.

The constraints introduced by the stitching as well as the interaction between orientations are essential for comprehensive characterisation of the material. The importance of stacking sequence—the order in which the orientations are laid and subsequently formed—was shown by Hallander et al. (Hallander et al., 2013) on a prepreg hot drape forming process. It should be noted Hallander's work focuses on inter-ply shear (between the plies) rather than intra-ply shear (within the plies) as described above for in-plane shear—both of which influence forming. Jimenez Martin et al. (Martin et al., 2022b) followed this using NCF forming to show the existence of a predominant orientation driving the wrinkling result when combined with other orientations. The most prevalent orientations are 0°/90° and 45°/135°s. More recent studies have started to investigate non-orthogonal orientations (0°/45°s). This study uses a non-orthogonal biaxial NCF format (0°/45°) previously shown under picture frame loading conditions in Guzman et al.'s work (Guzman-Maldonado et al., 2019). The use of this NCF is key to achieve layups with the appropriate amounts of fibres in each orientation. Areal weight becomes instrumental in this case allowing each layer within a stitched NCF to be tailored to the required weight for the structure's loading requirements. As areal weight is often informed by the application, this parameter tends to remain constant in studies in the literature, and its effect on formability is not known.

To further tailor the NCF layup to the structure as well as stabilise the preform during handling, toughening veils and binders may be added. As such, most studies concentrate on the influence of these on the resultant mechanical properties of the composite (Heieck, 2015). Hallander et al. (Hallander et al., 2016) used thermoplastic veil to increase the friction between prepreg layers during forming. Though this suggests veil has a direct influence in forming through friction, the results of the study may only be true for prepreg and not dry fabric NCF forming.

Generally, studies published on the effect of NCF architecture on formability are limited in the variety of samples shown as well as the test set up used, with most studies choosing a controlled uniaxial loading set up. Though this may be beneficial in terms of repeatability and ease of sample loading, key boundary

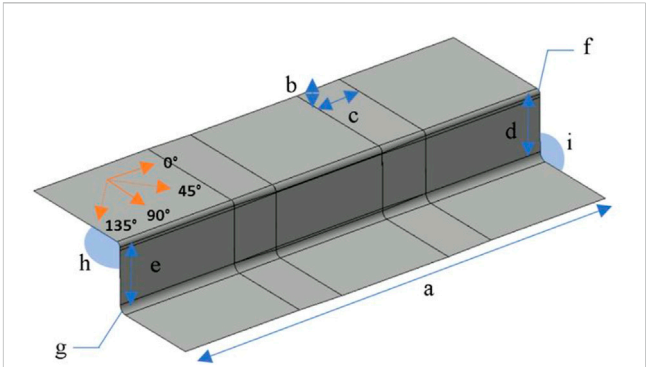


FIGURE 1  
Geometry used for forming trials.

TABLE 1 Geometry dimensions.

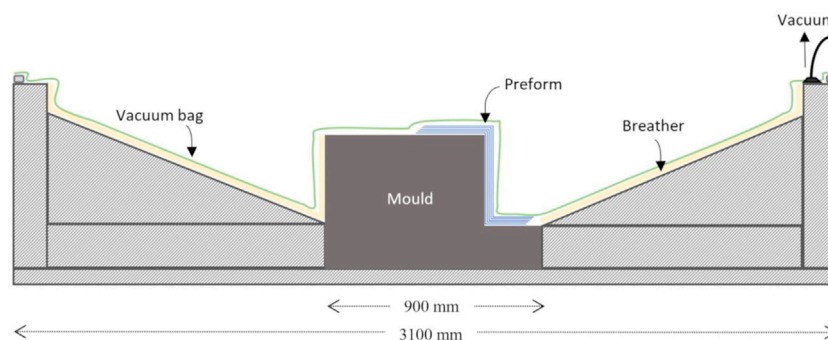
Dimension	Number
Length [a] (mm)	2000
Ramp height to length ratio [b:c]	1:40
Web height ratio [d:e]	1:1
Convex to concave corner radius ratio [f:g]	1:2
Top surface/web to bottom surface/web angle ratio [h:i]	1:1

conditions relevant to an industrial forming process are not addressed in these studies. This study aims to bridge the gap between benchtop test studies and industrial forming processes by introducing a 2 m span geometry with a single diaphragm forming set up leading to a repeatable wrinkle shape and pattern that more closely represents industrial forming processes. Established methods readily available in the literature for characterising wrinkles, both on woven and NCF dry fabrics, as well as prepreg, are drawn upon. The extensive matrix of NCF samples allows investigation of a number of parameters influencing architecture and subsequent formability in a realistic multiple-factor-at-a-time design of experiments. Parameters include: NCF orientation, addition of veil, stitch length and type and areal weight balance. The large geometry size and type combined with the NCF formats chosen add knowledge key to the field of NCF forming with a view to industrial structures. Orthogonal and non-orthogonal biaxial orientations will be considered in this paper.

## 2 Methodology

### 2.1 Geometry

Forming experiments were carried out on the geometry shown in Figure 1. The geometry contains two ramps with a gradient of 1:40 receding towards the centre of the geometry creating an excess in fabric length. Ramps are common in aerostructures for weight and loading optimization of the



**FIGURE 2**  
Tooling and geometry set up to ensure constant diaphragm kinematics.

**TABLE 2** NCF specifications.

ID	Orientation	Areal weight balance
NCF1	0°/90°	unbalanced
NCF2	0°/45°	unbalanced
NCF3	45°/135°	balanced

structure. The length of the geometry is approximately 2 m, a sizeable increase from any forming geometries currently available in the literature. Table 1 provides a legend for the labels used in Figure 1 including dimensions. Due to industrial input which generated this design, dimensions can only be provided in relative or qualitative terms, the same holds true for some of the material properties provided in this paper.

The NCF plies were placed on the geometry upper surface and left to drape over the vertical web and rest on the lower surface under its own weight. The plies for each forming trial were 'fixed' on the same location on the upper surface using tape to avoid them from slipping down the vertical surface and enable a repeatable preform location per trial. A non-reusable diaphragm was sealed around four raised edges surrounding the geometry. The bagging was sealed to these raised edges to ensure that the order of drape, an influential parameter in resultant preform wrinkling is controlled for each drape trial. Further, a high elongation vacuum bagging film was used to enable stretching over the complex shape and reduce bridging in corners. A cross-section diagram of the tooling and geometry is shown in Figure 2.

During forming, when full vacuum is applied, the diaphragm contacts the top surface first, followed by the male or convex radius and outside edge of the bottom surface. The last surface the diaphragm meets is the female or concave radius. This creates a 'clamping effect' on the flange area of the preform where most of the wrinkling was observed. The preform surface was scanned while still under vacuum with a Hexagon Absolute Arm and interrogated for wrinkle dimensions using Polyworks software.

## 2.2 Materials

Three carbon fibre NCF orientations were used to create the preforms. The specification of each is shown in Table 2.

Using these NCFs, the matrix of trials seen in Table 3 was carried out. Six plies were placed all at once on the geometry. This number was chosen to show significant wrinkling used to assess the effect of the parameter change. The stitch and loop side of the materials have been shown with the fibre orientation highlighted in red. In the case of unbalanced areal weight NCF formats, the heavier areal weight has been underlined. The placement of veil or binder has been shown through the use of "V" and "B" respectively. Cells have been highlighted to show the change in parameter used as a sensitivity study. This reflects constraints typical to an industrial matrix, far from the idealised one factor at a time matrix of trials. The sensitivity studies on the different parameters were therefore not all available for all three NCF formats.

## 2.3 Wrinkle characterisation

A number of metrics were considered in order to characterise the resultant wrinkling to allow detailed comparisons.

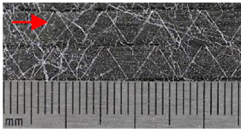
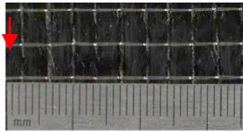

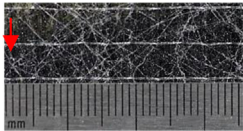



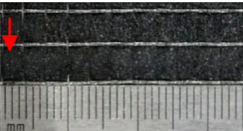

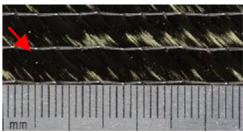
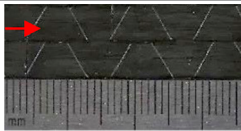
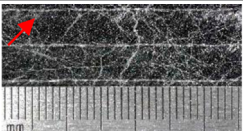
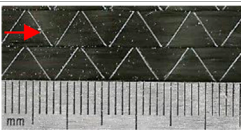
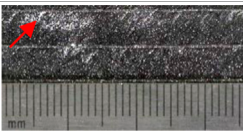
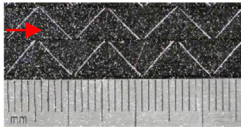
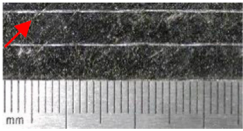

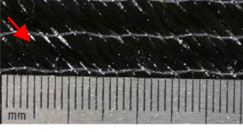


### 2.3.1 Shape

A qualitative assessment of the shape of the wrinkles was made on the basis of the colour maps generated, see Figure 3.

### 2.3.2 Size

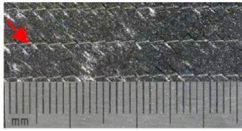
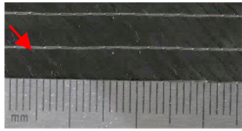
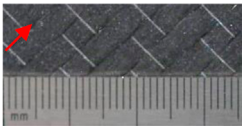
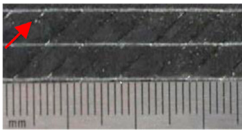
To capture the size of the wrinkle, three characteristic metrics were considered, including amplitude, wavelength, and aspect ratio. These measures were obtained by sampling the wrinkles along their length, as shown in Figure 3. Wavelength (shown in blue) are sampled perpendicular to the wrinkle direction vector (labelled in white). An aspect ratio is computed at each sampling location. Wrinkle amplitude was measured relative to the upper surface of the outermost ply (coloured in grey in Figure 3). A lower limit of 0.4 mm out-of-plane height was used in all trials to filter out the "noise" of the overall NCF surface (caused by the stitching or tow edges).

TABLE 3 Matrix of trials.

Trial ID	NCF ply sequence	Veil	Stitch length (mm)	Stitch type	Stitch side	Loop side
1a	[V/0°/90°] <sub>6</sub>	Yes	3.6	Tricot loop		
1b	[0°/90°/V] <sub>6</sub>	Yes	3.6	Tricot loop		
1c	[0°/90°/B] <sub>6</sub>	No	3.6	Tricot loop		
1d	[0°/90°/B] <sub>6</sub>	No	3.1	Tricot loop		
2a	[V/0°/135°] <sub>6</sub>	Yes	3.1	Tricot pillar		
2b	[0°/45°/V] <sub>6</sub>	Yes	3.1	Tricot pillar		
2c	[0°/45°/B] <sub>6</sub>	No	4	Tricot loop		
2d	[B/0°/45°/B] <sub>6</sub>	No	5.1	Tricot loop		
3a	[V/45°/135°] <sub>6</sub>	Yes	2.2	Tricot Pillar		
3b	[V/135°/45°/B] <sub>6</sub>	Yes	2.2	Pillar		

(Continued on following page)

TABLE 3 (Continued) Matrix of trials.

Trial ID	NCF ply sequence	Veil	Stitch length (mm)	Stitch type	Stitch side	Loop side
3c	[B/45°/135°] <sub>6</sub>	No	2.2	Pillar		
3d	[B/135°/45°/B] <sub>6</sub>	No	5.1	Tricot Loop		

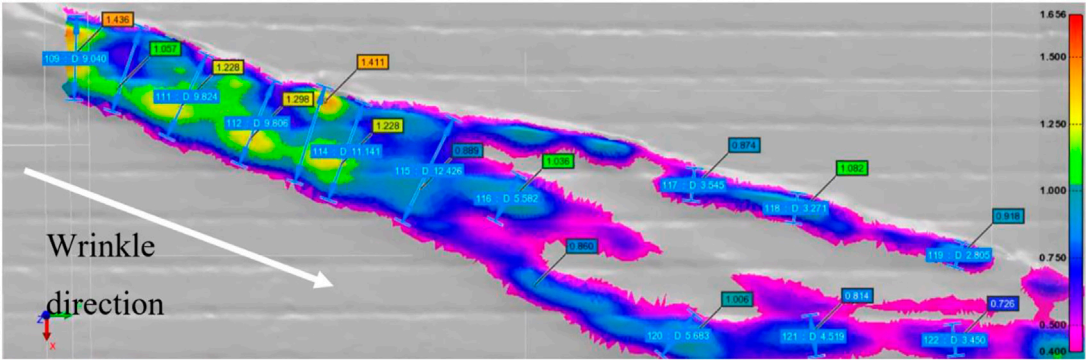


FIGURE 3 Example of sampling points for wrinkle width and height shown along wrinkle length with colour map showing out-of-plane heights.

2.3.3 Location

The location of the wrinkle within the part geometry was assessed both qualitatively through visual inspection of the colour maps as well as through coupling wrinkle amplitude with one of two axes of the plane on which wrinkles were found.

Wrinkling was only assessed on the outermost ply while the preform was still under maximum vacuum. Wrinkling was observed to propagate through the stack of six plies during removal of the plies from the geometry. However, no assessment was made of these as the plies were not heated or ‘binder activated’ and therefore no longer consolidated to the geometry once vacuum was released to observe the inner plies.

3 Results

3.1 Wrinkle shape

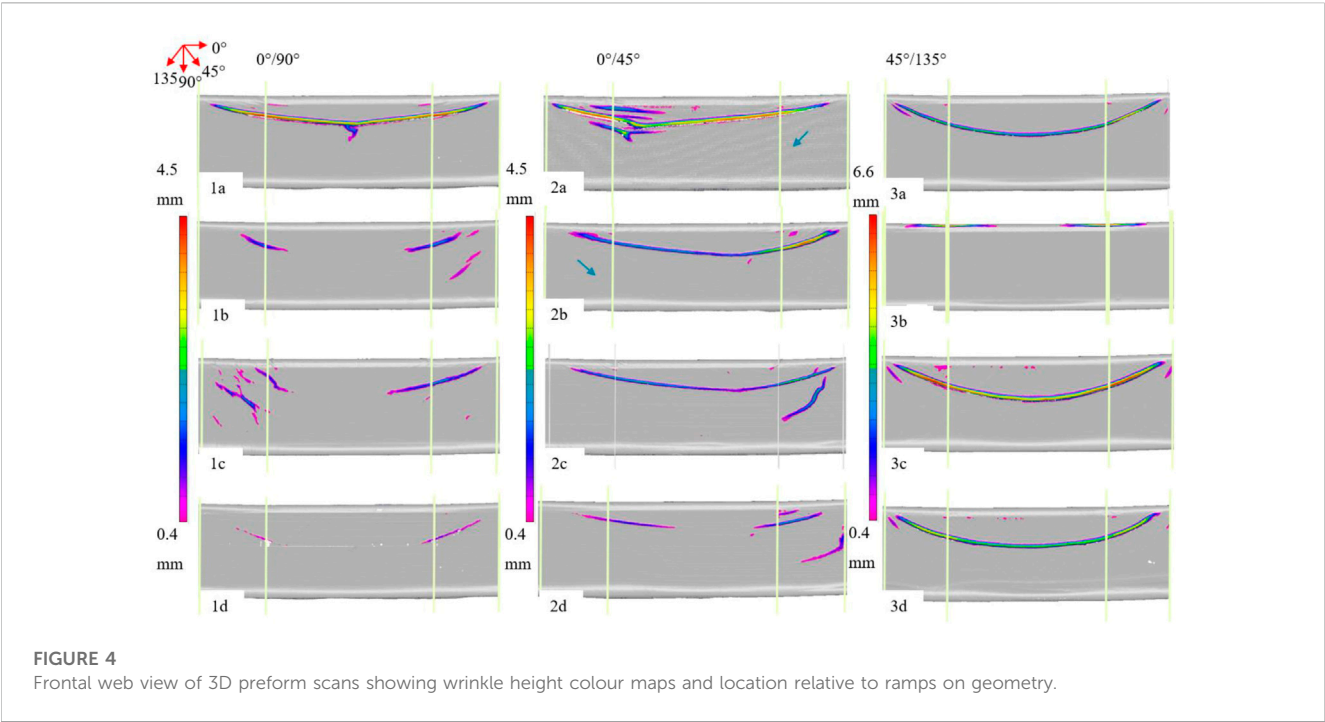
The scanned preform results, labelled by Trial ID, are shown in Figure 4. Colour maps show the distribution of out-of-plane heights along the wrinkle, with the scale adjusted for each NCF orientation for viewing purposes. The lower end value of the scale has been adjusted to filter out the “noise” caused by the texture of the NCF preform (0.4 mm). A front-on view to the geometry web surface is

chosen as this was the area where most of the wrinkling occurred. A rosette shows the orientation of the fibres as seen on the web. Vertical lines show the start and end of both left and right ramps on the geometry.

The images show most of the wrinkling initiates on the outside edges of both ramps and descends diagonally down towards the centre plane forming a crescent shape. Not all preforms connect at the centre to form a continuous wrinkle, as seen in most of the 0°/90° trials (1b-d). The 45°/135°s on the other hand all seem to show a continuous and symmetric “smile” wrinkle (3a, 3c-d), except for the veiled heavier (areal weight) format (3b). This trial is different in appearance from all others with wrinkling occurring on the upper (convex) radius of the geometry rather than on the web surface. Both wrinkles however are still located around the ramp regions, suggesting it is geometry driven. The distinct wrinkling is likely caused by the combination of veil with pillar stitch pattern, pointing at an interaction between these two parameters.

All wrinkling patterns are approximately symmetric in appearance, though there are differences in overall wrinkle heights between left and right wrinkles, with the 0°/45° layouts showing the least symmetry. In fact, the shape of these is seen to change depending on whether the orientation is a 0°/45° or a 0°/135°, as observed when comparing trial 2a to trials 2b-d. Additional shorter wrinkles are also observed in some of these trials.





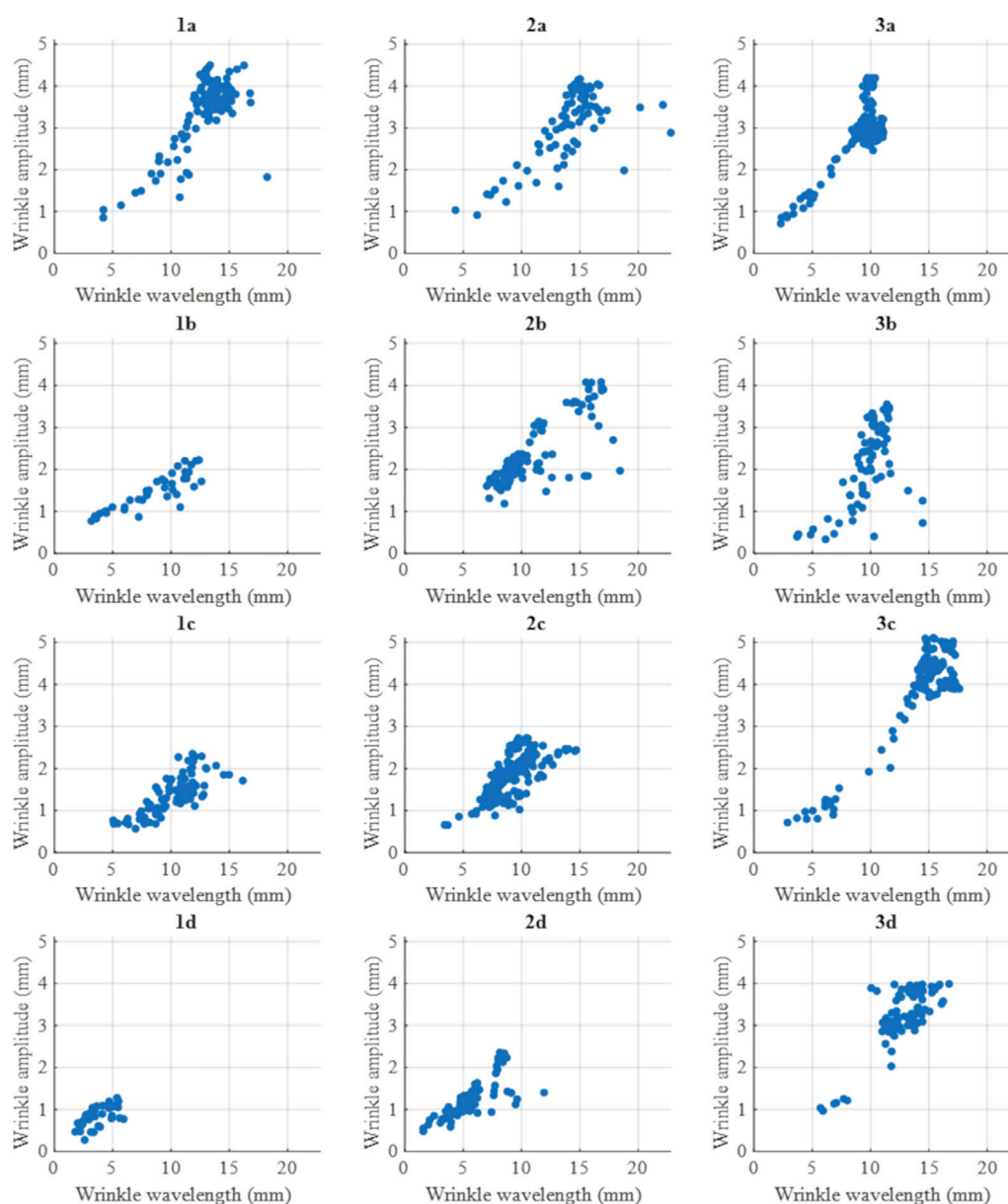
**FIGURE 4**  
Frontal web view of 3D preform scans showing wrinkle height colour maps and location relative to ramps on geometry.

**TABLE 4** Maximum wrinkle amplitude values (mm).

			NCF 1 (0°/90°)	NCF 2 (0°/45°)	NCF 3 (45°/135°)
a	Amplitude	Avg ± st. dev	3.4 ± 0.8	2.9 ± 1.0	2.8 ± 0.7
		Max	4.5	4.2	4.2
	Wavelength	Avg ± st. dev	13.0 ± 2.2	14.1 ± 2.9	9.3 ± 1.9
		Max	18.2	22.8	11.1
b	Amplitude	Avg ± st. dev	1.4 ± 0.4	2.4 ± 0.7	5.9 ± 0.4
		Max	2.2	4.1	6.6
	Wavelength	Avg ± st. dev	8.2 ± 3.0	11.0 ± 2.9	5.4 ± 1.5
		Max	12.6	18.5	7.2
c	Amplitude	Avg ± st. dev	1.4 ± 0.4	1.9 ± 0.5	3.8 ± 1.2
		Max	2.4	2.7	5.1
	Wavelength	Avg ± st. dev	10.2 ± 2.2	9.3 ± 1.9	14.2 ± 3.5
		Max	16.2	14.7	17.6
d	Amplitude	Avg ± st. dev	0.9 ± 0.2	1.3 ± 0.5	3.2 ± 0.7
		Max	1.3	2.4	4.0
	Wavelength	Avg ± st. dev	3.7 ± 1.2	5.9 ± 2.0	12.6 ± 1.9
		Max	5.9	11.9	16.7

As well as differences in preform results between NCF orientations, the effect of the NCF architecture is shown. Results show noticeably higher wrinkling on the veiled preforms, especially those with veil applied on the 0° fibres (1a, 2a). For the 45°/135°s the opposite effect was observed with more noticeable wrinkling on the non-veiled preforms. A higher stitch length on the 0°/45°s and 45°/135°s (2d and 3d) showed lower wrinkling whereas on the 0°/90°s (3c), the effect was the opposite with a slight increase in stitch length





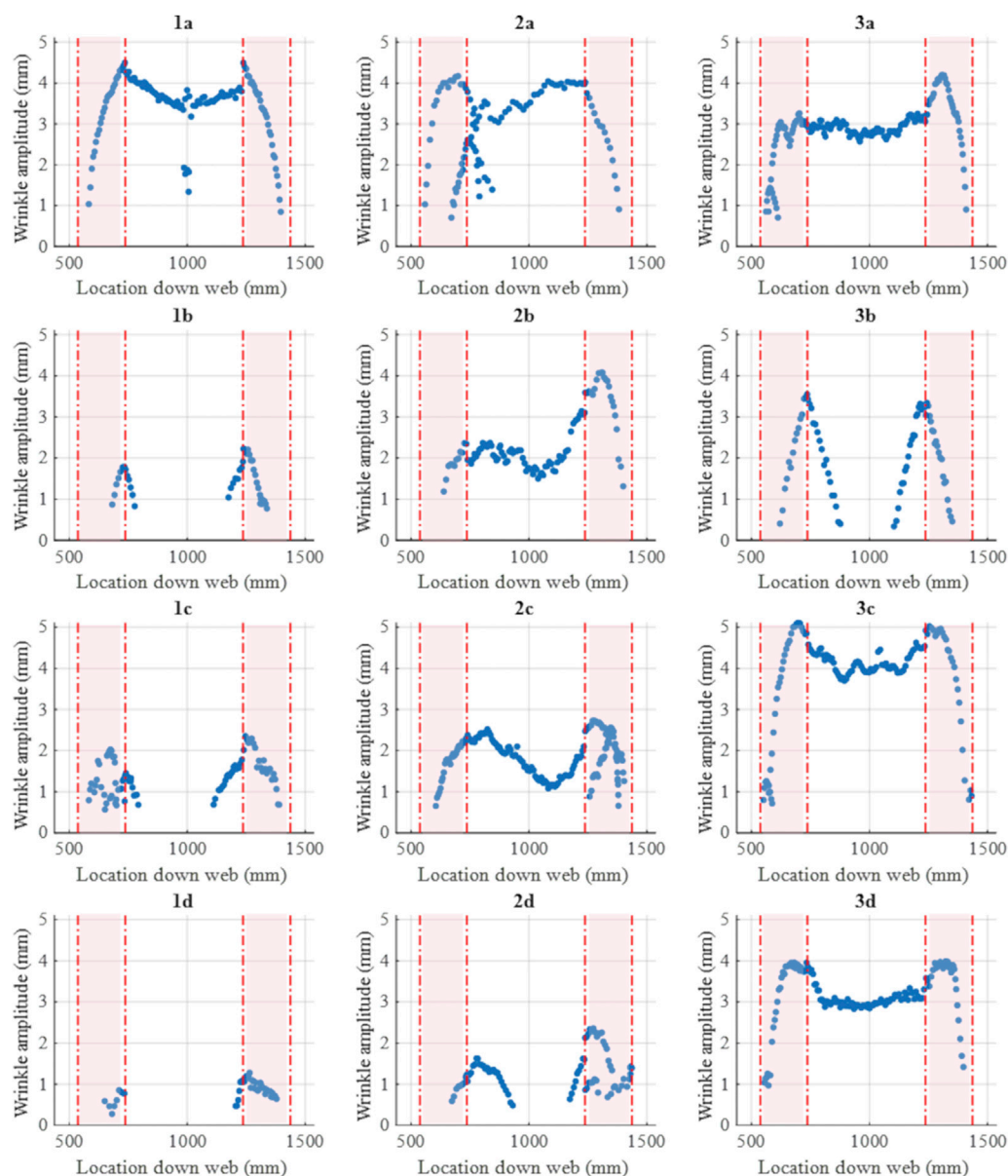
**FIGURE 5**  
Wrinkle amplitude vs. wavelength plots.

(from 3.1 to 3.6) showing higher wrinkling (3c vs. 3d). This shows the importance of tailoring NCF parameters dependent on orientation.

## 3.2 Wrinkle size

Wrinkle amplitude and wavelength values are shown in Table 4. Results show the highest out-of-plane values for Trials 3b and c, suggesting the combination of pillar stitch pattern on a 45°/135° NCF drives this. Overall results show higher wrinkle amplitude values for veiled materials, with the

45°/135° NCFs showing overall higher wrinkling. The lowest amplitude value (1d) correlated with the smallest visible wrinkling observed in 1d shown in Figure 4. Maximum wrinkle wavelengths on the other hand did not match those with maximum wrinkle amplitudes, with veiled trials (1a, 2a, 2b) showing overall wider wrinkling. The opposite was observed for non-veiled 45°/135°s (3c and 3d). Stitch length had a minimal effect in both wrinkle wavelength and amplitude for 0°/45°s and 45°/135°s, whereas a larger difference in wrinkle wavelength between the 0°/90° trials (1c and d) was observed, with the shorter stitching resulting in lower overall wrinkling. This same trend however was not able to be assessed for 0°/45°s



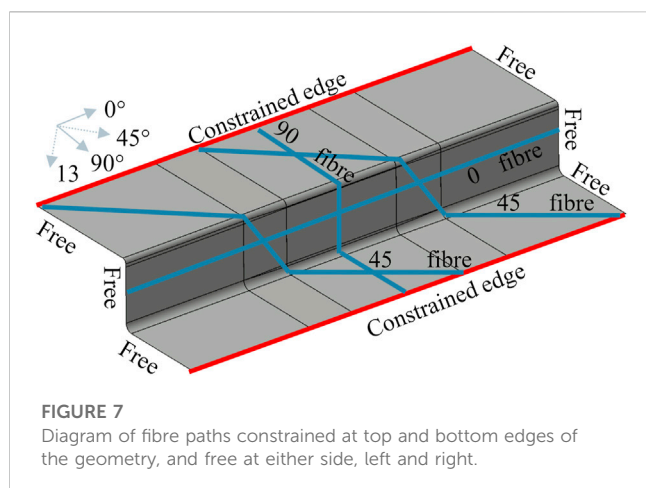
**FIGURE 6**  
Wrinkle amplitude vs. location along web showing location of ramps.

and  $45^\circ/135^\circ$  as other material parameters may have affected the result (e.g. the change in stitch pattern in the case of the  $45^\circ/135^\circ$  between 3c and 3d). Higher standard deviation values were observed for wrinkle wavelengths over wrinkle amplitudes. However no clear link is observed between NCF parameters and standard deviation. This points at NCF parameters being sensitive to a number of wrinkle metrics and reinforces the use of several methods, both visual and numerical to characterise them.

Discrepancies in maximum and average values for each trial ID are observed in both wrinkle amplitude and wavelength values. Overall, the tabulated results help show the distribution of sample values from the wrinkles shown in the colour maps. Scatter plots for wrinkle amplitude vs. wavelength values for all trials are shown in

Figure 5. A linear relationship between amplitude and wavelength is observed in all trials, with amplitude increasing as wavelength increases. This shows wrinkle aspect ratio (ratio of amplitude to wavelength) is specific to the NCF format or trial (1a, 2a, etc). Not all trials however, show a perfectly linear correlation, with some, for example 3c showing a changing aspect ratio value for higher wrinkle values.

Data points were sampled from all wrinkles observed on the geometry web and have not been distinguished for those showing several separate wrinkles. This again shows aspect ratio as a material driven parameter, as data points from different wrinkle instances but for the same NCF material can be best fitted together. In fact, no relationship is observed between number of wrinkles and resultant level of scatter. As the wrinkles were sampled uniformly along their



length, shorter or smaller wrinkles contain a smaller number of samples plotted, as is the case for 1d for example where the wrinkling is overall low and the distribution highly clustered. In most cases the scatter increases at higher wrinkle amplitude and wavelength values. The 45°/135°s show an increase in gradient with higher amplitudes for the same wavelength recorded at higher values. The effect of veil on the 0°s for the 0°/90°s shows as a higher aspect ratio (1a vs. 1b and 1c). This effect is not as discernible for the 0°/45°s. Stitch length on the other hand does not seem to have an effect on aspect ratio, but rather on absolute maximum values.

### 3.3 Wrinkle location

The wrinkle colour maps shown in Figure 4 pointed at asymmetry in both the shape of the wrinkle as well as the distribution of amplitude along the wrinkle. This has been plotted in Figure 6. Wrinkle amplitude values sampled have been shown against their respective location along the length of the web. The area of the ramps is shaded on the graphs. Results show the maximum amplitude values tend to occur on the inner ramp edges, where these meet the flat central plane. Amplitude then decreases in this central plane in the case of continuous wrinkles that join at the centre, or more generally decrease towards the end of the wrinkle. This is also observed for the individual wrinkles surrounding the larger wrinkles (2a, 1c, 2c, 2d) and shows in the form of an upside down “v” shape on the plots. Overall, a sharper increase to the maximum point or “peak” of the wrinkle is observed in the veiled preforms (1a–3b). This is most noticeable in the 45°/135°s where 3c and 3d show flatter peaks. The asymmetry in the 0°/45°s can be observed with one side showing a higher peak amplitude than the other.

## 4 Discussion

This study has presented a comprehensive matrix of forming trials to show the effect of NCF material architecture on out-of-plane wrinkling. Though the matrix is far from an idealised “one factor at a time” full factorial design, the combined effect of NCF material parameters has been shown where individual parameters could not be isolated. For example, the distinctive

corner wrinkling observed in trial 3b was stipulated to be likely due to the combination of veil with pillar stitch pattern. This itself points at a strong interaction between these two parameters. The singular effect of a pillar over a tricot stitch however cannot be isolated due to the likely interaction with other material parameters. Further studies would therefore benefit from a one-factor at a time approach to Design of Experiments. Different methods have also been presented for characterising the resultant wrinkling. This is of relevance as some trends or hypotheses that are visible through some methods are not visible in others. The location of 3b for example, by comparison to all other trials, showed wrinkling in the top radius, rather than on the geometry web. The assessment of the wrinkling can then be based not just on wrinkle dimensions but on whether the location on the structure is critical. Overall, the general similarities in location and shape of the wrinkling point at these being geometry driven. The recess ramp feature causes an excess in fibre length in the centre of the geometry. The diaphragm kinematics (as described in the Methodology) result in this excess occurring between the “clamped” or “tensioned” regions of the preform on the upper and lower surfaces. This leads to the characteristic “smile” wrinkle observed in the centre of the ramps on the flange of the geometry. The reader is referred to the kinematic model of the geometry shown by Jimenez Martin et al. in (Martin et al., 2022a). Sjölander et al. (Hallander et al., 2015), using a similar recess ramp geometry stipulated that the wrinkling was a result of interaction between two layers with specific fibre orientations or due to compression of the entire stack. The differences in wrinkle size (amplitude, wavelength) point at material driven behaviour in forming.

When comparing wrinkle shapes, similarities between trials of the same NCF orientation are observed. The 0°/45°s (2a–d) for example show an asymmetric “smile” wrinkle, i.e. the “trough” of the wrinkle occurs to one side rather than in the centre as is the case for the 45°/135°s. The side (towards left or right ramp) that the trough occurs in depends on whether the NCF is a 0°/45° or a 0°/135°, as seen when comparing 2a to trials 2b–d. This side also shows higher out-of-plane wrinkle values than the longer side of the wrinkle. This is due to an area of the 45° (or 135°) fibres having a free edge at the side of the preform, as shown in Figure 7. The free edge is a result of the sequence of the diaphragm contact points on the geometry, leading to an upper and a lower constrained edge with free edges to the left and right of the geometry. This creates a tension or ‘clamping’ effect across the height of the geometry flange. The area between ‘45 fibre path 1’ and ‘45 fibre path 2’ is fully constrained on both upper and lower edges, whereas the area to the right of ‘45 fibre path 2’ sees a free edge. This phenomenon was shown by Guzman et al. (Guzman-maldonado et al., 2022) in the form of an increase in shear observed in this triangular region of fibres. However, as not enough tension (the tension in this case is provided by the diaphragm) is applied in the direction of the fibres as was stipulated in Guzman’ work, the result instead is higher out-of-plane wrinkling. This may also explain why the amplitude profile for the 45°/135°s over the length of the geometry decreases in the centre between the two ramps, as the fibres are all constrained in this region (by the two constrained edges shown in Figure 4) and therefore tensioned more than those with a free edge. The tension results in lower out-of-plane wrinkling.

Preforms with added veil showed overall wider amplitude wrinkling and higher thickness due to the added weight of the veil. The higher amplitude may be due to the additional inter-ply friction created by the veil, as pointed out by Hallander et al. in their study on prepreg (Hallander et al., 2013). The addition of veil also contributes to a higher overall areal weight, likely leading to an increase in bending stiffness, this in turn may contribute to the resultant higher level of wrinkling, both in amplitude and in number of wrinkles. In fact, Boisse et al. (Boisse et al., 2011) showed the direct effect of bending stiffness on number of wrinkles: a higher bending stiffness led to less wrinkles and hence more shearing in the material.

As the veiled material formats showed overall less distributed separate wrinkling, this suggests the addition of veil on NCFs significantly increases the bending stiffness properties. The orientation on which veil is applied was also shown to be an important parameter for unbalanced NCF formats ( $0^\circ/90^\circ$  and  $0^\circ/45^\circ$ ). With both formats weighted towards the  $0^\circ$  fibres, a difference in resultant wrinkling was observed dependent on which orientation the veil was applied on. Results showed overall higher wrinkling for formats with veil applied on the  $0^\circ$  fibres, showing a higher areal weight exacerbates the influence of veil on the preform. The addition of veil on the  $45^\circ/135^\circ$ s however did not show observable differences in number of wrinkling and showed an opposite effect to the  $0^\circ/90^\circ$ s and  $0^\circ/45^\circ$ s in terms of wrinkle amplitude: veiled  $45^\circ/135^\circ$ s showing lower wrinkle amplitude, whilst veiled  $0^\circ/90^\circ$ s and  $0^\circ/45^\circ$ s leading to higher wrinkle amplitudes. This highlights the complex interaction between NCF parameters and the need to tailor them dependent on orientation.

## 5 Conclusion

This study has presented a matrix of trials realistic of an industrial campaign, carried out on a much larger scale geometry with representative features for aerostructures than is currently available in the literature. Results show that whereas location and shape of the wrinkling are driven by geometry, wrinkle size and its defining parameters (amplitude, wavelength, aspect ratio) are driven by the parameters defining NCF architecture. The interaction between these leads to complex wrinkling, characterised both numerically and graphically. The key trends extracted include:

- location and shape of the wrinkling are mainly geometry driven whereas wrinkle amplitude and width are mainly material driven
- non-orthogonal  $0^\circ/45^\circ$  NCF's show asymmetric wrinkling due to the difference in constrained edges seen by the two fibre orientations
- veiled NCFs showed overall higher wrinkling, though the effect changes dependent on other material variables such as stitch and orientation
- $45^\circ/135^\circ$ s showed overall higher wrinkling over the  $0^\circ/90^\circ$  and  $0^\circ/45^\circ$  formats.

Conflicting trends observed previously in the literature, for example with regards to veil, have also been shown to differ dependent on which NCF architecture variables these are combined with, once again highlighting the challenge of identifying single key parameters to formability. Trends extracted also differ between wrinkle characterisation methods chosen, showing the complexity in attempting to use these as a single metric for formability. The study therefore shows the importance of using several characterisation methods and not reducing wrinkling definitions to a single data point or set. Overall, the study has showcased the sensitivity of resultant preform wrinkling to NCF architecture and the importance of wrinkle characterisation methods to analyse the sensitivity. The results from the study may impact future process modelling approaches to defect prediction, for example through highlighting key parameters that may influence the model result.

## Data availability statement

The datasets presented in this article are not readily available because the raw data required to reproduce these findings are subject to industrial confidentiality. Requests to access the datasets should be directed to James Kratz, james.kratz@bristol.ac.uk.

## Author contributions

CJ: Conceptualization, Methodology, Validation, Formal analysis, Investigation, Data Curation, Writing—Original Draft, Visualization. VM: Conceptualization, Writing—Review and Editing, Supervision. TM: Conceptualization, Resources, Writing—Review and Editing, Supervision, Funding acquisition. JK: Conceptualization, Writing—Review and Editing, Supervision, Funding acquisition.

## Funding

The research presented was supported by the Airbus, part funded by the UK's Aerospace Technology Institute, and the EPSRC through the Centre for Doctoral Training in Composites Manufacture (EP/L015102/1) and the Programme Grant "Certification for Design—Reshaping the Testing Pyramid" (CerTest, EP/S017038/1). The support received is gratefully acknowledged.

## Conflict of interest

Authors CJ and TM were employed by the company Airbus UK. The remaining authors declare that the research was conducted in the absence of any commercial or financial relationships that could be construed as a potential conflict of interest.

## Publisher's note

All claims expressed in this article are solely those of the authors and do not necessarily represent those of their affiliated

organizations, or those of the publisher, the editors and the reviewers. Any product that may be evaluated in this article, or claim that may be made by its manufacturer, is not guaranteed or endorsed by the publisher.

## References

- Bardl, G., Nocke, A., Hübner, M., Gereke, T., Pooch, M., Schulze, M., et al. (2018). Analysis of the 3D draping behavior of carbon fiber non-crimp fabrics with eddy current technique. *Compos Part B [Internet]* 132, 49–60. doi:10.1016/j.compositesb.2017.08.007
- Boisse, P., Hamila, N., Vidal-Sallé, E., and Dumont, F. (2011). Simulation of wrinkling during textile composite reinforcement forming. Influence of tensile, in-plane shear and bending stiffnesses. *Compos Sci. Technol. [Internet]* 71 (5), 683–692. doi:10.1016/j.compscitech.2011.01.011
- Chen, S., Joesbury, A. M., Yu, F., Harper, L. T., and Warrior, N. A. (2021). Optimisation of intra-ply stitch removal for improved formability of biaxial non-crimp fabrics. *Compos Part B Eng.* 229, 109464. doi:10.1016/j.compositesb.2021.109464
- Guzman-maldonado, E., Bel, S., Bloom, D., Fideu, P., and Boisse, P. (2022). Materials & Design Experimental and numerical analyses of the mechanical behavior during draping of non-orthogonal bi-axial non-crimp fabric composite reinforcements. *Mater Des. [Internet]* 218, 110682. doi:10.1016/j.matdes.2022.110682
- Guzman-Maldonado, E., Wang, P., Hamila, N., and Boisse, P. (2019). Experimental and numerical analysis of wrinkling during forming of multi-layered textile composites. *Compos Struct. [Internet]* 208, 208–223. doi:10.1016/j.compstruct.2018.10.018
- Hallander, P., Åkermo, M., Mattei, C., Petersson, M., and Nyman, T. (2013). Composites: Part A an experimental study of mechanisms behind wrinkle development during forming of composite laminates. *Compos Part A [Internet]* 50, 54–64. doi:10.1016/j.compositesa.2013.03.013
- Hallander, P., Sjölander, J., and Åkermo, M. (2015). Forming induced wrinkling of composite laminates with mixed ply material properties; an experimental study. *Compos Part A Appl. Sci. Manuf. [Internet]* 78, 234–245. doi:10.1016/j.compositesa.2015.08.025
- Hallander, P., Sjölander, J., Petersson, M., and Åkermo, M. (2016). Interface manipulation towards wrinkle-free forming of stacked UD prepreg layers. *Compos Part A Appl. Sci. Manuf. [Internet]* 90, 340–348. doi:10.1016/j.compositesa.2016.07.013
- Heieck, F. (2015). Binder application methods for textile preforming processes. *APRIL - Adv. Preform Manuf. Industrial LCM-Processes*, 1–16.
- Lomov, S. (2016). *Non-crimp fabric composites: Manufacturing, properties and applications*. Cambridge: Woodhead Publishing Series in Composites Science and Engineering.
- Martin, C. J., Maes, V., McMahon, T., and Kratz, J. (2022). Large scale forming of non-crimp fabrics for aerostructures. *Key Eng. Mat.* 926, 1387–1398. doi:10.4028/p-809h64
- Martin, C. J., Maes, V. K., McMahon, T., and Kratz, J. (2022). The role of bias extension testing to guide forming of non-crimp fabrics. *Front. Mater.* 9, 1–13. doi:10.3389/fmats.2022.825830
- Nosrat, F., Gereke, T., and Cherif, C. (2016). Composites: Part A analyses of interaction mechanisms during forming of multilayer carbon woven fabrics for composite applications. *Compos PART A [Internet]* 84, 406–416. doi:10.1016/j.compositesa.2016.02.023
- Thompson, A. J., Said, B. E., Belnoue, J. P., and Hallett, S. R. (2018). Modelling process induced deformations in 0/90 non-crimp fabrics at the meso-scale. *Compos Sci. Technol. [Internet]* 168, 104–110. doi:10.1016/j.compscitech.2018.08.029
- Turk, M. A., Vermes, B., Thompson, A. J., Belnoue, J. P-H., Hallett, S. R., and Ivanov, D. S. (2019). Mitigating forming defects by local modification of dry preforms. *Compos Part A Appl. Sci. Manuf.* 128, 105643. doi:10.1016/j.compositesa.2019.105643
- Viisainen, J. V., and Sutcliffe, M. P. F. (2021). Characterising the variability in wrinkling during the preforming of non-crimp fabrics. *Compos Part A [Internet]* 149, 106536. doi:10.1016/j.compositesa.2021.106536





## OPEN ACCESS

## EDITED BY

Baris Caglar,  
Delft University of Technology,  
Netherlands

## REVIEWED BY

Mohammad Ghaedsharaf,  
Polytechnique Montréal, Canada  
Muhammad Ali,  
Khalifa University, United Arab Emirates

## \*CORRESPONDENCE

Stephan Maidl,  
✉ stephan.maidl@tum.de

## SPECIALTY SECTION

This article was submitted to  
Polymeric and Composite Materials,  
a section of the journal  
Frontiers in Materials

RECEIVED 19 December 2022

ACCEPTED 06 February 2023

PUBLISHED 23 February 2023

## CITATION

Maidl S, Hilbck M, Kind K and Drechsler K  
(2023), Optical inspection of the braid  
formation zone during manufacturing of  
preforms from reinforcement fibers for  
defect detection purposes.  
*Front. Mater.* 10:1127476.  
doi: 10.3389/fmats.2023.1127476

## COPYRIGHT

© 2023 Maidl, Hilbck, Kind and Drechsler.  
This is an open-access article distributed  
under the terms of the [Creative  
Commons Attribution License \(CC BY\)](#).  
The use, distribution or reproduction in  
other forums is permitted, provided the  
original author(s) and the copyright  
owner(s) are credited and that the original  
publication in this journal is cited, in  
accordance with accepted academic  
practice. No use, distribution or  
reproduction is permitted which does not  
comply with these terms.

# Optical inspection of the braid formation zone during manufacturing of preforms from reinforcement fibers for defect detection purposes

Stephan Maidl\*, Maximilian Hilbck, Kalle Kind and Klaus Drechsler

Chair of Carbon Composites, Department of Aerospace and Geodesy, TUM School of Engineering and Design, Technical University of Munich, Garching, Germany

Braiding is a highly automated process for manufacturing preforms directly from reinforcement yarns at large production volumes. The quality of braided textiles and the stability of the process can however be negatively affected by defects that occur during braiding. If such defects can be detected from fine process anomalies early during their formation, the process can be interrupted and countermeasures can be introduced before the defect aggravates and gets braided into the product. Current sensor modules for defect detection during braiding however involve problems of either late response times, process impairments or a lack of applicability to braiding of composite parts. In an effort to overcome these drawbacks, the paper at hand proposes to optically monitor the braid formation zone by means of a single camera (no process impairments). An associated image analysis algorithm creates a measure for the angular distance of each individual braiding yarn to its neighboring yarns and tracks the yarns as they rotate around the overbraidable mandrel (typical for braiding of composite parts). Since braiding yarns typically exhibit distinct curvatures as they span from the bobbins towards the center of the braiding machine due to frictional yarn-yarn interaction, a change in yarn curvature and thus in angular yarn distance is an early sign of a defect-characteristic anomaly in yarn tension (early response). If implemented on a real-time capable computing device, an apparatus according to the presented method can be retrofitted to existing production lines for braiding process monitoring. It then contributes to the reduction of error correction times since countermeasures are quicker to implement as long as the defect has not aggravated, yet. Furthermore, scrap material rates can be reduced as anomalies can be detected before they manifest in the braided structure.

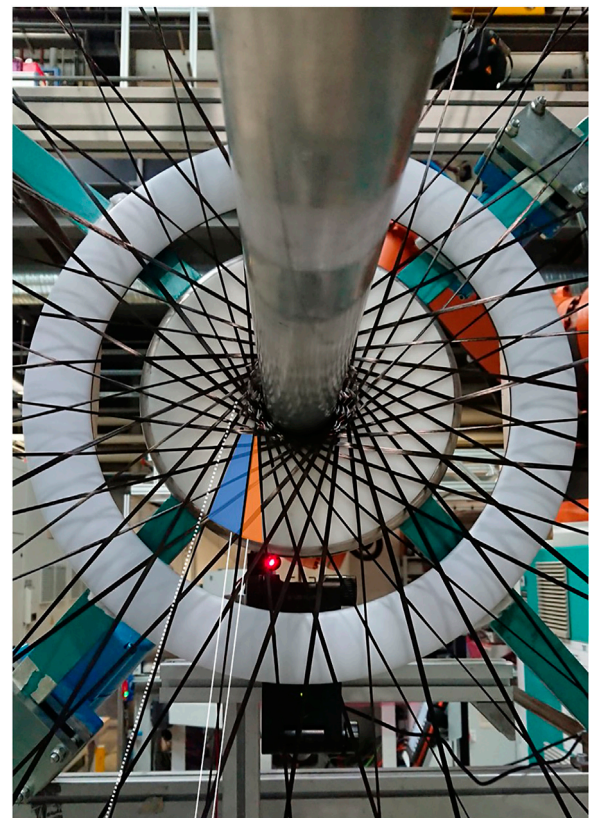
## KEYWORDS

braiding defects, defect detection, online process monitoring, optical inspection, image analysis, automated quality control

## 1 Introduction

Having been practiced as a social art of bonding strands of human hair in a pleasant fashion for at least 22,000–30,000 years (Kohen, 1946; White, 2006), the principle of braiding is nowadays applied as a textile production process with applications in a wide range of economic sectors such as the marine industry (e.g., mooring ropes or fishing nets),

the sports and leisure industry [e.g., climbing ropes or parachute cords (Michael et al., 2016)], electrical engineering and oil hydraulics (e.g., electric shielding or protection of hoses) or medical technology [e.g., stents (Aibibu et al., 2016)]. More specifically, braiding of reinforcement fibers in order to manufacture preforms for composite parts has well-known applications in the automotive [e.g., pillars for passenger compartments (Hill, 2003; Bulat et al., 2016)], aviation [e.g., helicopter landing gears (Thuis, 2004a; 2004b)], space [e.g., rocket nozzles (van Ravenhorst and Akkerman, 2016b; van Ravenhorst, 2018)] as well as in the sports and leisure industry [e.g., lightweight bicycle rims (Kind and Drechsler, 2015; Bulat et al., 2016; Zuurendonk, 2018)]. During braiding of these often hollow structures that may be curved and show a varying cross-section, typical defects such as a generally “fuzzy” braid due to frictional yarn abrasion, yarn loops due to a loss in tension of a single yarn or local yarn gaps and yarn breakages due to an increased tension of an individual yarn may occur (Ebel et al., 2013; Ebel et al., 2016). A particular process anomaly, namely the fibrous ring, is regarded as the most relevant cause for braiding defects. A fibrous ring is an accumulation of broken carbon filaments at the bobbin (braiding spool) which impedes the yarn from unwinding properly from the spool (Ebel et al., 2016; Mierzwa et al., 2016). This causes an increase in tension of the respective yarn that may eventually lead to a distortion of the regular braid structure in the form of a local yarn gap and eventually to a breakage of the yarn. Mierzwa et al. (2018) and Mierzwa (2019) investigated the effect of local yarn gaps in biaxially braided multilayer specimens on their strength. They found a deterioration of up to 36% in tensile and of up to 33% in compressive strength when the braided preforms with local yarn gaps were infiltrated with resin by the Vacuum Assisted Process. By contrast, they did not find significant effects when the preforms were injected with resin by means of the Resin Transfer Molding (RTM) Process. The authors concluded that an excessive fiber undulation in the braided plies on top of the yarn gap was created when a flexible upper tooling (here: vacuum bag) was used during resin infusion and caused the excessive knock-down in strength. In case of a rigid upper tooling (here: RTM tool), a local yarn gap did not cause additional fiber undulation and hence no significant knock-down in strength. Ebel et al. (2013); Ebel et al. (2016) conducted endurance braiding tests in order to quantify the extent of machine downtime due to the necessity of manually rethreading yarns that had broken because of fibrous rings at the braiding spools. In an extreme case scenario with unsuitable parameters during rewinding of the yarns on the braiding spools, they observed a downtime of 26% of the total duration of a test. Despite of these investigations constituting extreme cases, the above figures show that monitoring systems for the braiding process can on the one hand serve as quality assurance and on the other hand as a measure to increase production output and reduce scrap material rates during braiding. The latter point is particularly valid because a process anomaly can often be resolved with little effort if it is detected early (e.g., removal of a fibrous ring with scissors by hand). If an anomaly has evolved through various stages to a major failure event (e.g., a yarn breakage), the braided preform usually needs to be scrapped and time-consuming effort is required to reset the machine to an acceptable state (e.g., rethreading of a broken yarn).



**FIGURE 1**

Braiding formation zone during braiding with  $n_{\text{yarn}} = 64 \text{ 24 k}$  carbon yarns; curvature of one yarn indicated by a tangential white-dotted line; yarn with purposefully increased tension marked by two solid white lines; increased distance to the preceding yarn marked by blue color; reduced distance to the succeeding yarn marked by orange color; image taken from (Maidl et al., 2022) and adapted.

## 2 Current sensor modules for braiding process monitoring

In order to detect braiding process anomalies, several approaches already exist. Most widely used sensors are rudimentary, stationary switches that jut into the tracks of the bobbin carriers (c.f. Maidl et al., 2018). Upon breakage of a yarn, a movable member of the yarn tensioning unit of the bobbin carrier, e.g., a lever or a slider, changes its position and/or orientation compared to the usual operating mode. When the defective carrier passes by a stationary sensor, the switch gets pushed and a control signal to stop the braiding machine is generated. This approach comes with particularly low installation effort and costs. However, it is only capable of detecting an anomaly when a yarn has already broken. It does not give an early warning which could be used as a trigger to intervene and avoid a larger failure event.

An approach that allows the generation of an early warning comprises a force sensor with a skid attached to it (Lenkeit, 1997). The skid gets in contact with the braiding yarns as they pass by and the force sensor measures the induced reaction force. This way, yarns with increased tension that are about to break can be

identified as can yarns with a reduced tension that may lead to a yarn loop in the braid. A disadvantage of this approach is however that the additional yarn contact may cause additional yarn damage, particularly when the braiding machine operates at high speeds which imply a high relative velocity between the yarn and the skid. When brittle reinforcement fibers such as carbon or glass are braided, it is generally agreed that unnecessary yarn contact needs to be avoided for reasons of an accumulation of yarn damage.

Branscomb (2007) and Branscomb and Beale (2011) proposed an optical inspection of the movement of the braiding point. The braiding point is the point in the center of a braiding machine where, during braiding of a rope or a cord, the braiding yarns meet and form the braided strand. During regular braiding, the braiding point rests stationary in the center of the machine due to a balance of forces from the circularly arranged braiding yarns. If a yarn tension anomaly is present, the braiding point moves outside the center of the machine because of imbalanced yarn forces. This optical inspection also works without any additional yarn contact and therefore incurs no additional yarn damage. The problem of this approach is however that during braiding of composite preforms, a distinct braiding point that is free to move does not exist in most cases. Instead, the reinforcement fibers are usually braided onto rigidly guided mandrels (e.g., by a robot). Hence, the described concept cannot be applied for braiding of composite structures.

Nevertheless, there are optical inspection approaches of the braid formation zone that can be applied in composites braiding (cf. Figure 1 for a view of the braid formation zone). The underlying detection concept is based on the fact that braiding yarns are slightly curved as they span from the bobbin towards the center of the machine due to frictional interaction between yarns that circulate through the machine in opposite directions (van Ravenhorst and Akkerman, 2016a; van Ravenhorst, 2018). When a braiding yarn shows an increased tension, its curvature is reduced. When a yarn shows a reduced tension, its curvature is in turn more pronounced. Brockmanns et al. (2014) conclude in their patent application that from a force sensor with a skid attached to it according to Lenkeit (1997) not only the force amplitude created by the passing-by of each yarn but also the time interval between the force impulses can be measured. Furthermore, yarn contact and thus yarn damage can be avoided by measuring the time intervals between circulating braiding yarns by means of an optical sensor. Due to natural process fluctuations such as vibrating yarns, such a discrete distance measurement was however experimentally determined by means of a light barrier in the braid formation zone to be prone to false positive and false negative defect detections (Maidl et al., 2022).

The paper at hand is therefore intended to provide a solution for an optical inspection of the braid formation zone that

- is capable of giving an early warning before defective braid is produced,
- incurs no additional yarn damage,
- is suitable for the use case of braiding of composite structures on a mandrel and
- allows a robust process monitoring by eradicating false positive or false negative defect detections that may stem from natural process fluctuations.

### 3 Materials and methods

The fact that braiding yarns do not follow a straight line but exhibit a curved shape instead is indicated in Figure 1. A straight dotted line that is tangential to one of the yarns shows an increasing distance to the respective yarn the closer the yarn is to the center of the braid formation zone. Additionally, another yarn marked by two solid lines is purposefully set under an anomalously high tension in Figure 1, thereby resembling a situation that occurs when a braiding defect, such as a fibrous ring, is present. The consequence is that the curvature of this yarn is reduced, resulting in an increased angular distance to its succeeding yarn (cf. blue area in Figure 1) and a reduced angular distance to its preceding yarn (cf. orange area in Figure 1). This deviation in angular yarn distances results in different time intervals of the circulating braiding yarns passing by a discrete sensor that is placed close to the center of the braid formation zone (e.g., a light barrier of which the red laser is visible in Figure 1). Brockmanns et al. (2014) propose to use such a deviation from regular time intervals as a defect detection criterion. Since this was—given natural process fluctuations—shown to be an unreliable criterion (Maidl et al., 2022), a video camera and an associated image analysis algorithm are applied to track the yarns during the braiding process in the paper at hand. The idea behind this approach is that a yarn distance measurement is not only carried out at a discrete position in the braid formation zone but that distance measurements for each yarn are constantly made as the yarns circulate around the center of the machine (ideally at each video frame). This way, a multitude of yarn distance measurements is available for each braiding yarn as it completes a full 360° revolution through the machine. An averaging over several yarn distance measurements is then able to even out naturally occurring process fluctuations (e.g., vibrations or temporary stick-slip movement of the yarns).

In order to validate the above-described detection principle and to illustrate a possible way on how to determine over how many video frames the yarn distance measurements need to be averaged, the following experimental study was conducted. A cylindrical mandrel with a diameter of  $d = 65 \text{ mm}$  and a length of  $l = 2.5 \text{ m}$  was overbraided with Tenax®-E HTS40 carbon yarns from Teijin Carbon Europe GmbH under a braiding angle of  $\varphi = 45^\circ$ . The RF 1/128–100 braiding machine from HERZOG GmbH that was used for the experiments was set to a speed of horn gear rotation of  $r = 130 \text{ rpm}$ . For an optimal spreading of the braiding yarns, the braiding ring was mechanically actuated by shaker motors at a frequency of approximately 13 Hz. The number of braiding yarns was varied between  $n_{\text{yarn}} = 32$  and  $n_{\text{yarn}} = 64$ . The reason for varying the yarn number was to evaluate the effect of less overall curvature of the braiding yarns on the detection principle. If a comparatively low number of braiding yarns (here:  $n_{\text{yarn}} = 32$ ) is used, the overall frictional interaction between the yarns is reduced because there are less yarn crossing points in the braid formation zone. This results in less yarn curvature compared to the use of a larger yarn number (here:  $n_{\text{yarn}} = 64$ ), making it potentially more difficult to detect a change in angular yarn distances. Furthermore, the filament count of the yarns was varied between 6 k (400 tex), 12 k (800 tex) and 24 k (1600 tex). Similar to the variation in yarn





**FIGURE 2**

Barrel tensioner screwed onto a bobbin carrier in order to create a consistent level of elevated tension of a single yarn during the braiding experiments with a simulated defect.

number, the idea behind varying the thickness of the threads was to capture a potential change in frictional yarn interaction. When thinner yarns (here: 6 k) are used, the deflection of each yarn at a crossing point and also the contact area between two touching yarns is smaller compared to the case of thicker braiding yarns (here: 12 k or 24 k). This may result in less overall frictional interaction, less yarn curvature and consequently to a more difficult defect detection by angular yarn distances. The sizing material for the 12 k and 24 k yarns was of the type F13 (epoxy) and of the type E13 (polyurethane) for the 6 k yarns because Teijin Carbon Europe GmbH does not deliver the three thicknesses of HTS40 yarns with the exact same type of sizing. Moreover, the tension of the braiding yarns was varied. During regular braiding without any replication of a defect (reference experiments), the tension of all braiding yarns was set to  $\sim 4$  N by applying standard 350 g-yarn tension springs as delivered by HERZOG GmbH in the bobbin carriers. In order to be able to repeatedly create the same level of process anomaly, the tension of a single braiding yarn was increased to  $\sim 20$  N,  $\sim 35$  N

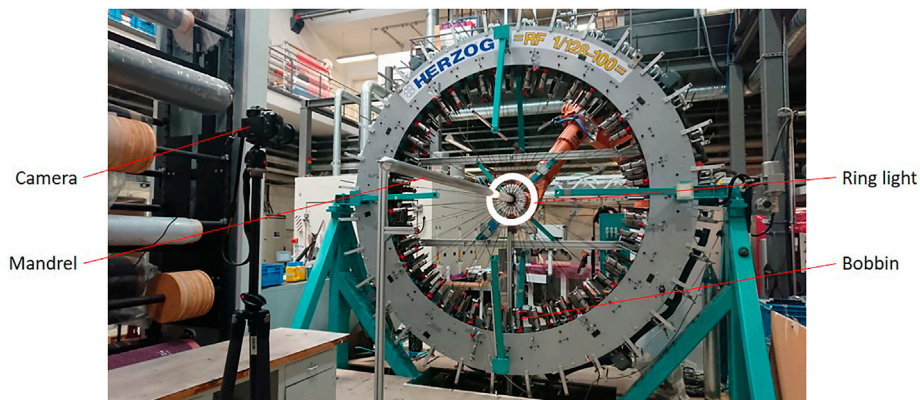
and  $>45$  N by means of a barrel tensioner that was attached to one bobbin carrier (cf. Figure 2) and by changing the tension spring inside the respective bobbin carrier to ratings of 600 g and 950 g. The above-described test plan was carried out full factorially. Given the large number of braiding tests and the amount of data generated from each test, each experiment configuration was tested once.

For the recording the braiding experiments, a Nikon D3300 SLR camera with a resolution of  $1920 \times 1080$  pixels and a frame rate of  $frame\ rate = 25\ fps$  was aligned with the mandrel axis and placed at a distance of about 3.3 m to the braiding machine. No obstruction of the camera view on the braid formation zone was present during the experiments discussed in the paper at hand. For considerations on an obstruction of the camera view, e.g., by support structures, the mandrel or another handling robot, the reader is referred to the outlook section of this article. A ring light as backlight illumination (cf. Figure 3) in combination with an ISO value of the camera of 400 and an aperture setting of  $\frac{1}{8}$  eliminated any disturbing light reflections from the shimmering sizing of the carbon yarns. The exposure time of the camera was set to 0.002 s in order to obtain video frames without significant motion blur of the yarns. This value was calculated by allowing an error due to motion blur of 1 pixel at the outside edge of the ring light (outside  $\varnothing$  252.5 mm). The circumferential yarn speed at the outside edge of the ring light was calculated from the set speed of horn gear rotation and linear down-scaling by intercept theorems. A possible vibration of the braiding yarns was neglected in the calculation of the exposure time of the camera. A visual inspection of the acquired video frames did not show any motion blur of the braiding yarns and therefore legitimized this simplification.

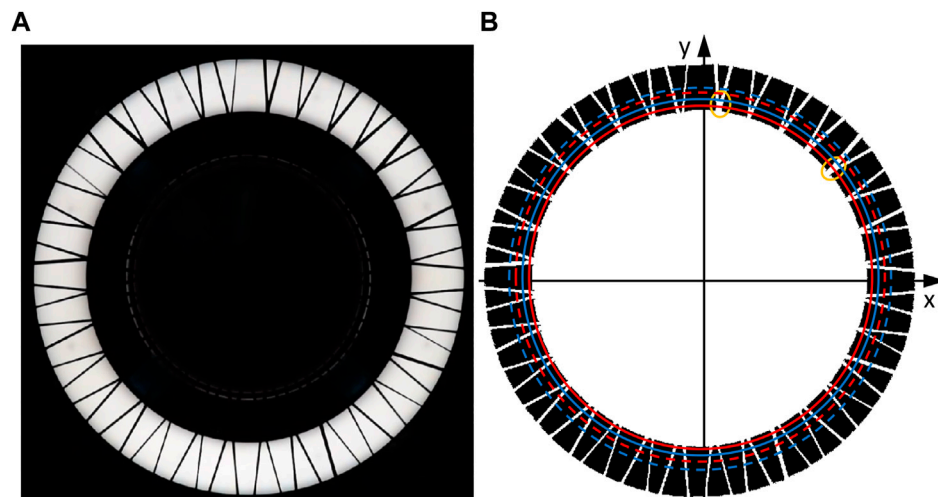
## 4 Image analysis algorithm

Figure 4A shows an exemplary video frame acquired by the above-described camera setup during braiding with  $n_{yarn} = 64$  12 k braiding yarns at a speed of horn gear rotation of  $r = 130\ rpm$ . Due to the camera settings, all parts of the image that are not illuminated by the ring light appear dark. Additionally, the braiding yarns distinctly shadow the ring light without any motion blur or disturbing light reflections. Figure 4B depicts the working principle of the image analysis algorithm, which was implemented in MATLAB R2021a. In a preprocessing step, the image is first complemented by the “imcomplement”-function and then binarized by the “imbinarize”-function. After that, all parts of the video frame that are not illuminated by the ring light are cropped from the image by white masks. This makes the braiding yarns appear as white objects in Figure 4B.

During the subsequent main processing, a first pair of imaginary concentric circles close to the inner edge of the ring light is drawn into the image (cf. solid red and blue circles in Figure 4B). The outer circle of this pair is 10 pixels larger in radius than the inner circle. It is then checked if both circles intersect with a white object as many times as there are braiding yarns in the braiding test. Three cases may result from this check. The first case is that the number of intersections equals the number of braiding yarns for both circles. In this case, the measurement algorithm can continue. The second case is that the number of intersections only equals the number of braiding yarns for the outer circle. In this case, the outer circle is

**FIGURE 3**

Experimental setup of the RF 1/128–100 braiding machine from HERZOG GmbH equipped with a ring light behind the braid formation zone, a cylindrical mandrel that is overbraided with carbon yarns and a camera that monitors the illuminated braid formation zone.

**FIGURE 4**

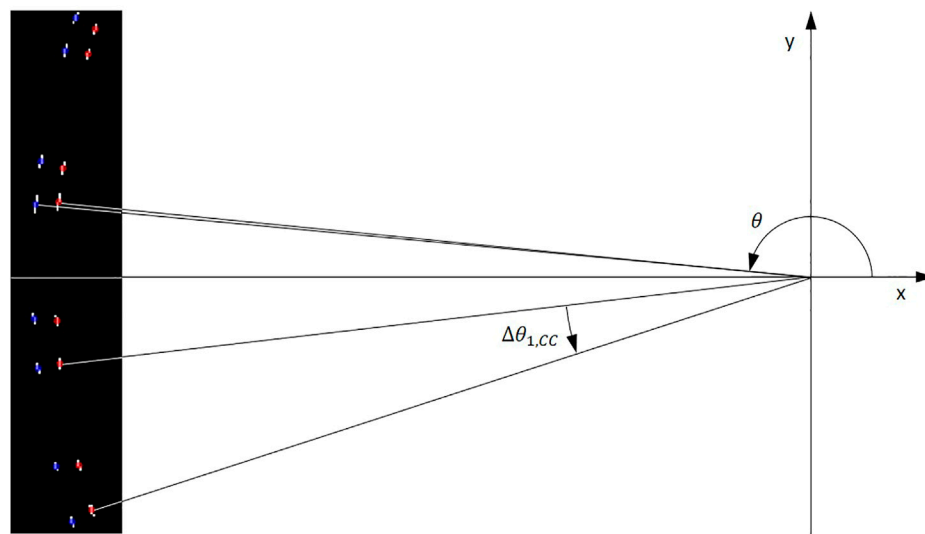
Exemplary video frame acquired by the camera that monitors the braid formation zone (A); identical video frame after preprocessing by the image analysis algorithm (B); two pairs of imaginary circles (solid and dashed circles) drawn-in for a visualization of the working principle of the main processing of the algorithm; two orange ellipses mark areas where the circle in solid blue intersects with yarn crossing points.

taken as the new inner circle and a new outer circle is drawn that is 10 pixels larger in radius than the new inner circle (previous outer circle). Then, the check for the number of intersections is run again. In the third case, the number of yarn intersections does not equal the number of braiding yarns for the outer circle. This is the case in Figure 4B. Two orange ellipses mark areas where the outer circle only intersects with one white object where in fact two braiding yarns cross each other. The number of intersections for the outer circle is in this case 62, which is two less than the number of braiding yarns  $n_{yarn} = 64$ . In this case, a whole new pair of circles is drawn into the image, whereby the inner circle of the new pair is 10 pixels larger in radius than the previous outer circle (cf. dashed red and blue circles in Figure 4B). The check for the number of yarn intersections is carried out in a loop until the first case of the

yarn number being equal to the number of braiding yarns  $n_{yarn}$  is reached or until no new outer circle can be drawn because the algorithm has reached the outer edge of the ring light with its imaginary circles. If the algorithm has reached the outer edge of the ring light without reaching the first case, the respective video frame is dropped and cannot be taken into account for the analysis. If the first case could be reached with a video frame, then the next step of measuring the angular yarn distances can be carried out.

For each of the intersection objects of inner and outer circle, their centroid is calculated by the “regionprops”-function. Exemplary intersection objects and their centroids are depicted in Figure 5. For each centroid on the inner circle, the corresponding centroid on the outer circle, which originates from the same yarn as the respective centroid on the inner circle, is found by means of a nearest





**FIGURE 5**

Close-up of white intersection objects resulting from the video frame in Figure 4; centroids of inner and outer intersection objects marked by red and blue dots, respectively; exemplary measurement of the polar angle  $\theta$  of two intersection objects that originate from the same yarn for an identification of the direction of yarn rotation; exemplary visualization of the angular yarn distance  $\Delta\theta_{1,CC}$  between two neighboring yarns of counterclockwise (CC) direction of rotation.

neighbor search (“knnsearch”-function). Plausibility checks in the form that the distance between corresponding centroids must not exceed 11 pixels or be less than 9 pixels are implemented in order to avoid wrong assignments of centroids that are located closely to points of yarn intersections. This is of particular importance because in the next step, the decision whether a yarn circulates in clockwise or in counterclockwise direction through the braiding machine is based on the difference in polar angles  $\theta \in ]-\pi; +\pi]$  of corresponding centroids from the inner and outer circle. In Figure 5, the polar angles  $\theta$  with respect to the center of the braiding machine are drawn in for a pair of corresponding centroids from the inner (red dot) and outer circle (blue dot). Since the polar angle  $\theta$  of the point on the inner circle is smaller than the one of the point on the outer circle, this pair of centroids is stipulated to originate from a counterclockwise yarn. If the polar angle  $\theta$  from the point on the inner circle was larger than the one of the corresponding point on the outer circle, then the pair of centroids would be stipulated to originate from a clockwise yarn. Exceptions for the case of two corresponding centroids being located on different sides of the negative  $x$ -axis (transition  $-\pi \rightarrow \pi$ ) are taken account of in the implementation of the image analysis algorithm. After all pairs of corresponding centroids are assigned to a direction of rotation, a further plausibility check is implemented in the form that there must be  $\frac{n_{yarn}}{2}$  assignments for each of the two directions of yarn rotation. If this plausibility check cannot be passed, the respective video frame is dropped and the algorithm continues with the next video frame. If this plausibility check is passed, the polar angles  $\theta$  for the centroids on the inner circle of both directions of rotation are separately sorted in ascending order. The angular distances of the yarns of both directions of rotation are then calculated by the difference between adjacent polar angles  $\theta$  in the two sorted arrays for the two directions of rotation. In Figure 5, the angular distance of two adjacent centroids from a counterclockwise (CC) yarn is exemplarily indicated by  $\Delta\theta_{1,CC}$ .

The final post processing comprises the two steps of averaging the yarn distance measurements per direction of rotation over several video frames and a visualization of the defective yarn in the acquired video frames. Figure 6 exemplarily shows angular yarn distance measurements of the counterclockwise yarns during braiding with the 12 k yarns and an increased tension of a single yarn of  $\sim 35$  N for the first nine video frames that passed all plausibility checks described above and therefore could be evaluated. Apart from a general scatter in the data, which reflects the nature of the braiding process and caused a stationary light barrier to be found to be unsuitable for braiding process monitoring (Maidl et al., 2022), a distinct pattern of a particular larger yarn distance directly followed by a smaller yarn distance appears to propagate from yarn distance numbers 24–25 in frame 1 to yarn distance numbers 27–28 in frame 15. This distinct propagating pattern reflects the fact that a yarn with an elevated tension, which creates a systematic deviation in yarn distances, moves in counterclockwise direction through the braiding machine. The distinct pattern moves from left to right through the diagrams in Figure 6 because the calculated yarn distances appear sorted from polar angles of  $-\pi$  to  $+\pi$  (counterclockwise direction in Figure 4) along the  $x$ -axes in the diagrams. However, the pattern is not always clearly distinguishable from the natural process scatter (particularly frames 2, 5 and 15) or are not visible at all (particularly frames 7 and 10). This is why an averaging over several video frames is crucial for a stable process monitoring. This averaging is carried out by shifting the  $x$ -axes in the diagrams in Figure 6 according to the speed of horn gear rotation of the braiding machine so that the distinct defect-characteristic pattern, graphically speaking, remains stationary (at the same  $x$ -axis value) in the diagrams. This shifting is carried out by the following operations: At first, the polar angle of the yarn in the third quadrant that is closest to the negative  $x$ -axis in the first video frame of a braiding experiment is calculated (“first yarn”,  $i = 1$ ). An

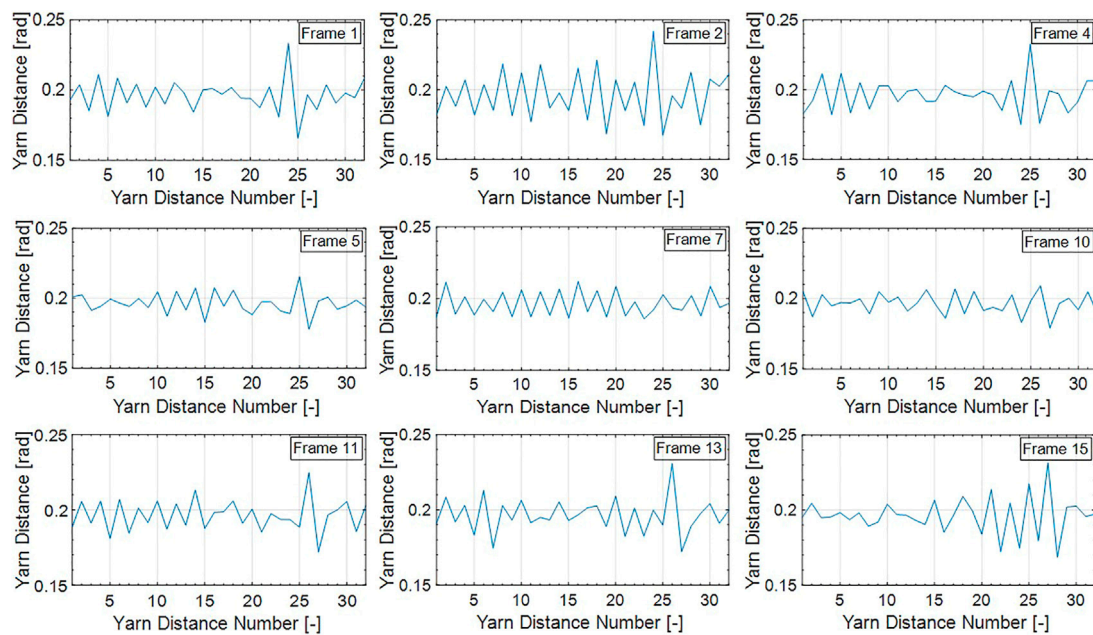


FIGURE 6

Yarn distance measurement results of counterclockwise yarns of the first 15 frames of the braiding experiment with  $n_{yarn} = 64$  12 k yarns and an elevated tension of a single counterclockwise yarn of  $\sim 35$  N.

isolated measurement of the angle  $\theta_{i=1,CC,n_{frame}=1}$  would however be subject to yarn vibrations. This is why, for a more exact calculation, the actual position of each yarn  $\theta_{i,CC,n_{frame}=1}$  is measured, corrected by the theoretical yarn spacing and then averaged.

$$\theta_{i=1,CC,n_{frame}=1,mean} = \text{mean} \left( \theta_{i,CC,n_{frame}=1} - \frac{2\pi}{n_{yarn}} \cdot (i-1) \right), \quad (1)$$

$$\text{whereby } i = \left\{ 1; 2; \dots; \frac{n_{yarn}}{2} \right\}$$

Secondly, the expected position of the “first yarn” at frame number  $n_{frame}$  due to its movement is calculated by

$$\theta_{i=1,CC,n_{frame},expected} = \text{wrapToPi} \left( \theta_{i=1,CC,n_{frame}=1,mean} + \frac{\frac{n_{frame}}{\text{frame rate}}}{t_{360^\circ}} \cdot 2\pi \right) \quad (2)$$

whereby  $t_{360^\circ}$  is the time it takes a yarn to complete a full  $360^\circ$  revolution around the center of the braiding machine according to the set machine speed. The function “wrapToPi” is applied in order to project the obtained value from the function argument to the interval  $]-\pi; +\pi]$ . Thirdly, of all the polar angles in the  $n$ th frame  $\theta_{i,CC,n_{frame}}$ , the closest match to the expected position of the “first yarn” ( $i = 1$ ) from the first frame of the experiment is calculated by means of the “knnsearch”-function.

$$\text{Index}_{n_{frame}} = \text{knnsearch}(\theta_{i,CC,n_{frame}}, \theta_{i=1,CC,n_{frame},expected}), \quad (3)$$

$$\text{whereby } i = \left\{ 1; 2; \dots; \frac{n_{yarn}}{2} \right\}$$

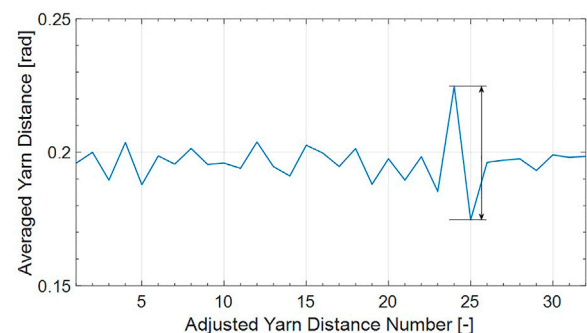


FIGURE 7

Averaged yarn distance measurements calculated from the nine diagrams shown in Figure 6 after shifting the x-axis by Formula 1 through Formula 4; prominence of defect-characteristic pattern indicated by a double arrow.

The index of the closest match minus 1 then equals the offset of the measured angular yarn distances from the  $n$ th frame compared to the first video frame of the experiment.

$$\text{offset}_{n_{frame}} = \text{Index}_{n_{frame}}(1) - 1 \quad (4)$$

The negative of this offset value is then applied in the “circshift”-function to shift the sorted array of angular yarn distances in a way that each position of the array corresponds to the same yarn throughout the monitoring process. The above formulae are written and explained for the case of monitoring counterclockwise (CC) yarns. In case clockwise (C) yarns shall be

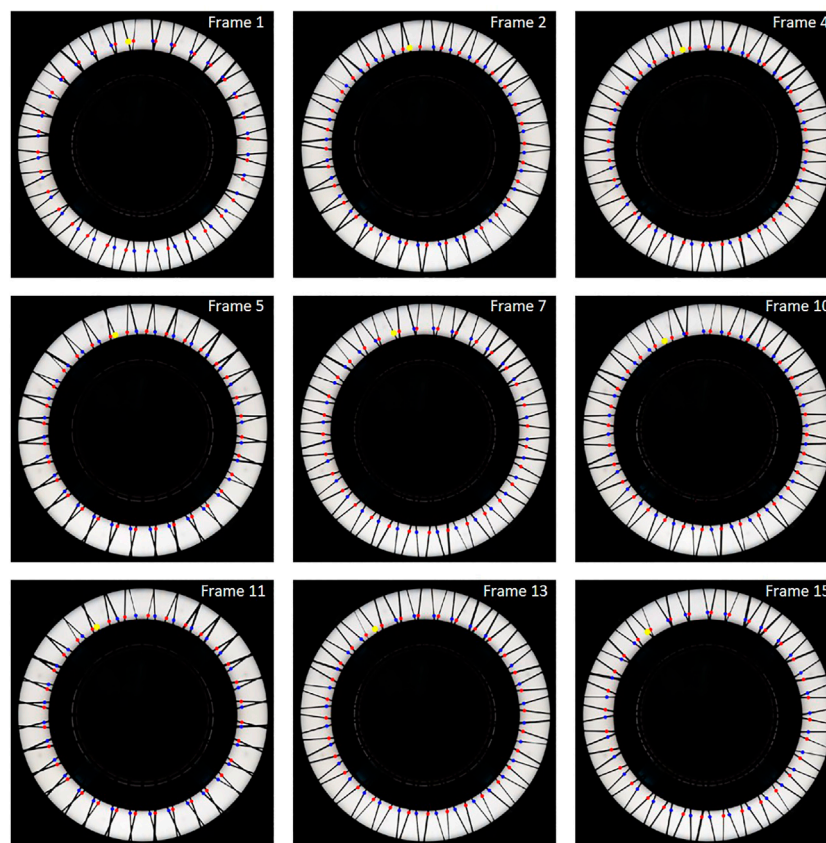


FIGURE 8

Video frames corresponding to the yarn distance diagrams from Figure 6; clockwise yarns marked by red dots; counterclockwise yarns marked by blue dots; defective yarn as identified from the characteristic pattern in Figure 7 marked by a yellow dot.

monitored, the “+”-sign in Formula 2 needs to be replaced by a “-”-sign. Additionally, not the negative but the positive offset value from Formula 4 needs to be applied in the “circshift” function in order to keep a moving defective yarn and its corresponding yarn distance measurements at the same position in the array of angular yarn distance values over the duration of the braiding experiment.

Once each position in the array of angular yarn distance values corresponds to the distance between the same two yarns for all acquired video frames, an average in yarn distance can be calculated for each pair of yarns over a certain number of video frames (length of averaging window). The result of such an averaging over the nine diagrams from Figure 6 that represent measurements from counterclockwise yarns is illustrated in Figure 7. It can be observed that random deviations in angular yarn distances have significantly evened out. Furthermore, between yarn distance number 24 and 25, a distinct defect-characteristic spike has formed in the diagram. The prominence of this defect-characteristic spike is marked with a double arrow. This measure is used in the following results section as a value to compare the deviation in yarn distances over the different experiment variants.

From the position of the defect-characteristic pattern in Figure 7, the yarn with anomalously high tension can be identified to be the 25th counterclockwise yarn in the first video frame of the experiment counting from the negative

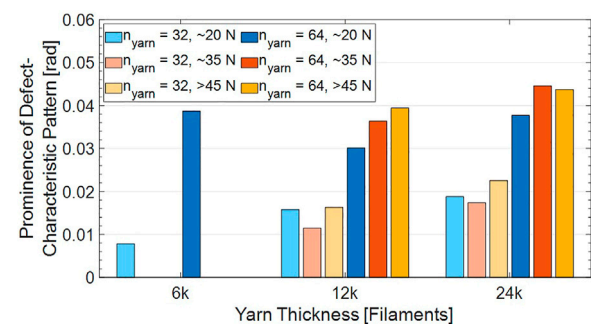


FIGURE 9

Prominence of the defect-characteristic pattern after averaging over the complete duration of each braiding experiment with a simulated defect.

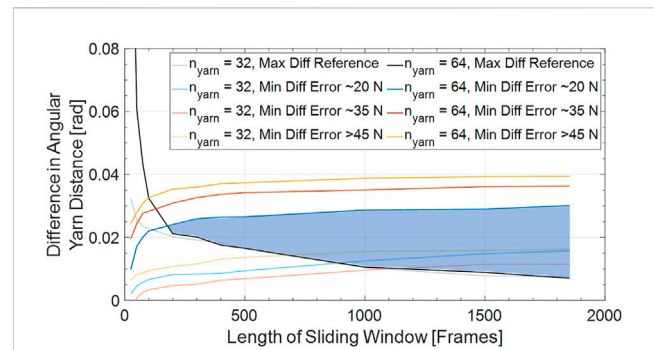
$x$ -axis in mathematically positive direction. Figure 8 shows a visualization of the detection result of the above-described image analysis algorithm for the first nine analyzable video frames of the braiding experiment already illustrated in Figure 6. The clockwise yarns are marked by red dots and the counterclockwise yarns are marked by blue dots. The defective yarn as identified by the

algorithm is marked by a yellow dot. It can be observed that the marks lie at different radial distances from the center of the camera view. This is due to the fact that the image analysis algorithm had to apply different radii for the pair of circles in order that both circles intersect one-to-one with each braiding yarn. Furthermore, it can be seen that the defective yarn moves in counterclockwise direction through the sequence of images. On close inspection by eye, one can even correlate distinct deviations in angular yarn distances from the diagrams in Figure 6 to the distances of the yellow-marked yarn to its neighboring yarns in the respective frames in Figure 8.

## 5 Results and discussion

The prominences of the defect-characteristic pattern as marked in Figure 7 were analyzed for the different variants of the braiding experiments. For the diagram shown in Figure 9, all available video frames of a braiding experiment were taken into account for the averaging step. The standard deviations are not drawn-in on purpose because they would not provide any meaningful information given the natural scatter of the angular yarn distances as described above. Additionally, no data is shown for the 6 k yarns and elevated tensions of ~35 N and >45 N, respectively. The reason for this is that these thin yarns could not sustain these high elevated tensions and broke during the braiding tests. It can be observed that the defect-characteristic spike in the averaged yarn distance measurement is generally more pronounced if  $n_{\text{yarn}} = 64$  braiding yarns are used compared to  $n_{\text{yarn}} = 32$  yarns. Furthermore, a trend towards a stronger deviation in angular yarn distances at the defective yarn can be identified the thicker the braiding yarns are. Only the variant with  $n_{\text{yarn}} = 64$  k yarns and an elevated tension of a single yarn of ~20 N does not comply with this trend. Moreover, within an experiment group of the same yarn number  $n_{\text{yarn}}$  and the same yarn thickness, a trend towards an increasing prominence of the defect-characteristic spike in the averaged angular yarn distance measurement is observable the higher the level of the yarn tension anomaly is. However, several experiments with an elevated tension of ~35 N do not monotonously fit into this trend. Nevertheless, the overall picture of the trend towards stronger deviations in angular yarn distances with increasing yarn tension anomaly is still maintained because the variant with the highest tension (>45 N) consistently creates stronger deviations than the variant with the least yarn tension anomaly (~20 N).

The fact that in variants with  $n_{\text{yarn}} = 64$  yarns the deviations in yarn distances that are more clearly identifiable than in variants with  $n_{\text{yarn}} = 32$  yarns is well explainable by a higher level of frictional interaction in the braid formation zone when  $n_{\text{yarn}} = 64$  yarns are used. A higher number of yarns creates a higher number of yarn crossing points, higher frictional forces between the yarns and thus a more pronounced curvature of the yarns during regular braiding. If the yarns exhibit a more pronounced curvature, the principle of detecting a change in curvature due to changes in yarn tension is better applicable. A similar explanation relying on different levels of frictional interaction between the braiding yarns can also be provided for the trend of increasing prominence of the defect-characteristic pattern the thicker the yarns are. Thicker yarns cause the yarns to be deflected by a larger angle at each yarn



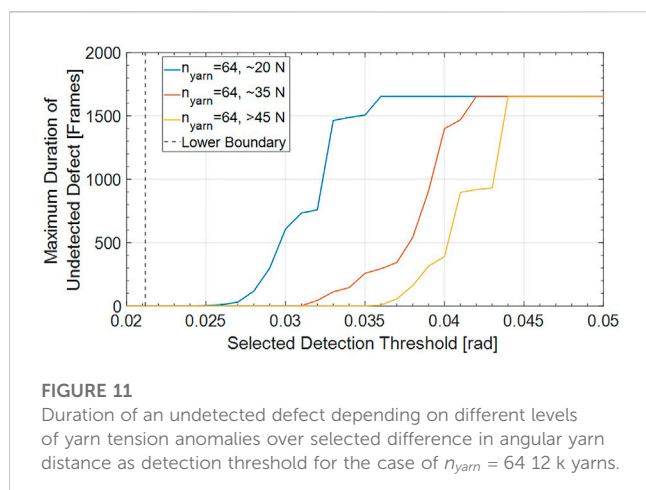
**FIGURE 10**

Comparison of maximum difference in angular yarn distance resulting from random process fluctuations during flawless reference measurements with minimum of defect-characteristic pattern during measurements with a replicated defect over different lengths of sliding averaging windows for the braiding experiments with 12 k yarns; blue-marked area indicates combinations of lengths of averaging windows and differences in angular yarn distances as possible detection thresholds for a defect detection without any false negative or false positive detections for  $n_{\text{yarn}} = 64$  12 k yarns.

crossing point in the braid formation zone. Additionally, the contact area at crossing points between thicker yarns is larger compared to thinner yarns. The overall trend of a more pronounced defect-characteristic pattern the stronger the deviation in tension of a single yarn is can be expected from the detection principle. The curvature of the defective yarn is reduced due to its increased tension, leading to the detectable deviations in angular yarn distances. A reason for the fact that the variants with an elevated tension of a single yarn of ~35 N do not monotonously fit into the overall trend can be that a screw-on barrel tensioner was used on the respective bobbin carrier to achieve a significant portion of the elevated tension. Given the fact that the yarn tension slightly varies on an unmodified carrier depending on the filling degree of the bobbin, a multiplication of slight yarn tension inputs to the barrel tensioner may lead to more pronounced variations in yarn tension output according to the Euler-Eytelwein frictional law (frictional rope equation). Furthermore, environmental variables such as moisture could not be controlled in the manufacturing laboratory, which are also known to influence frictional yarn interaction during braiding.

In Figure 9, all available video frames of an experiment variant were taken into account for the calculation of the prominence of the defect-characteristic pattern. From a process monitoring perspective, it is however of interest how long the averaging window of video frames actually needs to be in order to reliably detect a defect. This relation is analyzed at the example of the group of experiments with the 12 k yarns in Figure 10. On the x-axis, the number of video frames taken into account for the averaging step described in Section 4 is varied. It can be observed that the smaller the averaging window is, the more pronounced the maximum of random yarn distance variations from flawless reference measurements appears in the diagram (cf. curves labeled as “Max Diff Reference”). With increasing length of the sliding averaging window, random deviations in yarn distances are increasingly evened out. By contrast, the minimum deviation in angular yarn distance that





results from the defective yarn increases with increasing length of the averaging window (cf. curves labeled as “Min Diff Error”). For the case of  $n_{yarn} = 64$  braiding yarns, the curve of maxima of random deviations in angular yarn distance during regular braiding intersects with the lowest curve of minima of systematic deviations in yarn distances due to a process error at a length of an averaging window of 200 video frames. At 200 frames and beyond, a blue-marked area is opened up where the maximum curve of random deviations during regular braiding lies below the curve of minima of systematic deviations during defective braiding. This means if a combination of length of averaging window and detection threshold in terms of difference in angular yarn distance between neighboring yarns from the blue-marked area was chosen, no false positive or false negative defect detections occurred during the conducted braiding tests.

Given the fact that a minimum length of the averaging window of 200 frames is required for a reliable defect detection at a frame rate of  $frame\ rate = 25\ fps$  for the case of  $n_{yarn} = 64$ , a latency of 8 s is incurred in the presented monitoring approach. The set speed of horn gear rotation of  $r = 130\ rpm$  and a number of 32 horn gears in the braiding machine results in  $t_{360^\circ} = 7.38\ s$  for a full  $360^\circ$  revolution of a yarn through the braiding machine. Within this context, a lead time of 8 s, corresponding to about one full revolution of the braiding machine, can be regarded as acceptable, particularly given the fact that already a comparatively small yarn tension increase of  $\sim 20\ N$  is reliably detected in the braiding experiments. Such small increases in yarn tension do not lead to yarn breakages that are time-consuming to resolve. The picture is however different for the case of  $n_{yarn} = 32$  braiding yarns. Only at a length of the averaging window of about 1100 frames and beyond, no false positive or false negative defect detections would have occurred in the conducted experiments. This results in approximately 44 s of lead time and thus six full revolutions of the braiding machine that need to be taken into account for an averaging of measured yarn distances. From practical experience and also from the data presented by Maidl et al. (2018) and Maidl et al. (2020), it may well be the case that a yarn with a fibrous ring at its braiding spool has already broken within this time period and has caused the braided preform to be defective due to a missing yarn.

Even though it is a positive finding that a biaxial braid of at least  $n_{yarn} = 64$  braiding yarns can reliably be monitored by the proposed approach without any false positive or false negative defect detections, the authors would like to point out that it is not absolutely necessary to avoid false negative detections at all costs. This is because the defect detection algorithm is programmed to work on *sliding* averaging windows. Sticking with the example of a window length of 200 frames, it may for instance be the case that a defect is not detected (false negative) on video frames 1–200. However, when the algorithm takes frames 2–201 into account, the defect might get detected, resulting in a time delay of only 0.04 s (one frame). Figure 11 illustrates this relation for the exemplary case of  $n_{yarn} = 64$  12 k braiding yarns and a length of the averaging window of 200 frames. As lower boundary, the maximum of random deviations in yarn distances from flawless reference measurements is drawn-in. Any detection threshold below this value would have resulted in false positive defect detections in the conducted experiments. Given the comparatively high number of 25 fps, even small percentages of false positive detections are not acceptable because this would cause an alarm every few seconds and make a productive braiding impossible. For a length of the averaging window of 200 frames, the upper boundary of the blue-marked area in Figure 10 lies at 0.025 radians. The diagram in Figure 11 however shows that even if higher detection thresholds are chosen, the defect is still detected but only missed for a small number of frames. If, for instance, a level of yarn tension increase of  $\sim 20\ N$  shall be detected, a detection threshold of 0.026 radians would have led to the defect being detected with a maximum delay of only 10 frames. If the detection threshold was set to 0.036 radians, this level of process anomaly would not be detected at all (saturation of the curve at total number of frames per braiding experiment). Nevertheless, the highest level of yarn tension increase ( $>45\ N$ ) would still be detected at this threshold. The detection of such a high level of process anomaly is then only delayed by a maximum of 8 frames. This shows that whereas the lower boundary in Figure 10 needs to be regarded as a “strict” boundary, the upper boundary of the blue-marked area in Figure 10 can be seen as a “soft” boundary. It is therefore advisable to choose a detection threshold that is well above the “strict” lower boundary to avoid false positive defect detections due to process scatter and rather accept a limited number of false negative defect detections.

## 6 Conclusion and outlook

A newly developed camera-based monitoring approach for a simultaneous tracking of all braiding yarns during the process was presented in the paper at hand. As a principle for anomaly detection, the associated image processing algorithm relies on an analysis of angular yarn distances of braiding yarns of the same direction of circulation through the machine. In an experimental study comprising flawless reference braiding tests and braiding tests with purposefully introduced yarn tension anomalies of varying severity as well as a variation of yarn number  $n_{yarn}$  and yarn thickness, the new method was shown to be in principle capable of reliably identifying an anomalously tensed yarn during braiding of preforms for composite parts. Also, since the method is purely



optical, no additional yarn contact and thus yarn damage is induced. It was found that the method can even out naturally occurring process fluctuations and distinguish them from systematic process anomalies by applying an averaging window over several video frames. In case of  $n_{\text{yarn}} = 64$  12 k carbon yarns and a moderate yarn tension anomaly of  $\sim 20$  N, an averaging window of 200 frames (8 s given the applied frame rate of 25 fps) was sufficient in order not to create any false positive or false negative defect detections. Given such a short averaging window and thus latency time, a braiding defect, such as for instance the fibrous ring mentioned in the beginning of this article, can therefore be detected early during its formation. The braiding machine can be stopped before an eventual yarn breakage occurs and the production of defective braid can be prevented. Due to the fact that the above-described algorithm allows a precise identification of the defective yarn, operating personnel may be provided with a light signal in order to avoid a time-consuming search for the defective yarn among a potentially large number of braiding yarns. The error can swiftly be spotted, its cause can be found and manually be resolved. A limitation to the provided proof of concept is however that the presented method of measuring angular yarn distances as a sign of process anomalies only works if there is sufficient friction between the braiding yarns that creates significant yarn curvature. In the conducted braiding experiments, this prerequisite could not be maintained if only  $n_{\text{yarn}} = 32$  braiding yarns were used. If more than the investigated  $n_{\text{yarn}} = 64$  braiding yarns shall be monitored, the approach is expected to function even better because frictional interaction and thus yarn curvature is even more pronounced due to the further increased number of yarn crossings in the braid formation zone. However, if for instance  $n_{\text{yarn}} = 128$  braiding yarns and more shall be monitored, the authors recommend the use of a ring light that is larger in diameter than the chosen one (outside  $\varnothing$  252.5 mm) in order to be able to monitor the angular yarn distances at a greater radial distance from the center of the braiding machine. This is necessary for high numbers of braiding yarns  $n_{\text{yarn}}$  because the yarns are spaced too closely together at small radial distances from the center of the machine. This would cause the imaginary circles of the image analysis algorithm to constantly intersect with yarn crossing points and the criterion of as many yarn intersections of the pair of imaginary circles as there are yarns in the machine would never be possible to satisfy.

For reasons of providing a proof of concept, the experiments in the paper at hand only cover braiding of a cylindrical mandrel. The strength of the braiding process, particularly in comparison to filament winding, is however that also parts that are curved can be produced. If such curved parts need to be braided, the camera view to parts of the braid formation zone may be obstructed by a curved mandrel. A similar obstruction of the camera view occurs when a second handling robot is used so that the overbraidable mandrel is grabbed at both ends. The algorithm presented in the paper at hand does however not require a full view on the braid formation zone. The criterion that the imaginary circles of the image analysis algorithm need to intersect with yarns as many times as there are yarns in the braiding machine can be modified with limited effort. It is for instance possible to let the algorithm operate independently on four quarters of the braid formation zone. In

such a modification of the algorithm, the number of yarn intersections of the imaginary circles in a quarter needs to equal  $\frac{n_{\text{yarn}}}{4}$ . It is furthermore not required that it is always the same quarter of the braid formation zone that the view is obstructed to, e.g., in case of a complex path of the guiding robots. Each individual braiding yarn can still be tracked and its distances to neighboring yarns can still be correctly averaged over the independent quarters of the braid formation zone according to [Formula 1](#) through [Formula 4](#). Hence, it is possible to deploy the proposed image analysis algorithm on real-time capable computing devices and retrofit the optical monitoring to existing braiding machines also for the production of complexly shaped preforms. The proposed modification of the algorithm of operating only on sections of the braid formation zone can also be used as a method in order not to be forced exclude entire video frames from the analysis if the respective frames fail to pass the plausibility checks introduced in [Section 4](#). Instead, only the areas of the braid formation zone in a video frame that cannot unambiguously be analyzed can be excluded from the analysis (e.g., due to unfavorable locations of the yarn crossing points with respect to the imaginary circles). The remaining areas can then still be taken into account for the analysis and potentially reduce the required length of the averaging window and thus latency time of the detection method.

As discussed, the detection principle relies on frictional interaction between the braiding yarns. If other yarns than dry carbon yarns also with potentially different types of sizing shall be braided (e.g., glass or aramid fibers) it may be the case that their frictional properties vary from those of carbon yarns. This is why further experiments with these different types of yarn materials are required to assess the defect detection capabilities of the proposed approach. Furthermore, there may be yarns that are partly transparent for the ring shaped backlight illumination (e.g., glass fibers). The brightness thresholds for the binarization during the image preprocessing may have to be modified for such yarn types. Finally, it needs to be acknowledged that if triaxial braids with additional  $0^\circ$ -fibers compared to the investigated biaxial braid shall be monitored, the algorithm as presented is not functional since neighboring intersection objects would not exclusively correspond to moving braiding yarns. The current distinction between clockwise and counterclockwise yarns by comparison of polar angles  $\theta$  as illustrated in [Figure 5](#) needs to be amended for the case of  $0^\circ$ -yarns, e.g., by introducing a third case if the polar angles  $\theta$  of intersection objects originating from the same yarn on the inner and outer imaginary circle are similar.

## Data availability statement

The raw data supporting the conclusion of this article will be made available by the authors, without undue reservation.

## Author contributions

SM Conceptualization, Methodology, Software, Validation, Formal analysis, Investigation, Writing—original draft, Writing—review and

editing, Visualization, Project administration, Funding acquisition. MH Conceptualization, Methodology, Writing—review and editing. KK Writing—review and editing, Supervision. KD Resources, Writing—review and editing, Supervision.

## Funding

The authors thankfully acknowledge the funding provided by the German Federal Ministry for Economic Affairs and Climate Action under the scheme “Zentrales Innovationsprogramm Mittelstand (ZIM)” for the project “IMoFlecht: Inline Monitoringsystem zur Überwachung hochqualitativer Flechtprodukte” (Funding Code: ZF4004324HB9).

## References

- Aibibu, D., Hild, M., and Cherif, C. (2016). “An overview of braiding structure in medical textile: Fiber-based implants and tissue engineering,” in *Advances in braiding technology: Specialized techniques and applications*. Editor Y. Kyosev (Duxford: Woodhead Publishing), 171–190.
- Branscomb, D. J. (2007). *A machine vision and sensing system for braid defect detection, diagnosis and prevention during manufacture*. Master Thesis, Auburn, United States of America: Auburn University.
- Branscomb, D. J., and Beale, D. G. (2011). Fault detection in braiding utilizing low-cost USB machine vision. *J. Text. Inst.* 102, 568–581. doi:10.1080/00405000.2010.498174
- Brockmanns, K.-J., Kümpers, F.-J., Baumgart, G., and Leifeld, M. (2014). Radialflechtmaschine. German patent application DE102012223127A1.
- Bulat, M., Ahlborn, H., Gnädinger, F., and Michaelis, D. (2016). “Braided carbon fiber composites,” in *Advances in braiding technology: Specialized techniques and applications*. Editor Y. Kyosev (Duxford: Woodhead Publishing), 383–394.
- Ebel, C., Brand, M., and Drechsler, K. (2013). “Effect of fiber damage on the efficiency of the braiding process,” in 11th Composites Week @ Leuven and TexComp-11 Conference, Leuven, Belgium.
- Ebel, C., Mierzwa, A., and Kind, K. (2016). “Yarn damage during braiding of reinforcement fibers for composites,” in *Advances in braiding technology: Specialized techniques and applications*. Editor Y. Kyosev (Duxford: Woodhead Publishing), 319–354.
- Hill, J. (2003). Adhesively bonded structural composites for Aston Martin vehicles. Available at: <https://www.audiclubsouthafrica.co.za/yabbfiles/Attachments/b01.pdf> (Accessed October 31, 2021).
- Kind, K., and Drechsler, K. (2015). *Method for the production of braided CFRP bicycle rims*, 15. Amiens, France: SAMPE Europe Conference.
- Kohen, M. (1946). The venus of willendorf. *Am. Imago* 3, 49–60.
- Lenkeit, J. (1997). Verfahren zur Zugkraftmessung an laufenden Fäden einer Fadengruppe sowie Vorrichtung zur Ausübung des Verfahrens. *German Patent Specification DE19730965C1*. Germany: Tensometric-Meßtechnik Ströhmann & Co GmbH.
- Maidl, S., Fernández Villalba, Á., Kind, K., and Drechsler, K. (2020). Development of sensor integrated braiding rings for the automated detection of braiding defects. *Mater. Today Proc.* 34, 74–81. doi:10.1016/j.matpr.2020.01.194
- Maidl, S., Putze, L., Kind, K., and Drechsler, K. (2022). “Automated detection of yarn gaps during radial braiding of carbon fiber by means of light barriers,” in ECCM20 - 20th European Conference on Composite Materials, Lausanne, Switzerland.
- Maidl, S., Sabieraj, M., Mierzwa, A., Ebel, C., and Drechsler, K. (2018). Investigating the unwinding behavior of technical yarns and development of a new sensor system for the braiding process. *IOP Conf. Ser. Mater. Sci. Eng.* 406, 012065. doi:10.1088/1757-899X/406/1/012065
- Michael, M., Kern, C., and Heinze, T. (2016). “Braiding process for braided ropes,” in *Advances in braiding technology: Specialized techniques and applications*. Editor Y. Kyosev (Duxford: Woodhead Publishing), 225–243.
- Mierzwa, A., Ebel, C., and Drechsler, K. (2018). Auswirkungen lokaler Garnlücken auf die mechanischen Eigenschaften geflochtener Kohlenstofffaser-Kunststoff-Verbunde. *Zeitschrift Kunststoffechnik/J. Plastics Technol.* 14, 146–173. doi:10.3139/o999.02012018
- Mierzwa, A., Ebel, C., Harbers, T., and Drechsler, K. (2016). “Investigation on creation of fibrous rings and their influence on the braided preform quality,” in ECCM17 - 17th European Conference on Composite Materials, Munich, Germany.
- Mierzwa, A. (2019). Zur Entstehung und Auswirkung von Garnlücken in Carbonbiaxialgeflecht. *Dissertation*. Munich, Germany: Technical University of Munich.
- Thuis, H. (2004a). “Composite landing gear components for aerospace applications,” in ICAS 2004 - 24th International Congress of the Aeronautical Sciences, Yokohama, Japan.
- Thuis, H. (2004b). The development of composite landing gear components for aerospace applications. <https://citeseerx.ist.psu.edu/viewdoc/download?doi=10.1.1.157.3791&rep=rep1&type=pdf> (Accessed October 31, 2021).
- van Ravenhorst, J. H., and Akkerman, R. (2016a). A yarn interaction model for circular braiding. *Compos. Part A Appl. Sci. Manuf.* 81, 254–263. doi:10.1016/j.compositesa.2015.11.026
- van Ravenhorst, J. H., and Akkerman, R. (2016b). “Overbraiding simulation,” in *Advances in braiding technology: Specialized techniques and applications*. Editor Y. Kyosev (Duxford: Woodhead Publishing), 431–455.
- van Ravenhorst, J. H. (2018). *Design tools for circular overbraiding of complex mandrels*. Dissertation. Twente, Netherlands: University of Twente.
- White, R. (2006). The women of brassempouy: A century of research and interpretation. *J. Archaeol. Method Theory* 13, 250–303. doi:10.1007/s10816-006-9023-z
- Zuurendonk, B. (2018). *Carbon fibre composite rim: An automation feasibility study*. Master Thesis. Delft, Netherlands: Delft University of Technology.

## Conflict of interest

The authors declare that the research was conducted in the absence of any commercial or financial relationships that could be construed as a potential conflict of interest.

## Publisher's note

All claims expressed in this article are solely those of the authors and do not necessarily represent those of their affiliated organizations, or those of the publisher, the editors and the reviewers. Any product that may be evaluated in this article, or claim that may be made by its manufacturer, is not guaranteed or endorsed by the publisher.



## OPEN ACCESS

## EDITED BY

Lode Daelemans,  
Ghent University, Belgium

## REVIEWED BY

Marco Gigliotti,  
École Nationale Supérieure de  
Mécanique et d'Aérotechnique, France  
Quentin Govignon,  
IMT Mines Albi-Carmaux, France

## \*CORRESPONDENCE

Vincent K. Maes,  
✉ [vincent.maes@bristol.ac.uk](mailto:vincent.maes@bristol.ac.uk)

## SPECIALTY SECTION

This article was submitted to Polymeric  
and Composite Materials,  
a section of the journal  
Frontiers in Materials

RECEIVED 18 December 2022

ACCEPTED 24 February 2023

PUBLISHED 09 March 2023

## CITATION

Maes VK, Radhakrishnan A, Lombetti D  
and Kratz J (2023), Zonally heated tooling  
for moulding complex and highly tapered  
composite parts.  
*Front. Mater.* 10:1126932.  
doi: 10.3389/fmats.2023.1126932

## COPYRIGHT

© 2023 Maes, Radhakrishnan, Lombetti  
and Kratz. This is an open-access article  
distributed under the terms of the  
[Creative Commons Attribution License](https://creativecommons.org/licenses/by/4.0/)  
(CC BY). The use, distribution or  
reproduction in other forums is  
permitted, provided the original author(s)  
and the copyright owner(s) are credited  
and that the original publication in this  
journal is cited, in accordance with  
accepted academic practice. No use,  
distribution or reproduction is permitted  
which does not comply with these terms.

# Zonally heated tooling for moulding complex and highly tapered composite parts

Vincent K. Maes<sup>1\*</sup>, Arjun Radhakrishnan<sup>1</sup>, Diego Lombetti<sup>2</sup> and James Kratz<sup>1</sup>

<sup>1</sup>Bristol Composites Institute, University of Bristol, Bristol, United Kingdom, <sup>2</sup>Composite Technology Facility, Rolls-Royce Plc, Bristol, United Kingdom

Curing of composite material parts often rely on slow cure cycles to manage exotherms and avoid hot or cold spots in the part. This is especially true for larger, thicker and/or geometrically complex parts, which suffer from unevenness in heating between different regions of the part stemming from thickness variations and made worse by the use of convection heating in ovens and autoclaves. An alternative technology for moulding is using heated tooling, which improves the energy efficiency of the process but can also significantly increase the tooling costs. However, the true power of heated tooling is in the ability to tailor the temperature profile in different regions. By introducing zonal heating, significantly faster process cycles can be achieved, hence improving production rates. Using cure simulation, two identical components are analysed, one part produced using convection heating (i.e., oven) and the second made using direct heating (i.e., heated tooling). The zonal approach was tuned based on numerical models and shows a reduction of 17.5% in terms of cure time and the experimental trials found an approximate 45% reduction in energy consumption.

## KEYWORDS

moulding, zonally heated tooling, tapered composites, energy efficiency, cure simulation

## 1 Introduction

Moulding composite materials is an energy-intensive activity, generally relying on ovens and autoclaves, and is required to produce the final shape of the component and achieve the desired material properties. To meet quality requirements, slower heat rates and longer dwells are often used, especially for larger, thicker and/or geometrically complex parts in an attempt to maintain homogenous temperature profiles throughout the part as it cures (i.e., avoid hot or cold spots which result in undesirable cure gradients). This is because ovens and autoclaves, which transfer heat through convection, can leave large and/or complex parts with significant thermal gradients, which in turn lead to residual stresses and potential distortions or even damage in the final cured part if not mitigated. Even with slower heating rates and intermediate dwells introduced to cure cycles, thick and complex parts can often experience huge variations in the rate of cure resulting in some regions transitioning from liquid to glassy before other regions. The cure gradients lead to residual stresses which increase part warpage and can lead to microcracking or delamination (Bogetti and Gillespie, 1991). To resolve this, various studies have looked into using optimization of the cure cycles (i.e., fine-tuning of ramp rates and dwell times and temperatures) to manage the exotherm resulting in more even temperatures and hence cure development throughout the part, though generally at the cost of increased cure times (Struzziero and Skordos, 2017).

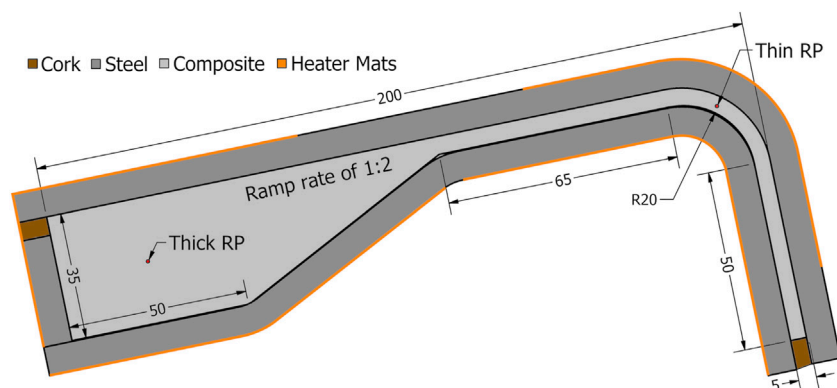


FIGURE 1

2D cross-sectional view of design, incl. tooling and qualitative indication of heater mat positions, with key part dimensions in millimetres.

Alternatively, a different approach to introducing heat could be used, such as direct conduction in the form of heated tooling (Marsh, 2003; Progoulakis, 2004; Rzgar, 2015). With heated tooling, heat is introduced directly to the tool surfaces or volume through heated fluid circulation (Abdallah et al., 2016) or heating elements (Athanasopoulos et al., 2013). While this improves the energy efficiency of the process, it also significantly increases the tooling costs and is hence generally not adopted in the industry for large parts. However, the true power of heated tooling is not in reducing the energy consumed for a standard cure cycle (i.e., as a direct replacement to an oven or autoclave process), but rather in the ability to tailor the temperature profile applied to different regions (Weiland et al., 2017). By introducing zonal heating, significantly faster process cycles can be achieved while reliably meeting the optimal part quality by reaching moulding temperatures quicker and more uniformly (Smith et al., 2013) even for complex parts with thick tooling. A faster cure cycle using heated tooling then brings savings both in reducing the energy bill as well as in allowing greater throughput, hence allowing more parts to be produced using a smaller factory footprint.

This work seeks to demonstrate the ability of zonally heated tooling to produce large thickness variation parts to the same or better quality standards as compared to traditional single zone (i.e., oven and autoclave) curing with faster cure cycles. Quality within the context of this work is measured by the variation in degree of cure within the part through-out the cure cycle, where a more homogeneous development of degree of cure is considered to be indicative of good quality whereas large differences in degree of cure between different regions of the part are considered to imply poor quality. To carry out the work, cure simulations are used to investigate two identical components. One part relied on the oven for heat with a traditional convection heating cycle and the second used electric cartridges with different temperature profiles to achieve an accelerated and zonally defined heating cycle. Experimental parts were then produced to confirm the simulation results and allow for energy measurements to be made. These measurements, taken during both cure set-ups, allows assessment of the gains in terms of energy efficiency when shifting from indirect convection heating in an oven to direct heating with heater mats.

## 2 Methodology

### 2.1 Part and tooling material and geometry

The part design was chosen to contain both thick and thin regions, as well some overall geometric complexity that would influence the air flow around it when heated using an oven. The cross-section of the design is shown in Figure 1. The physical part is a 150 mm deep extrusion of this shape. The tooling shown is made from 3 parts of 8 mm thick 304 stainless steel which were bent to shape and finished using CNC machining for exact part dimensions and smooth lay-up surface. Post machining the tool thickness was reduced slightly for the lower part around the corner where thickness was 6 mm. The pieces are brought together to form a two-sided tool and cork is used as shown in to fill gaps on either side of the part. These gaps are introduced to allow a nearly closed mould at the start of cure while also accommodating compaction during cure.

The composite material chosen in this work is SHD MTC400, an epoxy resin, which is reinforced with a twill fabric made of T700 carbon fibre of 415 gsm aerial weight and with 38% resin weight content. This material was chosen as an aerospace representative grade system, i.e., it has a glass transition temperature around 200°C, and in part due to its reactivity which makes it challenging to cure thicker parts without incurring significant exotherms that cause an internal overshoot of temperature above the target cure temperature. In extreme cases the heat from the exotherm can result in deterioration of the matrix, but even with minor overshoots can result in elevated internal stresses. For the analysis and prediction of the thermal behaviour during the cure cycle, the key material parameters include the density,  $\rho$ , specific heat capacity,  $c_p$ , and conductivity,  $\kappa$ . These are provided in Table 1, for both the composite and tooling material, as well as the cork and are representative of standard values for these materials. No material testing was conducted on any of the materials used. For the composite material the specific heat capacity and conductivity in-plane and through-thickness are based on previous work on similar materials and are given as functions of temperature,  $T$ , and Degree of Cure (DoC),  $\alpha$ , as follows:

TABLE 1 Thermal properties of composites material, steel, and cork.

Property	Unit	Composite material	304 stainless steel (Lewis et al., 1977)	Cork (Ashby et al., 2018)
$\rho$	[kg/m <sup>3</sup> ]	1586.0	7930.0	240.0
$c_p$	[J/(kg·K)]	Eq. 1	502.416	1900.0
$\kappa$	[W/(m·K)]	Eqs 2, 3	16.2	0.04

TABLE 2 Cure kinetic parameters for MTC 400 resin system (Gaska, 2021).

Parameter	Units	Value
$A_1$	[1/s]	$2.97 \times 10^6$
$E_1$	[J/mol]	$1.36 \times 10^5$
$A_2$	[1/s]	$1.28 \times 10^{11}$
$E_2$	[J/mol]	$9.82 \times 10^4$
$m$	[-]	0.8473
$n$	[-]	2.4065
$D$	[-]	28.504
$\alpha_{c0}$	[-]	1.326
$\alpha_{cT}$	[1/K]	$5.73 \times 10^{-3}$
$R$	[J/(mol·K)]	8.314

$$\begin{aligned} c_p(T) &= 2.411 \cdot T + 1168.0, & (1) \\ \kappa_{11}(T, \alpha) &= \kappa_{22}(T, \alpha) = 4.2207 + 0.0085818 \cdot T + 0.027922 \cdot \alpha, & (2) \\ \kappa_{33}(T, \alpha) &= 0.7344 - 0.001 \cdot T + 0.3924 \cdot \alpha - 0.0015 \cdot T \cdot \alpha. & (3) \end{aligned}$$

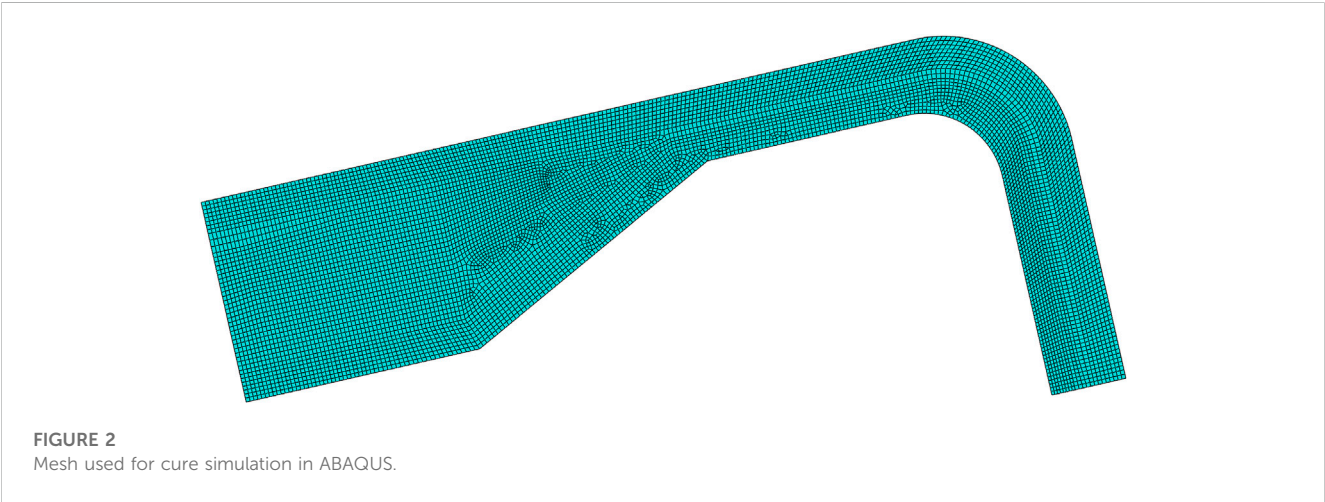
The final component required to define the material system is the cure kinetics, defined by the DoC rate function, see Eq. 4, and the total heat of reaction, H, which is taken as 543 J/g (Gaska, 2021). The coefficients of the cure kinetics are given in Table 2.

$$\frac{d\alpha}{dt}(T, \alpha) = \frac{\left( A_1 \cdot \exp\left(-\frac{E_1}{R \cdot T}\right) + A_2 \cdot \exp\left(-\frac{E_2}{R \cdot T}\right) \cdot \alpha^m \right) \cdot (1 - \alpha)^n}{1 + \exp(D \cdot (\alpha + \alpha_{c0} - \alpha_{cT} \cdot T))} \quad (4)$$

## 2.2 Numerical model and cure cycle selection

The numerical model used to run the cure simulations was set up using the heat transfer analysis in ABAQUS, a simplified 2D cross-sectional approach was used relying on the width of the part being sufficient to allow the part to be approximated by its midplane. Meshing was done using a mixture of quadrilateral and triangular elements and a target element edge length of 1 mm, to ensure sufficient elements in the thinner region to capture any through thickness gradients, see Figure 2. The analysis was transient with an initial homogeneous temperature 20°C and initial time stepping of 30 s and a constraint on the maximum change in temperature in any material point of 2°C for any single time step. This was needed to ensure any exotherms were sufficiently time resolved. The ABAQUS solver was allowed to adjust the time steps down to meet the target maximum temperature change but was prevented from taking time steps greater than 30 s.

For the oven cure simulation, the entire outer edge of the tooling and cork was simulated as having convection heating using the surface film interaction condition. The heat transfer coefficient was set to 10 W/(m<sup>2</sup>·K) and the sink temperature was set to be the air temperature profile as programmed into the oven controller and confirmed *via* thermocouple. For the heated tooling assisted cure, the same boundary edges were divided into three regions, two of which correspond to regions with different target temperature profiles and the third correspond to gaps between the heater mats where a convection boundary condition was applied using the same heat transfer coefficient of 10 W/(m<sup>2</sup>·K) but now using a sink temperature of 20°C, simulating room temperature heat leakage. The first of the heater mat regions contained the





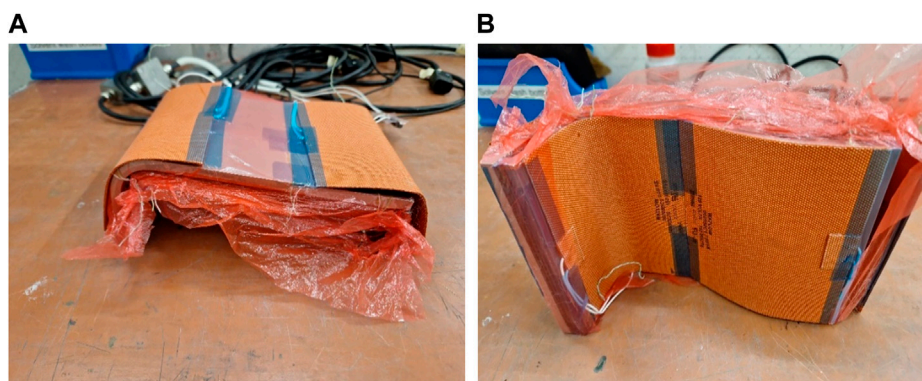


FIGURE 3

Part, pre-bagging, with heater mats on top surface (A) and bottom surface (B), showing placement and gaps.

boundaries of the thick and ramped regions and the second heater mat region contained the boundaries of the thin and corner regions. Figure 3 shows the part prior to bagging, showing the placement of the heaters and the gaps.

For each of these set-ups, a two-stage cure cycle was manually tuned to limit the exotherm occurring in the thick region to be around the target final cure temperature of 120°C. For the heated tooling model, the zonal heating was further used to target a more even heat up rate and DoC development throughout the composite material volume. To check these metrics, two reference points (RP) were used to extract the local temperature and DoC throughout the cycle in the centre of the thick region, Thick RP, and in the centre of the corner, Thin RP, as indicated in Figure 1.

## 2.3 Manufacturing and experimental set-up

The lay-up surface was treated with 5 coats of release agent before each part was manufactured. In addition, release film was used between the lay-up surface and the first ply. The pre-preg material, with a nominal cured ply thickness of 0.43 mm, was cut to size by hand. For the thick region a total of 82 plies were used and for the thin region a total of 12 plies were used, resulting in a theoretical cured thickness of 35.26 and 5.16 mm in these regions, respectively. During lay-up, cold de-bulks were used at regular intervals to reduce thickness build up. In the middle of the stack, thermocouples were introduced at the approximate location matching the RPs, as identified in Figure 1, to allow comparison of thermal profiles between the simulation and the experiments. The thermal profile was combined with the cure kinetics model to predict the cure development in these regions for the manufactured parts.

Thermocouples were also added on the outer surface of the tooling to track the boundary condition. In the case of the zonal heating experiment, an additional set of thermocouples were needed on the outside surface of the tool as input to the controller units. The entire tool part assembly, including heater mats for the zonally heated experiment, was then bagged and a final thermocouple was added externally to the bag to track ambient air temperature. Bag integrity was checked with no drop in vacuum observed within 10 min of disconnecting the vacuum hose. Both oven and heater mat

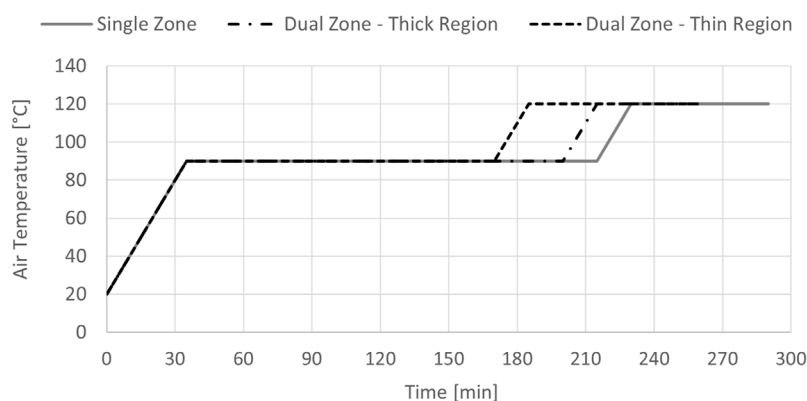
experiments took place in a Carbolite oven, in the case of the heater mat experiment the oven served as a heat proof chamber and was turned off. Vacuum was maintained using an external vacuum pump that remained on at maximum vacuum, indicated on the pump's gauge at 30 mHg, throughout the cure cycle. For the oven cured part, the oven temperature set point was controlled using the in-built controller, while for the zonally heated cured part the four heater mats were each managed by a separate external Watlow PID controller which was fed by a single power unit.

For both curing cycles, an Energy Logger (TinyLogger) was used to monitor the average current drawn by either the oven or the central power unit used to power all the heater mats, at an interval of 30 s. The TinyLogger was also plugged into the lab main circuit to allow monitoring of the voltage and hence allow computation of the power used. As the TinyLogger used can only measure a single power output it was not possible to measure the heater mats individually. An affordable system for parallel power measurements is being developed to allow future studies to capture readings of individual heater mats. The thermocouples were monitored using a datalogger (PicoLogger) at the same interval of 30 s. However, as the ovens/heater mat controllers, PicoLogger Laptop, and TinyLogger were not connected the data sets are not time synchronised as they are manually started one at a time. However, the data is synchronised post-manufacturing using timestamps as the different devices were within 10 s of one another which is considered acceptable given the multi-hour nature of the cure cycle.

## 3 Results

### 3.1 Cure cycle design

The baseline cure cycle for this material for standard thickness laminates is a single hold cure at a temperature anywhere between 80°C and 135°C, with a hold time of 16 h for the low temperature cure and only 1 h at the higher temperature. Due to the reactivity of the material and the thickness of the chosen part, however, the higher hold temperature is not viable due to the exothermic peak of up to 235°C that would be generated, according to the model, in such



**FIGURE 4**  
Air temperature profiles for single and dual zones.

a scenario. For this reason, an intermediate dwell at 90°C was introduced. At this temperature the material begins to react, and the thick region experiences a mild exotherm that brings this region up to around 120°C, the targeted final cure temperature. The second ramp then brings the rest of the part to this temperature for the final hold and cure.

The final cure cycles are given in Figure 4, where the initial ramp rate and hold temperature are identical for both the single zone and the dual zone cure cycles. Ramp rates were kept to 2°C/min to ensure even heating in both scenarios. While both the oven and heater mats are capable of heating faster, this can cause thermal gradients within the oven or across the heater mats that are undesirable when attempting to create a more homogeneous temperature profile within the part. For the single zone (i.e., oven) scenario, the second ramp is delayed allowing thick region exotherm to pass before additional heat is added to the system which would otherwise worsen the peak temperature caused by the exotherm. On the other hand, the dual zone (i.e., heater mat) scenario allows the second ramp to initiate earlier in the thin region only. This separation of the regions also allows the overall cure cycle to be reduced by 17.5% while ensuring uniform final DoC throughout the part. In the single zone cure, due to the delay in ramping up to the final temperature, the thin region lags in cure development requiring the overall cure cycle to be extended in order to allow it to catch up and achieve a part with roughly even cure throughout at the end of the final dwell.

### 3.2 Exotherm and degree of cure

Using the selected cure cycles, single zone and dual zone simulations were carried out and parts were made using an oven and heater mats for experimental validation. The thermal profiles at the selected RPs for the single zone oven cure are as shown in Figure 5 for both simulation and experiment. The figure also shows the oven air temperature and tool temperature above the thick RP as well as power measurements. The experimental thermal profiles for the tool for the thin region and simulation results are not included as no discernible differences were found between them and the corresponding RP thermal profiles.

These temperature profiles show the significant difference in temperature between the thick and thin regions, which is present both in the simulations and the experimental measurements. In the simulation the maximum difference is around 20°C, while for the experiments it was around 34°C. The experimental data shows an additional delay in the temperature and consequently an elevated exotherm. From previous experience it is known that the effective heat transfer in the oven is variable and hence it is expected the difference stems from the heat transfer being lower during the experimental trial than simulated. Thermal lag between the air, tool, and thick region is also highlighted by the experimental temperature profiles. From the power data it can be seen that there is a spike in energy usage both during the initial and secondary ramps.

For the dual zone heater mat approach, as shown in Figure 6, the differences between the thick and thin regions in both simulation and experimental profiles are smaller. For the simulation, the thick and thin region have a closely matching temperature profile. In the experiment, the thin region was found to follow the simulated response closely, but the thick region experienced an exotherm of roughly 20°C which was not predicted by the simulation. The thick region also shows a thermal lag not found in the simulation. The tool temperature thermocouples, which are directly under the heater mat, show no lag and hence confirm the heater mats are following the target cure cycles well. For thin section, the tool temperature shows a decent match to the RP. Finally, the air temperature shows a rise from 20°C to around 40°C, exemplifying the passive heat loss within this set-up. It is evident from the power data that the heater mats require less energy to achieve the required cure cycle.

The differences in the thermal profiles result in a difference in the cure development. For the single zone cure, the degree of cure development, calculated by feeding the simulated and measured temperature profiles to the cure kinetics model is shown in Figure 7. For the simulation, the maximum difference in DoC between the thick and thin region, occurring just after the exothermic peak, is around 0.3, with the thick region surpassing a DoC of 0.9 while the thin region is still below 0.6 (gel point). Such a large DoC variation implies that the polymer in the thick region will begin to gel and carry load while the thin region is still in liquid form. Combined with

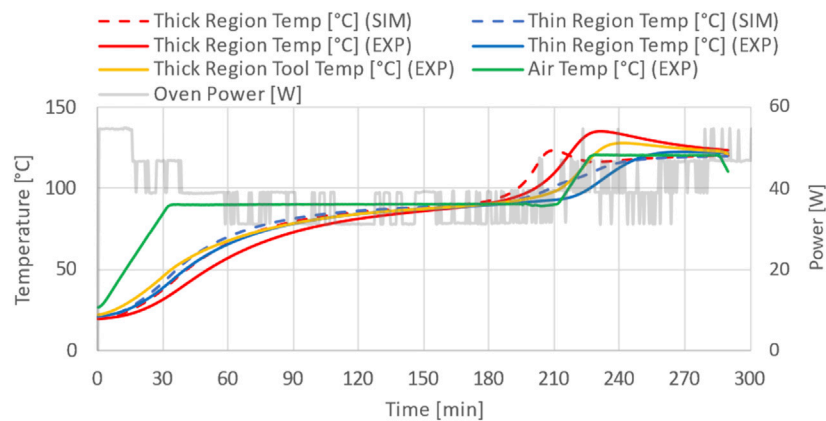


FIGURE 5

Temperature as simulated and experimentally measured at mid-thickness in thick and thin region for single zone cure, accompanied by the power usage of the oven as measured.

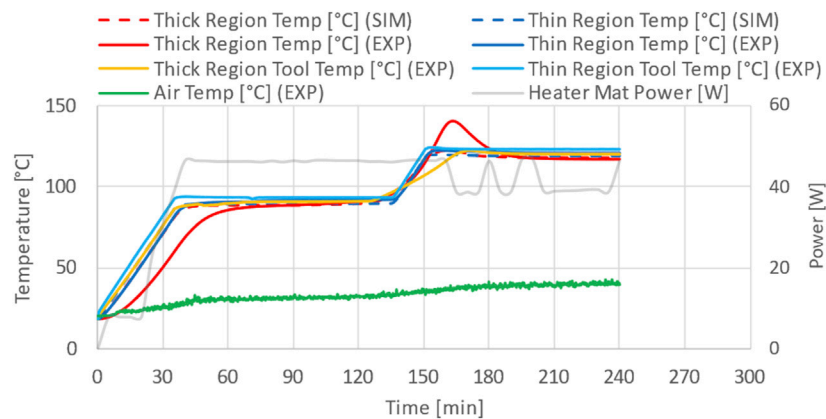


FIGURE 6

Temperature as simulated and experimentally measured at mid-thickness in thick and thin region for dual zone cure, accompanied by the power usage of the heater mats as measured.

the thermal gradient this can result in internal thermal stresses and potential distortions and/or micro-cracking. For the experimental data, the degree of cure profiles are still similar, appearing mostly to be shifted in time. The overall comparison between the thick and thin region still shows a large difference in degree of cure development, with a maximum delta of 0.43.

For the dual zone heater mat approach, the degree of cure development as computed using the temperature profiles are shown in Figure 8. From these it can be observed that the difference in degree of cure development between thick and thin region are reduced for both the simulation and experimental data. This validates the ability of zonal heating to avoid some of the complications cause by using the oven as the separate thermal control for the thin and thick regions can create a better match in DoC development in both regions. In the dual zone approach, the maximum difference in DoC is reduced to below 0.05 which occurs well before gelation with the DoC being effectively identical from 0.2 onwards for the simulated data. For the experimental data the match

is not as close but is still improved significantly compared to the oven cure, with the maximum difference in DoC being reduced to 0.18 and showing a very close match beyond the gel point.

Overall, it can be observed that the dual zone heating approach allows very close match in thermal history and DoC development even though the thickness ratio is 1:7 with the thick region exotherming which the thin region does not do. This close match in DoC development is taken to be indicative of superior quality as DoC gradients have been linked to residual stresses (Bogetti and Gillespie, 1991). Even though the match is not as close as predicted by the simulation, the experiments still show the dual zone approach to achieve better cure development homogeneity.

### 3.3 Energy usage

Integrating the power measurements taken during the two cure approaches by the TinyLogger, it is possible to compare the overall

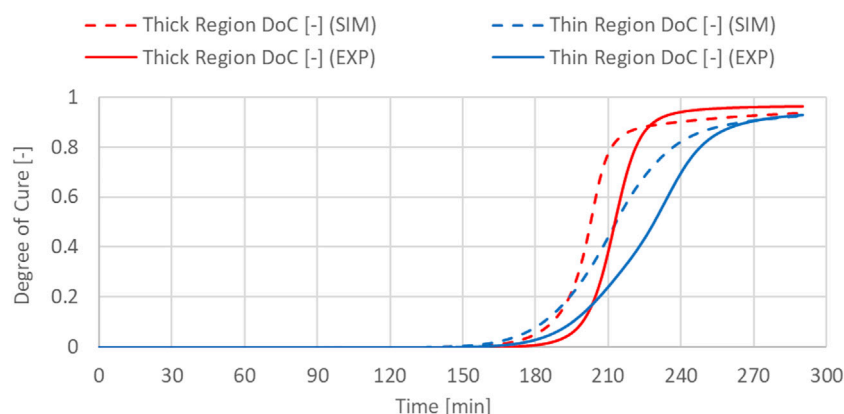


FIGURE 7

Degree of Cure calculated using simulated and measured temperature data at mid-thickness in thick and thin region for single zone cure.

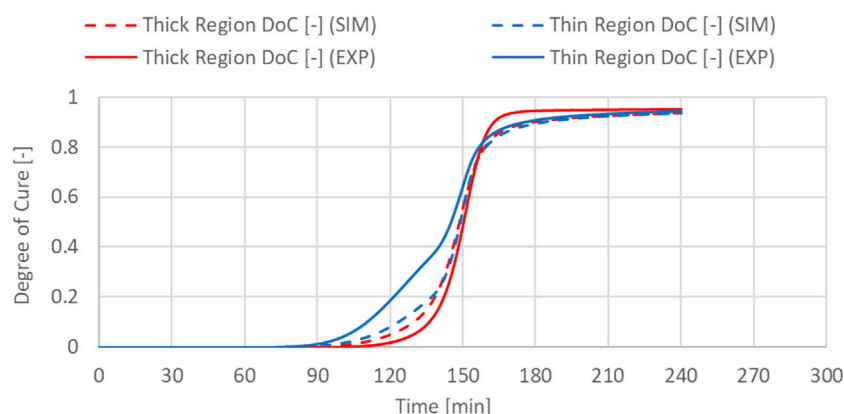


FIGURE 8

Degree of Cure calculated using simulated and measured temperature data at mid-thickness in thick and thin region for dual zone cure.

energy usage of single zone oven curing and dual zone heater mat curing. For the single zone part the total energy consumption was 0.278 kWh, while for the dual zone curing to total energy consumption was measured as only 0.154 kWh. This represents an energy saving of around 45%. This value is affected by both the size and efficiency of the oven as well as the exothermic nature of the part. It is also worth noting that for the zonal heated part, where the oven was off, the ambient air temperature inside the oven was observed to increase to around 40°C from 20°C.

## 4 Discussion

The key observations from the numerical and experimental trials relate to the improved efficiency, both in terms of time and energy consumed, and the improved part quality, in terms of closer match in DoC development throughout the part. In reality, these changes are the compound effect of both the switch to direct heating and multi-zonal

heating. A more nuanced analysis, which separates these two effects would require an additional part to be made using the heater mats with a single zone thermal profile. As this part is missing, the energy savings cannot be accurately split between the two factors. However, the changes in part quality through improved homogeneity of the cure development can be attributed solely to the use of dual zone heating.

The gains observed for the multi-zone, direct heated part were initially predicted from the simulations and then largely confirmed in the experiments. However, the experiments did show a noticeable exotherm not predicted by the simulations. This can be attributed to several approximations involved in the model. The first approximations are the thermal properties of the composite materials, which were not characterised in this study but based on previous studies on similar systems. Characterisation of the conductivity properties of this specific system could refine these properties and hence improve predictions. The second set of approximations, is expected to contribute significantly to the thermal lag and subsequent exothermic peak, is the heat loss to the

ambient air. This approximation is fed by two aspects; the 2D nature of the simulation and the heat transfer coefficient. The oven heat transfer coefficient is naturally low due to the slow air circulation speed and ambient pressure. It is furthermore dependent on the ambient air conditions as the oven used is not a perfectly sealed system (i.e., access ports through which the wires of the thermo-couples and heater mats are passed). This makes it difficult to accurately characterise the heat transfer between the oven air and the part, especially in the case of the dual zone heater mat cured part as for this the oven is turned off and hence there is even less air circulation. The difference in actual heat transfer during the cure cycle and the approximated heat transfer coefficient used in the simulation can easily differ enough to obtain the observed increase in the exotherm of 15.1°C overshoot for single zone oven curing and 20.4°C overshoot for the dual zone heater mat based curing as the temperature overshoot is very sensitive to the efficiency with which the heat generated can be shed to the air. Improved prediction could be possible using a 3D model as it can capture heat transfer across the sides of the part, which would be a source of heat gain in the oven model and heat loss in the heater mat model. There will, likely, always be a limit to the accuracy of the simulations. Therefore improved robustness of the cure cycle and management of the exotherm could be achieved by using machine learning techniques such as those developed by Humfeld et al. (2021) to adaptively control the set points of the heater mats based on the thermocouple data and the numerical model.

Alternatively, the behaviour of the dual zone approach could be improved by using a closed system using a liquid heat exchanger. This would allow an equally efficient heat addition and extraction rather than efficient heat addition from the heater mats and inefficient heat extraction from convection to the ambient oven air. Use of a liquid heat exchanger would then also allow better insulation of the part, which would likely result in further energy savings. However, such a system is more complex, expensive, and space consuming, than using heater mats.

## 5 Conclusion

In this study a thick and complex part was simulated to evaluate the ability of zonally controlled heated tooling to better manage the exotherm and allow for a more even thermal and cure development profile. Numerical simulations were used to design both the single and dual zone cure cycles. The predictions were experimentally checked using trial parts with embedded thermocouples. The experimental results showed an exotherm not predicted by the simulation. This difference is expected to stem from approximations used for the thermal properties of the composite material, the low and variable heat transfer in the oven, which is difficult to characterise and simulate, and the use of a 2D model instead of a full 3D simulation.

However, the experimental trials confirmed the improvements in matching DoC development as was predicted by the simulations. Large spatial gradients in vicinity of the gelation are known to result in larger residual stresses that are detrimental to part quality and performance. The dual zone approach reduced such spatial gradients in temperature and DoC. This reduction can be attributed to the independent thermal control (tuning) of the thick and thin zones, leading to similar thermal history and cure development, without worsening the exotherm from added heat.

Furthermore, compared to single zone oven, dual zone heater mat approach was able to reduce the cycle time by 17.5% with experimental measurements showing a reduction of 45% in energy consumption. The reduced energy consumption is achieved through the combination of reduced cycle time and the shift to more efficient direct heating of the tool surface.

In future work, more advanced direct heating systems are of interest for improved control. This will then allow cure cycles that use heating, active cooling, and reheating (Kim and Lee, 1997). Combined with the zonal approach demonstrated here, this is expected to further improve the management of the exotherm and reduce the cure cycle time while matching thermal history and DoC development throughout the part.

## Data availability statement

The raw data supporting the conclusion of this article will be made available by the authors, without undue reservation.

## Author contributions

VM: conceptualization, data curation, formal analysis, funding acquisition, investigation, methodology, project administration, visualization, writing—original draft, writing—review and editing. AR: conceptualization, funding acquisition, investigation, methodology, writing—review and editing. DL: conceptualisation, funding acquisition, supervision, writing—review and editing. JK: conceptualisation, funding acquisition, methodology, project administration, supervision, writing—review and editing.

## Funding

This work was supported through the Bristol Impact Acceleration Account under the EPSRC grant EP/R511663/1 as well as by the Future Composites Manufacturing Research Hub under the EPSRC grant EP/P006701/1. The support is gratefully acknowledged.

## Acknowledgments

This work was carried out at the Bristol Composite Institute under the supervision and with the assistance of the technical staff. Their input is gratefully acknowledged.

## Conflict of interest

Author DL was employed by the company Rolls-Royce Plc.

The remaining authors declare that the research was conducted in the absence of any commercial or financial relationships that could be construed as a potential conflict of interest.



## Publisher's note

All claims expressed in this article are solely those of the authors and do not necessarily represent those of their affiliated

organizations, or those of the publisher, the editors and the reviewers. Any product that may be evaluated in this article, or claim that may be made by its manufacturer, is not guaranteed or endorsed by the publisher.

## References

- Abdalrahman, R., Grove, S., Kyte, A., and Rizvi, M. J. (2016). Numerical simulation and experimental verification of heating performance of an integrally water-heated tool. *J. Reinf. Plastics Compos.* 35 (8), 671–687. doi:10.1177/0731684415626804
- Ashby, M., Shercliff, H., and Cebon, D. (2018). "Appendix A: Data for engineering materials," in *Materials: Engineering, science, processing and design*. 4th ed. (Butterworth-Heinemann).
- Athanasopoulos, N., Koutsoukis, G., Vlachos, D., and Kostopoulos, V. (2013). Temperature uniformity analysis and development of open lightweight composite molds using carbon fibers as heating elements. *Compos. Part B Eng.* 50, 279–289. doi:10.1016/j.compositesb.2013.02.038
- Bogetti, T. A., and Gillespie, J. W. (1991). Two-dimensional cure simulation of thick thermosetting composites. *J. Compos. Mater.* 25 (3), 239–273. doi:10.1177/002199839102500302
- Gaska, K. (2021). *SHD MTC400 cure kinetics and rheology (internal report)*. Bristol.
- Humfeld, K. D., Gu, D., Butler, G. A., Nelson, K., and Zobeiry, N. (2021). A machine learning framework for real-time inverse modeling and multi-objective process optimization of composites for active manufacturing control. *Compos. Part B Eng.* 223, 109150. doi:10.1016/j.compositesb.2021.109150
- Kim, J. S., and Lee, D. G. (1997). Development of an autoclave cure cycle with cooling and reheating steps for thick thermoset composite laminates. *J. Compos. Mater.* 31 (22), 2264–2282. doi:10.1177/002199839703102203
- Lewis, J. R. (1977). "Chapter 19: Physical properties of stainless steels," in *Handbook of stainless steels*. Editors D. Peckner and I. M. Bernstein (New York: McGraw-Hill).
- Marsh, G. (2003). Mould tool heating - the oven-free alternative. *Reinf. Plast.* 47 (11), 38–41.
- Progoulakis, I. (2004). *Heated tooling for aerospace composites manufacture*. University of Plymouth.
- Rzgar, A. (2015). *Integrally- heated tooling for polymer composites*. University of Plymouth Research Theses.
- Smith, A. W., Goyette, K., Kazanas, C., and Hubert, P. (2013). *Development of a heated tooling solution to improve process flexibility for out-of-autoclave prepregs* in Proceeding of the International SAMPE Technical Conference.
- Struzziero, G., and Skordos, A. A. (2017). Multi-objective optimisation of the cure of thick components. *Compos. Part A Appl. Sci. Manuf.* 93, 126–136. doi:10.1016/j.compositesa.2016.11.014
- Weiland, J. S., Hubert, P., and Hinterhölzl, R. M. (2017). Thermal dimensioning of manufacturing moulds with multiple resistively heated zones for composite processing. *J. Compos. Mater.* 51 (28), 3969–3986. doi:10.1177/0021998317695422



## OPEN ACCESS

## EDITED BY

Christophe Binetruy,  
Ecole Centrale de Nantes, France

## REVIEWED BY

Steven Le Corre,  
Université de Nantes, France  
Khubab Shaker,  
National Textile University, Pakistan

## \*CORRESPONDENCE

Masoud Bodaghi,  
✉ masoud.bodaghi@list.lu

## SPECIALTY SECTION

This article was submitted to Polymeric  
and Composite Materials,  
a section of the journal  
Frontiers in Materials

RECEIVED 23 January 2023

ACCEPTED 13 March 2023

PUBLISHED 22 March 2023

## CITATION

Bodaghi M, Delfrari D, Lucas M,  
Senoussaoui N-L, Koutsawa Y, Uğural BK  
and Perrin H (2023), On the relationship  
of morphology evolution and thermal  
conductivity of flax reinforced  
polypropylene laminates.  
*Front. Mater.* 10:1150180.  
doi: 10.3389/fmats.2023.1150180

## COPYRIGHT

© 2023 Bodaghi, Delfrari, Lucas,  
Senoussaoui, Koutsawa, Uğural and  
Perrin. This is an open-access article  
distributed under the terms of the  
[Creative Commons Attribution License  
\(CC BY\)](https://creativecommons.org/licenses/by/4.0/). The use, distribution or  
reproduction in other forums is  
permitted, provided the original author(s)  
and the copyright owner(s) are credited  
and that the original publication in this  
journal is cited, in accordance with  
accepted academic practice. No use,  
distribution or reproduction is permitted  
which does not comply with these terms.

# On the relationship of morphology evolution and thermal conductivity of flax reinforced polypropylene laminates

Masoud Bodaghi<sup>1\*</sup>, Doriane Delfrari<sup>1</sup>, Margot Lucas<sup>1</sup>,  
Noha-Lys Senoussaoui<sup>1</sup>, Yao Koutsawa<sup>1</sup>, Burcu Karaca Uğural<sup>2</sup>  
and Henri Perrin<sup>1</sup>

<sup>1</sup>Luxembourg Institute of Science and Technology (LIST), Hautcharage, Luxembourg, <sup>2</sup>Head Office, BPREG, Bornova, Izmir, Türkiye

This paper focuses on the morphology evolution in the forming process of unidirectional flax reinforced polypropylene composite laminates. The link between the morphology evolution and thermal conductivity during consolidation stages is investigated. Hot press forming allows to manufacture several composite laminates at different consolidation stages as a function of the compaction thickness. Microscopic evolution of the laminates in terms of morphology and porosity fractions are evaluated by scanning electron microscopy and X-ray microtomography ( $\mu$ -CT). Hot disk technique is applied to measure the thermal conductivity of the laminates in in-plane and transverse directions. It is found that the in-plane thermal conductivity almost linearly increases with the reduction of porosity fraction. However, the transverse thermal conductivity remained constant. Beside the proposed relations, a theoretical model, based on a two-level Mori-Tanaka homogenization method is proposed. Considering the three-phases material (i.e., porosity, fiber, and polymer matrix), there is a good agreement between the experiment data and model predictions, but limited predictivity for porosity level above 15% certainly due to simplifying assumptions used in the predictive model.

## KEYWORDS

thermal conductivity, flax fiber, hot press forming, consolidation, porosity

## 1 Introduction

Given the increasing demand for fiber reinforced polymer composites from aerospace to marine and infrastructure industry sectors, the global solidarity solution is sustainable composite products with the lowest ecological footprint during and at the end of their service life has been a major industry driver of polymer composite materials. Natural fiber reinforced composites can potentially reduce the global dependence on the petroleum-based fibers such as glass and carbon. In addition, a shift from thermoset composites to the thermoplastic counterparts accelerates manufacturing cycle, improves toughness and impact strength, and allows a reliable recycling process. Therefore, natural fiber reinforced thermoplastic composites will be a material platform for circular economy.

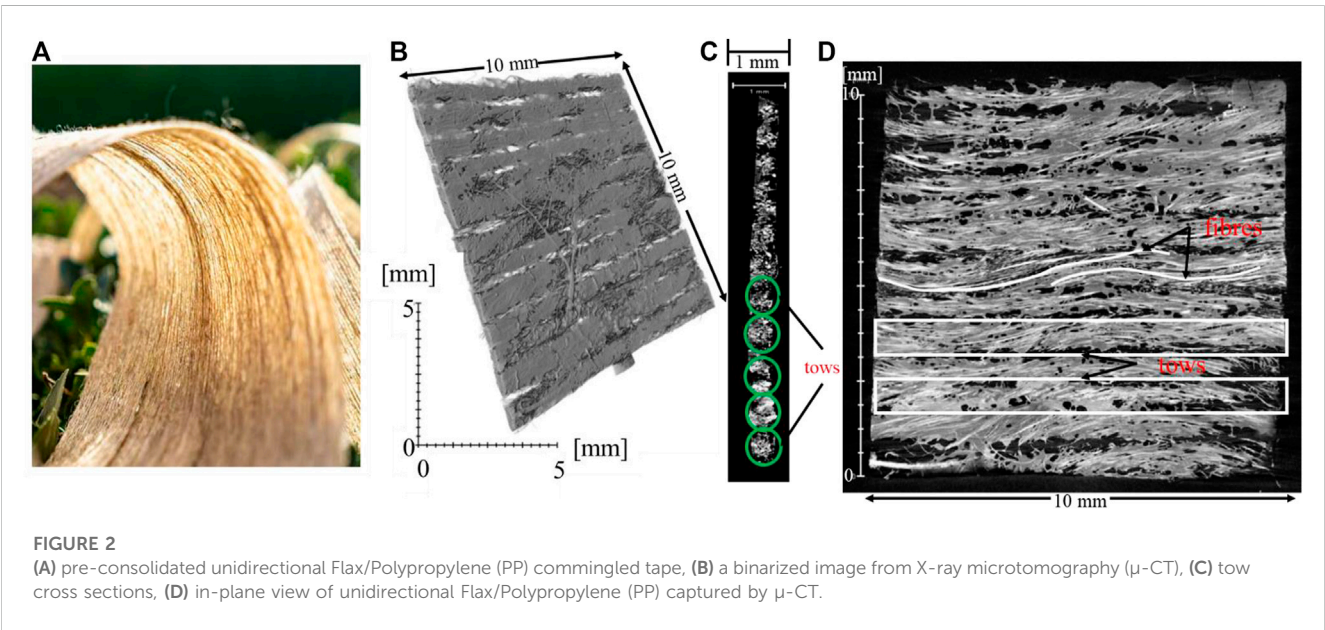
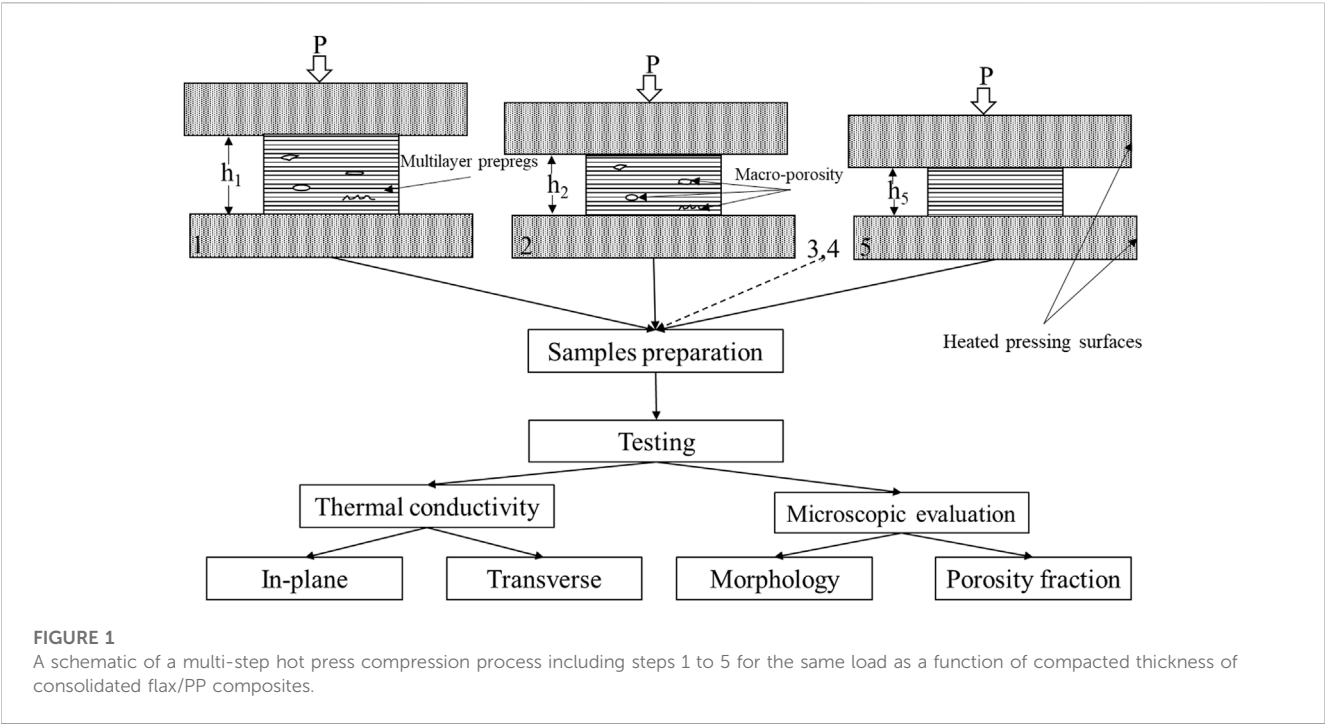
**TABLE 1** Experimental study of thermal conductivity measurements of different types of natural fiber reinforced thermoplastic or thermoset composites.

References	Composite		Fabric structure	V <sub>f</sub> (%) range	Manufacturing technique	Thermal conductivity (W/mK) range		Test method
	Fiber	Resin				In-plane	Transverse	
Mishra et al. (2020)	Flax	Epoxy	plain weave	35–37	Hand lay-up and hot press molding	----	0.27–0.31	C-therm TCi
	Jute		twill weave				0.25–0.26	
			Unidirectional					
			Matt					
Wang et al. (2020)	Bamboo	polypropylene fiber	Non-woven	36–74	hot press molding		0.03–0.35	HotDisk transient plane source (TPS) –2500s
Zheng (2014)	Hemp	----	Unidirectional	100	-----	----	0.12	Numerical modelling
Mounika et al. (2012)	Bamboo	Polyester	Unidirectional	15–60	Hand lay-up and hot press molding		0.18–0.21	Guarded heat floy meter
Thilagavathi et al. (2010)	mix (bamboo, banana, and jute fibers)	polypropylene fiber	Non-woven	49.4	Web formation and subsequent needle-punching machine	-----	0.03	ASTM D 737
Li et al. (2008)	flax (NaOH treatment)	high density polyethylene	Powder	6.8–21.9	Extrusion	-----	0.32–0.42	Line-source
Behzad and Sain (2007)	Hemp	Acrylic polymer	Random	50–80	Vacuum infusion	0.74–0.97	0.18–0.28	Davidson&James
Takagi et al. (2007)	Bamboo	Poly lactic acid (PLA)	Chopped random	61.8	hot press molding	-----	0.34	Hot wire
Kim et al. (2006)	mix (kenaf/ hemp/flax/ sisal)	maleated polypropylene	Chopped random	38–42	hot press molding	-----	0.05–0.06	ASTM-C518 (steady state)
Mangal et al. (2003)	Pineapple leaf	phenol formaldehyde and coupling agent	Unidirectional	-----	Fiber treatment	-----	0.12–0.22	HotDisk TPS

The standard materials for continuous natural fiber reinforced thermoplastic composites are prepreg or semipreg (comingled yarn-based fabric). These semi-products open the way to new forming techniques such as hot press forming (Ouagne et al., 2010; Bourmaud et al., 2016; Derbali et al., 2018), automated prepreg tape placement (Lukaszewicz et al., 2012; van Hoa et al., 2017; Donough et al., 2022), or new welding techniques (Ageorges et al., 2001; Ageorges and Ye, 2002; Yousefpour et al., 2004; Fu et al., 2022). One of the very influent parameters of the forming techniques is the temperature (Guzman-Maldonado et al., 2016). The careful design of temperature cycle can maximize the process window and minimize the porosity volume fraction of fabricated composites (Hernández et al., 2013). Improper process design could lead to a porosity volume fraction of 30% (Madsen et al., 2007). Porosity formation during thermoplastic prepreg consolidation is referred to the empty spaces between the stacked prepreg layers (inter-layer porosities) and within the layers (intra-layer porosities).

Certain increase in the processing temperature of stacked prepreg layers decreases the resin viscosity, enhances the

impregnation property of a thermoplastic resin to a reinforcing fiber, and hence evolves contact layers (Saenz-Castillo et al., 2019). But temperature must be kept below a maximum value to avoid the thermal degradation of natural fiber reinforcing thermoplastic composites (Gassan and Bledzki, 2001; van de Velde and Baetens, 2001; Fujihara et al., 2004). A well-consolidated natural fiber reinforcing thermoplastic composites must be conducted within a narrow window of opportunity. Recognizing the thermal properties such as thermal conductivity at processing temperatures are important parameters to simulate the temperature gradient inside the composite during a forming process (Li et al., 2008). Barasinski et al. (Barasinski et al., 2011) observed non-continuous temperature field between layers during thermoplastic tape placement process due to the existence of inter-layer porosities. They remarked that the evolution of the layer contacts improves the thermal conductivity across the material. The thermal conductivity of fiber and polymer within a prepreg makes an important contribution to the heat transfer. On the other hand, porosities across the composite volume can significantly influence the thermal behavior of a stacked prepreg during a thermoforming process.

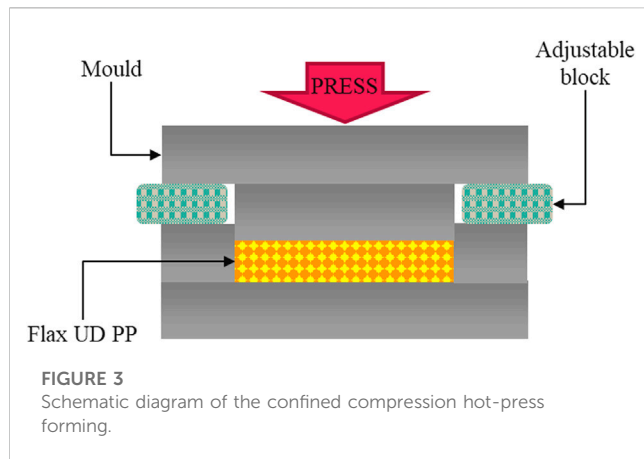


**TABLE 2** The technical specifications of the Flax/Polypropylene (PP) commingled unidirectional fabric (BPREG, 2022).

Supplier	Fibre content (wt%)	Polymer type	Consolidated ply thickness (mm)	Width (cm)	Areal density (g/m <sup>2</sup> )
BPREG	50	semi-crystalline Polypropylene (PP)	0.3	60	300

Given the lower value of the thermal conductivity of air compared with a solid, the incorporation of porosity into a stacked prepreg decreases its thermal conductivity.

Nonetheless, no author addressed the link between the porosity fraction and thermal conductivity, especially when the morphology of a composite laminate is evolving during a consolidation or forming process.



## 1.1 Previous work and objectives

Although much research has been carried out on natural fiber composites, little is known about the relationship of thermal conductivity and the microstructure evolution of natural fiber reinforced thermoplastic composite during forming process. Existing studies majorly focused on the relationship of transverse thermal conductivity and fiber content for the fully consolidated natural fiber reinforced polymer composites (see Table 1).

Thermal conductivity of stacked prepreg layers is not a simple function of the thermal conductivities of its components, (i.e., polymer, and fiber) during a consolidation step. It is strongly affected by porosity fraction, pore geometries and microstructural evolution. The relation between fibres microstructure and its evolution during processing has been documented in the literature (Dumont et al., 2010; Latil et al., 2011; Dumont et al., 2017). The effect of microstructure characteristics such as fibre diameter and orientation angle on the conductivity of fibrous media has been also discussed (Fu and Mai, 2003; Han and Chung, 2011; Lu et al., 2021). However, the effect of microstructure on the thermal conductivity, accounting for the third phase (porosity), has yet to be evaluated. Thermoplastic prepreg materials contain a relatively high level of initial porosity content (intra-layer porosity) (5%–10%) (Zhang et al., 2017). Because of the rough prepreg surface, large inter-layer porosities are expected for multi-layered prepreg. Intra-layer porosities are as important a limiting factor as inter-layer porosities in thermal conductivity. During the consolidation, after the thermoplastic composites is heated, a compression pressure is applied to reduce intra- and inter-layer porosities. A few papers have reported the correlation between microstructure evolutions as a function of inter-layer porosity fraction and thermal conductivity during a consolidation process. Most of these studies simplified the geometry of inter-layer porosities rather than a complete porosity measurement. Lee and Springer (il Lee and Springer, 1987) modelled the degree of layer contact evolution as a function of temperature and pressure by using a succession of rectangular asperities. Although Yang and Pitchumani (Yang and Pitchumani, 2001) improved the geometrical description of layer contact evolution, the literature (Mantell and Springer, 1992; Ageorges et al., 2001; Lamèthe et al., 2005; Tierney and Gillespie, 2006; Khan et al., 2010) widely applied the model of (il Lee and Springer, 1987). Levy et al. (Lévy et al., 2014) made use of Lee and Springer's model (il Lee and Springer, 1987) to relate

layer contact evolution between layers of a laminate and internal thermal contact resistance under constant pressure and isothermal conditions. However, those works were developed for a thin layer which is composed of two phases: a composite phase and an air phase. They also ignored the incorporation of the intra-layer porosities into their model. The reduction of intralayer porosities is dominated by the porosity consolidation under the effect of a compaction pressure. After the compression of a stacked prepreg, the thickness is changing, and the resin flows to fill the porosities. Depending on the spatial distribution and local content of intra-layer porosity within prepreps, some intra-layer porosities are difficult to be removed (Zhang et al., 2017), (Simacek et al., 2013). To our best knowledge, the sole study in the view of microstructure of plant fiber and composite has been provided by Liu et al. (Liu et al., 2014). They showed that the transverse thermal conductivity of unidirectional abaca fiber/epoxy composite manufactured by resin transfer molding (RTM) increases by decreasing porosity fraction and increasing weakest linkage strength. Porosities in thermosetting composites can be washed out with resin flow, bleeding introduced high pressure, vibration, and vacuum in RTM process (Mehdikhani et al., 2019). Intralayer and interlayer porosities in thermoplastic composites is hard to be eliminated due to the high viscosity of thermoplastic resins ( $10^5$ – $10^9$  mPa s for thermoplastic melt vs. 30–200 mPa s) that results in significantly limited resin flow comparing to thermosetting counterparts such as epoxy (van Rijswijk and Bersee, 2007).

The objective of the present work is to determine thermal conductivity in in-plane and transverse directions at different porosity fractions as a function of compacted thickness of consolidated composites. During the consolidation step (Figure 1), the load ( $p$ ) is applied on the flax fibre thermoplastic prepreg above the melting temperature of semi-crystalline polypropylene (PP). This load forces the molten thermoplastic to be impregnated into the flax fabrics while gradually removing porosities. Change at the thicknesses ( $h_1 > h_2 > \dots > h_5$ ) will be the controlling parameter for the morphology evolution and obtained porosity fraction. Thermal conductivities are measured at five different consolidation stages by using a Hot disk technique. Finally, a correlation with theoretical values, based on measured and estimated inputs parameters is proposed. Figure 1 represents the steps involved in the evolution of composite microstructure at different consolidation stages for the same load ( $p$ ).

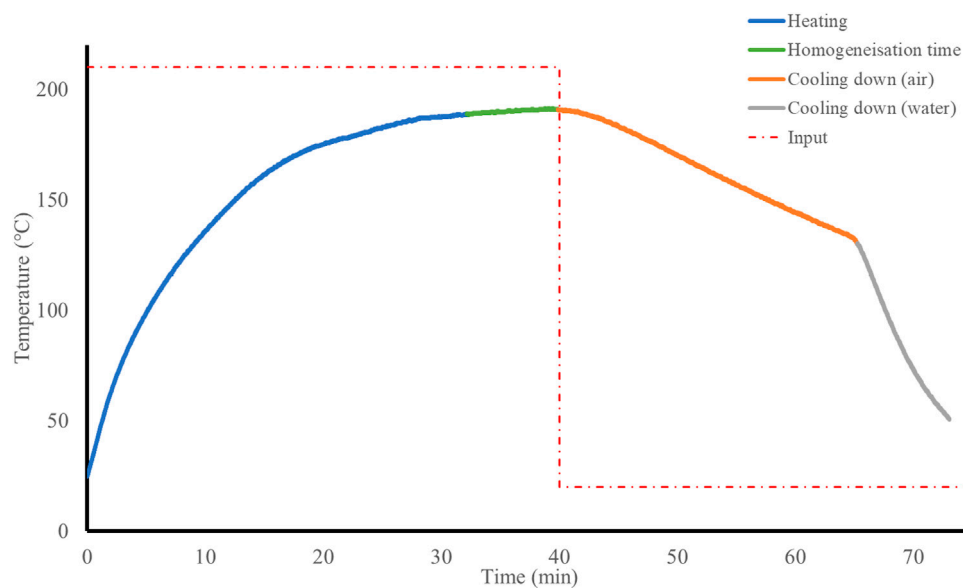
## 2 Experiments

### 2.1 Materials

The tested material is a pre-consolidated unidirectional Flax/semi-crystalline Polypropylene (PP) commingled tape (Figure 2A) supplied by BPREG. The main properties of the fabric are summarized in Table 2.

With X-ray microtomography ( $\mu$ -CT), Figure 2B shows white rodlike porosities in a pre-consolidated unidirectional Flax/Polypropylene (PP) commingled tape. The cross-sectional images of fibre tows are shown in Figure 2C. The width of ellipse-shaped tow cross sections (green in Figure 2C) is around 600  $\mu$ m. The in-plane view of a tow captured by  $\mu$ -CT has a deviation from a straight





**FIGURE 4**  
Heating and cooling cycles during the consolidation process of the Flax/PP preregs.

**TABLE 3 Series of experiments for morphology evolution and thermal conductivity measurements. The thickness percentage reduction was calculated relative to the primary consolidation stage.**

Thickness percentage reduction	0%	7%	12%	20%	25%
Consolidation stages	1 (primary consolidation)	2	3	4	5 (fully consolidated)
Spacer blocks for the first series of experiments (mm)	5.80	5.40	5.0	4.60	4.30
Spacer blocks for the second series of experiments (mm)	16.60	15.50	14.60	13.10	12.50

line as shown in Figure 2D. This inherent deviation, which is not visible by naked eye, is due to the tow twisting during the manufacturing process of a pre-consolidated unidirectional Flax/PP commingled tape.

## 2.2 Fabrication of neat PP and its composite laminates

The thermal conductivity of a polymer composite is influenced by several factors including, fiber direction, fiber volume fraction, moisture content, porosity fraction and polymer type. The major contributors to the thermal conductivity changes are fiber and porosity fractions and the conductive characteristics of polymer and fiber. In this study, in addition to the composite samples, one sample of neat PP was also manufactured by a hot-press forming process.

### 2.2.1 Neat PP manufacturing

To minimize the thermal degradation during hot-press forming, the thermal behavior of PP polymer was characterized by differential scanning calorimetry (DSC) and thermal gravimetric analysis (TGA). The test specimen was dried at 80°C for 1 hour. DSC

results showed melting temperature of 165°C for PP. The isothermal TGA results at 190°C for 2 h determined 2 wt% degradation of PP. Accordingly, the neat PP plates were fabricated by hot press forming at 190°C as follows: polypropylene fibers were placed inside a preheated square mold having dimensions of 100 × 100 mm<sup>2</sup>. The plate thickness was adjusted by using picture frame of 15 mm. Subsequently, the mold was closed with a pressure of 10 bars for 10 min. The plate was demolded at temperatures below 30°C. Finally, the samples were cut from the plates for thermal conductivity measurements.

### 2.2.2 Consolidation of unidirectional Flax/PP composite

To avoid the thermal degradation, after oven drying at 80°C for one night, isothermal TGA of dried flax fibre at 190°C was also performed for 2 h. The TGA results showed a negligible degradation (>1%) of flax fibres. The consolidation process is like the one applied for the fabrication of neat PP. In this work, only the influence of the mold cavity nominal thickness on the porosity fraction, morphology evolution and thermal conductivity is considered. At each consolidation iteration, the subsequent change in cavity height is applied to the thickness of the consolidated flax/PP composite. The reference sample was defined from the minimum achievable

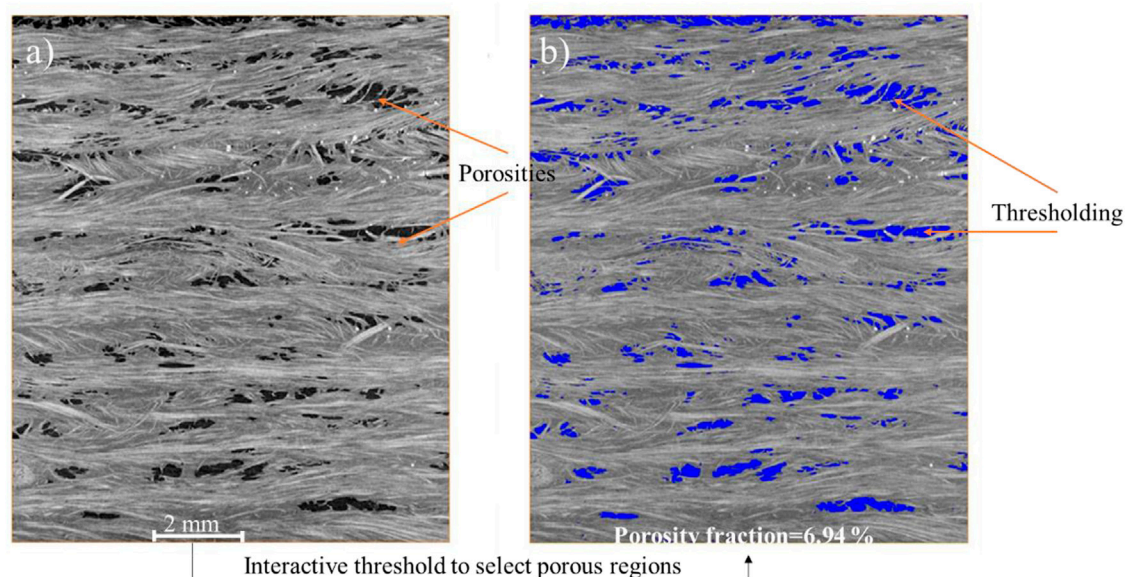


FIGURE 5

(A) A grayscale tomographic slice of the flax/PP specimen with 7% thickness reduction relative to the base line (i.e., consolidation stage 2), (B) the image of tomographic slice of the flax/PP specimen processed by Avizo software, highlighting porous regions in blue.



FIGURE 6

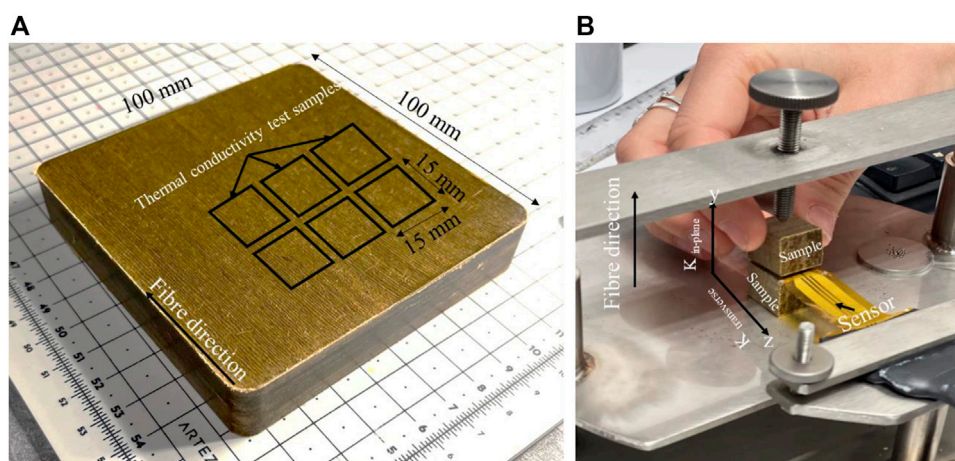
Fully consolidated ten-layer flax/PP composite: (A) cross-sectional morphology of consolidated image, (B) 3D image of fibers from micro-CT, (C) 3D image of porosities from micro-CT with the following operating conditions: voltage: 70 kV; current: 160  $\mu$ A, isotropic voxel size:  $6 \times 6 \times 6 \mu\text{m}$ , scan time: 90 min.

thickness at which the porosities are almost eliminated, and fiber volume fraction reaches to its maximum. In this study, our reference sample was achieved at the cavity height of 2.3 mm. Based on the obtained reference thickness, four intermediate consolidation states were conducted by changing mold cavity with the same pressure load. The percentages of thickness reduction were 0%, 7%, 12%, 20%, 25% relative to the thickness of the primary consolidation. The mould tooling and Flax/PP assembly inside the cavity is shown in Figure 3. The upper and bottom compaction surfaces were steel plates. Consolidation process as follows: the composite from a dried stack of Flax/PP prepreg layers (after oven drying at 80°C for one night) was molded and subsequently closed with a gap of 50  $\mu\text{m}$  to

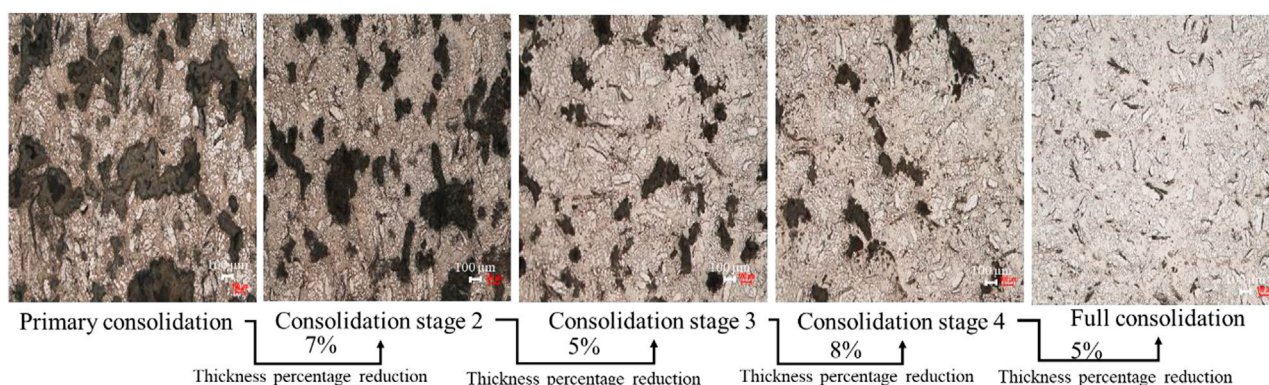
outflow the excess molten polymer during compression stage. The mold was put on a hot-press machine preheated to 200°C. As soon as the mold reached to the temperature of 190°C, it was held for 10 min without compression to allow the PP to start melting and percolating through the fibers. Subsequently, the assembly was pressed at 1 mm/min constant closing speed to reach the target thickness and held for 10 min for consolidation. The target thickness was adjusted by standard spacer blocks (see Figure 3).

During the consolidation, the applied pressure (10 bar) forced the molten polymer to fill the empty spaces between and inside the fibre tows while eliminating porosities. During the cooling period, the pressure applied was maintained until the temperature of the





**FIGURE 7**  
Schematic illustration of thermal conductivity measurement by using Hot Disk technique. (A) sample preparation, (B) TPS assembly.



**FIGURE 8**  
SEM observations for microstructure changing of flax/pp composites under consolidation stages: morphology changes as a function of the thickness percentage reduction at different consolidation stages.

mold cavity dropped down to 50°C for demolding the consolidated laminate. Improper cooling cycle will generate residual stresses and influence the fiber rearrangement and capillary flow within the fibre tows. For the semi-crystalline PP matrix, a higher cooling rate yields higher residual stresses. The magnitude of the stresses varies depending on several parameters such as number of plies, fibre volume fraction, and processing conditions. To limit the residual stresses, two-rate cooling profile was applied. As shown in Figure 4, the temperature of the composite was reduced to 130°C at the cooling rate of  $-2.5^{\circ}\text{C}/\text{min}$  by air and subsequently the cooling rate was increased to  $-10.5^{\circ}\text{C}/\text{min}$  by water to reduce the temperature of the composite to 50°C.

## 2.3 Sample preparation

Two series of consolidation tests were performed on the Flax/PP prepreg. The first series of experiments were planned for the

assessment of porosity fractions and morphology evolutions by consolidation of 17 Flax/PP prepreg layers. Consolidation was divided into five stages, which contributed to the change in the laminate thickness under the same applied pressure  $P$ . Depending on the consolidation's stages, the thickness was reduced from 5.8 mm to 4.5 mm. The second series of experiments were planned for the determination of the in-plane and through-thickness thermal conductivities of Flax/PP composites. To make free-edge effect consolidation, each layer was first punched to the final part dimension. During the consolidation stages, a confined compression mould with a gap of 0.05 mm between upper and bottom mould was used, enabling the air/gas removal without squeezing out the fibres from the mould cavity. Finally, to avoid potential surface effects at the edge area, all samples were cut 10 mm far from the edges.

The thickness of composite samples should be at least 10 mm for thermal conductivity measurements (EN ISO 22007-2:2015, 2015). The samples for thermal conductivity measurements were

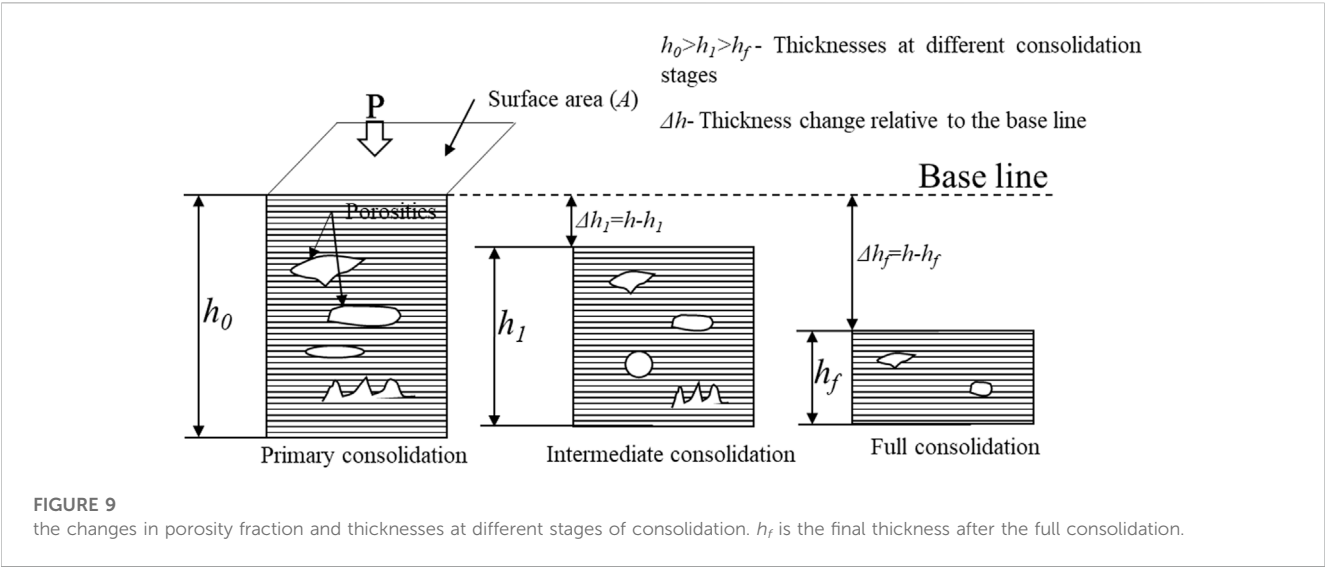


TABLE 4 Porosity volume fractions relative to the corresponding consolidation stages.

Consolidation stage [lamine thickness (mm)]	Volume of sample (mm <sup>3</sup> )	Volume of a porosity (μm <sup>3</sup> )		Volume of total porosity (mm <sup>3</sup> )	Porosity volume fraction (%)
		Min	Max		
Primary consolidation (5.80)	555.12	$8.480 \times 10^{-6}$	99.562	107.51	19.36
2 (5.40)	554.44	$6.86 \times 10^{-6}$	101.918	112.33	20.26
3 (5.00)	569.54	$6.86 \times 10^{-6}$	19.91	53.76	9.44
4 (4.60)	555.27	$8.48 \times 10^{-6}$	0.964	14.08	2.53
Full consolidation (4.3)	584.50	$8.48 \times 10^{-6}$	0.0075	0.085	0.01

approximately three times thicker than those samples used for the measurements of porosity fractions and morphology evolution. Depending on the consolidation’s stages, the thicknesses of samples for thermal conductivity measurements were reduced from 16 mm to 12 mm by consolidation of 60 Flax/PP prepreg layers. Table 3 shows series of experiments planned for the fabrication of composites consolidated at different thicknesses.

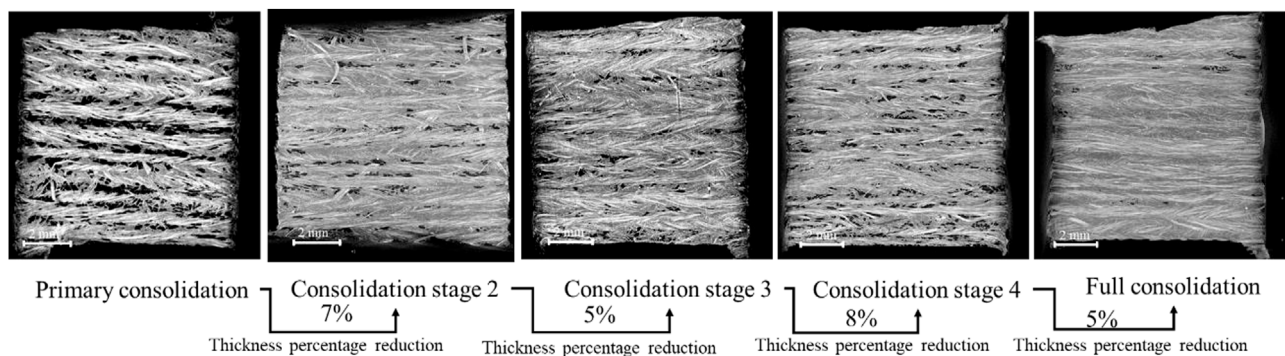
## 2.4 Testing

### 2.4.1 Porosity fraction and morphology evolution

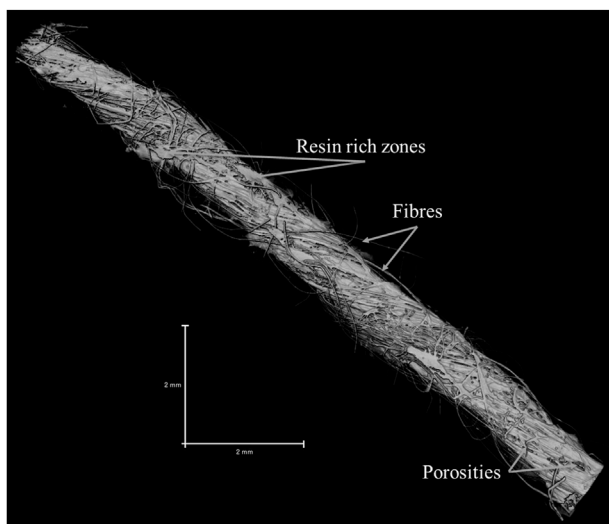
#### 2.4.1.1 Porosity fraction

An Image-based technique, which is a common tool for the assessment of the void content of composites (Machado et al., 2022), was used to assess the porosity fraction. Due to high porosity content, especially for the primary consolidation case, X-ray micro-computed tomography (μ-CT) was employed to obtain three-dimensional (3D) images of porosities inside the consolidated samples. The porosity fraction was estimated from segmented 3D images. As the focus of the current study was to address the relationship of porosity fraction and thermal conductivity, the authors will not discuss the detailed porosity

characteristics such as shape, location, and spatial distribution. The individual samples (10 mm × 10 mm) were scanned on a EasyTOM high-end CT system from RX Solutions with the following operating conditions: voltage: 50 kV; current: 200 μA, isotropic voxel size: 20 × 20 × 20 μm, scan time: 90 min 2,100 radiographic projections were acquired with the rotation step of 0.12° with the exposure time of one second for each projection. The voxel size means that only porosities equal to or larger than equivalent diameters, which is the ratio of the surface area of a pore to its perimeter, of 20 μm were accounted. The reconstruction of the X-ray projections to tomographic slices was performed with RX act software from RX solutions (RX Solutions, 2022). The segmentation and data processing were conducted using the 2D/3D image analysis software Avizo. Another Avizo software feature is the ability to calculate the porosity and analyze the pore connectivity (Li et al., 2021). The porosity fraction of flax/PP at different consolidation stages was then estimated by Avizo. The interactive thresholding module of the Avizo software was applied to return a binary image (porosities in black and flax/pp in gray) (Figure 5A). In the interactive thresholding, the classification of the pore phase and the solid phase (Flax/PP) was performed automatically based on shape characteristics of the image histogram. The module smoothed the histogram to two



**FIGURE 10**  
μ-CT images of samples at different consolidation stages.



**FIGURE 11**  
The longitudinal view of a flax/pp fibre tow.

distinguishable peaks, and the valley between these peaks was selected as the threshold value. As the acquired images showed a roughly bimodal histogram, they are appropriated to the interactive thresholding (Sankur, 2004; Jensen et al., 2014). Subsequently a color threshold was imposed to highlight the porosity regions for the estimation of porosity fraction (Figure 5B).

#### 2.4.1.2 Morphology evolution

The cross-sectional morphology evolution of consolidated samples was examined by a pressure-controlled FEI Quanta FEG 200 scanning electron microscope (SEM) from FEI Company (Oregon, United States). For the investigation of morphology evolution, the samples were embedded in low viscosity resin and subsequently were polished to obtain scratch-free surface finishes. The samples with a size of  $12 \times 15 \times 15$  mm were cleaned and dried at  $80^\circ\text{C}$  for 1 hour and immediately were transferred to the SEM chamber to minimize the moisture absorption of the composites.

Figure 6 shows cross-sectional (6a) and 3D view (6b and c) of a fully consolidated ten-layer Flax/PP composites. The cross-sectional view from Figure 6A reveals the homogeneous distribution of fiber inside the polymer matrix. A fiber volume fraction of 34% and a porosity fraction of 0.7% through the segmented 3D image were estimated by applying Avizo software, confirming the well-consolidated reference sample.

#### 2.4.2 Thermal conductivity measurement

The measurements of thermal conductivity of all composites were conducted at the room temperature and normal pressure by using Hot disk technique [i.e., transient plane source (TPS)]. The sample size used for the measurements was  $15 \times 15 \text{ mm}^2$  (Figure 7A). The Hot Disk is a TPS 2500 S from Hot Disk instruments with a Kapton-insulated sensor in the form of a bifilar spiral with the design number of 7,577 ( $a = 2.001 \text{ mm}$  radius) (Figure 7B). Both in-plane and transverse thermal conductivities were measured according to EN ISO 22007-2: 2015. Assuming the conductive pattern to be in the y-z plane of a coordinate system, the in-plane and transverse thermal conductivities were measured, correspondingly (Figure 7B).

For each consolidation stage (Table 3, five configurations), six samples were cut using water jet to produce thermal conductivity test samples (Figure 5A). The Kapton sensor was sandwiched between two samples (Figure 5B). The thermal conductivity of testing samples was determined by monitoring temperature increase of sensor for 10 s due to an input power per unit area, which was increased from 20 to 50 mW with the 10 mW steps. These measurements were repeated three times for each consolidation stage.

## 3 Results and discussion

### 3.1 Porosity fraction and morphology evolution

The SEM images of morphology evolution from primary consolidation to full consolidation are shown in Figure 8. Based on the consolidation results on Flax/PP specimens of different



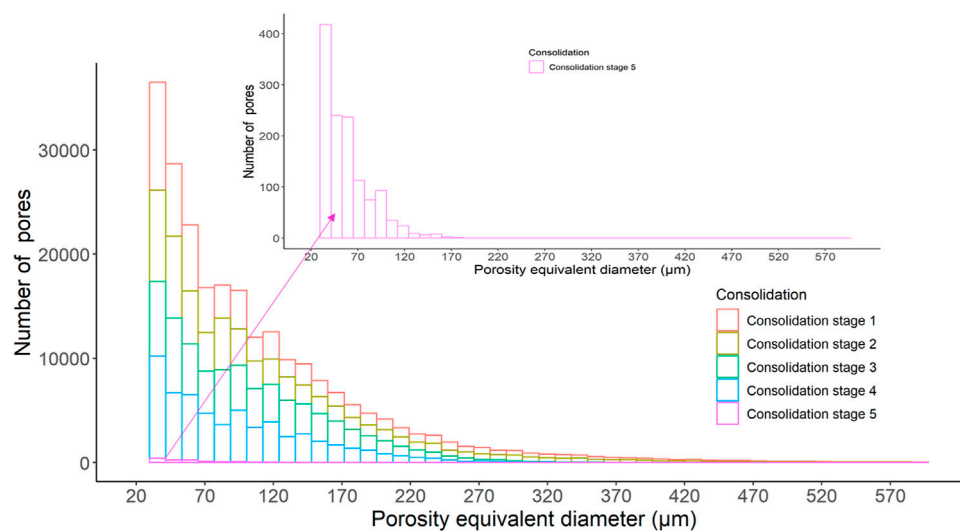


FIGURE 12

The frequency of the distribution of porosity equivalent diameter at different consolidation stages.

**TABLE 5 Comparison of the thermal conductivity values obtained for the neat PP. It should be noted that the type of PPs in terms of its amorphous or semicrystalline structure was not addressed by the Refs.**

Refs	Supplier	Average thermal conductivity at 25°C (W/(m.k))
Current study (semi-crystalline)		0.16
Muratov et al., (2021) (semi-crystalline)	PP, Borealis	0.18
Krause et al. (2019)	PP, Moplen HP400R	0.26
Chen et al. (2017)	PP, MoplenRP344RK	0.22
Krause and Pötschke (2016)	PP, 579S (sabic)	0.26
Han and Fina (2011)	Not specified	0.11
Weidenfeller et al. (2004)	Minelco B.V. & RTP s.a.r.l	0.22

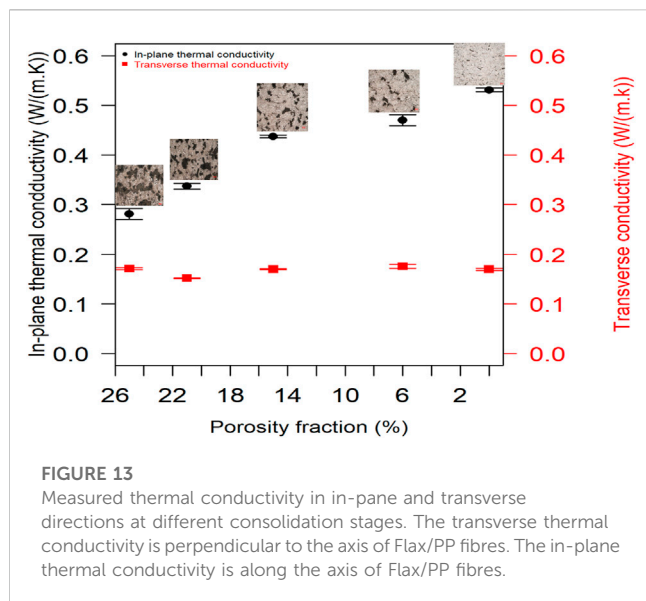
thickness, when the compression load was applied to the specimens, a decrease in volume is due to the fiber rearrangement (Figure 6 in white color) and a reduction of porosity fraction (Figure 8 in black color). According to Terzaghi (Terzaghi, 1943), a change in volume directly affects the porosity fraction of a saturated porous medium (i.e., flax/PP prepreg), which is evident from Figure 8.

Considering the Terzaghi's one-dimensional consolidation theory, and assuming incompressible fluid, a correlation between the volume of porosity fraction and thickness changes can be explained schematically by Figure 9. Due to the applied pressure ( $p$ ), the prepreg layers experienced the stress and the porous regions filled by the resin at higher thickness reduction reducing the volume of specimens at different consolidation stages (Nixon-Pearson et al., 2017). This effect is negligible for full consolidation specimen since the void content was below 0.7% from X-ray CT scans.

Therefore, decreasing the thickness from 5.8 mm to 4.3 mm results in a large reduction of the porosity volume fraction from 19.36% to 0.01% at constant pressure (Table 4).

The specific micro-mechanism of the porosity reduction at different consolidation stages includes coupled mechanism of stress equilibrium between porosity internal pressure and porosity compression by applied pressure and porosity filling with the resin flow. Surface tension between the porosities and resin works together with porosity internal pressure and the applied pressure, governing stress equilibrium and whether the porosities should collapse or grow. At the fibre tow scale, as the temperature during the hot press forming was constant, the contribution of resin viscosity which affects the rate of resin flow and critical time for the porosity reduction was not addressed in the current study.

Figure 10 shows extensive inter and intra-layer porosities for the primary consolidation. In the hot press forming process, air entrapment, dissolved and adsorbed moisture and volatiles such as plasticizer in the PP may cause the nucleation and growth of porosities during the forming processing (Figure 10). Consolidation at lower thicknesses tend to show both reduced porosity size and reduced amount of low fiber density areas. A complaint network of



fiber and viscous matrix exhibits various flow and deformation mechanisms depending on applied conditions. Moreover, inadequate resin impregnation into the fibre tows can cause additional porosities. For porosities inside the fiber tow regions, after applying the pressure, the laminate thickness is reduced, and the resin flows through the fibre tows to fill the porosities due to squeezing flow from resin rich zones to fill porous regions (Wang and Gutowski, 1991; Shuler and Advani, 1996; Simacek et al., 2013).

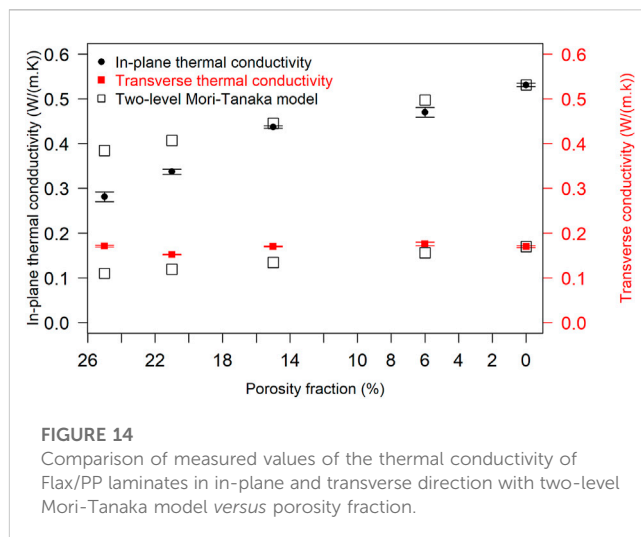
Porosities in Flax/PP composites can be due to the initial porosities in the Flax/PP commingled layers or can be caused due to the air entrapment between layers during laminations. The porosities can vary in size from 20 to 50 microns in the zones of poor impregnation. The initial porosities in the prepreg are generated during the manufacturing of the pre-consolidated unidirectional Flax/Polypropylene (PP) commingled tape (Figure 11).

Previous studies revealed that individual porosity characteristics, i.e., porosity content, diameter and aspect ratio are statically distributed in a volume of the consolidated thermoplastic laminate. Figure 12 shows the distribution of the void equivalent diameter at each consolidation stage. As an overall trend, the number of voids sharply skewed right as the porosity equivalent diameter increases, indicating a high small porosity content in the range of 20–100  $\mu\text{m}$  at the each of the consolidation stages. As the consolidation extended from stage 1–5, the maximum number of pores reduced 98%. The authors plan to publish the detailed determination of the statistics of porosity characteristics in Flax/PP laminate.

## 3.2 Thermal conductivity

### 3.2.1 Thermal conductivity of PP

The reported thermal conductivity values for the pure consolidated polypropylene (Table 5) can range between 0.1 and 0.3 W/(m.K) at 25°C. Because the thermal conductivity of a polymer, particularly consolidated PP, is a complex function of temperature,

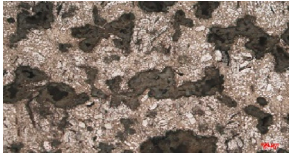

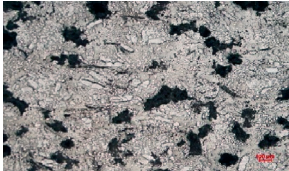
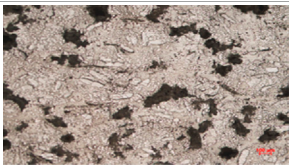



pressure, molecular weight distribution and chain structure (Patti and Acierno, 2020). For the current study, both in-plane and transverse thermal conductivity of the neat PP polymer plate were measured around 0.16 W/(m.K), which is well within the reported range. As the thermal conductivity has the same value in the principal directions, the neat PP was regarded as a homogeneous material.

### 3.2.2 Thermal conductivity of Flax/PP

The measured thermal conductivities of unidirectional Flax/PP composites in in-plane and transverse directions are plotted as a function of porosity fraction in Figure 13. As the porosity fraction decreases, the in-plane thermal conductivity increases. An increase of 70% occurs from in-plane conductivity equal to 0.28 [W/(m.K)] for the porosity fraction of 25% to 0.53 [W/(m.K)] for the porosity fraction of almost 0%. A decrease in porosity leads to a rise in the number of contact points as well as an increase in the volume of flax/PP fraction (with reference to Figures 6, 8) with much higher thermal conductivity than the thermal conductivity of the air gaps (inter and intra layer porosities) [0.026 W/(m.K)] (Liu et al., 2012) in the whole volume. From Figure 13, it is indicated that the in-plane thermal conductivity is dependent on the degree of Flax/PP fibre packing. At full consolidation stage containing approximately 0% porosity (Figures 10, 13), Flax/PP fibres are very densely packed and touch each other, leading to the highest thermal conductivity (Barasinski et al., 2011; Lévy et al., 2014). As stated in the literature, the transfer of heat in non-metals such as polymer composites can be explained by the flow of phonons or propagation of lattice vibrational energy (Slack, 1979; Ishida and Rimdusit, 1998). Consequently, the maximum packing of the flax fibre in the matrix is one way to maximise the formation of highly thermal conductive networks. Unlike in-plane conductivity, as the porosity fraction decreases the transverse thermal conductivity remains almost constant with an average thermal conductivity of 0.167 W/(m.K). Since Flax/PP commingled fibres consist of flax fibres that are radially arranged around the axis of PP fibres, the thermal path tends to be formed axially rather than transversely cross it. Moreover, as it is also obvious from Figure 13, the in-plane thermal conductivity values are much higher than the transverse

**TABLE 6 Morphology evolution and thermal conductivity at different the consolidation stages of flax/PP. As there is no change in transverse thermal conductivity, the results are not presented.**

Consolidation stage (%)	Morphology evolution	Porosity fraction (%)	Fiber volume fraction (%)	In-plane thermal conductivity (W/(m.K))	
				Experiment	Model
Primary consolidation		25	25	0.28	0.38
7		21	27	0.33	0.40
12		15	29	0.43	0.44
20		6	32	0.47	0.49
25		0	34	0.53	0.53

ones at the corresponding porosity fractions of Flax/PP laminates. Because thermal conductivity of pure flax fibres along their axis is 1.232 W/(k.m) while transversely to their main axis is 0.17 W/(k.m). These results are consistence with the thermal conductivity measurements for hemp (Behzad and Sain, 2007), flax (Li et al., 2008), bamboo (Takagi et al., 2007), and banana (Annie Paul et al., 2008) embedded into thermoplastic polymers. Therefore, since thermal resistance along the axis of Flax/PP fibre is less than the thermal resistance across the axis, the most portion of heat is transferred along the Flax/PP axis.

3.3 Model analysis of thermal conductivity

The two-level homogenization method proposed in (Naili et al., 2022) for elastic composites and extended to thermal and electrical conductivity in (Koutsawa et al., 2022) is used here to predict the

effective thermal conductivity of the three-phase (flax fibers, pores, and polypropylene matrix) NFRC. The two-level method is based on nested homogenization levels. At the deepest level, the real matrix material is homogenized with a first family of reinforcements. The effective material thus obtained plays the role of a fictitious matrix which is reinforced with another set of reinforcements to constitute an upper-level composite. This procedure is repeated until all reinforcements families have been taken in account. In this study, the Mori–Tanaka model (Mori and Tanaka, 1973) is used at a given level to homogenize the basic two-phase composite. The derivation of Mori–Tanaka’s model is based on an approximate use of Eshelby’s solution (Eshelby, 1957). It is assumed that each inclusion in the real representative volume element (RVE) behaves as if it were isolated in the real matrix. The body is infinite and subjected to the average matrix strains in the real RVE as the far field (remote) strain. The Mori–Tanaka model is very successful in predicting the effective properties of two-phase

composites. In theory, it is restricted to moderate volume fractions of inclusions (less than 25%) but in practice it can give good predictions well beyond this range. The two-level method can deliver excellent predictions when the right choice of the nested homogenization levels is made. It is shown that for reinforcements with different material properties, when going from the deepest level to the upper level, the inclusions should be added from the most compliant to the most rigid. More details on the model's equations can be found in (Koutsawa et al., 2022).

Reverse calculation based on the reference material is used to determine the model input parameters for the flax fibre. Thus, a flax fibre in-plane thermal conductivity of 1.232 W/(m.K) and a transverse thermal conductivity of 0.170 W/(m.K) were determined and used in the theoretical model. The theoretical values present a good agreement with experiments (Figure 14) for low and moderate porosity fractions ( $\leq 15\%$ ). The gap between the model and the experimental data for high porosity fractions ( $> 15\%$ ) can be explained by the simplifying assumptions used in the model regarding the pores' size, aspect ratio and spatial distribution. Indeed, for this first attempt, the pores are assumed to be spherical and randomly distributed in the microstructure. Therefore, extended experimental data will be required for a better description of the microstructure in the theoretical predictive model.

## 4 Conclusion

In this study, the link between the porosity fraction, morphology evolution and the thermal conductivity of flax fiber reinforced polypropylene composite was investigated. A hot plate forming process experiment allowed to manufacture several plates with different porosity contents depending on the consolidation stages. Subsequently, hot disk technique was applied to measure the thermal conductivity in in-plane and transverse directions. SEM and as micro-CT were used to analysis the cross sections of the laminates in terms of morphology and porosity fractions. Finally, a theoretical model, based on a two-level Mori-Tanaka homogenization method is proposed.

The results of the study as summarized in Table 6 suggested that.

- (1) Transverse thermal conductivity was much lower than in-plane thermal conductivity. This means that the most portion of heat is transferred axially along the Flax/PP fibre where each fibre is surrounded with the PP rather than transversely across it.
- (2) In-plane thermal conductivity almost linearly increased with the reduction of porosity fraction. However, the transverse thermal conductivity remained constant. The flax fibre compaction into the matrix is one way to increase the Flax/PP interfaces, improving thermal conductive networks.
- (3) Considering the three-phases material (porosity, fiber, and polymer matrix), the model results were in a good agreement with experiments, but limited predictivity for porosity fraction above 15%. The aspect ratio for this range of consolidation cannot be considered as spherical and the typical channel shape of porosity must be integrated in the theoretical model.
- (4) The morphology evolution should be included in the thermal simulation of composite laminate forming process. The future study aims at developing a simulation tool for the coupling of

the microstructure evolution and heat transfer in the hot press forming technique.

We will also address the effects of moisture content on the thermal conductivity of the fully consolidated Flax/PP composite in the future work.

## Data availability statement

The raw data supporting the conclusion of this article will be made available by the authors, without undue reservation.

## Author contributions

MB: Validation, Methodology, Formal analysis, Visualization, Investigation, Writing-original Draft, Review and Editing, DD: Data Curation, Formal analysis, Review and Editing, N-LS: Methodology, Investigation, ML: Methodology, Investigation, YK: Software, Numerical analysis, Review and Editing. BU: Material supply, material characterisation, HP: Conceptualization, Methodology, Supervision, Validation, Formal analysis, funding acquisition, Visualization, Investigation, Review and Editing.

## Funding

The Luxembourg National Research Fund (FNR) for funding Structural composite material, NATALINA under the research grant INTER/MERA/19/13991124 in frame of M-ERA.Net.

## Acknowledgments

The authors acknowledge the support from the Luxembourg National Research Fund (FNR) for funding Structural composite material, NATALINA under the research grant INTER/MERA/19/13991124 in frame of M-ERA.Net. The authors greatly appreciate Loïc Borghini and Sébastien Klein for their support in sample manufacturing and preparation, Régis Vaudemont and Benoit Marcolini for thermal analysis. The authors also gratefully thank the NATALINA's project partners BPREG and KAREL KALIP and their funding agency TUBITAK.

## Conflict of interest

Author BU was employed by BPREG.

The remaining authors declare that the research was conducted in the absence of any commercial or financial relationships that could be construed as a potential conflict of interest.

## Publisher's note

All claims expressed in this article are solely those of the authors and do not necessarily represent those of their affiliated



organizations, or those of the publisher, the editors and the reviewers. Any product that may be evaluated in this article, or

claim that may be made by its manufacturer, is not guaranteed or endorsed by the publisher.

## References

- Ageorges, C., Ye, L., and Hou, M. (2001). Advances in fusion bonding techniques for joining thermoplastic matrix composites: A review. *Compos Part A Appl. Sci. Manuf.* 32, 839–857. doi:10.1016/s1359-835x(00)00166-4
- Ageorges, C., and Ye, L. (2002). “State of the art in fusion bonding of polymer composites,” in *Fusion bonding of polymer composites* (London: Springer), 7–64. doi:10.1007/978-1-4471-0171-0\_2
- Annie Paul, S., Boudenne, A., Ibos, L., Candau, Y., Joseph, K., and Thomas, S. (2008). Effect of fiber loading and chemical treatments on thermophysical properties of banana fiber/polypropylene commingled composite materials. *Compos Part A Appl. Sci. Manuf.* 39 (9), 1582–1588. doi:10.1016/j.compositesa.2008.06.004
- Barasinski, A., Leygue, A., Soccarr, E., and Poitou, A. (2011). *In situ* consolidation for thermoplastic tape placement process is not obvious. *AIP Conf. Proc.* 1353, 948–953. doi:10.1063/1.3589638
- Behzad, T., and Sain, M. (2007). Measurement and prediction of thermal conductivity for hemp fiber reinforced composites. *Polym. Eng. Sci.* 47 (7), 977–983. doi:10.1002/pen.20632
- Bourmaud, A., le Duigou, A., Gourier, C., and Baley, C. (2016). Influence of processing temperature on mechanical performance of unidirectional polyamide 11-flax fibre composites. *Ind. Crops Prod.* 84, 151–165. doi:10.1016/j.indcrop.2016.02.007
- BPREG (2022). Technical sheet. Available at: [www.bpreg.com](http://www.bpreg.com).
- Chen, L., Xu, H. F., He, S. J., Du, Y. H., Yu, N. J., Du, X. Z., et al. (2017). Thermal conductivity performance of polypropylene composites filled with polydopamine-functionalized hexagonal boron nitride. *PLoS One* 12 (1), e0170523. doi:10.1371/journal.pone.0170523
- Derbali, I., Terekhina, S., Guillaumat, L., and Ouagne, P. (2018). Rapid manufacturing of woven comingled flax/polypropylene composite structures. *Int. J. Material Form.* 12 (6), 927–942. doi:10.1007/s12289-018-01464-1
- Donough, M. J., Shafaqst John, N. A., Philips, A. W., and Gangadhara Prusty, B. (2022). Process modelling of *in-situ* consolidated thermoplastic composite by automated fibre placement – a review. *Compos. Part A Appl. Sci. Manuf.* 163, 107179. doi:10.1016/j.compositesa.2022.107179
- Dumont, P. J. J., Orgéas, L., Hubert, M., Vermeulen, B., Vroman, P., Rolland du Roscoat, S., et al. (2010). “Compression moulding of flax fibre reinforced composite materials,” in The 10th International Conference on Flow Processes in Composite Materials (FPCM10), Monte Verità, Ascona, CH, July 11–15, 2010.
- Dumont, P., Orgéas, L., Martoia, F., Budtova, T., and Vincent, M. (2017). “Mise en œuvre des composites à fibres lignocellulosiques,” in *Composites polymères et fibres lignocellulosiques Propriétés, transformation et caractérisation*, Vol. 5, 159–211.
- EN ISO 22007-2:2015 (2015). *Plastics-Determination of thermal conductivity and thermal diffusivity*.
- Eshelby, J. D. (1957). The determination of the elastic field of an ellipsoidal inclusion, and related problems. *Proc. R. Soc. Lond A Math. Phys. Sci.* 241 (1226), 376–396. doi:10.1098/rspa.1957.0133
- Fu, S. Y., and Mai, Y. W. (2003). Thermal conductivity of misaligned short-fiber-reinforced polymer composites. *J. Appl. Polym. Sci.* 88 (6), 1497–1505. doi:10.1002/app.11864
- Fu, X., Wu, X., Huang, G., Li, W., Kang, S., Wang, L., et al. (2022). Fusion bonding possibility for incompatible polymers by the novel ultrasonic welding technology: Effect of interfacial compatibilization. *ACS Omega* 7 (17), 14797–14806. doi:10.1021/acsomega.2c00255
- Fujihara, K., Huang, Z.-M., Ramakrishna, S., and Hamada, H. (2004). Influence of processing conditions on bending property of continuous carbon fiber reinforced PEEK composites. *Compos Sci. Technol.* 64 (16), 2525–2534. doi:10.1016/j.compscitech.2004.05.014
- Gassan, J., and Bledzki, A. K. (2001). Thermal degradation of flax and jute fibers. *J. Appl. Polym. Sci.* 82 (6), 1417–1422. doi:10.1002/app.1979
- Guzman-Maldonado, E., Hamila, N., Naouar, N., Moulin, G., and Boisse, P. (2016). Simulation of thermoplastic prepreg thermoforming based on a visco-hyperelastic model and a thermal homogenization. *Mater. Des.* 93, 431–442. doi:10.1016/j.matdes.2015.12.166
- Han, S., and Chung, D. D. L. (2011). Increasing the through-thickness thermal conductivity of carbon fiber polymer–matrix composite by curing pressure increase and filler incorporation. *Compos Sci. Technol.* 71 (16), 1944–1952. doi:10.1016/j.compscitech.2011.09.011
- Han, Z., and Fina, A. (2011), 36. Oxford, 914–944. doi:10.1016/j.progpolymsci.2010.11.004 Thermal conductivity of carbon nanotubes and their polymer nanocomposites: A review. *Prog. Polym. Sci.* 7
- Hernández, S., Sket, F., González, C., and Llorca, J. (2013). Optimization of curing cycle in carbon fiber-reinforced laminates: Void distribution and mechanical properties. *Compos Sci. Technol.* 85, 73–82. doi:10.1016/j.compscitech.2013.06.005
- il Lee, W., and Springer, G. S. (1987). A model of the manufacturing process of thermoplastic matrix composites. *J. Compos Mater* 21 (11), 1017–1055. doi:10.1177/002199838702101103
- Ishida, H., and Rimdusit, S. (1998). Very high thermal conductivity obtained by boron nitride-filled polybenzoxazine. *Thermochimica* 320, 177–186. doi:10.1016/s0040-6031(98)00463-8
- Jensen, S., Samanta, S., Chakrabarti-Bell, S., Regenauer-Lieb, K., Siddique, K. H. M., and Wang, S. (2014). Automated thresholding and analysis of microCT scanned bread dough. *J. Microsc.* 256 (2), 100–110. doi:10.1111/jmi.12163
- Khan, M. A., Mitschang, P., and Schledjewski, R. (2010). Identification of some optimal parameters to achieve higher laminate quality through tape placement process. *Adv. Polym. Technol.* 29 (2), 98–111. doi:10.1002/adv.20177
- Kim, S. W., Lee, S. H., Kang, J. S., and Kang, K. H. (2006). Thermal conductivity of thermoplastics reinforced with natural fibers. *Int. J. Thermophys.* 27 (6), 1873–1881. doi:10.1007/s10765-006-0128-0
- Koutsawa, Y., Rauchs, G., Fiorelli, D., Makradi, A., and Belouettar, S. (2022). A multi-scale model for the effective electro-mechanical properties of short fiber reinforced additively manufactured ceramic matrix composites containing carbon nanotubes. *Compos. Part C. Open Access* 7, 100234. doi:10.1016/j.jcomc.2022.100234
- Krause, B., and Pötschke, P. (2016). Electrical and thermal conductivity of polypropylene filled with combinations of carbon fillers. *AIP Conf. Proc.* 1779. doi:10.1063/1.4965494
- Krause, B., Rzeczkowski, P., and Pötschke, P. (2019). Thermal conductivity and electrical resistivity of melt-mixed polypropylene composites containing mixtures of carbon-based fillers. *Polym. (Basel)* 11, 1073–1076. doi:10.3390/POLYM11061073
- Lamèthe, J. F., Beauchêne, P., and Léger, L. (2005). Polymer dynamics applied to PEEK matrix composite welding. *Aerosp. Sci. Technol.* 9 (3), 233–240. doi:10.1016/j.ast.2005.01.008
- Latil, P., Orgéas, L., Geindreau, C., Dumont, P. J. J., and Rolland du Roscoat, S. (2011). Towards the 3D *in situ* characterisation of deformation micro-mechanisms within a compressed bundle of fibres. *Compos Sci. Technol.* 71 (4), 480–488. doi:10.1016/j.compscitech.2010.12.023
- Lévy, A., Heider, D., Tierney, J., Gillespie, J., and Levy, A. (2014). Inter-layer thermal contact resistance evolution with the degree of intimate contact in the processing of thermoplastic composite laminates. *Compos. Mater.* 48 (4), 491–503. doi:10.1177/0021998313476318
- Li, X., Tabil, L. G., Oguocha, I. N., and Panigrahi, S. (2008). Thermal diffusivity, thermal conductivity, and specific heat of flax fiber–HDPE biocomposites at processing temperatures. *Compos Sci. Technol.* 68 (7–8), 1753–1758. doi:10.1016/j.compscitech.2008.02.016
- Li, Y., Chi, Y., Han, S., Zhao, C., and Miao, Y. (2021). Pore-throat structure characterization of carbon fiber reinforced resin matrix composites: Employing Micro-CT and Avizo technique. *PLoS One* 16 (9), e0257640. doi:10.1371/journal.pone.0257640
- Liu, K., Takagi, H., Osugi, R., and Yang, Z. (2012). Effect of physicochemical structure of natural fiber on transverse thermal conductivity of unidirectional abaca/bamboo fiber composites. *Compos Part A Appl. Sci. Manuf.* 43 (8), 1234–1241. doi:10.1016/j.compositesa.2012.02.020
- Liu, K., Zhang, X., Takagi, H., Yang, Z., and Wang, D. (2014). Effect of chemical treatments on transverse thermal conductivity of unidirectional abaca fiber/epoxy composite. *Compos Part A Appl. Sci. Manuf.* 66, 227–236. doi:10.1016/j.compositesa.2014.07.018
- Lu, J., Kan, A., Zhu, W., and Yuan, Y. (2021). Numerical investigation on effective thermal conductivity of fibrous porous medium under vacuum using Lattice-Boltzmann method. *Int. J. Therm. Sci.* 160, 106682. doi:10.1016/j.ijthermalsci.2020.106682
- Lukasiewicz, D. H. J. A., Ward, C., and Potter, K. D. (2012). The engineering aspects of automated prepreg layup: History, present and future. *Compos B Eng.* 43 (3), 997–1009. doi:10.1016/j.compositesb.2011.12.003
- Machado, J. M., Tavares, J. M. R. S., Camanho, P. P., and Correia, N. (2022). Automatic void content assessment of composite laminates using a machine-learning approach. *Compos Struct.* 288, 115383. doi:10.1016/j.compstruct.2022.115383
- Madsen, B., Thygesen, A., and Lilholt, H. (2007). Plant fibre composites - porosity and volumetric interaction. *Compos Sci. Technol.* 67 (7–8), 1584–1600. doi:10.1016/j.compscitech.2006.07.009

- Mangal, R., Saxena, N. S., Joshi, G. P., and Thomas, S. (2003). Measurement of effective thermal conductivity and thermal diffusivity for assessing the integrity of fiber to matrix bond in natural fiber composite. *Indian J. Pure Appl. Phys.* 41 (9), 712–718.
- Mantell, S. C., and Springer, G. S. (1992). Manufacturing process models for thermoplastic composites. *J. Compos. Mater.* 26 (16), 2348–2377. doi:10.1177/002199839202601602
- Mehdikhani, M., Gorbatiikh, L., Verpoest, I., and v Lomov, S. (2019). Voids in fiber-reinforced polymer composites: A review on their formation, characteristics, and effects on mechanical performance. *J. Compos. Mater.* 53 (12), 1579–1669. doi:10.1177/0021998318772152
- Mishra, R., Wiener, J., Militky, J., Petru, M., Tomkova, B., and Novotna, J. (2020). Bio-composites reinforced with natural fibers: Comparative analysis of thermal, static and dynamic-mechanical properties. *Fibers Polym.* 21 (3), 619–627. doi:10.1007/s12221-020-9804-0
- Mori, T., and Tanaka, K. (1973). Average stress in matrix and average elastic energy of materials with misfitting inclusions. *Acta Metall.* 21 (5), 571–574. doi:10.1016/0001-6160(73)90064-3
- Mounika, M., Ramaniah, K., Ratna Prasad, A. V., Rao, K. M., Hema, K., and Reddy, C. (2012). Thermal conductivity characterization of bamboo fiber reinforced polyester composite. *J. Mater. Environ. Sci.* 3 (6), 1109–1116.
- Muratov, D. S., Vanyushin, V. O., Luchnikov, L. O., Degtyaryov, M. Y., Kolesnikov, E. A., Stepashkin, A. A., et al. (2021). Improved thermal conductivity of polypropylene filled with exfoliated hexagonal boron nitride (hBN) particles. *Mater Res. Express* 8 (3), 035010. doi:10.1088/2053-1591/abed0f
- Naili, C., Doghri, I., and Demey, J. (2022). Porous materials reinforced with short fibers: Unbiased full-field assessment of several homogenization strategies in elasticity. *Mech. Adv. Mater. Struct.* 29 (20), 2857–2872. doi:10.1080/15376494.2021.1880674
- Nixon-Pearson, O. J., Belnoue, J. P. H., Ivanov, D. S., Potter, K. D., and Hallett, S. R. (2017). An experimental investigation of the consolidation behaviour of uncured prepreps under processing conditions. *J. Compos. Mater.* 51 (13), 1911–1924. doi:10.1177/0021998316665681
- Ouagne, P., Bizet, L., Baley, C., and Bréard, J. (2010). Analysis of the film-stacking processing parameters for PLLA/flax fiber biocomposites. *J. Compos. Mater.* 44 (10), 1201–1215. doi:10.1177/0021998309349019
- Patti, A., and Acierio, D. (2020). “Thermal conductivity of polypropylene-based materials,” in *Polypropylene - polymerization and characterization of mechanical and thermal properties* (London, UK: IntechOpen). doi:10.5772/intechopen.84477
- RX Solutions (2022). *RX ACT software*. Chennai, TN: RX solutions.
- Saenz-Castillo, D., Martín, M. I., Calvo, S., Rodríguez-Lence, F., and Güemes, A. (2019). Effect of processing parameters and void content on mechanical properties and NDI of thermoplastic composites. *Compos Part A Appl. Sci. Manuf.* 121, 308–320. doi:10.1016/j.compositesa.2019.03.035
- Sankur, B. (2004). Survey over image thresholding techniques and quantitative performance evaluation. *J. Electron Imaging* 13 (1), 146. doi:10.1117/1.1631315
- Shuler, S. F., and Advani, S. G. (1996). Transverse squeeze flow of concentrated aligned fibers in viscous fluids. *J. Newt. Fluid Mech.* 65, 47. doi:10.1016/0377-0257(96)01440-1
- Simacek, P., Advani, S. G., Gruber, M., and Jensen, B. (2013). A non-local void filling model to describe its dynamics during processing thermoplastic composites. *Compos Part A Appl. Sci. Manuf.* 46, 154–165. doi:10.1016/j.compositesa.2012.10.015
- Slack, G. A. (1979). The thermal conductivity of nonmetallic crystals. *Solid State Phys.* 34, 1–71. doi:10.1016/S0081-1947(08)60359-8
- Takagi, H., Kako, S., Kusano, K., and Ousaka, A. (2007). Thermal conductivity of PLA-bamboo fiber composites. *Adv. Compos. Mater. Official J. Jpn. Soc. Compos. Mater.* 16 (4), 377–384. doi:10.1163/156855107782325186
- Terzaghi, K. (1943). *Theoretical soil mechanics*. Hoboken, NJ, USA: John Wiley & Sons. doi:10.1002/9780470172766
- Thilagavathi, G., Pradeep, E., Kannaian, T., and Sasikala, L. (2010). Development of natural fiber nonwovens for application as car interiors for noise control. *J. Industrial Text.* 39 (3), 267–278. doi:10.1177/1528083709347124
- Tierney, J., and Gillespie, J. W. (2006). Modeling of *in situ* strength development for the thermoplastic composite tow placement process. *J. Compos. Mater.* 40 (16), 1487–1506. doi:10.1177/0021998306060162
- van de Velde, K., and Baetens, E. (2001). Thermal and mechanical properties of flax fibres as potential composite reinforcement. *Macromol. Mater. Eng.* 286 (6), 342–349. doi:10.1002/1439-2054(20010601)286:6<342::AID-MAME342>3.0.CO;2-P
- van Hoa, S., Duc Hoang, M., and Simpson, J. (2017). Manufacturing procedure to make flat thermoplastic composite laminates by automated fibre placement and their mechanical properties. *J. Thermoplast. Compos. Mater.* 30 (12), 1693–1712. doi:10.1177/0892705716662516
- van Rijswijk, K., and Bersee, H. E. N. (2007). Reactive processing of textile fiber-reinforced thermoplastic composites - an overview. *Compos. Part A Appl. Sci. Manuf.* 38 (3), 666–681. doi:10.1016/j.compositesa.2006.05.007
- Wang, C., Zuo, Q., Lin, T., Anuar, N. I. S., Mohd Salleh, K., Gan, S., et al. (2020). Predicting thermal conductivity and mechanical property of bamboo fibers/polypropylene nonwovens reinforced composites based on regression analysis. *Int. Commun. Heat Mass Transf.* 118, 104895. doi:10.1016/j.icheatmasstransfer.2020.104895
- Wang, E. L., and Gutowski, T. G. (1991). Laps and gaps in thermoplastic composites processing. *Compos. Manuf.* 2, 69–78. doi:10.1016/0956-7143(91)90182-G
- Weidenfeller, B., Höfer, M., and Schilling, F. R. (2004). Thermal conductivity, thermal diffusivity, and specific heat capacity of particle filled polypropylene. *Compos Part A Appl. Sci. Manuf.* 35 (4), 423–429. doi:10.1016/j.compositesa.2003.11.005
- Yang, F., and Pitchumani, R. (2001). A fractal Cantor set based description of interlaminar contact evolution during thermoplastic composites processing. *J. Mater. Sci.* 36 (19), 4661–4671. doi:10.1023/A:1017950215945
- Yousefpour, A., Hojjati, M., and Immarigeon, J. P. (2004). Fusion bonding/welding of thermoplastic composites. *J. Thermoplast. Compos. Mater.* 17 (4), 303–341. doi:10.1177/0892705704045187
- Zhang, D., Heider, D., and Gillespie, J. W. (2017). Determination of void statistics and statistical representative volume elements in carbon fiber-reinforced thermoplastic prepreps. *J. Thermoplast. Compos. Mater.* 30 (8), 1103–1119. doi:10.1177/0892705715618002
- Zheng, G. Y. (2014). Numerical investigation of characteristic of anisotropic thermal conductivity of natural fiber bundle with numbered lumens. *Math. Probl. Eng.* 2014, 1–8. doi:10.1155/2014/506818



## OPEN ACCESS

## EDITED BY

Veronique Michaud,  
Swiss Federal Institute of Technology  
Lausanne, Switzerland

## REVIEWED BY

Bodo Fiedler,  
Hamburg University of Technology,  
Germany  
Andrey Aniskevich,  
University of Latvia, Latvia

## \*CORRESPONDENCE

Behnam Ashrafi,  
✉ Behnam.Ashrafi@cnrc-nrc.gc.ca  
Mostafa Yourdkhani,  
✉ yourd@colostate.edu

## SPECIALTY SECTION

This article was submitted to  
Polymeric and Composite Materials,  
a section of the journal  
Frontiers in Materials

RECEIVED 15 February 2023

ACCEPTED 06 March 2023

PUBLISHED 23 March 2023

## CITATION

Naseri I, Ashrafi B, Jakubinek M,  
Martinez-Rubi Y and Yourdkhani M  
(2023), Rapid and facile preparation of  
nanocomposite film heaters for  
composite manufacturing.  
*Front. Mater.* 10:1166986.  
doi: 10.3389/fmats.2023.1166986

## COPYRIGHT

© 2023 Naseri, Ashrafi, Jakubinek,  
Martinez-Rubi and Yourdkhani. This is an  
open-access article distributed under the  
terms of the [Creative Commons  
Attribution License \(CC BY\)](#). The use,  
distribution or reproduction in other  
forums is permitted, provided the original  
author(s) and the copyright owner(s) are  
credited and that the original publication  
in this journal is cited, in accordance with  
accepted academic practice. No use,  
distribution or reproduction is permitted  
which does not comply with these terms.

# Rapid and facile preparation of nanocomposite film heaters for composite manufacturing

Iman Naseri<sup>1</sup>, Behnam Ashrafi<sup>2\*</sup>, Michael Jakubinek<sup>3</sup>,  
Yadienka Martinez-Rubi<sup>3</sup> and Mostafa Yourdkhani<sup>1,4\*</sup>

<sup>1</sup>Department of Mechanical Engineering, Colorado State University, Fort Collins, CO, United States,  
<sup>2</sup>Aerospace Research Centre, National Research Council Canada, Montreal, QC, Canada, <sup>3</sup>Security and  
Disruptive Technologies Research Centre, Emerging Technologies Division, National Research Council  
Canada, Ottawa, ON, Canada, <sup>4</sup>School of Advanced Materials Discovery, Colorado State University, Fort  
Collins, CO, United States

Nanocomposite film heaters are promising for out-of-oven (OoO) and energy-efficient curing of fiber-reinforced polymer composites. However, the current techniques for manufacturing nanocomposite film heaters are intensive in terms of time and energy and require expensive resources. In this work, we present a facile and rapid approach for preparation of nanocomposite film heaters with excellent heat generation properties based on a frontally polymerizable resin system. This approach enables rapid fabrication of nanocomposite films within a few minutes and without the need for using expensive equipment, making it suitable for mass production of nanocomposite film heaters. Various characterization techniques are used to determine the morphology, composition, and mechanical properties of nanocomposite films. The electrothermal performance of nanocomposite film heaters are then evaluated under various conditions. Nanostructured heaters exhibit excellent Joule heating properties, where temperatures as high as  $\sim 132^{\circ}\text{C}$  can be reached within only 2 min using a low input power density of  $\sim 2\text{ W cm}^{-2}$ . Finally, a nanocomposite film heater is used for OoO curing of a small composite panel with minimal energy consumption. Using this approach, 0.1 MJ of energy is consumed during the 4-h cure cycle of a commercial prepreg system, which would otherwise require at least 40.5 MJ of energy to cure using a convection oven.

## KEYWORDS

out-of-oven curing, frontal polymerization, dicyclopentadiene, Joule heating, fiber-reinforced composites, energy-efficient, rapid manufacturing

## 1 Introduction

Fiber-reinforced polymer composites (FRPCs) exhibit excellent specific mechanical properties, chemical stability, and fatigue resistance, making them an ideal material for designing lightweight and durable structures in a variety of industries including aerospace, wind energy, defense, construction, and marine (Zhang et al., 2021; Chen et al., 2023). However, the widespread use of FRPCs in various applications is limited by their underlying challenging manufacturing processes. The traditional technology for manufacture of polymer composites involves elevated-temperature curing of the matrix thermoset resin for several hours (up to 24 h) in an autoclave or oven (Schlimbach and Ogale, 2012; Lee et al., 2018). This process is highly intensive in terms of time, energy, carbon footprint, and

resources. In addition, the production rate and size of components are limited by the internal dimensions and availability of ovens and autoclaves.

Composite layups are typically heated in an autoclave or oven *via* convection, which is highly inefficient in terms of energy consumption, as a significant amount of energy is required to heat up a large volume of gas inside the equipment (Liu et al., 2020). Developing alternative heating methods that enable fast and efficient heating of a composite layup has been the focus of extensive research over the past decade. One of the alternative heating approaches is using electromagnetic waves (e.g., infrared, microwave, and ultraviolet) for supplying the energy required for composite curing. Although each of these radiation curing methods offers distinct advantages, they are challenging to use at an industrial scale due to their specific limitations. For example, the high cost of microwave ovens, use of special tooling materials, and microwave shielding effect of carbon fibers are key issues that limit the widespread adoption of microwave heating technique for composite processing (Nuhiji et al., 2019; Galos, 2021). Direct conductive heating is a promising heating method, which can substantially reduce the energy demand of curing process while eliminating the need for expensive autoclaves or ovens (Yue et al., 2022). In this curing approach, heat is directly supplied to the composite layup *via* conduction, either from a heated mold or direct resistive heating of a conductive material (Tu et al., 2022). The latter approach is advantageous as the acquisition and maintenance of heated tools are costly. In direct resistive heating approach, the heat required for curing of the matrix thermoset resin is supplied by passing electric current through a conductor, in which the electric energy is converted into heat *via* Joule's effect (Silva et al., 2017; Moreira et al., 2021). A wide range of conductive materials including carbon fiber, metal meshes, and nanocomposite films have been used as a resistive element for direct heating of composite layups (Yao et al., 2019; Chen et al., 2020; Karalis et al., 2021). Nanocomposite films in particular show a great promise for curing polymer composites in part because of their excellent electrothermal conversion efficiency, low thermal mass, and deformability (Bobinger et al., 2019; Xu et al., 2021). Additionally, nanocomposite films can be integrated into a composite layup and remain advantageous in service conditions by imparting new functionalities (e.g., de-icing, damage sensing) to the host composite structure (Tarfaoui et al., 2019; Groo et al., 2020; Naseri et al., 2022).

Adoption of direct conductive curing technique using nanocomposite film heaters requires developing new approaches for scalable, rapid, and inexpensive preparation of nanocomposite films with excellent electrothermal properties. There are two main approaches for preparation of nanocomposite film heaters. In the more traditional approach, conductive nanoparticles (e.g., carbon nanotubes, graphene) are added to the polymer matrix of composites *via* solvent-based or direct mechanical mixing techniques to enhance the electrical conductivity of the matrix polymer for heat generation *via* Joule's effect. While these approaches are useful for bulk preparation of polymer nanocomposites, they suffer from the challenging processing steps, safety hazards, and limited amount of nanoparticles that can be added to polymers (Chakraborty et al., 2011; Wan Dalina et al., 2019). For example, in preparation of carbon nanotube-

modified polymers, often less than 1 wt.% of nanotubes can be added to polymers, as increasing the nanotube content substantially increases the resin viscosity and makes the processing conditions quite challenging (Ma et al., 2010). Additionally, it is extremely difficult to evenly disperse all nanotubes, resulting in agglomeration of nanoparticles in the polymer matrix and degradation of the mechanical properties of produced nanocomposites compared to the pristine polymer (Isaza M et al., 2018; Zeinedini et al., 2018; Xia et al., 2020). An alternative approach for preparation of polymer nanocomposite heaters with a high content of nanoparticles is creation of papers of nanoparticles followed by impregnation of the produced nanostructured papers by the polymer resin (Khan et al., 2015). Buckypaper, which is a macroscopic assembly of carbon nanotubes, is one of such papers that has been produced at large scales and allows for creating polymer nanocomposites with a high concentration of nanoparticles (up to 30 vol.%) while enabling easier and safer handling of nanoparticles compared to bulk processing methods (Lopes et al., 2010). The high concentration of nanotubes in buckypaper results in a high electrical conductivity in produced nanocomposites, which is crucial for obtaining the desired electrothermal performance *via* Joule heating effect; therefore, produced heaters deliver superior electrothermal properties compared to nanocomposite heaters produced using bulk mixing approaches. The preparation process of nanocomposite films typically involves infiltration of the nanoparticle network with a thermosetting resin (e.g., epoxy) under vacuum and often at elevated temperatures to reduce the resin viscosity and facilitate the impregnation of the highly dense, porous network of nanotubes (Ribeiro et al., 2017). Following the infiltration step, the material is cured in an oven according to the cure cycle of the thermosetting resin, which can typically take several hours to obtain a fully crosslinked polymer network. These processing steps make the manufacturing process of nanocomposite heaters slow and arduous.

Recently, frontal polymerization (FP) has emerged as an energy-efficient and rapid approach for curing of thermoset resins and their composites (Robertson et al., 2018; Pojman, 2022; Suslick et al., 2022; Ziaee et al., 2022). In FP, a monomer solution containing a latent catalyst is heated locally to activate the latent catalyst and initiate an exothermic polymerization reaction. The released heat is used to activate more catalyst and polymerize more resin. As a result, a self-propagating reaction wave is formed that propagates through the monomer solution until all available monomers are converted to polymer (Pojman, 2012; Ziaee and Yourdkhani, 2021; Naseri and Yourdkhani, 2022). FP has been demonstrated for a wide range of resin systems including cyclic olefins, epoxies, and acrylates (Mariani et al., 2008; Klikovits et al., 2017; Dean et al., 2020). Dicyclopentadiene (DCPD), a member of the cyclic olefin family, is one of the FP resin systems, which is of great interest due to its excellent front properties, long and tunable pot life, very low viscosity of  $\sim 1.5 \times 10^{-3}$  Pa s, and excellent thermo-mechanical properties of resulting polydicyclopentadiene (pDCPD) polymer (Rui et al., 2014; Robertson et al., 2017; Centellas et al., 2022).

The aim of this study is to introduce a facile approach for rapid and energy-efficient fabrication of thermoset-based nanocomposite film heaters at room temperature without using any vacuum conditions or ovens. To achieve this goal, we use a low-viscosity resin ( $\eta \sim 1.5 \times 10^{-3}$  Pa s) based on dicyclopentadiene (DCPD) that can readily impregnate buckypaper networks at room temperature



and ambient pressure. Following the rapid impregnation, the DCPD-based resin is cured *via* through-thickness frontal polymerization. In this work, we first evaluate the quality of the produced nanocomposite films by characterizing their composition, morphology, and mechanical properties using various techniques including scanning electron microscopy, thermogravimetric analysis, and tensile testing. Then, electrodes are connected to the opposite sides of the nanocomposite films to create film heaters and determine the electrothermal performance of resulting heaters in response to various static and dynamic electrical loading conditions. Upon characterization of the electrothermal performance of film heaters, they are used to demonstrate direct conductive heating and curing of a composite panel using a commercial prepreg system.

## 2 Experimental

### 2.1 Materials

Dicyclopentadiene (DCPD), 5-ethylidene-2-norbornene (ENB), second-generation Grubbs' catalyst (GC2), and phenylcyclohexane (PCH) were purchased from Sigma Aldrich. DCPD is solid at room temperature; therefore a 95:5 wt.% solution of DCPD:ENB was prepared to depress the melting point of the resin solution. The DCPD/ENB solution will be referred to as DCPD resin hereafter in this article. Tributyl phosphite (TBP) was obtained from TCI America. PCH is used to facilitate the dissolution of the GC2 catalyst in the resin solution, whereas TPB is used as an inhibitor to control the reactivity and pot life of the resin system. In a typical experiment, 3.21 mg of GC2 was measured and dissolved in 1 mL of PCH. An appropriate amount of TBP (1 M equivalent with respect to GC2) was added to the GC2/PCH solution *via* a volumetric syringe. This solution was then added to 5 mL of DCPD and thoroughly mixed. Buckypaper with an average thickness of 60  $\mu\text{m}$  was prepared in-house using multiwalled carbon nanotubes (Nanocyl NC7000) and based on the vacuum filtration technique following the procedure described in our previous work (Ashrafi et al., 2017). A silver-filled conductive paste (ConductiveX) was used for attaching copper electrodes to buckypaper films. A unidirectional carbon fiber prepreg (AX-6201XL, Axiom) was used for fabrication of composite panels.

### 2.2 Preparation and characterization of nanocomposite films

Differential scanning calorimetry (DSC) measurements were carried out on uncured DCPD resin as well as pDCPD films cured at various temperatures to determine an appropriate cure cycle for preparation of nanocomposites. For measurement of the total heat of reaction of the uncured resin, ~3 mg of resin was transferred into an aluminum hermetic DSC pan and sealed. DSC measurements were performed from 25°C to 250°C at a heating rate of 5°C min<sup>-1</sup>. The residual heat of reaction of cured pDCPD films was similarly measured by transferring 5 mg of cured resin into a DSC pan, followed by heating from 25°C to 250°C at a heating rate of 5°C min<sup>-1</sup>. Degree of cure was

calculated as  $\alpha = 1 - H_r/H_t$ , where  $\alpha$  is the degree of cure and  $H_t$  and  $H_r$  are the total heat of reaction of the liquid resin and the residual heat of reaction of the cured films, respectively. A Discovery HR-2 Rheometer (TA Instrument) with a 40 mm flat geometry and a gap of 500  $\mu\text{m}$  was used to determine the rheological properties of the DCPD resin containing 1 M equivalent of inhibitor with respect to Grubbs' catalyst. Time-sweep measurements were performed at 23°C with a frequency of 1 Hz. The wettability of pristine buckypaper by the DCPD resin was characterized by measuring the static contact angle at room temperature using a goniometer (Rame-Hart Instrument). A droplet of the DCPD resin was placed on the surface of a buckypaper specimen, and the contact angle was immediately measured. Five measurements were carried out and the average value is reported.

Nanocomposite films were prepared by droplet casting of resin onto the surface of buckypaper (Figure 1). Upon dropping a few droplets of resin, the resin was observed to quickly saturate the nanotube network, after which the excess resin was removed using a lint-free wipe. Through-thickness frontal polymerization was initiated by heating the DCPD-impregnated buckypaper using a laboratory-scale hot plate at ~140°C. Since the thickness of the film is low (~100–200  $\mu\text{m}$ ), the propagation of the FP reaction through the thickness of the film was not noticeable and the overall cure process, from initiation to full cure, was completed within a few minutes. In other words, the resin was used here as a cure-on-demand resin system rather than as a self-propagating FP resin system. Thermogravimetric analysis (TGA) was used to determine the resin and nanotube contents in the nanocomposite films, according to the procedure reported in our previous work (Ashrafi et al., 2010). Calculation of resin or nanotube content requires performing TGA experiments on neat polymer, pristine buckypaper, and nanocomposite film. TGA measurements were carried out from 25°C to 600°C at a heating rate of 10°C min<sup>-1</sup> under nitrogen environment. A 30-min hold was also added to the temperature profile at 470°C to obtain an accurate weight measurement of the residue from each specimen at this processing temperature. Two measurements were performed on each material. The resin content in the nanocomposite is calculated as (Ashrafi et al., 2010),

$$w_R = \frac{(m_F - m_C + w_I(1 - m_F))}{(m_F - m_R)} \quad (1)$$

$$1 = w_R + w_F + w_I \quad (2)$$

$w_R$  and  $w_F$  are weight fraction of resin and carbon nanotube in the nanocomposite film,  $m_R$ ,  $m_F$ , and  $m_C$  are residual mass of neat resin, pristine buckypaper, and nanocomposite film measured at 470°C, respectively. The concentration of solid (i.e., metal) impurities in pristine buckypaper ( $w_I$ ) was determined by performing an additional TGA measurement on pristine buckypaper specimens from 25°C to 1,000°C at a heating rate of 10°C min<sup>-1</sup> under air environment. The impurity content of the pristine buckypaper was calculated to be 9.5%. Scanning electron microscopy (SEM) was performed using a JEOL JSM-5800 field emission scanning electron microscope to observe the morphology of buckypaper films after impregnation. The cross-section of the nanocomposite film was sputter-coated with a 10 nm thick layer of gold and imaged at an accelerating voltage of 15 kV. Tensile tests were performed on

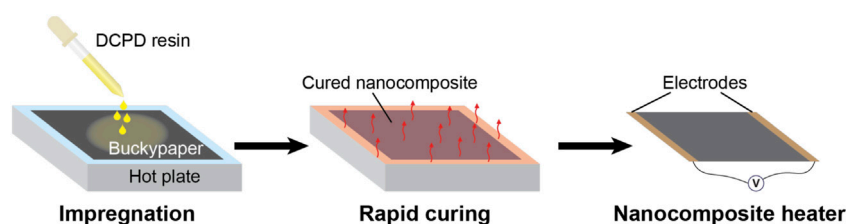


FIGURE 1

Schematic representation of the fabrication process of the nanocomposite film heater. A sample of buckypaper is first impregnated by the DCPD resin using droplet casting approach, followed by rapid curing via frontal polymerization. Nanocomposite film heaters are then prepared by connecting two copper electrodes to the two opposite sides of the produced films.

rectangular specimens ( $2 \times 30 \text{ mm}^2$ ) to determine the mechanical properties of pristine buckypaper and nanocomposite films. All tests were performed at a displacement rate of  $1 \text{ mm min}^{-1}$ . Electrothermal performance of nanocomposite films were characterized using specimens with an effective heating area of  $10 \times 20 \text{ mm}^2$ . Copper electrodes were attached to both ends of the nanocomposite films using a silver-filled conductive paste. A vacuum pressure of  $81.3 \text{ kPa}$  was applied to the heaters by vacuum-bagging them on a glass substrate to simulate boundary conditions that heaters undergo during the composite manufacturing process. Various voltages were supplied to the heater films using a direct current (DC) power supply (9206, B&K Precision). The voltage and current data during electrothermal tests were recorded to determine the power consumption. The temperature at the center of the heater was measured using a K-type thermocouple and recorded by a LabView program.

## 2.3 Composite fabrication

For fabrication of composite panels, a nanocomposite heater with an effective heating area of  $30 \times 30 \text{ mm}^2$  was used. Eight plies of a unidirectional prepreg ( $40 \times 30 \text{ mm}^2$ ) were cured using the nanocomposite heater placed on top of the layup and separated from prepreg plies using a release film. The input power to the heater was gradually increased to  $\sim 8.9 \text{ W}$  within 45 min to increase the temperature of the heater to  $82^\circ\text{C}$  at a heating rate of  $1.3^\circ\text{C min}^{-1}$  and then the input power was held unchanged for 3 h to simulate the cure cycle recommended by the prepreg manufacturer (3 h at  $82^\circ\text{C}$ ). Two K-type thermocouples were used to measure the temperature profiles at the bottom and top of the layup during the curing process. An infrared thermal camera (FLIR T540) was also used to monitor the spatial distribution of temperature during the cure cycle. A control composite panel was also prepared using the same layup strategy but with curing the layup in an oven at  $82^\circ\text{C}$  for 3 h. The degree of cure of the composite panels produced using direct conductive heating and oven curing approaches were determined using DSC measurements. The residual heat of reaction of the cured composites was measured by transferring 15 mg of the cured composites into a DSC pan, followed by heating from  $25^\circ\text{C}$  to  $250^\circ\text{C}$  at a heating rate of  $5^\circ\text{C min}^{-1}$ . The total heat of reaction of the uncured prepreg was measured by performing DSC

measurements on 5 mg specimens of the uncured prepreg using the same experimental procedure.

## 3 Results and discussion

### 3.1 Characterization of DCPD resin

Facile fabrication of buckypaper-based nanocomposites with a high density of nanotubes and low void content requires using a resin system that has a low initial viscosity and long pot life at room temperature while being rapidly curable at elevated temperatures and also having good compatibility with buckypaper for easy impregnation. Additionally, the resulting polymer nanocomposite should exhibit excellent thermomechanical properties. DCPD meets such requirements and is a promising resin for facile preparation of polymer nanocomposite films; therefore, we studied processing of buckypaper impregnated with the DCPD cure-on-demand resin system to explore the feasibility of fabrication of pDCPD-buckypaper nanocomposite films under mild processing conditions compared with traditional approaches used for epoxy resins. The results of room-temperature rheological measurements on the DCPD resin show that the initial viscosity of the resin remained unchanged for approximately 2 h, after which it slowly increased and reached a value of  $750 \text{ Pa s}$  after 5 h (Figure 2A); however, no gelation was observed within 5 h of the measurement (Figure 2B). As opposed to conventional epoxy resins, which have a high initial viscosity and short pot life, the low initial viscosity along with the long pot life of the DCPD resin enable facile impregnation of buckypaper at room temperature and ambient pressure without the need for adding any solvents, which is highly desirable from the processing point of view. In addition, while the DCPD resin is stable for a few hours at room temperature, it rapidly cures at elevated temperatures and yields a fully cured solid polymer within a few minutes. Figure 2C shows the results of DSC measurements on an uncured DCPD resin sample as well as a sample cured at  $100^\circ\text{C}$  for 5 min. The tall and sharp exothermic peak observed in the thermal profile of the uncured resin sample, which indicates the range of cure temperature, clearly disappeared in the thermal profile of the cured sample. As a result, a high degree of cure ( $\sim 93\%$ ) could be achieved by curing the resin for only 5 min. Contact angle measurements were also carried out to evaluate the wettability of buckypaper by the DCPD resin (Figure 2D). While an initial contact angle of  $17.3^\circ \pm$

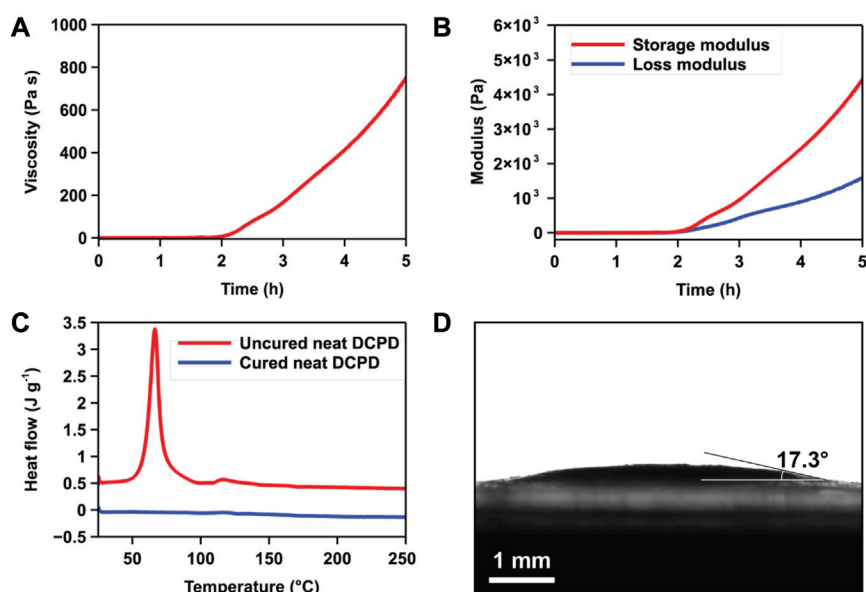


FIGURE 2

Characterization of DCPD resin system (A, B) Time-sweep viscosity and modulus profiles of an uncured DCPD resin containing 1 M equivalent of inhibitor with respect to Grubbs' catalyst at 23°C. (C) Thermal profile of an uncured resin sample and a pDCPD film sample cured at 100°C for 5 min. (D) Contact angle measurement for a droplet of DCPD resin on the buckypaper substrate.

TABLE 1 Degree of cure of various samples measured using DSC experiments.

Material	Cure temperature (°C)	Cure time (min)	Degree of cure (%)
pDCPD film	100	5	93.8 ± 1.2
pDCPD film	120	5	99.1 ± 0.3
pDCPD film	140	5	99.4 ± 0.1
Nanocomposite film	140	5	98.2 ± 0.4
Oven-cured FRPC panel	82	180	96.3 ± 0.1
Heater-cured FRPC panel	82	180	91.3 ± 0.05

0.8° was formed between the DCPD resin and buckypaper, the resin completely infused into the porous structure of buckypaper within a few seconds, demonstrating the excellent compatibility of the resin and carbon nanotube network.

### 3.2 Characterization of nanocomposite films

The appropriate cure temperature for preparation of nanocomposite films was determined by heating the neat DCPD resin samples for 5 min at various temperatures (100, 120, and 140°C) and measuring the degree of cure of the resulting pDCPD films using DSC experiments. The degree-of-cure data obtained from DSC measurements are presented in Table 1. An increase in the cure temperature from 100°C to 140°C increased the degree of cure of pDCPD films from 93.8% to 99.4%, indicating that fully cured pDCPD films can be prepared by heating the material for 5 min at 140°C. DSC measurements were also conducted on a

nanocomposite film sample cured according to the developed cure cycle (i.e., heating for 5 min at 140°C) to determine the degree of cure of polymer in the nanocomposite film. A high degree of cure of ~98.2% was obtained for the cured nanocomposite film, further verifying that highly cured nanocomposite films can be prepared using the developed cure cycle. The microstructure of the cured nanocomposite samples was examined by performing SEM imaging on the cross-section of cured nanocomposite films. Figures 3A, B show the SEM micrographs of the nanocomposite sample at two different magnifications. The low-magnification image (Figure 3A) indicates that a thin (~10 µm) layer of neat resin is formed on the film surface, caused by the incomplete removal of the excess surface resin during the drop casting process. The average thickness of nanocomposite films is ~77 µm, caused by the swelling of the nanotube network by the impregnated resin as well as the formation of the surface resin layer. The image captured at the higher magnification (Figure 3B) demonstrates the high quality of impregnation and low volume fraction of pores in the

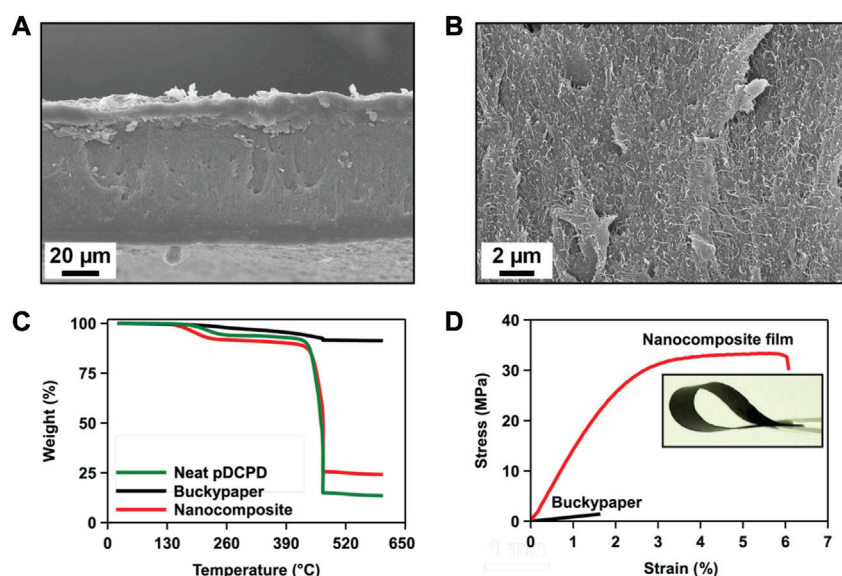


FIGURE 3

Characterization of polymer nanocomposite films. (A, B) Scanning electron microscopy (SEM) micrographs from the cross-section of a nanocomposite film. (C) TGA profiles of pristine buckypaper, neat cured pDCPD film, and nanocomposite film. (D) Tensile stress-strain curves of pristine buckypaper and nanocomposite films. The inset shows a nanocomposite film bent using a tweezer.

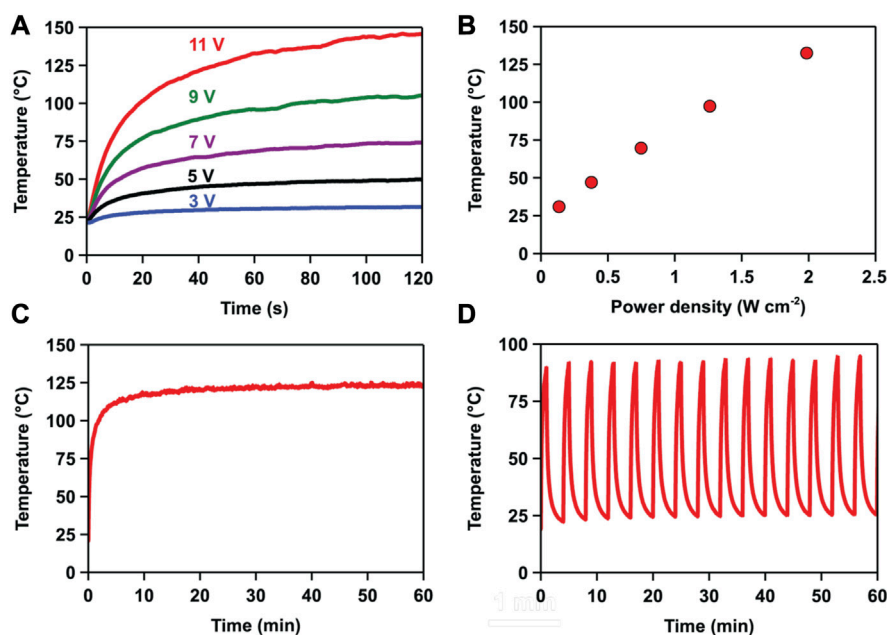


FIGURE 4

Evaluation of the electrothermal performance of produced nanocomposite films. (A) Temperature profiles of a nanocomposite film heater in response to various input voltages. (B) Relationship between input power density and steady-state temperature. (C) Static electrothermal stability test at a constant input voltage of 9 V. (D) Cyclic stability test by varying the input voltage between 0 and 9 V.

produced nanocomposite film, which are necessary for producing films with good mechanical performance. Nanotube content is one of the key factors that affect the mechanical and electrothermal

properties of nanocomposite films. TGA measurements were performed to determine the carbon nanotube content in cured nanocomposite films (Figure 3C). The residual masses of



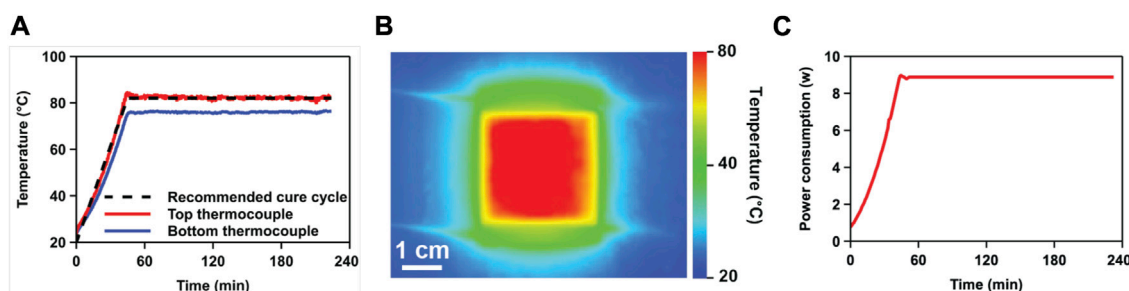


FIGURE 5

Direct conductive curing of a FRPC panel using a nanocomposite film heater. (A) Temperature profiles measured at the bottom and top of the composite layup during the cure cycle. (B) Thermal infrared image of the nanocomposite film heater during composite manufacturing. (C) Power consumption profile recorded during the cure cycle.

constituents and nanocomposite at 470°C were used to determine the carbon nanotube content in produced nanocomposites using Eqs 1, 2. A carbon nanotube content of ~12.6 wt.% was calculated, which is high enough to ensure excellent heat generation capability in nanocomposite films. Compared to the pristine buckypaper, which is mechanically weak and fragile, the nanocomposite films are mechanically robust and can withstand various forms of deformation including twisting and bending. Tensile tests were performed on pristine buckypaper and nanocomposite film specimens to compare the mechanical properties of the buckypaper before and after impregnation and encapsulation by the polymer resin (Figure 3D). In pristine buckypaper, carbon nanotubes in the porous network are held together only *via* van der Waals forces and physical entanglement resulting in poor tensile properties. Impregnation of the porous structure of buckypaper with the matrix polymer enhances the mechanical robustness of the paper, where its tensile strength is increased 22-fold from 1.4 MPa to 31.3 MPa and its tensile modulus is increased 5-fold from 0.150 to 0.708 GPa.

Use of the produced nanocomposite film heaters for successful conductive curing of FRPCs first requires characterizing the Joule heating performance of the nanocomposite films. We performed electrothermal tests on nanocomposite film specimens by applying various voltages across the specimens and measuring their time-dependent temperature profiles (Figure 4A). An increase in the applied input voltage results in an increase in the heating rate as well as the steady-state temperature of film heaters. The nanocomposite film heaters demonstrate an excellent electrothermal performance, where a temperature of ~132°C can be reached in 2 min using a low input voltage of 11 V (equivalent power consumption of 6.16 W). The measured linear relationship between the input power density and steady-state temperature also demonstrates that the heat generation in the nanocomposite heaters follows Joule's law (Figure 4B). Another important requirement for using nanocomposite films as a heater for curing of FRPCs is the stability and reproducibility of their electrothermal properties, as they must survive long and repeated cure cycles for composite manufacturing. The electrothermal stability of nanocomposite heaters were evaluated by applying both static and dynamic electric loads on the heater films and measuring their temperature response. Figure 4C shows the temperature response

of a heater to an input voltage of 9 V when continuously applied for 1 h. After the initial transient stage, temperature remains almost unchanged, demonstrating the stable and reliable electrothermal performance of the nanocomposite heater. The response of the heater to a cyclic electric load was also measured to evaluate the reproducibility of heat generation by produced film heaters; the results of the cyclic electrothermal stability tests reveal that the temperature profile of the heater follows a similar pattern for a given electric loading condition, indicating the good reproducibility of the observed electrothermal properties in the nanocomposite films (Figure 4D).

### 3.3 Composite fabrication

Following the successful demonstration of the Joule heating performance of the produced buckypaper-DCPD nanocomposite films, we used the films as a heat source for direct conductive heating and curing of carbon FRPC laminates. Composite layups were prepared by stacking eight small ( $4 \times 3 \text{ cm}^2$ ) plies of an out-of-autoclave carbon fiber prepreg on a polyisocyanurate foam tool and placing the film heater (effective heating area of  $3 \times 3 \text{ cm}^2$ ) on top of the prepreg stack. A thin layer of a release film was used under the film heater to separate it from the prepreg stack for easy removal and reuse of the heater following the curing process. The layup was then vacuum bagged, and then the cure process was initiated by supplying power to the film heater to generate heat according to the recommended cure cycle. Figure 5A shows temperature profiles measured using two thermocouples placed in the center of the composite layup at the top and bottom surfaces of the laminate during the applied cure cycle. The input power to the film heater was gradually increased until the temperature at the top (heater side) of the laminate reached the cure temperature of the prepreg (i.e., 82°C), after which the power was maintained unchanged for 3 h. A steady-state temperature of ~76°C was measured at the bottom of the layup, which is slightly lower than the required cure temperature, caused by heat losses through tooling boundaries; however, the temperature distribution across the laminate is sufficient for proper curing of the composite laminate. Infrared thermal imaging was also used to monitor

the spatial distribution of temperature throughout the top surface of the layup during the curing process. A uniform heat generation and temperature distribution was observed in the composite layup (Figure 5B), indicating the effectiveness of the nanocomposite film heater for uniform heating and curing of the composite laminate. The energy consumption of this direct conductive curing approach was calculated from the power consumption profile recorded during the applied cure cycle (Figure 5C). Using this approach, only 0.1 MJ of energy was required to successfully cure the composite laminate, whereas curing the same composite panel using a small convection oven in our laboratory (internal volume of 0.17 m<sup>3</sup>) is estimated to require 40.5 MJ of energy. The degree of cure of the composite laminate cured by the nanocomposite film heater was determined using DSC measurements. As a control, the degree of cure of a similar composite panel cured using the traditional, bulk oven curing approach was also measured. The degree of cure of the composite panels made using the heater and oven curing approaches was 91.3% and 96.3%, respectively (Table 1). The slightly lower degree of cure obtained in conductive curing approach is attributed to the observed temperature gradient across the thickness of the layup. This issue can potentially be mitigated by modifying the cure cycle by increasing the dwell temperature and/or the cure time or alternatively by placing the heater on the bottom (tool side) of the composite layup.

## 4 Conclusion

In this work, we used a frontally curable thermoset resin with a low initial resin viscosity to fabricate buckypaper-based polymer nanocomposites. The low viscosity of the resin system allows for quick impregnation of the carbon nanotube network at room temperature and ambient pressure. Following the impregnation step, complete curing of the matrix resin was achieved in a few minutes via through-thickness heating of the material. Produced nanocomposite films are mechanically robust and exhibit excellent electrical conductivity and electrothermal performance, which are ideal for using the films as a heater for curing of fiber-reinforced polymer composites. Finally, a nanocomposite film heater was used to cure a carbon fiber composite panel using a low energy consumption of 0.1 MJ, which is 350 times less than the energy required for producing a similar panel using the conventional oven curing approach.

## References

- Ashrafi, B., Guan, J., Mirjalili, V., Hubert, P., Simard, B., and Johnston, A. (2010). Correlation between Young's modulus and impregnation quality of epoxy-impregnated SWCNT buckypaper. *Compos. Part A: Appl. Sci. Manuf.* 41, 1184–1191. doi:10.1016/j.compositesa.2010.04.018
- Ashrafi, B., Jakubinek, M. B., Martinez-Rubi, Y., Rahmat, M., Djokic, D., Laqua, K., et al. (2017). Multifunctional fiber reinforced polymer composites using carbon and boron nitride nanotubes. *Acta Astronaut.* 141, 57–63. doi:10.1016/j.actaastro.2017.09.023
- Bobinger, M. R., Romero, F. J., Salinas-Castillo, A., Becherer, M., Lugli, P., Morales, D. P., et al. (2019). Flexible and robust laser-induced graphene heaters photothermally scribed on bare polyimide substrates. *Carbon* 144, 116–126. doi:10.1016/j.carbon.2018.12.010
- Centellas, P. J., Yourdkhani, M., Vyas, S., Koohbor, B., Geubelle, P. H., and Sottos, N. R. (2022). Rapid multiple-front polymerization of fiber-reinforced polymer composites. *Compos. Part A: Appl. Sci. Manuf.* 158, 106931. doi:10.1016/j.compositesa.2022.106931
- Chakraborty, A. K., Plyhm, T., Barbezat, M., Necola, A., and Terrasi, G. P. (2011). Carbon nanotube (CNT)-epoxy nanocomposites: A systematic investigation of CNT dispersion. *J. Nanoparticle Res.* 13, 6493–6506. doi:10.1007/s11051-011-0552-3
- Chen, J., Wang, Y., Liu, F., and Luo, S. (2020). Laser-Induced graphene paper heaters with multimodally patternable electrothermal performance for low-energy manufacturing of composites. *ACS Appl. Mater. Interfaces* 12, 23284–23297. doi:10.1021/acsami.0c02188

## Data availability statement

The original contributions presented in the study are included in the article/supplementary material, further inquiries can be directed to the corresponding authors.

## Author contributions

MY and BA directed the research. IN performed the experiments. MJ and YM-R fabricated the buckypaper samples. All authors participated in discussions and writing the manuscript.

## Funding

This work was supported by the New Beginning Ideation Fund from the National Research Council Canada (Grant Agreement no. 967242).

## Acknowledgments

Authors would like to thank the staff members of Colorado State University Analytical Resources Core Facility (RRID: SCR\_021758) for their assistance with performing SEM, TGA, and DSC experiments.

## Conflict of interest

The authors declare that the research was conducted in the absence of any commercial or financial relationships that could be construed as a potential conflict of interest.

## Publisher's note

All claims expressed in this article are solely those of the authors and do not necessarily represent those of their affiliated organizations, or those of the publisher, the editors and the reviewers. Any product that may be evaluated in this article, or claim that may be made by its manufacturer, is not guaranteed or endorsed by the publisher.

- Chen, X., Cheng, S., Wen, K., Wang, C., Zhang, J., Zhang, H., et al. (2023). *In-situ* damage self-monitoring of fiber-reinforced composite by integrating self-powered ZnO nanowires decorated carbon fabric. *Compos. Part B: Eng.* 248, 110368. doi:10.1016/j.compositesb.2022.110368
- Dean, L. M., Wu, Q., Alshangiti, O., Moore, J. S., and Sottos, N. R. (2020). Rapid synthesis of elastomers and thermosets with tunable thermomechanical properties. *ACS Macro Lett.* 9, 819–824. doi:10.1021/acsmacrolett.0c00233
- Galos, J. (2021). Microwave processing of carbon fibre polymer composites: A review. *Polym. Polym. Compos.* 29, 151–162. doi:10.1177/0967391120903894
- Groo, L., Nasser, J., Zhang, L., Steinke, K., Inman, D., and Sodano, H. (2020). Laser induced graphene in fiberglass-reinforced composites for strain and damage sensing. *Compos. Sci. Technol.* 199, 108367. doi:10.1016/j.compscitech.2020.108367
- Isaza, M. C. A., Herrera Ramírez, J., Ledezma Sillas, J., and Meza, J. (2018). Dispersion and alignment quantification of carbon nanotubes in a polyvinyl alcohol matrix. *J. Compos. Mater.* 52, 1617–1626. doi:10.1177/0021998317731151
- Karalis, G., Tzounis, L., Dimos, E., Mytafides, C. K., Liebscher, M., Karydis-Messinis, A., et al. (2021). Printed single-wall carbon nanotube-based Joule heating devices integrated as functional laminae in advanced composites. *ACS Appl. Mater. Interfaces* 13, 39880–39893. doi:10.1021/acsmami.1c10001
- Khan, F., Kausar, A., and Siddiq, M. (2015). A review on properties and fabrication techniques of polymer/carbon nanotube composites and polymer intercalated buckypapers. *Polymer-Plastics Technol. Eng.* 54, 1524–1539. doi:10.1080/03602559.2015.1021486
- Klikovits, N., Liska, R., D'Anna, A., and Sangermano, M. (2017). Successful UV-induced RICFP of epoxy-composites. *Macromol. Chem. Phys.* 218, 1700313. doi:10.1002/macp.201700313
- Lee, J., Ni, X., Daso, F., Xiao, X., King, D., Gómez, J. S., et al. (2018). Advanced carbon fiber composite out-of-autoclave laminate manufacture via nanostructured out-of-oven conductive curing. *Compos. Sci. Technol.* 166, 150–159. doi:10.1016/j.compscitech.2018.02.031
- Liu, Y., van Vliet, T., Tao, Y., Busfield, J. J. C., Peijs, T., Bilotti, E., et al. (2020). Sustainable and self-regulating out-of-oven manufacturing of FRPs with integrated multifunctional capabilities. *Compos. Sci. Technol.* 190, 108032. doi:10.1016/j.compscitech.2020.108032
- Lopes, P. E., van Hattum, F., Pereira, C. M. C., Nóvoa, P. J. R. O., Forero, S., Hepp, F., et al. (2010). High CNT content composites with CNT Buckypaper and epoxy resin matrix: Impregnation behaviour composite production and characterization. *Compos. Struct.* 92, 1291–1298. doi:10.1016/j.compstruct.2009.11.003
- Ma, P.-C., Siddiqui, N. A., Marom, G., and Kim, J.-K. (2010). Dispersion and functionalization of carbon nanotubes for polymer-based nanocomposites: A review. *Compos. Part A: Appl. Sci. Manuf.* 41, 1345–1367. doi:10.1016/j.compositesa.2010.07.003
- Mariani, A., Fiori, S., Bidali, S., Alzari, V., and Malucelli, G. (2008). Frontal polymerization of diurethane diacrylates. *J. Polym. Sci. Part A: Polym. Chem.* 46, 3344–3352. doi:10.1002/pola.22675
- Moreira, I. P., Sanivada, U. K., Bessa, J., Cunha, F., and Figueiro, R. (2021). A review of multiple scale fibrous and composite systems for heating applications. *Molecules* 26, 3686. doi:10.3390/molecules26123686
- Naseri, I., and Yourdkhani, M. (2022). Rapid and energy-efficient frontal curing of multifunctional composites using integrated nanostructured heaters. *ACS Appl. Mater. Interfaces* 14, 50215. doi:10.1021/acsmami.2c15415
- Naseri, I., Ziaee, M., Nilsson, Z. N., Lustig, D. R., and Yourdkhani, M. (2022). Electrothermal performance of heaters based on laser-induced graphene on aramid fabric. *ACS Omega* 7, 3746–3757. doi:10.1021/acsomega.1c06572
- Nuhji, B., Swait, T., Bower, M. P., Green, J. E., Day, R. J., and Scaife, R. J. (2019). Tooling materials compatible with carbon fibre composites in a microwave environment. *Compos. Part B: Eng.* 163, 769–778. doi:10.1016/j.compositesb.2019.01.047
- Pojman, J. A. (2022). "Cure-on-Demand composites by frontal polymerization," in *Encyclopedia of materials: Plastics and polymers* (Elsevier), 85–100. doi:10.1016/B978-0-12-820352-1.00201-7
- Pojman, J. A. (2012). "Frontal polymerization," in *Polymer science: A comprehensive reference* (Elsevier), 957–980. doi:10.1016/B978-0-444-53349-4.00124-2
- Ribeiro, B., Botelho, E. C., Costa, M. L., and Bandeira, C. F. (2017). Carbon nanotube buckypaper reinforced polymer composites: A review. *Polímeros* 27, 247–255. doi:10.1590/0104-1428.03916
- Robertson, I. D., Dean, L. M., Rudebusch, G. E., Sottos, N. R., White, S. R., and Moore, J. S. (2017). Alkyl phosphite inhibitors for frontal ring-opening metathesis polymerization greatly increase pot life. *ACS Macro Lett.* 6, 609–612. doi:10.1021/acsmacrolett.7b00270
- Robertson, I. D., Yourdkhani, M., Centellas, P. J., Aw, J. E., Ivanoff, D. G., Goli, E., et al. (2018). Rapid energy-efficient manufacturing of polymers and composites via frontal polymerization. *Nature* 557, 223–227. doi:10.1038/s41586-018-0054-x
- Ruiti, A., Sanna, D., Alzari, V., Nuvoli, D., and Mariani, A. (2014). Advances in the frontal ring opening metathesis polymerization of dicyclopentadiene. *J. Polym. Sci. Part A: Polym. Chem.* 52, 2776–2780. doi:10.1002/pola.27301
- Schlimbach, J., and Ogale, A. (2012). "Out-of-autoclave curing process in polymer matrix composites," in *Manufacturing techniques for polymer matrix composites (PMCs)* (Elsevier), 435–480. doi:10.1533/9780857096258.3.435
- Silva, V. L. M., Santos, L. M. N. B. F., and Silva, A. M. S. (2017). Ohmic heating: An emerging concept in organic synthesis. *Chem. Eur. J.* 23, 7853–7865. doi:10.1002/chem.201700307
- Suslick, B. A., Hemmer, J., Groce, B. R., Stawiasz, K. J., Geubelle, P. H., Malucelli, G., et al. (2022). Frontal polymerizations: From chemical perspectives to macroscopic properties and applications. *Chem. Rev.* doi:10.1021/acs.chemrev.2c00686
- Tarfaoui, M., El Moumen, A., Boehle, M., Shah, O., and Lafdi, K. (2019). Self-heating and deicing epoxy/glass fiber based carbon nanotubes buckypaper composite. *J. Mater. Sci.* 54, 1351–1362. doi:10.1007/s10853-018-2917-9
- Tu, R., Liu, T., Steinke, K., Nasser, J., and Sodano, H. A. (2022). Laser induced graphene-based out-of-autoclave curing of fiberglass reinforced polymer matrix composites. *Compos. Sci. Technol.* 226, 109529. doi:10.1016/j.compscitech.2022.109529
- Wan Dalina, W. A. D., Mariatti, M., and Tan, S. H. (2019). Multi-walled carbon nanotubes buckypaper/epoxy composites: Effect of loading and pressure on tensile and electrical properties. *Polym. Bull.* 76, 2801–2817. doi:10.1007/s00289-018-2530-8
- Xia, Q., Zhang, Z., Liu, Y., and Leng, J. (2020). Buckypaper and its composites for aeronautic applications. *Compos. Part B: Eng.* 199, 108231. doi:10.1016/j.compositesb.2020.108231
- Xu, F., Aouraghe, M. A., Xie, X., Zheng, L., Zhang, K., and Fu, K. K. (2021). Highly stretchable, fast thermal response carbon nanotube composite heater. *Compos. Part A: Appl. Sci. Manuf.* 147, 106471. doi:10.1016/j.compositesa.2021.106471
- Yao, X., Falzon, B. G., and Hawkins, S. C. (2019). Orthotropic electro-thermal behaviour of highly-aligned carbon nanotube web based composites. *Compos. Sci. Technol.* 170, 157–164. doi:10.1016/j.compscitech.2018.11.042
- Yue, C., Zhang, Y., Lu, W., Zhang, Y., Wang, P., Li, Y., et al. (2022). Realizing the curing of polymer composite materials by using electrical resistance heating: A review. *Compos. Part A: Appl. Sci. Manuf.* 163, 107181. doi:10.1016/j.compositesa.2022.107181
- Zeinedini, A., Shokrieh, M. M., and Ebrahimi, A. (2018). The effect of agglomeration on the fracture toughness of CNTs-reinforced nanocomposites. *Theor. Appl. Fract. Mech.* 94, 84–94. doi:10.1016/j.tafmec.2018.01.009
- Zhang, Z., Liu, R., Li, W., Liu, Y., Pei, Z., Qiu, J., et al. (2021). Frontal polymerization-assisted 3D printing of short carbon fibers/dicyclopentadiene composites. *J. Manuf. Process.* 71, 753–762. doi:10.1016/j.jmapro.2021.10.014
- Ziaee, M., Johnson, J. W., and Yourdkhani, M. (2022). 3D printing of short-carbon-fiber-reinforced thermoset polymer composites via frontal polymerization. *ACS Appl. Mater. Interfaces* 14, 16694–16702. doi:10.1021/acsmami.2c02076
- Ziaee, M., and Yourdkhani, M. (2021). Effect of resin staging on frontal polymerization of dicyclopentadiene. *J. Polym. Sci.* 59, 1732–1739. doi:10.1002/pol.20210285



## OPEN ACCESS

## EDITED BY

Baris Caglar,  
Delft University of Technology,  
Netherlands

## REVIEWED BY

Masoud Bodaghi,  
Luxembourg Institute of Science and  
Technology (LIST), Luxembourg  
Miro Duhovic,  
Leibniz-Institut für Verbundwerkstoffe,  
Germany

## \*CORRESPONDENCE

Oliver Döbrich,  
✉ oliver.doebrich@zhaw.ch

## SPECIALTY SECTION

This article was submitted to Polymeric  
and Composite Materials,  
a section of the journal  
Frontiers in Materials

RECEIVED 30 January 2023

ACCEPTED 14 March 2023

PUBLISHED 30 March 2023

## CITATION

Döbrich O and Brauner C (2023),  
Machine vision system for digital twin  
modeling of composite structures.  
*Front. Mater.* 10:1154655.  
doi: 10.3389/fmats.2023.1154655

## COPYRIGHT

© 2023 Döbrich and Brauner. This is an  
open-access article distributed under the  
terms of the [Creative Commons  
Attribution License \(CC BY\)](#). The use,  
distribution or reproduction in other  
forums is permitted, provided the original  
author(s) and the copyright owner(s) are  
credited and that the original publication  
in this journal is cited, in accordance with  
accepted academic practice. No use,  
distribution or reproduction is permitted  
which does not comply with these terms.

# Machine vision system for digital twin modeling of composite structures

Oliver Döbrich<sup>1\*</sup> and Christian Brauner<sup>2</sup>

<sup>1</sup>School of Engineering, Institute of Materials and Process Engineering, ZHAW Zurich University of Applied Sciences, Winterthur, Switzerland, <sup>2</sup>School of Engineering, Institute of Polymer Engineering, FHNW University of Applied Sciences and Arts Northwestern Switzerland, Windisch, Switzerland

Although the structural design of composite structures has already been carried out on a virtual level, composite mechanical properties remain sensitive to fiber orientation and therefore to the quality and reliability of the production process. Considering both manual single-unit manufacturing and advanced mass-unit fabrication, requirements on the production quality may differ, but certainty on the achieved result is crucial. A digital twin model, deterministically derived from produced parts, can be transferred into a virtual simulation environment to check for potential deviations of fiber alignment, resulting from variations in source material or composite production. Transferring that deterministic information into a virtual simulation environment allows for an estimation of the part's structural potential despite any possible deviations by carrying out numerical simulation predictions on that model. This step of quality assessment can help reduce scrap parts by relying on simulation data that may demonstrate the feasibility of parts despite the containment of deviations with an otherwise uncertain impact. Therefore, further steps toward digitalization of the composite production process chain, especially on the characterization of the production quality, are aspired. In this contribution, a vision system based on a Microsoft Azure Kinect RGB-D camera is introduced which is used to digitalize the composite preform configuration from machine vision data by evaluating the achieved local fiber orientation as result of the complex preform draping process by digital image processing. A digital workflow is introduced that enables to feed the captured real-world data back into a digital environment where numerical simulations with the "as-built" fiber orientation can be carried out. The obtained results are used for assessing production quality and composite performance in the presence of possible deviations. The system, which consists of a camera array of consumer grade, can acquire real-world data and then transfer the data into a virtual environment.

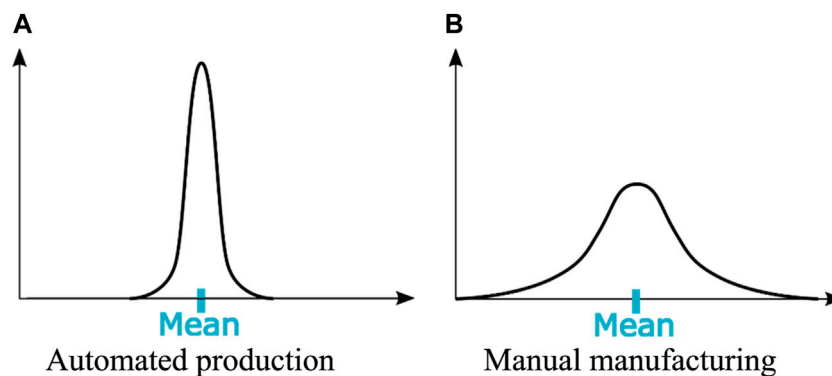
## KEYWORDS

machine vision, composite, digital twin, modeling, finite element analysis

## 1 Introduction

Composite components have excellent mechanical properties at a low specific density compared to conventional construction materials such as metals. This combination results in a wide range of applications for components in the high-performance sector. For fiber-based composite components, the orientation of the fiber is crucial for the exploitation of the mechanical potential.





**FIGURE 1**  
Schematic deviation from aspired production results depending on the production method. (A) Automated production. (B) Manual manufacturing.

Since the manufacturing of complex-shaped parts from composite materials is a sequential process characterized by either manual or automated handling of unstable and flexible reinforcement fabrics, deviations from an ideal “as-planned” configuration are likely to be observed. The deviations can vary depending on the robustness of the process, as shown in Figure 1.

The designing of composite parts is regularly carried out with only small reserves in mechanical capacity due to the general lightweight motivation and high material costs when using fiber-reinforced composites. Deviations in fiber orientation and defects from the manufacturing process may result in reduced structural stiffness or unpredicted failure due to reduced strength. Therefore, the use of machine vision to digitalize the quality assessment of composite production is aspired.

Nevertheless, due to the high cost and effort, fiber orientation is rarely digitally verified in practice. In this paper, a system that determines the fiber orientation at the ply level of a complex-shaped textile-reinforced composite part during preforming processes using an inexpensive RGB-D camera is presented. The Azure Kinect camera, initially launched by Microsoft for entertainment purposes, can provide both depth measurement for obtaining geometry data and texture information using an RGB sensor. A point cloud captured by the time-of-flight (TOF) IR camera is used to detect positioning of the structural geometry to identify the position in space and allocate location-based data such as fiber orientation. Based on the color image taken by the camera, the local texture is projected onto the component geometry, and the orientation of the fiber is determined using open-source image analysis. The system presented in this paper is characterized by low investment costs and a high degree of automation as well as open-source Python libraries, which allows a customization of the system and enhances the system flexibility and usability.

## 2 State of the art

Optical evaluation systems are already being used in composite research, as well as in the composite industry. Algorithms for image analysis are applied at the material level to analyze geometrical features, such as voids, or at the structural level to observe

macroscopic features such as fiber orientation or global defects like wrinkles.

Early computational evaluation methods were based on camera images where edge detection algorithms were applied on fast Fourier transformed images of technical reinforcement braids (Lian et al., 2000; Mersmann, 2011). Stationary cameras were used on these steady production processes where no geometrical information was required. The obtained values were used for quality assessment (Lian et al., 2000) and process control (Mersmann, 2011; Lekandis and Vosniakos, 2020), simple damage detection (Wilhelmsen and Ostrom, 2016), and for importing material relevant input data (fiber orientation) into a virtual environment finite element analysis (FEA) models for further use in numerical simulation (Stender et al., 2019; Döbrich et al., 2021). Studies on using composite machine vision in material research to study the fatigue behavior of glass–fiber-reinforced composites are also found in the literature (Song et al., 2022). In addition, studies on using machine vision systems to investigate wrinkling caused by shearing in dry textile drape processes are found (Döbrich et al., 2013; Pasco et al., 2019).

The field of view for those applications is rather small and is limited to a specific section of composite parts or composite production processes. The digital image evaluation at the component level of composite structures is carried out by hand-guided or robot-guided camera systems (Kunze et al., 2020; Döbrich et al., 2021). Commercially available systems are provided by Hexagon (Sweden, formerly Apodius) [hand-guided inspection system (Stender et al., 2019; Antoniou et al., 2020; Döbrich et al., 2021)] or CIKONI (Germany) [robot-guided Hexagon system (Pasco et al., 2019)]. These systems can easily adapt to the shape of the structural part (Malhan et al., 2018). However, the process is time-consuming and requires either manual guidance or a geometry-specific teaching of the robotic guidance system. Another setback is that generally only the visible top layer is evaluable. This requires a sequential examination of every single layer that is draped over or added to a stack of reinforcement layers. Time- and labor-consuming semi-automated evaluation methods directly increase the assessment time when they must be carried out multiple times. However, common RGB camera images have been proved to be sufficient for the evaluation of fiber orientation features (Lian et al., 2000; Mersmann, 2011; Stender et al., 2019).

The introduced systems mostly rely on expensive hardware and specific software packages and are vulnerable to changes in environmental conditions. The general requirement for a diffuse illumination system is pointed out by most of the authors from the relevant literature due to the reflecting nature of technical reinforcement fibers, especially mandatory for analyzing carbon fibers. To address this particular challenge, novel inspection systems have been introduced that make use of the polarization effects found in carbon fibers (Ernst et al., 2016). By using this effect, fiber trace and thus fiber orientation can be determined not only on the dry textile or unconsolidated prepreg but also on the composite parts, since the polarization effect only affects the fiber and not the matrix (Atkinson et al., 2021; Schommer et al., 2023).

However, it is also not possible to analyze layers within the composite, since here, too, only the surface of reinforcement textiles and composites can be considered. Systems that can evaluate a stack of reinforcement layers are known as well. Micro-CT scans (Desplentere et al., 2005), as well as X-ray micro-CT scans (Bernardini et al., 1999a), have been used to build composite unit cell models to predict the mechanical properties. An application of this technique at the structural level is difficult to carry out and generally limited by the sample size, the duration of the method, and the costs. The eddy current sensor data can be used to evaluate the result of the preforming process (Bardl et al., 2016). Unfortunately, this technique is limited to carbon or metal fibers due to the need of electrical conductivity within the material.

In the summary of the already existing systems, it can be stated that the extraction of composite-related data is possible by simple RGB image evaluation. Composite materials are suitable for such an optical evaluation due to their heterogeneous structure, where the most important features can be determined at the mesoscopic level (yarn level). However, currently, image analysis is only used in stationary cameras for simple and continuous processes, such as braiding, where information on the positioning in space is not important, and relevant information can be extracted by observing a planar field of interest or by systems that apply an extended effort in terms of camera guidance for capturing complex geometries along with local features like fiber orientation. Methods that allow an analysis of the entire reinforcement stack are only applicable with advanced analysis methods and expensive technology, whereas sequential ply-by-ply analyses are only implemented with non-stationary systems, for which the evaluation time is high and therefore an industrial implementation is unlikely.

Therefore, a system is introduced that does not rely on manual or guided camera/sensor movement but offers an environmental observing stationary camera array that is able to capture the geometry and the texture information in a single shot. The system is fast enough that a sequential evaluation of multiple layers can be carried out without additional expenses in process time and therefore be applicable in mass consumer industries, whereas the open-source software libraries and the use of consumer hardware make it suitable for small manufacturing enterprises and research institutes. The mutual determination of structural geometry and composite relevant features derived from image processing along with adaptable open-source algorithms characterizes the novelty of the introduced system.

## 3 Hardware and approach

### 3.1 Material

A twill woven fabric prepreg system composed of 200 tex carbon HT-3k multifilament yarns and epoxy resin produced by Krempel Group (Fa. Krempel GmbH, Vaihingen, Germany) was studied. The characteristics of the material are shown in Table 1 along with an image of the material.

### 3.2 Utilizable camera hardware

The approach presented in this contribution introduces a fiber orientation evaluation system based on the Microsoft Azure Kinect camera (Figure 2A). Recently, the third-generation Kinect cameras have been introduced not only for entertainment and gaming purposes but also for industrial applications. The current generation Kinect camera is equipped with a 1-MP depth sensor (IR-TOF) and a 12-MP camera for RGB image capturing. The Azure cameras are especially low-priced compared to existing composite evaluation products and come with a sync port to set up a camera array, as shown in Figure 2B.

### 3.3 Stationary machine vision approach

The developed method for the detection of fiber orientation using the Microsoft Azure Kinect camera is shown in Figure 3. The camera array a) captures a single RGB image and a single point cloud per camera b) which is merged in regards to the positioning of the cameras by performing a rigid body transformation of the point clouds related to the designated master camera's position (Figure 5), according to Eq. (1). The combined point cloud contains all points captured by the camera array. These are points captured not only from the composite part itself but also related to the surroundings (mounting, positioning table, etc.) and the environment (opposite cameras, respective tripods, other objects in the lab/tool shop, etc.). By the definition of a space of interest, that is, related to the composite part size and position within the camera array, captured points outside the designated space can be removed from the merged point cloud. The remaining point cloud is still very dense and must be used for meshing of the surface of composite parts. The number of points within the point cloud exceeds the number of points required for a useful mesh. A relevant mesh size can be derived from the textile characteristics, such as yarn density and yarn count, as the fiber orientation will be evaluated using the captured RGB image locally cropped onto the mesh element size. The captured point cloud density depends on the object distance from the camera. Related values are shown in Table 2.

Therefore, MeshLabs open API accessible by Python library PyMeshLab (Muntoni and Cignoni, 2021) was used to reduce the number of points to meet the desired mesh size (10 mm for the material introduced in Section 3.1). The simplified cloud was meshed using ball pivot meshing algorithms c), as shown in Figure 6. The meshing was performed using Python's Open3D library (Zhou et al., 2018).

TABLE 1 Krempel KGBX 2508 prepreg system.

	Material property		Image
Fabric material: Twill 2/2 weave	Weft density	~6/cm	
	Warp density	~6/cm	
	Areal density	245 g/m²	
Prepreg system	Prepreg thickness	0.28 mm	
	Mass content resin	44 m%	
	Areal density	440 g/m²	

Utilizable camera hardware.

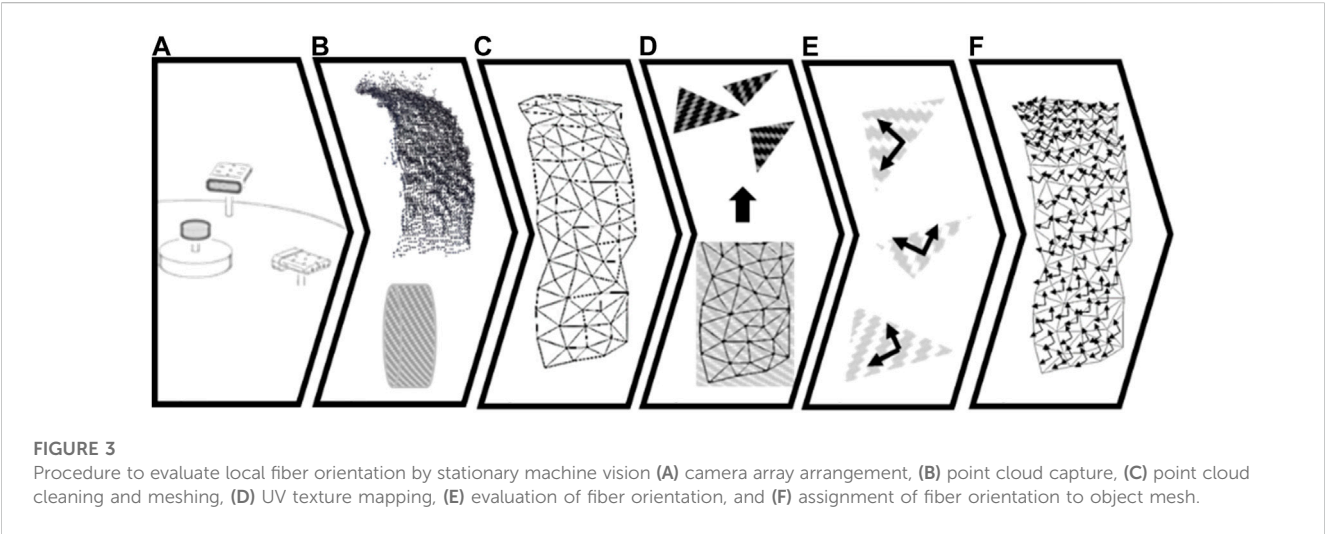
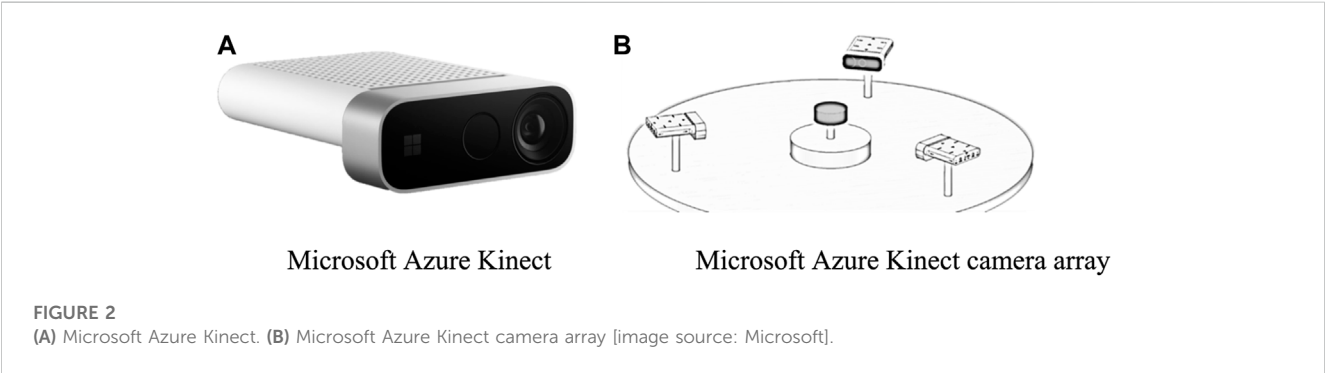
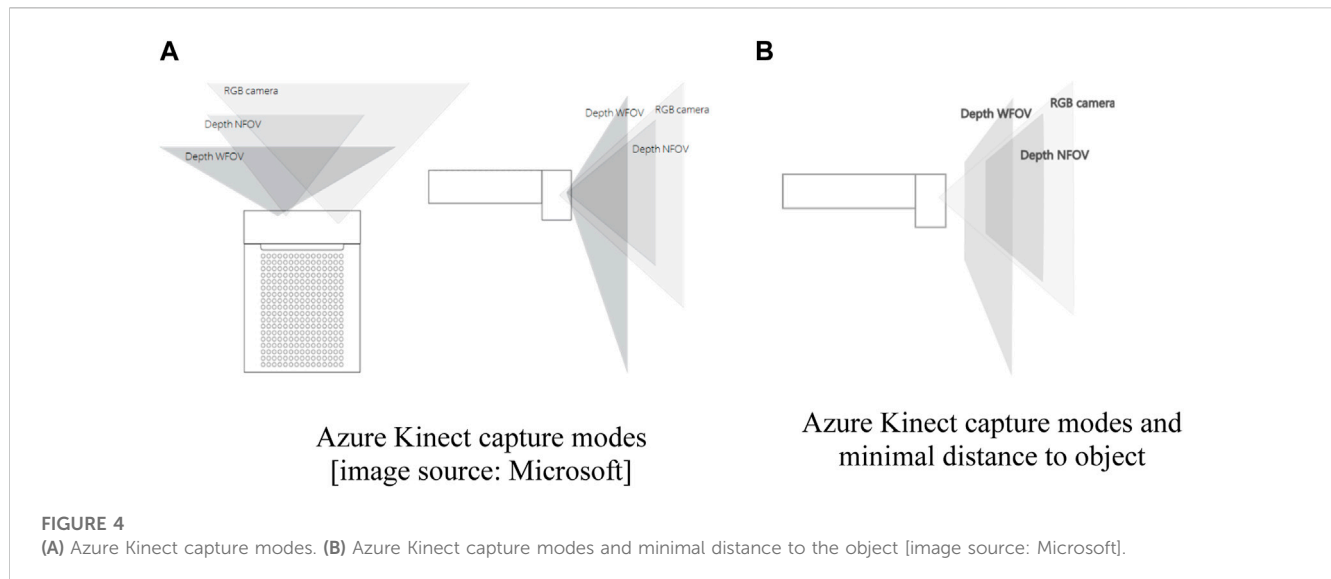


TABLE 2 Distance-related point cloud density.

Object distance from the camera (m)	Average distance between captured points (mm)
0.5	0.9
1.0	1.7
1.5	2.8
2.0	3.8



By using UV-transformation, the texture image related to every element of the generated mesh is taken from the captured RGB color image and cropped to the size of interest related to the mesh element size  $d$ ). For these images, the main orientations, not in regard to fiber orientation, but in regard to color gradients within the picture, are determined  $e$ ) using image processing methods, like the histogram of oriented gradients (HOG) (Lindeberg, 1998) and edge detection algorithms (Dalal and Triggs, 2005) available in Python's Open-Source Computer Vision (OpenCV) library (Bradski, 2000). Particularly, for continuous fiber surface textures, the color gradient and the main trace of the edges correlate with the main fiber orientations (Lian et al., 2000). The established orientation vector (or several vectors when observing biaxial reinforcement textiles) must be transformed considering the positioning of the surface element toward the camera to account for tilted surfaces causing distortions in the captured image  $f$ ).

With regard to the positioning of the investigable composite part, the distance to the camera is dependent on the camera's capturing mode, narrow field of view (NFOV) or wide field of view (WFOV), as shown in Figure 4. A minimum distance of 25 cm is achievable in WFOV. However, better results have been achieved in NFOV, which also corresponds to the RGB camera's field of view. The TOF sensor shows different sensitivities in NFOV, as shown in Figure 4B. Therefore, a distance of 50 cm from the camera has proven to be recommendable by several trial studies. The size of the structural part that is to be investigated does not necessarily need to fit in this field of view as this field can be extended by another camera. A recommendation related to a minimum size cannot be made as this has not been investigated. However, the point cloud density shown in Table 2 can be used as orientation as it indicates the sensitivity of the camera.

This general approach is applicable to a single RGB-D camera only. However, when pursuing a stationary camera system, an increasing number of cameras forming the array improves the level of detail in the captured point cloud and increases the possibility to capture the whole structural geometry in a single shot. The low investment costs for consumer hardware cameras

make this upscale considerable. Depending on the composite structural geometry, the number of cameras required for capturing all surfaces and details may vary. For very complex geometries containing undercuts or surfaces not visible to an observer from outside, this stationary approach may even be insufficient. The number of cameras may be reduced for complex geometries by using a rotatable mounting for the composite structure. This allows for captures from multiple angles by a single camera, which is ruled out in this study.

## 4 Experiments

### 4.1 Capturing of structural geometry

To use Microsoft Azure Kinect cameras as a camera array, a rigid transformation matrix must be set up for every slave camera to transform the captured information into the master camera coordinate system, according to Eq. (1). The rotation matrix and the transformation vector can be found by using a least-square fitting method (Arun et al., 1987). For this, a calibration pattern needs to be captured for every camera, and the specific parameters  $\vec{t}$  (transformation vector) and  $R$  (rotation matrix) can be determined from three points observed using every individual slave camera and the master camera itself. Afterward, the points captured by every slave camera can be transformed into the master camera coordinate system, resulting in a single cloud containing every point captured by all cameras in the array (within the space of interest), as shown in Figure 5.t

$$T(\vec{v}) = R\vec{v} + \vec{t}. \quad (1)$$

For converting the point cloud into a surface mesh, ball pivoting (Bernardini et al., 1999b) is used as part of the Open3D library (Zhou et al., 2018). The meshing can be adjusted by parameters to regulate the point distance and element size. An example of the result obtained from this step is shown in Figure 6.



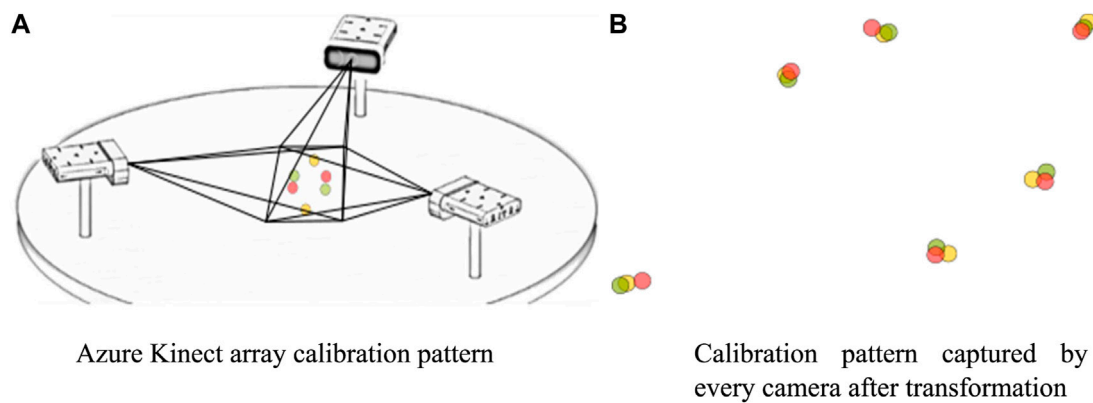


FIGURE 5

Determination of a rigid transformation matrix from the slave camera to the master camera. **(A)** Azure Kinect array calibration pattern. **(B)** Calibration pattern captured by every camera after transformation.

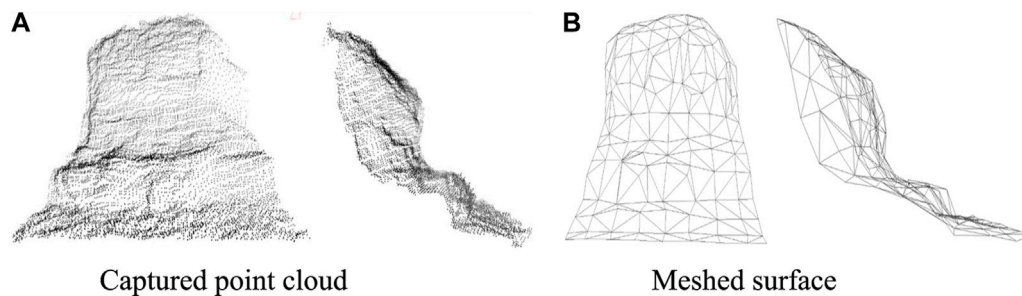


FIGURE 6

Point cloud and meshed surface derived from ball pivot meshing algorithms (Bernardini et al., 1999b). **(A)** Captured point cloud. **(B)** Meshed surface.

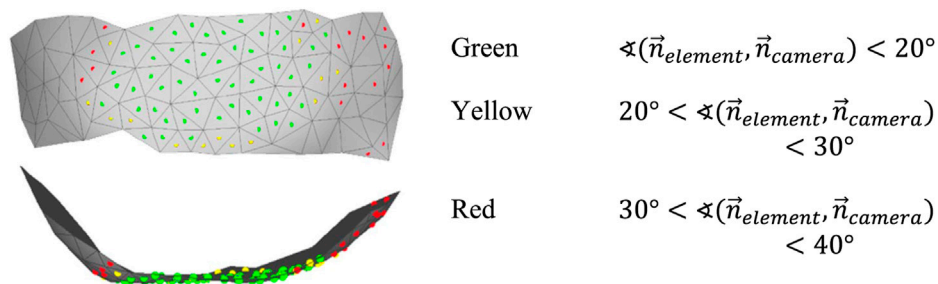


FIGURE 7

Evaluation of element orientation toward the camera.

## 4.2 UV-transformation of the surface texture

To map the surface texture captured by the RGB camera onto the corresponding mesh element, a pre-evaluation is conducted to determine the alignment of the elements toward the camera. The texture that is to be evaluated must not be tilted too much to guarantee a successful examination and assignment of the fiber

orientation. Therefore, the element normal vector  $\vec{n}$  is calculated from the element node coordinates. The angle toward the specific camera that captured the respective image is calculated, and the “element quality” is evaluated by ranking the elements, as shown in Figure 7. Depending on the category obtained for every element, an assignment of fiber orientation is carried out only on the respective element which has not been captured by another camera in the

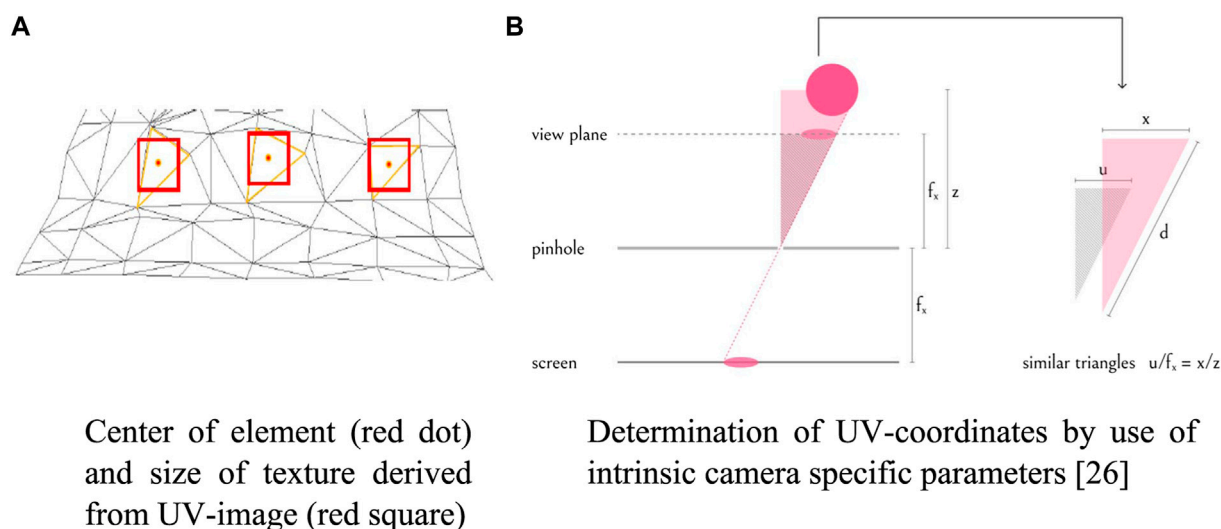


FIGURE 8

Basic parameters used in UV-transformation. (A) Center of element (red dot) and size of texture derived from the UV image (red square). (B) Determination of UV-coordinates using intrinsic camera-specific parameters (From depth map to point cloud, 2020).

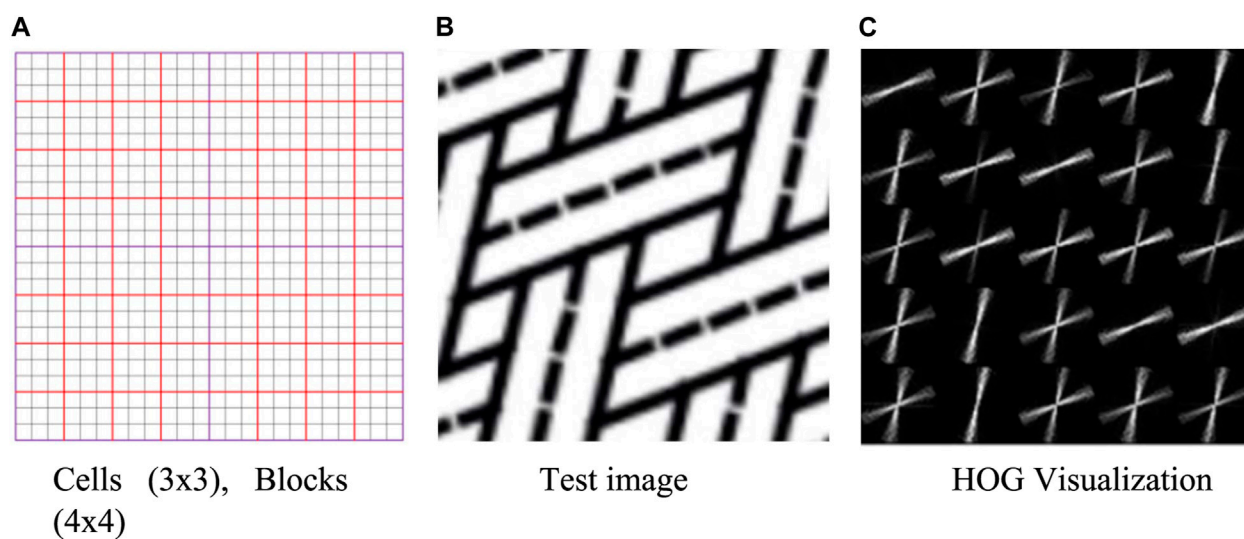


FIGURE 9

Histogram of oriented gradients. (A) Cells (3 x 3) and blocks (4 x 4). (B) Test image. (C) HOG visualization.

array. If the elements' normal vector is too far off the camera's normal vector, it is not evaluated at all.

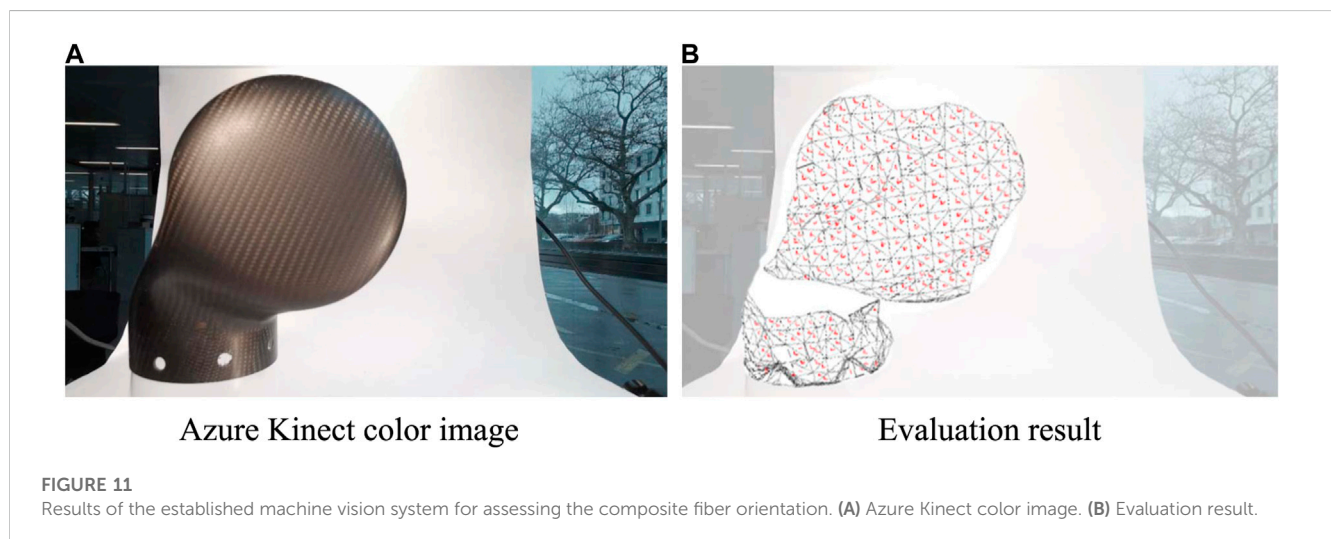
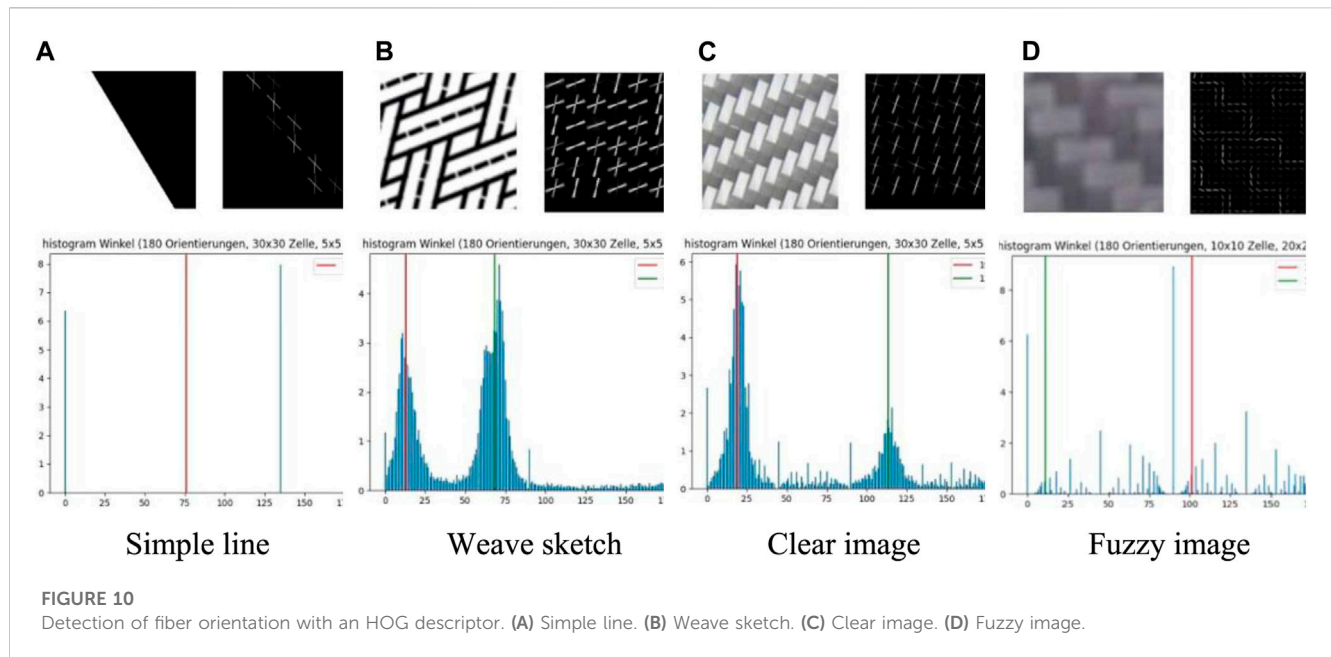
The texture that corresponds to the location of every element must be determined by UV-transformation. In general, the captured color image is 2D, containing texture information in a UV system. The point cloud and the derived mesh exist in an XYZ-Cartesian coordinate system. By performing UV-transformation, every location in XYZ-space becomes related to the specific area in the UV image. For this, the center of the elements is used as a reference. By using the intrinsic parameters and the focal length of the camera setting (specific for every camera), the position of every point in XYZ-space can be

observed on the UV image on the camera's digital sensor, as shown in Figure 8 and explained in Eq. (2).

$$\text{With: } x = \frac{uz}{f_x}, u = \frac{x}{z}f, \text{ and } v = \frac{y}{z}f. \quad (2)$$

### 4.3 Histogram of oriented gradient descriptor

The histogram of oriented gradients (HOG) is formed from feature vectors of images or image sections. In contrast to pure edge



detection methods, the feature vector of the HOG primarily contains information about the color gradient in discrete directions within a certain evaluation cell. These direction vectors are displayed in a histogram or by plotting them onto the specific area of the image (Figure 9C). The HOG plot represents the main orientation of lines in the test image (Figure 9B) for every evaluation cell (Figure 9A). For textile textures, the main orientation of surface texture gradients is assumed to be in correlation with the trace of the reinforcement yarns, namely, the local fiber orientations. The orientation gradients are classified into a defined number of angles. Therefore, the number of existing main orientations can be evaluated by investigating the histogram's local maxima. The number of local maxima corresponds to the number of local fiber systems (1—UD reinforcement, 2—weave, and 3—open reed weave). The algorithms used for the presented results are part of the OpenCV library (Bradski, 2000).

## 5 Results

The evaluation of image sections captured by the Microsoft Azure Kinect camera is shown in Figures 10C, D. The quality of data that is provided by applying HOG algorithm depends significantly on the image quality. Therefore, adequate illumination (strong, diffuse) and a certain maximal distance (depending on the reinforcement rapport and yarn count) for capturing texture images are required. However, the main orientations could be evaluated successfully even for fuzzy images, but the system is also flexible in this regard that Microsoft Azure Kinect embedded RGB camera may be substituted with an even better camera to capture more detailed images of the texture in the first place. The main orientations have been determined by finding the local maxima along the histogram of orientation vectors. For the test

image (Figure 10A), one main direction is assigned, whereas two directions have been found for the images showing weave textures (Figures 10B–D).

Figure 11 shows the result of the evaluation system. The sample geometry prepared from twill woven carbon fiber prepregs in a manual and sequential preform draping process is determined using the infrared depth sensor, and a meshed surface topology could be generated. Texture evaluation is only carried out for elements that are oriented toward the camera within the introduced tolerances. The local fiber orientations are determined by the HOG algorithm and mapped onto the discrete elements of the meshed surface. The result presented is created with a single shot and covers most of the structural surface parts visible for a single camera. The introduced algorithm has been executed on a local personal computer, although the Azure Kinect camera can be used for Microsoft Azure cloud computing services. The average duration for evaluation of a single shot performed by one camera (including all the steps shown in Figure 3) was  $4\text{ s} < t_{\text{compute}} < 8\text{ s}$ .

## 6 Conclusion

A novel machine vision approach is introduced that enables the evaluation of composite material local fiber orientation along with the corresponding location on the structure by scanning the surface texture and the geometry by utilizing RGB-D camera of consumer-grade that is capable of examining composite parts at the structural level by a single shot. The utilized cameras can be built up as a camera array that allows for a multi-shot evaluation within the same time frame as a single shot. The introduced methods are efficient for the quantification of the orientation values. The element-wise evaluation can be used directly as input for FEA simulation to carry out “as-built” numerical simulations, digitalize processes, assess the production quality, and archive production data. The low investment costs and the availability of the introduced methods by relying on open-source libraries can boost the application in the composite industry, especially for small- and middle-scale businesses, and help increase the digitalization by enabling the digital twin pre-processing of composite materials and structures. The simple, fast, and supervision-free method is suitable for mass consumer production since production processes can be observed without the handling of cameras or manually initiating the scanning process. The system mainly targets the sequential processes found in draping of complex composite structures or the stacking of reinforcement layers. In future, continuous production processes are targeted, for which the fast evaluation algorithms and the

possibility to move the workload into a cloud service are beneficial. However, data-related challenges occurring when capturing, evaluating, and storing of continuous data are to be pursued.

## Data availability statement

The original contributions presented in the study are included in the article/Supplementary Material; further inquiries can be directed to the corresponding author.

## Author contributions

Study conception, conceiving the idea, collecting data, analysis and interpretation of results, drafting the manuscript, preparation, and design: OD. Supervision of the project: CB.

## Funding

The research was supported by Open Access Funding by Zurich University of Applied Sciences (ZHAW).

## Acknowledgments

The authors would like to thank their Student Matthias Hansmann for his support, effort, and work toward this project.

## Conflict of interest

The authors declare that the research was conducted in the absence of any commercial or financial relationships that could be construed as a potential conflict of interest.

## Publisher's note

All claims expressed in this article are solely those of the authors and do not necessarily represent those of their affiliated organizations, or those of the publisher, the editors, and the reviewers. Any product that may be evaluated in this article, or claim that may be made by its manufacturer, is not guaranteed or endorsed by the publisher.

## References

- Antoniou, A., Mikkelsen, L. P., Goutianos, S., Bagemiel, O., Gebauer, I., Flindt, R., et al. (2020). Influence of the glass non-crimp fabric intrinsic undulation on the stiffness of the composite ply: A micromechanical approach. *IOP Publ.* 942 (1), 012017. doi:10.1088/1757-899x/942/1/012017
- Arun, K. S., Huang, T. S., and Blostein, S. D. (1987). Least-squares fitting of two 3-D point sets. *IEEE Trans. pattern analysis Mach. Intell.* PAMI-9 (5), 698–700. doi:10.1109/tpami.1987.4767965
- Atkinson, G. A., O'Hara Nash, S., and Smith, L. N. (2021). Precision fibre angle inspection for carbon fibre composite structures using polarisation vision. *Electronics* 10, 2765. doi:10.3390/electronics10222765
- Bardl, G., Nocke, A., Cherif, C., Pooch, M., Schulze, M., Heuer, H., et al. (2016). Automated detection of yarn orientation in 3D-draped carbon fiber fabrics and preforms from eddy current data. *Compos. Part B Eng.* 96, 312–324. doi:10.1016/j.compositesb.2016.04.040
- Bernardini, F., Mittleman, J., Rushmeier, H., Silva, C., and Taubin, G. (1999). The ball-pivoting algorithm for surface reconstruction. *IEEE Trans. Vis. Comput. Graph.* 5 (4), 349–359. doi:10.1109/2945.817351
- Bernardini, F., Mittleman, J., Rushmeier, H., Silva, C., and Taubin, G. (1999). The ball-pivoting algorithm for surface reconstruction. *IEEE Trans. Vis. Comput. Graph.* 5 (4), 349–359. doi:10.1109/2945.817351



- Bradski, G. (2000). The openCV library. *Dr. Dobb's J. Softw. Tools Prof. Program.* 25 (11), 120–123.
- Dalal, N., and Triggs, B. (2005). "Histograms of oriented gradients for human detection," in Proceedings of the 2005 IEEE computer society conference on computer vision and pattern recognition (CVPR'05), San Diego, CA, USA, June 2005 (IEEE), 886–893.
- Desplentere, F., Lomov, S. V., Woerdeman, D. L., Verpoest, I., Wevers, M., and Bogdanovich, A. (2005). Micro-CT characterization of variability in 3D textile architecture. *Compos. Sci. Technol.* 65 (13), 1920–1930. doi:10.1016/j.compscitech.2005.04.008
- Döbrich, O., Anderegg, A., Gort, N., and Brauner, C. (2021). Machine vision for as-built modeling of complex draped composite structures. *Materials* 14 (3), 682. doi:10.3390/ma14030682
- Döbrich, O., Gereke, T., and Cherif, C. (2013). A finite element based approach for the accurate determination of the shear behaviour of textiles with the picture-frame shear test. *Key Eng. Mater.* 554. Trans Tech Publications Ltd, 1105–1115.
- Ernst, J., Junger, S., and Tschekalinskij, W. (2016). *U.S. Patent No. 9*. Washington, DC: U.S. Patent and Trademark Office.
- From depth map to point cloud (2020). Published online: Map for robots. [www.medium.com](http://www.medium.com).
- Kunze, Eckart, Schwarz, B., Weber, T., Muller, M., Bohm, R., and Gude, M. (2020). Forming analysis of internal plies of multi-layer unidirectional textile preforms using projectional radiography. *Procedia Manuf.* 47, 17–23. doi:10.1016/j.promfg.2020.04.110
- Lekanidis, S., and Vosniakos, G. C. (2020). Machine vision support of VARI process automation in composite part manufacturing. *Int. J. Mechatronics Manuf. Syst.* 13 (2), 169–183. doi:10.1504/ijmms.2020.109799
- Lian, B., Jiang, L., McGrath, J. J., and Jaranson, J. (2000). Quantitative determination of morphological features of triaxially braided composites by the use of machine vision. *Compos. Sci. Technol.* 60 (2), 159–166. doi:10.1016/s0266-3538(99)00115-3
- Lindeberg, T. (1998). Edge detection and ridge detection with automatic scale selection. *Int. J. Comput. Vis.* 30, 117–156. doi:10.1023/a:1008097225773
- Malhan, R. K., Kabir, A. M., Shembekar, A. V., Shah, B., Gupta, S. K., and Centea, T. (2018). "Hybrid cells for multi-layer prepreg composite sheet layup," in Proceedings of the 2018 IEEE 14th International Conference on Automation Science and Engineering (CASE) (IEEE), 1466–1472.
- Mersmann, C. (2011). Industrializing metrology—machine vision integration in composites production. *CIRP Ann.* 60 (1), 511–514. doi:10.1016/j.cirp.2011.03.056
- Muntoni, A., and Cignoni, P. (2021). *PyMeshLab*. Zenodo.
- Pasco, C., Khan, M., and Kendall, K. (2019). A novel discrete method of shear angle measurement for in-plane shear properties of thermoset prepreg using a point-tracking algorithm. *J. Compos. Mater.* 53 (14), 2001–2013. doi:10.1177/0021998318813193
- Schommer, D., Duhovic, M., Hoffmann, T., Ernst, J., Schladitz, K., Moghiseh, A., et al. (2023). Polarization imaging for surface fiber orientation measurements of carbon fiber sheet molding compounds. *Compos. Commun.* 37, 101456. doi:10.1016/j.coco.2022.101456
- Song, S., Jing, J., and Cheng, W. (2022). Online monitoring system for macro-fatigue characteristics of glass fiber composite materials based on machine vision. *IEEE Trans. Instrum. Meas.* 71, 1–12. doi:10.1109/tim.2022.3151142
- Stender, S., Magura, N., Fischer, K., and Emonts, M. (2019). Function-orientated production of FRP components. *Lightweight Des. Worldw.* 12 (1), 18–25. doi:10.1007/s41777-018-0065-1
- Wilhelmsen, C. A., and Ostrom, L. T. (2016). IEEE, 316–322. Remote aircraft composite inspection using 3D imaging. Proceedings of the 2016 9th International Conference on Human System Interactions (HSI) July 2016. Portsmouth, UK
- Zhou, Q. Y., Park, J., and Koltun, V. (2018). *Open3D: A modern library for 3D data processing*. arXiv preprint arXiv:1801.09847.



## OPEN ACCESS

## EDITED BY

Veronique Michaud,  
Swiss Federal Institute of Technology  
Lausanne, Switzerland

## REVIEWED BY

Xingzhe Wang,  
Lanzhou University, China  
Remko Akkerman,  
University of Twente, Netherlands

## \*CORRESPONDENCE

A. J. de Wit,  
✉ Bert.de.Wit@nlr.nl

RECEIVED 31 January 2023

ACCEPTED 12 April 2023

PUBLISHED 27 April 2023

## CITATION

de Wit AJ, van Hoorn N, Straathof LS and  
Vankan WJ (2023), Numerical simulation  
of inductive heating in thermoplastic  
unidirectional cross-ply laminates.  
*Front. Mater.* 10:1155322.  
doi: 10.3389/fmats.2023.1155322

## COPYRIGHT

© 2023 de Wit, van Hoorn, Straathof and  
Vankan. This is an open-access article  
distributed under the terms of the  
[Creative Commons Attribution License](#)  
(CC BY). The use, distribution or  
reproduction in other forums is  
permitted, provided the original author(s)  
and the copyright owner(s) are credited  
and that the original publication in this  
journal is cited, in accordance with  
accepted academic practice. No use,  
distribution or reproduction is permitted  
which does not comply with these terms.

# Numerical simulation of inductive heating in thermoplastic unidirectional cross-ply laminates

A. J. de Wit\*, N. van Hoorn, L. S. Straathof and W. J. Vankan

Royal Netherlands Aerospace Centre—NLR, Amsterdam, Netherlands

Thermoplastic Composites can be re-melted allowing them to be joined via welding. This is an attractive alternative to conventional methods that are used to join thermoset composite parts such as mechanical fastening and adhesive bonding. In this work the inductive heating of uni-directional (UD) plies of thermoplastic carbon fiber reinforced polymer (CFRP) laminates is investigated. The focus is on developing a numerical electromagnetic and thermal simulation model that captures the main processes involved in eddy current generation and heat generation, in particular in the interface areas of the UD plies. A measurement technique has been developed to obtain the electric properties of the ply material. Furthermore, to support the modelling of both the induction heating equipment and work piece a field measurement of the magnetic field surrounding the coil and work piece has been developed. Inductive heating experiments were carried out on several thick composite laminate plates with different ply lay-ups to compare and validate the electro-magnetic-thermal simulation model. The measured surface temperatures were compared with the results from the simulation model. The results of this work can be used to support the design of UD-ply laminates to improve their ability to be welded via inductive heating. In addition, the results of this work can be used to assist in pre-determining induction welding equipment settings and heating times.

## KEYWORDS

eddy currents, thermoplastic composites, numerical simulation, electro-magnetic, inductive heating, thermal analysis, joule heating

## 1 Introduction

In the Large Passenger Aircraft Platform 2 of the European R&D program Clean Sky 2, a Multifunctional Fuselage Demonstrator (MFFD) for single aisle aircraft is developed that serves as a platform for examining the full potential of Thermoplastic (TP) composites. This TP composite MFFD shall demonstrate the benefits of integrating various functionalities and help future European airliner production to become faster, greener, and more competitive. Significant weight reduction and thus environmental improvements of aircraft are expected as a result of innovative manufacturing, assembly, and installation processes. These innovations in turn will drive down costs and improve product competitiveness to European aeronautics. The TP composite MFFD consists of an assembly of multifunctional building blocks for the next-generation fuselage and cabin. Development of advanced joining technologies and effective use of materials is necessary to enable a competitive assembly.

One example of such advanced joining techniques is induction welding (Christopoulos, 1990). TP composites can be re-melted allowing them to be joined *via* welding (Mitschang,

et al., 2000). At present, the inductive heating of woven fabric composites is well documented and understood (Yousefpour, et al., 2004). Several heating mechanisms take place in the induction heating of TP carbon fiber reinforced polymer (CFRP). The extent in which each mechanism contributes to the heating process, depends on the material that is heated and the process parameters that are applied. However, a Uni-Directional (UD) CFRP material is more difficult to heat than a weave CFRP material. According to literature (Ahmed, et al., 2006) this could be due to the absence of a current returning path that is naturally embedded in the weave.

The objective of this work is to develop 3D electromagnetic simulation models coupled to 3D thermal simulation models that can provide insight into the inductive heating of UD plies of thermoplastic CFRP laminates. Investigations include the influence of the UD plies and the ply interfaces on the eddy current generation and heat generation inside a UD CFRP laminate when placed inside an electromagnetic field that is induced by a coil. First, basic steps for modelling eddy current generation in a CFRP laminate are introduced. Second, a numerical simulation model based on electromagnetic Finite Element (FE) analysis is introduced. This model is extended with an updated version of a cross-ply interface model (de Wit, et al., 2021) previously developed by the authors. The updated interface model is constructed analogous to a surface implementation (Cheng, et al., 2021) but is extended to a volumetric implementation in this work. Third, electrical conductivity measurements were performed to determine necessary material parameters for the numerical modelling. Furthermore, magnetic field measurements near the induction welding equipment were performed to obtain confidence in the electromagnetic modelling of the setup. Fourth, inductive heating measurements were carried out and compared with the results obtained from the simulation models. Finally, the main conclusions and steps for further research are presented.

## 2 Electromagnetic modelling

For induction welding (IW) of TP CFRP, the electromagnetic properties of the plies and the laminate layout are of key importance for the electromagnetic behavior of the electromagnetic eddy currents that emerge in the CFRP composite laminate. Apart from the magnetic permeability and magnetic permittivity, the electric conductivity of the material is a key determinant for the eddy current density distribution in the laminate. Although these properties depend on temperature and frequency, in the current study these properties are kept constant.

### 2.1 Cross-ply laminates and ply interfaces

Induction heating is accomplished *via* Eddy currents that are generated in the carbon fibers through the magnetic field from a coil. For Eddy currents to occur, closed loops of electrically conductive paths are necessary. Hence, current flowing along the fibers has to be able to return back along another set of fibers. If there is sufficient galvanic connection a conductive loop is created. Typically, in

woven fabrics this is easily established as the fibers make contact in the weave. For UD material this contact is not evident.

If insufficient contact between fibers is present such as in UD material, the only way for current to flow in a closed loop is *via* capacitive coupling through the polymer matrix. For most polymers this can only occur at very high frequencies (several MHz). In such cases additional heat is generated *via* dielectric losses in the polymer. Since equipment that can operate at frequencies of several MHz is not applicable in our setup this form of heating is not considered.

For UD material another option remains to create electrical closed loops. When UD material is stacked at different angles with respect to each other cross-ply interfaces are formed that close the current loop (O'Shaughnessy et al., 2016). This is shown in Figure 1.

At these interfaces contact resistance forms an additional heating mechanism in addition to the Joule Heating coming from the fiber resistance (Kim et al., 2000). These cross-fiber contacts result in a more isotropic in-plane conductivity and increased out-of-plane conductivity in this interface layer. To incorporate this important effect, the augmented electric conductivity properties in the cross-ply interfaces must be included in the FE model.

### 2.2 Cross-ply interface definition

In this work we develop an approach for solid FE modelling of electromagnetic eddy currents in cross-ply laminates including their cross-ply interfaces. To develop the interface concept, we consider a small two-ply laminate sample with arbitrary thickness ( $t$ ), width ( $w$ ) and length ( $L$ ). Furthermore, two interface cases are considered. The first consists of a [0,0] UD laminate and the second of a [0,90] cross-ply laminate. The  $x$ -axis is taken along the two-ply laminate length direction,  $y$ -axis is taken along the two-ply width direction and  $z$ -axis along the thickness of the two-ply thickness direction. Each ply has a total thickness of  $t_{ply}$ . The cross-section is sketched in Figure 2.

In the region around the interface between the plies, a cross-ply interface layer of arbitrary but finite thickness  $t_{int}$  per ply is introduced, see Figure 2. This interface layer is considered to have the augmented anisotropic electric conductivity properties. Furthermore, these properties are taken homogeneous throughout the whole interface. The in-plane conductivities in the interface layer are assumed to result from the combination or mixture of the conductivities of the two plies. The out-of-plane conductivity in the interface layer is taken equal to the out-of-plane conductivity (or resistivity) of the considered cross-ply.

### 2.3 Electric resistances of plies and interface

The anisotropic resistance tensor for each of the two plies (ply 1 and ply 2) in the small laminate sample (recall Figure 2) contains the resistances of each of the two plies in the three directions  $x, y, z$ , see Figure 3.

Hence, the resistances are written as:

$$R_{pi} = [R_{pi,1}^{pi}, R_{pi,2}^{pi}, R_{pi,3}^{pi}], i = 1, 2 \quad (1)$$

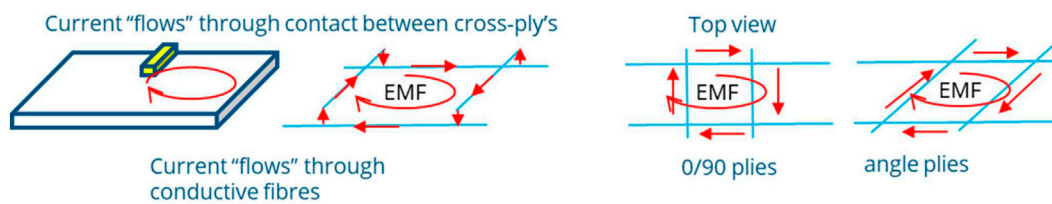


FIGURE 1

Cross-ply's form a closed loop such that current can 'flow' through the plies. EMF stands for electromagnetic field.

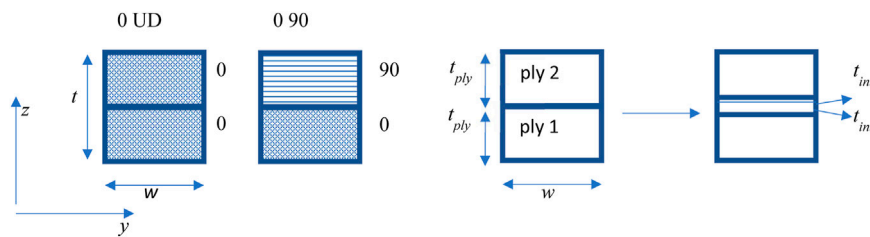


FIGURE 2

Front view of the small 2-ply laminate sample. A UD [0,0] and a cross-ply [0,90] laminate are shown. The 0 fibers are oriented in x-direction. Each ply has a total thickness  $t_{ply}$ . The cross-ply interface layer of arbitrary finite thickness  $t_{int}$  per ply is considered in between the ply. Hence, the interface layer thickness is  $2 \cdot t_{int}$ .

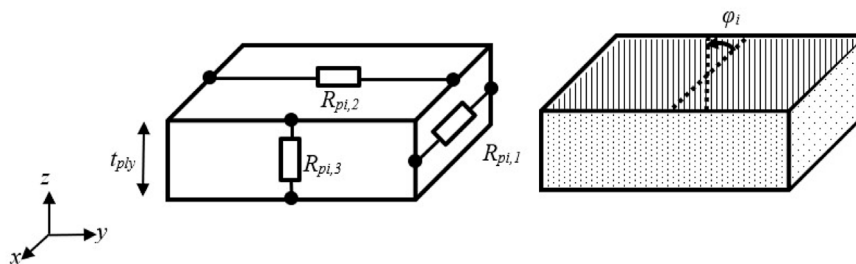


FIGURE 3

Illustration of the anisotropic resistances (left) and fiber orientation expressed by ply angle  $\varphi_i$  (right) for a single ply in the small laminate sample.

In Eq. 1,  $i$  is the ply index and each ply can have arbitrary ply orientation, expressed by a ply angle  $\varphi_i$ . The resistances of a ply in the small laminate sample at an arbitrary ply angle  $\varphi_i$  can be determined by assuming a linear relation between the resistance in fibre direction ( $R_{11}$ ) and the resistance in transverse direction ( $R_{22}$ ) of a single ply, see (Cheng, et al., 2021). In this work however, this relation is considered non-linear:

$$R_{pi,1}^{\varphi_i} = \alpha R_{11} + \beta R_{22}, R_{pi,2}^{\varphi_i} = \beta R_{11} + \alpha R_{22}, i = 1, 2 \quad (2)$$

$$\alpha = (\cos \varphi_i)^2, \beta = (\sin \varphi_i)^2 \quad (3)$$

Since the interface layer has finite thickness (recall Figure 2 right), the total resistance in each direction  $x, y, z$  of the small two-ply laminate sample must be equal to the total resistance of the sample without the interface layer (Figure 2 left). This yields that the resistance of the whole interface is equal to the combined resistance of its components. Hence,

the lower half of the interface that contains the ply 1 properties and the upper half of the interface that contains the ply 2 properties.

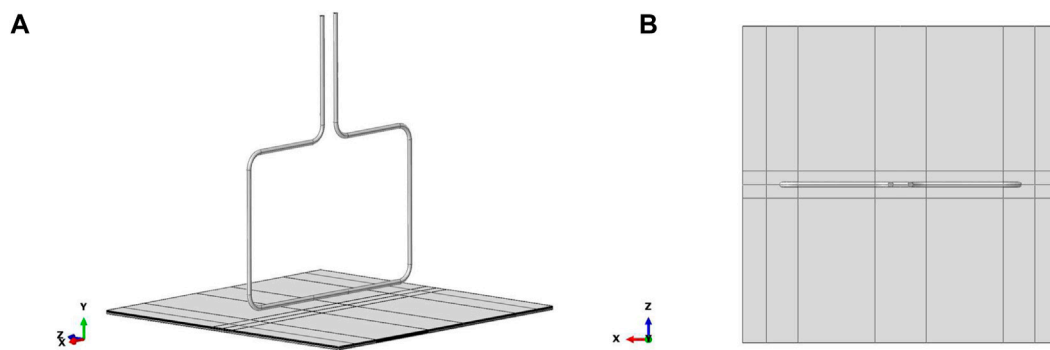
Consequently, the in-plane resistances of the interface, i.e., in  $x, y$  directions, are composed of the parallel resistances of the interface components:

$$R_{ij} = \frac{R_{i1,j} R_{i2,j}}{R_{i1,j} + R_{i2,j}}, j = 1, 2 \quad (4)$$

Here  $R_{i,j}$  is the resistance of the whole interface in direction  $j$ , and  $R_{i1,j}$  is the lower interface component resistance and  $R_{i2,j}$  is the upper interface component resistance, in direction  $j$ , with  $j = 1, 2, 3$  that refers to the  $x, y, z$  directions.

The out-of-plane resistance of the interface, i.e., in  $z$  direction, is composed of the serial interface component resistances, and an additional ply-contact resistance. In (Xu, et al., 2018) this ply-





**FIGURE 4**  
(A) Overall lay-out of the coil and laminate. (B) Top view of the coil above the laminate.

contact resistivity (denoted by  $\rho_c$ ) is determined experimentally for two-ply laminate samples.

## 2.4 Numerical simulation model electromagnetic field

The electromagnetic simulations are carried out in the FE package Abaqus (Simulia, 2023). In Abaqus a time-harmonic eddy current analysis procedure is used, which assumes that a time-harmonic excitation such as an alternating current in the coil results in a time-harmonic electromagnetic response of electric and magnetic field with the same frequency everywhere in the domain.

The equations involved solving the inductive heating of thermoplastic material are presented in generic terms following the outline in (Chen, 2016). The electric and magnetic fields are governed by Maxwell's equations

$$\nabla \cdot \mathbf{E} = \rho_E; \nabla \cdot \mathbf{B} = 0; \nabla \times \mathbf{E} = -\frac{\partial \mathbf{B}}{\partial \tau}; \nabla \times \mathbf{H} = \mathbf{J} + \frac{\partial \mathbf{D}}{\partial \tau} \quad (5)$$

Where  $\rho_E$  the electric charge density,  $\mathbf{E}$  the electric field,  $\mathbf{B}$  the magnetic induction,  $\mathbf{D}$  the electric flux density,  $\mathbf{J}$  the electric current density,  $\mathbf{H}$  the magnetic field and  $\tau$  corresponds to time. The following constitutive relations are substituted:

$$\mathbf{D} = \epsilon_0 \epsilon_r \mathbf{E}; \mathbf{B} = \mu_0 \mu_r \mathbf{H}; \mathbf{J} = \sigma \cdot \mathbf{E} \quad (6)$$

Where  $\epsilon_0$  absolute permittivity,  $\epsilon_r$  relative permittivity,  $\mu_0$  absolute magnetic permeability,  $\mu_r$  relative permeability and  $\sigma$  the conductivity tensor.

The joule heating is computed via:

$$\dot{Q} = \mathbf{J}^T \cdot \bar{\sigma}^{-1} \cdot \mathbf{J} \quad (7)$$

This joule heating is used to calculate the temperature distribution of the thermoplastic laminate by the heat equation:

$$\rho c_p \frac{\partial T}{\partial \tau} - \nabla \cdot (\bar{\lambda} \nabla T) = \dot{Q} \quad (8)$$

Where  $\rho$  is the density,  $c_p$  the specific heat coefficient,  $\lambda$  the thermal conductivity tensor.

In the case of eddy current analysis it is typical that large portions of the model consist of electrically non-conductive regions such as air. In such case the problem becomes ill-conditioned and Abaqus uses an iterative solution technique to prevent a negative impact on the computed electric and magnetic fields. In some cases this technique may not work and Abaqus advises to add artificial electrical conductivity to convert to a solution. It is recommended to set this artificial conductivity about five to eight orders of magnitude less than that of the conductors in the model. As will be shown in the next section, the electric conductivity in ply direction is an order of magnitude four higher than in the non-ply direction. Hence, it is difficult to add artificial conductance and not affect the computed results in out-of-ply directions in Abaqus.

### 2.4.1 Model geometry, load and boundary conditions

To capture 3D effects of the induction setup a 3D FEA model is constructed. The overall lay-out of the coil and laminate is shown in Figure 4. A top view of the lay-out showing the coil centered above the laminate is shown in Figure 4B.

The distance between coil and laminate is 14 [mm]. The coil cross section has an outer diameter of 6.35 [mm] and inner diameter of 4.35 [mm]. The overall dimensions of the coil and its position with respect to the laminate are shown in Figure 4, Figure 5.

To reduce the computational effort and make use of symmetry conditions in the model only 1/4th of the model is included in the Abaqus model. Therefore, the symmetry plane parallel to the coil winding is modeled as a perfect magnetic conductor, see Figure 6.

The boundary condition for the parallel symmetry plane is written as:

$$\mathbf{n} \times \mathbf{H} = 0 \quad (9)$$

This corresponds to the assumption that the current field is mirrored in this symmetry plane.

Perpendicular to the coil, the symmetry plane is modelled as a perfect magnetic insulator, see Figure 6. The boundary condition is written as:

$$\mathbf{n} \times \mathbf{A} = 0; \nabla \times \mathbf{A} = \mathbf{B} \quad (10)$$

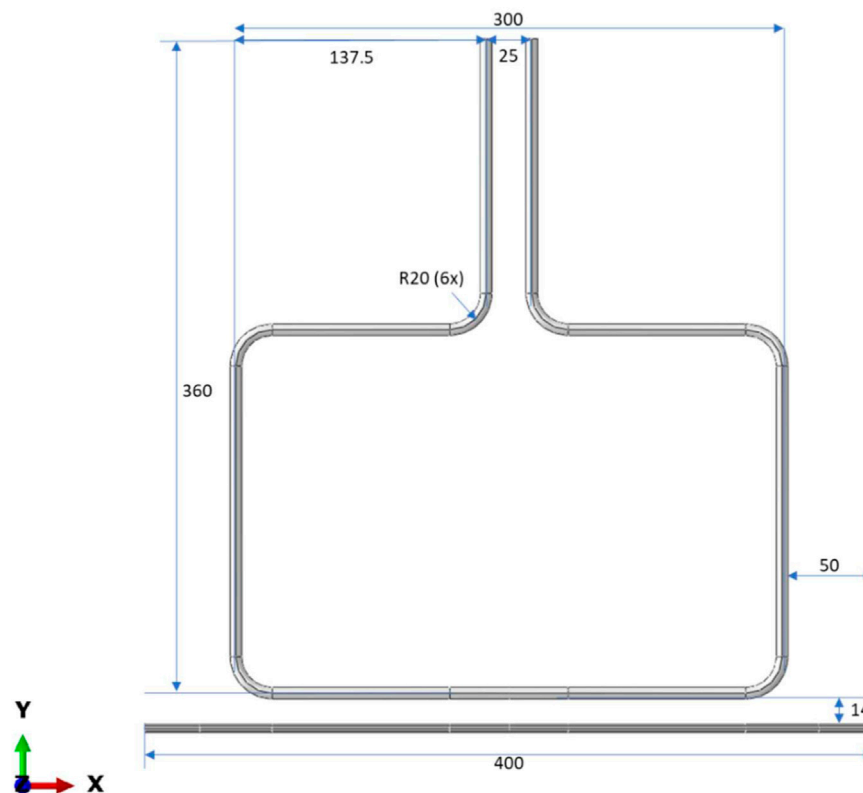


FIGURE 5

Dimensions of the coil in [mm] and position with respect to the laminate.

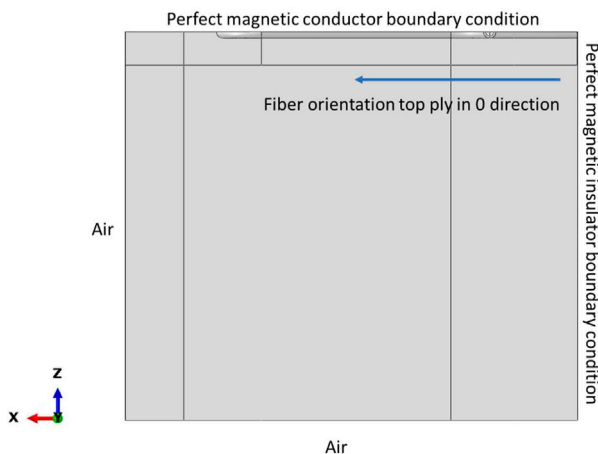


FIGURE 6

Model of 1/4th of the geometry. On the symmetry plane a perfect magnetic conductor boundary condition is applied. On the anti-symmetry plane a perfect magnetic insulator boundary condition is applied. At the two remaining edges of the plate a volume of air is modelled.

Which corresponds to the assumption that the magnetic field normal to the symmetry plane equals zero and the current cannot have a tangential component.

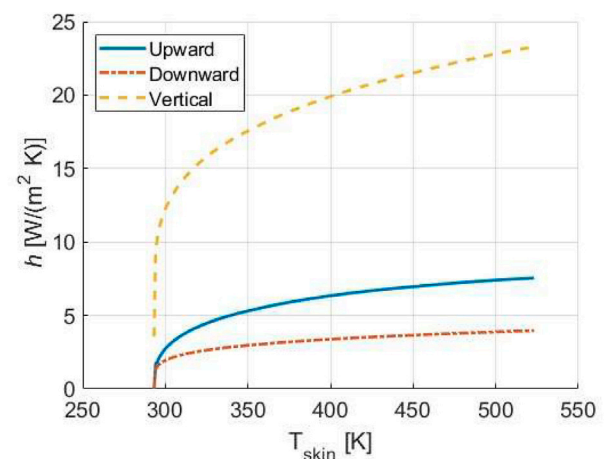


FIGURE 7

Convection coefficients used on the top and bottom surface of the plate and the external sides exposed to the surrounding air.

Because the laminates considered in this work have a ply orientation of  $0^\circ$  or  $90^\circ$  these symmetry conditions can also be applied to the composite laminate. Furthermore, surrounding the coil and laminate a box of air is modelled with dimensions  $400 \times 400 \times 500$  mm. The external surfaces of this box of air are assumed magnetic insulators:

**TABLE 1** Material properties for the air, coil and AS4D/PEKK taken from (Grouve, et al., 2020) unless indicated otherwise. Furthermore, dimensions and applied loading that were applied to the model.

Property	Symbol	Value
Ply thickness		0.138 [mm]
Number of plies		36 [-]
Laminate surface area 1/4th model		200 × 200 [mm <sup>2</sup> ]
Laminate thickness		5 [mm]
Coil cross-section outer diameter		6.35 [mm]
Coil cross-section inner diameter		4.35 [mm]
Coil distance to laminate		14 [mm]
Coil applied frequency		194 [kHz]
Coil applied current		199.5 [A]
Absolute permittivity of Air, Coil, C/PEKK ply	$\epsilon_0$	8.85E-12 [F/m]
Relative electric permittivity of C/PEKK ply	$\epsilon_r$	3.7 [-]
Relative electric permittivity of Air, Coil	$\epsilon_r$	1 [-]
Magnetic permeability of Air, Coil, C/PEKK ply	$\mu_0$	4 $\pi$ /1E7 [H/m]
Relative magnetic permeability of Air, Coil, C/PEKK ply	$\mu_r$	1 [-]
Electrical conductivity of Air, Coil	$\sigma$	1 [S/m]
Initial and room temperature	$T_a$	23 [°C]
Heat transfer coefficient	$h$	See Figure 7
Thermal conductivity	$\lambda$	See Figure 8
Density	$\rho$	See Figure 9
Specific heat coefficient	$c_p$	See Figure 10
Electrical conductivity of C/PEKK Longitudinal ply direction Off axis in-plane direction Off axis the thickness direction	$\sigma_{11}$ $\sigma_{22}$ $\sigma_{33}$	33,500 [S/m] (NLR Section 3.1) 8.865 [S/m] 0.055 [S/m]
Electrical conductivity of C/PEKK interface [0,90]]		
Longitudinal and off-axis	$\sigma_{11}$	16,752 [S/m] (computed Section 2.3)
Through thickness	$\sigma_{22}$	0.27 [S/m] (computed Section 2.3)
Laminate lay-up		UD [0] <sub>36</sub> Cross-ply [0,90] <sub>9s</sub> Cross-ply grouped [0 <sub>3</sub> ,90 <sub>3</sub> ] <sub>3s</sub>

$$\mathbf{n} \times \mathbf{H} = \mathbf{0} \quad (11)$$

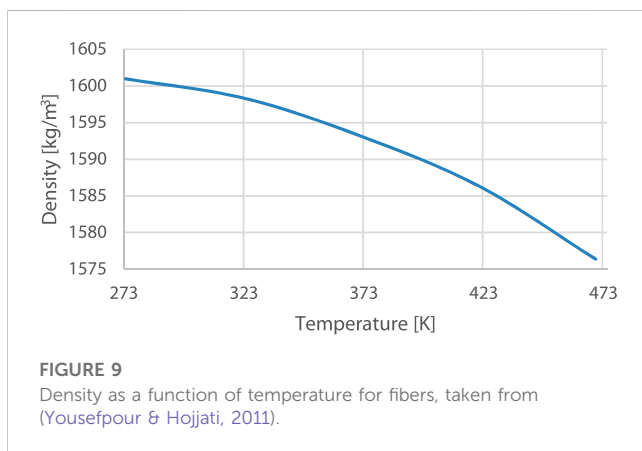
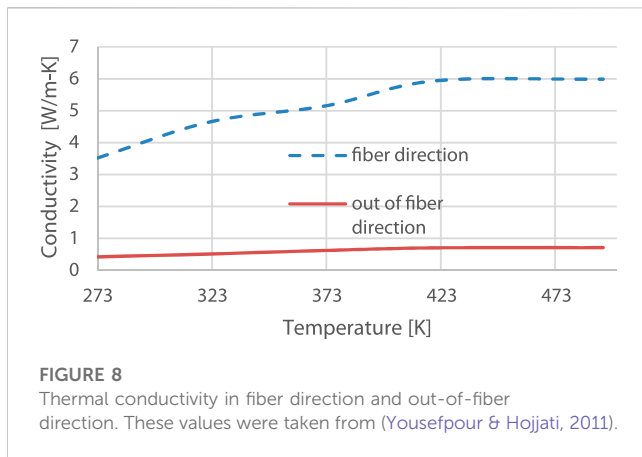
For the thermal simulation model only the geometry of the thermoplastic plate was considered. Hence, the boundary conditions with respect to air were modelled *via* a film coefficient:

$$-\lambda_n \frac{\partial T}{\partial \mathbf{n}} = h(T_{skin} - T_a) \quad (12)$$

Where  $h$  is the so-called film coefficient and  $T_a$  the ambient or in this case room temperature.  $\lambda_n$  is the thermal conductivity along the unit normal on the surface  $\mathbf{n}$ . The convective heating coefficients for each surface of the plate are computed using the approach outlined

in (Moser, 2012). For completeness the computed coefficients are shown in Figure 7.

The one-quarter model consists of a composite laminate with dimensions 200 [mm]x200 [mm] and 36 plies. Each ply has a thickness of 0.138 [mm]. Hence, the laminate thickness equals 5 [mm]. The coil consists of a single rectangle of which one-quarter is modelled. The coil is assumed to have homogenous material properties. To prevent Abaqus to calculate eddy currents for the volume of the coil that are then subtracted from the applied current load a conductivity of 1 [S/m] is used. Furthermore, a current of 199.5 [A] is applied



in circumferential direction of the coil at a frequency of 194 [kHz].

## 2.4.2 Material properties

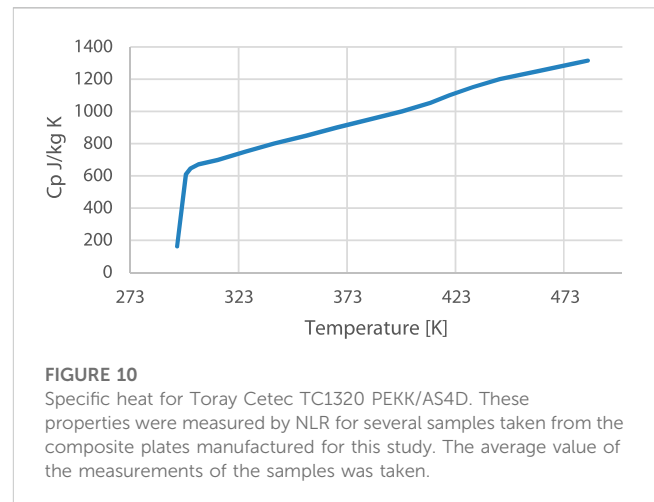
The material properties that are used in the present model for the air, coil and laminate are listed in Table 1.

The air surrounding the 1/4th coil and laminate is a box of 400 [mm] x 400 [mm] x 500 [mm]. Each ply is modeled separately and considered an homogenous anisotropic sheet. For meshing two elements are used in thickness direction for each ply, see Figure 11.

The whole model comprises 2.3 M EMC3D8 elements. A larger model did not fit on our current available computer hardware. Furthermore, in previous work (de Wit, et al., 2022) the mesh density that corresponds to this number of elements was found sufficient to capture both magnetic field and eddy current field. The interfaces between plies are taken as 10% of ply thickness. The interfaces consume 2 elements in thickness direction from each ply except for top and bottom ply that only assign one element to the interface.

## 3 Experiments to support the modelling

Although material data sheets include recognized standards for mechanical and thermal material properties, electrical properties are



less common to be included. For UD material, an additional property involving the cross-ply electrical properties is application specific. Furthermore, to obtain confidence in the electromagnetic modelling field measurements were done on the induction heating setup to compare and validate the modelling approach.

## 3.1 UD ply electrical conductivity measurements

The anisotropic electrical conductivity of a single ply was characterized by measuring the resistance as outlined in (de Wit, et al., 2022). For completeness, the procedure is summarized here. A measurement in the longitudinal, transverse, and through-thickness direction was performed. For the experimental setup unconsolidated strips of UD tape material with a thickness of 0.21 [mm] were clamped between electrodes. For the resistance measurements in longitudinal direction (i.e., fibre direction) a 6.35 [mm] wide and 1,000 [mm] long specimen was used. For the resistance measurement in the transverse and through-thickness direction shorter specimens of 20 [mm] were used and the clamping devices were adjusted.

Five samples were used for each measurement and the Direct-Current (DC) resistance, as well as, the Alternating-Current (AC) impedance. The impedance was measured at several frequencies, that is: 50 [Hz], 25 [kHz], 50 [kHz], 75 [kHz], and 100 [kHz]. Each specimen was measured at two instances to exclude the influence of the test setup and clamping procedure. By using the specimen dimensions the resistance in Ohm was transformed to conductivity in [S/m].

The AC conductivity measurements were extrapolated to the frequency of the induction welding simulation (for this measurement, 384 [kHz]). The results of the longitudinal conductivity measurements were compared with values found in the literature for AS4D/PEKK. For two types of AS4D/PEKK Table 2 shows the electrical conductivity values compared to values obtained from literature.



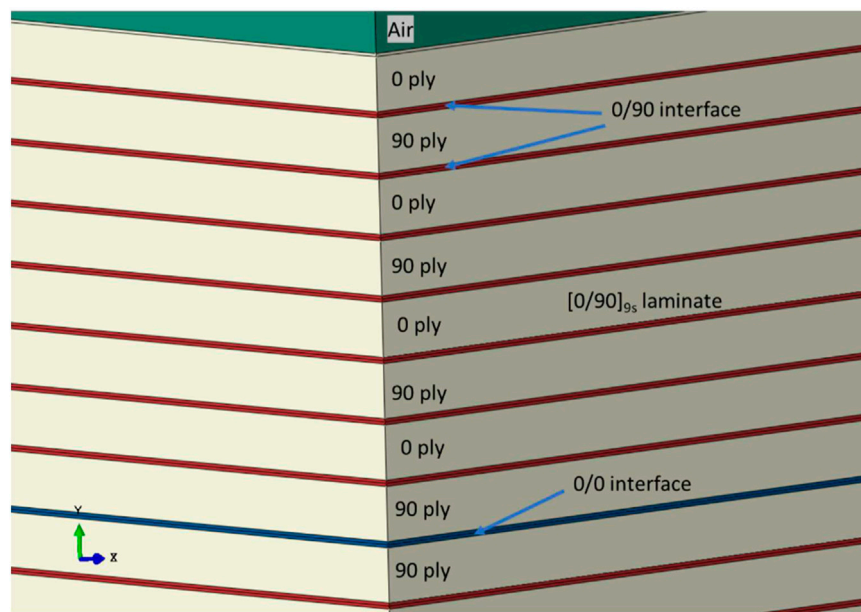


FIGURE 11

Modelling of plies and interfaces for a  $[0/90]_{9s}$  laminate. Each interface layer consists of a part of the top ply and a part of the bottom ply.

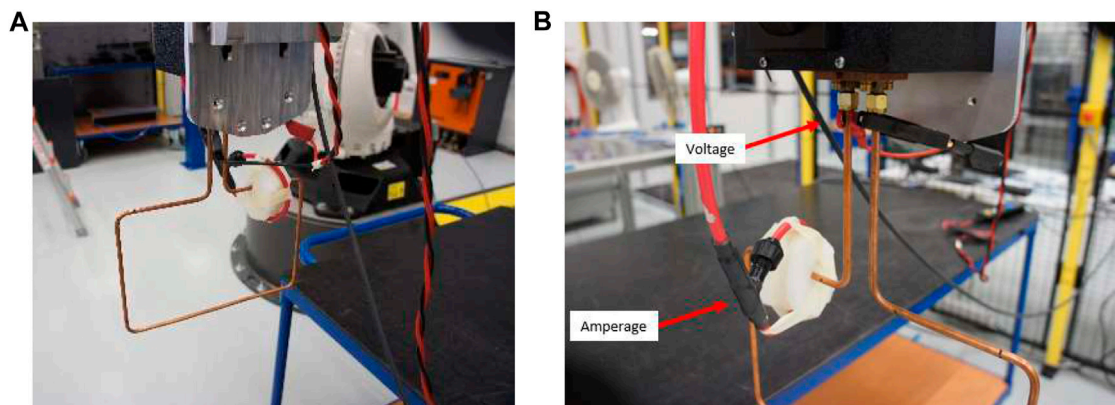


FIGURE 12

(A) Measurement of the Voltage and (B) Amperage applied to the coil.

The values found are in close agreement with those obtained by (Grouve, et al., 2020) (Buser, et al., 2022). For the interface modelling conductivity properties have to be assigned to the interface elements as well. Such values can be determined *via* a similar measuring approach as outlined. Unfortunately, the measured electrical conductivity properties showed little consistency. It is the intention of the authors to repeat these measurements in future works.

## 3.2 Experimental magnetic field measurements

To obtain confidence in the numerical electromagnetic simulations, measurements were performed on the magnetic

field surrounding the induction coil to compare the values with those obtained through simulation. The magnetic field was measured near the induction coil in the presence of air with no workpiece, with an aluminum workpiece, and a composite workpiece. In addition, the applied electrical load that is necessary for the FEA model was verified by measuring the current in the induction coil.

### 3.2.1 Experimental setup

Induction coils are designed with a specific application in mind. Therefore, many shapes and forms can be found for which different electromagnetic fields are constructed. In addition, the eddy currents that are generated in the workpiece are dependent on the coil shape and placement. Induction coils applied for

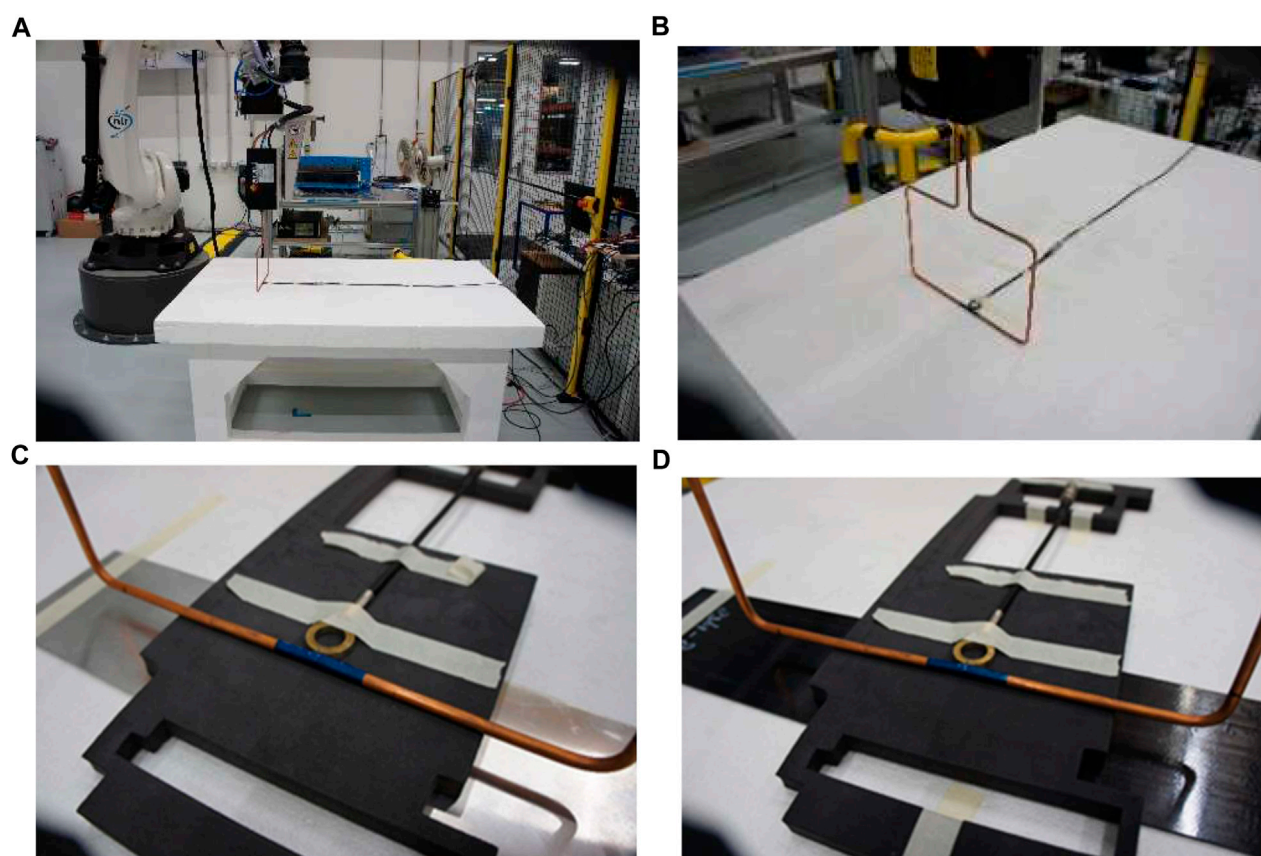


FIGURE 13

(A) The test setup for measuring the magnetic field around the induction coil. (B) Coil used to measure the magnetic field surrounding the induction coil and workpiece. Measurement of the magnetic field strength above the aluminum (C) and composite (D) plate.

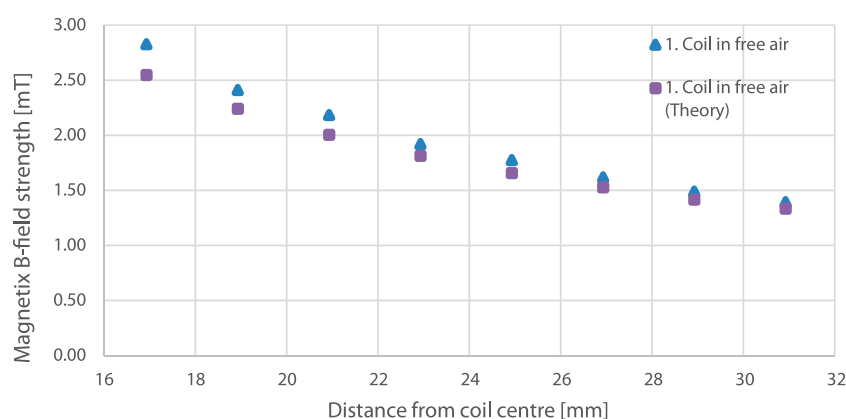


FIGURE 14

Magnetic B-field strength that was measured and the theoretical values computed with Eq. 13.

studying inductive heating in composites, for instance (Grouve, et al., 2020), (Cheng, et al., 2021), usually have a different orientation and shape than the inductive heating equipment at NLR that was designed for welding long and slender structures. The inductive heating equipment corresponds to a setup

developed by KVE Composites Group (Kok & Van Engelen). The generator consists of an Ambrell EASYHeat 83,100 LI that generates 10 [kW] at a frequency in the range of 150–400 [kHz]. The equipment is mounted on a KUKA KR 240 R2700 PRIME robot arm.

**TABLE 2** Electrical conductivity properties found in literature and measured by NLR for AS4D/PEKK.

Solvay AS4D/PEKK	
o(Grouve, et al., 2020) $\sigma_{11}$	31,307 $\pm$ 50 [S/m]
o(Buser, et al., 2022) $\sigma_{11}$	36,900 [S/m]
oThis work $\sigma_{11}$	36,399 $\pm$ 632 [S/m]
Toray Cetec TC1320 AS4D/PEKK	
o(Grouve, et al., 2020) $\sigma_{11}$	18,900 $\pm$ 180 [S/m]
oThis work $\sigma_{11}$	33,468 $\pm$ 803 [S/m]

To capture the main characteristics of the electromagnetic field a long slender coil was used (dimensions listed in 2.4.1) that the authors expect to create a uniform field over a larger distance in the workpiece, see [Figure 12A](#).

An operator of the induction equipment has the option to choose the coil amperage. Based on this amperage, the induction machine applies an optimal frequency. It is unknown if the applied current matches the actual current in the coil. For electromagnetic simulations in Abaqus ([Simulia, 2023](#)) it is necessary to confirm the current in the induction coil. Therefore, the amperage and voltage in the coil were measured with a setup as shown in [Figure 12B](#).

After the current measurements the coil was placed on a Styrofoam table that does not interfere with the magnetic field. For measuring the magnetic field a probe was used. The circular probe is made of a non-magnetic material (i.e., brass). The probe has an inner diameter of approximately 15 [mm] and a thickness of 5 [mm]. Using a known constant magnetic field the probe has been calibrated.

In order to measure the magnetic field close to the coil the magnetic field probe is positioned next to the coil as shown in [Figures 13A, B](#).

The probe was connected to an oscilloscope for data acquisition in the frequency domain. The magnetic field that was captured inside the magnetic field probe was measured.

For the measurements with aluminium plate and composite plate a non-conductive material was placed in between the coil and workpiece to fix the positioning of the field probe, see [Figures 13C, D](#). As a result, the coil and the probe have a constant spacing of 14 [mm] with the workpiece.

For the measurements in free air, with the aluminium plate, and with the composite plate the coil was moved horizontally in steps of 2 mm away from the probe. At each step the induction welding equipment was activated for 2 seconds to minimise heating of the

workpiece. In this time, a measurement was taken and the frequency response from 100 [kHz] to 300 [kHz] was logged.

From basic electromagnetism theory, see [Equation 13](#), it is known that magnetic flux density (B) decreases for increasing distance from the coil (r).

$$B = \frac{\mu_0 I}{2\pi r} \quad (13)$$

where  $\mu_0$  is absolute magnetic permeability and  $I$  is applied current.

Therefore, the magnetic field decreases within the probe inner surface. To compare the theoretical values, the probe measurements (and in the next section the simulation results) have to be recomputed to represent the average value over the probe inner area. It is assumed that the magnetic field is uniform in the length direction of the coil and the simulation and theoretical data is averaged using a circular integral corresponding to the probe inner diameter.

### 3.2.2 Measurement results and discussion

The voltage and amperage measurements were performed prior to the magnetic field measurement. Here the input amperage was increased from approximately 50 [A] to 200 [A]. The measured RMS values of the amperage and voltage are listed in [Table 3](#).

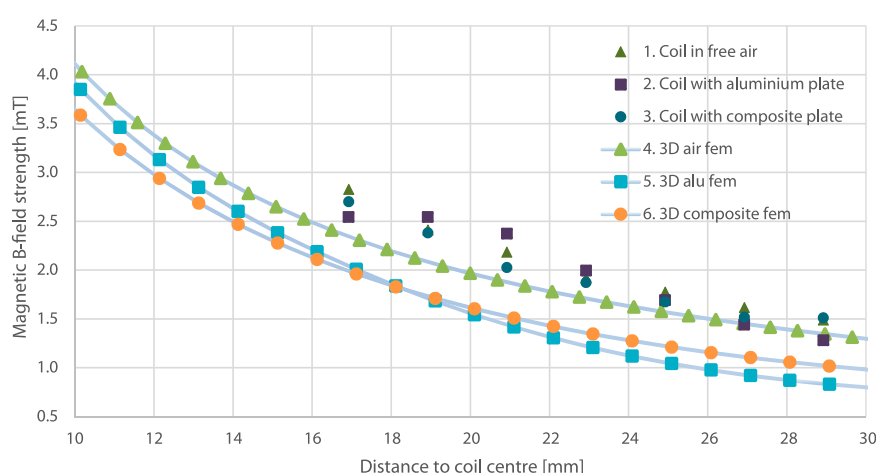
From [Table 3](#) it is observed that the optimal frequency set by the induction welding equipment decreases for increasing amperage. This is because at higher amperages a lower frequency is required to obtain the same induction power. The measured RMS amperage is slightly lower compared to the input amperage. From the detailed time response of the amperage signal it is observed that variations in time could be the cause of these differences.

For the magnetic B-field measurements an input amperage of 199.5 [A] at 193 [kHz] is used. The accuracy of the magnetic B-field measurements is determined by comparing the theoretical values of the magnetic B-field strength with the measured values, see [Figure 14](#). Here the theoretical values are averaged over the probe inner diameter.

The results are in good agreement and follow the same trend. A difference of 4%–11% between the theory and the experiment is observed for each measurement. There are several aspects that could be the cause of this difference. Firstly, the theory is based on Direct-Current (DC) while for the experiment Alternating-Current (AC) at a relatively high frequency is used. Secondly, the probe is calibrated in a constant AC magnetic field that differs from the varying magnetic field. Despite theoretically correct averaging of the theoretical data over the inner area of the probe this could differ from reality. Thirdly, a slight position inaccuracy of the probe (e.g., in the order of 0.5 [mm]) will significantly affect the result, especially

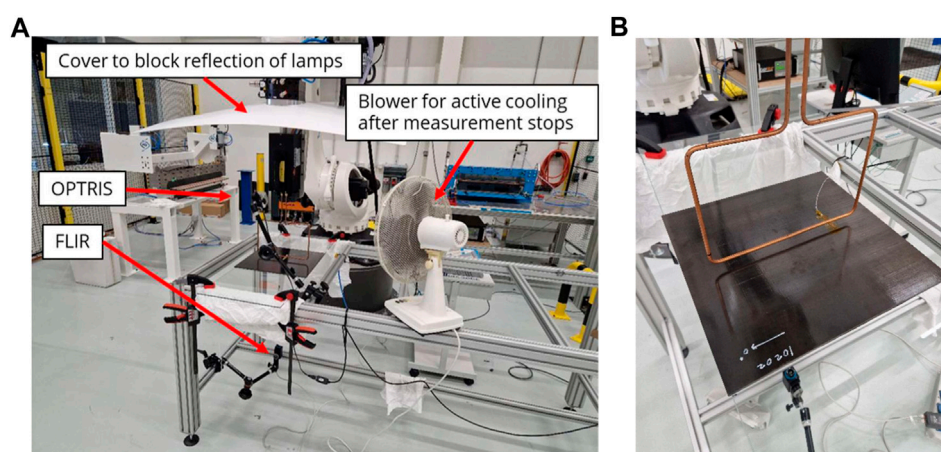
**TABLE 3** RMS values of applied amperage and frequencies as measured.

Input amperage [A]	Input frequency [kHz]	Measured RMS amperage [A]	Measured RMS voltage [V]
50.4	201	43.2	45.0
100.8	200	91.0	94.3
149.1	195	141.6	138.2
199.5	193	191.0	183.2



**FIGURE 15**

Magnetic B-field strength computed at a distance from the coil using a 3 D FEA simulation model that was introduced in Section 2.4 *versus* the measured values.



**FIGURE 16**

Measurement setup for the inductive heating measurements. (A) Key components of the measurement setup. (B) White marking on the laminate corresponds to the 0° ply orientation. Furthermore, the positioning of the thermocouple below the coil can be seen.

for the measurements closest to the coil. Because the coil that was used to measure the magnetic field strength has a certain thickness the measurements could not be conducted closer to the coil than 17 [mm].

The results of the magnetic B-field strength measurements and the simulated values *via* FEA are shown in Figure 15.

The measurements in air and with a composite workpiece are in good agreement. As can be expected the composite plate has a negligible effect on the magnetic field. The measured magnetic B-field strength for the aluminium plate is lower than expected near the coil. The reason has not been determined but may be due to the averaging of B-field strength values of the field probe area that was used to compute the measurement values. Furthermore, as can be seen from the results plotted in Figure 15 the simulated values for the 3D electromagnetic model are close to the values measured near the coil. It is expected that further mesh refinement would improve

these results as was shown in previous work with a 2 D model (de Wit, et al., 2022).

## 4 Experiments to validate the modelling

Inductive heating measurements were carried out to obtain data to compare the numerical simulation model results with measurements on equipment that captures key aspects of our induction welding equipment.

### 4.1 Experimental setup

The inductive heating measurements were performed on three square plates. The material consisted of Toray



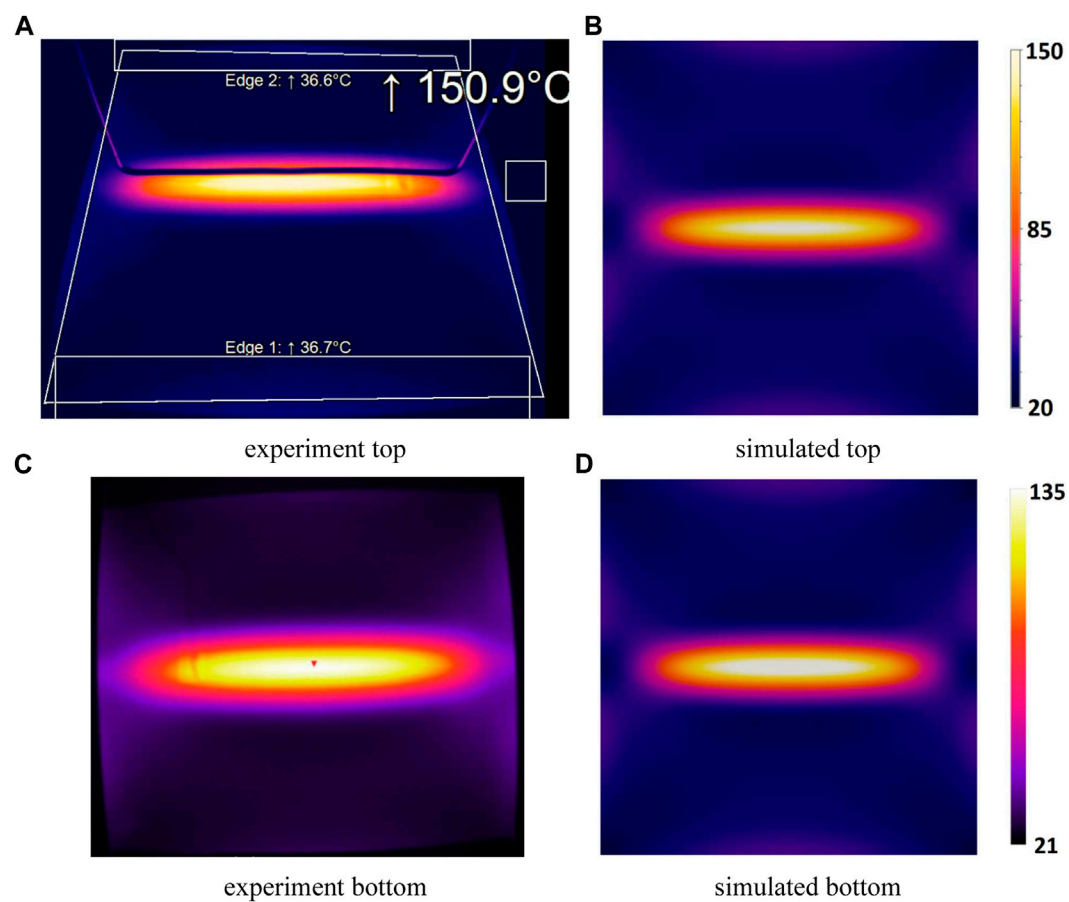


FIGURE 17

Temperature contour plot for the cross ply  $[0,90]_{9s}$  plate (A1). (A–C) correspond to measurements whereas (B–D) correspond to simulated values.

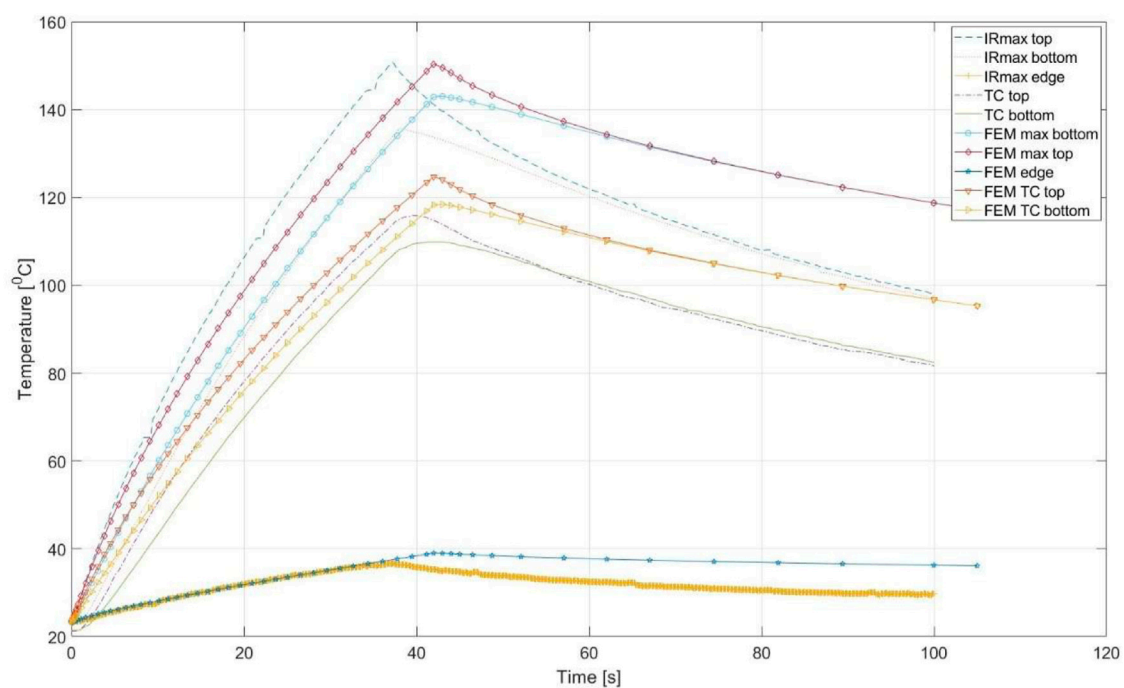


FIGURE 18

Temperature measurements cross-ply  $[0,90]_{9s}$  plate (A1). The surface temperatures were measured via Optris (top surface), FLIR (bottom surface) and two thermocouples placed 100 [mm] from the edge underneath the coil. The FEM values were taken from the simulation model.



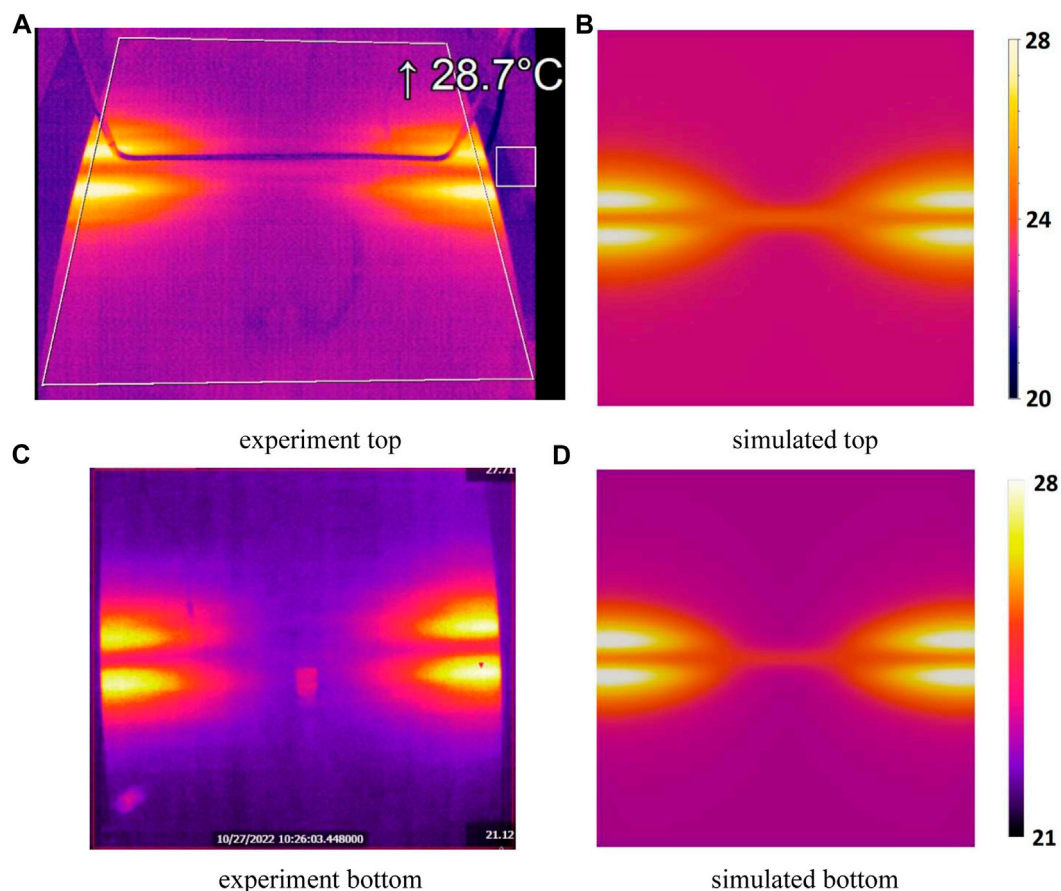


FIGURE 19

Temperature contour plot for the UD  $[0]_{36}$  plate (A2). (A–C) Some increment in temperature is observed near the edges of the plate. (B–D) Temperature contour plot from the simulations.

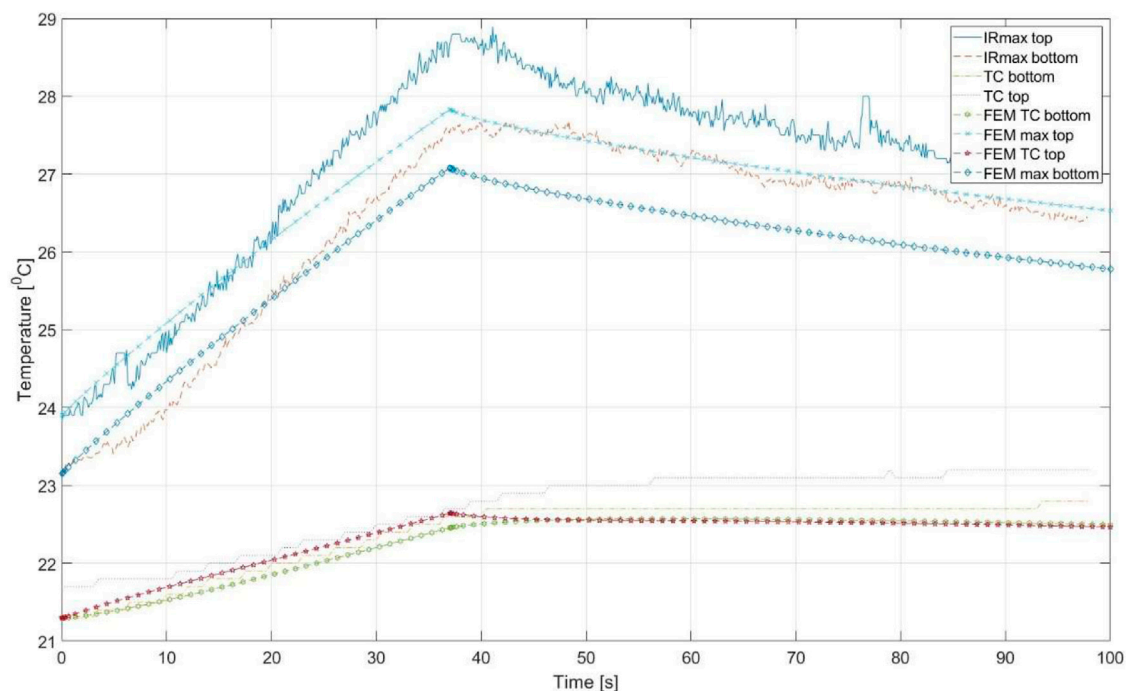
TC1320 PEKK AS4D, the ply thickness was approximately 0.138 [mm] and the global dimensions were 400 [mm] x 400 [mm] x 5 [mm]. Three different lay-ups were manufactured, plate A2, a Uni-Directional (UD)  $[0]_{36}$ , plate A1, a cross ply  $[0,90]_{9s}$  and plate A3, a cross-ply grouped  $[0_3,90_3]_{3s}$ . The three plates were manufactured via Automatic Fibre Placement (AFP) as three sub packages of 500 [mm] x 500 [mm] UD plates. After AFP these plates were then consolidated inside an autoclave at 8 [bar].

Each plate was placed inside the inductive heating equipment and was supported at the edges by a glass plate. Hence, except for a 30 [mm] support on either side the entire composite plate was hanging freely in the air. The coil was placed at a distance of 14 [mm] above the surface of the plate and was aligned with the center of the plate as shown in Figure 16. The  $0^\circ$  direction was aligned with the length direction of the coil.

The surface temperature of the plate was measured by two infrared (IR) cameras. An Optris PI 640 measured the top of the plate and a FLIR A35 the bottom of the plate. The top camera was positioned at an angle with the plate surface to ensure visibility under the coil, while the bottom camera was

positioned perpendicular to the bottom surface. Furthermore, two thermocouples were located at top and bottom at 100 [mm] from the edge of the plate and below the coil (200 [mm] from the other edge). The coil was centred above the plate, 200 [mm] from the far edges and 50 [mm] on either side of the closest edges.

To compare the temperature measurements with the results from the simulation the plate was heated up to a temperature where no melting or other thermal effects that are not part of the modelling were expected. The plate was therefore heated from room temperature (approx. 22  $^\circ\text{C}$ ) until 150  $^\circ\text{C}$  and then cooled down to approximately 100  $^\circ\text{C}$ . After reaching 100  $^\circ\text{C}$  the measurement was stopped and a fan was turned on to speed up the cooling process until room temperature. The necessary equipment settings were determined using the  $[0,90]_{9s}$  plate which reached 150  $^\circ\text{C}$  after 37 [s] and then was passively cooled down for another 60 [s] via natural convection. These settings were applied to the other plates as well. A frequency of approximately 194 [kHz] and an Amperage of 199.5 [A] was used for this heating process and was used throughout the other heating experiments as well.



**FIGURE 20**  
Recorded and computed temperatures for the UD  $[0]_{36}$  plate (A2).

## 4.2 Measurement and simulation results and discussion

A1 Cross ply  $[0,90]_{9s}$  After some tuning for the top and bottom of each plate a contour plot of the measured temperatures was created and a similar colour spectrum was used for the simulated values. The results are shown in Figure 17.

As can be seen from Figure 17 (a) and (c), not only the plate underneath the coil increases in temperature but also the edges of the plate rise in temperature via a pattern that is typical for this plate geometry and coil. Using the FLIR software for the bottom of the plate we did not manage to create more contrast. Still some edge heating can be observed. The contour plots taken from the simulated plate shown in Figure 17 (b) and (d) are in good agreement with the results of the experiments.

From each of the surface measurements the maximum temperatures were taken. In addition, the maximum temperature at the edges further away from the coil were taken and combined in a graph together with the measurements from the thermocouples and the FEM calculated values. The results are shown in Figure 18.

The Optris camera recalibrates several times during the measurement and therefore a jump in the recorded temperature is visible. As can be seen from Figure 18 the Optris and FLIR camera measure immediately the turning off of the induction coil whereas the thermocouples require some time to heat up and cool down before measuring a change in temperature. Therefore the peak temperature is a smooth curve on the thermocouple graph rather than the sudden jump that is seen with the IR cameras.

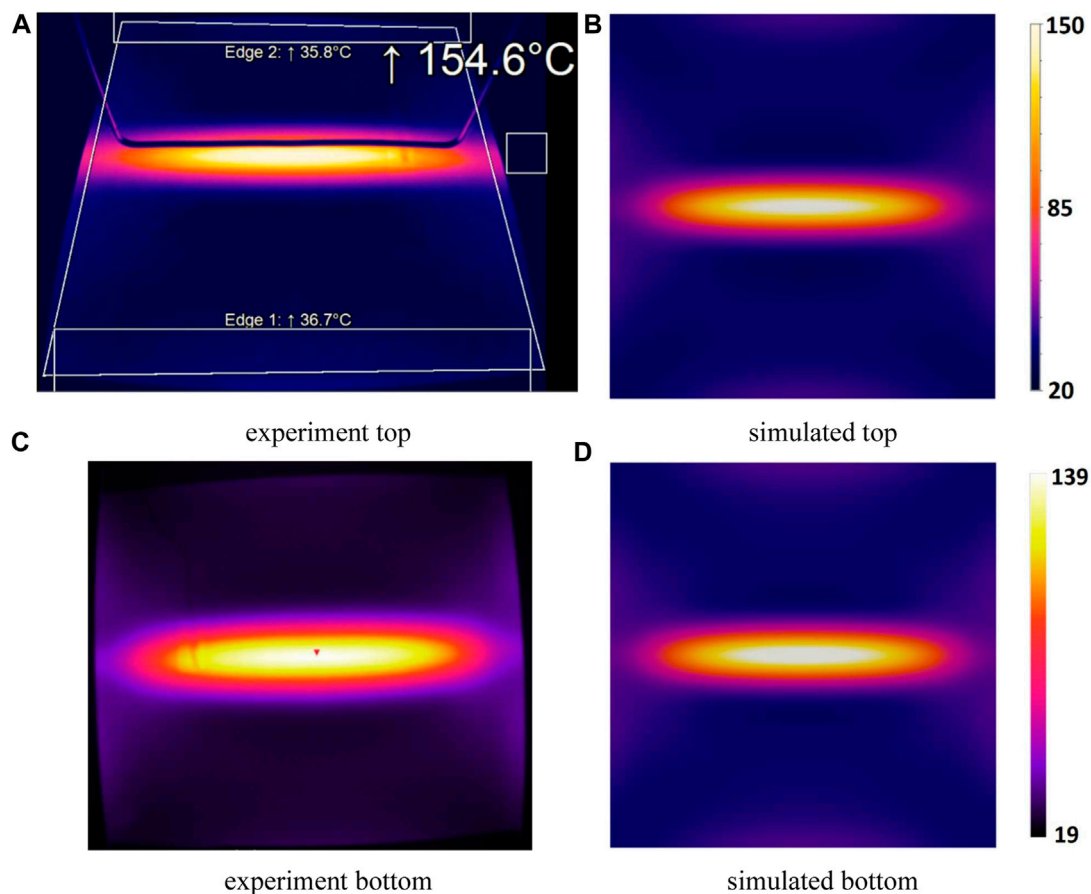
The simulated values are in qualitative agreement with the measured values. The top surface of the plate in the simulation

model reached  $140^{\circ}\text{C}$  in 37 [s] whereas the measurements showed  $151^{\circ}\text{C}$ . Therefore, the simulation of the inductive heating was continued until 42 [s] when the maximum surface temperature was equal to  $151^{\circ}\text{C}$ . Furthermore, the difference between top and bottom maximum surface temperature is larger for the experiments (approximately  $15^{\circ}\text{C}$ ) as compared to the simulated values (approximately  $5^{\circ}\text{C}$ ). Since conductive thermal properties were taken from literature, rather than measured properties some deviation may be expected there. Finally, as can be seen from the cooling part of the graph, the drop in temperature measured during the experiments is somewhat larger than what was computed. Hence, the film coefficients applied to the model to represent the convective cooling should be a bit higher than those that were computed.

A2, Uni-Directional (UD)  $[0]_{36}$  The UD plate is expected not to heat up at all. Since all plies are running parallel to the coil there is no current return path *via* cross-ply interfaces. However, some plies might be in contact in longitudinal direction. Simulations of this type of plate suggest heating due to small eddy currents that are generated in the laminate supposedly due to a non-zero electric conductivity in the longitudinal fiber direction. Hence, plate A2 was used to prove that this phenomenon occurs in practice. As can be seen from the thermal images in Figure 19 there is a slight increase in temperature at the edges of the plate

The edges of the plate contribute to generation of a current return path and corresponding joule heating. The simulation model shows a similar heating pattern. For completeness, the measured and calculated temperatures as recorded for the A2 plate are shown in Figure 20.

Note that the maximum temperatures are located near the edges of the plate instead of underneath the coil. Furthermore,



**FIGURE 21**

Temperature plot of top and bottom temperatures of the grouped cross-ply  $[0_3,90_3]_{3s}$  plate (A3). (A) and (C) correspond to measurements whereas (B) and (D) correspond to simulated values.

the thermocouples that are placed 100 [mm] away from the edge underneath the coil record only a minor increase in temperature, approximately 1.5 [°C] whereas the maximum temperature at the top increases to almost 29 [°C] from room temperature (23 [°C]). Furthermore, as we can see from the temperature graph the top and bottom maximum recorded values differ slightly as well as the thermocouple values. This is partly due to the fact that the Optis and FLIR camera did not register the same room temperature and always showed a difference of approximately 1 [°C]. We did not locate any other heat sources that would cause the top of the plate to be warmer than the bottom. During the heating of the other two plates A1 and A3 this temperature difference was not an issue but for this case the difference is visible in the graph.

Comparing the simulated values with those recorded during the measurements the values are in good agreement. In both the experiment and the simulation the heating was 37 [s] and the difference in maximum temperature is only 1.5 [°C]. The results for the thermocouples are in good agreement although the temperature increment is very little.

A3, a grouped cross-ply  $[0_3,90_3]_{3s}$ . The third plate consisted of less cross-ply interfaces and initially we expected *via* coarse mesh FE analysis that this plate would heat up less than the cross-ply plate A1.

The A1 plate has 34 cross-ply interfaces, whereas the A3 plate has only 10 cross-ply interfaces. However, the temperature plot in Figure 21 shows that after 37 [s] of inductive heating the plate reached a temperature of approximately 155 [°C] which is roughly the same temperature as the A1 plate (recall Figure 17) that reached 151 [°C].

One possibility is that in addition to the cross-ply interfaces having an effect on the surface temperature also the current penetration depth (Christopoulos, 1990) is of influence. The higher the electric conductivity of the workpiece the less deep the eddy currents penetrate and instead form at the surface of the workpiece. This would lead to higher top surface temperatures. Through conduction effects within the laminate the bottom surface temperature could then also increase. For the A3 plate the bottom surface temperature is slightly higher than that of the A1 plate as can be seen in Figure 22 that shows a recording of the maximum IR measurements and the thermocouple measurements for the A3 plate.

The top of the plate reaches a maximum temperature of approximately 155 [°C] and the bottom a temperature of approximately 139 [°C]. For the A1 plate the top reached 151 [°C] and the bottom 136 [°C]. Hence, the difference between the two measurements is small and therefore both plates are considered to heat up similarly. A probable cause could be that

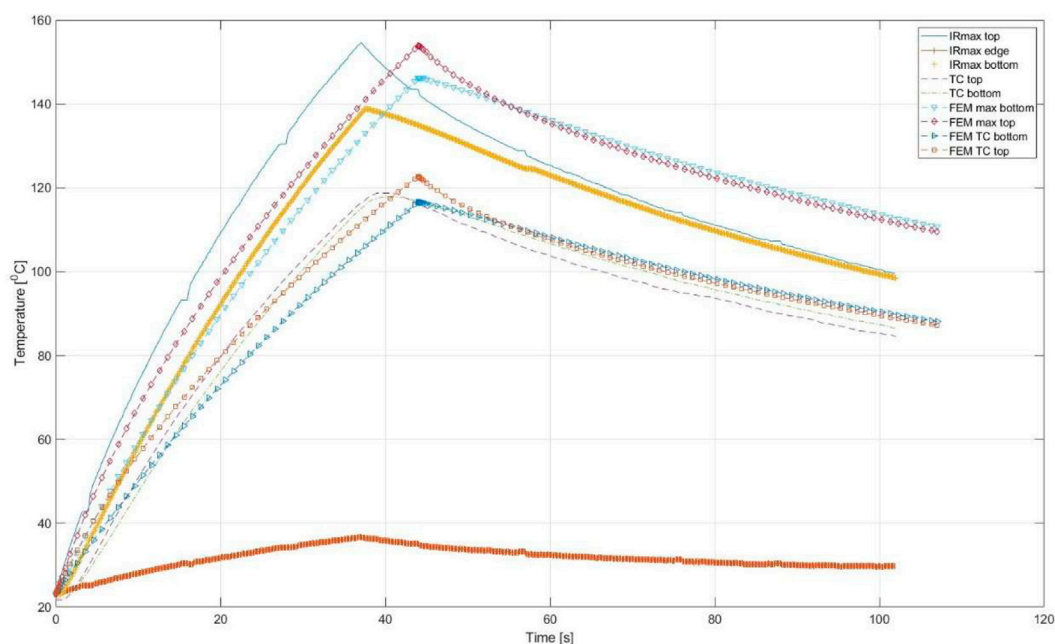


FIGURE 22

Temperature measurements of the grouped cross-ply  $[0_3,90_3]_s$  plate (A3).

the number of cross-ply interfaces does not have to be significant in order for a relatively thick laminate to heat up.

For the simulated A3 plate the maximum temperature reaches 151 [°C] after 44.6 [s] whereas the A1 plate reached 151 [°C] after 44 [s]. Furthermore, in the simulation for plate A3 after 37 [s] the temperature is 138 [°C]. For plate A1 in the simulation for the plate A1 after 37 [s] the temperature is 140 [°C]. Hence, in the simulations the A1 plate heats up slightly faster than the A3 plate. However, this difference is considered small and may be also due to the mesh not capturing every effect as we could not further refine the mesh for such a thick plate.

## 5 Conclusions and further work

Several experimental tests were developed to obtain material properties and verify the electromagnetic simulation approach. The measured material properties were compared with data found in literature and showed good agreement. The results of the magnetic field measurements and applied load on the coil supported the modelling steps for building the electromagnetic FE model. The thermal experiments showed that increasing the number of cross-ply interfaces may not always lead to higher temperature at the laminate upper and lower surfaces. Finally, the results from the simulations were in good agreement with the data recorded for the thermal experiments. Some further improvements in the modelling require the measuring of each relevant material property of the material over the relevant temperature range. The authors intend to further improve on the developed measurement techniques to include through the thickness measurements of the electrical conductance and to develop a simplified 3D FE model that is less computationally demanding than the current 3D approach. The results of the present

work will be used for further investigation of inductive welding of long and slender joints.

## Data availability statement

The raw data supporting the conclusion of this article will be made available by the authors, without undue reservation.

## Author contributions

AdW and WV contributed to conception and design of the study. NvH and LS setup the experiments and recorded the data. AdW wrote the first draft of the manuscript. NvH and WV wrote sections of the manuscript. All auteurs contributed to manuscript revision.

## Funding

This project has received funding from the Clean Sky 2 Joint Undertaking (JU) under grant agreement No 945583. The JU receives support from the European Union's Horizon 2020 research and innovation programme and the Clean Sky 2 JU members other than the Union.

## Conflict of interest

The authors declare that the research was conducted in the absence of any commercial or financial relationships that could be construed as a potential conflict of interest.



## Publisher's note

All claims expressed in this article are solely those of the authors and do not necessarily represent those of their affiliated

organizations, or those of the publisher, the editors and the reviewers. Any product that may be evaluated in this article, or claim that may be made by its manufacturer, is not guaranteed or endorsed by the publisher.

## References

- Ahmed, T., Stavrov, D., Bersee, H., and Beukers, A. (2006). Induction welding of thermoplastic composites - an overview. *Compos. Part A Appl. Sci. Manuf.* 37, 1638–1651. doi:10.1016/j.compositesa.2005.10.009
- Buser, Y., Bieleman, G., Wijskamp, S., and Akkerman, R. (2022). "Characterisation of orthotropic electrical conductivity of unidirectional c/pack thermoplastic composites," in Proceedings of the 20th European Conference on Composite Materials - Composites Meet Sustainability, Lausanne, Switzerland, June 2022.
- Chen, L. (2016). *Finite element methods for Maxwell equations*. Oakland, CA, USA: University of California.
- Cheng, J., Wang, B., Xu, D., Qiu, J., and Takagi, T. (2021). Resistive loss considerations in the finite element analysis of eddy current attenuation in anisotropic conductive composites. *NDT E Int.* 119–102403. doi:10.1016/j.ndteint.2021.102403
- Christopoulos, C. (1990). *An introduction to applied electromagnetism*. Toronto, OA, Canada: Wiley.
- de Wit, A. J., van Hoorn, N., Nahuis, B. R., and Vankan, W. J. (2022a). "Numerical simulation of eddy current generation in uni-directional thermoplastic composites," in Proceedings of the 20th European Conference on Composite Materials - Composites Meet Sustainability, Lausanne, Switzerland, June 2022.
- de Wit, A. J., van Hoorn, N., Nahuis, B. R., and Vankan, W. J. (2021). *Prediction of thermo-mechanic effects through numerical simulation of induction heating of thermoplastic composites*. Amsterdam, Netherlands: Royal Netherlands Aerospace Centre - NLR.
- de Wit, A. J., van Hoorn, N., Straathof, L. S., and Vankan, W. J., 2022b. Eddy current simulation and experiments for assessments of inductive heating in uni-directional thermoplastic composites. International Congress on Welding Additive Manufacturing and associated Non Destructive Testing, June 2022, Paris, France, .
- Grouve, W., Vrugink, E., Sacchetti, F., and Akkerman, R. (2020). Induction heating of UD C/PEKK cross-ply laminates. *Procedia Manuf.* 47, 29–35. doi:10.1016/j.promfg.2020.04.112
- Kim, H. J., Yarlagaadda, S., Shevchenko, N. B., Fink, B. K., and Gillespie, J. W. (2000). Development of a numerical model to predict in-plane heat generation patterns during induction processing of carbon fiber-reinforced prepreg stacks. *Jounral Compos. Mater.* 37 (16), 1461–1483. doi:10.1177/0021998303034460
- Moser, L. (2012). *Experimental analysis and modeling of susceptorless induction welding of high performance thermoplastic polymer composites*. Kaiserslautern, Germany: Kaiserslautern: Institute für Verbundwerkstoffe GmbH. PhD thesis.
- O'Shaughnessey, P. G., Dubé, M., and Villegas, I. F. (2016). Modeling and experimental investigation of induction welding of thermoplastic composites and comparison with other welding processes. *J. Compos. Mater.* 50 (21), 2895–2910. doi:10.1177/0021998315614991
- Simulia (2023). *Abaqus 2023 theory manual*. Rhode Island: Dassault Systèmes Simulia Corp.
- Xu, X., Ji, H., Qui, J., Cheng, J., Wu, Y., and Takagi, T. (2018). Interlaminar contact resistivity and its influence on eddy currents in carbon fiber reinforced polymer laminates. *NDT E Int.* 94, 79–91. doi:10.1016/j.ndteint.2017.12.003
- Yousefpour, A., Hojjati, M., and Immarigeon, J.-P. (2004). Fusion bonding/welding of thermoplastic composites. *J. Thermoplast. Compos. Mater.* 17, 303–341. doi:10.1177/0892705704045187
- Yousefpour, A., and Hojjati, M. (2011). *Welding thermoplastics and thermoplastic composite materials*. Hoboken, NJ, US: John Wiley & Sons.



## OPEN ACCESS

## EDITED BY

Chung Hae Park,  
IMT Lille Douai, France

## REVIEWED BY

Emmanuelle Vidal-Salle,  
Institut National des Sciences Appliquées  
de Lyon (INSA Lyon), France  
Luise Kärger,  
Karlsruhe Institute of Technology (KIT),  
Germany  
Samir Allaoui,  
Université de Reims  
Champagne-Ardenne, France

## \*CORRESPONDENCE

P. D. Mulye,  
✉ Paris-Dilip.Mulye@ec-nantes.fr

RECEIVED 28 February 2023

ACCEPTED 17 May 2023

PUBLISHED 12 June 2023

## CITATION

Mulye PD, Morañay L, Binetruy C,  
Comas-Cardona S, Leygue A and  
Guillon D (2023), Unified numerical  
process modeling of forming and  
consolidation for thermoplastic  
composites with prepreg patches.  
*Front. Mater.* 10:1176482.  
doi: 10.3389/fmats.2023.1176482

## COPYRIGHT

© 2023 Mulye, Morañay, Binetruy,  
Comas-Cardona, Leygue and Guillon.  
This is an open-access article distributed  
under the terms of the [Creative  
Commons Attribution License \(CC BY\)](#).  
The use, distribution or reproduction in  
other forums is permitted, provided the  
original author(s) and the copyright  
owner(s) are credited and that the  
original publication in this journal is  
cited, in accordance with accepted  
academic practice. No use, distribution  
or reproduction is permitted which does  
not comply with these terms.

# Unified numerical process modeling of forming and consolidation for thermoplastic composites with prepreg patches

P. D. Mulye<sup>1,2\*</sup>, L. Morañay<sup>2</sup>, C. Binetruy<sup>1</sup>, S. Comas-Cardona<sup>1</sup>,  
A. Leygue<sup>1</sup> and D. Guillon<sup>3</sup>

<sup>1</sup>Nantes Université, École Centrale Nantes, CNRS, GeM, Nantes, France, <sup>2</sup>Altair Engineering France, Valbonne, France, <sup>3</sup>Pôle Ingénierie Polymères & Composite, CETIM, Technocampus Composites, Bouguenais, France

The main idea behind “Quilted Stratum Process” (QSP®) is to create a flat blank made of unidirectional/woven thermoplastic prepreg patches instead of using uniformly shaped prepreg stack as is the case with standard thermostamping process. Thus, using QSP®; one can manufacture components with complex geometries by using nearly rectangular patches while still maintaining a short cycle time similar to the standard thermostamping process. The use of near-rectangular patches results in a significant material saving which is a necessity for a sustainable product development. During standard thermostamping and/or QSP®; the consolidation phase plays a key role in the strength and quality of the final product. This becomes even more important in the case of unidirectional thermoplastic prepreps where mechanisms such as transverse squeeze flow can impact not only the in-plane dimensions of the prepreg but also the fibre orientations within the prepreg. This work presents a unified modeling approach that combines a novel pinching shell element, a new elasto-plastic constitutive model for pinching shell in order to provide a unified solution to simulate both forming and consolidation-flow using a shell-based approach. This unique unified approach of simulating forming and consolidation provides a set of additional outputs such as the through-thickness stress, final deformed shape of the plies including the squeeze flow effect and the changes in the orientation of fibres within the plies during and after the process. This work finally demonstrates how this information can help the manufacturers to design better tooling based on the outcomes of the numerical process simulation in order to achieve a desired product quality. Additionally, one can also steer the final fibre orientation which results from the initial position of the patch, its forming and squeeze flow.

## KEYWORDS

process simulation, forming, consolidation, shell element, prepreps

## 1 Introduction

The classical thermostamping process for manufacturing composite parts has been around for many years. A modified version of this process called “Quilted Stratum Process” (QSP®) (Guillon et al., 2016) has been developed in 2012 by CETIM, Centrale Nantes and other partners. The motivation behind this advanced manufacturing technology is to

strategically optimize a component's performance while reducing material wastage without compromising the production process efficiency.

QSP<sup>®</sup> shares several features with the standard composite thermostamping process. However, the main idea behind this process is to use unidirectional (UD) or woven thermoplastic prepreg patches instead of using uniformly shaped prepreg stack as is the case with standard thermostamping process. By using smaller and near-rectangular patches; the flat prepreg geometry can be optimally subdivided so as to fit maximum number of patches within a given size of the prepreg sheet at the prepreg cutting phase (Figure 1) which reduces the material wastage. This reduction in material wastage not only decreases the production cost but also reduces the environmental impact, thereby creating a more sustainable solution compared to the classical thermostamping process. In addition, by choosing the specific prepreg patches for specific locations, one provides an additional degree of freedom in the design of the part using QSP<sup>®</sup> (Irisarri et al., 2019). It is true that some material overlap might be required in case of QSP<sup>®</sup> (Figure 1). However, in case of classical thermostamping; the material corresponding to the areas that inside the circular shapes in (Figure 1) is wasted. This wastage, in general much bigger than the extra material needed for the overlap can be avoided by using QSP<sup>®</sup>. Further, by using specific patches at specific locations on the part, one can create local strengthening of the part [refer to Figure 6 from Guillon et al. (2016) to see an example of a local strengthening of a component]. On the other hand, in case of a classical thermostamping process, this kind of local strengthening may not be easy to obtain and it would have to be a global strengthening (using multiple plies everywhere instead of just specific locations) which would require much more material.

In order to embrace the idea of “one-shot-manufacturing”; it is important to consider all the major features of a given manufacturing process and their impact on the final product. Thus numerical simulation of a process and its inclusion into the product design pipeline is very important. Driven by the anisotropic nature of fabric coupled with its interaction with the polymer in case of prepreps, numerical simulation of a standard composite forming process itself poses several challenges. However for QSP<sup>®</sup>, there are some additional challenges in the physical process and its numerical modeling because of the usage of prepreg patches: the inability to use a blank holder, the possible long distance sliding of prepreg patches during forming (Schell et al., 2016) and the transverse squeeze flow occurring during consolidation especially for UD prepreps.

The overview of the modeling of a classical composite forming process can be found in (Lim and Ramakrishna, 2002; Dörr et al., 2017a) the latter addresses the available industrial solutions for simulation of UD's. For an even more recent review about the advances in composite forming, one can refer to (Boisse et al., 2022). In 2018, it has been showed in the review article (Bussetta and Correia, 2018) that the major focus of the research in composite forming simulation has been on the forming phase of the process and more specifically, on the modeling of in-plane shear and tension to predict changes in fibre orientations and prediction of wrinkles.

However, during standard thermostamping and/or QSP<sup>®</sup>; the forming stage is almost always followed by a consolidation stage which is relatively less explored. Consolidation stage helps in removal of porosities, healing ply-ply interfaces, improving

the surface quality and controlling the thermo-mechanical transformations of the material at the onset of the cooling phase. Thus, the consolidation phase plays a key role in the strength and quality of the final product.

During the consolidation process of thermoplastic prepreps, there exists a through-thickness normal (transverse) stress also referred to as “Pinching Stress” (Soulat et al., 2006) which in fact is the main driving mechanism of the consolidation phase. The modeling of the consolidation phase becomes even more important in the case of unidirectional thermoplastic prepreps where mechanisms such as transverse squeeze flow can impact not only the in-plane dimensions of the prepreg but also the fibre orientations within the prepreg (Sorba et al., 2017). The mechanism of the transverse squeeze flow is schematically shown in Figure 2. In this mechanism, due to the consolidation pressure, the thickness of the composite layer reduces, creating a resin movement within the ply which in turn convects the fibres with it (provided there is a room for the material to flow in-plane) and modifies the fibre orientations. It is to be noted that the resin-rich layer exists at the ply-ply interface in almost all types of layups as discussed in (Sorba et al., 2017). This resin-rich layer facilitates the movement of the fibres in the adjacent layers even in the case of multidirectional layups which has been demonstrated in their work on a stack configuration of  $[0^\circ/90^\circ]_6$ .

The experimental evidence of the transverse squeeze flow and its influence on the final component is demonstrated in Figure 3. Figure 3A shows the initial and final deformed shape of a UD stack of  $[0^\circ]_5$  after undergoing a 25% consolidation. Due to the inextensibility of the fibres, the major deformations occur along the direction orthogonal to the fibres. This transverse stretching can be very high (in this case the final width was 1.5 times the original width). Figure 3B shows an industrial scale component manufactured by CETIM which has a UD patch at the top in its stacking configuration. It can be seen that the initial width of 78 mm can increase by as much as 30% at several locations due to the transverse squeeze flow. In summary, the mechanisms such as in-plane shear and tension are relatively well established in the literature both in terms of simulation as well as their characterization. On the other hand, the mechanisms such as the squeeze flow and simulation of consolidation are not yet standardized, even though their influence on the final deformed shape is obvious.

In order to incorporate both forming and consolidation phases into the process simulation, a natural strategy could be to use a two-step approach to simulate forming and consolidation phases serially one after the other. This is motivated by the fact that the primary mechanisms occurring in forming and consolidation phases are quite different. However, this strategy poses several practical challenges from a numerical simulation point of view.

Without the pinching shell element, the two-step approach would be: 1) perform the forming simulation using classical shell elements 2) export the deformed mesh and other data after the forming phase 3) add a hexahedral elements layer (to model through thickness compressive behavior during consolidation) in between the plies modeled with classical shell elements 4) perform consolidation phase simulation.

This two-step approach was tested on an industrial model and the practical challenges that were observed were as follows [discussed in more detail in (Mulye, 2021)]:

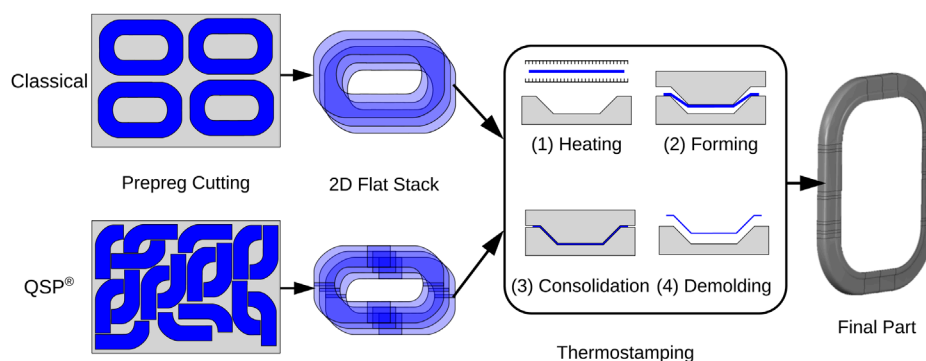


FIGURE 1

A schematic representation of a full workflow of a thermostamping process for a classical process as well as QSP<sup>®</sup> for a demonstrator of an aircraft window frame from a SHERLOC QSP<sup>®</sup> project (Thomas J and Charlotte, 2019) (a part of CLEAN SKY 2 initiative).

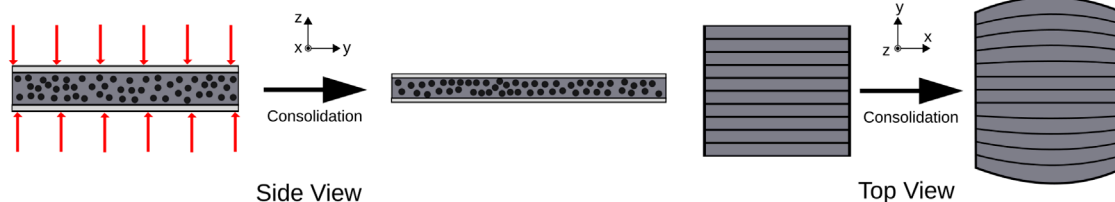


FIGURE 2

A schematic representation of a transverse squeeze flow mechanism for a single unidirectional ply (without any lateral constraints) during the consolidation phase of the thermostamping process.

- At the end of the forming stage, the shell components (plies) are already in a 3D deformed configuration and often there could be regions with a very small gap between the plies. This results in a very small thickness of hexahedral elements that are added in such regions. This in turn results in a very small time-step for consolidation.
- Because the nature of the Type-25 contact in Altair Radioss™ (constant penalty stiffness) that is added between the plies (during forming); often the midsurfaces of the plies can themselves interpenetrate making it impossible to add a hexahedral layer in such locations.
- A user intervention is needed to make a decision about the resolution of the above two points. This makes it challenging to make the whole process automated which can be a big hurdle from an industrial point of view.

Besides, it has been shown in (Soulat et al., 2006) that porosities in some regions can get removed during *forming* phase itself indicating a possibility of a local consolidation even during the forming phase. Thus, creating a global split of the forming and consolidation phases may not be possible. This has motivated us to develop a unified modeling strategy that can be used for both forming and consolidation phases without the need to explicitly separate them.

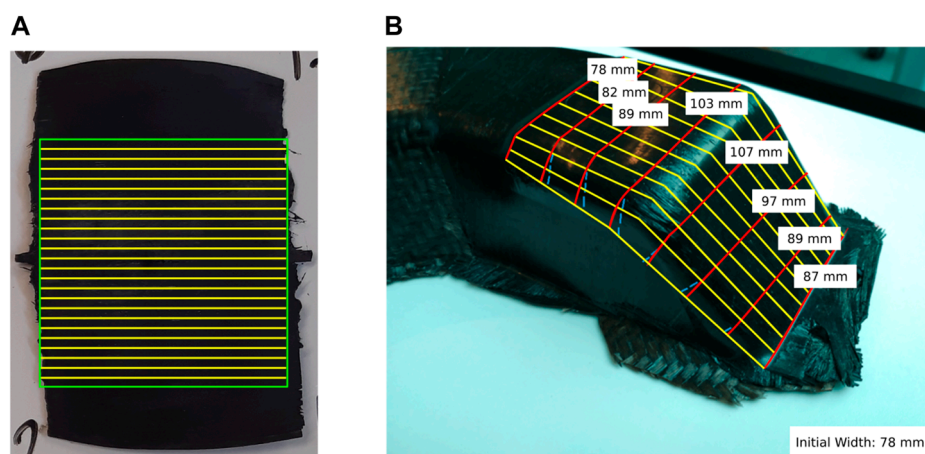
In the literature, the forming phase is predominantly modeled using shell elements whereas there have been three main directions for modeling consolidation process from the point of view of

the finite element used in the numerical simulation: 1) solid (hexahedral) element based approach 2) solid-shell element based approach 3) shell element based approach.

The solid elements can readily capture a 3D stress state without requiring any changes in the existing element formulations or modifications in the constitutive models. The numerical modeling of consolidation process conducted in (Belnoue et al., 2016; 2018) used C3D8 solid elements of ABAQUS/Standard to model each individual ply with a specific user material model. A solid element with 27 nodes with a mixed formulation for velocity, pressure and fibre tension was used in (Sorba et al., 2017) to model transverse squeeze flow by modeling the UD prepreps as a transversely isotropic viscous fluid (Rogers, 1989). Solid elements face challenge when they are thin (the thickness of a prepreg is usually small compared to its in-plane dimensions) suffer from a small time-step in the case of an explicit solver and are too stiff/rigid in bending mode due to the transverse shear locking phenomenon.

A solid-shell element has a 3D stress state and is able to overcome the limitation of the transverse shear locking and therefore can also be used for bending modes. A novel prismatic solid-shell element with seven nodes (SB7y19) was developed in (Xiong, 2017; Xiong et al., 2018; 2019) to model forming and consolidation in a unified manner, however effects such as transverse squeeze flow were not modeled as the focus was more on the woven prepreps instead of UD. A new hexahedral solid-shell element capable of pinching (SB9) was developed in (Dia et al., 2020) also to perform a unified simulation of forming and consolidation. Based on the





**FIGURE 3**

Experimental evidence of the transverse squeeze flow mechanism. **(A)** Final deformed shape of a flat  $[0^\circ]_5$  stack after consolidation (the initial shape is shown in green color and the initial fibre orientations are shown in yellow color); **(B)** Final deformed shape of a unidirectional patch of an industrial component manufactured using QSP<sup>®</sup> by CETIM (the fibre orientations are shown in yellow color and the final width measurements at various locations are shown).

work of (Schwarze and Reese, 2011), a new user element was implemented and extended in (Schäfer et al., 2020; Schäfer et al., 2021) with a major focus on the investigation of various locking mechanisms. Overall, the solid-shell elements show a good potential and when coupled with a selective mass scaling, they can be used to simulate forming and consolidation on an industrial scale. However, a demonstration on a full-scale industrial model with many plies and prepreg patches (QSP<sup>®</sup>) is not available in the literature yet.

Even though the shell elements have shown tremendous potential for forming phase simulation which involves large deformations, large bending, large rotations; the classical 3-parameter (Kirchhoff-Love theory) or 5-parameter (Reissner-Mindlin theory) shells cannot be used for modeling consolidation as they are based on a plane stress assumption (i.e.,  $\sigma_{zz} = 0$ ). So they cannot have a pinching stress. However, a 6-parameter shell proposed in (Simo et al., 1990) has a possibility of stretching of the director vector with a linear displacement field along the thickness direction. Thus, it can have a  $\sigma_{zz} \neq 0$  and  $\epsilon_{zz} \neq 0$ ; however it suffers from a Poisson thickness locking which can be resolved either by decoupling pinching stress and bending strains (Soulat et al., 2006) or by using a quadratic interpolation of displacement along the thickness (Parisch, 1991; Sansour and Bufler, 1992). Further, a 7-parameter shell (Büchter and Ramm, 1992; Büchter et al., 1994) which is by far the most comprehensive shell formulation can also have a pinching stress. further discussion about this type of shell can be found in (Bischoff and Ramm, 1997; 2000; Brank et al., 2002).

In conclusion, developing a purely shell element based approach for modeling consolidation can be impactful as the current typical simulation workflow involves shell elements for modeling forming. Thus, having a shell element that can be used for both forming and consolidation phases in a unified manner can be beneficial as it would require no or very little change to the current workflow in the industries. To the best of our knowledge, there is no unique numerical solution that is able to address both forming and consolidation phases (with or without long distance sliding of

prepreg patches) together in a unified manner that is solely based on the shell approach.

This work presents such a shell-based unified modeling approach that combines a novel pinching shell element, elasto-plastic constitutive model for pinching shell and the interply adhesion model (Mulye et al., 2020) in order to provide a unified solution to model both forming and consolidation-flow. This unique unified approach of simulating forming and consolidation provides a set of additional outputs such as the through-thickness stress, the final deformed shape of the plies including the squeeze flow effect and the changes in the orientation of fibres within the plies during and after the process. This information is useful as it helps in identifying the regions which will have a good consolidation quality versus the regions with poor consolidation quality. Also, assuming good consolidation is achieved, by observing the changes in the fibre orientations caused by the squeeze flow, one can determine whether the component meets or not the required quality in terms of strength. Using this information, and by performing several design and process simulation iterations; one is able to obtain a better final design of the mold and/or stack itself that incorporates all the necessary ingredients of the full manufacturing process.

## 2 Objectives and content of the study

The main objectives of this study are fourfold:

- Develop a new shell element (QBATP) by extending the hourglass-free full-integration 4-node QBAT shell element of Altair Radioss<sup>™</sup> so as to include a transverse normal (pinching) stress
- Propose a novel elasto-plastic constitutive model for the QBATP shell to model the behavior of the nearly incompressible melt polymer during the consolidation phase and propose a practical method for its characterization

- Create and validate a modeling strategy using the above two points in order to provide a unified approach of process modeling of forming and consolidation
- Demonstrate the use of this strategy to improve the mold design for thermoplastic composites

### 3 A full-integration pinching shell (QBATP)

As discussed above, the three-dimensional stress state cannot be modeled with the classical 5-parameter Mindlin shells which are built with a plane-stress assumption ( $\sigma_{zz} = 0$ ). To overcome this, a new 4-noded 6-parameter shell element (referred to as QBATP which stands for “Quadrilateral BAToz Pinching shell element”) has been developed by extending the existing hourglass-free full-integration 5 parameter shell element in Altair Radioss™ known as QBAT (Altair Engineering, 2018). The QBAT element is based in the Q4y24 element discussed in Batoz and Dhatt (1992) which in turn is based on the MITC4 element discussed in Bathe et al. (1975), Dvorkin and Bathe (1984). The functionality of the pinching stress has been added by introducing additional nodal degrees of freedom to the existing QBAT formulation, discussed in this section.

In this work, a 6-parameter shell element (linear displacement interpolation through thickness) was chosen and the Poisson thickness locking was avoided by decoupling the normal pinching stress and the bending (discussed further in Section 3.3). The 7-parameter shell (quadratic displacement interpolation through thickness) would have readily solved the Poisson thickness locking problem without any modifications to the constitutive model. However, the choice of 6-parameter shell over a 7-parameter shell in this work was mainly driven by the associated computational cost which would be lower in case of a 6-parameter shell because of lesser degrees of freedom per node compared to a 7-parameter shell.

#### 3.1 Concept of pinching and shell element description

A typical geometry of a general shell element can be represented as shown in Figure 4A by a three-dimensional mid-surface  $\bar{\mathbf{x}}_p(\xi, \eta)$  representing the points located on the mid-surface. With this, the position of a general point  $\bar{\mathbf{x}}_q(\xi, \eta, \zeta)$  within the shell can be written as follows,

$$\bar{\mathbf{x}}_q(\xi, \eta, \zeta) = \bar{\mathbf{x}}_p(\xi, \eta) + z(\zeta) \bar{\mathbf{n}}(\xi, \eta) \quad \text{where} \quad z = \frac{1}{2}\zeta h \quad (1)$$

and  $\xi, \eta$  and  $\zeta$  are the parametric coordinates and  $h$  is the thickness of the shell. In general, the nodal fiber direction  $\zeta$  may not correspond to the mid-surface normal  $\bar{\mathbf{n}}$  but the QBAT shell element is built with a postulate that they are equivalent as was the case with the Q4y24 developed in (Batoz and Dhatt, 1992). This remains true for the case with a uniform thickness within an element or in case of a *mild-taper* conditions as discussed in (Oñate, 2013). Also, it is considered that the mid-surface represented by the vector  $\bar{\mathbf{x}}_p$  is continuous however the normals could be discontinuous across elements as shown in

Figure 4B. With this description, the displacements for the general point  $\bar{\mathbf{x}}_q$  are given by,

$$\bar{\mathbf{u}}_q = \bar{\mathbf{x}}_q^{t_0+\Delta t} - \bar{\mathbf{x}}_q^{t_0} = \bar{\mathbf{x}}_p^{t_0+\Delta t} + \frac{\zeta}{2} h^{t_0+\Delta t} \bar{\mathbf{n}}^{t_0+\Delta t} - \bar{\mathbf{x}}_p^{t_0} - \frac{\zeta}{2} h^{t_0} \bar{\mathbf{n}}^{t_0} \quad (2)$$

Using the first order approximation of Taylor series for  $h^{t_0+\Delta t}$  and  $\bar{\mathbf{n}}^{t_0+\Delta t}$  we get,

$$\begin{aligned} \bar{\mathbf{u}}_q = & \underbrace{\bar{\mathbf{x}}_p^{t_0+\Delta t} - \bar{\mathbf{x}}_p^{t_0}}_{\text{Term 1}} + \underbrace{\frac{\zeta}{2} h^{t_0} (\bar{\mathbf{n}}^{t_0+\Delta t} - \bar{\mathbf{n}}^{t_0})}_{\text{Term 2}} \\ & + \underbrace{\frac{\zeta}{2} (h^{t_0+\Delta t} - h^{t_0}) \bar{\mathbf{n}}^{t_0}}_{\text{Term 3}} \end{aligned} \quad (3)$$

The **Term 1** in Eq. 3 corresponds to the displacement DoFs of the mid-surface of the shell. The **Term 2** corresponds to the rotation DoFs of the mid-surface. The **Term 3** corresponds to the change in thickness. This phenomenon is neglected in the case of classic shell theories; as the fiber (not to be confused with the fibres that provide reinforcements for the composites) is assumed to be inextensible (Belytschko et al., 2013). As a result, only the first two terms are considered for the classical shells. However, the **Term 3** is not neglected for the six or seven parameter shells. This term is the basis of creating an additional nodal degree of freedom locally referred to as the “Pinching degree of freedom.” Taking into account the **Term 3** in the shell formulation, it is possible to have a non-zero transverse normal stress  $\sigma_{zz}$ .

The geometry of QBATP shell is shown in Figure 4C which consists of four nodes on the mid-surface of the shell. The corresponding reference element in the isoparametric space along with the local node numbering convention is shown in Figure 4E. Classical bilinear shape functions and their derivatives are used to interpolate a nodal degree of freedom. Within the element, each node ( $i$ ) has six local degrees of freedom; three for standard mid-surface displacements ( $U_{1i}, U_{2i}, U_{3i}$ ), two for rotations ( $\theta_{1i}, \theta_{2i}$ ) and additionally one for the pinching displacement ( $U_i^p$ ) as follows:

$$[\mathbf{U}_i]_{(6 \times 1)} = [U_{1i} \quad U_{2i} \quad U_{3i} \quad \theta_{1i} \quad \theta_{2i} \quad U_i^p]^T \quad (4)$$

which are defined with respect to the orthonormal coordinate system ( $\bar{\mathbf{t}}_{1i}, \bar{\mathbf{t}}_{2i}$  and  $\bar{\mathbf{n}}_i$ ) defined at each node as shown in Figure 4F. Additionally, one must define the covariant basis vectors ( $\bar{\mathbf{a}}_1$  and  $\bar{\mathbf{a}}_2$ ) (which will be used in the calculating strains in the next section) as shown in Figure 4D, which are not necessarily orthogonal to each other. Further discussion about their derivation can be found in the **Supplementary Material** (Section 1) of this article.

The pinching DoFs are defined with respect to the mid-surface. The pinching displacement  $U^p$  corresponds to the displacement of the artificial nodes located at the top and bottom surface of the shell. This being a relative degree of freedom, a sign convention needs to be defined. The increase of thickness is considered positive, i.e.,  $U^p > 0$  whereas a reduction of the thickness is considered to be negative, i.e.,  $U^p < 0$ .

#### 3.2 Calculation of strain-rates and strain

Strain rates are calculated based on the rate of deformation tensor. The calculation of the strain rates is split into four

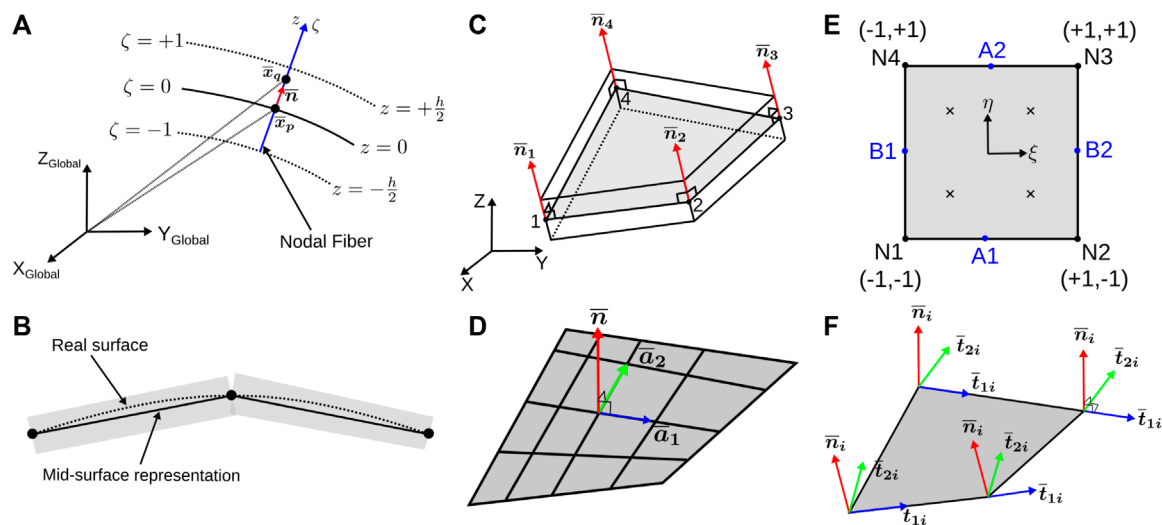


FIGURE 4

QBATP shell element: (A) Formulation and representation of the nodal fiber; (B) Representation of QBATP shell element; (C) Representation of the geometry of the element; (D) Covariant basis for the shell; (E) Reference element in isoparametric space; (F) Nodal orthogonal coordinate systems.

strain interpolation matrices 1) Membrane  $[B_m]$  2) Curvatures  $[B_b]$  3) Pinching  $[B_p]$  and 4) Transverse shear  $[B_{ts}]$ . The details for the individual strain rate matrices can be found in the [Supplementary Material](#) (Section 2) of this article.

The membrane strain-rate is calculated as follows:

$$\begin{bmatrix} \dot{\epsilon}_{xx} \\ \dot{\epsilon}_{yy} \\ \dot{\epsilon}_{xy} \end{bmatrix} = [B_m] [V] \quad (5)$$

Where the  $[B_m]$  matrix is given by:

$$[B_m] = \begin{bmatrix} B_{m1} & B_{m2} & B_{m3} & B_{m4} \end{bmatrix} \quad (6)$$

$$B_{mi} = \begin{bmatrix} \bar{t}_1^T N_{ix} & 0 & 0 & 0 \\ \bar{t}_2^T N_{iy} & 0 & 0 & 0 \\ \bar{t}_1^T N_{iy} + \bar{t}_2^T N_{ix} & 0 & 0 & 0 \end{bmatrix}$$

The rates of curvature are calculated as follows:

$$\begin{bmatrix} \dot{\chi}_{xx} \\ \dot{\chi}_{yy} \\ \dot{\chi}_{xy} \end{bmatrix} = [B_b] [V] \quad (7)$$

Where the  $[B_b]$  matrix is given by:

$$[B_b] = \begin{bmatrix} B_{b1} & B_{b2} & B_{b3} & B_{b4} \end{bmatrix} \quad (8)$$

$$B_{bi} = \begin{bmatrix} \bar{t}_1^T Nbc_{1i} & s_{1i} N_{ix} & 0 \\ \bar{t}_2^T Nbc_{2i} & s_{2i} N_{iy} & 0 \\ \bar{t}_1^T Nbc_{2i} + \bar{t}_2^T Nbc_{1i} & s_{1i} N_{iy} + s_{2i} N_{ix} & 0 \end{bmatrix}$$

The pinching strain-rate is calculated as follows:

$$\begin{bmatrix} \dot{\epsilon}_{zz} \end{bmatrix} = [B_p] [V] \quad (9)$$

Where the  $[B_p]$  matrix is given by:

$$[B_p] = \begin{bmatrix} B_{p1} & B_{p2} & B_{p3} & B_{p4} \end{bmatrix} \quad (10)$$

$$B_{pi} = \begin{bmatrix} 0 & 0 & 0 & 0 & 0 & \frac{2N_i}{h} \end{bmatrix}$$

While considering the transverse shear behavior, it is important to consider the phenomenon of “Transverse Shear Locking.” This occurs mainly because of the inability of the  $C^0$  shell finite elements to reproduce a pure bending behavior. The coupling between the normal and shear strains for linear elements results in a parasitic transverse shear strains in case of pure bending. This therefore, leads to numerical stiffening in bending creating a poor convergence. There are several solutions discussed in the literature to avoid this type of locking. Methods such as reduced integration of the transverse shear as discussed in (Oñate, 2013), usage of  $C^1$  elements as discussed in (Belytschko et al., 2013), the “Enhanced Assumed Strain” (EAS) method proposed in (Simo and Rifai, 1990) and the “Assumed Natural Strain” (ANS) method first proposed in (Hughes and Tezduyar, 1981) can be used. This idea of “Assumed Natural Strain” (ANS) method has been discussed in (Dvorkin and Bathe, 1984) and further used for Q4y24 element in (Batoz and Dhait, 1992). In this work, the same approach has been used for the QBATP elements. The method interpolates the transverse shear strain from the values of the covariant components of the transverse shear strains at four edge mid-points (A1, A2, B1, B2) as follows [Figure 4E](#),

$$\gamma_\xi = \frac{1-\eta}{2} \gamma_\xi^{A1} + \frac{1+\eta}{2} \gamma_\xi^{A2} \quad (11)$$

$$\gamma_\eta = \frac{1-\xi}{2} \gamma_\eta^{B1} + \frac{1+\xi}{2} \gamma_\eta^{B2}$$

With this, the transverse shear strain-rate is calculated as follows:

$$\begin{bmatrix} \dot{\epsilon}_{xz} \\ \dot{\epsilon}_{yz} \end{bmatrix} = [C^0]^T [B_{ts}] [V] \quad (12)$$

Where the  $[C^0]$  is the local basis at  $z = 0$  (Refer to Section 1 in [Supplementary Material](#)) and the  $[B_{ts}]$  matrix is given by:

$$[B_{ts}] = \begin{bmatrix} B_{ts}^1 & B_{ts}^2 & B_{ts}^3 & B_{ts}^4 \\ (2 \times 24) & (2 \times 6) & (2 \times 6) & (2 \times 6) \end{bmatrix} \quad (13)$$

$$[B_{ts}^1] = \begin{bmatrix} -nA1^T & +AS1_{A1}^T & 0 \\ -nB1^T & +AS1_{B1}^T & 0 \end{bmatrix} \quad (14)$$

$$[B_{ts}^2] = \begin{bmatrix} +nA1^T & +AS2_{A1}^T & 0 \\ -nB2^T & +AS1_{B2}^T & 0 \end{bmatrix} \quad (15)$$

$$[B_{ts}^3] = \begin{bmatrix} +nA2^T & +AS2_{A2}^T & 0 \\ +nB2^T & +AS2_{B2}^T & 0 \end{bmatrix} \quad (16)$$

$$[B_{ts}^4] = \begin{bmatrix} -nA2^T & +AS1_{A2}^T & 0 \\ +nB1^T & +AS2_{B1}^T & 0 \end{bmatrix} \quad (17)$$

### 3.3 Elastic constitutive model

The incremental form of the elastic constitutive model discussed in [Soulat et al. \(2006\)](#) was used in this work as a first step. It is to be noted here that the final modeling strategy is as follows: each ply in a multi-layer composite stack is modeled individually. Each of these plies consists of two shell element components with shared coincident nodes (discussed later in more detail in [Section 4](#) of this work). In brief, one shell component would represent fibres using an anisotropic elastic material model, whereas the other shell components would represent the melt polymer using an elasto-plastic constitutive model developed and discussed later in [Section 4](#). Developing an elastic constitutive model serves as the first step in order to validate the shell element itself before continuing with the next developments.

The membrane and bending contributions to the stress which use the corotational framework are as follows:

$$\begin{bmatrix} \Delta\sigma_{xx} \\ \Delta\sigma_{yy} \\ \Delta\sigma_{zz} \\ \Delta\sigma_{xy} \\ \Delta\sigma_{yz} \\ \Delta\sigma_{xz} \end{bmatrix} = \begin{bmatrix} \frac{E(1-\nu)}{(1+\nu)(1-2\nu)} & \frac{E\nu}{(1+\nu)(1-2\nu)} & \frac{E\nu}{(1+\nu)(1-2\nu)} & 0 & 0 & 0 \\ \frac{E\nu}{(1+\nu)(1-2\nu)} & \frac{E(1-\nu)}{(1+\nu)(1-2\nu)} & \frac{E\nu}{(1+\nu)(1-2\nu)} & 0 & 0 & 0 \\ \frac{E\nu}{(1+\nu)(1-2\nu)} & \frac{E\nu}{(1+\nu)(1-2\nu)} & \frac{E(1-\nu)}{(1+\nu)(1-2\nu)} & 0 & 0 & 0 \\ 0 & 0 & 0 & \frac{E}{2(1+\nu)} & 0 & 0 \\ 0 & 0 & 0 & 0 & \frac{E}{2(1+\nu)} & 0 \\ 0 & 0 & 0 & 0 & 0 & \frac{E}{2(1+\nu)} \end{bmatrix} \times \begin{bmatrix} \Delta\epsilon_{xx} \\ \Delta\epsilon_{yy} \\ \Delta\epsilon_{zz} \\ \Delta\epsilon_{xy} \\ \Delta\epsilon_{yz} \\ \Delta\epsilon_{xz} \end{bmatrix} + \begin{bmatrix} \frac{E}{1-\nu^2} & \frac{E\nu}{1-\nu^2} & 0 & 0 & 0 & 0 \\ \frac{E\nu}{1-\nu^2} & \frac{E}{1-\nu^2} & 0 & 0 & 0 & 0 \\ 0 & 0 & 0 & 0 & 0 & 0 \\ 0 & 0 & 0 & \frac{E}{2(1+\nu)} & 0 & 0 \\ 0 & 0 & 0 & 0 & \frac{E}{2(1+\nu)} & 0 \\ 0 & 0 & 0 & 0 & 0 & \frac{E}{2(1+\nu)} \end{bmatrix} \times \begin{bmatrix} z\Delta\chi_{xx} \\ z\Delta\chi_{yy} \\ 0 \\ z\Delta\chi_{xy} \\ 0 \\ 0 \end{bmatrix} \quad (18)$$

where the  $\Delta\epsilon_{ij}$  correspond to the change of membrane strains whereas the  $\Delta\chi_{ij}$  correspond to the change of curvatures.

Compared to the classic QBAT shell, the modifications are as follows:

- The membrane stiffness matrix for the QBATP element does not use the plane stress assumption. Therefore, it is similar to the full three-dimensional stiffness matrix for elasticity.
- QBATP element has an additional stress compared to QBAT shell, i.e., the transverse normal stress  $\sigma_{zz}$ .
- $\sigma_{zz}$  has been decoupled from the bending DoFs in order to avoid pinching locking (or Poisson thickness locking) as discussed in more detail in [Soulat et al. \(2006\)](#). This assumption of decoupling can and will result in errors such as the underestimation of the total strain energy. However, we believe that in composite applications; it is rare to find a material point that is undergoing forming and consolidation at the same time (which is where one will expect the most errors because of this assumptions). Each material point in a ply can switch from forming to consolidation at a different time during the entire process, but the material point is either undergoing forming (i.e., bending) or consolidation (i.e., transverse normal compression) at a given instant.

In this work, the through-thickness integrations are calculated explicitly without at each gauss points performing numerical integration. This approach is referred to as a “global approach” as it does not use any integration points in the thickness direction.

### 3.4 Stress internal force relationship

The internal force vector ( $F_{int}$ ) for the element is then calculated as,

$$F_{int}^{elem} = \int_{elem} B^T \sigma dV \quad (19)$$

This three-dimensional integration is then split into a through-thickness integration and subsequently a surface integration over the element's mid-surface. The stress resultants are calculated as follows:

$$\begin{aligned} N_x &= \int_{-\bar{h}/2}^{\bar{h}/2} \sigma_{xx} dz, & N_y &= \int_{-\bar{h}/2}^{\bar{h}/2} \sigma_{yy} dz, & N_z &= \int_{-\bar{h}/2}^{\bar{h}/2} \sigma_{zz} dz \\ N_{xy} &= \int_{-\bar{h}/2}^{\bar{h}/2} \sigma_{xy} dz, & N_{yz} &= \int_{-\bar{h}/2}^{\bar{h}/2} \sigma_{yz} dz, & N_{xz} &= \int_{-\bar{h}/2}^{\bar{h}/2} \sigma_{xz} dz \end{aligned} \quad (20)$$

And the stress couples are calculated as follows:

$$M_x = \int_{-\bar{h}/2}^{\bar{h}/2} \sigma_{xx} z dz, \quad M_y = \int_{-\bar{h}/2}^{\bar{h}/2} \sigma_{yy} z dz, \quad M_{xy} = \int_{-\bar{h}/2}^{\bar{h}/2} \sigma_{xy} z dz \quad (21)$$

This results into a  $F_{int}$  vector for the element as follows,

$$[F_{int}] = \begin{bmatrix} \dots & F_{1i} & F_{2i} & F_{3i} & M_{1i} & M_{2i} & F_i^p & \dots \end{bmatrix}^T \quad (22)$$

These are then assembled after performing necessary coordinate transformations into separate vectors for global Forces ( $F_{int}^g$ ), global Moments ( $M_{int}^g$ ) and global Pinching force ( $F_{int}^{gp}$ ) as discussed in [Soulat et al. \(2006\)](#).



### 3.5 External force and pinching pressure

In order to apply an external load for pinching the element, a surface type of loading for pinching has been developed. It is referred to as 'Pinching pressure' in this work. This involves application of an equal and opposite surface pressure load ( $P$ ) on the top and bottom sides of the shell. The external pinching force at each node ( $i$ ) of the element is calculated as,

$$\mathbf{F}_{\text{ext}}^p(i) = \frac{1}{4} (2P) A \bar{\mathbf{n}} \quad (23)$$

Where  $A$  is the area of the element and  $\bar{\mathbf{n}}$  is the normal to the mid-surface at the center of the element.

It is to be noted here that the development of the pinching pressure type of loading is purely done to test the shell element under external pinching load. It serves as a checkpoint before beginning the development of the interaction between the contact forces and the pinching degrees of freedom. In thermostamping applications, one cannot actually apply a pinching load directly. Pinching/consolidation will occur through contact forces, and it will get transmitted from one ply to the other through contact forces. This physics of contacts and their interaction with pinching degrees of freedom has been implemented in Altair Radioss™ details of which can be found in Mulye (2021).

### 3.6 Dynamic system of equations

The assembly of internal and external forces, moments and pinching forces results in the following global dynamic system of equations (Eq. 24). It consists of three sets of equations each corresponding to displacements, rotations and pinching displacements respectively.

$$\begin{aligned} \mathbf{M} \ddot{\mathbf{U}} &= \mathbf{F}_{\text{ext}} - \mathbf{F}_{\text{int}} \\ \mathbf{I} \ddot{\boldsymbol{\theta}} &= \mathbf{M}_{\text{ext}} - \mathbf{M}_{\text{int}} \\ \mathbf{M}^p \ddot{\mathbf{U}}^p &= \mathbf{F}_{\text{ext}}^p - \mathbf{F}_{\text{int}}^p \end{aligned} \quad (24)$$

Where  $\mathbf{M}$  and  $\mathbf{M}^p$  are lumped mass matrices corresponding to the displacements and pinching displacements respectively.  $\mathbf{I}$  is the diagonal moment of inertia. An explicit central difference scheme that falls under the broad category of Newmark family schemes with  $\alpha = 1/2$  and  $\beta = 0$  is used in Altair Radioss™ (Altair Engineering, 2018) to solve this system of equations in order to obtain the velocities and displacements at each time-step.

Further, selective mass scaling has been added for this element to increase its critical time-step. In the case of QBATP element; an approach inspired from the technique of the acceleration filtering for solid elements (Olovsson et al., 2004) was used. This approach is similar to the selective mass scaling for solid-shell elements discussed in Cocchetti et al. (2013). This allowed one to selectively increase the mass corresponding only to the pinching DoFs ( $\mathbf{M}_p$ ) without changing the mass for the classical DoFs ( $\mathbf{M}$ ). A detailed discussion about selective mass scaling for QBATP shell element can be found in Section 3.4 of Mulye (2021). With the implementation of the selective mass scaling, the time-step of the QBATP shell element does not depend on its thickness. This comes at a price that the dynamic effects along the thickness can no longer be modeled.

However forming and consolidation can be considered to be quasi-steady processes for which it is a fair assumption to neglect the dynamic effects along the thickness direction.

Additionally, in order to use QBATP shell element for the simulation of forming and consolidation; it is necessary to add the capability of pinching within the contact interface. This capability has been added for the Type-25 contact interface in Altair Radioss™ and has been validated with a test case discussed in Mulye (2021).

It is important to mention here all the code developed in this work can be accessed within the GitHub repository of OpenRadioss (Altair Engineering, 2022).

### 3.7 Validation

Before performing any full-scale unified simulation using the QBATP shells, it is necessary to validate the shell element itself which is done using various numerical tests. Even though only three of the numerical validations tests are discussed in this section, other numerical tests can be found in Mulye (2021) and the corresponding simulation input files can be found in the Supplementary Material (Section 5) of this article.

#### 3.7.1 Uniform crushing under pressure test

The objective of this numerical test is to compare the QBATP element (with selective mass scaling) with the BRICK8 element of Altair Radioss™ under a uniform pinching pressure and also compare the results with the values reported in Soulat et al. (2006). The geometry consists of flat plate of size 50 mm × 50 mm with an initial thickness of 4 mm which was meshed with an element size of 10 mm. The material properties of  $E = 120$  GPa and  $\nu = 0.3$  were used. This being a quarter model; appropriate symmetry conditions were applied as shown in the test setup (Figure 5A). All elements were loaded and then unloaded with a peak pinching pressure of 10,000 MPa. The position of the node located at point C with respect to point A in X direction (Figure 5B) and the evolution of the thickness (Figure 5C) were compared with the reference solutions which showed a good match.

It is to be noted that such a high value of applied pressure (10,000 MPa) has been chosen for two reasons: 1) In order to compress a material of high stiffness ( $E = 120$  GPa) to about 8% compaction; we need to apply a high pressure. For composites, the through thickness Young's modulus would not be so high and so the actual compaction pressure needed would be much lesser. 2) This test was conducted in order to reproduce the work of Soulat et al. (2006) so it was necessary to keep the exact same numerical test conditions including the applied pressure.

#### 3.7.2 Large bending of cantilever test

The objective of this numerical test is to check if the locking [due to the addition of pinching as demonstrated in Soulat et al. (2006)] is avoided for a large deflection case, which is very common in a typical forming scenario. It is to be noted that this test has been performed on a linear elastic material and not on a composite material as the main objective of this test is to ensure that there is no numerical locking. The geometry consists of a cantilever beam of size 400 mm × 20 mm × 20 mm and a force of 250 N was



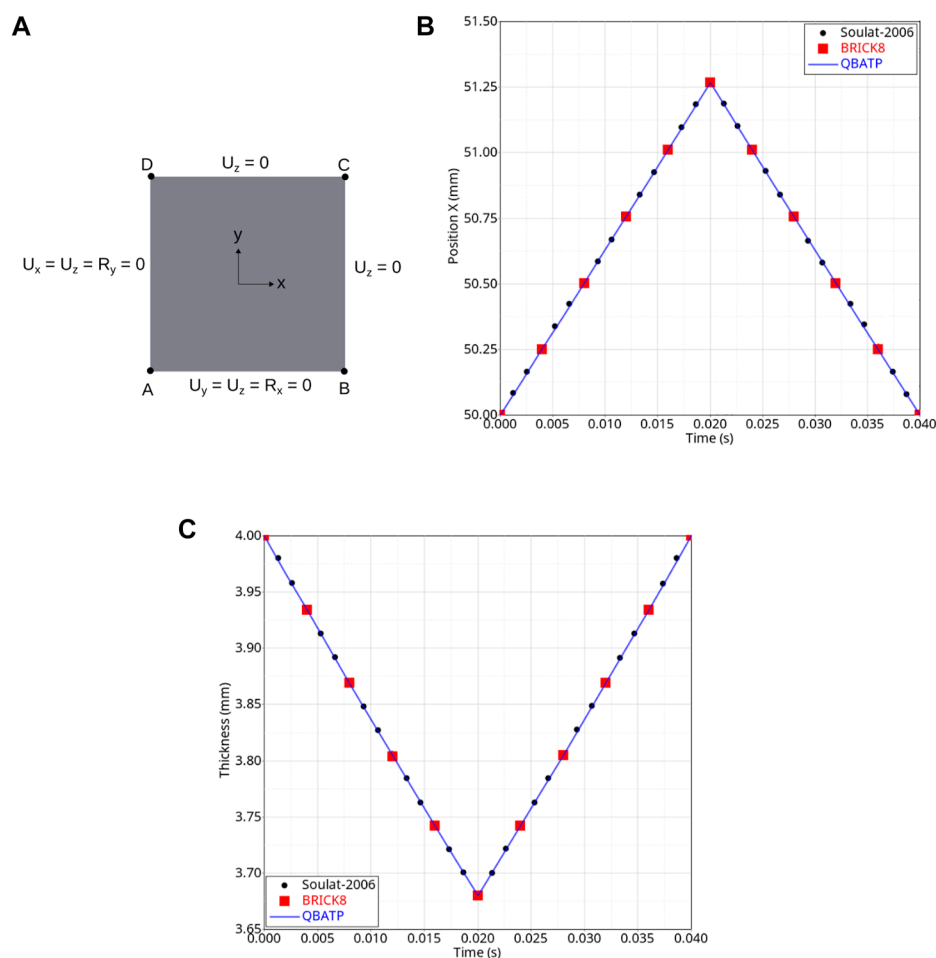


FIGURE 5

QBATP validation test: uniform crushing under pressure: a comparison of solutions obtained using QBATP shells, BRICK8 elements and from Soulat et al. (2006). (A) Geometry (top view) and setup of the test; (B) Comparison of the evolution of the relative position in X direction (in mm) of point C with respect to point A; (C) Comparison of the evolution of the thickness (mm).

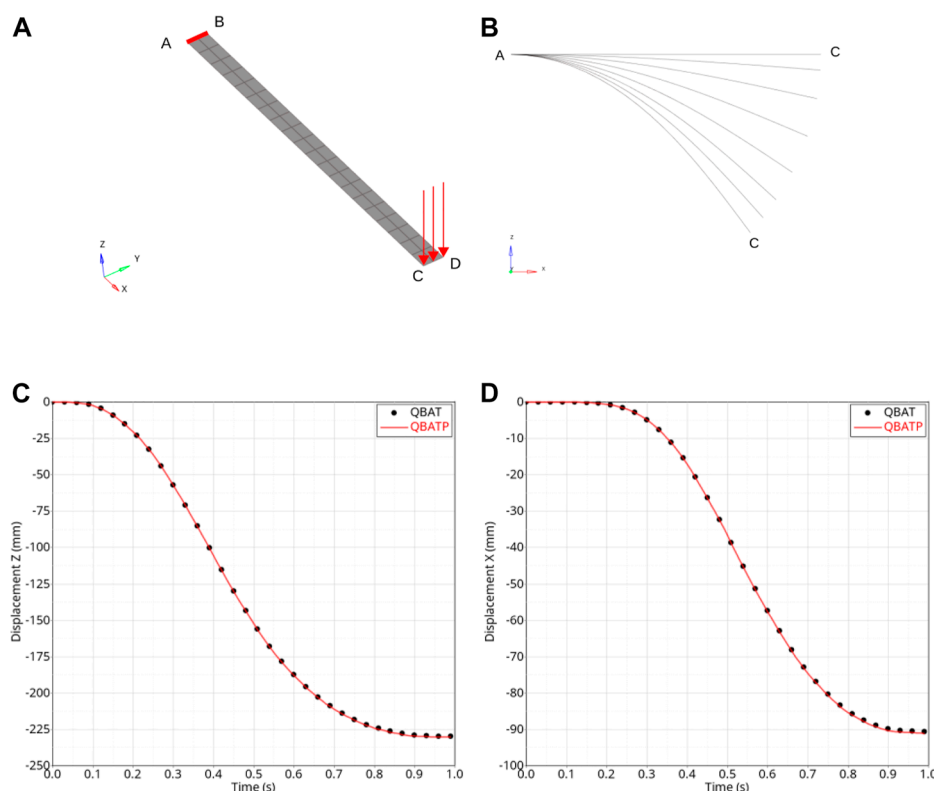
progressively applied on one end of the beam whereas the other end was fixed (Figure 6A). The material properties of  $E = 1,000$  MPa,  $\nu = 0.3$  were used. The large deflection due to this load (Scale 1:1) can be seen in Figure 6B. The evolution of displacement of point C in Z direction (Figure 6C) and X direction (Figure 6D) using the QBATP element showed a good match with the ones obtained using QBAT element thereby demonstrating that the locking due to pinching has been avoided for QBATP elements. For a quantitative comparison with the values reported in the literature, the final Z displacement value (Bisshopp and Drucker, 1945) was 224 mm (reduced integration shell element), the one obtained using QBAT elements (full integration without pinching) was 229.95 mm while the one obtained using QBATP elements was measured to be 230.36 mm.

### 3.7.3 Non-uniform pinching pressure test

In a typical consolidation process, it can often occur that some regions undergo much higher consolidation than others. The objective of this test is to simulate this scenario which has been done by applying the pinching pressure only on one part of the

model and the results are compared with the BRICK8 element. The model under consideration is exactly the same as in Section 3.7.1, i.e., the uniform crushing under pressure test, except the application of the pinching pressure. In this test, a linearly increasing pinching pressure (from 0 and up to 10,000 MPa) was applied only on the elements highlighted in red color (Figure 7A). The displacement field in Y (mm) for both BRICK8 and QBATP meshes shows a good match (Figure 7B). Furthermore, the evolution of pinching displacements (Z) for nodes N1-N4 (refer to Figure 7A for their locations) was compared with the BRICK8 model (Figure 7C) which show a good correlation. The slight difference between the displacements is due to the difference between the mid-surface normals (used to apply the pinching pressure load for QBATP elements) and the top-surface normals (used for applying the pressure load for BRICK8 elements).

Based on the tests discussed in this section along with several other tests discussed in Mulye (2021) and in the Supplementary Material (Section 5) of this article, it can be concluded that the QBATP element can be considered as a suitable candidate to model forming and consolidation in a unified manner.



**FIGURE 6**

QBATP validation test: large bending of a cantilever: a comparison of solutions obtained using QBATP shells, QBAT elements and from Bisshopp and Drucker (1945), Soulat et al. (2006). (A) Geometry and setup of the test; (B) Side view of the evolution of the deformed shape of the cantilever; (C) Comparison of the evolution of the Z displacement (mm) of point C; (D) Comparison of the evolution of the X displacement (mm) of point C.

## 4 Elasto-plastic constitutive model compatible with the pinching shell

This section focuses on the development of a constitutive model for the nearly incompressible thermoplastic melt polymer which is a key ingredient in the numerical modeling of the consolidation phase.

The transverse squeeze flow behavior occurring during the consolidation is predominantly governed by the nearly incompressible melt polymer. As stated in Bussetta and Correia (2018), a thermoplastic polymer behaves as a visco-elastic material at room temperature and as a visco-plastic material at higher temperature. Various modeling strategies for the behavior of polymer described in the literature can be classified into two main categories; one is followed by the composite forming community whereas a different approach is followed by the consolidation and rheology community.

An isotropic-viscoelastic constitutive model was used in Cherouat and Billoët (2001) to model the behavior of the polymer where a membrane element was used for its modeling. Using a micro-mechanical approach and without explicitly modeling fibres and matrix separately (Harrison et al., 2002); used a constitutive model for prepreps which was based on the viscosity of matrix, weave pattern and initial spacing between fibres. Polypropylene polymer was modeled using a Maxwell model in Willems et al. (2006) and the dependence of viscosity on strain rate was modeled

using a power law. It was observed that simulation tests with viscosity and without viscosity resulted in a very small difference in terms of deformation. Based on this observation the simulation performed in Vanclooster et al. (2009) did not consider the matrix viscosity. Similarly, viscous effects were not considered in Khan et al. (2015), Gong et al. (2016), Gong et al. (2018) even though they used elastic, anisotropic hyperelastic and neo-hookean constitutive models for the polymer respectively. In this broad category of modeling the behavior of melt polymer for forming applications, many researchers have demonstrated that the viscous effects of the matrix can be neglected in the simulation without significantly impacting the final results. On the contrary, several works have been published where the viscous effects were modeled and their influence was investigated for shear (Haanappel et al., 2014; Machado et al., 2016) and bending (Alshahrani and Hojjati, 2017; Dörr et al., 2017b).

Even though there have been several attempts at modeling the consolidation behavior for a woven prepreg, the literature for the UD prepreps is predominantly focused on the modeling of squeeze flow phenomenon. The research focused on the modeling of transverse squeeze flow relies on the idea that a thermoplastic UD prepreg behaves as a continuum that can be modeled with a Transversely Isotropic Fluid (TIF) model (Rogers, 1989). This modeling approach is known as the “Ideal Fibre Reinforced fluid Model” (IFRM) approach. Finite element analysis using this technique was performed with the assumption of plane stress

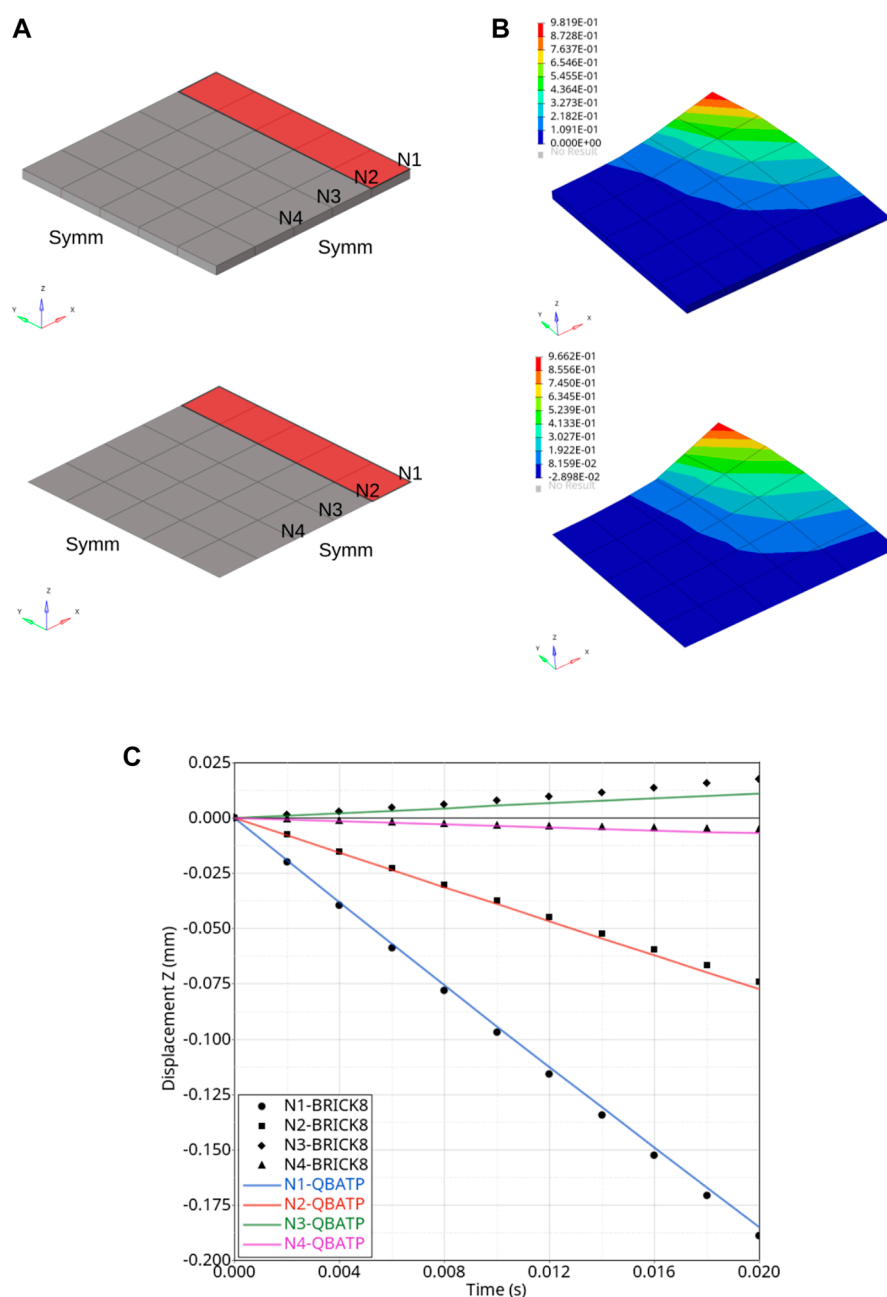


FIGURE 7

QBATP validation test: nonuniform pinching pressure: a comparison of solutions obtained using QBATP shells and BRICK8 elements. (A) Geometry, mesh and setup of the test; (B) Comparison of the final deformed shape (scaled 10X) and Y displacement field (mm); (C) Comparison of the Z (pinching direction) displacement field (mm) at nodes N1–N4.

resulting in a 2D scenario in O’Bradaigh and Pipes (1991). Simulations on a full three dimensional model were performed in Sorba et al. (2017) along with the explicit modeling of the interfacial resin-rich layer.

Based on the literature review, it appears that there is no standardized approach to its modeling probably due to the complexities and challenges involved in its characterization. With this in mind, several modeling choices are made in this work that not only simplify the numerical aspects of the modeling but also reduce

the complexity in the characterization procedure. They are discussed below:

- Following the approach predominantly used by composite forming community; viscous effects are not modeled within the prepreg. A plasticity-based approach is chosen in order to emulate the flow of melt polymer. For processes like QSP<sup>®</sup>, modeling the irreversibility with large deformation along with a failure criteria (which could be developed in the future) is more

important than modeling the viscous effects. This is because if the UD patches experience any kind of severe loading along the direction orthogonal to fibres, they can fail. Thus plasticity has been given a preference in terms of modeling compared to viscous effects. The viscous effects could be further added to this model in the future.

- The core idea of modeling the squeeze flow based on the IFRM model is to model the prepreg as an equivalent single continuum without differentiating between polymer and fibres, which automatically includes the coupling between the two phases. In this work, this interaction is achieved by overlapping two shell elements (one for polymer and one for fibres) with shared and coincident nodes.

The modeling strategy followed in this work is as follows: each ply contains two shell element components with shared coincident nodes. One of these two components represents fibres whereas the other represents polymer. The shell for fibres is modeled using a full integration standard shell element (QBAT) of Altair Radioss™ and uses an anisotropic elastic material model (Law-58). On the other hand, the shell for polymer is modeled using the full integration pinching shell element (QBATP) developed in the previous section and shall use an elasto-plastic constitutive model (referred to as Law-91) that will be discussed next.

## 4.1 Global plasticity for a pinching shell

In order to model the behavior of the nearly incompressible melt polymer during consolidation; a new elasto-plastic constitutive model has been developed that is compatible with the QBATP shell element. This is inspired from the global plasticity model proposed by Ilyushin (Ilyushin, 1948) for classical shells. The Von-Mises yield criterion ( $f$ ) is defined directly in terms of deviatoric stress resultants ( $\bar{N}^{dev}$ ) and stress couples ( $\bar{M}$ ) as follows,

$$f = \sqrt{16(\bar{M}_{eq}^t)^2 + (\bar{N}_{eq}^t)^2} - \sigma_y \quad (25)$$

$$\bar{M}_{eq}^2 = \bar{M}_x^2 + \bar{M}_y^2 - \bar{M}_x \bar{M}_y + 3\bar{M}_{xy}^2$$

$$\bar{N}_{eq}^2 = \frac{3}{2} [(\bar{N}_x^{dev})^2 + (\bar{N}_y^{dev})^2 + (\bar{N}_z^{dev})^2 + 2(\bar{N}_{xy})^2]$$

The model uses linear isotropic hardening with radial return and a linear equation of state is used to correlate pressure, specific volume and bulk modulus. Selective reduced integration is performed for the spherical part of stress in order to avoid volumetric locking.

Also note that, the following assumptions are made (for the sake of simplicity) in the development of this model.

- For the criterion, the coupling term of the membrane and bending part is not considered. For the locations that are undergoing consolidation, it is reasonable to assume that they would be predominantly under a membrane (non-bending) stress state rather than a bending stress state thereby justifying the choice of neglecting the coupling term.
- The contribution of transverse shear is also not considered in the criterion. Thus, the resultants  $N_{yz}$  and  $N_{xz}$  are always updated assuming elastic behavior. This is not a strong assumption, since for thin shells it has been shown in Dujc

and Brank (2012) that the results obtained by considering the elastic response for transverse shear showed no significant difference when plasticity was considered for transverse shear.

## 4.2 Algorithm

Using the modified yield criterion for pinching shell, the step by step algorithm is given below:

1. Calculate the deviatoric part of resultant of normal stresses  $\{\bar{N}^n\}$  using,

$$P^n = \frac{1}{3} (\bar{N}_{xx}^n + \bar{N}_{yy}^n + \bar{N}_{zz}^n)$$

$$\{\bar{N}_{dev}^n\} = \begin{Bmatrix} \bar{N}_x^{dev} \\ \bar{N}_y^{dev} \\ \bar{N}_z^{dev} \end{Bmatrix} = \begin{Bmatrix} \bar{N}_x^n + P^n \\ \bar{N}_y^n + P^n \\ \bar{N}_z^n + P^n \end{Bmatrix} \quad (26)$$

2. Calculate a trial deviatoric stress resultant  $\{\bar{N}_{dev}^t\}$  assuming elastic response ( $G$  is the elastic shear modulus).

$$\{\bar{N}_{dev}^t\} = \{\bar{N}_{dev}^n\} + 2G\{\Delta\epsilon_{dev}\} \quad (27)$$

3. Calculate other trial stress resultants ( $\bar{N}_{xy}^t$ ) and trial stress couples ( $\bar{M}_x^t, \bar{M}_y^t, \bar{M}_{xy}^t$ ) as in the case of the elastic constitutive model.
4. Calculate  $P^{n+1}$  assuming a linear equation of state ( $g$ ) and performing a selective reduced integration to avoid volumetric locking ( $K$  is the bulk modulus).

$$P^{n+1} = g(K, \rho^{n+1}, \rho^0) \quad (28)$$

5. Calculate the updated yield stress based on the equivalent plastic strain and hardening modulus (HM) as,

$$\sigma_y = \sigma_y^0 + HM \epsilon_p^{eq} \quad (29)$$

6. Calculate the modified yield criterion calculated in Eq. 25.
7. If  $f \leq 0$ , it implies that the material is not undergoing plastic loading signifying  $\epsilon_p^{eq} = 0$ .

$$\{\bar{N}_{dev}^{n+1}\} = \{\bar{N}_{dev}^t\}$$

$$\{\bar{N}^{n+1}\} = \{\bar{N}_{dev}^{n+1} - P^{n+1}\}$$

$$\bar{N}_{xy}^{n+1} = \bar{N}_{xy}^t$$

$$\{\bar{M}^{n+1}\} = \{\bar{M}^t\} \quad (30)$$

8. If  $f > 0$ , it means that the material is undergoing plastic loading. Thus, a factor for radial return ( $R$ ) needs to be calculated with subsequent updates in the stress resultants, stress couples and equivalent plastic strain.

$$R = \frac{\sigma_y}{\sqrt{16(\bar{M}_{eq}^t)^2 + (\bar{N}_{eq}^t)^2}}$$

$$\{\bar{N}^{n+1}\} = \{\bar{N}_{dev}^t\} R - P^{n+1}$$

$$\bar{N}_{xy}^{n+1} = \bar{N}_{xy}^t R$$

$$\{\bar{M}^{n+1}\} = \{\bar{M}^t\} R$$

$$\Delta\epsilon_p^{eq} = f / (E + HM) \quad (31)$$

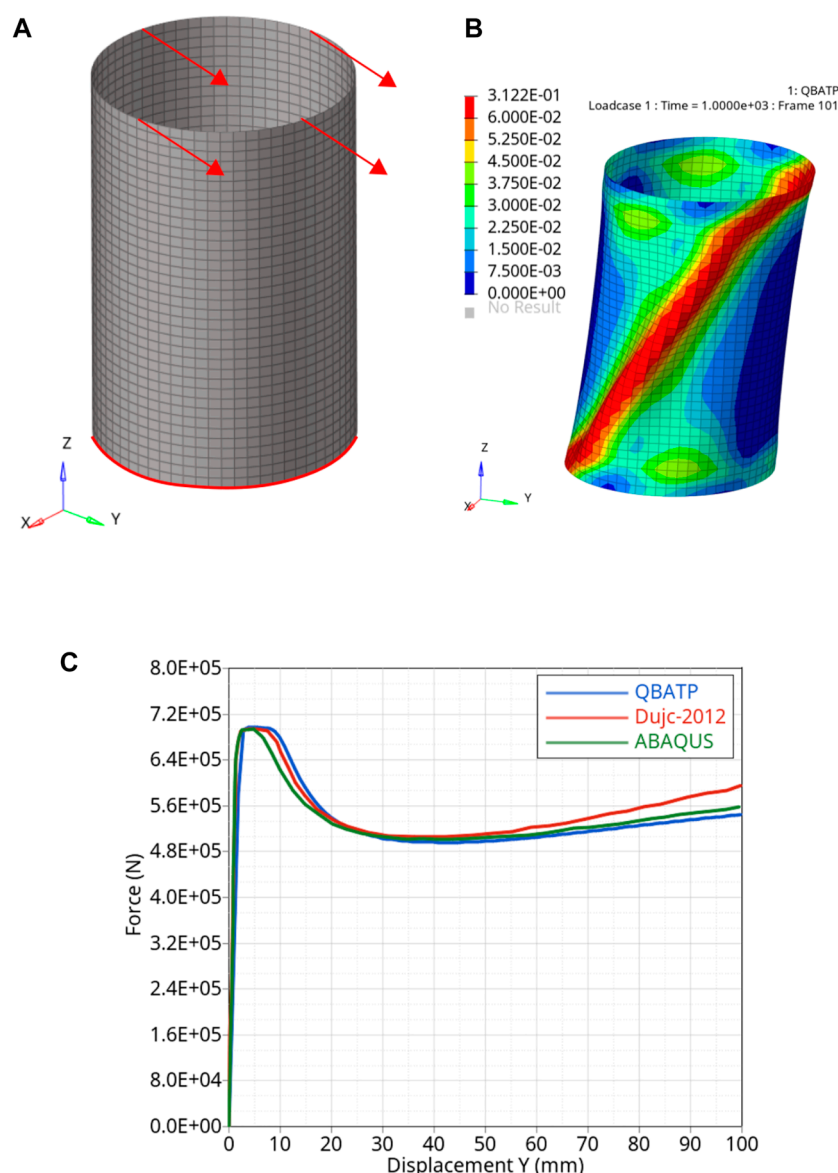


FIGURE 8

QBATP element with elasto-plastic constitutive model validation test: cylinder under shear loading: a comparison of solutions obtained using QBATP shells, ABAQUS and from Dujc and Brank (2012). (A) Geometry, mesh and setup of the test; (B) Visualization of the deformation and the equivalent plastic strain field ( $\epsilon_p^{eq}$ ) for QBATP shells; (C) Comparison of the reaction force in Y direction (N) vs. displacement in Y direction (mm).

### 4.3 Validation

Even though only one of the numerical validations tests is discussed in this section, other numerical tests can be found in Mulye (2021).

The objective of this test is to replicate a benchmark test from Dujc and Brank (2012) consisting of a hollow cylinder with elastic perfectly plastic material properties undergoing large shear. In this test, a hollow cylinder of radius  $r = 285$  mm, height  $H = 850$  mm and thickness  $h = 5$  mm undergoes shear loading (Figure 8A). The lower edge was fixed in all degrees of freedom and an imposed velocity was applied on the top edge in Y direction until a displacement of 100 mm is reached (Figure 8B). All other

DoFs on this edge were constrained. The material properties were set to:  $E = 210,000$  MPa,  $\nu = 0.3$ ,  $\sigma_y = 240$  MPa and hardening modulus (HM) was set to 0 making it a case of perfectly plasticity. Reaction force in the Y direction obtained from the simulation was plotted against the Y displacement of the top edge (Figure 8C). It was found that the response of QBATP element was fairly close to the response obtained by Dujc and Brank (2012). It was also found to be very similar in response to the ABAQUS result involving S4R elements [curve reproduced from Dujc and Brank (2012)].

With this validation test along with the several other tests described in Mulye (2021), it was considered that the constitutive model has been validated.



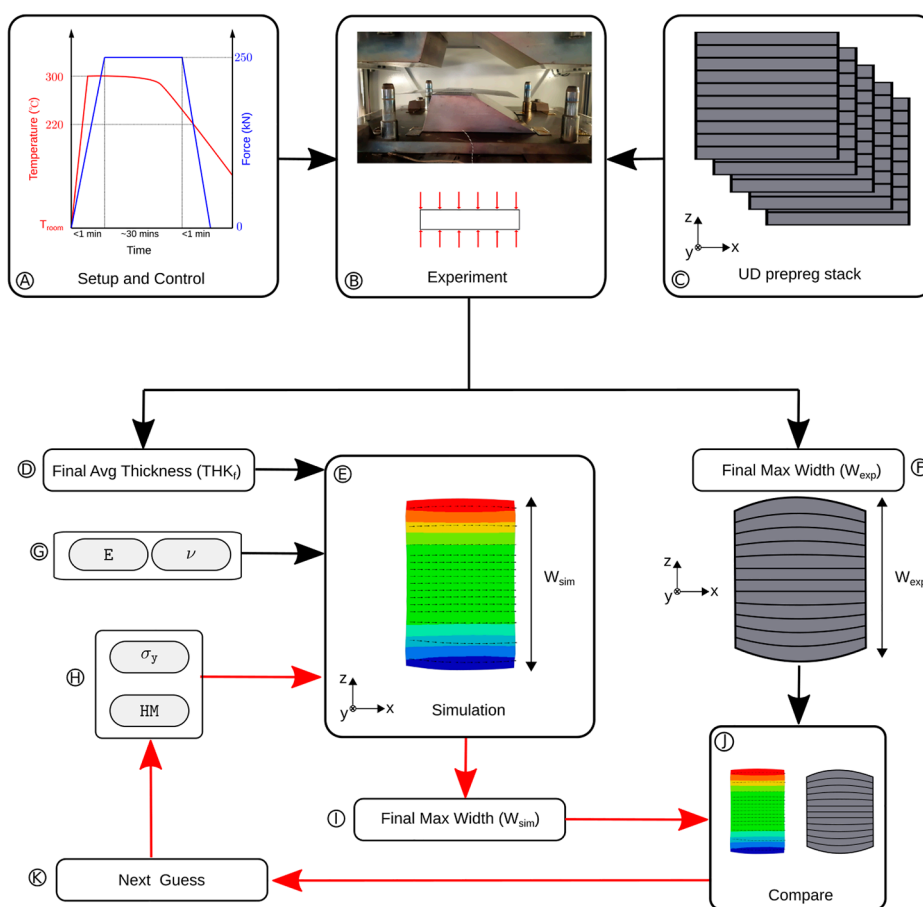


FIGURE 9

A schematic representation of the characterization strategy for the four material parameters of the elasto-plastic constitutive model.

#### 4.4 Characterization of the constitutive model

This constitutive model requires four parameters: Young's modulus ( $E$ ), Poisson's ratio ( $\nu$ ), Yield stress ( $\sigma_y$ ) and isotropic hardening modulus ( $HM$ ). Due to the very low stiffness of the melt polymer and the absence of fibres in the in-plane transverse direction; the classic uniaxial tensile test could not be used. Therefore, an alternative approach was considered. The parameters  $E$  and  $\nu$  were obtained using the Tait equation,

$$V_p(T, P) = V_p(T, 0) [1 - C(T)] \ln \left[ 1 + \frac{P}{B(T)} \right] \quad (32)$$

where  $V_p$  is the specific volume of polymer,  $T$  is the temperature,  $P$  is the pressure and other variables ( $B(T)$  and  $C(T)$ ) are material parameters. The material parameters for PA-66 polymer tabulated in Table 1 in Wang et al. (1992) were used. The parameters are:  $C(T) = 0.0894$ ,  $V_p(T, 0) = 0.7657e^{0.00066T}$  and  $B(T) = 3226e^{-0.00504E-3T}$ . Further, by assuming a linear equation of state and assuming an isothermal process; the bulk modulus of the polymer ( $K$ ) was found to be 226.46 MPa. In future work, these assumptions can be resolved by implementing a specific and temperature dependent equation of state. The incompressibility of melt polymer is the motivating factor to use Poisson's ratio ( $\nu$ ) as

0.495. Using, the bulk modulus and Poisson's ratio, the Young's modulus was calculated using  $E = 3K(1 - 2\nu)$  and it was found to be 6.8 MPa.

To obtain the remaining two material parameters yield stress ( $\sigma_y$ ) and hardening modulus ( $HM$ ), a UD consolidation test is proposed here in which the UD stack is squeezed in a flat mold at a high temperature equivalent to QSP®. The final deformed shape obtained from the process is used to characterize these two parameters. The key idea here is to use the flat sections of the actual mold to characterize the constitutive model avoiding the need for a dedicated setup for characterization. This point makes it highly suitable for industrial use where a dedicated characterization campaign is often difficult to conduct as it can impact the design cycle time and cost significantly.

It is worth mentioning that an attempt was made to use a Digital Image Correlation technique was attempted by marking an initial grid on the specimen so that the local deformations could be studied. However, due to the squeeze flow occurring at such a high temperature, the markings were spread thereby making it impossible to study local deformations with this approach.

The workflow for the characterization procedure is shown in Figure 9. The stack of UD prepreps undergoes consolidation in the flat sections of the mold. A schematic representation of the temperature and loading cycles is shown in. After the completion

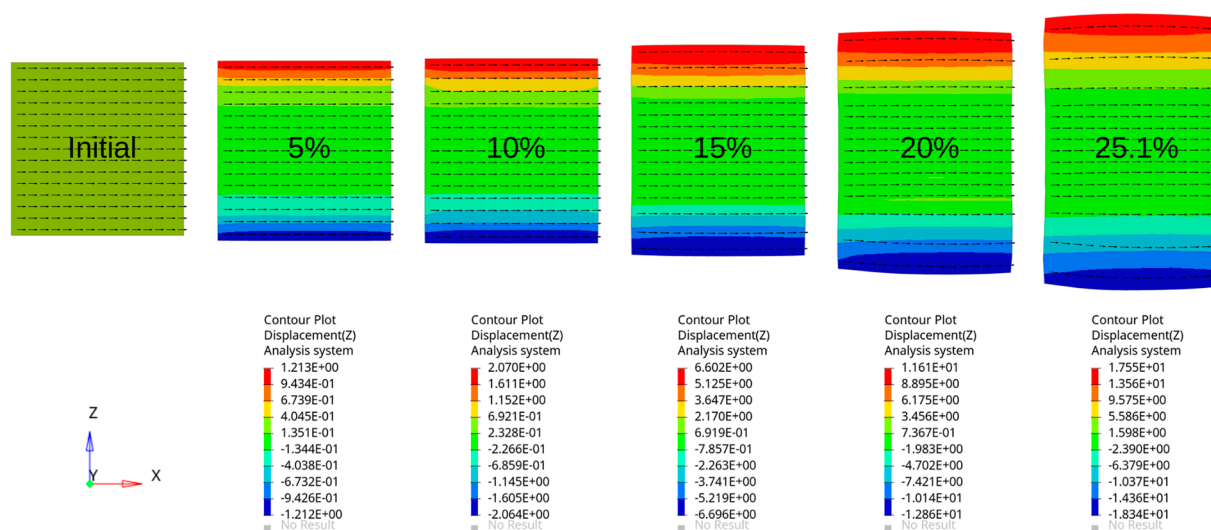


FIGURE 10

Deformation of a flat  $[0^\circ]_5$  stack undergoing various degrees of consolidation (5%–25.1%).

of the consolidation experiment, one can measure the final average thickness and final maximum width using the deformed shape of the sample.

Due to the use of the industrial hydraulic press, this is representative of industrial conditions. Thus neither the accurate compaction force nor the punch displacement can be controlled during the test. This also is a typical situation in the industrial setups where these quantities cannot be controlled or measured very precisely. Thus, the characterization strategy was planned solely based on the final deformed shape after consolidation.

The final deformed shape can be subdivided into two quantities: out of plane deformation (thickness reduction) and in-plane deformation (increase of width and length due to the transverse squeeze flow). These two are the only outputs needed for the characterization method proposed here.

## 4.5 Experimental procedure

The characterization in this work is carried out on UD plies. The UD ply tapes used in this work consist of Glass fibres impregnated with PA-66 polymer ( $V_f = 60\%$ ). The specification for the same is given by Celestran<sup>®</sup> CFR-TP PA-66 GF60-02 (Supplier: TICONA). The experimental campaign on a stack of UD prepreps with a configuration  $[0^\circ]_5$  and dimensions 60 mm  $\times$  60 mm. The total initial thickness was measured to be 1.55 mm. The experiments were conducted using the Omega mold shown in Figure 9, mounted on a hydraulic press of 750 kN capacity. Only one sample was tested for this campaign. Metal spacers of appropriate thicknesses were used as a way to restrict the maximum amount of consolidation.

Referring back to Figure 9, the value of the final average thickness serves as an input to the simulation. Also, the material parameters obtained using Tait equation and incompressibility condition (E and  $\nu$ ) are input to the simulation. Using these inputs, a set of simulations were performed by varying the values for  $\sigma_y$  and HM for the material. The final maximum width obtained from

the simulation ( $W_{sim}$ ) was compared with the final maximum width obtained from the experiments ( $W_{exp}$ ) in the block. This difference ( $W_{sim} - W_{exp}$ ) served as a quantitative measure in order to perform the simulations with the next guess of  $\sigma_y$  and HM. This feedback loop is indicated by the red colored arrows in Figure 9. A set of simulations consisting of 25 simulations with a range of values for the parameters  $\sigma_y = [0.05, 0.1, 0.25, 0.5, 1]$  MPa and  $HM = [0.05, 0.1, 0.25, 0.5, 1]$  MPa were performed. Based on the obtained results and comparing the quantity ( $W_{sim} - W_{exp}$ ), a further refinement in the material properties was performed. Thus, the set of values for which the difference ( $W_{sim} - W_{exp}$ ) was minimum were chosen as the material parameters. They were  $\sigma_y = 0.1$  MPa and  $HM = 0.105$  MPa. In future, a dedicated optimization framework can be used in order to obtain more precise values of the material parameters and also multiple experimental repetitions should be done in order to identify the sensitivity of the experiments and thereby the variation of the  $W_{exp}$ .

## 4.6 Consolidation process modeling of thermoplastic UD prepreps

In this section, various test cases of consolidation of UD thermoplastic prepreps are discussed with the aim to demonstrate the capabilities of using the elasto-plastic constitutive model developed in this work along with the QBATP element in order to do consolidation process modeling.

### 4.6.1 Flat $[0^\circ]_5$ case

Even though the characterization of constitutive model was carried out using this prepreg stack configuration; only the maximum final width of the specimen was used for the characterization. Thus, it is interesting to observe the overall final shape and to compare that with the experimental observations.

For the simulation, a flat UD ply of dimensions 60 mm  $\times$  60 mm and a thickness of 1.55 mm was modeled between two flat

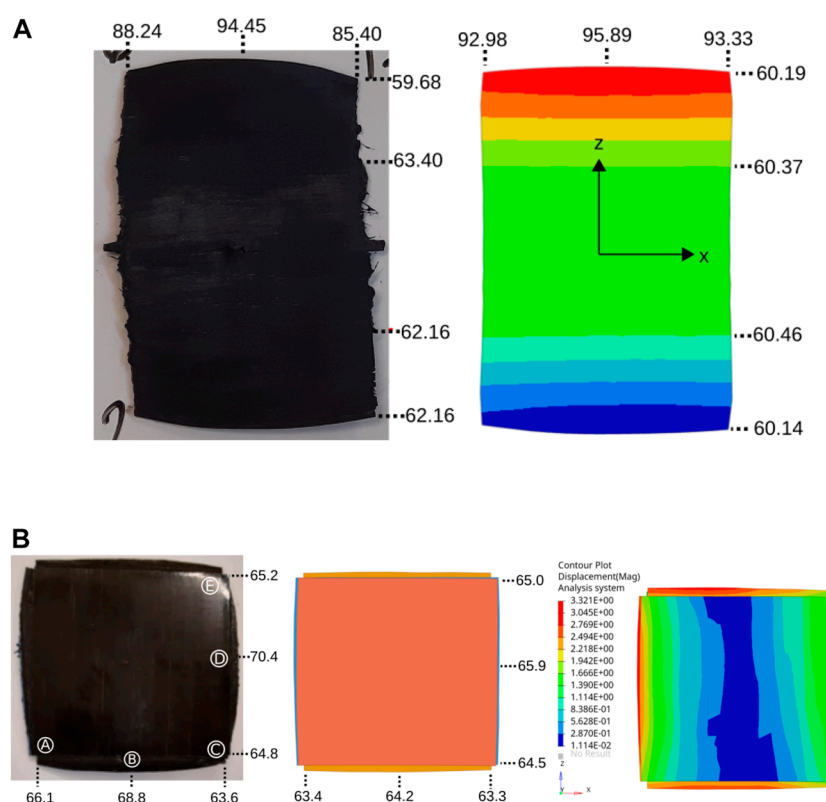


FIGURE 11

Comparison of the numerical simulation and experimental observations for (A) a flat unidirectional  $[0^\circ]_5$  stack; (B) a flat  $[0^\circ/90^\circ]_2$  stack (numbers indicate the dimensions measured at various locations of the stack).

molds. The punch and die are given elastic material properties. The summary of the material properties used for this simulation is given in the [Supplementary Material](#) (Section 3). An imposed displacement is applied on the flat punch which induces a transverse squeeze flow in the prepreg stack whereas the die is fixed in all DoFs. The simulation is run until a final average thickness of 1.161 mm was obtained which corresponds to a total consolidation of 25.1%. The displacement field along direction Z at various stages of the consolidation is shown in [Figure 10](#). The final deformed shape obtained from the simulation is compared to the experiment in [Figure 11A](#). Fibres being nearly inextensible, the displacements along X are very small as indicated by the measurements at various locations. It can be observed that even though some curvature is seen in the simulation depicting the barreling effect, it does not match exactly with the experiment. This difference could have come from the ply-mold interaction and the heat transfer happening at their interface which is not modeled in the simulation.

#### 4.6.2 Flat $[0^\circ/90^\circ]_5$ case

Another consolidation experimental test is conducted with a stack of the configuration  $[0^\circ/90^\circ]_2$  where each ply is of the size  $60\text{ mm} \times 60\text{ mm} \times 0.31\text{ mm}$ . This is motivated by a similar previous work discussed in [Sorba \(2017\)](#). Starting with an initial average stack thickness of 1.225 mm; a consolidation operation was performed until the final average stack thickness of 1.19 mm was achieved. The loading and boundary conditions are exactly the same as that of

the  $[0^\circ]_5$  case. Also, the material properties are same (except the direction of the fibres).

The in-plane deformations observed from the simulations are compared with those obtained from the experiments in [Figure 11B](#). The width predictions at the corners (locations, and are predicted quite well from the simulation (with a difference of less than 1 mm). Also, the deformation patterns at the corners are predicted with a good accuracy. However, the amount of widening predicted by the simulation at the midpoints of sides of the stack (locations and) is less than what has been observed in the experiments. A further investigations both from the point of view of numerical and experimental work can be helpful in identifying and resolving the differences observed in the results of the simulation and the experiment. As discussed in [Sorba et al. \(2017\)](#), the presence of a thin polymer layer at the interface in cross-ply stacks enhances layer spreading.

## 5 Unified numerical process modeling of forming and consolidation

With all the above ingredients (i.e., QBATP shell element and elasto-plastic constitutive model for melt polymer) implemented and validated, one can attempt to perform a unified numerical process simulation of forming and consolidation. In addition to the modeling strategy discussed already, the ply-ply interaction is

modeled with Type-25 contact law in Altair Radioss<sup>TM</sup> with interply adhesion as discussed in Mulye et al. (2020).

## 5.1 Unified approach testing and validation

The objective of this section is to use all the novel pinching shell element, elasto-plastic constitutive model for pinching shell coupled with the interply adhesion in order to test the unified approach to model both forming and consolidation flow. This has been done for the following two cases.

### 5.1.1 Revisiting the industrial model from CETIM

In this section, the industrial model from CETIM discussed previously in Mulye et al. (2020) is revisited but with the updated modeling strategy that consists of using the QBATP element with the elasto-plastic constitutive model. Note that in Mulye et al. (2020), only the forming phase was simulated using the classical shell elements.

The considered industrial model (Figure 12) has a prepreg stack consisting of 9 plies of different shapes, fibre architectures (UD/woven) and fibre orientations. The woven prepreg plies are TEPEX<sup>®</sup> dynalite 101-RG600(x) (Supplier: BOND LAMINATES). The UD ply tapes are Celestran<sup>®</sup> CFR-TP PA-66 GF60-02 (Supplier: TICONA). A mesh size of 4 mm was used which generated a total 29,653 nodes consisting of 48,404 quadrilateral elements. The material parameters and parameters related to the interply adhesion are taken from Mulye et al. (2020). In terms of computational time for simulating this model, it took about 2 h with 4 threads with shared memory processing on a local computer [Intel(R) Xeon(R) CPU E3-1545M v5 @ 2.90GHz (x86\_64)] with the natural time-step of the model.

Overall, with reference to the final deformed shape, the results of simulation with unified approach were found to be comparable with the ones obtained from the experiment (refer to the Section 6 in Supplementary Material to see a qualitative comparison between the two). However, now with this new unified approach, one now has access to additional information such as the through-thickness normal stress.

The maximum initial stack thickness is 3.5 mm. Thus, a rough estimate can be made to predict that the consolidation phase will begin when the distance between the punch and die reduces to 3.5 mm (after adjusting for the thicknesses of die and punch themselves). Based on this prediction, the transverse normal stress for all plies was plotted along with the magnitude of contact force experienced by the punch at various instants during the simulation. Figure 13A is obtained when the punch-die distance is 4.78 mm which is before the beginning of the consolidation as per estimate. As expected, there is neither a noticeable  $\sigma_{zz}$  nor any contact force on the flat portions of the punch. After the consolidation begins, one should observe the development of a through-thickness stress in the regions which undergo consolidation. As a consequence, one should observe a reaction force on the punch in that region. This was observed in the Figure 13B. As the consolidation phase continues further, the stress field intensifies and spreads into other regions as more regions come in contact with the molds and begin experiencing consolidation pressure. Finally, at the end of consolidation phase; Figure 13C shows the state of the stress and

reaction force. At this stage, the distance between the die and punch is 3.22 mm (which amounts to  $\approx 8\%$  consolidation).

As expected, it can be seen that the maximum compressive stress is on the flat section of the top face of the component. Whereas, other regions are contributing less in the sharing of the consolidation pressure. This can be qualitatively cross-verified with the observed contact force plot. Ply-wise through-thickness normal stress is an important information which can be used in the design of the mold and/or stack. This helps in identifying which regions will have a poor quality of consolidation. The regions with lower consolidation are likely to have higher porosities and therefore are possible sites of weakness/failure for the component. Thus, based on the information obtained from this type of simulation, one can either modify the mold design or the stack itself, in order to have a better consolidation behavior.

Similar to the exercise performed in Mulye et al. (2020), the fibre orientations after the simulations using the unified approach were compared at various locations with those obtained from the experiments. The fibre orientations obtained from the unified simulation approach are listed in the Supplementary Material (Section 4). Even though a detailed analysis of the comparison can be found in Mulye (2021); overall when compared for all faces, the fibre orientations predicted by the unified simulation were on an average  $5.4^\circ$  away from the experiments. This value is similar to the value obtained with a pure forming solution (which was  $5.9^\circ$  degrees).

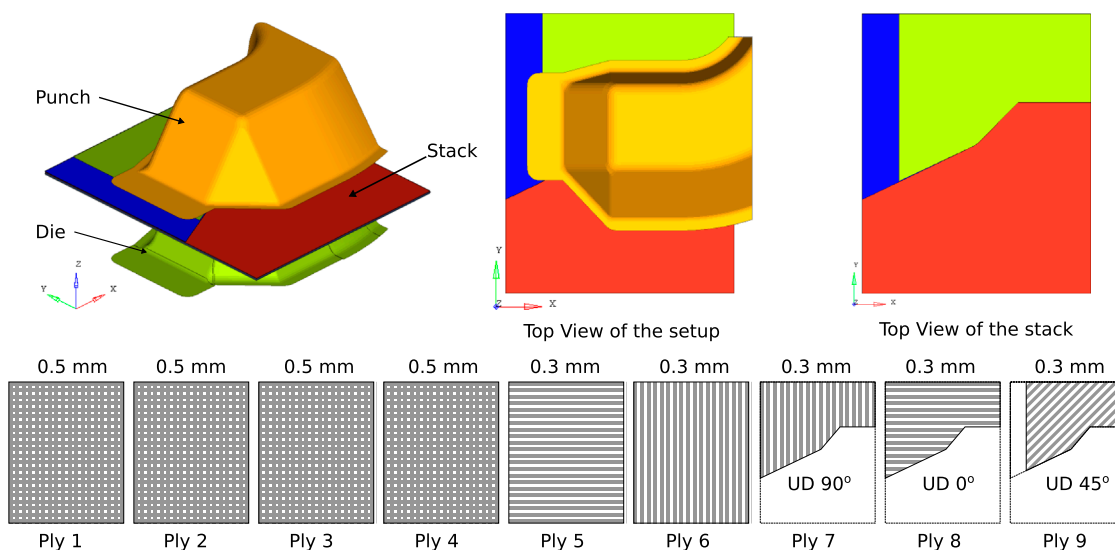
This verification is essential since there are several changes in the modeling approach for the forming approach compared to the unified approach such as the usage of QBATP elements with elasto-plastic constitutive model and other consequences of the pinching behavior both within the components as well as at the interfaces.

It is perhaps expected that in this component, there is not much of a squeeze flow to be observed because of mainly two reasons. First, the compressive loading predominantly passed through a zone on the top face (Figure 13C). Second, due to the overall stack configuration, there may not be enough room for the squeeze flow to occur. This may not be the case with other components and stacking sequences. An example designed to show the squeeze flow on a semi-industrial component is discussed next.

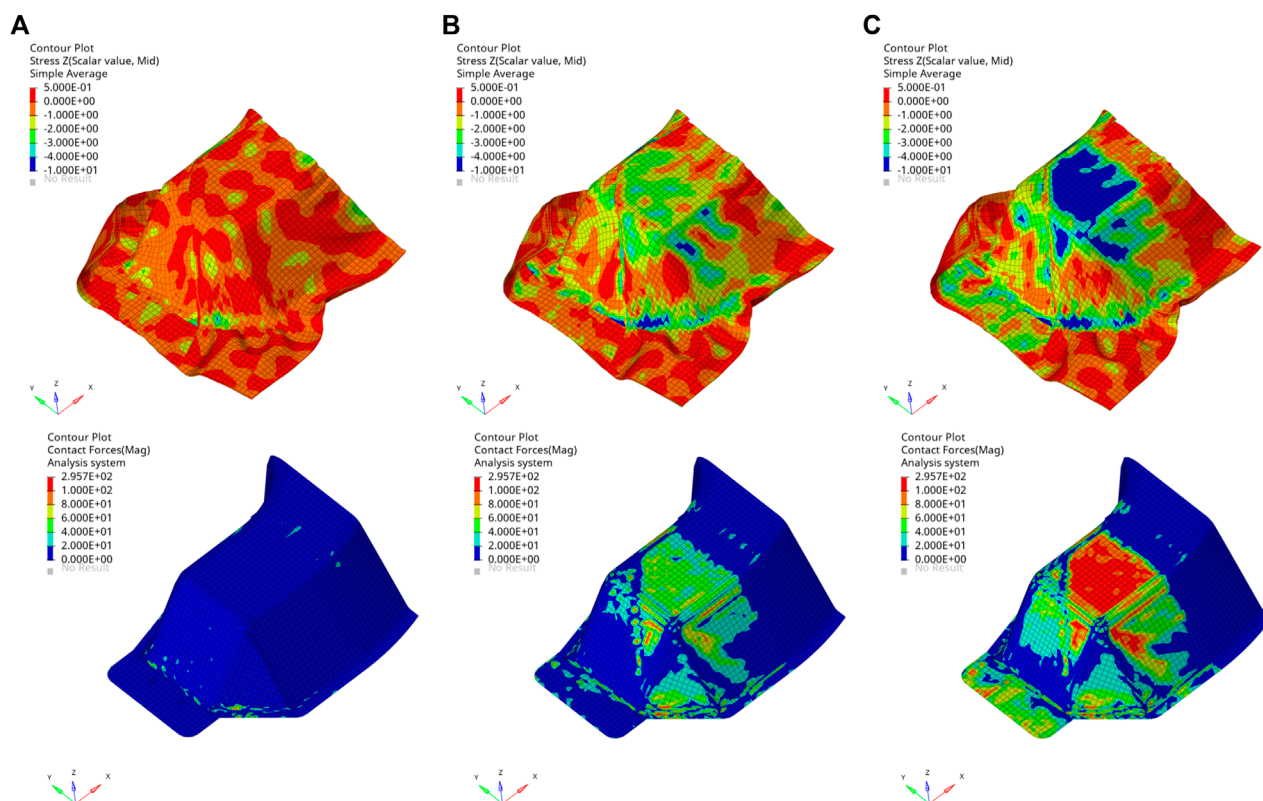
### 5.1.2 Numerical simulation of a UD ply

To validate this unified approach, a semi-industrial model designed by CETIM was considered. It consists of a flat UD ply stack  $[0^\circ]_4$  of dimensions 420 mm  $\times$  60 mm and thickness of 0.31 mm each resulting in a total stack thickness of 1.24 mm. The fibres are oriented along the X direction (Figure 14A). The UD ply tapes used in this work consist of Glass fibres impregnated with PA-66 polymer Celestran<sup>®</sup> CFR-TP PA-66 GF60-02 (Supplier: TICONA). The unified numerical simulation consisting of 6,000 deformable shell elements took around 10 min on a local computer [Intel(R) Xeon(R) CPU E3-1545M v5 @ 2.90GHz (x86\_64)] using the natural time-step of the model.

In order to quantitatively compare the results of the unified forming and consolidation simulation with the experiments, the final widths (in mm) were measured at various locations of the ply in both experiments and simulation (Figure 14B). Ideally it would have been interesting to compare the field of the displacement/strains in the ply using Digital Image Correlation

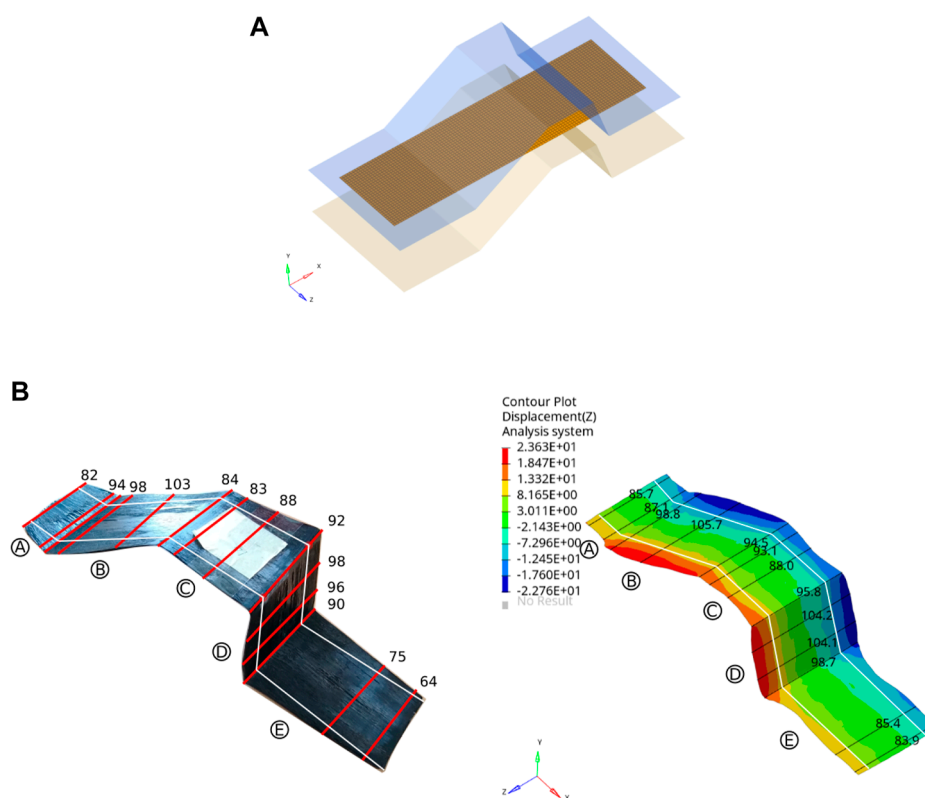
**FIGURE 12**

Numerical model of the industrial component designed by CETIM showing its geometry and the prepreg stack configuration (Ply 1 to 9: from bottom to the top of the stack).

**FIGURE 13**

Results of the unified numerical simulation of the forming and consolidation for QSP®: Field of the transverse normal stress  $\sigma_{zz}$  in MPa (top) and field of the magnitude of the contact force in N on the punch (bottom): (A) Before consolidation phase begins; (B) During the consolidation phase; (C) After the consolidation phase (final state).





**FIGURE 14**

Experimental validation of the unified numerical simulation of a unidirectional ply on Omega mold: (A) Geometry, setup and mesh; (B) Width comparison between experiments and the numerical simulation results (measurements are in mm and the initial width is shown with the white lines).

(DIC) technique. We tried to mark the grid on the initial ply before it undergoes consolidation in order to perform a DIC during or after consolidation. However, because of the squeeze-flow these marked lines spread (turning into a patch of paint). So it becomes nearly impossible to perform DIC on such a sample. Therefore, we have chosen to measure dimensions at several locations and compare them with the simulation. Since, the ply thickness is what is controlled in the simulation (through the application of imposed displacement on the punch), and because there is no significant change in the dimensions along the fibre directions; only the width measurements from the simulation at various locations were compared to the experimental measurements.

Based on the comparison, several observations can be made. With the exception of face, all other faces have better results. Considering all faces, the average of absolute errors in the widths calculated from simulation and obtained from the experiments was found to be 7.1 mm. Also, the maximum width predicted by the simulation is 105.7 mm (on face) which is close to the experimentally observed value which is 103 mm.

There are several possible hypotheses that can explain the difference of results on face such as, 1) thermal effects such as the temperature inhomogeneity in the mold 2) geometrical effects such as imperfect parallelism of the mold 3) process related effects such as a possible local deformations (bending) of the mold itself.

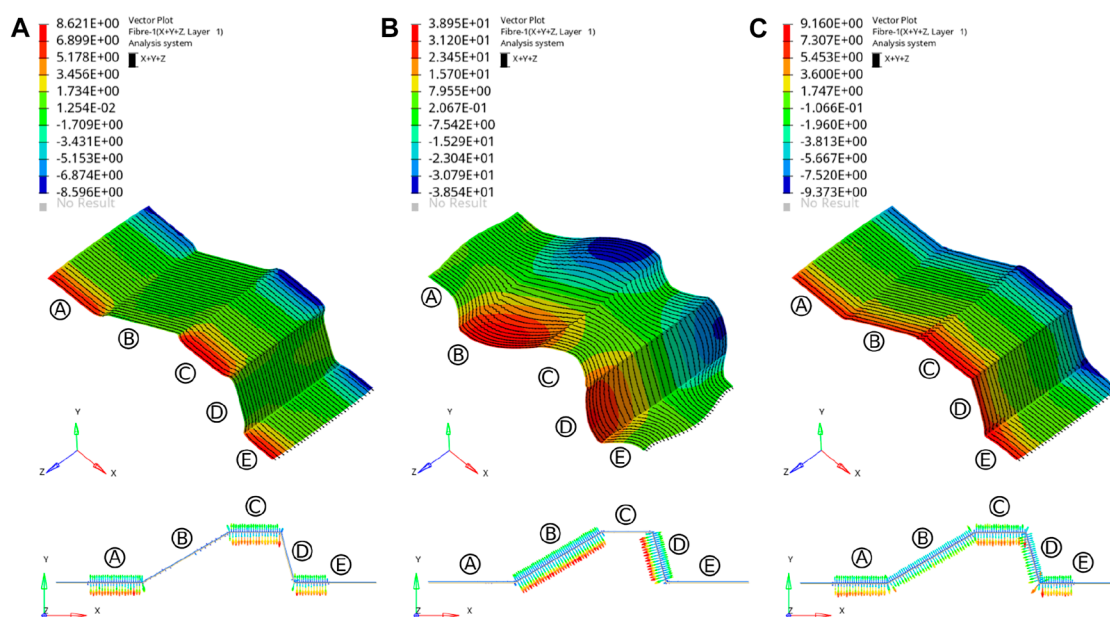
In summary, the two validation tests presented above show that the simulation using the unified approach are able to model

the squeeze flow behavior. It is also able to predict the final deformed shape with a reasonable accuracy with this modeling approach.

## 6 Application: improving the mold and part design

This section demonstrates how the unified simulation strategy for forming and consolidation (when included in the iterative design pipeline) can help in improving the mold design for thermoplastic composites. To show the iterative design process for this demonstrative example, the geometry of punch was locally modified by translating nodes normal to their plane using Hypermesh. The modifications are done based on the observed deformations from simulation. The original design (Section 5.1.2) is referred to here as **Design-1** shown in Figure 15A. Recalling that the consolidation was found to occur only in zones, and. On the other hand, the zones and experienced no noticeable consolidation.

Based on this observation, the nodes on faces and of the punch were moved inwards (orthogonally to the face) by a small distance of about 0.6 mm (which was later found to be significant) to arrive at **Design-2**. The simulation outcomes of **Design-2** are shown in Figure 15B. It showed the exact opposite trend as that of **Design-1**. The consolidation was found to occur in zones and whereas the



**FIGURE 15**  
Iterative design change in the mold geometry with the use of a unified numerical process modeling of forming and consolidation: field of the Z displacement in mm (top) and reaction force distribution (bottom) for: (A) Design-1; (B) Design-2; (C) Design-3.

other zones, and showed no significant consolidation. Again, this is evident from the reaction force distribution plot (**Figure 15B**). This provided an indication that for a good consolidation in all zones, the geometry of the punch should be somewhere in between **Design-1** and **Design-2**.

Also, an important observation can be made with respect to the fibre orientation distribution for various designs. By tuning the mold design and thereby tweaking the amount of squeeze flow occurring in each zone, it was possible to maintain the straightness of the fibres in case of **Design-3** which was not possible with the initial designs **Design-1** and **Design-2** where the local barreling type effect made significant changes in the fibre orientations.

Based on this conclusion, **Design-3** was created this time by moving the nodes on faces and by 0.1 mm with respect to the **Design-1**. The simulation on this design, showed a relatively uniform distribution of consolidation on all faces as shown in **Figure 15C**.

This demonstrates how the unified solution proposed in this work can help the manufacturers to design better tooling based on the outcomes of the numerical process simulation that considers forming, consolidation and potential transverse squeeze flow in order to achieve a desired product quality and part design.

## 7 Conclusion

In summary, it has been shown that the simulation of forming and consolidation phases of QSP<sup>®</sup> can be performed using a shell element based unified approach. With the use of the novel pinching shell element (QBATP) and the elasto-plastic constitutive model for the melt polymer (based on four parameters); one can simulate and predict the squeeze flow behavior with a reasonable

accuracy. Additionally due to the use of pinching shell elements in this approach; one has access to additional ply level information such as transverse normal stress which can be used to design the mold and/or the stack itself by incorporating the effects of the consolidation phase together with the forming phase.

## Data availability statement

The original contributions presented in the study are included in the article/**Supplementary Material**, further inquiries can be directed to the corresponding author.

## Author contributions

LM and CB contributed to the conceptualization of this work. LM and AL were involved in the methodology. PM worked on the development of the software with a guidance from LM. SC-C led the experimental campaign in this work. The formal analysis, investigation and writing was carried out by PM. This was supervised by LM, CB, and SC-C. DG provided resources which include previous experimental data and equipment from CETIM. All authors contributed to the article and approved the submitted version.

## Funding

The authors would like to express their gratitude towards ANRT (CIFRE 2017/1621) for the financial support.

## Conflict of interest

PM and LM were employed by Altair Engineering France.

The remaining authors declare that the research was conducted in the absence of any commercial or financial relationships that could be construed as a potential conflict of interest.

## Publisher's note

All claims expressed in this article are solely those of the authors and do not necessarily represent those of their affiliated

organizations, or those of the publisher, the editors and the reviewers. Any product that may be evaluated in this article, or claim that may be made by its manufacturer, is not guaranteed or endorsed by the publisher.

## Supplementary material

The Supplementary Material for this article can be found online at: <https://www.frontiersin.org/articles/10.3389/fmats.2023.1176482/full#supplementary-material>

## References

- Alshahrani, H., and Hojjati, M. (2017). Bending behavior of multilayered textile composite prepreps: Experiment and finite element modeling. *Mater. Des.* 124, 211–224. doi:10.1016/j.matdes.2017.03.077
- Altair Engineering (2022). OpenRadioss source code. Available at: <https://github.com/OpenRadioss/OpenRadioss>.
- Altair Engineering (2018). *Radioss theory manual*. France: Mecalog Sarl.
- Bathe, K., Ramm, E., and Wilson, E. (1975). Finite element formulations for large deformation dynamic analysis. *Int. J. Numer. methods Eng.* 9, 353–386. doi:10.1002/nme.1620090207
- Batoz, J., and Dhatt, G. (1992). *Modélisation des structures par éléments finis*. Paris: Coques. Hermès.
- Belnoue, J.-H., Nixon-Pearson, O., Ivanov, D., and Hallett, S. (2016). A novel hyper-viscoelastic model for consolidation of toughened prepreps under processing conditions. *Mech. Mater.* 97, 118–134. doi:10.1016/j.mechmat.2016.02.019
- Belnoue, J.-H., Nixon-Pearson, O., Thompson, A., Ivanov, D., Potter, K., and Hallett, S. (2018). Consolidation-driven defect generation in thick composite parts. *J. Manuf. Sci. Eng.* 140, 071006. doi:10.1115/1.4039555
- Belytschko, T., Liu, W., Moran, B., and Elkhodary, K. (2013). *Nonlinear finite elements for continua and structures*. United States: John Wiley & Sons.
- Bischoff, M., and Ramm, E. (2000). On the physical significance of higher order kinematic and static variables in a three-dimensional shell formulation. *Int. J. Solids Struct.* 37, 6933–6960. doi:10.1016/S0020-7683(99)00321-2
- Bischoff, M., and Ramm, E. (1997). Shear deformable shell elements for large strains and rotations. *Int. J. Numer. Methods Eng.* 40, 4427–4449. doi:10.1002/(sici)1097-0207(19971215)40:23<4427::aid-nme268>3.0.co;2-9
- Bisshopp, K., and Drucker, D. (1945). Large deflection of cantilever beams. *Q. Appl. Math.* 3, 272–275. doi:10.1090/qam/13360
- Boisse, P., Akkerman, R., Carlone, P., Kärger, L., Lomov, S. V., and Sherwood, J. A. (2022). Advances in composite forming through 25 years of esaform. *Int. J. Material Form.* 15, 39. doi:10.1007/s12289-022-01682-8
- Brank, B., Korelc, J., and Ibrahimbegović, A. (2002). Nonlinear shell problem formulation accounting for through-the-thickness stretching and its finite element implementation. *Comput. Struct.* 80, 699–717. doi:10.1016/S0045-7949(02)00042-1
- Büchter, N., and Ramm, E. (1992). 3d-extension of nonlinear shell equations based on the enhanced assumed strain concept. *Comput. Methods Appl. Sci.* 1992, 55–62.
- Büchter, N., Ramm, E., and Roehl, D. (1994). Three-dimensional extension of nonlinear shell formulation based on the enhanced assumed strain concept. *Int. J. Numer. methods Eng.* 37, 2551–2568. doi:10.1002/nme.1620371504
- Bussetta, P., and Correia, N. (2018). Numerical forming of continuous fibre reinforced composite material: A review. *Compos. Part A Appl. Sci. Manuf.* 113, 12–31. doi:10.1016/j.compositesa.2018.07.010
- Cherouat, A., and Billoët, J. (2001). Mechanical and numerical modelling of composite manufacturing processes deep-drawing and laying-up of thin pre-impregnated woven fabrics. *J. Mater. Process. Technol.* 118, 460–471. doi:10.1016/S0924-0136(01)00987-6
- Cocchetti, G., Pagani, M., and Perego, U. (2013). Selective mass scaling and critical time-step estimate for explicit dynamics analyses with solid-shell elements. *Comput. Struct.* 127, 39–52. doi:10.1016/j.compstruc.2012.10.021
- Dia, M., Hamila, N., Abbas, M., and Gravouil, A. (2020). A nine nodes solid-shell finite element with enhanced pinching stress. *Comput. Mech.* 65, 1377–1395. doi:10.1007/s00466-020-01825-1
- Dörr, D., Brymerski, W., Ropers, S., Leutz, D., Joppich, T., Kärger, L., et al. (2017a). A benchmark study of finite element codes for forming simulation of thermoplastic ud-tapes. *Procedia CIRP* 66, 101–106. doi:10.1016/j.procir.2017.03.223
- Dörr, D., Schirmaier, F. J., Henning, F., and Kärger, L. (2017b). A viscoelastic approach for modeling bending behavior in finite element forming simulation of continuously fiber reinforced composites. *Compos. Part A Appl. Sci. Manuf.* 94, 113–123. doi:10.1016/j.compositesa.2016.11.027
- Dujc, J., and Brank, B. (2012). Stress resultant plasticity for shells revisited. *Comput. Methods Appl. Mech. Eng.* 247, 146–165. doi:10.1016/j.cma.2012.07.012
- Dvorkin, E., and Bathe, K. (1984). A continuum mechanics based four-node shell element for general non-linear analysis. *Eng. Comput.* 1, 77–88. doi:10.1108/eb023562
- Gong, Y., Peng, X., Yao, Y., and Guo, Z. (2016). An anisotropic hyperelastic constitutive model for thermoplastic woven composite prepreps. *Compos. Sci. Technol.* 128, 17–24. doi:10.1016/j.compscitech.2016.03.005
- Gong, Y., Xu, P., Peng, X., Wei, R., Yao, Y., and Zhao, K. (2018). A lamination model for forming simulation of woven fabric reinforced thermoplastic prepreps. *Compos. Struct.* 196, 89–95. doi:10.1016/j.compstruct.2018.05.004
- Guillon, D., Lemasçon, A., and Callens, C. (2016). “QSP®: An innovative process based on tailored preforms for low cost and fast production of optimized thermoplastic composite parts,” in Proceedings of the 17th European Conference on Composite Materials ECCM17, Munich, Germany, 26–30th June 2016.
- Haanappel, S., Ten Thije, R., Sachs, U., Rietman, B., and Akkerman, R. (2014). Formability analyses of uni-directional and textile reinforced thermoplastics. *Compos. Part A Appl. Sci. Manuf.* 56, 80–92. doi:10.1016/j.compositesa.2013.09.009
- Harrison, P., Clifford, M., Long, A., and Rudd, C. (2002). Constitutive modelling of impregnated continuous fibre reinforced composites micromechanical approach. *Plastics, Rubber Compos.* 31, 76–86. doi:10.1179/146580102225001409
- Hughes, T., and Tezduyar, T. (1981). Finite elements based upon mindlin plate theory with particular reference to the four-node bilinear isoparametric element. *J. Appl. Mech.* 48, 587–596. doi:10.1115/1.3157679
- Ilyushin, A. (1948). *Plasticity [in Russian]*. Moscow–Leningrad: gostekhzdat.
- Irisarri, F., Macquart, T., Julien, C., and Espinassou, D. (2019). A novel design method for the fast and cost-effective manufacture of composite parts employing the quilted stratum process. *Compos. Part B Eng.* 158, 364–372. doi:10.1016/j.compositesb.2018.09.070
- Khan, M., Reynolds, N., Williams, G., and Kendall, K. (2015). Processing of thermoset prepreps for high-volume applications and their numerical analysis using superimposed finite elements. *Compos. Struct.* 131, 917–926. doi:10.1016/j.compstruct.2015.06.056
- Lim, T., and Ramakrishna, S. (2002). Modelling of composite sheet forming: A review. *Compos. Part A Appl. Sci. Manuf.* 33, 515–537. doi:10.1016/S1359-835X(01)00138-5
- Machado, M., Fischlschweiger, M., and Major, Z. (2016). A rate-dependent non-orthogonal constitutive model for describing shear behaviour of woven reinforced thermoplastic composites. *Compos. Part A Appl. Sci. Manuf.* 80, 194–203. doi:10.1016/j.compositesa.2015.10.028
- Mulye, P. D. (2021). “Unified numerical modeling of forming and consolidation of thermoplastic composites with prepreg patches,” (France: École centrale de Nantes). Ph.D. thesis.
- Mulye, P., Hemmer, J., Morancay, L., Binetruy, C., Leygue, A., Comas-Cardona, S., et al. (2020). Numerical modeling of interply adhesion in composite forming of viscous discontinuous thermoplastic prepreps. *Compos. Part B Eng.* 191, 107953. doi:10.1016/j.compositesb.2020.107953
- O’Bradaigh, C., and Pipes, B. (1991). Finite element analysis of composite sheet-forming process. *Compos. Manuf.* 2, 161–170. doi:10.1016/0956-7143(91)90135-4

- Olovsson, L., Unosson, M., and Simonsson, K. (2004). Selective mass scaling for thin walled structures modeled with tri-linear solid elements. *Comput. Mech.* 34, 134–136. doi:10.1007/s00466-004-0560-6
- Oñate, E. (2013). *Structural analysis with the finite element method. Linear statics: Volume 2: Beams, plates and shells*. Berlin, Germany: Springer Science & Business Media.
- Parisch, H. (1991). An investigation of a finite rotation four node assumed strain shell element. *Int. J. Numer. Methods Eng.* 31, 127–150. doi:10.1002/nme.1620310108
- Rogers, T. (1989). Squeezing flow of fibre-reinforced viscous fluids. *J. Eng. Math.* 23, 81–89. doi:10.1007/bf00058434
- Sansour, C., and Bufler, H. (1992). An exact finite rotation shell theory, its mixed variational formulation and its finite element implementation. *Int. J. Numer. Methods Eng.* 34, 73–115. doi:10.1002/nme.1620340107
- Schäfer, B., Dörr, D., and Kärger, L. (2021). “Potential and challenges of a solid-shell element for the macroscopic forming simulation of engineering textiles,” in ESAFORM 2021 - 24th International Conference on Material Forming, Online event, 14 Apr 2021 → 16 Apr 2021. doi:10.25518/esaform21.883
- Schäfer, B., Dörr, D., and Kärger, L. (2020). Reduced-integrated 8-node hexahedral solid-shell element for the macroscopic forming simulation of continuous fibre-reinforced polymers. *Procedia Manuf.* 47, 134–139. doi:10.1016/j.promfg.2020.04.154
- Schell, J., Amory, L., and Guillon, D. (2016). Movement of patches during thermoforming: Experiment and simulation. *AIP Conf. Proc.* 1769, 170032.
- Schwarze, M., and Reese, S. (2011). A reduced integration solid-shell finite element based on the eas and the ans concept—Large deformation problems. *Int. J. Numer. Methods Eng.* 85, 289–329. doi:10.1002/nme.2966
- Simo, J., and Rifai, M. (1990). A class of mixed assumed strain methods and the method of incompatible modes. *Int. J. Numer. methods Eng.* 29, 1595–1638. doi:10.1002/nme.1620290802
- Simo, J., Rifai, M., and Fox, D. (1990). On a stress resultant geometrically exact shell model. part iv: Variable thickness shells with through-the-thickness stretching. *Comput. methods Appl. Mech. Eng.* 81, 91–126. doi:10.1016/0045-7825(90)90143-a
- Sorba, G., Binetruy, C., Leygue, A., and Comas-Cardona, S. (2017). Squeeze flow in heterogeneous unidirectional discontinuous viscous prepreg laminates: Experimental measurement and 3d modeling. *Compos. Part A Appl. Sci. Manuf.* 103, 196–207. doi:10.1016/j.compositesa.2017.10.007
- Sorba, G. (2017). “Experimental study and numerical modelling of squeeze flow in laminate viscous discontinuous composites,” (France: École centrale de Nantes). Ph.D. thesis.
- Soulat, D., Cheruet, A., and Boisse, P. (2006). Simulation of continuous fibre reinforced thermoplastic forming using a shell finite element with transverse stress. *Comput. Struct.* 84, 888–903. doi:10.1016/j.compstruc.2006.02.011
- Thomas J, P. P., and Charlotte, L. (2019). “Process simulation to assist in the design of a tp composite window frame,” in SAMPE Europe Conference, Madrid, Spain, 3 – 5 October 2023.
- Vanloooster, K., Lomov, S., and Verpoest, I. (2009). Experimental validation of forming simulations of fabric reinforced polymers using an unsymmetrical mould configuration. *Compos. Part A Appl. Sci. Manuf.* 40, 530–539. doi:10.1016/j.compositesa.2009.02.005
- Wang, Y., Chia, W., Hsieh, K., and Tseng, H. (1992). Specific volume of molten thermoplastic polymer composite at high pressure. *J. Appl. Polym. Sci.* 44, 1731–1736. doi:10.1002/app.1992.070441005
- Willems, A., Lomov, S., Vandepitte, D., and Verpoest, I. (2006). “Double dome forming simulation of woven textile composites,” in The ninth international conference on material forming ESAFORM, Glasgow, United Kingdom, April 26–28, 2006, 747–750.
- Xiong, H., Hamila, N., and Boisse, P. (2019). Consolidation modeling during thermoforming of thermoplastic composite prepregs. *Materials* 12, 2853. doi:10.3390/ma12182853
- Xiong, H., Maldonado, E., Hamila, N., and Boisse, P. (2018). A prismatic solid-shell finite element based on a dkt approach with efficient calculation of through the thickness deformation. *Finite Elem. Analysis Des.* 151, 18–33. doi:10.1016/j.finel.2018.08.003
- Xiong, H. (2017). “Simulation of forming, compaction and consolidation of thermoplastic composites based on solid shell elements,” (France: Université de Lyon). Ph.D. thesis.



## OPEN ACCESS

## EDITED BY

Ahmed Barhoum,  
Dublin City University, Ireland

## REVIEWED BY

Senthilkumar Krishnasamy,  
King Mongkut's University of Technology  
North Bangkok, Thailand  
Senthil Muthu Kumar Thiagamani,  
Kalasalingam University, India

## \*CORRESPONDENCE

Wassim Guerfala,  
✉ wassim.guerfala@ec-nantes.fr

RECEIVED 28 February 2023

ACCEPTED 29 May 2023

PUBLISHED 15 June 2023

## CITATION

Guerfala W, Rozycki P and Binetruy C  
(2023), Development of flax/basalt/  
PA11 bio-composites: optimal  
formulation and modelling of the quasi-  
static behaviour.  
*Front. Mater.* 10:1176408.  
doi: 10.3389/fmats.2023.1176408

## COPYRIGHT

© 2023 Guerfala, Rozycki and Binetruy.  
This is an open-access article distributed  
under the terms of the [Creative  
Commons Attribution License \(CC BY\)](#).  
The use, distribution or reproduction in  
other forums is permitted, provided the  
original author(s) and the copyright  
owner(s) are credited and that the original  
publication in this journal is cited, in  
accordance with accepted academic  
practice. No use, distribution or  
reproduction is permitted which does not  
comply with these terms.

# Development of flax/basalt/PA11 bio-composites: optimal formulation and modelling of the quasi-static behaviour

Wassim Guerfala<sup>1,2\*</sup>, Patrick Rozycki<sup>1</sup> and Christophe Binetruy<sup>1</sup>

<sup>1</sup>Institut de recherche en génie civil et mécanique, UMR CNRS 6183, Ecole centrale Nantes, Nantes Université, Nantes, France, <sup>2</sup>Department Body in White Research and Innovation Unit, Bertrandt, Vélizy, France

Environmental impact is becoming increasingly important in the automotive industry, with car manufacturers looking to reduce CO<sub>2</sub> emissions through cleaner engines and structural weight reduction. Composite materials offer an excellent alternative to standard steels with significant weight reduction and the ability to produce functional parts (Rangappa et al., *Polymer Composites*, 2022, 43, 645–691), (Jeyaguru et al., *Polymer Composites*, 2022, 43, 3902–3914), (Sanjay et al., *Journal of Cleaner Production*, 2018, 172, 566–581). The main objective of this study is to investigate the potential of a new and unique hybrid bio-composite material combining flax and basalt fibers and PA11 polymer. This material design is studied with the idea of reducing the moisture sensitivity, variabilities, and uncertainties of vegetal fibers by the presence of basalt fibers. The first step consists of developing a new hybrid composite material and studying its quasi-static mechanical behaviour when subjected to different humidity levels. Then, a multi-scale non-linear homogenization approach is proposed to support the interpretation of the characterization test results. The experimental results show the benefits of the hybridization. In fact, the hybrid composite is 20% stiffer than the flax/PA11 composite, 8% lighter than the basalt/PA11 composite and has a reduced dispersion of its mechanical properties, 52% lower than the flax/PA11 composite. Considering the promising properties of the hybrid composite, we have investigated the possibility of developing the front hood of a sports car using this material. The first results highlight a potential mass gain of 18% at iso-performance with the original front hood. The following steps will be devoted to the numerical and experimental validation.

## KEYWORDS

composite materials, natural fibers, hybrid composite, homogenization, thermo-compression

## Introduction

The application of composite materials remains limited in the automotive industry due to various technical, economic, and environmental constraints. Knowledge of the technical aspects of manufacturing (processes and production rate), the mechanical behaviour of these heterogeneous materials (behaviour law and simulation tools) and their lifespan are still insufficient for mass production. On the economic aspect, the high price of fibers, such as carbon fibers, and the high manufacturing cost related to cycle time are the main obstacles to developing these materials. Furthermore, the environmental impact became increasingly



critical with new European regulations for reducing the CO<sub>2</sub> emission and the Carbone footprint of the life cycle automotive structures. The main objective of this research is to define a new concept for semi-structural automotive parts (hood, door, dashboard ...) that can meet the various industrial requirements while respecting environmental regulations. Therefore, the initial work has focused on selecting materials from a wide range of vegetal fibers and bio-sourced polymers with suitable properties. Then, a focus was made on the characterization of hybrid composite materials through various quasi-static mechanical tests at different humidity levels. Hybridization is a frequently employed process to create intermediate properties between the two original materials (Swolfs et al., 2019).

Hybridization can result in a trade-off between mechanical properties and economic cost in order to meet the application requirements. Several recent studies show that the mechanical properties can be adapted by using hybridizations based on basalt fiber laminates with other natural fibers (Raponi et al., 2022), (Fargassa et al., 2018), (Petrucchi et al., 2013), intending to provide a more durable material. These studies mainly focused on the impact and mechanical characterization properties of a basalt/flax hybrid composite. All the composites involved were thermoset composites (epoxy, vinylester) with laminate hybridization. This study analyzed an original combination of flax and basalt fibers and a thermoplastic matrix (PA11) with a fabric scale hybridization by co-weaving. This work focuses on the effect of hybridization on mechanical properties. Then the effect of hygrometry on the evolution of the mechanical behavior of the composite (with three levels of hygrometry). Finally, the hybridization interest in reducing the dispersion of the mechanical properties of the studied material.

Various bio-composite materials based on natural fibers and bio-sourced matrices are used in industry (Nasimudeen et al., 2021), (Mohit et al., 2022), (Jeyaguru et al., 2022b) motivated by mass reduction (Jeyaguru et al., 2022c), (Jeyaguru et al., 2022d), (Chandrasekar et al., 2022), (Jeyaguru et al., 2023) environmental impact limitation (Mohit et al., 2022), (Chandrasekar et al., 2020), (Baley et al., 2017), (Fragassa et al., 2015) good recyclability (Bourmaud and Baley, 2007). The choice of these materials is essential and is linked to the final properties required for the semi-structural parts. Therefore, different matrices and fibers have been compared according to manufacturing constraints, processing conditions, environmental impact, and economic requirements.

The hybridization concept uses two or more fibers reinforcing the same matrix. It provides sufficient flexibility to design the optimal material (Senthilkumar et al., 2022), (Athith et al., 2018), (Kumar et al., 2020). The main idea is to mitigate the weaknesses of one of the fibers while keeping the advantages of the other (s) (Senthilkumar et al., 2019), (Shahroze et al., 2019), (El Hadi et al., 2019). This composite material offers many advantages but requires in-depth study to define the best combination of compatible fibers (Shahroze et al., 2019). The mechanical properties of the hybrid composite (fiber A and fiber B) are often the weighted average of the respective mechanical properties of both fibers. A better combination can create a synergetic effect that improves the hybrid composite properties compared to composites reinforced with only one type of fibre (Senthilkumar et al., 2019), (Shahroze et al., 2019).

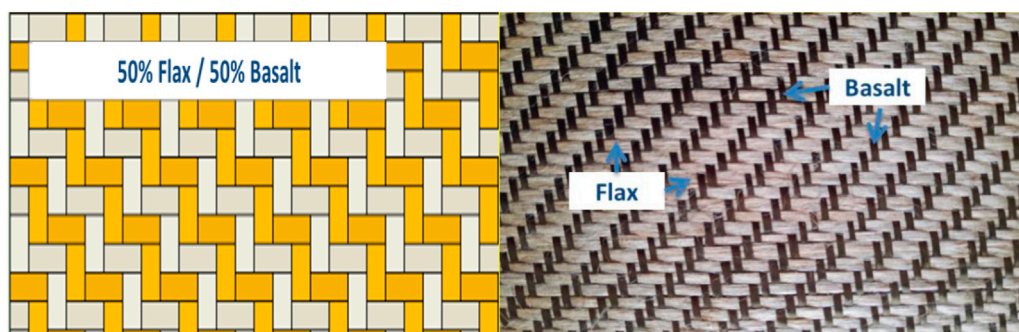
There are two leading families of fibers: synthetic and natural (mineral fibers, plant fibers and animal fibers) (Swolfs et al., 2014). Natural fibers, whose mechanical properties are similar to those of glass fibers were studied. Mineral fibers have good mechanical and thermal properties due to their chemical composition based on silicon (e.g., asbestos, basalt). Plant fibers are available in a wide range depending on the type of plant and its origin (leaves, stems, seeds or fruits) (Baley et al., 2017), (Bourmaud and Baley, 2009).

A first selection of natural fibres was made based on studies of bio-composite materials and their application fields (Baley et al., 2017), (Fragassa et al., 2015). The industrial aspect of fibre production (quantity and quality of the products) represented an essential factor in this selection. The following fibres were selected: hemp, sisal, ramie, jute, flax and basalt. In the second step, specific constraint functions were defined, which reflect the industrial requirements: structural lightness, mechanical performance, cost, environmental impact and durability. It was decided to select flax and basalt as fibre reinforcement and a PA11 matrix from Arkema (Fragassa et al., 2015). These different constituents are compatible and have complementary mechanical properties. Flax fiber has good mechanical properties (Baley et al., 2017), (Baley and Bourmaud, 2014a) and low density (1.4 g/cm<sup>3</sup>) (Baley et al., 2017), while basalt fiber provides high stiffness (Young's modulus of 93 GPa) (Baley et al., 2017), high moisture resistance (water absorption rate of 0.03%) (Baley et al., 2017) and excellent temperature resistance (maximum application temperature: 850°C) (Baley et al., 2017). The choice of a thermoplastic matrix and natural fibers improves the recyclability of this hybrid bio-composite.

This article is structured as follows. First part concerns the results of the experimental study of the developed materials, basalt/PA11, flax/PA11 and hybrid5050/PA11 for different directions (0°/45°/90°). The second part concerns the moisture influence on the evolution of the mechanical behaviour of materials since both the flax fiber and the PA11 matrix are sensitive to moisture (Bourmaud and Baley, 2009), (Baley and Bourmaud, 2014a) and (Destaing et al., 2016). As this hybrid material is new, the interpretation of the experimental results is accompanied by the micromechanical analysis of the representative volume element (RVE) of the hybrid composites using the finite element method. To this end, the computational model uses Multiscale Designer (Altair) to predict the mechanical response of different RVEs beyond elastic regimes to understand the effects of flax fiber variability, its hybridization with basalt fibers and the influence of moisture on macroscale properties. The predictions are compared with experimental results.

## Materials and methods

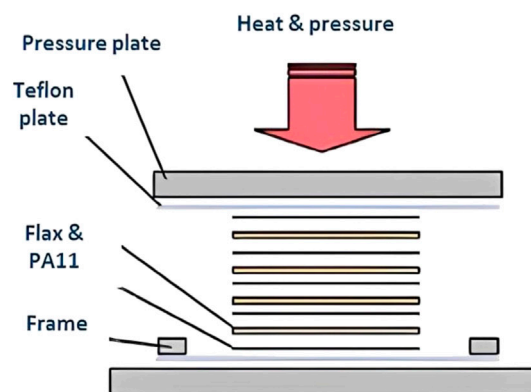
In this research work, the mechanical behaviour of the thermoplastic matrix PA11 and the composite materials flax/PA11, basalt/PA11 and hybrid5050/PA11 was investigated at three humidity levels (RH0, RH50 and RH85) and the ambient temperature of 23°C. The fibre distribution for the hybrid5050/PA11 composite is 50% flax fibre and 50% basalt fibre. The flax fibres used were supplied by the company Depestele in France, the basalt fibres were provided by the company Isomatex in Belgium and the PA11 polyamide matrix was developed by Arkema in France.



**FIGURE 1**  
Hybrid5050/PA11 fabric Twill2X2.



**FIGURE 2**  
Hydraulic press SCAMEX.



Depestele weaved together the flax and basalt fibres to get the hybrid composite hybrid5050/PA11 (Figure 1).

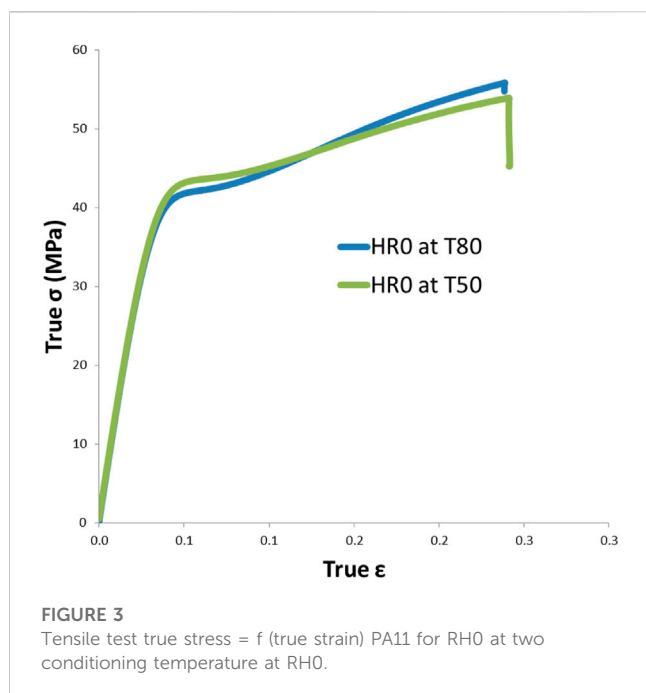
Table 1 shows the mechanical properties of the PA11 matrix, flax and basalt fibers. The indices 1, 2, and 3 refer to the principal axes of the fiber, with axis 1 referring to the fiber axis (Nasimudeen et al., 2021).

## Fabrication of composites

The choice of manufacturing depends on the selected materials' characteristics and the application's constraints. There is a wide variety of manufacturing processes for composite materials (Swolfs et al., 2019); each technology depends on several parameters. Indeed, the melting temperature, matrix viscosity, fiber length, thermal resistance, or geometric complexity of the manufactured parts must be considered. The thermo-compression process was chosen because of the matrix's thermoplastic nature, the flax fibre's

temperature sensitivity and the short cycle time compatible with automotive production. It was applied for the different composite materials; flax/PA11 (twill, 4 plies, 2 mm thick, Vf 42%), basalt/PA11 (UD, 8 plies, 4 mm thick, Vf 27%) and hybrid5050 (twill, 4 plies and 2 mm thick, Vf 33%).

Thermo-compression allows forming composite parts with prepreps by combining pressure and temperature for a relatively short cycle time (Baley and Bourmaud, 2014b). An experimental study has defined the thermo-compression parameters (Supplementary Figure S1). The temperature is maintained at 220°C for 3 min during the heating phase and 23°C for 5 min during the cooling phase. The material is kept under a pressure of 5 bars during heating and 3 bars during cooling. The objective is to ensure proper impregnation of the fibers without risking the degradation of the flax fibers. A pre-drying phase of the fabrics was carried out to reduce the hygrometric effect on the prepreg impregnation quality and improve the composite's desorption (Barbulée et al., 2014).



1. The first composite plates were produced by thermocompression with a hydraulic press SCAMEX of 75 tons of clamping, equipped with heated platens of 1 m<sup>2</sup> (Figure 2)

The final panels have been manufactured using industrial methods to consider the imperfections inherent in this type of production. The specimens were then cut out using a water jet. For composites, parallelepiped specimens were used. The specimens' dimensions are as follows: 2 mm thick, 25 mm wide and 250 mm long overall, they are in accordance with ISO 527 standard (the equivalent of ASTM D638 for tensile testing of reinforced and unreinforced polymers). The specimens used for the quasi-static tests of the PA11 thermoplastic matrix are of the dumbbell type. Their dimensions are defined as follows: 4 mm thick, 10 mm wide and a zone of interest of length 80 mm. The specimens were manufactured by the extrusion method by the a polymer materials laboratory.

## Moisture absorption and desorption test

Given the sensitivity of the materials studied (thermoplastic matrix and vegetal fibers) to humidity (Bourmaud and Baley, 2009), (Barbulée et al., 2014), three standard levels of hygrometry (RH0—dry climate, RH50 - standard climate and RH85—humid climate) were analyzed for the matrix and composites in order to evaluate their effect on mechanical properties.

First, it was necessary to identify two experimental protocols: the first concerns the drying of the material, which allows a return to a dry state (RH0). The second is designed to ensure the samples are returned to a moist environment (RH50 and RH85). In both cases, gravimetric measurements were carried out to monitor the evolution of the specimen masses and determine the days required to dry or age the specimens. In order to return the material to a dry state,

samples were placed in an oven (Binder VD-115 equipped with a Vaccubrand PC3001 pumping unit) under vacuum at 80°C. This temperature was chosen in accordance with the instructions of the matrix supplier and the data reported in the literature on the thermal resistance of the flax fibers (no impact on their mechanical properties) (Bourmaud and Baley, 2009), (Barbulée et al., 2014). For ageing at RH50 and RH85, samples were placed in a climatic chamber (BINDER KMF115) at 80°C, the same temperature for drying and ageing in accordance with supplier's instructions. Some mechanical tensile tests were performed to verify that the drying temperature processes did not affect the mechanical behaviour of the composites (Figure 3).

In order to maintain the moisture content of the different materials during the characterization tests, the specimens were packed in batches of five in specific bags.

The moisture variation  $M_t$  is calculated using

$$M_t = \frac{m_t - m_0}{m_0} \quad (1)$$

With  $m_0$  initial mass,  $m_t$  sample mass

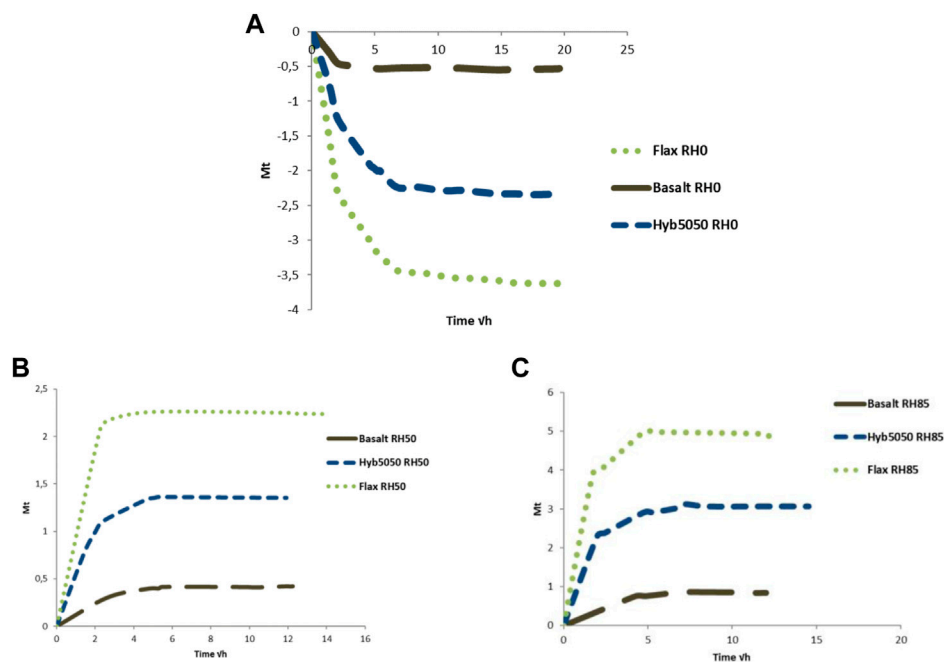
Gravimetric measurements were carried out on each material studied to follow the sample mass's evolution during conditioning. These measurements allow determining the variation of the humidity  $M_t$  for each material and identifying the time required for desiccation and sorption. Figure 4 shows the  $M_t$ 's evolution and the humidity sensitivity (RH0, RH50 and RH85) for each material.

As shown in Figure 4, the basalt/PA11 composite has the highest moisture resistance and a shorter drying time than the flax/PA11 composite. The humidity ratio of the basalt/PA11 composite (0.5%) is relatively low compared to that of the flax/PA11 composite (3.6%). As expected, the hybrid5050/PA11 composite is intermediate in moisture resistance (2.32%) between the flax/PA11 and basalt/PA11 composites.

The moisture variation for RH50 plotted in Figure 4 shows a significant difference between the composites Basalt/PA11 (0.42% moisture content) and Lin/PA11 (2.22% moisture content); in fact, the basalt fibers are mineral fibers and have excellent moisture resistance (Raponi et al., 2022), (Fargassa et al., 2018). Regarding the hyb5050/PA11 composites, the moisture uptake (1.33%) remains lower than that of flax, indicating that the hybridization allows reducing the moisture sensitivity. Similarly, for RH85 in Figure 4, the same behavior is observed; the basalt has the lowest moisture content (0.83%), while that of the flax/PA11 composite (4.89%). The 5,050/PA11 hybrid shows 37% less moisture than the flax/PA11 composite.

## Mechanical tests

The main objectives of the experimental phase were to identify the mechanical characteristics (Young's modulus, Shear modulus, Poisson's ratio, strength and strain at failure . . . ) of the PA11 matrix and the composites flax/PA11, basalt/PA11 and hybrid50/50. Then to understand the evolution of their mechanical behavior according to the different humidity ranges RH0, RH50, and RH85 the quasi-static tensile and in-plane shear tests were carried out on a universal testing machine (INSTRON 5584), according to the ISO527 (ASTM



**FIGURE 4**  
Moisture variation (Mt) as a function of the square root of time: (A)-desorption (RH0), (B) sorption (RH50) and (C) sorption (RH85).

D3039). The samples' dimensions are selected per the ISO 527 standard.

Quasi-static tests have been carried out in the dry state RH0 at ambient temperature (+23°C) and for different directions (0°/45°/90°). The choice of the hygrometry level was made to eliminate their effect on the mechanical behaviour of the composite, as flax fibers are sensitive to humidity and high temperature (Baley et al., 2017), and to understand the impact of the hybridization on the mechanical properties and mechanical behaviour of the hybrid5050/PA11 material. The 0° orientation provides the longitudinal mechanical properties, the 45° orientation gives the shear properties and the 90° orientation provides the transverse mechanical properties of the composite. The second part of the experimental study highlights the effect of humidity for three humidity levels, RH0, RH50, and RH85, for the composite materials basalt/PA11, flax/PA11 and hybrid 5,050/PA11 as well as for the PA11 matrix.

Five samples were used for each of the tests reported in [Supplementary Table S2](#) to ensure the reproducibility of the results.

A digital image correlation (DIC) method has been adopted to determine the strain field of the specimens. A high-resolution camera (STEMMER GT6600) is used to capture images during the tensile test, which are then processed using the VIC-2D software to calculate the strain field.

Analysis of the monotonic tensile tests provides the stiffness, strength and deformation at the failure of these materials. Due to their geometrical symmetries, unidirectional composite laminates are considered to be transversely isotropic materials (Baley et al., 2005). This hypothesis allows to simplify the relationships between stresses and strains for the different orientations. The calculated stresses and strains are local and are extracted from the quantities

measured in the global machine plan ([Supplementary Figure S2](#)). [Supplementary Table S3](#) shows the quantities calculated as a function of the different laminates in the global coordinate system ( $O, \bar{x}_1, \bar{x}_2, \bar{x}_3$ ), the tensile test being performed in the  $\bar{x}_1$  direction.

## Experimental study

[Figure 5](#) compares the different mechanical behaviors of the flax/PA11, basalt/PA11 and hyb5050/PA11 composites. True stresses were calculated to take into account the potential effects of large deformations. The true stress  $\sigma$  and strain  $\varepsilon$  are determined from:

$$\sigma = \sigma_n (1 + \varepsilon_n) \quad (2)$$

$$\varepsilon = \ln (1 + \varepsilon_n) \quad (3)$$

$$\varepsilon_n = \frac{l - l_0}{l_0} \quad (4)$$

$$\sigma_n = \frac{F}{S_0} \quad (5)$$

$\varepsilon_n$ : nominal strain  $\sigma_n$ : nominal stress

F: applied force  $S_0$ : samples initial section

l: samples length  $l_0$ : samples initial length

The basalt/PA11 composite is stiffer than the hybrid 5,050/PA11 and flax/PA11 composites for the 0° direction due to the relatively high mechanical properties of the basalt fiber (Singha, 2012) compared to the flax fiber (Baley et al., 2017). Furthermore, the basalt/PA11 composite is unidirectional, and the hybrid5050/PA11 and flax/PA11 composites are balanced. The deformation of the basalt composites is relatively higher than that of the hybrid

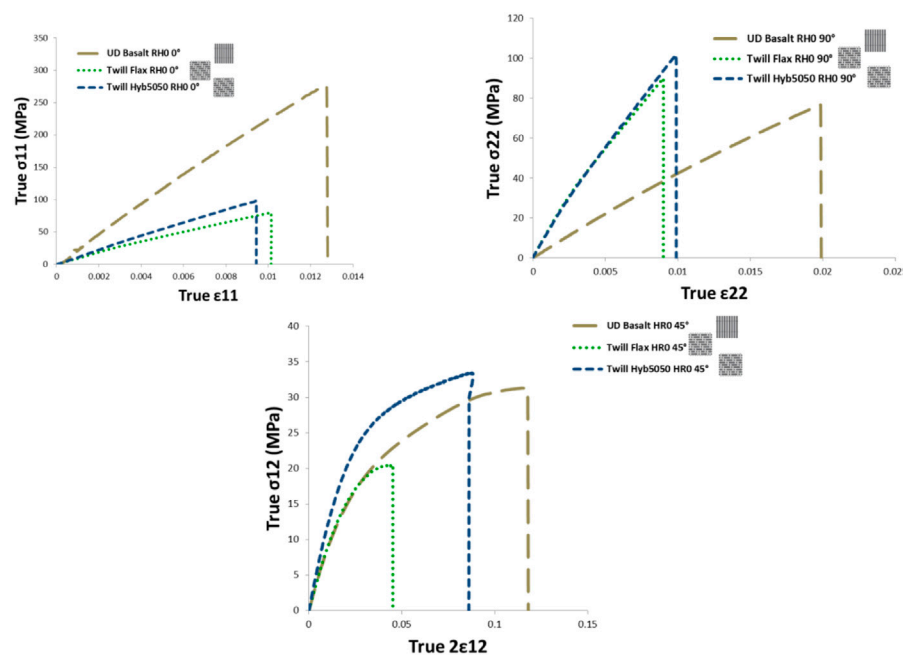


FIGURE 5

True stress vs. true strain in the global coordinate system for the flax/PA11, Hyb5050/PA11 and basalt/PA11 composites for RH0 and 0°, 45°, and 90° at 23°C.

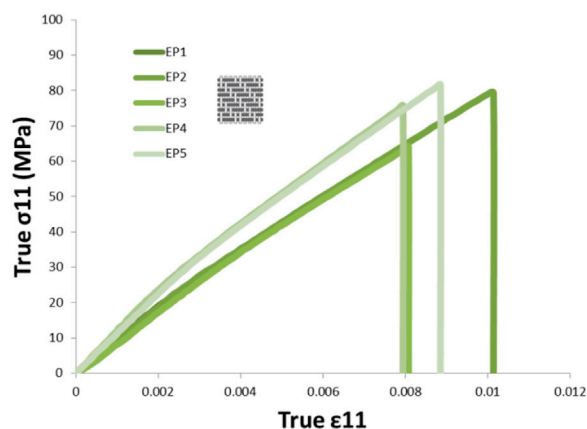


FIGURE 6

Global true stress vs. true strain for tensile testing of flax/PA11 0° for RH0 at 23°C.

5,050/PA11 and flax/PA11 composites for the different directions (0° and 90°). As conclusion, the hybridization has improved the mechanical characteristics of the hybrid 5,050/PA11 *versus* the flax/PA11 composite. Figure 5 shows that the hybrid composite is 20% stiffer than the flax composite. As expected, the Young modulus E22 of the unidirectional basalt/PA11 is significantly lower than the hybrid5050/PA11 and flax/PA11 woven composites (Figure 5). Also, the longitudinal and transverse Young's moduli of the 5,050/PA11 and Flax/PA11 are very similar because they are made from balanced twill fabrics. The different mechanical properties

of the studied composites are reported in Table 3. It is important to emphasize that it is possible to have a more consistent comparison if fibre content  $V_f$  for the hybrid5050/PA11 and flax/PA11 composites were the same. In fact, the fibre content for the different composites: flax/PA11 ( $V_f$  42%), basalt/PA11 ( $V_f$  27%) and hybrid5050/PA11 ( $V_f$  33%) are different. This difference in fibre content is due to the process of powdering the fabric during the pre-impregnation manufacturing (50% by weight for the fibres, 50% by weight for the matrix). The hybrid5050/PA11 composite would have better mechanical properties with a higher fibre content, thus highlighting the interest in hybridization.

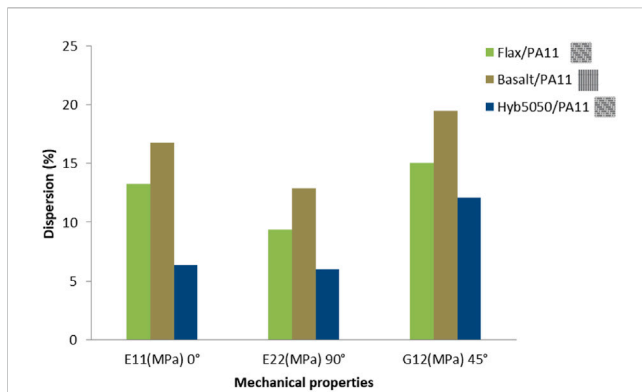
Figure 6 shows the typical dispersion of the mechanical behaviour for the flax/PA11 composite. This dispersion is essentially due to the plant nature of the flax fibers. Indeed, the mechanical characteristics of flax fibers depend on the nature of the fibers, the growth conditions (temperature and humidity), and the treatment carried out to process these fibers (Baley et al., 2017).

Dispersions are defined by:

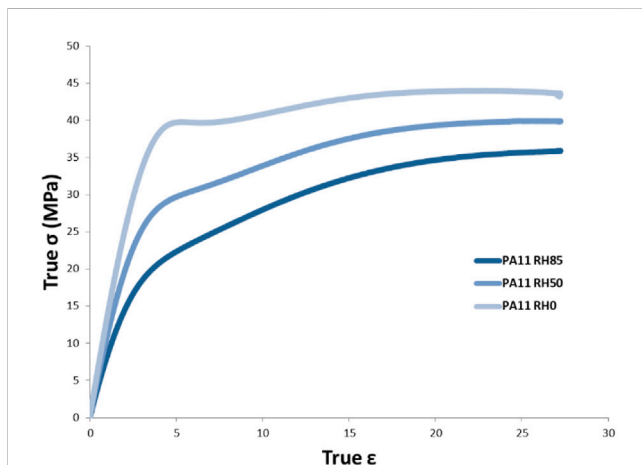
$$Dispersion = \frac{\text{standard deviation}}{\text{Main value}} \times 100 \quad (6)$$

The hybridization of flax fibers with basalt fibers reduced the scatter of the mechanical properties of the flax/PA11 composite. As a result, the hybrid5050/PA11 composite shows a lower dispersion of Young's modulus compared to both basalt/PA11 and flax/PA11 composites for the different directions (0°, 45° and 90°) as shown in Figure 7. Also, the dispersion of the different mechanical properties is more pronounced for the 45° direction compared to the 0° and 90° directions. Although basalt, due to its chemical composition and manufacturing





**FIGURE 7**  
Mechanical property dispersion for basalt/PA11, flax/PA11 and hybrid5050/PA11 composites for directions 0°, 45°, and 90°.



**FIGURE 8**  
Global true stress vs. true strain for the tensile test of PA11 for RH0, RH50, and RH85 at 23°C.

process (Shubhalakshmi et al., 2016), (Singha, 2012) has good mechanical stability like glass fiber, a considerable dispersion is noticed for its different mechanical properties (E11, E22, and G12). This is related to manufacturing defects; a deviation in the orientation of fibers for the composite UD basalt/PA11 composite was found.

The hybridization of flax and basalt fibers created a synergy that allowed a lower dispersion of the mechanical properties of the hybrid5050/PA11 composite. In conclusion, the dispersion depends on the nature of the fibers, the type of fabric (UD or twill) and the orientation of the composite.

The second phase of the experimental study investigates the effect of moisture on the evolution of the mechanical behaviour of our materials, the matrix PA11, flax/PA11, basalt/PA11 and Hybrid 5,050/PA11 composites. This part aims to understand and quantify the evolution of the mechanical properties of materials for the three humidity levels RH0, RH50 and RH85. Then, it will enable to verify the interest of hybridization in reducing the material's sensitivity to humidity.

Figure 8 shows the typical response of the PA11 matrix during quasi-static tensile tests for the three moisture levels RH0, RH50, and RH85.

The different Young's moduli of PA11 are reported in [Supplementary Table S4](#). They show that moisture promotes the plasticization of the material and reduces stiffness.

Figure 9 shows the evolution of the mechanical properties of flax/PA11, hybrid5050/PA11 and basalt/PA11 for the three moisture levels RH0, RH50 and RH85:

From the values in [Table 4](#), it can be seen that there is a decrease in the mechanical properties of the different composites. The Flax/PA11 composite shows a similar significant decrease in its mechanical properties for RH50 and RH85. The longitudinal modulus E11 decreases from 10,100 MPa (RH0) to 7,918 MPa for RH50 and 5,001 MPa for RH85, i.e., a decrease of 21% for RH50% and 50% for RH85. This decrease can be explained by the sensitivity of both the flax fiber (Bourmaud and Baley, 2009), (Abida et al., 2020), (Fabre et al., 2017) and the PA11 matrix (Destaing et al., 2016). The evolution of the properties of flax fiber is related to its microscopic structure. The matrix is mainly composed of hemicellulose and lignin. The cellulose fibrils are helically oriented at the microfibril angle ([Supplementary Figure S3](#)). The physical properties of natural fibers are mainly determined by their chemical and physical composition, structure, percentage of cellulose, microfibril angle, cross-section and degree of polymerization. The lower the microfibrillar angle, the higher the stiffness and strength of the fiber; the higher the microfibrillar angle, the higher the elongation at break. It can be seen that the microfibrillar angle increases with increasing humidity, which explains the evolution of the stiffness of the flax/PA11 composite.

For the hybrid5050/PA11 composite, a moderate decrease in mechanical properties as a function of humidity was observed compared to the flax/PA11 composite. Indeed, for the longitudinal Young's modulus E11 a decrease of 7% at RH50% and 27% at RH85; the basalt fiber has considerably reduced the hybrid5050/PA11 sensitivity to moisture, as shown in [Table 4](#).

A comparison of the mechanical properties of the studied composites for the different moisture contents is represented in [Figure 10](#).

Although the basalt fiber has a good moisture sensitivity (Rozycki et al., 2018), its mechanical properties were reduced for RH50 and RH85 compared to the dry state RH0 ([Figure 10](#)). E11 drops from 23,300 MPa (RH0) to 17,893 MPa (RH50) and 19,570 MPa for RH85. For the basalt/PA11 composite, the variation in mechanical properties essentially depends on the sensitivity of PA11 to humidity, bearing in mind that fiber content (27%) is relatively low (Coussa et al., 2017). However, an improvement in the mechanical properties was observed from RH50 to RH85 in all directions (0°, 45°, and 90°). The improvement in the mechanical properties of the basalt/PA11 composite at RH85 could be related to a modification of the fiber/matrix interface, which could allow a better adhesion between the basalt fiber and the PA11 matrix.

Following the mechanical characterisation tests of the different materials studied, a microscopic study was conducted using a Scanning Electron Microscope ([Figure 11](#)). There are different damage mechanisms for composite materials depending on the nature of the fibres, the matrix and the fabric used. The damage modes are fibre breakage, fibre/matrix debonding and matrix

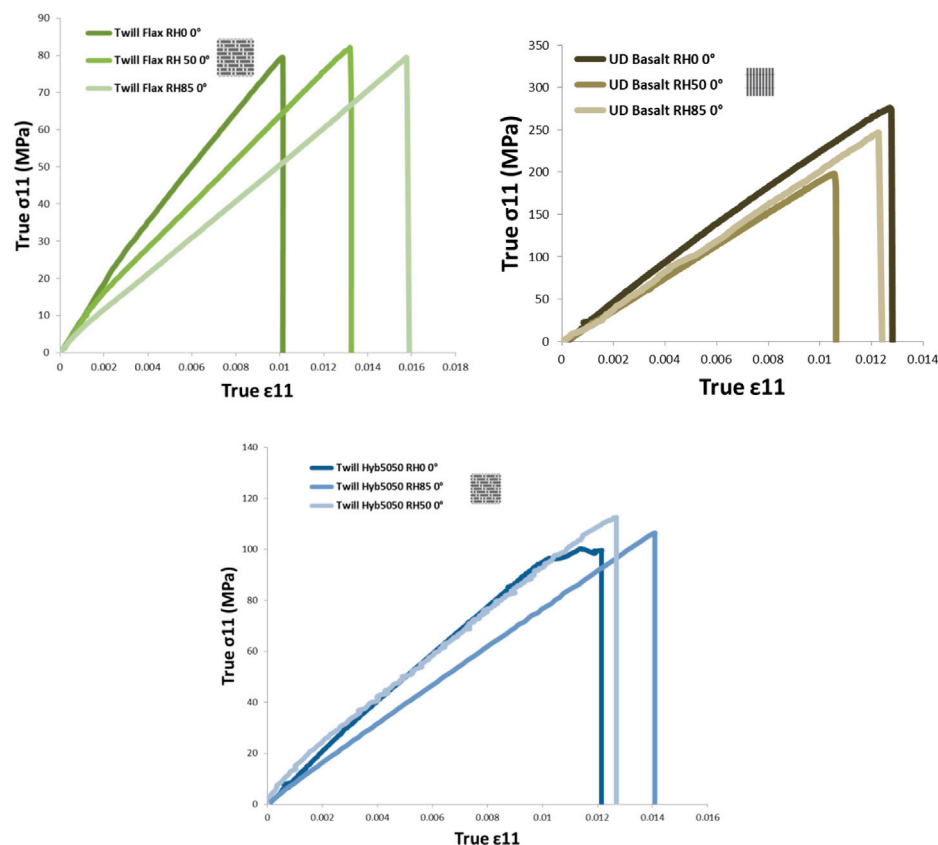


FIGURE 9

Global true stress vs. true strain for the tensile test of flax/PA11, hyb5050/PA11 and basalt/PA11 0° for RH0 RH50 and RH85 at 23°C.

cracking. The analysis of the SEM results (Figure 12) shows that fibre breakage as the damage mode for the flax/PA11 composite is fibre breakage and fibre/matrix delamination for the basalt/PA11 composite. These damage modes were retained for the hyb5050/PA11 composites.

## Numerical study

The second part of the research work is devoted to the numerical study based on homogenization methods; it allows the prediction of the mechanical behaviour of a heterogeneous material from the mechanical properties of its phases. It will be able to determine the effective properties at the macroscopic scale of the material from a Representative Elemental Volume (REV) that depends on the scale of hybridization. In this study, a numerical method based on a multi-scale homogenization (Supplementary Figure S4) will be used to capture the geometrical features of the materials under study and to integrate the hygrometry that impacts the behaviour of the composite.

The multi-scale numerical homogenization method is divided into two phases. The first phase concerns the homogenization of the constituents (fiber and matrix) at the microscopic scale. It provides the behaviour of the polymer reinforced by the fiber tow. The second phase represents homogenization at the macroscopic scale (fiber tow

and matrix). It allows having the behaviour of the studied composite (Rozycki et al., 2018). Initially, the elastic phase of the composite material's mechanical behavior is studied. Therefore, this part focuses on the determination of the effective properties for the following composite materials: flax/PA11 (twill), basalt/PA11 (UD), and hybrid5050/PA11 (twill) for RH0.

Multiscale Designer, developed by Altair, is used as a numerical homogenization tool to predict effective properties (Altair Multiscale Designer User Manual, 2021). Macro homogeneous linear material properties are calculated using either a forward homogenization problem (Yuan and Fish, 2008) or an inverse optimization problem. It allows the prediction of the mechanical properties of different types of composite (UD, twill, etc.) from the intrinsic properties of their fiber and matrix components and their spatial distribution. This tool allows different types of REV to be represented, depending on the composite studied (UD, twill, with or without the fiber/matrix interface) (Supplementary Figure S5) and uses the periodic boundary conditions.

The REV type (Supplementary Figure S5) was chosen for its ability to integrate two different fibers (flax and basalt fiber) to represent a hybrid composite. The first numerical study is carried out without adding an interface between the matrix and fibers due to the lack of information on their mechanical properties.

The REV dimensions were defined from the micrographic inspection of the different composite materials (Supplementary

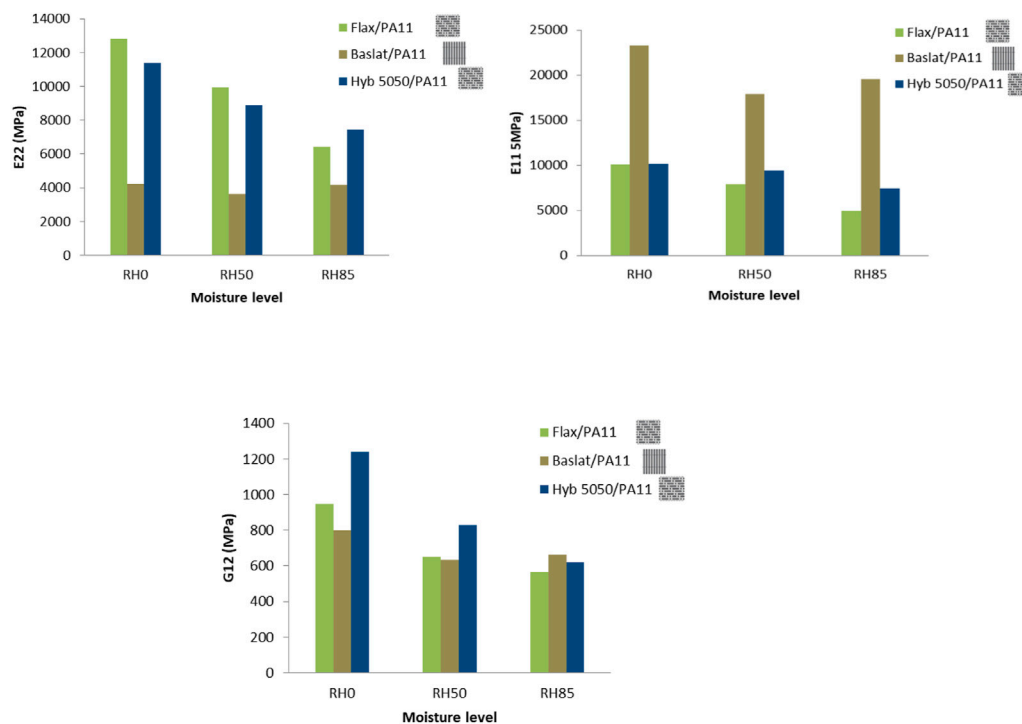


FIGURE 10

Comparison of the mechanical properties E11, E22 and G12 for flax/PA11, basalt/PA11 and hybrid 5,050/PA11 composites, for RH0, RH50 and RH85 at 23°C.



FIGURE 11

Scanning electron microscope (SEM).

Figure S6) using the image processing tool Image J. The following dimensions were determined: Tow major radius  $r_y$ , Tow minor radius  $r_z$  and Tow spacing  $s_y$  (Supplementary Figure S7).

Supplementary Figure S7 presents the different REV dimensions for the flax/PA11 composite: the tow major radius ( $r_y$ ), the minor tow radius ( $r_z$ ), the tow spacing ( $s_y$ ) and the fiber volume fraction ( $V_f$ ). This unit cell does not include the crimp of the twill weave.

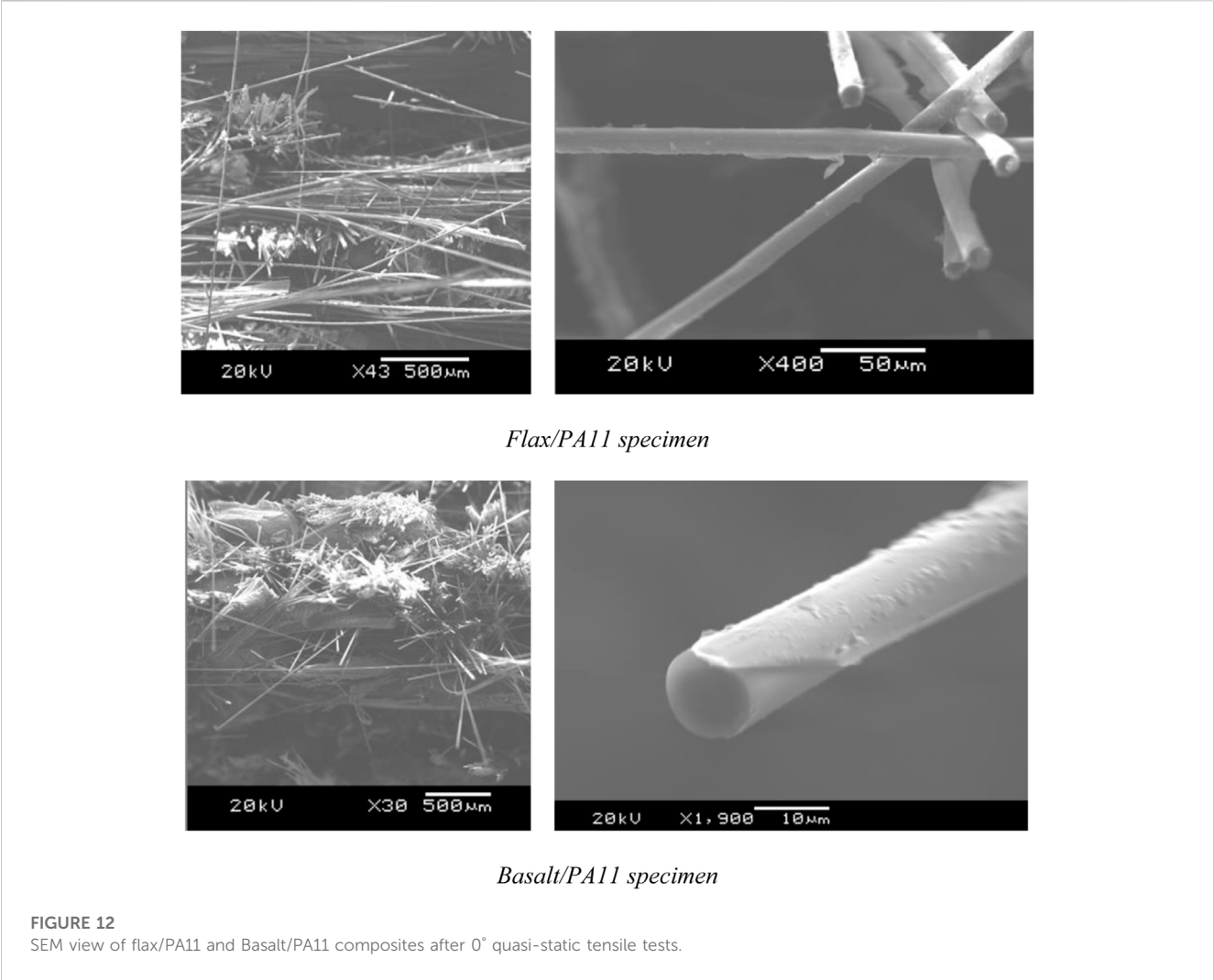
The multi-scale homogenization was carried out using the intrinsic properties of flax fibers, basalt fibers and PA11 (Table 1) according to their volume fractions and arrangements (Table 2). The indices 1, 2, and 3 refer to the main axes of the fiber, with axis 1 referring to the direction of the fiber (Baley et al., 2017).

These numerical simulations will be used to compare and correlate the numerical results with the experimental results. In order to make a consistent comparison between the different composite materials, The experimental characterization tests will be extended by studying the composites with an identical fiber content and similar weave ( $V_f$  of 42% and balanced twill). Supplementary Table S6 shows the different materials that will be examined using the homogenization method.

The numerical and experimental results are compared in Table 5. The error between the numerical and experimental results is calculated from:

$$\text{Error} = \frac{\text{Experimental} - \text{Numerical}}{\text{Experimental}} \quad (7)$$

A significant difference was found between the experimental and numerical properties, reflected in a high error value for all the flax/PA11, basalt/PA11 and hybrid5050/PA11 composites. This can be explained by the limitation of including the fiber/matrix interface and the flax/basalt interface for the hybrid composite (Destaing et al., 2016). The type of VER has a strong influence on the numerical results. On the other hand, a difference could be



**TABLE 1 Mechanical properties of flax and basalt fibers and the PA11 matrix for RH0** The description of the different composite materials is shown in **Table 2**.

Mechanical properties	Basalt (Dhand et al., 2015)	Flax (Baley et al., 2017)	PA11 (Destaing et al., 2016)
Longitudinal Young's modulus $E_{f_1}$ (MPa)	89,000	52,000	1,400
Transverse Young's modulus $E_{f_2}$ (MPa)	—	8,000	—
Longitudinal shear modulus $G_{f_{12}}$ (MPa)	—	2,410	—
Transverse shear modulus $G_{f_{23}}$ (MPa)	—	2,930	—
Poisson's ratio	0.2	0.4	0.06
Density (g/cm3)	2.7	1.4	1.03

**TABLE 2 Fiber volume fraction and density of the studied composites.**

	Flax/PA11	Basalt/PA11	Hyb5050/PA11
Vf (Vol.)	42%	27%	33%
Density (g/cm <sup>3</sup> )	1.18	1.48	1.36
Fabric	Twill	UD	Twill

observed between the intrinsic mechanical properties of the materials used and the values available in the bibliography.

Then we were interested in the mechanical behaviour of the composite for the linear elastic and the non-linear parts. Predefined constitutive law in Multiscale Designer (Rate-independent plasticity (RI) model) was used to represent the stress-strain curve for PA11 using the constitutive model in Eq. 8

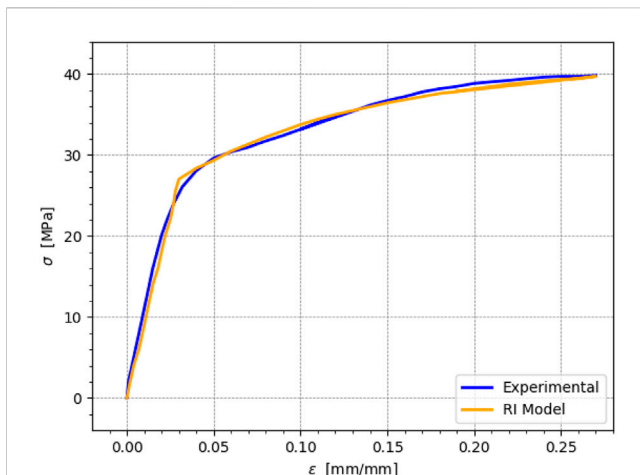


FIGURE 13

Comparative curves of experimental results and numerical simulation for PA11 at RH50.

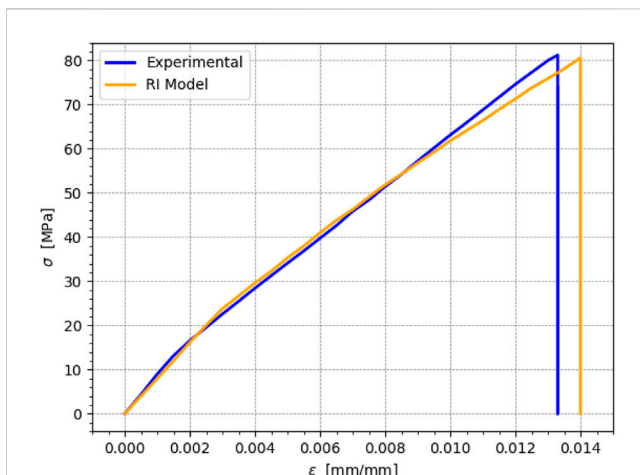


FIGURE 14

Comparative curves of experimental results with numerical simulation for flax/PA11 (0° and RH50).

$$\sigma = \sigma_y + (\sigma_1 - \sigma_y) \left[ 1 - e^{-\delta \left( \epsilon - \frac{\sigma}{E} \right)} \right] + H \left( \epsilon - \frac{\sigma}{E} \right) \quad (8)$$

Where  $\sigma_y$  is the yield strain,  $\sigma_1$  is the ultimate strain,  $H$  is the linear term for the hardening law and  $\delta$  is the exponent for the evolution law.

This model provides a good fit for the experimental data, as shown in Figure 13.

An inverse homogenization was performed to determine the mechanical properties of the flax fiber from the experimental curves. Table 6 shows the mechanical properties of the flax fiber at RH0, RH50, and RH85.

These fiber properties are used to perform a numerical homogenization and to verify the correlation between the RI model and the experimental results at RH 50° and 0° direction at

ambient temperature. Figure 14 shows good agreement between the experiment and model.

To achieve our study on the effect of hybridization on the evolution of the mechanical behavior for the hybrid composite, a focus on the different types of hybridization was made, which depends on the scale of hybridization. In fact, there are three scales of hybridization: the laminate scale, the layer scale by co-weaving and the fiber scale by commingling two different fibers. Most of the research to date has focused on the study of hybrid laminates. Initial work has focused on analyzing hybrid layer scale composites; studying the other scales will allow the best type of hybridization for better mechanical properties. A specific REV was developed on Hypermesh for each scale of hybridization presented in Supplementary Figure S8.

The effective properties of the hybrid composites are presented in Table 6.

The numerical simulations show that the hybrid composite made of commingled fibres and the hybrid co-woven composite have the same mechanical properties. In fact, the hybridization is carried out in the same layer. Only the distribution of the fibres in the same layer was modified with an equal distribution in the longitudinal and transverse directions. The behaviour of the composite is balanced in both directions of the material. However, the results show a difference in the mechanical properties of the laminated composite with the mixed fibre composite and the co-woven composites. The longitudinal properties are also different from the transverse properties. This difference is related to the nature of the fabrics, in fact a combination of flax twill and basalt UD layer was used. These results show the effect of the nature of the hybridization on the mechanical properties of the hybrid composite material.

## Results and discussion

The results were analyzed with the aim of understanding the benefits of hybridization by comparing the three composite materials flax/PA11, basalt/PA11 and hybrid5050/PA11. The second part was dedicated to the impact of hygrometry on the evolution of the mechanical behaviour of the different composites materials for three moisture levels RH0, RH50 and RH85. Finally, a comparison of hybridization levels was analyzed using multi scale homogenization. The different mechanical behaviors of the flax/PA11, basalt/PA11 and hyb5050/PA11 composites are presented in Figure 5 and their mechanical properties are reported in Table 3. As expected the basalt/PA11 composite is stiffer than the hybrid 5,050/PA11 and flax/PA11 composites for the 0° direction due to the high mechanical properties of the basalt fiber (Singha, 2012). The hybridization has improved the mechanical characteristics of the hybrid 5,050/PA11 compared to the flax/PA11 composite. The hybrid composite is 20% stiffer than the flax composite (Figure 4). Furthermore, Figure 7 shows that the hybrid5050/PA11 composite has a lower dispersion of Young's modulus



**TABLE 3 Mechanical characteristics of Hybrid5050/PA11, basalt/PA11 and flax/PA11 composites for RH0 and for directions (0°/45°/90°) at 23°C.**

	Flax		Basalt		Hyb 50 50	
0°	E11(MPa)	$\nu_{12}$	E11(MPa)	$\nu_{12}$	E11(MPa)	$\nu_{12}$
	10,100 ± 1,340	0.04 ± 0.02	23,300 ± 3900	0.18 ± 0.02	10,220 ± 650	0.05 ± 0.05
	$\sigma_{11}$ failure (MPa)	$\epsilon_{11}$ failure	$\sigma_{11}$ failure (MPa)	$\epsilon_{11}$ failure	$\sigma_{11}$ failure (MPa)	$\epsilon_{11}$ failure
	60 ± 11	0.008 ± 0.01	255 ± 37	0.01 ± 0.001	70 ± 17	0.01 ± 0.04
90°	E22(MPa)	$\nu_{21}$	E22(MPa)	$\nu_{21}$	E22(MPa)	$\nu_{21}$
	12,807 ± 1,200	0.05 ± 0.153	4,220 ± 545	0.032 ± 0.07	11,400 ± 680	0.50 ± 0.2
	$\sigma_{22}$ failure (MPa)	$\epsilon_{22}$ failure	$\sigma_{22}$ failure (MPa)	$\epsilon_{22}$ failure	$\sigma_{22}$ failure (MPa)	$\epsilon_{22}$ failure
	75 ± 4	0.007 ± 0.002	57 ± 4	0.015 ± 0.01	85 ± 3	0.008 ± 0.0003
45°	G12(MPa)		G12(MPa)		G12(MPa)	
	949 ± 143		801 ± 156		1,240 ± 150	
	$\sigma_{12}$ failure (MPa)	2 $\epsilon_{12}$ failure	$\sigma_{12}$ failure (MPa)	2 $\epsilon_{12}$ failure	$\sigma_{12}$ failure (MPa)	2 $\epsilon_{12}$ failure
	35 ± 5	0.06 ± 0.032	54 ± 10	0.14 ± 0.04	55 ± 5	0.1 ± 0.02

E11, Longitudinal elastic modulus; E22, Transverse elastic modulus; G12, Shear modulus;  $\sigma_{11}$  failure; Longitudinal stress at break;  $\epsilon_{11}$  failure, Longitudinal strain at break;  $\sigma_{22}$  failure, Transverse stress at break;  $\epsilon_{22}$  failure, Transverse strain at break;  $\sigma_{12}$  failure, Shear stress at break; 2  $\epsilon_{12}$  failure, Shear strain at break;  $\nu_{12}$ , Poisson coefficient 12;  $\nu_{21}$ , Poisson coefficient 21.

**TABLE 4 Young Modulus of hyb5050/PA11, basalt/PA11 and flax/PA11 composites for RH0, RH50 & RH85 and for directions (0°/45°/90°) at 23 °C.**

		Flax/PA11	Basalt/PA11	Hybrid5050/PA11
RH0	E11(MPa)	10,100 ± 1,340	23,300 ± 3900	10,220 ± 650
	E22(MPa)	12,807 ± 1,200	4,220 ± 545	11,400 ± 680
	G12(MPa)	949 ± 143	801 ± 156	1,240 ± 150
RH50	E11(MPa)	7,918 ± 1,295	17,893 ± 3402	9,440 ± 392
	E22(MPa)	9,950 ± 1,000	3619 ± 443	8,886 ± 401
	G12(MPa)	650 ± 284	632 ± 310	828 ± 90
RH85	E11(MPa)	5,001 ± 479	19,570 ± 1,481	7,462 ± 360
	E22(MPa)	6,434 ± 1,061	4,191 ± 397	7,428 ± 175
	G12(MPa)	566 ± 231	664 ± 91	623 ± 62

versus basalt/PA11 and flax/PA11 composites for the different directions (0°, 45°, and 90°). Using flax and basalt fibers provided a synergy which reduces the dispersion of the mechanical properties of the hybrid5050/PA11 composite.

The evolution of the mechanical properties of flax/PA11, hybrid5050/PA11 and basalt/PA11 for the three moisture levels RH0, RH50, and RH85 is presented in Figure 9. Table 4 shows a decrease in the mechanical properties of the different composites. The Flax/PA11 composite had a significant loss of its mechanical properties for RH50 and RH85. For the hybrid5050/PA11 composite, a moderate modification in mechanical properties was observed compared to the flax/PA11 composite. Indeed, for the longitudinal Young's modulus E11 a decrease of 7% at RH50% and 27% at RH85.

For the multiscale homogenization a comparison between numerical and experimental results was reported in Table 5 through error calculation. High error value was observed for all the flax/PA11, basalt/PA11 and hybrid5050/PA11 composites. The first explanation is related to the limitation of including the fiber/matrix interface and the flax/basalt interface for the hybrid composite (Destaing et al., 2016). Also, VER size and type have a strong influence on the numerical results. On the other hand, the difference between the intrinsic mechanical properties of the materials used and the values available in the bibliography could be observed. For the hybridization levels, the effective properties of the hybrid composites are presented in Table 6. The hybrid composite made of commingled fibres and the

**TABLE 5 Comparative table of numerical/experimental mechanical properties of Flax/PA11, basalt/PA11, hyb5050/PA11 composites for RH0.**

	Flax			Basalt			Hybrid5050		
	E11	E22	G12	E11	E22	G12	E11	E22	G12
Experimental (MPa)	10,100	12,807	949	23,283	4,220	801	10,218	11,395	1,240
Numerical (MPa)	9,970	9,970	1,090	25,060	2,204	1,040	15,000	15,000	1,090
Error %	1.3	22	−15	−8	47	−30	−47	−32	12

**TABLE 6 Numerical simulation results for different hybrid composite materials.**

	E11 (MPa)	E22 (MPa)	G12 (MPa)
Comminglingfibers	15,000	15,000	1,090
Co-weaving	15,000	15,000	1,090
Laminating	18,800	6,140	1840

hybrid co-woven composite have the same mechanical properties. In fact, the hybridization is carried out in the same layer.

## Conclusion and references

The main objective of this study is to highlight the interest in using biocomposite materials in structural parts by understanding their mechanical behaviour.

Firstly, natural fibers and thermoplastic matrices were studied to determine the best fibre/matrix combination. The thermo-compression parameters, i.e., temperature, dwelltime and pressure were then validated to meet the industrial requirements. The second phase was devoted to the experimental characterization of the different flax, basalt and hybrid composites and the PA11 matrix. This part aimed to identify the mechanical properties of the studied materials in the dry state and at room temperature, then the influence of humidity on the evolution of the mechanical properties of the matrix and the different flax/PA11, basalt/PA11 and hybrid5050/PA11 composites was analyzed. The results of the characterization tests highlight the interest of hybridization. Indeed, the use of basalt fibers with flax fibers improves the mechanical performance of the hybrid composite compared to the flax/PA11 composite and reduces its density by increasing the potential mass gain compared to the basalt/PA11 composite. Furthermore, the hybridization allowed a significant reduction in the scatter of the mechanical properties of the hybrid5050/PA11 compared to the flax/PA11 and the basalt/PA11 composites. The results of the experimental study are in agreement with those obtained in published research works. Indeed, hybridization improves the mechanical performance of the hybrid composite and reduces its sensitivity to moisture, especially when a plant fibre is combined with a synthetic fibre that has a low moisture absorption (Nasimudeen et al., 2021), (Jeyaguru et al., 2022b), (Jeyaguru et al., 2022d), (Jeyaguru et al., 2023). The research work of (Almansour et al., 2017; Almansour et al., 2018) approved that positive impact of using basalt fibres with flax/vinylester composite on the interlaminar fracture toughness. Basalt fibres enhance the durability and limited the sensitivity of flax fibres. Likewise, (Fiore et al., 2016), confirmed and prove a better durability for an hybrid composite with two external basalt layers. (Raponi et al., 2022). shows that the intraply arrangement of flax and basalt was especially useful in improving the tensile properties of flax-based laminates by 116% and 69% for ultimate strength and modulus.

In the second part of this paper, the multiscale numerical homogenization approach is used to determine the effective properties of the studied materials and to compare the numerical results with the experimental values. It also allowed to understand the influence of hygrometry on the composite behaviour and to complete our empirical study by homogenizing new composite

materials with identical fiber content and weave. The significant discrepancy requires the study and the integration of the fiber-matrix interface and the verification of the intrinsic properties of the flax fiber through a reverse homogenization based on the experimental curves. It helped to understand the effect of moisture on the mechanical behaviour of plant fibres. The numerical tool allows us to compare the three scales of hybridization; the laminate scale, the layer scale (by co-weaving) and the fibre scale (by blending two different fibres), and helps us to make the appropriate choice of hybridization for the intended application.

## Data availability statement

The original contributions presented in the study are included in the article/Supplementary Material, further inquiries can be directed to the corresponding author.

## Author contributions

WG: carried out experimental and numerical works, wrote the draft paper. CB and PR: contributed to conception and design of the study, contributed to manuscript revision, read, and approved the submitted version. All authors contributed to the article and approved the submitted version.

## Acknowledgments

The authors acknowledge the support of the company Bertrandt for the funding of this research work.

## Conflict of interest

WG was employed by the company Department Body in White Research and Innovation Unit, Bertrandt.

The remaining authors declare that the research was conducted in the absence of any commercial or financial relationships that could be construed as a potential conflict of interest.

## Publisher's note

All claims expressed in this article are solely those of the authors and do not necessarily represent those of their affiliated organizations, or those of the publisher, the editors and the reviewers. Any product that may be evaluated in this article, or claim that may be made by its manufacturer, is not guaranteed or endorsed by the publisher.

## Supplementary material

The Supplementary Material for this article can be found online at: <https://www.frontiersin.org/articles/10.3389/fmats.2023.1176408/full#supplementary-material>

## References

- Abida, M., Gehring, F., Mars, J., and Vivet, A. (2020). Hygro-mechanical coupling and multiscale swelling coefficients assessment of flax yarns and flax/epoxy composites. *Compos. Part A Appl. Sci. Manuf.* 136. doi:10.1016/j.compositesa.2020.105914
- Almansour, F. A., Dhakal, H. N., and Zhang, Z. Y. (2017). Effect of water absorption on Mode I interlaminar fracture toughness of flax/basalt reinforced vinyl ester hybrid composites. *Compos. Struct.*, 168:813–825. doi:10.1016/j.compstruct.2017.02.081
- Almansour, F. A., Dhakal, H. N., and Zhang, Z. Y. (2018). Investigation into Mode II interlaminar fracture toughness characteristics of flax/basalt reinforced vinyl ester hybrid composites. *Compos. Sci. Technol.* 154, 117–127. doi:10.1016/j.compscitech.2017.11.016
- Altair Multiscale Designer User Manual, 2021.
- Atthith, D., Sanjay, M. R., Gowda, Y., Madhu, P., Arpitha, G. R., Yogesha, B., et al. (2018). Effect of tungsten carbide on mechanical and tribological properties of jute/sisal/E-glass fabrics reinforced natural rubber/epoxy composites. *J. Industrial Text.* 48, 713–737. doi:10.1177/1528083717740765
- Baley, C., and Bourmaud, A. (2014). Average tensile properties of French elementary flax fibers. *Mater. Lett.* 122, 159–161. doi:10.1016/j.matlet.2014.02.030
- Baley, C., and Bourmaud, A. (2014). Average tensile properties of French elementary flax fibers. *Mater. Lett.* 122, 159–161. doi:10.1016/j.matlet.2014.02.030
- Baley, C., Bourmaud, A., and Scida, D. (2017). Influence of the scattering of flax fibres properties on flax/epoxy woven ply stiffness. *Mater. Des.* 122, 136–145. doi:10.1016/j.matdes.2017.02.094
- Baley, C., Morvan, C., and Grohens, Y. (2005). «Influence of the absorbed water on the tensile strength of flax fibers». *Macromol. Symp.* 222, p195–p202. doi:10.1002/masy.200550425
- Barbulee, A., Jernot, J. P., Bréard, J., and Gomina, M. (2014). Damage to flax fibre slivers under monotonic uniaxial tensile loading. *Compos. Part A Appl. Sci. Manuf.* 64, 107–114. doi:10.1016/j.compositesa.2014.04.024
- Bourmaud, A., and Baley, C. (2007). Investigations on the recycling of hemp and sisal fibre reinforced polypropylene composites. *Polym. Degrad. Stab.* 92, 1034–1045. doi:10.1016/j.polymdegradstab.2007.02.018
- Bourmaud, A., and Baley, C. (2009). Rigidity analysis of polypropylene/vegetal fibre composites after recycling. *Polym. Degrad. Stab.* 94, 297–305. doi:10.1016/j.polymdegradstab.2008.12.010
- Chandrasekar, M., Shahroze, R. M., Senthil Muthu Kumar, T., Senthilkumar, K., Ishak, M. R., Rajini, N., et al. (2022). Influence of a silica aerogel filler on the mechanical, thermal, and physical properties of flax/epoxy composite. *Mech. Compos. Mater.* 58 (N°2), 383–396.
- Chandrasekar, M., Siva, I., Kumar, T. S. M., Senthilkumar, K., Siengchin, S., and Rajini, N. (2020). Influence of fibre inter-ply orientation on the mechanical and free vibration properties of banana fibre reinforced polyester composite laminates. *J. Polym. Environ.* 28, 2789–2800. doi:10.1007/s10924-020-01814-8
- Coussa, et al. (2017). Influence of rate effects on the mechanical behaviour of thermoplastic matrix woven composites. *JNC 20-Ecole Des. PontsParisTech.*
- Destaing, F., Jouannot-Chesney, P., Gomina, M., and Bréard, J. (2016). Choice between film or powder of PA11 for processing flax fiber reinforced composites. *Revue des Compos. des Matériaux Avancés n°3* 26, 435–449. doi:10.3166/rcma.26.435-449
- Dhand, V., Mittal, G., Rhee, K. Y., Park, S. J., and Hui, D. (2015). A short review on basalt fiber reinforced polymer composites. *Composites: Part B*, 166–180.
- El Hadi, S., Scida, D., Pac, M. J., and Ayad, R. (2019). Mode-I interlaminar fracture toughness of flax, glass and hybrid flax-glass fibre woven composites: Failure mechanism evaluation using acoustic emission analysis. *Polym. Test.* 75, 246–253. doi:10.1016/j.polymertesting.2019.02.022
- Fabre, V., Quandalle, G., Billon, N., and Cantournet, S. (2017). Time-Temperature-Water Content equivalence on dynamic mechanical response of polyamide 6. *Polymer* (6), 2–3.
- Fargassa, C., Pavlovic, A., and Santulli, C. (2018). Mechanical and impact characterization of flax and basalt fibervinylester composites and their hybrids. *Compos. Part B* 137, 247–259.
- Fiore, V., Calabrese, L., Di Bella, G., Scalici, T., Galtieri, G., Vakenza, A., et al. (2016). Effects of aging in salt spray conditions on flax and flax/basalt reinforced composites: Wettability and dynamic mechanical properties. *Compos. B* 93, 35–42. doi:10.1016/j.compositesb.2016.02.057
- Fragassa, C., Santulli, C., Pavlović, A., and Šljivić, M. (2015). Improving performance and applicability of green composite materials by hybridization. *Contemp. Mater.* 6, 35–43. doi:10.7251/comen1501035f
- Jeyaguru, S., Thiagamani, S. M. K., Pulikkalparambil, H., Siengchin, S., Krishnasamy, S., Muthukumar, C., et al. (2022). Mechanical, absorption, and swelling properties of jute/kenaf/banana reinforced epoxy hybrid composites: Influence of various stacking sequences. *Polym. Compos.* 43, 8297–8307. doi:10.1002/pc.26999
- Jeyaguru, S., Thiagamani, S. M. K., Pulikkalparambil, H., Siengchin, S., Krishnasamy, S., Muthukumar, C., et al. (2022). Mechanical, acoustic and vibration performance of intra-ply Kevlar/PALF epoxy hybrid composites: Effects of different weaving patterns. *Polym. Compos.* 43, 3902–3914. doi:10.1002/pc.26665
- Jeyaguru, S., Thiagamani, S. M. K., Pulikkalparambil, H., Siengchin, S., Krishnasamy, S., Rajkumar, A. G., et al. (2022). Effects of different weaving patterns on thermomechanical and dynamic mechanical properties of Kevlar/pineapple leaf fiber hybrid composites. *Polym. Compos.* 43, 4979–4997. doi:10.1002/pc.26764
- Jeyaguru, S., Thiagamani, S. M. K., Pulikkalparambil, H., Siengchin, S., Subramaniam, J., Rangappa, S. M., et al. (2022). Mechanical, acoustic and vibration performance of intra-ply kevlar/PALF epoxy hybrid composites: Effects of different weaving patterns. *Polym. Compos.* 43, 3902–3914. doi:10.1002/pc.26665
- Jeyaguru, S., Thiagamani, S. M. K., Rangappa, S. M., and Siengchin, S. (2023). Experimental studies on the absorption, swelling and erosion performance of hybrid woven Kevlar/hemp reinforced epoxy composites. *Express Polym. Lett.* 17 N°4, 353–372. doi:10.3144/expresspolymlett.2023.26
- Kumar, T. S. M., et al. (2020). *Influence of fillers on the thermal and mechanical properties of biocomposites: An overview, biofibers and biopolymers for biocomposites.* Springer, 111–133.
- Mohit, H., Rangappa, S. M., Siengchin, S., Gorbatiyuk, S., Manimaran, P., Alka Kumari, C., et al. (2022). A comprehensive review on performance and machinability of plant fiber polymer composites. *Polym. Compos.* 43, 608–623. doi:10.1002/pc.26403
- Nasimudeen, N. A., Karounamurthy, S., Selvarathinam, J., Thiagamani, S. M. K., Pulikkalparambil, H., Krishnasamy, S., et al. (2021). Mechanical, absorption, and swelling properties of Vinyl Ester based natural fibre hybrid composite. *Appl. Sci. Eng. Prog.* 14 N°4, 680–688.
- Petrucchi, P., Santulli, C., Puglia, D., Sarasini, F., Torre, L., and Kenny, J. M. (2013). Mechanical characterisation of hybrid composite laminates based on basalt fibres in combination with flax, hemp and glass fibres manufactured by vacuum infusion. *Mater. Des.* 49, 728–735. doi:10.1016/j.matdes.2013.02.014
- Rangappa, S. M., Siengchin, S., Parameswaranpillai, J., Jawaid, M., and Ozbakkaloglu, T. (2022). Lignocellulosic fiber reinforced composites: Progress, performance, properties, applications, and future perspectives. *Polym. Compos.* 43, 645–691. doi:10.1002/pc.26413
- Raponi, E., Boria, S., Giammaria, V., Fischer, B., Pörnbacher, J., Sarasini, F., et al. (2022). Effect of basalt intraply hybridization on the damage tolerance of flax laminates: Experimental analysis and analytical modeling under low-velocity impact. *Compos. Struct.* 287, 115270. doi:10.1016/j.compstruct.2022.115270
- Rozycki, P., Mbacke, M., and Dau, A. (2018). *Multiscale homogenization of a glass-PA66 fabric composite behaviour for crash studies, ECCM18-18th European conference on composite materials*, 24–28.
- Sanjay, M. R., Madhu, P., Jawaid, M., Senthamarakannan, P., Senthil, S., and Pradeep, S. (2018). Characterization and properties of natural fiber polymer composites: A comprehensive review. *J. Clean. Prod.* 172, 566–581. doi:10.1016/j.jclepro.2017.10.101
- Senthilkumar, K., Rajini, N., Saba, N., Chandrasekar, M., Jawaid, M., and Siengchin, S. (2019). Effect of alkali treatment on mechanical and morphological properties of pineapple leaf fibre/polyester composites. *J. Polym. Environ.* 27, 1191–1201. doi:10.1007/s10924-019-01418-x, No.
- Senthilkumar, K., Subramaniam, S., Ungtrakul, T., Kumar, T. S. M., Chandrasekar, M., Rajini, N., et al. (2022). Dual cantilever creep and recovery behavior of sisal/hemp fibre reinforced hybrid biocomposites: Effects of layering sequence, accelerated weathering and temperature. *J. Industrial Text.* 51, 2372S–2390S. doi:10.1177/1528083720961416
- Shahroze, R. M., Chandrasekar, M., Senthilkumar, K., Senthilmuthukumar, T., Ishak, M. R., and Asyraf (2019). A review on the various fibre treatment techniques used for the fibre surface modification of the sugar palm fibres. *Proc. Seminar Enau Kebangsaan*, 48–52.
- Shubhalakshmi, B. S., Jagannatha Reddy, H. N., and Arjun, K. (2016). *International journal of engineering sciences and research technology*, 2277–9655. ISSN,p.
- Singha, K. (2012). A short review on basalt fiber. *Int. J. Text. Sci.*, 19–28.
- Swolfs, Y., Verpoest, I., and Gorbatiyk, L. (2019). Recent advances in fibre-hybrid composites: Materials selection, opportunities and applications. *Int. Mater. Rev.* 64, 181–215. doi:10.1080/09506608.2018.1467365
- Swolfs, Y., Gorbatiyk, L., and Verpoest, I. (2014). *Fiber hybridization in polymer composites: A review, composite Part A: Applied science and manufacturing*, 181–200.
- Toumis, R. B., Renard, J., Monin, M., and Nimdum, P. (2013). Fatigue damage modelling of continuous E-glass fibre/epoxy composite. *Procedia Eng.* 66, 723–736. doi:10.1016/j.proeng.2013.12.126
- Yuan, Z., and Fish, J. (2008). Toward realization of computational homogenization in practice. *Int. J. Numer. Methods Eng.* 73 (3), 361–380. doi:10.1002/nme.2074



## OPEN ACCESS

## EDITED BY

Lode Daelemans,  
Ghent University, Belgium

## REVIEWED BY

Doojin Lee,  
Chonnam National University,  
Republic of Korea  
Pietro Russo,  
National Research Council (CNR), Italy

## \*CORRESPONDENCE

R. M. Santos,  
✉ rmsantos@inegi.up.pt

RECEIVED 03 March 2023

ACCEPTED 08 June 2023

PUBLISHED 21 June 2023

## CITATION

Borges C, Chicharo A, Araújo A, Silva J  
and Santos RM (2023), Designing of  
carbon fiber-reinforced polymer (CFRP)  
composites for a second-life in the  
aeronautic industry: strategies towards a  
more sustainable future.  
*Front. Mater.* 10:1179270.  
doi: 10.3389/fmats.2023.1179270

## COPYRIGHT

© 2023 Borges, Chicharo, Araújo, Silva  
and Santos. This is an open-access article  
distributed under the terms of the  
[Creative Commons Attribution License](#)  
(CC BY). The use, distribution or  
reproduction in other forums is  
permitted, provided the original author(s)  
and the copyright owner(s) are credited  
and that the original publication in this  
journal is cited, in accordance with  
accepted academic practice. No use,  
distribution or reproduction is permitted  
which does not comply with these terms.

# Designing of carbon fiber-reinforced polymer (CFRP) composites for a second-life in the aeronautic industry: strategies towards a more sustainable future

Carolina Borges<sup>1</sup>, A. Chicharo<sup>1</sup>, A. Araújo<sup>1,2</sup>, J. Silva<sup>1</sup> and  
R. M. Santos<sup>1,2\*</sup>

<sup>1</sup>Materials and Composite Structures Unit, Institute of Science and Innovation in Mechanical and Industrial Engineering (INEGI), Porto, Portugal, <sup>2</sup>LAETA—Associated Laboratory of Energy, Transports and Aeronautics, Porto, Portugal

Over the last few years, the use of carbon fiber-reinforced polymer composites (CFRP) in the aeronautic sector has significantly increased, given these materials' outstanding properties. Consequently, the accumulation of composite residues is becoming an environmental hurdle. Therefore, in a world where sustainability and circularity remain on the lead, the replacement of thermosets by thermoplastics as polymeric matrices emerges as a promising technique, given the recyclability of these materials. Following this perspective, in this work, carbon fiber-reinforced polymer (CFRP) composite "residues" were incorporated into a poly(etheretherketone) (PEEK) matrix, as a strategy towards a more sustainable future, aiming at developing novel compounds for the aeronautic industry. The influence of two different fiber sizes (<600 and 600–1000 µm) on the neat PEEK properties was assessed through formulations developed using a co-rotating twin screw-extruder, under optimized processing conditions. Furthermore, the potential thermo-oxidative degradation, and the recycling feasibility of the neat PEEK and its compounds, were evaluated by submitting the materials to several thermo-mechanical cycles. The results showed that PEEK compounds were successfully prepared, and presented a good fiber distribution and absence of fiber agglomerates. A positive impact on the mechanical performance of PEEK was found by the incorporation of 3.3 wt.% of short carbon fibers (sCF) with larger sizes (600–1000 µm). The reprocessing of neat PEEK and its compounds for 15 consecutive cycles demonstrated their remarkable thermo-mechanical stability, without any sign of degradation or irreversible loss of properties. The fiber length and fiber length distribution of reprocessed compounds showed that major variations occurred after the first extrusion cycle, especially for larger sizes.

## KEYWORDS

composites, recycling, compounding, extrusion, circular economy

## 1 Introduction

Carbon fiber-reinforced polymer (CFRP) composites scored tremendous scope of application in several flourishing sectors, including aerospace, construction, automotive, and wind energy fields, owing to their outstanding in-plane mechanical properties combined with lower density (Yao et al., 2018; Li and Englund, 2017; Pimenta and Pinho, 2011). Moreover, the soaring demand



for CFRPs in these sectors stems from their ease of integration, multifunctionality, and freedom in design of complex geometries and structures (Vo Dong et al., 2018; Zhang et al., 2020a; Giorgini et al., 2020; Butenegro et al., 2021). With all its major employers holding a substantial share in the modern economy, in 2020 the aviation, aerospace, and defense segments remained in the lead, in terms of share growth in the global CFRP composites market, reaching up to \$7.0 billion, and by 2030 it is foreseen to reach \$15.4 billion (Nikhil and ChidanandEswara, 2022).

Regarding the aerospace industry, CFRP composites are mainly applied to interiors, engine blades, propellers/rotors, brackets, single-aisle and wide-body wings, and nowadays, these materials represent up to 40% of modern aircraft. An example is the Boeing 787 Dreamliner passenger plane, which is composed by approximately 50% of composite materials by weight in the main body, parts of the tail, wings, and fuselage, becoming the most fuel-efficient aircraft (Fortune Business Insights, 2023). Furthermore, structural components based on CFRP composites can lead not only to a significant weight reduction but also to an important decrease of carbon dioxide (CO<sub>2</sub>) emissions by up to 20%, during operations. In fact, CO<sub>2</sub> is the primarily emitted greenhouse gas, and its reduction can lead to global warming and climate change mitigation (Al-Lami et al., 2018).

Supported by sustainable and energy-efficiency trends, the global growth of CFRPs usage has unavoidably brought about a concomitant increase in production wastes and end-of-life (EoL) components (e.g., from decommissioned aircraft) (Pulkkinen, 2022), (Meng et al., 2020). According to the International Air Transport Association (IATA), nearly around 16,000 commercial passenger and cargo planes have been retired worldwide in the past 35 years and every year up to 700 jets are getting closer to the end of their operational lives. Moreover, the UK-based aerospace strategy consultancy, NAVEO, projected that at least 11,000 passenger and cargo planes will be officially retired from service over the next 10 years (Petrauskaitė, 2022), (IATA, 2022). For aircrafts containing CFRPs in their composition, it is estimated that by 2025, 8,500 will be discarded, which will roughly translate to more than 154,000 tons of carbon fibers (CFs) (Meng et al., 2020), (Carberry, 2006), (Alves et al., 2018). Under this scenario, and towards a more circular economy, aircraft decommissioning is becoming an uppermost concern, involving a multidisciplinary process that encompasses environmental, operational, safety, legal, and economic aspects (Elsayed and Roetger, 2022).

Nevertheless, associated to traditional CFRPs design, manufacturing, and application, great challenges arise: the difficulty in reusing and recycling these materials, as well as the lack of sustainable and profitable recycling methodologies. These drawbacks are mainly promoted by i) their complex composition at different scales (fibers, matrix, and fillers), ii) the crosslinked nature of thermoset matrices, not allowing them to be remolded, reshaped, or recycled, and iii) their combination with other materials (metal fixings, honeycombs, among others). In the recent past, the main disposal routes of EoL composite structures include graveyards, landfills, or incineration, which are at the bottom of the waste management hierarchy. Therefore, turning CFRP “wastes” into a valuable material resource and closing the loop in the CFRP life cycle becomes primordial (Li and Englund, 2017), (Pimenta and Pinho, 2011).

Regardless of the different recycling methodologies, and their inherent advantages or disadvantages, mechanical recycling is the most technologically mature CFRP recycling method, which generally

consists of reducing the material size to be further incorporated as a reinforcement or filler into new matrices (e.g., polymers, cement, among others) (Butenegro et al., 2021), (Giorgini et al., 2020), (Meng et al., 2020), (Oliveux et al., 2015; Vincent et al., 2019; Gao et al., 2022). Beyond mechanical methods, chemical recycling is a promising and complementary alternative to overcome the challenges inherent to traditional CFRP composites, allowing the recovery of valuable CFs through the depolymerization of the network structure by the cleavage of specific bonds presented in cured thermosets. However, chemical recycling demands harsh conditions, including high temperatures and pressures, and involves the presence of solvents and the production of various by-products (Liu et al., 2022), (Zhang et al., 2020b).

In an ever-evolving world, the development of more sustainable materials with improved properties and functionalities, ensuring they fit into the category of circular economy materials, is also an essential aspect to meet industrial demands, and prevent environmental and safety risks. In this sense, the replacement of thermosets by thermoplastics seems to be a promising route, and so far, significant efforts have been devoted to developing high-performance and -temperature polymers from the poly(aryletherketone) (PAEK) family, with special focus on poly(etheretherketone) (PEEK), for highly demanding applications (Lu et al., 2019a; Sudhin et al., 2020; Alshammari et al., 2021).

PEEK is a semi-crystalline thermoplastic with good chemical resistance, flame retardancy, low moisture absorption, and recyclability. This material is also known by its remarkable thermal stability provided by the presence of ether linkages in the molecular chain, which also imparts the possibility of being processable via cost-efficient and faster processes, such as injection molding and extrusion. However, its unusual mechanical performance is strongly dependent on the degree of crystallinity and crystalline morphology, which are influenced by the thermal history and processing conditions applied to the material. Therefore, the further structural reinforcement of PEEK with recovered CFRP “residues” or recycled CFs opens a new horizon for designing composite materials with enhanced mechanical wear and impact resistance, which are properties mainly required for the aeronautic industrial field (Lu et al., 2019b; Pedoto et al., 2022; Lu et al., 2023).

An overview of the literature reveals that few studies have been conducted aiming at establishing correlations between the orientation state of fibers, fiber length, fiber/matrix interface, and matrix crystallinity with the overall mechanical performance and microstructure of the recycled PEEK compounds (Zhang et al., 2012; Kumar, et al., 2008; Hirayama et al., 2017; Nakashima et al., 2017; Li et al., 2018; Subhedar et al., 2020). Thus, in the present work, carbon fiber-reinforced thermoplastic “residues” (rCFRT), resulting from the design, production and optimization of an aeronautic demo case (bracket), were milled and reused for the development of novel compounds. Two fiber sizes of rCFRT were selected and incorporated into a neat PEEK matrix to study their influence on the mechanical performance, thermal transitions and crystallinity degree, and rheological properties of the matrix. In addition, the developed compounds were further submitted to continuous thermo-mechanical cycles to investigate their potential thermo-oxidative degradation and recycling feasibility. The fiber length size and distribution, after several thermomechanical cycles, were also evaluated. The final objective of this work will be to reach the most suitable formulation, with tailored properties, which will be applied to develop another demo case by injection molding: an airplane bracket.



Afterward, three demo cases will be combined to produce a window frame by *in situ* welding.

## 2 Experimental part

### 2.1 Materials

The two materials used in this work were: 1) PEEK 150G pellets supplied by Victrex® (Lanchashire, United Kingdom), and 2) a low melt poly (aryletherketone), LMPAEK, unidirectional carbon fiber prepreg tapes. PEEK has a Newtonian plateau melt viscosity of 130 Pa.s at 400°C, a density of 1.30 g/cm<sup>3</sup> at 25°C, and was used as a polymeric matrix. The “residues” from the carbon fiber reinforced low melt thermoplastics (rCFRT) were milled in a granulator (Rapid Granulator 200-24K®) with a 4 mm grid. All materials were previously dried overnight in an oven at 120°C and then subjected to a granulometric analysis by sieving in a sieve shaker (AS200 Analytical, Retsch®). The results are depicted in Figure 1.

The largest amount of rCFRT is in the range between 600 and 1,000 µm. Therefore, in this work, the incorporation of two different particle sizes was considered i) < 600 and ii) 600–1,000 µm.

### 2.2 Development of novel recycled compounds based on rCFRT

The development of novel recycled compounds, based on two different rCFRT sizes, was conducted in an intermeshing co-rotating twin-screw extruder (Coperion GmbH ZSK 26 Mc) with L/D = 40, with screws rotating at 200 rpm, to ensure adequate hydrodynamic shear stresses and residence times for the dispersion of rCFRT. Downstream accessories were coupled to the extruder, including a water-cooling bath, counter-current air dryer, and rotating knife. The loading of rCFRT was set at 5 wt% (selected based on a preliminary study

conducted through i) rCFRT incorporations up to 10 wt%, without significant mechanical reinforcement of the compound between 5 and 10 wt%, and an assumption considering ii) the possible scarcity of the available “residues,” with 5 wt% being a reasonable loading that guarantees the existence of enough rCFRT to be incorporated). In addition, it is relevant to state that in the bulk, this percentage only represents 3.3 wt% of CFs, since the LMPAEK tapes are constituted by 66% of CF weight fraction and 34% of PAEK. The screw configuration contains three mixing zones consisting of kneading blocks with different staggering angles, with the aim of melting the polymer and inducing dispersive mixing, separated by conveying sections. Extruded filaments with a 3 mm diameter were slowly cooled to ensure appropriate material recrystallization, and were then pelletized. The extrusion parameters were adjusted for each developed compound to ensure processing stability, and the data are presented in Table 1.

Table 1 shows the effect of reinforced PEEK with 5 wt% of rCFRT on the extrusion processing parameters, including pressure drop, and melt temperature. Since the melt temperature of compounds is similar to neat PEEK, significant increments in the melt viscosity or viscous dissipation with an incorporation of 5 wt% of rCFRT are not expected. However, it is important to note that even when extrusion processing conditions were adjusted (e.g., temperature profile), the incorporation of rCFRT had an adverse effect on processability, inducing a significant increase in the melt pressure, from 22–23 to 30–31 bar.

### 2.3 Samples preparation by injection and compression molding

Neat PEEK and its compounds containing 5 wt% of rCFRT were prepared by injection or compression molding, depending on the characterization technique requirements. For tensile tests, the materials were previously dried and injected in the form of type 1A specimens, according to ISO 527-2 standard, using an Engle ES 200/45 HL-V machine. Based on the safety data sheet provided by Victrex®,

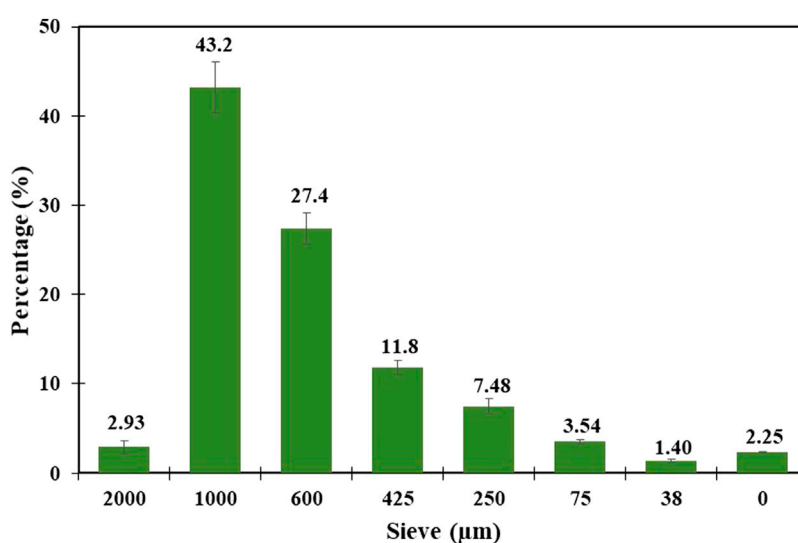


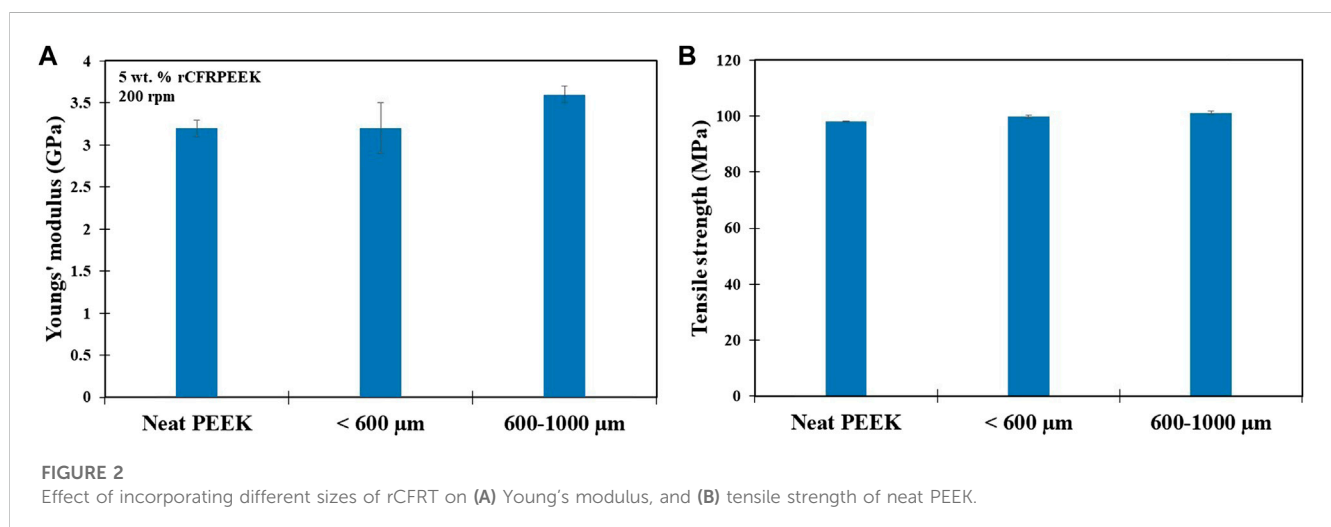
FIGURE 1  
Granulometric analysis of the rCFRT.

**TABLE 1** Adjusted extrusion processing conditions for each compound.

Formulation	Temperature profile (°C)	Pressure (bar)	Melt temperature (°C)
Neat PEEK	365-365-370-370-365-365-365-365-370	22–23	365–366
< 600 µm	360-365-365-370-370-370-375-375-375-375	28–30	364–365
600–1,000 µm	360-365-365-370-370-370-375-375-375-375	30–31	365–366

**TABLE 2** Injection molding conditions.

Formulation	Injection temperatures (°C)	Mold temperature (°C)	Screw rotation (L/min)	Counter pressure (bar)	Injection pressure (bar)
Neat PEEK	350–380	210	100	50	857
< 600 µm	340–380	210	100	100	781
600–1,000 µm	340–380	210	100	100	781



the recommended tool temperatures to obtain crystalline components with PEEK stand between 170 and 200°C. The barrel temperature range must stand between 350 and 380°C. PEEK compounds required increased barrel temperatures (maximum 20°C). Table 2 displays the injection molding conditions applied for injected bars.

For the rheological characterization, disks with 25 mm diameter and 1 mm thick were also prepared by compression molding in a hot plate press SATIM TYPE PML 1, at 390°C for 30 min.

## 2.4 Compounds' characterization

### 2.4.1 Stress-strain behavior

The influence of different rCFRT sizes on the quasi-static mechanical behavior of neat PEEK was evaluated using an INSTRON 4208® universal instrument (INSTRON, Massachusetts, United States), with a load cell of 5 kN and a constant crosshead speed of 2 mm/min until 4 mm displacement, followed by 10 mm/min up to mechanical failure. The data analysis

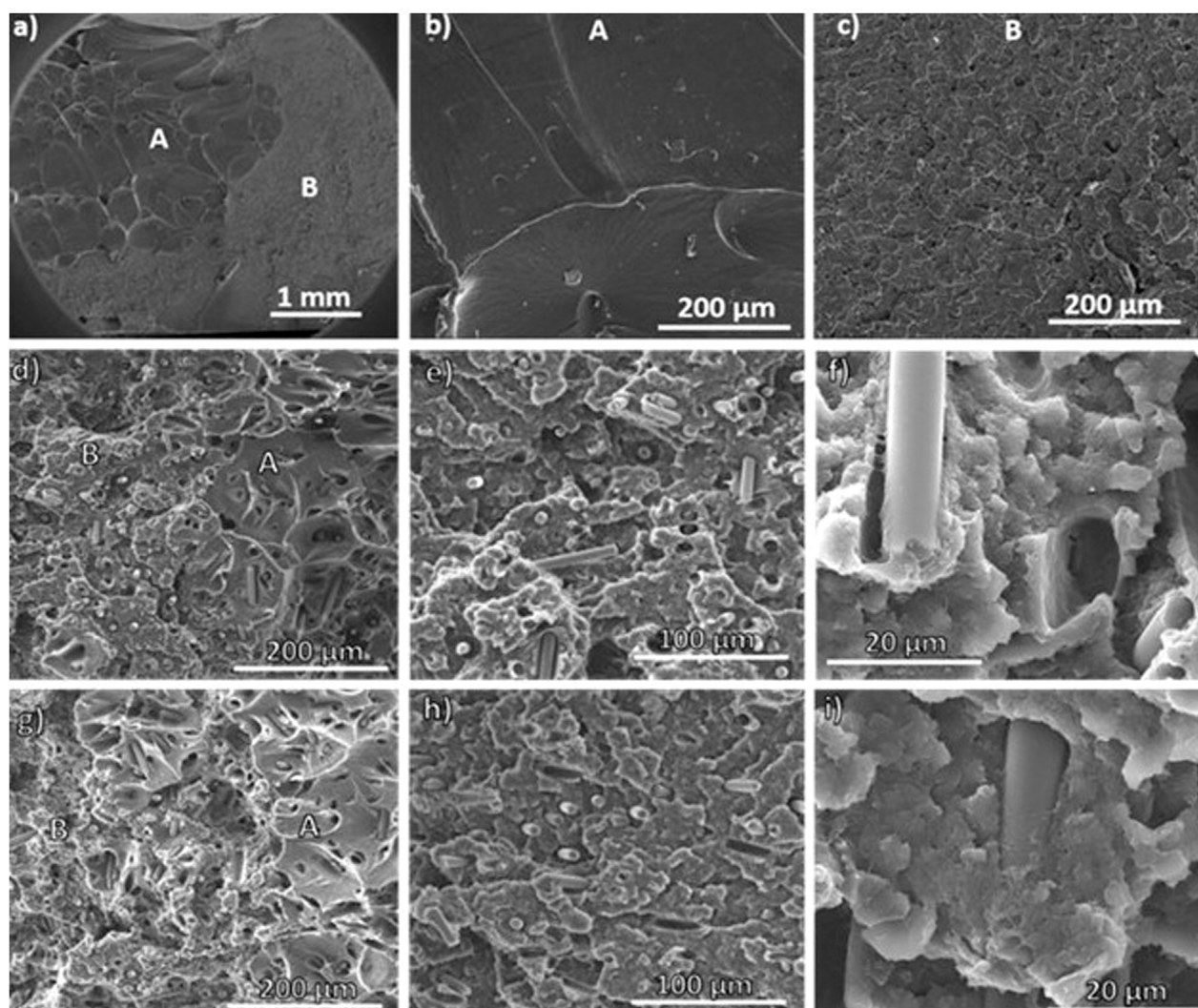
was assessed by means of ISO-527 standard tensile tests to determine compounds' ultimate tensile strength and Young's modulus.

### 2.4.2 Fractured surface observation by scanning electron microscopy (SEM)

The fractured surface of the tensile test specimens was observed using a High resolution (Schottky) Environmental Scanning Electron Microscope (FEI Quanta 400 FEG ESEM/EDAX Genesis X4M). Before the analysis, the samples were coated with a gold/palladium (Au/Pd) thin film for 120 s, and with a 15 mA current (SPI Module Sputter Coater).

### 2.4.3 Crystallization degree evaluation by differential scanning calorimetry (DSC)

The comparison between the crystallization degree and thermal transitions of neat PEEK and its compounds was assessed by DSC (TA Instruments Q20 model®, New Castle DE, United States). Samples were heated from 100.0 to 380.0°C at a heating rate of 30.0°C/min, under a nitrogen atmosphere. Afterwards, the samples were cooled up to



**FIGURE 3**  
SEM images of the specimens' fractured surface after mechanical testing: (A–C) for neat PEEK, and compounds containing (D–F) <600, and (G–I) 600–1,000  $\mu\text{m}$  rCFRT.

100.0°C and heated again from 100.0 to 380.0°C at 30.0°C/min. The reported results are the average of three tested samples, and the crystallinity degree of compounds was calculated as follows:  $X_c = \frac{\Delta H_m}{\alpha \times \Delta H_{100\%}} \times 100$  (Lu et al., 2019c).

Where,  $X_c$  is the samples crystallinity degree,  $\Delta H_m$  is the melting enthalpy during the second heating,  $\Delta H_{100\%} = 130 \text{ J/g}$  (Lu et al., 2019c) is the melting enthalpy for fully crystalized PEEK, and  $\alpha$  is the mass fraction of PEEK in the compound.

#### 2.4.4 Rheology

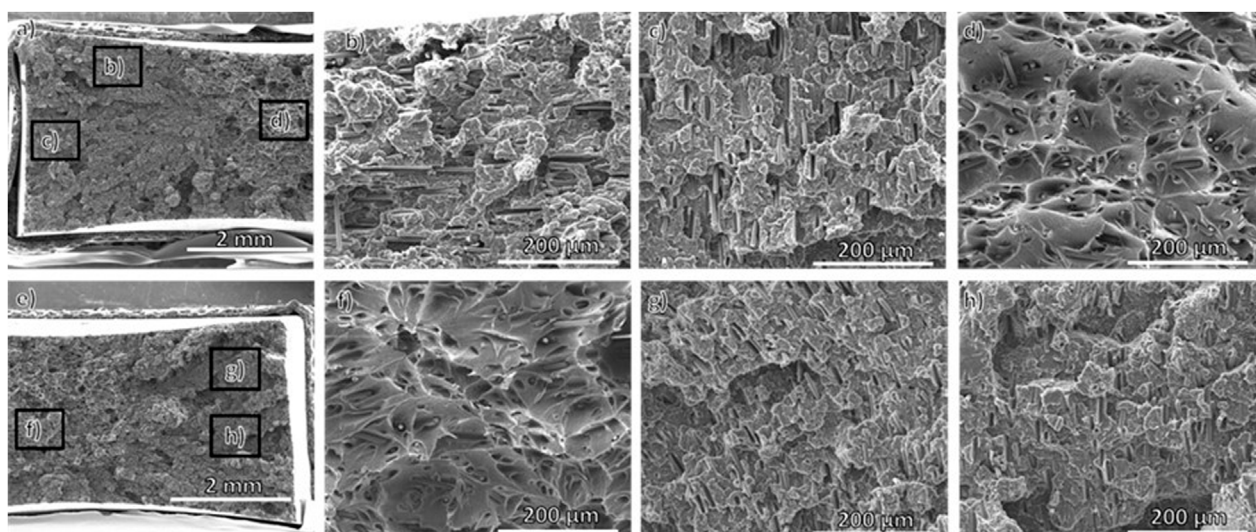
The rheological properties of neat PEEK and its compounds were determined on a Discovery Hybrid Rheometer DHR-1 (TA Instruments LTD®, New Castle, United States), equipped with a parallel plate geometry with a diameter of 25 mm, and a gap of less than 1 mm was applied, at 370°C. Small amplitude oscillatory shear (SAOS) experiments were performed on the samples at an angular frequency sweep from 0.1 to 100 rad/s. The linear viscoelastic response

was determined with strain amplitude sweeps from 0.05 to 12.5%, and a strain of 5% was selected for the frequency sweep tests.

#### 2.4.5 Assessment of the compounds' thermo-mechanical stability and recycling feasibility

Neat PEEK and its compounds were submitted to consecutive reprocessing cycles with the aim to evaluate their thermo-mechanical stability and recycling feasibility. For the purpose, all compounds were subjected to 15 consecutive extrusion cycles by using the same twin-screw extruder and processing conditions described in Section 2.2. When leaving the extruder, the monofilaments were cooled in water and dried in a counter-current air dryer. Afterwards, the compounds were fed again to the extruder and the procedure was repeated 14 consecutive times. Neat and reprocessed PEEK were then characterized by Fourier Transform Infrared Spectroscopy (FTIR), using an Agilent Technologies Cary 630 spectrophotometer with an Attenuated Total Reflectance accessory (ATR) at a resolution of  $4 \text{ cm}^{-1}$  and an average of





**FIGURE 4**  
SEM images denoting sCFs orientation in the tensile specimens: particle size (A–D) <600 and (E–H) 600–1,000  $\mu\text{m}$ .

140 scans. In addition, the mechanical properties of reprocessed PEEK were evaluated under conditions described previously, and the fiber length size and fiber length distribution were assessed.

#### 2.4.6 Assessment of the compounds' fiber length and fiber length distribution after thermo-mechanical reprocessing cycles

Aiming to determine the potential fiber length reduction of the developed PEEK compounds submitted to several thermo-mechanical reprocessing cycles, the PEEK matrix of each recycled compound was removed by acid digestion, according to ASTM D3171-15. Samples with 1 g were placed in a beaker, to which 20 mL of 95%–98% sulfuric acid was carefully added. The mixture was placed on a hot plate, at 100°C for 60 min. Afterwards, 40 mL of hydrogen peroxide was added, drop by drop, to oxidize the matrix. Finally, when the solution appeared clear, CFs were washed with distilled water and acetone. After drying the fibers in an oven, at 100°C for at least 1 h, it was possible to carry out both fiber length size and fiber length distribution analysis. Optical microscopy of recovered fibers was observed by a Zeiss Axioplan 2 microscope coupled to a Zeiss AxioCam ICc 3 camera, equipped with a 6-place turret currently outfitted with 6 objectives from 5 to 100 $\times$ . Scanned images of the fibers were analyzed using ImageJ software, and a scale resolution was set, in which 1 pixel corresponds to 0.8  $\mu\text{m}$ .

### 3 Results and discussion

#### 3.1 Particle size influence on the neat PEEK properties

The influence of two different particle sizes of rCFRT (<600 and 600–1,000  $\mu\text{m}$ ) on the tensile properties of neat PEEK is shown in Figure 2.

The measured tensile properties of neat PEEK, in terms of both elastic modulus and tensile strength, are similar to the values revealed by the manufacturer (4.1 GPa and 100.0 MPa vs.  $3.2 \pm 0.1$  GPa and  $98.2 \pm 0.1$  MPa), suggesting that a similar molecular orientation and crystallinity degree were attained in injection-molded testing samples. These observations were then confirmed by DSC data. Moreover, it can be observed that the incorporation of 5 wt% of rCFRT with larger sizes (600–1,000  $\mu\text{m}$ ) slightly increased the mechanical performance of neat PEEK, while a poor ability to reinforce the polymeric matrix with low load transfer efficiency seems to be attained through the incorporation of rCFRT with smaller sizes (<600  $\mu\text{m}$ ) (Sarasua et al., 1996), (Pan and Yapici, 2016). These results are in good agreement with studies reported in the literature (Sarasua et al., 1996; Pan and Yapici, 2016; Lu et al., 2019c).

In fact, several parameters affect the overall mechanical performance of the developed PEEK compounds, including the loading (Li et al., 2018), (Zhang et al., 2012), length (Kumar, et al., 2008), (Hirayama et al., 2017), (Unterweger et al., 2020), orientation (Subhedar et al., 2020) and dispersion level of fibers into a polymeric matrix (Nakashima et al., 2017), polymer viscosity (von Turkovich and Erwin, 2023), (Fu, et al., 2023), among others. For example, Zhang et al. (2012) showed that the strengthening mechanism of PEEK is improved by incorporating sCFs up to 10 wt%. Flexural (67.8%) and ultimate tensile strength (62.4%) enhancement were reported (Li et al., 2018) through the addition of 20 wt% of sCFs within a low-viscosity PEEK. Although higher sCFs dispersion levels are expected in polymers with a higher melt viscosity, fiber shortening can become worse due to the higher shear forces generated, limiting the reinforcement effect of sCFs (von Turkovich and Erwin, 2023), (Fu, et al., 2023). In addition, Unterweger et al. (2020) evaluated the influence of sCFs length (100–350  $\mu\text{m}$ ) on the mechanical properties of injection-molded composites, and the results revealed that an overall increase of both

tensile strength and elastic modulus was attained when the fiber length was increased.

After the tensile tests, the fractured surface of the specimens was observed, and the SEM images are depicted in Figure 3 A–C) for neat PEEK, D–F) < 600  $\mu\text{m}$  rCFRT, and G–I) 600–1,000  $\mu\text{m}$  rCFRT, respectively.

The surface of the injected-PEEK specimen evidences the presence of a smooth region, related to plastic deformation before breaking, and the appearance of necking (Figures 3A, B region A). Nevertheless, the observed necking (Chen et al., 2018) is concentrated in a region without widely spreading, while the remaining area of the specimen presents a more rough and brittle fracture surface (Figures 3A, C region B). Similar findings were observed for the PEEK compounds containing 5 wt% rCFRT, and Figures 3D, G exemplifies the regions A and B where an increased fracture roughness is visible when compared to the neat PEEK. The modified formulations showed that the sCFs are well distributed in the polymeric matrix (absence of fiber agglomerates), and sCFs pull-out and debonding are the predominant failure modes of the materials (Figures 3D, E, G, H). It is also depicted in Figures 3F, I sCFs coated with polymer sheath, which evidences the good compatibility/interaction between the fibers and the matrix. This is in agreement with the tensile results obtained, since the addition of the rCFRT did not promote a decrease of the materials' mechanical performance.

The specimens fractured surface observation also provided interesting insight on the sCFs orientation in the flow direction,

from transverse section of the tensile specimens, as depicted in Figure 4.

The SEM images, in Figure 4, showed strong CFs alignment parallel to the skin region of the specimen, associated to the rapid cooling (Xiaochun et al., 2018) and the bending load applied from the vertical direction to the injection mould surface (Murata and Kanno, 2021). The core of the sample presents a more random orientation or alignment along the flow direction (Figure 4D, F). It should be noted that no difference was found between the compounds containing different sizes of sCFs (Murata and Kanno, 2021).

The influence of incorporating 5 wt% of rCFRT, with different particle sizes, on the thermal transitions and crystallization degree of neat PEEK is summarized in Figure 5 and Table 3. The onset temperature of each peak and the maximum peak temperature were identified, and the enthalpy of each transition was calculated.

The heat flow variation of neat PEEK (raw-material, in pellet form), during the first heat ramp, showed the glass transition temperature ( $T_g$ ) at  $165.5^\circ\text{C} \pm 0.4^\circ\text{C}$ , and a single melting endotherm at  $353.1^\circ\text{C} \pm 0.9^\circ\text{C}$  that corresponds to the melting of the primary crystallization phase, where amorphous material nucleates and spherulitic growth occurs (higher temperature endotherm, HTE) (Pérez-Martín et al., 2022). Notice that a similar degree of crystallization was attained for the PEEK injected bars in comparison with raw-material, showing that the selected injection molding conditions were appropriate, confirming previous observations.

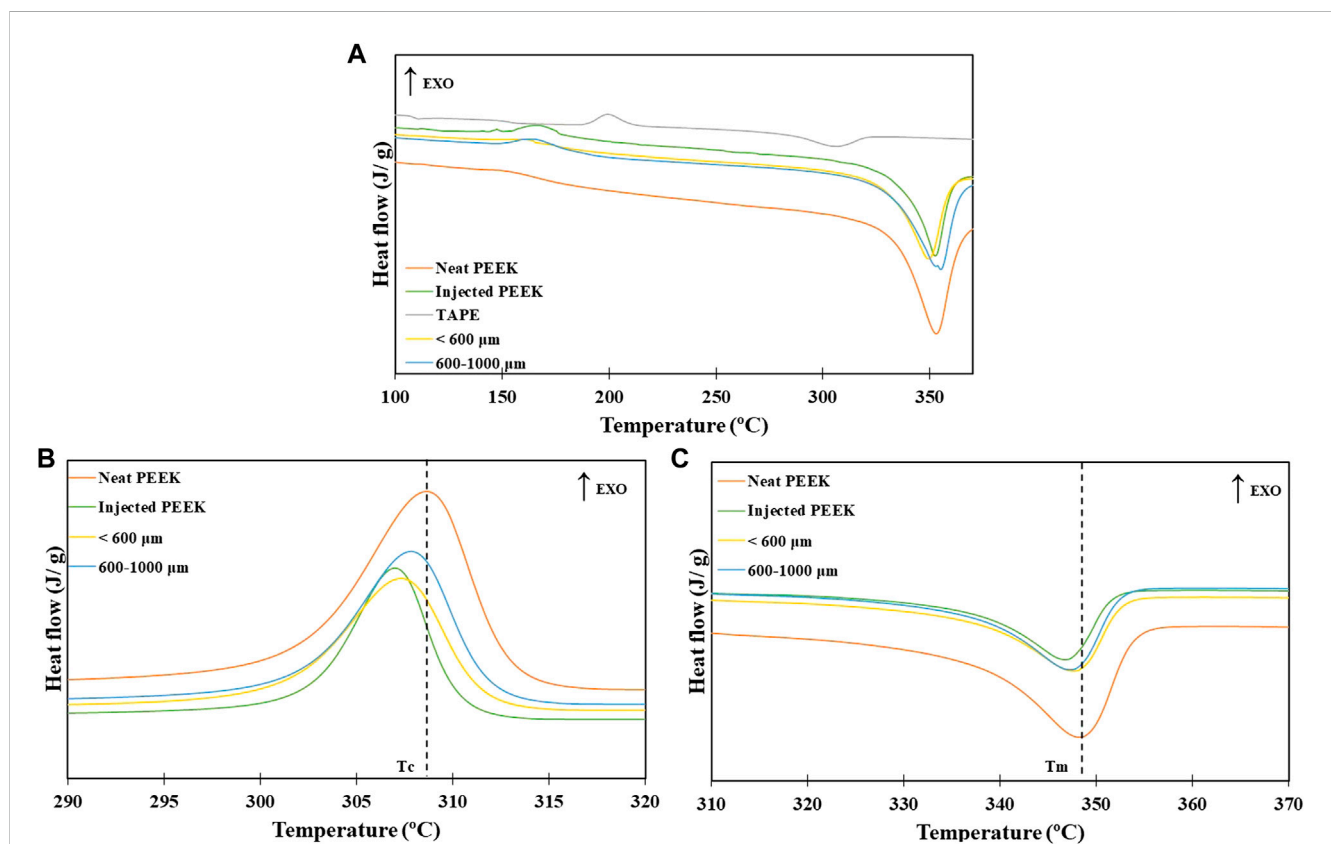


FIGURE 5  
DSC thermograms for neat PEEK, LMPAEK prepreg tape and rCFRT compounds: (A) first heating, (B) cooling, and (C) second heating.



TABLE 3 Average values for transition temperatures and crystallinity degree of the neat PEEK and its compounds.

	$T_g$ (°C)	$\Delta H_{m1}$ (J/g)	$T_{m1}$ (°C)	$\Delta H_{m2}$ (J/g)	$T_{m2}$ (°C)	$X_c$ (%)
Neat PEEK (raw-material, pellet form)	$165.5 \pm 0.4$	$55.4 \pm 3.5$	$353.1 \pm 0.9$	$40.5 \pm 0.5$	$347.0 \pm 0.3$	$31.2 \pm 0.4$
PEEK (injected bars)	$175.7 \pm 0.2$	$58.2 \pm 0.8$	$352.2 \pm 0.0$	$40.8 \pm 0.2$	$346.8 \pm 0.0$	$31.2 \pm 0.3$
< 600 $\mu\text{m}$	$169.0 \pm 4.1$	$54.9 \pm 0.2$	$350.4 \pm 1.2$	$38.8 \pm 1.4$	$347.3 \pm 0.3$	$29.8 \pm 0.9$
600–1,000 $\mu\text{m}$	$175.8 \pm 1.4$	$45.3 \pm 2.0$	$352.4 \pm 1.7$	$36.6 \pm 1.1$	$347.0 \pm 0.0$	$28.2 \pm 0.8$

The LMPAEEK prepreg tape exhibited a cold crystallization exotherm above  $T_g$ , at  $199.5^\circ\text{C}$  ( $\Delta H_{cc} = 6.3 \pm 0.4$  J/g). This behavior is related to the processing conditions applied during prepreg tape manufacturing, where a higher cooling rate from the melt can inhibit polymer chain reorganization and crystal structure formation (Pérez-Martín et al., 2021). Therefore, the amorphous phase present in the LMPAEEK prepreg tape undergoes cold crystallization during subsequent heating (Figure 5A).

The crystallization peak of compounds containing 5 wt% of rCFRT shifts to lower temperatures comparatively to PEEK (Figure 5B), indicating that the polymer recrystallization was slightly hindered in the presence of rCFRT, especially for those with larger dimensions (600–1,000  $\mu\text{m}$ ). However, the enthalpies associated to the first and second melting processes (Table 1) are different, suggesting that some residual stresses were generated during compounds manufacturing. In addition, it is important to note that the crystallization degree of PEEK compounds is lower than neat PEEK, which means that higher mechanical improvements through the incorporation of rCFRT could be achieved by controlling the processing conditions applied in the extrusion and injection molding.

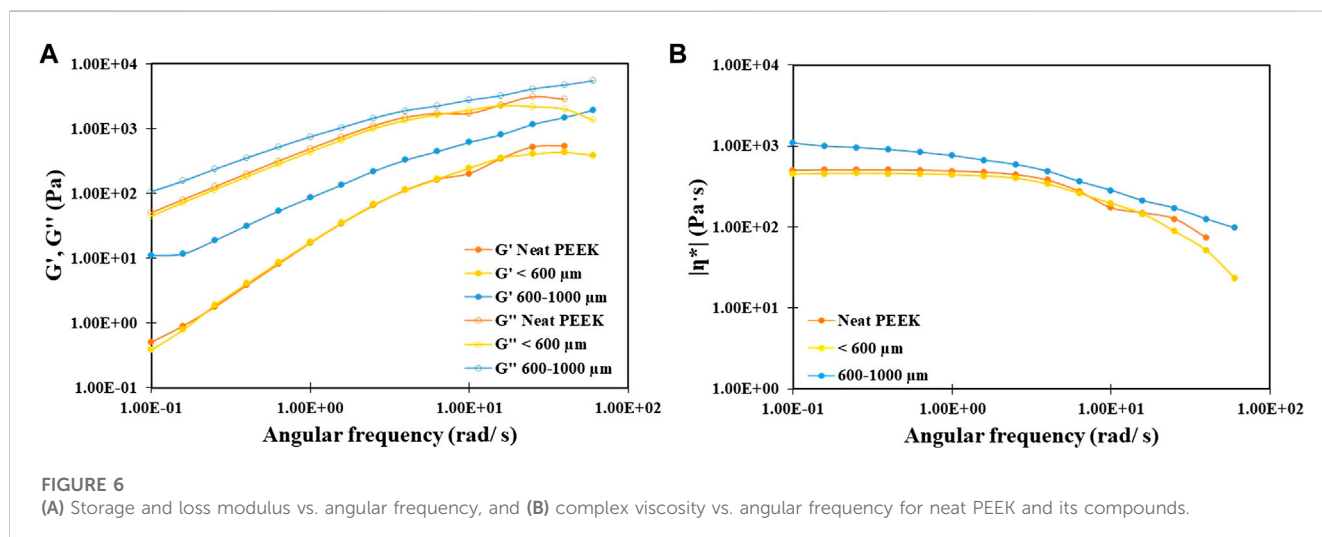
Since the incorporation of rCFRT can induce significant changes in the flow behavior of neat PEEK, and its processability limit, promoted by increments in the viscosity, the rheological properties were investigated (Rieger et al., 2019). The storage modulus ( $G'$ ) is the most sensible to structural changes, and it is closely related to the rigidity of the polymer

macromolecules and their entanglement, while the loss modulus ( $G''$ ) depends on the linkages that control the conformational changes of the chain segments, and the displacement of one chain in relation to another. Understanding their behavior provides essential information about the viscoelasticity of the material (Erбетта et al., 2014). Thus, the rheological characterization of neat PEEK and its compounds, including the  $G'$ ,  $G''$  and complex viscosity ( $|\eta^*|$ ) was performed, and the results are depicted in Figure 6.

For all tested formulations,  $G''$  remained virtually unchanged since its behavior is dominated by the flow of the viscous phase, which indicates that the viscous component of the material dominates the elastic counterpart, across almost all frequencies. Higher values of  $G''$  at the low angular frequency in comparison with neat PEEK were observed, mainly due to the presence of the solid phase (rCFRT) (Cox and Merz, 1958). Moreover, the incorporation of rCFRT slightly altered the complex viscosity of the polymeric matrix, becoming more pronounced for compounds containing larger particle sizes (600–1,000  $\mu\text{m}$ ).

### 3.2 Thermo-mechanical cycles influence on PEEK stability

The stability of neat PEEK during processing and reprocessing was evaluated, allowing to mimic its feasibility to be recycled without significant thermo-oxidative degradation and irreversible loss of properties (von Turkovich and Erwin, 2023). For this purpose, neat



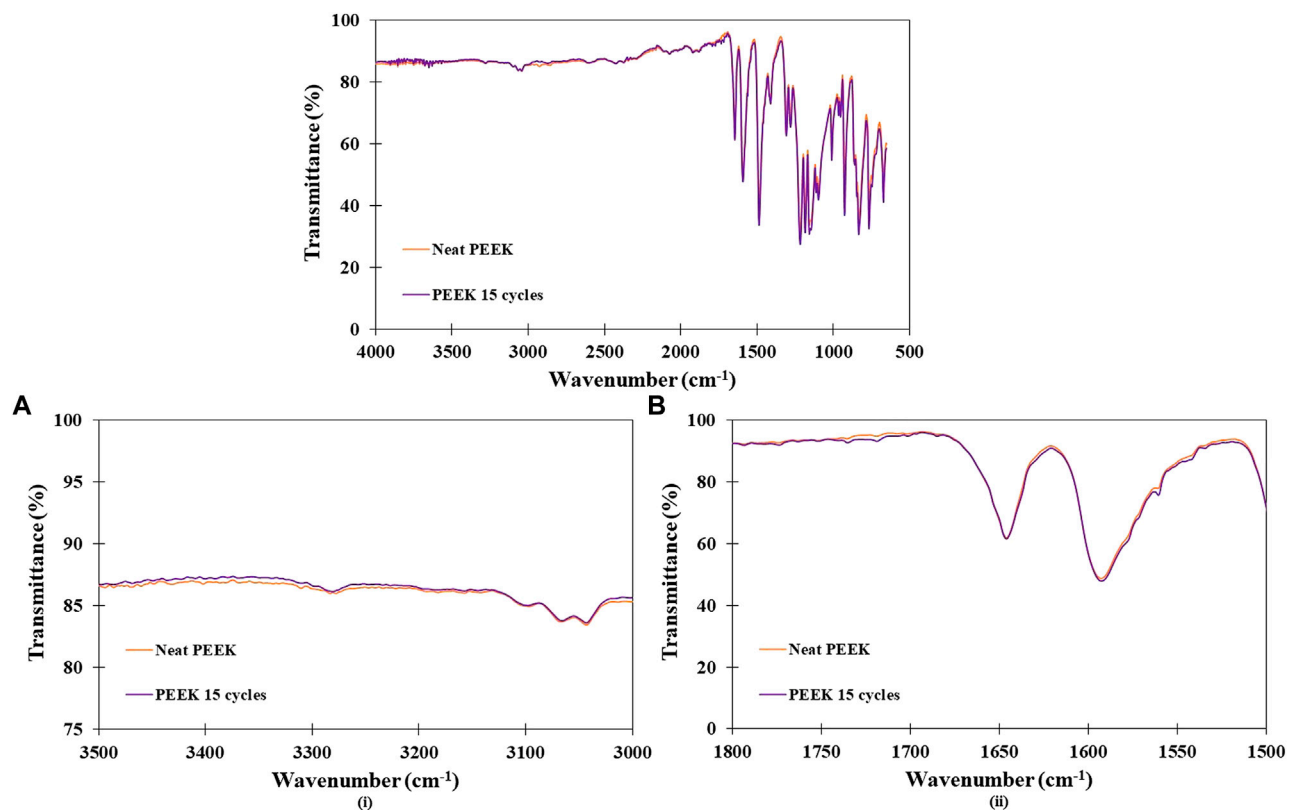


FIGURE 7

(A) ATR-FTIR spectra of neat and reprocessed PEEK for 15 cycles: (B) hydroxyl, and (C) carbonyl region.

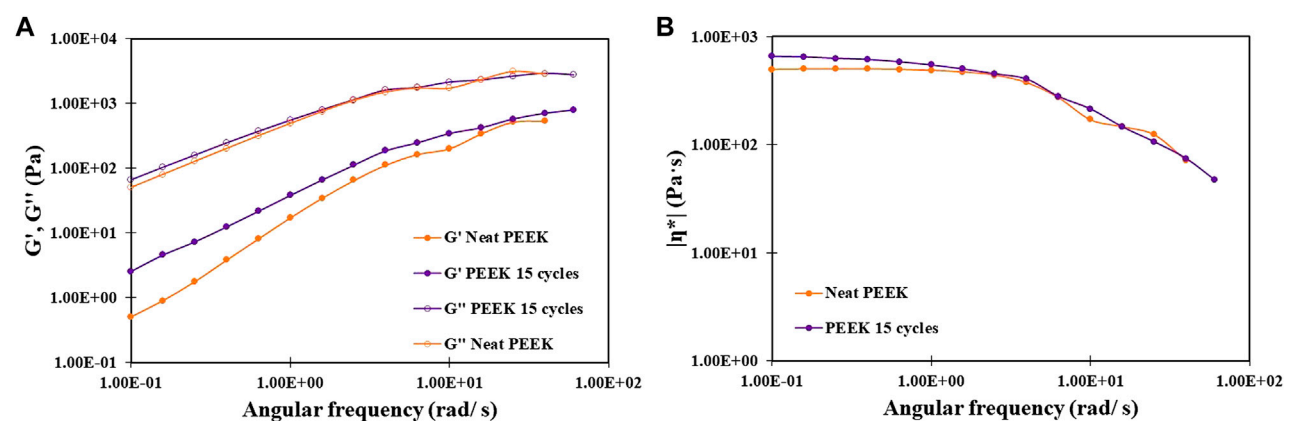


FIGURE 8

(A) Storage and loss modulus vs. angular frequency, and (B) complex viscosity vs. angular frequency for neat and reprocessed PEEK.

PEEK was subjected to 15 consecutive extrusion cycles under similar processing conditions. Chemical modifications that can occur on neat PEEK were followed by ATR-FTIR spectroscopy. The spectra of neat and reprocessed PEEK for 15 cycles are presented in Figure 7.

The neat PEEK showed characteristic absorption bands at 1,413, 1,490 and 1,596 cm<sup>-1</sup>, attributed to stretching of the phenyl ring, while C-H deformations are mainly found in the range of

1,200–600 cm<sup>-1</sup>. Aromatic hydrogens can be observed below 900 cm<sup>-1</sup> (Gaitanelis et al., 2022). The carbonyl stretching vibration appeared at 1,646 cm<sup>-1</sup>, and the bending motion of the (C-C(C=O)-C) group at 1,305 cm<sup>-1</sup>. In addition, absorption bands at 1,184 and 1,219 cm<sup>-1</sup> were found, and attributed to the symmetric and asymmetric stretching vibrations of the diphenyl ether group (C-O-C linkages) (Yaragalla et al., 2021).

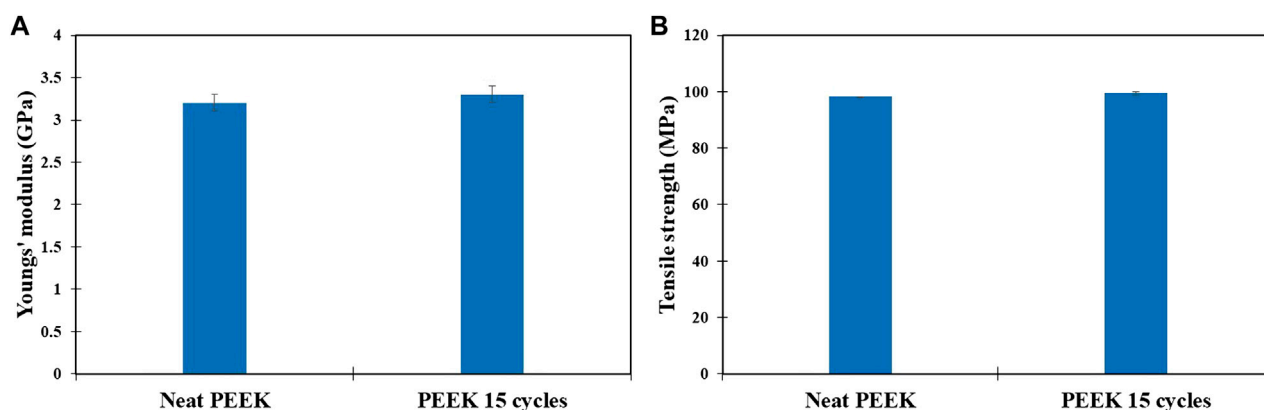


FIGURE 9  
(A) Young's modulus, and (B) tensile strength of neat and reprocessed PEEK.

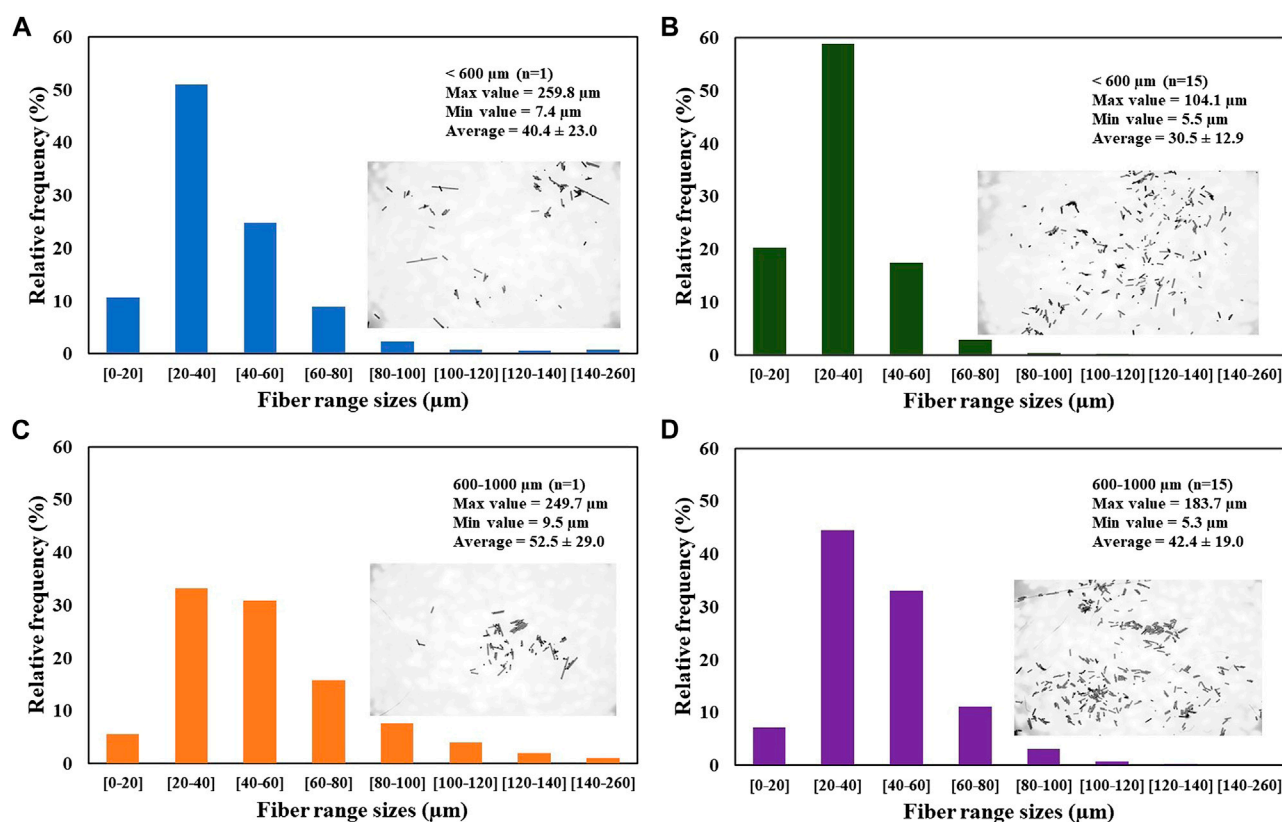


FIGURE 10  
Fiber length distribution histograms for each compound: (A) < 600  $\mu\text{m}$ , at  $n = 1$ ; (B) < 600  $\mu\text{m}$ , at  $n = 15$ ; (C) 600–1,000  $\mu\text{m}$ , at  $n = 1$  and (D) 600–1,000  $\mu\text{m}$ , at  $n = 15$ .

Thermo-oxidative and/or -mechanical degradation can induce the appearance of new absorption bands or a growth of the bands intensity in the region corresponding to carbonyl ( $1,600\text{--}1,800\text{ cm}^{-1}$ , Figure 8A) and hydroxyl ( $3,000\text{--}3,400\text{ cm}^{-1}$ , Figure 8B) stretching vibrations. Spectra modifications in non-aromatic hydrogen carbon bonds ( $2,800\text{--}3,000\text{ cm}^{-1}$ ), can be also observed depending on the

predominant degradation mechanism, e.g., crosslinking or chain scission.

The comparison of neat and reprocessed PEEK spectra showed similar absorption bands with the same intensities, proving that no degradation was found for PEEK upon 15 extrusion cycles. Moreover, rheological measurements were performed to support

TABLE 4 Compounds' fiber-length distribution.

	Maximum value ( $\mu\text{m}$ )	Minimum value ( $\mu\text{m}$ )	Average value ( $\mu\text{m}$ )
< 600 $\mu\text{m}$ ( $n = 1$ )	259.8	7.4	40.4 $\pm$ 23.0
< 600 $\mu\text{m}$ ( $n = 15$ )	104.1	5.5	30.5 $\pm$ 12.9
600–1,000 $\mu\text{m}$ ( $n = 1$ )	249.7	9.5	52.5 $\pm$ 29.0
600–1,000 $\mu\text{m}$ ( $n = 15$ )	183.7	5.3	42.4 $\pm$ 19.0

previous findings observed by ATR-FTIR, and to monitor the stability of reprocessed PEEK. The rheological results are illustrated in Figure 8.

Multiple heat treatment cycles, with prolonged heating above the polymer's melting temperature, may lead to a significant change in the polymer's viscosity, which is influenced by the degradation mechanism and kinetics, or the competition between crosslinking or scission (Colin and Tcharkhtchi, 2013), (Selvanarayanan, 2017). However, the collected viscoelastic data allows to state that 15 reprocessing cycles do not promote any changes on the rheological behavior of PEEK.

Therefore, based on these results, no irreversible changes in the properties of reprocessed PEEK are expected. Aiming at confirming these considerations, the mechanical performance of reprocessed PEEK was evaluated by stress-strain experiments, and the results are shown in Figure 9.

A similar mechanical behavior was found for neat and reprocessed PEEK for consecutive 15 extrusion cycles, showing the remarkable thermal stability of PEEK even when submitted to high shear stresses, temperatures, and residence times. An important contribution to the subject was reported by A.R. et al. (McLauchlin et al., 2014) where the reprocessability of PEEK through multiple injection molding cycles was evaluated, and the results showed that the tensile strength remained almost unchanged. In addition, McLauchlin, A. and co-workers (VICTREX, 2022) verified a similar behavior after 10 reprocessing cycles, showing the high recycling potential of this thermoplastic. Therefore, it can be concluded that the operating conditions selected for this study are suitable for the

PEEK processing and reprocessing without any signal of degradation or loss of properties.

### 3.3 Compounds' reprocessing influence on the material stability

The thermo-mechanical stability of PEEK compounds containing 5 wt% of rCFRT, with two different sizes, was also evaluated. The fiber length and fiber length distribution after 1 and 15 extrusion cycles were investigated, since it is well established in the literature that both extrusion and injection molding processes can induce fiber shortening, and consequently, a deterioration of the final mechanical properties of the compound (von Turkovich and Erwin, 2023), (Fu et al., 2002). There are three main causes related to this behavior: i) fiber/fiber interaction—abrasion between fiber surfaces induces stress concentrations, decreasing strength and leading to fiber fracture or bending stresses by fiber overlap, ii) fiber interaction with the polymeric matrix—viscous forces imparted by the polymer may originate fiber fracture, and iii) fiber contact with equipment surfaces occurs due to wear of the processing machine (von Turkovich and Erwin, 2023), (Fu et al., 2002).

The processing effect on fiber length was carried out for the first ( $n = 1$ ) and the last ( $n = 15$ ) extrusion cycle, allowing to compare the average values obtained from composite fiber length distribution among its recyclability. Figure 10 shows the fiber length distribution histograms for each compound, at  $n = 1$  and  $n = 15$ .

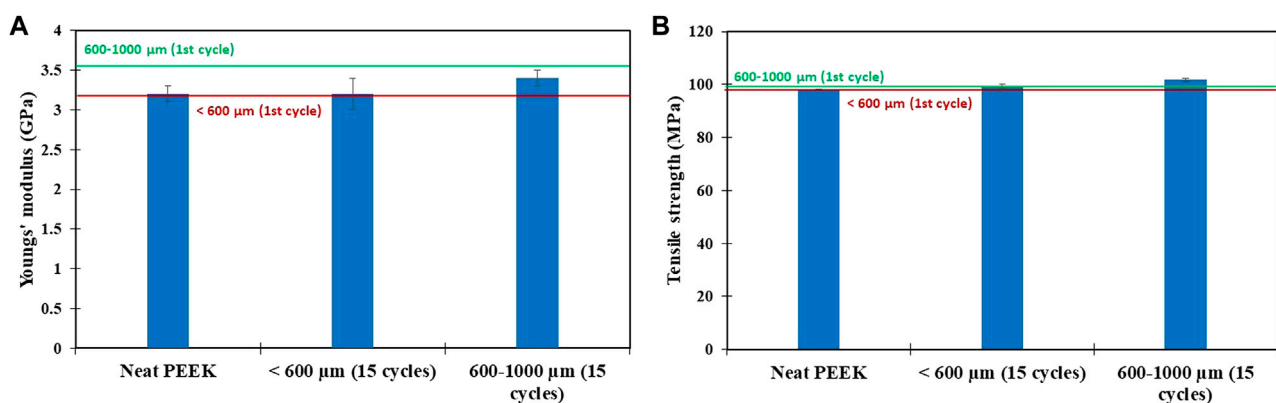


FIGURE 11  
(A) Young's modulus, and (B) tensile strength of neat PEEK and reprocessed compounds.

The results of the analysis of the obtained fiber length distribution of the compounds are represented in Table 4.

For both formulations, a significant decrease in fiber length was observed right after the first reprocessing cycle, although sCFs shortening is more pronounced for larger particle sizes. In addition, promoted by fiber breakage, the number of smaller fibers increased. After 15 extrusion cycles, this trend is maintained although the average fiber length decreases by being much lower.

Since the reinforcement of PEEK is related to the fiber length of rCFRT, the mechanical characterization of reprocessed compounds for 15 cycles was also assessed by uniaxial tensile tests, and the results are depicted in Figure 11.

It can be observed that reprocessed PEEK compounds containing 5 wt% of rCFRT, with different particle sizes, exhibited similar tensile strength behavior when compared to the PEEK compounds submitted to a single extrusion cycle. However, the formulation containing larger sCF particles demonstrated a slight decrease on the Young's modulus, in comparison to the same formulation submitted to a single extrusion cycle. Previous findings attained by optical microscopy support this behavior, once the pronounced reduction of fiber length occurred right after the first extrusion cycle, being more significant for larger sCF.

## 4 Conclusion

In this work, “waste” scraps from CFRP were incorporated into a thermoplastic matrix (PEEK), for a second-life in the aeronautic industry. The effect of two different fiber particle sizes (<600  $\mu\text{m}$  and 600–1,000  $\mu\text{m}$  rCFRT) on the mechanical, thermal and rheological properties of produced PEEK compounds, was assessed. The mechanical properties of the compounds did not increase significantly, which could be a result not only from the fiber breakage during material processing or the low content of rCFRT incorporation, but also from the lower degree of crystallization obtained. Nevertheless, the sCF were well distributed into the polymeric matrix and presented good fiber/matrix interface. In terms of the rheological characterization, it is concluded that the highest values of the storage modulus in the low angular frequency region are due to the presence of the solid phase, the viscous component of the material dominates the elastic counterpart across all frequencies, and the material viscosity slight increases in the presence of rCFRT.

Empowering an eco-friendly strategy, reprocessing studies were performed to evaluate the thermoplastic matrix and compounds' recyclability. For this purpose, the material was submitted to 15 consecutive extrusion cycles, for further characterization. Results obtained by ATR-FTIR showed that similar absorption bands with comparable intensities were obtained for both neat and reprocessed PEEK, proving that no degradation occurred nor loss of properties. These findings were

supported by viscoelastic and mechanical data. Therefore, it can be concluded that the selected processing and reprocessing conditions for the developing materials were appropriate. The fiber length and fiber length distribution upon 15 extrusion cycles were assessed and the mechanical behavior was also evaluated. It can be concluded that both formulations with different particle sizes exhibited similar tensile strength behavior, while the compound containing larger sCF showed a decrease of the Young's Modulus when compared to the same formulations submitted to a single extruder cycle. The results on the fiber length support this behavior once the pronounced reduction of fiber length occurred right after the first extrusion cycle, being more significant for larger sCF.

## Data availability statement

The raw data supporting the conclusion of this article will be made available by the authors, without undue reservation.

## Author contributions

Contributions on experimental work developed, including compounding and characterization: CB and AA; original draft: CB and AC; acquisition of the financial support for the project leading to this publication: RS and JS; conceptualization, formal analysis, and supervision: RS; review and editing: All. All authors contributed to the article and approved the submitted version.

## Funding

This work was supported by the Portuguese PT2020 program N°17/SI/2019, under the ReCAP: Recycled Composites for High-Performance Applications—aircraft components and support structures (46066) project.

## Conflict of interest

The authors declare that the research was conducted in the absence of any commercial or financial relationships that could be construed as a potential conflict of interest.

## Publisher's note

All claims expressed in this article are solely those of the authors and do not necessarily represent those of their affiliated organizations, or those of the publisher, the editors and the reviewers. Any product that may be evaluated in this article, or claim that may be made by its manufacturer, is not guaranteed or endorsed by the publisher.



## References

- Al-Lami, A., Hilmer, P., and Sinapius, M. (2018). Eco-efficiency assessment of manufacturing carbon fiber reinforced polymers (CFRP) in aerospace industry. *Aerosp. Sci. Technol.* 79, 669–678. doi:10.1016/j.ast.2018.06.020
- Alshammari, B. A., Alsuhybani, M. S., Almushaikeh, A. M., Alotaibi, B. M., Alenad, A. M., Alqahtani, N. B., et al. (2021). Comprehensive review of the properties and modifications of carbon fiber-reinforced thermoplastic composites. *Polymers* 13 (15), 2474. doi:10.3390/polym13152474
- Alves, S. M. C., da Silva, F. S., Donadon, M. V., Garcia, R. R., and Corat, E. J. (2018). Process and characterization of reclaimed carbon fiber composites by pyrolysis and oxidation, assisted by thermal plasma to avoid pollutants emissions. *J. Compos. Mater.* 52 (10), 1379–1398. doi:10.1177/0021998317724214
- Butenegro, J. A., Bahrami, M., Abenojar, J., and Martínez, M. Á. (2021). Recent progress in carbon fiber reinforced polymers recycling: A review of recycling methods and reuse of carbon fibers. *Materials* 14, 6401–6421. doi:10.3390/ma14216401
- Carberry, W. *Airplane recycling efforts benefit boeing operators*. Seattle, Washington D.C, United States:2006 Boeing AERO Magazine.
- Chen, C., Zhang, C., Liu, C., Miao, Y., Wong, S. C., and Li, Y. (2018). Rate-dependent tensile failure behavior of short fiber reinforced PEEK. *Compos B Eng.* 136, 187–196. doi:10.1016/j.compositesb.2017.10.031
- Colin, X., and Tcharkhtchi, A. (2013). Thermal degradation of polymers during their mechanical recycling. Recycling: Technological systems, management practices and environmental impact. *Nova Sci.*, 57–95.
- Cox, W. P., and Merz, E. H. (1958). Correlation of dynamic and steady flow viscosities. *J. Polym. Sci.* 28, 619–622. doi:10.1002/pol.1958.1202811812
- Elsayed, A., and Roetger, T. (2022). *Best practices and standards in aircraft end-of-life and recycling*. Montreal, Canada: ICAO.
- Erbetta, C. D. C., Manoel, G. F., Oliveira, A. P. L. R., e Silva, M. E. S. R., Freitas, R. F. S., and Sousa, R. G. (2014). Rheological and thermal behavior of high-density polyethylene (HDPE) at different temperatures. *Mater. Sci. Appl.* 5 (13), 923–931. doi:10.4236/msa.2014.513094
- Fortune Business Insights (2023). *Carbon Fiber Market Size, Share & COVID-19 Impact Analysis, By Precursor (PAN and Pitch), By Tow (Large Tow and Small Tow), By Application (Aviation, Aerospace & Defense, Automotive, Wind Turbines, Sports & Leisure, Construction, and Others), and Regional Forecast, 2023–2030*.
- Fu, S.-Y., Mai, Y.-W., Chui, E., Ching, Y., and Li, R. K. Y. (2002). Correction of the measurement of fiber length of short fiber reinforced thermoplastics. *Compos. Part A Appl. Sci. Manuf.* 33, 1549–1555. doi:10.1016/S1359-835X(02)00114-8
- Fu, S.-Y., Mai, Y.-W., Chui, E., Ching, Y., and Li, R. K. Y. Correction of the measurement of fiber length of short fiber reinforced thermoplastics.2023 Available: [www.elsevier.com/locate/compositesa](https://www.elsevier.com/locate/compositesa).
- Gaitanellis, D., Worrall, C., and Kazilas, M. (2022). Detecting, characterising and assessing PEEK's and CF-PEEK's thermal degradation in rapid high-temperature processing. *Polym. Degrad. Stab.* 204, 110096. doi:10.1016/j.polymdegradstab.2022.110096
- Gao, S., Qu, J., Li, H., and Kang, R. (2022). Effect of fiber type and content on mechanical property and lapping machinability of fiber-reinforced polyetheretherketone. *Polym. (Basel)* 14 (6), 1079. doi:10.3390/polym14061079
- Giorgini, L., Benelli, T., Brancolini, G., and Mazzocchi, L. (2020). Recycling of carbon fiber reinforced composite waste to close their life cycle in a cradle-to-cradle approach. *Curr. Opin. Green Sustain. Chem.* 26, 100368. doi:10.1016/j.cogsc.2020.100368
- Hirayama, D., Saron, C., Botelho, E. C., Costa, M. L., and Junior, A. C. A. (2017). "Polypropylene composites manufactured from recycled carbon fibers from aeronautic materials waste," in *Materials research* (São Carlos, Brazil: Universidade Federal de Sao Carlos), 526–531. doi:10.1590/1980-5373-MR-2016-1022
- IATA (2022). *Helping aircraft decommissioning*. Montreal, Canada: IATA.
- Kumar, K. S. S., Nair, C. P. R., and Ninan, K. N. (2008). Effect of fiber length and composition on mechanical properties of carbon fiber-reinforced polybenzoxazine. *Polym. Adv. Technol.* 19 (7), 895–904. doi:10.1002/pat.1056
- Li, F., Hu, Y., Hou, X., Hu, X., and Jiang, D. (2018). Thermal, mechanical, and tribological properties of short carbon fibers/PEEK composites. *High. Perform. Polym.* 30 (6), 657–666. doi:10.1177/0954008317715313
- Li, H., and Englund, K. (2017). Recycling of carbon fiber-reinforced thermoplastic composite wastes from the aerospace industry. *J. Compos Mater* 51 (9), 1265–1273. doi:10.1177/0021998316671796
- Liu, T., Shao, L., Zhao, B., Chang, Y. C., and Zhang, J. (2022). Progress in chemical recycling of carbon fiber reinforced epoxy composites. *Macromol. Rapid Commun.* 43 (23), 2200538. doi:10.1002/marc.202200538
- Lu, C., Ma, W., Ba, S., and Zhang, D. (2023). Resin content calculation of carbon fiber/poly (ether ether ketone) by thermogravimetric analysis. *Polym. Test.* 117, 107861. doi:10.1016/j.polymertesting.2022.107861
- Lu, C., Xu, N., Zheng, T., Zhang, X., Lv, H., Lu, X., et al. (2019a). The optimization of process parameters and characterization of high-performance CF/PEEK composites prepared by flexible CF/PEEK plain weave fabrics. *Polym. (Basel)* 11 (1), 53. doi:10.3390/polym11010053
- Lu, C., Xu, N., Zheng, T., Zhang, X., Lv, H., Lu, X., et al. (2019b). The optimization of process parameters and characterization of high-performance CF/PEEK composites prepared by flexible CF/PEEK plain weave fabrics. *Polym. (Basel)* 11 (1), 53. doi:10.3390/polym11010053
- Lu, C., Xu, N., Zheng, T., Zhang, X., Lv, H., Lu, X., et al. (2019c). The optimization of process parameters and characterization of high-performance CF/PEEK composites prepared by flexible CF/PEEK plain weave fabrics. *Polym. (Basel)* 11 (1), 53. doi:10.3390/polym11010053
- McLauchlin, A. R., Ghita, O. R., and Savage, L. (2014). Studies on the reprocessability of poly(ether ether ketone) (PEEK). *J. Mater Process Technol.* 214 (1), 75–80. doi:10.1016/j.jmatprotec.2013.07.010
- Meng, F., Cui, Y., Pickering, S., and McKechnie, J. (2020). From aviation to aviation: Environmental and financial viability of closed-loop recycling of carbon fibre composite. *Compos B Eng.* 200, 108362. doi:10.1016/j.compositesb.2020.108362
- Murata, Y., and Kanno, R. (2021). Effects of heating and cooling of injection mold cavity surface and melt flow control on properties of carbon fiber reinforced semi-aromatic polyamide molded products. *Polymers* 13, 587. doi:10.3390/polym13040587
- Nakashima, Y., Suganuma, H., Yamashita, S., and Takahashi, J. "Influence of strand dispersion method on mechanical properties of randomly oriented carbon fiber strand thermoplastic composites," in *Proceedings of the 21st International Conference on Composite Materials*, Xi'an, China, August 2017.
- Nikhil, M., Bilagi, C., and Eswara, P. (2022). Carbon fiber reinforced plastic (CFRP) market by raw material (polyacrylonitrile (PAN), petroleum pitch, and others), resin type (thermosetting and thermoplastic), and application (aerospace & defense, wind turbine, automotive, sports equipment, building & construction, and others). *Glob. Oppor. Analysis Industry Forecast*.
- Oliveux, G., Dandy, L. O., and Leeke, G. A. (2015). Current status of recycling of fibre reinforced polymers: Review of technologies, reuse and resulting properties. *Prog. Mater. Sci.* 72, 61–99. doi:10.1016/j.pmatsci.2015.01.004
- Pan, L., and Yapiçi, U. (2016). A comparative study on mechanical properties of carbon fiber/PEEK composites. *Adv. Compos. Mater.* 25 (4), 359–374. doi:10.1080/09243046.2014.996961
- Pedoto, G., Grandidier, J. C., Gigliotti, M., and Vinet, A. (2022). Characterization and modelling of the PEKK thermomechanical and creep behavior above the glass transition temperature. *Mech. Mater.* 166, 104189. doi:10.1016/j.mechmat.2021.104189
- Pérez-Martín, H., Mackenzie, P., Baidak, A., Ó Brádaigh, C. M., and Ray, D. (2021). Crystallinity studies of pekk and carbon fibre/PEKK composites: A review. *Compos. Part B Eng.* 223, 109127. doi:10.1016/j.compositesb.2021.109127
- Pérez-Martín, H., Mackenzie, P., Baidak, A., Ó Brádaigh, C. M., and Ray, D. (2022). Crystallisation behaviour and morphological studies of PEKK and carbon fibre/PEKK composites. *Compos Part A Appl. Sci. Manuf.* 159, 1–18. doi:10.1016/j.compositesa.2022.106992
- Petruskaite, G. (2022). The afterlife of retired aircraft: What are old planes turned into? *Aerotime Hub*.
- Pimenta, S., and Pinho, S. T. (2011). Recycling carbon fibre reinforced polymers for structural applications: Technology review and market outlook. *Waste Manag.* 31 (2), 378–392. doi:10.1016/j.wasman.2010.09.019
- Pulkkinen, A. (2022). The global composites market is driven by Carbon Fiber Reinforced Plastics. <https://nordicgrowth.com/en/the-global-composites-market-is-driven-by-carbon-fiber-reinforced-plastics/>.
- Rieger, D., Pola, M., Franče, P., Kadlec, J., Kovářík, T., and Kopačka, P. (2019). The effect of short carbon fibers on rheological behaviour and mechanical properties of metakaolin-slag geopolymer binder. *IOP Conf. Ser. Mater. Sci. Eng.* 613, 012050. doi:10.1088/1757-899X/613/1/012050
- Sarasua, J. R., Remiro, P. M., and Pouyet, J. (1996). Effects of thermal history on mechanical behavior of PEEK and its short-fiber composites. *Polym. Compos* 17 (3), 468–477. doi:10.1002/pc.10635
- Selvanarayanan, H. (2017). *Effects of thermal degradation on carbon reinforced PEEK composites*. Delft, Netherlands: TU Delft.
- Subhedar, K., (2020). Effect of fibre orientation on mechanical properties of carbon fibre composites SEE PROFILE Effect of fibre orientation on mechanical properties of carbon fibre composites. Available: <https://www.researchgate.net/publication/350809879>.
- Sudhin, S. A., Remanan, M., and Jayanarayanan, K. (2020). Comparison of properties of carbon fiber reinforced thermoplastic and thermosetting composites for aerospace applications. Available: [www.sciencedirect.com](https://www.sciencedirect.com).

- Unterweger, C., Mayrhofer, T., Piana, F., Duchoslav, J., Stifter, D., Poitzsch, C., et al. (2020). Impact of fiber length and fiber content on the mechanical properties and electrical conductivity of short carbon fiber reinforced polypropylene composites. *Compos. Sci. Technol.* 188, 107998. doi:10.1016/j.compscitech.2020.107998
- Victrex (2022). The use of regrind with VICTREX® PEEK. <https://www.victrex.com/>.
- Vincent, G. A., de Bruijn, T. A., Wijskamp, S., Abdul Rasheed, M. I., van Drongelen, M., and Akkerman, R. (2019). Shredding and sieving thermoplastic composite scrap: Method development and analyses of the fibre length distributions. *Compos. B Eng.* 176, 107197. doi:10.1016/j.compositesb.2019.107197
- Vo Dong, P. A., Azzaro-Pantel, C., and Cadene, A. L. (2018). Economic and environmental assessment of recovery and disposal pathways for CFRP waste management. *Resour. Conserv. Recycl.* 133, 63–75. doi:10.1016/j.resconrec.2018.01.024
- von Turkovich, R., and Erwin, L. (2023). Fiber fracture in reinforced thermoplastic processing. *Polym. Eng. Sci.* 63.
- Xiaochun, Y., Youhua, Y., Yanhong, F., Guizhen, Z., and Jinsong, W. (2018). Preparation and characterization of carbon fiber/polypropylene composites via a tri-screw in-line compounding and injection molding. *Adv. Polym. Technol.* 37 (8), 3861–3872. doi:10.1002/adv.22169
- Yao, S. S., Jin, F. L., Rhee, K. Y., Hui, D., and Park, S. J. (2018). Recent advances in carbon-fiber-reinforced thermoplastic composites: A review. *Compos. Part B Eng.* 142, 241–250. doi:10.1016/j.compositesb.2017.12.007
- Yaragalla, S., Zahid, M., Panda, J. K., Tsagarakis, N., Cingolani, R., and Athanassiou, A. (2021). Comprehensive enhancement in thermomechanical performance of melt-extruded peek filaments by graphene incorporation. *Polym. (Basel)* 13 (9), 1425. doi:10.3390/polym13091425
- Zhang, J., Chevali, V. S., Wang, H., and Wang, C. H. (2020a). Current status of carbon fibre and carbon fibre composites recycling. *Compos. Part B Eng.* 193, 108053. doi:10.1016/j.compositesb.2020.108053
- Zhang, J., Chevali, V. S., Wang, H., and Wang, C. H. (2020b). Current status of carbon fibre and carbon fibre composites recycling. *Compos. Part B Eng.* 193, 108053. doi:10.1016/j.compositesb.2020.108053
- Zhang, L., Li, M., and Hu, H. (2012). "Study on mechanical properties of PEEK composites," in *Advanced materials research* (Wollerau, Switzerland: Trans Tech Publications Ltd), 519–525. doi:10.4028/www.scientific.net/AMR.476-478.519



## OPEN ACCESS

## EDITED BY

Clemens Dransfeld,  
Delft University of Technology,  
Netherlands

## REVIEWED BY

Ewald Fauster,  
University of Leoben, Austria  
Miro Duhovic,  
Leibniz-Institut für Verbundwerkstoffe,  
Germany

## \*CORRESPONDENCE

Franz Maier,  
✉ franz.maier@afh-wels.at

RECEIVED 29 December 2022

ACCEPTED 26 June 2023

PUBLISHED 12 July 2023

## CITATION

Osterberger J, Maier F, Keller S and  
Hinterhölzl RM (2023), Evaluation of  
draping simulations by means of 3D laser  
scans and robot supported fiber angle  
scans.

*Front. Mater.* 10:1133788.

doi: 10.3389/fmats.2023.1133788

## COPYRIGHT

© 2023 Osterberger, Maier, Keller and  
Hinterhölzl. This is an open-access  
article distributed under the terms of the  
[Creative Commons Attribution License  
\(CC BY\)](https://creativecommons.org/licenses/by/4.0/). The use, distribution or  
reproduction in other forums is  
permitted, provided the original author(s)  
and the copyright owner(s) are credited  
and that the original publication in this  
journal is cited, in accordance with  
accepted academic practice. No use,  
distribution or reproduction is permitted  
which does not comply with these terms.

# Evaluation of draping simulations by means of 3D laser scans and robot supported fiber angle scans

Joachim Osterberger, Franz Maier\*, Sophia Keller and  
Roland Markus Hinterhölzl

Research Group for Lightweight Design and Composite Materials, University of Applied Sciences  
Upper Austria, Wels, AUT, Austria

In order to demonstrate the accuracy of macroscopic finite element draping simulations it is necessary to compare the results with experiments. In this work, a compact overview of evaluation methods for draping simulations based on experiments, in the recent literature, is provided. Then, a method using state of the art 3D laser scans (RS6, Hexagon) and robot supported fiber angle scans (FScan, Profactor) is described. The presented comparison of draping results with the tool geometry in 3D allows for an evaluation of wrinkles and bridging areas. For the evaluation of the edge contour, the commonly used method of projecting the edge contour on a 2D plane is extended to a comparison in 3D space. To determine fiber orientations and compare them with the predictions from simulations, a robot supported fiber angle sensor and a script-based mapping and comparison algorithm are used. The results are further analyzed statistically, to derive comparative figures to other results found in the literature. The location and dimensions of macroscopic manufacturing effects such as fiber bridging and wrinkles could be predicted accurately. The final component contour could be on average predicted within 5.2 mm. The fiber orientation could be predicted with a deviation of less than 2° for approx. 65% and within 6° for 95% of the part surface for UD laminas. Cross-ply laminas showed larger deviations, only 40% of the part surface was within 2° and 80% within 6°, compared to the experiment. Overall, the results for the presented methods show good agreement between multi-ply draping experiments and macroscopic simulations conducted with the Abaqus Fabric material model.

## KEYWORDS

draping, laser scan, fiber angle scan, simulation, draping simulation, simulation validation

## 1 Introduction

Macroscopic finite element (FE) forming simulations for manufacturing composite components have become increasingly important in the transportation industries over the last two decades. Demonstrating the accuracy builds the foundation for a reliable application and use of FE based draping simulations. Two main methods to validate draping simulations are commonly described in the literature. The first is to model mechanical testing procedures (i.e., virtual testing) and compare the simulation result with the measured response from experiments. This can also be used as an inverse approach to identify material parameters used in phenomenological material models. The second method is to perform draping

experiments on generic demonstrator geometries, typically with challenging features, such as curvatures, a double curvature, or tapered surfaces. Thus, the semifinished composites materials are exposed to complex deformation mechanisms. Depending on the used raw material, effects such as wrinkle formation can be easily triggered. This validation method provides details about the accuracy of the simulation results at quite extreme deformation conditions. Comparison methods typically focus on fiber orientations, wrinkle formation and position, and the edge contour in the deformed configuration. Various generic geometries are reported, whereby a complete hemisphere (Mohammed et al., 2000; Boisse et al., 2011; Peng and Ding, 2011; Bardl et al., 2016; Chen et al., 2016; Machado et al., 2016; Schirmaier et al., 2016; Han and Chang, 2018; Nasri et al., 2019; Mei et al., 2021) or hemispheric sections, combined with elongated sections (Willems, 2008; Vanclooster et al., 2009; Schug et al., 2018; Viisainen et al., 2021) are most common. Other methods include rectangular box shapes (Huang et al., 2021), potentially combined with a sinusoidal surface path (Leutz, 2016; Margossian, 2017; Osterberger et al., 2022) or tetrahedron geometries (Thompson et al., 2020; Chen et al., 2021; Viisainen et al., 2021). Geometries with sharp corner sections can potentially trigger large local deformations and wrinkle formation, depending on the raw material in use. Once the simulation has passed the validation on a generic demonstrator basis, the next step is to evaluate with increasingly complex application examples, e.g., egg box shape (Han and Chang, 2021a) or various complex preform geometries, as shown in (Alshahrani and Hojjati, 2017; Chen et al., 2017; Dörr et al., 2017; Mallach et al., 2017; Joppich, 2019). The different tooling geometries come with advantages and disadvantages depending on the material, for example, the hemisphere is very suitable for woven fabrics, while it damages UD-materials and leads to a large amount of wrinkles, due to large shear deformations (Leutz, 2016). Consequently, a wide range of geometries are proposed in the literature, making it challenging to generalize and compare results between studies.

Many different experimental methods to quantify the geometrical accuracy and manufacturing effects are proposed in the literature. For example, simple side-by-side comparison of simulation results with photographs (Margossian, 2017; Thompson et al., 2020; Huang et al., 2021), plotted stress- or strain results (Harrison et al., 2013; Chen et al., 2016; Alshahrani and Hojjati, 2017; Chen et al., 2017; Osterberger and Franz Maier, 2020; Han and Chang, 2021a), digital image correlation (DIC) measurements (Chen et al., 2021; Bai et al., 2022), and a 3D scan supported analysis (Dörr, 2019; Joppich, 2019; Osterberger et al., 2022) are used to evaluate wrinkling. Similarly, various methods are proposed to evaluate the edge contour, typically projected onto a plane. Common methods include a comparison with photographs (with or without grid points) and a simple ruler (with no specific standardized method or technique) (Mohammed et al., 2000; Leutz, 2016; Margossian, 2017; Nasri et al., 2019; Thompson et al., 2020; Han and Chang, 2021a; Mei et al., 2021; Rashidi et al., 2021), grid point analysis with a coordinate measurement machine (CMM) (Chen et al., 2016), analysis with DIC (Chen et al., 2021; Bai et al., 2022), up to 3D scan supported analysis (Dörr et al., 2017; Dörr, 2019; Joppich, 2019; Osterberger et al., 2022).

The simulated fiber angle distribution is typically validated by local comparison. Methods include a manual angle measurement

with a protractor (Mohammed et al., 2000), grid strain analysis with a CMM (Chen et al., 2016), orthogonal photographs for analysis at predefined points with ImageJ software (Harrison et al., 2013), the marker tracking method, or grid pattern tracking with DIC systems and suitable software (Vanclooster et al., 2009; Nasri et al., 2019; Rashidi et al., 2021; Bai et al., 2022), and fully robot supported fiber angle sensor scans, allowing precise tracking of fiber angles on complex geometries on the surface, as presented in (Leutz, 2016; Mallach et al., 2017; Margossian, 2017; Malhan et al., 2021), or by the use of the eddy current method (Bardl et al., 2016).

In this paper a set of methods to gauge the accuracy of the macroscopic FE simulation with Abaqus \*Fabric (Osterberger et al., 2022) is presented, on a single ply basis and with different thin layups. Single diaphragm forming is used as the automated draping process for our simulations and experiments. The method utilizes 3D laser scans (with a Hexagon RS6 laser scanner) for detailed evaluation of wrinkling and bridging from draping experiments, based on a comparison with the tooling geometry. A further investigation on the advantages of comparing the edge contour in 3D, rather than in 2D, as commonly found in recent literature, was conducted. Fiber angle orientations are measured with the robot supported FScan method, presented in (Leutz, 2016) and (Margossian, 2017), across the entire surface of the specimen.

## 2 Materials and methods

### 2.1 Material

For the experiments a carbon UD-prepreg (HexPly® M79/34%/UD300/CHS) with a low temperature curing epoxy system and an approximate ply thickness of 0.35 mm is used for the experiments.

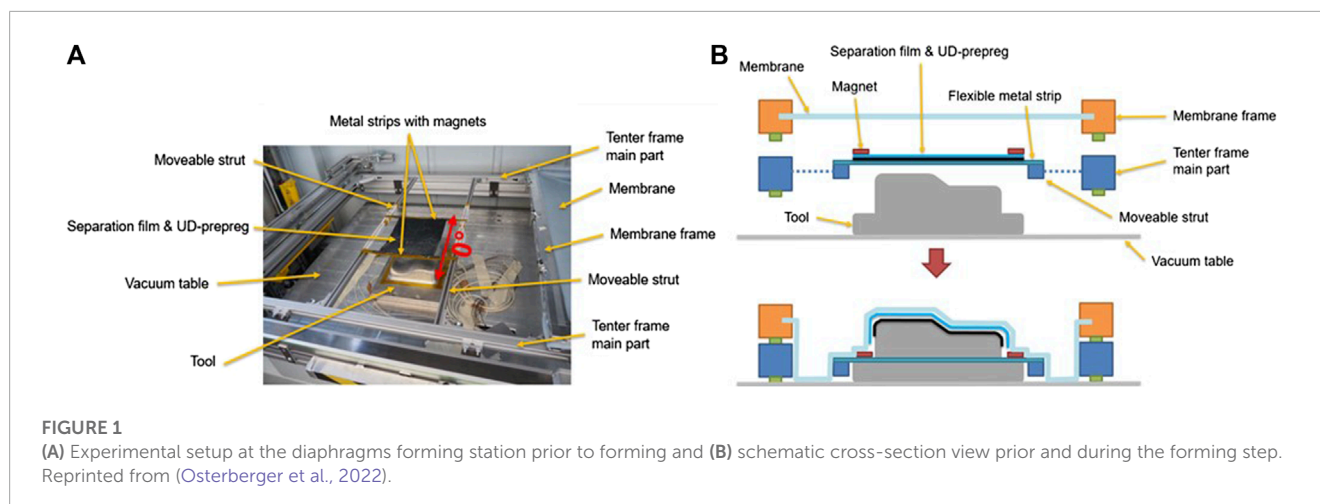
### 2.2 Experimental setup

All draping experiments are performed on a single diaphragm forming station with a generic double sine tool (~245 mm × 245 mm × 90 mm) according to the concept presented in (Osterberger et al., 2022). The blank laminate is fixed with a flexible magnetic clamping system and a PTFE separation film, used to prevent sticking to the membrane (c.f. Figure 1). The experiments are conducted with prepreg sheets of 260 × 220 mm in size. In addition to single ply experiments, the performance of four different layups was investigated: (0-0-0), (0-0-90), (0-90-0), (0-90), with three samples per layup. For more details on the experimental procedure the reader is referred to (Osterberger et al., 2022).

### 2.3 Simulation setup

The FE simulation uses the Abaqus \*Fabric material model and single ply modeling. Material characterization and modeling, as well as the FE model are shown in detail in (Osterberger et al., 2022). For the simulation of the four multi-layer laminates, the same basic setup was used, but modified in the following points: 1) Additional layers are modeled individually (as required for modeling the





approximated bending behavior) as independent parts in Abaqus, positioned exactly above each other. Thus, the plies are in initial contact with each other, with friction in between the layers and the tooling and separation film as defined in (Osterberger et al., 2022). 2) To ensure contact while maintaining a common edge contour, allowing for shear and friction movement between plies, a tie connection along the outer edge contour of the plies, maintaining the initial inter-ply distance, was assigned. Rotational degrees of freedom (DOF) for the affected nodes were set free. 3) Gravity is only applied for a short time at the beginning of the simulation to establish the initial sag of the laminate, allowing an accurate prediction of the location of first contact with the tool. This allows for higher mass-scaling, i.e., virtually increasing the material density to reduce the critical time increment and thus, reduce the computational time, than initially proposed. Increasing the density by a factor  $10^2$  reduces the simulation time to 6–8 h (8-times faster), with the same hardware as presented in (Osterberger et al., 2022).

## 2.4 3D scanning

A portable RS6 laser scanner system, mounted on a Romer Absolute-Arm 8,520 (Hexagon) with a reported accuracy of 0.026 mm ( $2\sigma$ ) was used for 3D scanning (Osterberger et al., 2022). Repeatability of the procedure was verified with a preliminary study. A slightly curved plate laminate (200 mm  $\times$  100 mm) made of PA6-UD tapes was scanned five times. Scans were then aligned and showed a maximum deviation of  $\pm 0.05$  mm for the surfaces at an edge length of 0.25 mm for the triangulated mesh.

The point cloud was obtained immediately after the forming step. The scanner allows for a scan rate of 300 Hz, however approximately 50% of measured points were filtered out to reduce calculation efforts, resulting in approximately 600,000 recorded points per second on a laser line with approximately 150 mm width. Scanning was completed within 1–2 min. After elimination of overlapping regions, about two million data points are used for comparison. The system enables 3D scans to be taken directly at the forming station without applying measurement markers or treatment with anti-reflexional coatings, which would compromise the surface for subsequent fiber angle scanning. The possible

occurrence of deformations due to relaxation or creep effects in the prepreg material was minimized by measuring directly after the forming step. To improve positional alignment some concise areas of the tooling are included in each 3D scan. The software Control X (V2022.1, Geomagic) is used for data analysis.

## 2.5 Comparison of deformed shape

To determine wrinkling and bridging in the draped laminate the generated point cloud is triangulated with 0.05 mm edge length. This is five times smaller than in the preliminary study and therefore reduces the potential discretization error. Alignment of the experiment and the simulation is performed using the tool. The procedure is summarized in Figure 2.

Initially, the coordinate system of a 3D scan of the blank tooling and the discretized tooling used for the draping simulation are aligned via best-fit. The aligned tooling geometry then serves as reference for the alignment process with the draping experiment. Segments of the tooling that are not covered by the laminate are used for a local best-fit alignment. These regions are marked green in the scan of the draping experiment in the top left corner of Figure 2. This ensures that the laminate in the simulation and the experiment is aligned correctly. In a subsequent step the scans of the draping experiments are modified and protruding parts of the tooling are removed. The extracted, draped laminate is then used for a comparison with the reference tool surface for a detailed evaluation of wrinkles (position and size) and bridging areas (height and size) with the so-called *3D Compare* tool in Control X. The deviations presented in this article are measured with the shortest distance method.

## 2.6 Comparison of edge contour

The correctly positioned scan of the draped geometry additionally serves as basis to extract the edge contour in 3D space. To compare it to the simulated edge contour, the draped geometry is exported from Abaqus (as triangulated mesh). Both geometries are already aligned via the tooling. The contour curves



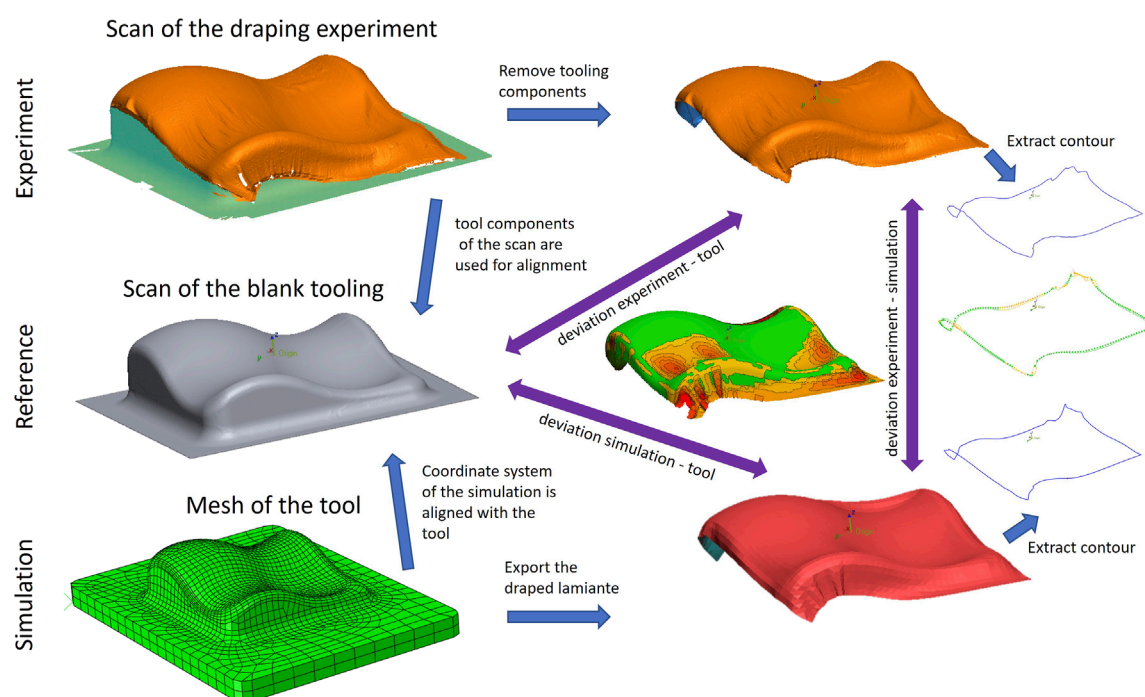


FIGURE 2

Summary of the alignment process and comparison methods used to evaluate the accuracy of the forming simulation.

for the simulation and the experiment are extracted and deviations are measured with the shortest distance method, with the *Curve Deviation* tool in Control X. A smooth contour curve is generated from the discrete scan and simulation data via spline-interpolation and thus, can introduce an error. This effect is increased near corners, folds, or incomplete sections of the scan and for coarse (triangulated) meshes. A mesh size of 0.05 mm for the experiments resulted in an observed local error of up to  $\pm 0.25$  mm. The mesh size of the geometry exported from the simulation depends on the element size and was 5 mm in our case. Unfortunately, it is not possible to define more interpolation points or refine the edge contour otherwise in an automated way. Thus, slight deviations from the original simulated contours were unavoidable. Observed deviations stay within approximately  $\pm 0.75$  mm in sharp corners and are negligible in rather straight sections. This sums up to  $\pm 1$  mm possible systematic deviation due to discretization and interpolation.

## 2.7 Statistical analysis

To sum up the deviation of the laminate to the tooling geometry over all experiments, histograms are generated. Manufacturing effects such as fiber bridging and wrinkles cause a deviation while areas that are in contact to the tooling result in a deviation close to zero. To ensure comparable results, the same mesh densities, i.e., the density of data points distributed across the surface for each experiment, are used. Thus, after visualizing the wrinkles and extracting the edge contour, the mesh density for all experiments was reduced to get approximately 30.000 elements, corresponding to an element edge length of approximately 1.4 mm for the triangulated

mesh. This is done for the geometry obtained from the experiment and the simulation. The deviation data is then exported to Matlab and histograms with an identical bin size are calculated, normalized, and averaged (in case of the experimental data).

## 2.8 Comparison of fiber angles

Fiber angles are measured using a photometric stereo sensor (FScan, Profactor), mounted on an industrial robot. The orientations are analyzed based on the directional dependency of the reflective properties of the material, with a reported root mean square error (RMSE) of up to  $1.5^\circ$  for prepreg materials (Zambal et al., 2015). For a detailed description of the comparison method, the reader is referred to (Keller et al., 2022). The procedure begins with placing the draped laminate, sitting on the tooling, on the measuring table and teaching the position of four reference points to the robot control system. This is done by moving a calibration tip to four dedicated locations on the tooling. These reference points allow for a coordinate transformation (via python script), where two reference points define the  $0^\circ$  or  $90^\circ$  direction. Subsequently, a robot path is planned with custom software from Profactor and the surface of the experiment is scanned automatically. The fiber angles across the surface are typically scanned in individual patches, that are stitched together and mapped onto the 3D geometry.

The orientation results, i.e., all measured points with their corresponding orientation vector, are exported (HDF5 file). A python script transforms the experimental data to the coordinate system of the simulation. A mapping algorithm (using a variation of the nearest neighbor method) is used to assign an average

orientation vector from the FScan data to the corresponding mesh element of the draping simulation. For each element, a virtual sphere with a radius of 3 mm, centered in the mesh element (5 mm mesh size), is used to search for all FScan data points within this volume. An average value is calculated and assigned as orientation vector for the respective mesh element. Hence, for each mesh element the measured and simulated (extracted from Abaqus results via python script) local fiber orientations are available as a 3D vector. However, a direct comparison of two vectors in a 3D space is typically not intuitive. To simplify the comparison and quantify the difference to a single number, the orientation vectors are projected on a reference plane, which is derived from three of the measured reference points. This allows to determine the element-wise difference between simulation and experiment. The resolution of this fiber orientation/deviation map depends on the element-size of the FEM mesh. The used comparison method implies some limitations and drawbacks which are examined in (Keller et al., 2022) and summed up in the discussion below. Results are visualized within Abaqus by coloring the elements depending on the deviation using a python macro.

### 3 Results

#### 3.1 Evaluation of deformed shape for single plies

For the evaluation on a single ply basis, a total of eight draping experiments were performed in the diaphragm station. Figure 3A illustrates deviations of the draping simulation and the tooling geometry, while Figures 3B–I shows deviations of the experiments to the tooling geometry. The 0° fiber direction is parallel to the global X-direction. A tolerance field of  $\pm 0.5$  mm is applied and set to a green color, indicating the material is in contact with the tool. The tolerance field is chosen slightly thicker than the ply thickness (0.35 mm), to compensate for systematic errors from FE meshing and alignment within the Control X software.

Aligning the meshed tool used for the FE analysis, with the 3D scan of the tooling, in order to align the coordinate systems of the simulation and the experiments, revealed a maximum local

deviation (discretization error) of 0.4 mm in the lower left corner. The average deviation across the entire surface was 0 mm, with standard deviation (STD) of 0.1 mm.

Bridging and wrinkling are clearly visible in the results of the ply-to-tool comparison in Figures 3B–I and even very fine wrinkles (width of 1–2 mm) within a bridging area can be visualized.

The region showing bridging in the upper left corners is reasonably similar for all experiments, though the maximum height differs between 5 mm in Figure 3B and a minimum of 3 mm in Figure 3G, where the large bridging area is split up into several smaller ones. The area spanned by the bridging laminate is slightly underestimated in the simulation. Fine local wrinkles within this bridging area tend to be in the upper half of this area and correspond to the wrinkle indicated in the simulation.

Some variations between experiments are present, despite the effort made for providing reproducible experiments. Figures 3C, D, F, H, show no (or hardly any) wrinkle, i.e., red/yellow region in the lower right corner, while Figures 3B, E, G, I clearly do. Thus, this fold in the lower right corner appears only in 50% of the experiments, while it was found in the simulation as shown in Figure 3A. This location is a local maximum of the double sine geometry, and the simulation revealed that the material is locally compressed in this area. Thus, small instabilities during forming, slight misalignments of tooling or laminate, or local inhomogeneities (asymmetries) in the material can cause this fold to be pushed sideways, where it can dissipate.

Other regions with fiber bridging, one on the tooling surface along the lower edge of the double sine and another at the lower left corner, appear in the simulation and are also present in all experiments, with similar dimensions and height.

The simulation cannot cover fine wrinkles due to the coarse mesh size (5 mm). The histograms of the averaged 3D deviations from all experiments and the simulation, are shown in Figure 4.

The histograms are well aligned, indicating that the simulation and experiments follow the same trends. Large deviations from the tooling geometry (above 1 mm) are slightly underestimated by the simulation. Slight differences in the range of 0–0.5 mm are expected as this area is affected by discretization errors, occurring at the rounded corner sections of the tooling.

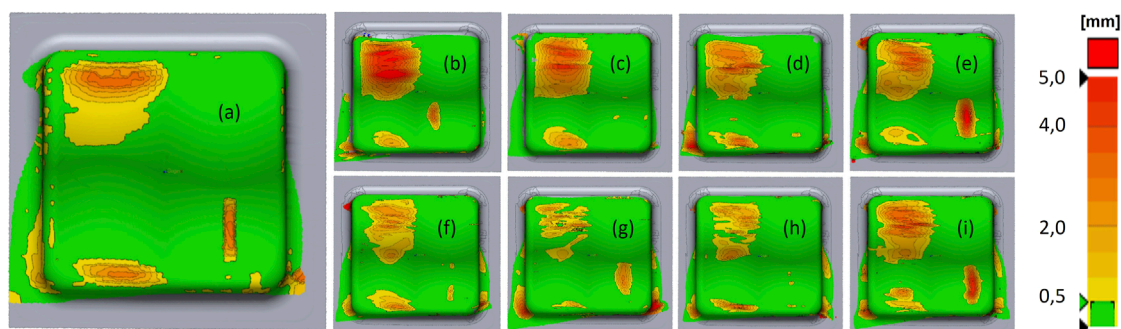


FIGURE 3

Comparison of the deformed shape from single ply (A) simulation and (B–I) experiments to the tool surface.

### 3.2 Evaluation of edge contour for single plies

For the analysis of the edge contour only five of the eight single ply experiments could be considered, due to an incomplete scan near the edge contour in the first three experiments (c.f. Figures 3B–D). Figure 5 shows a comparison of different views for the contour deviation of the part shown in Figure 3E. Figure 5A shows a projection onto a global X-Y plane, as it is commonly used in the literature. This method has some shortcomings when analysing complex 3D part geometries as out of plane deviation can visually disappear. This results in a discrepancy of arrow length and colour, where the latter is the reliable metric for the deviation. This becomes evident when comparing the regions 1 and 2 between views, as shown in Figures 5A–C. Thus, the contour deviation is presented in an isometric view. A tolerance field of  $\pm 3$  mm is chosen to consider for possible slight misalignment of the experiments and to consider systematic deviations coming from the chosen FE mesh discretization.

The largest local deviations of up to 20 mm are present in Figure 6C. For the experiments in Figures 6A, B the edge contour matches the simulated contour very well, with maximum deviations of less than 8 mm. Larger deviations occurring on opposite sides, as visible in Figures 6C–E indicate a misalignment of the laminate for the experiments. The experimental procedure must be further improved to prevent this in future experiments. The contour deviations across all experiments are summarized in a histogram (Figure 7). An average deviation of 5.2 mm, a median of 4.5 mm, 25% quartile of 2.3 mm and 75% quartile of 7.2 mm are measured. Only occasional outliers above 14 mm are found.

### 3.3 Evaluation of deformed shape for multi-ply laminates

To evaluate the accuracy of the simulation for multi-ply laminas, three experiments are performed per layup. The results are presented

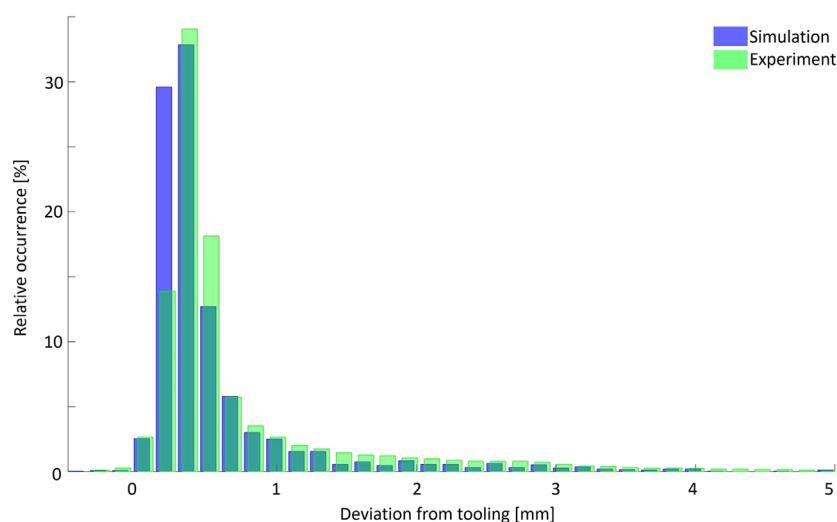


FIGURE 4

Summary of the 3D deviation distributions compared with the tool surface, on basis of eight single ply experiments vs. simulation in relative values.

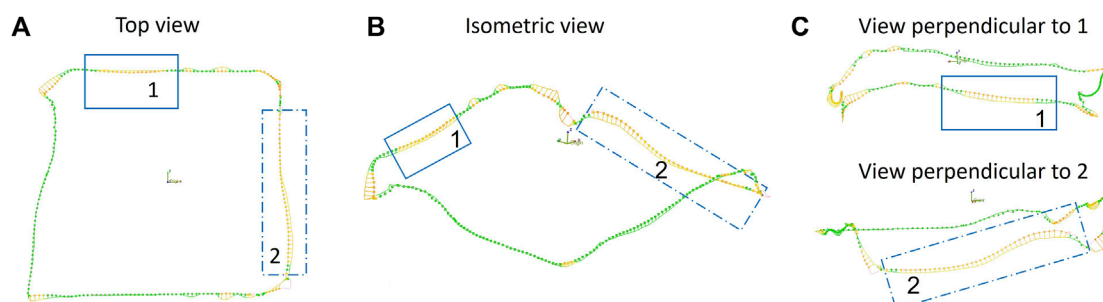
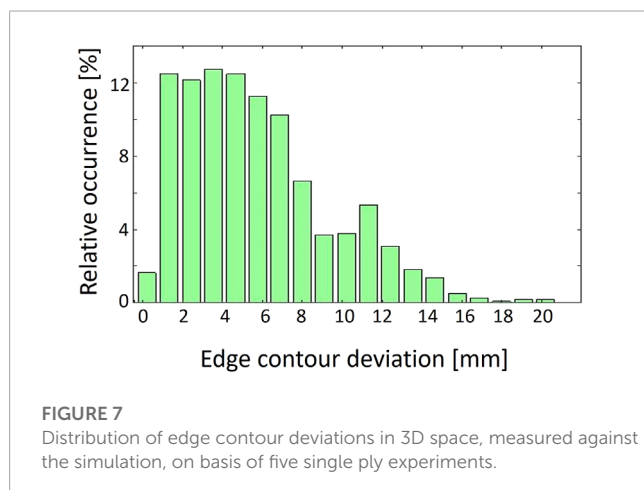
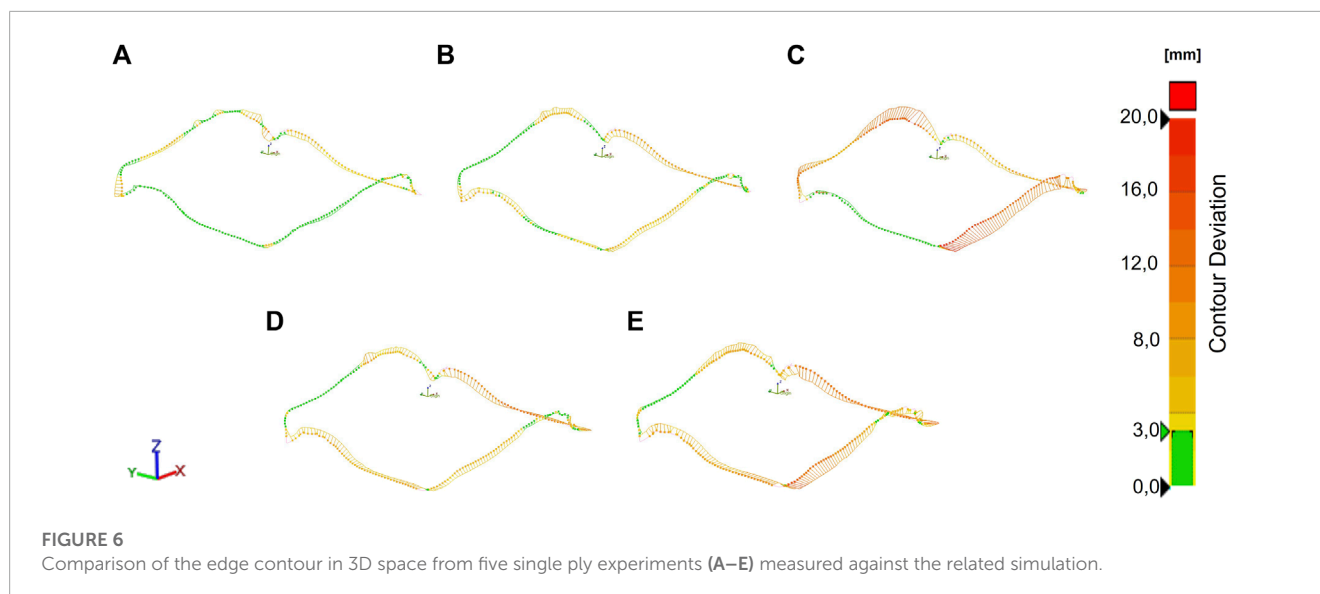


FIGURE 5

Comparison of the edge contour in (A) top (projected) view with (B) an isometric view; (C) Specific section could be further highlighted by adjusting the view, compromising the overall visibility.



in Figure 8. The  $0^\circ$  direction is aligned with the global X axis. The tolerance field for the green marked area varies between three-ply and two-ply layups due to the difference of lamina thickness. The range of the legend is kept at 5 mm, equivalent to the single ply experiments, while the tolerance field for three plies is defined with  $\pm 1.2$  mm and for two plies with  $\pm 0.85$  mm. Thus, a reasonably good comparability of 3D deviations at different laminate thicknesses is given.

In general, the simulations are capable of reproducing wrinkles and bridging areas on the top surface of the double sine tool geometry. Height and dimensions of wrinkles and bridging are captured with good accuracy for (0-0-0), (0-0-90) and (0-90) variants, however, in the (0-90-0) variant the bridging area in the upper left corner is overestimated. Deviations right at the laminate edges are generally overestimated and visible at the lower left corner of all simulations. This is caused by the tie connection enforced along the ply edges, preventing compression of the laminates in this area. However, this is a compromise allowing inter-ply movements, greatly improving the accuracy of the predicted contour.

A summary of the results shows that the FE simulation with Abaqus \*Fabric presented in (Osterberger et al., 2022) is able to predict the position, size and shape of macro wrinkles and bridging areas of laminates quite well. The apparent differences between the experiments are likely caused by slight inhomogeneities in the raw material and differences in the material placements. The resolution of fine wrinkles is limited by the coarse mesh size (5 mm) but is considered sufficient for the presented case.

### 3.4 Evaluation of edge contour for multi-ply laminates

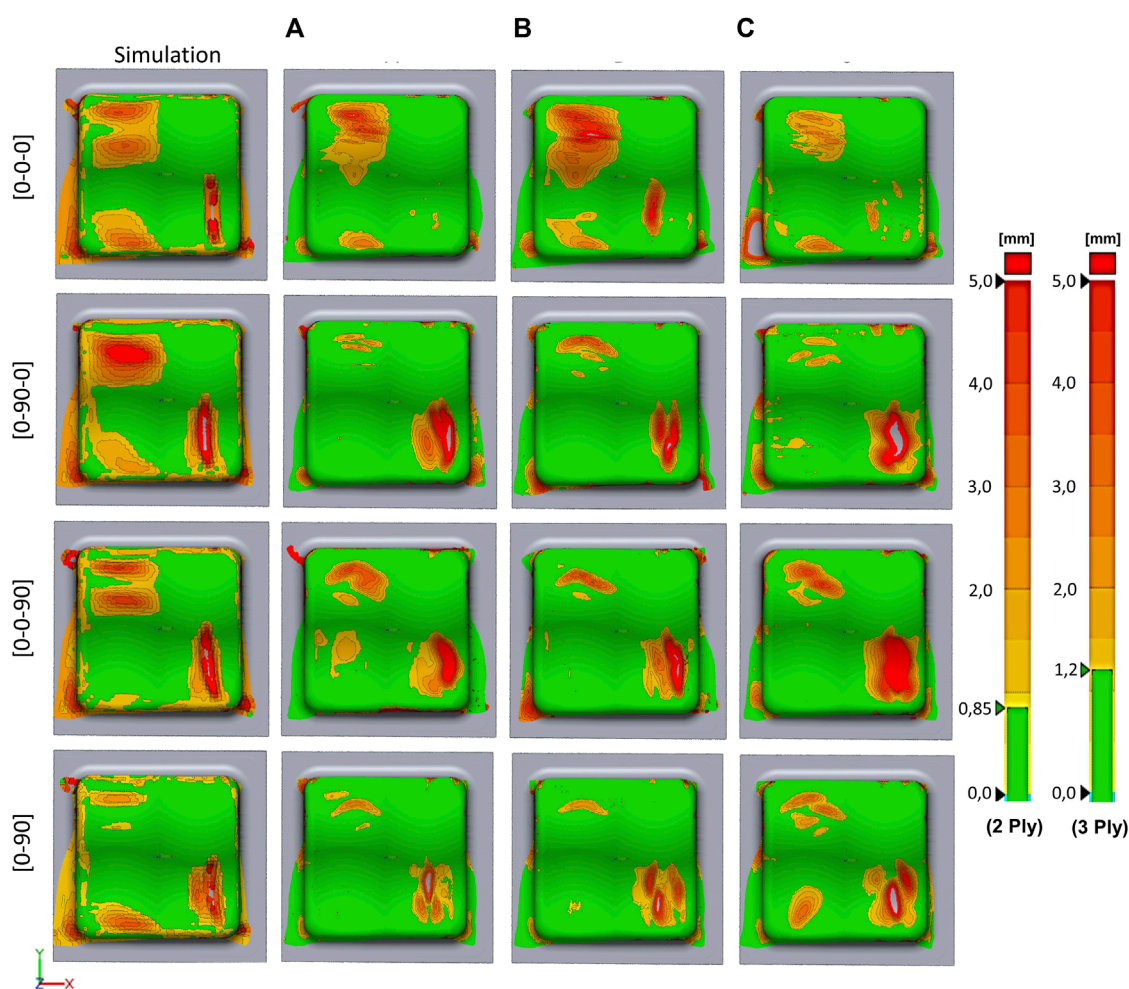
The results for the edge deviations, shown in Figure 9, correspond to the deformed shapes presented in Figure 8. The legend and the tolerance field are identical to the single ply experiments in Figure 6.

In general, very good agreement of the edge contour was observed. Only for the (0-0-90) lamina larger deviations, especially in Z direction are visible in the lower left corner in column A and C. It appears that the specimen was detached from tooling after the draping process. It is unclear if this was due to some imperfections in the material that reduced tack, or if it was caused by residual stresses, surpassing the tack locally. This highlights the importance of scanning parts with a viscoelastic prepreg material type immediately after forming. The data from Figure 9 is summarized using boxplots in Figure 10. The median deviation depended on the lay-up and was smallest for the (0-0-0) and (0-90) laminates with 2.3 mm, followed by the (0-90-0) laminate, and largest for the (0-0-90) laminates with up to 6.2 mm. Local outliers, probably caused by detaching errors of specimens in corners are included in these reported values.

### 3.5 Evaluation of fiber orientations for multi-ply laminates

In Figure 11 the comparison method for the fiber angle measurement is shown exemplarily. The local fiber angle alignment





**FIGURE 8**

Comparison of the deformed shape from simulations (left gap) with four different layups (0-0-0), (0-0-90), (0-90-0), (0-90), three experiments per layup [gaps (A, B, C)], measured against the tool surface. The left legend applies to 3 ply laminas and the right one to 2 ply laminas.

predicted by the simulation, is shown in Figure 11A, the results from the scanning experiments are provided in Figure 11C, both are relative to the global X direction. A comparison of these two results is given in Figure 11B, where good agreement between the two data sets is shown and large deviations only occur near the edges and folds. Sections including large folds could not be scanned and are therefore grayed out. Preliminary tests of the undeformed raw prepreg material have been conducted to determine the material quality and results for the fiber angle deviation are presented in Table 1. While in 92% of the area of the UD prepreg sheet local misalignments were within  $1.5^\circ$ , localized deviations up to  $3^\circ$  must still be expected.

The comparisons of fiber angle orientations from the FE simulations with the individual corresponding experiments are shown in Figure 12. The shares per interval, visualized in Figure 12, are summarized in Figure 13.

Best accuracy of fiber angles is reached for the (0-0-0) laminates, which is the only configuration where more than 80% of the surface was predicted within  $0^\circ$ – $4^\circ$ . For the other lay-ups only 60%–70% of the surface could be predicted within this range. This reduced

accuracy could either originate from the fabric material or the contact definition and is subject of further investigations. Deviations between simulation and experiments above  $12^\circ$  are rare with a share of less than 2% across all experiments.

A systematic error when projecting the direction vector onto a plane, that depends on the angle of inclination of the corresponding element, was observed. However, both experiment and simulation are affected in a similar manner by this projection distortion, canceling out the systematic error. However, in strongly inclined regions ( $>30^\circ$ ) with large differences in simulated and measured fiber angles, the observed difference might be amplified.

## 4 Discussion

The evaluation of wrinkles and folds based on the 3D deviation from the tooling, as shown in Figures 3, 8, comes with the advantage, that the position and height of even fine wrinkles can be identified and visualized accurately. This is a clear advantage over comparison methods based on photographs or strain representations, e.g.,



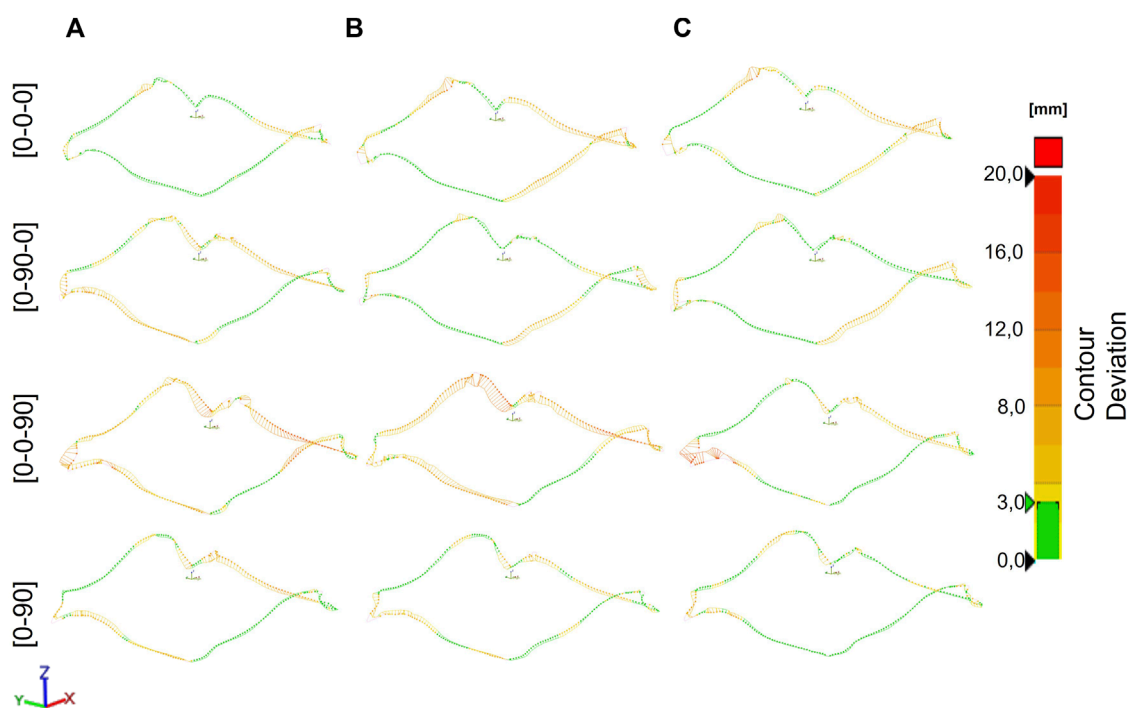


FIGURE 9

Comparison of the edge contour in 3D space from multi-ply experiments. Measured against the corresponding simulations. Four different layups (0-0-0), (0-0-90), (0-90-0), (0-90), three experiments per layup [gaps (A–C)], were realized.

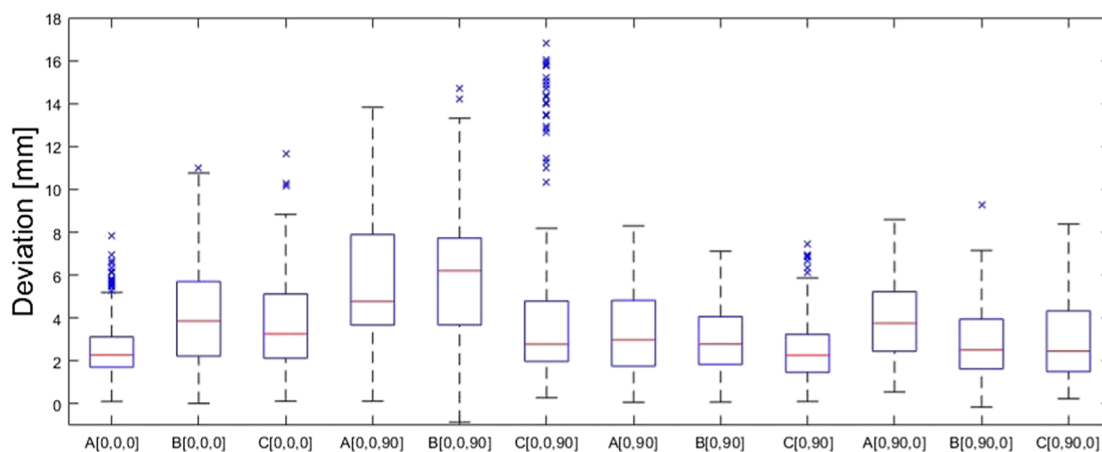


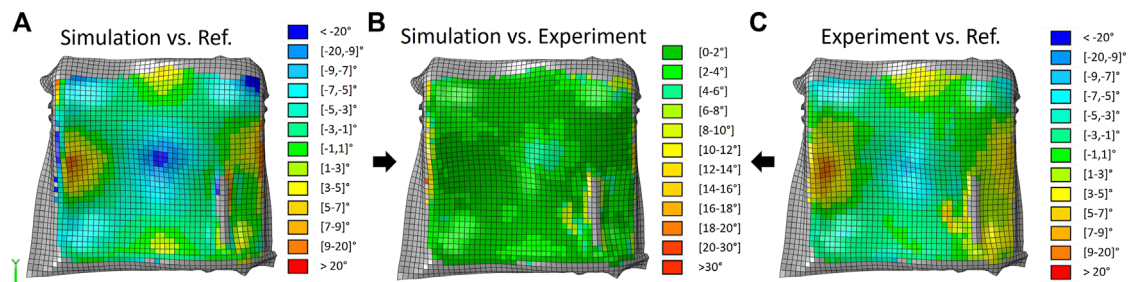
FIGURE 10

Boxplots of the edge contour analysis for all investigated specimens.

in (Chen et al., 2016; Margossian, 2017; Han and Chang, 2018; Thompson et al., 2020; Huang et al., 2021). In (Chen et al., 2021) and (Bai et al., 2022) a detection method for wrinkles is shown based on data from a DIC system. Separate section cuts or a full surface comparison of the recorded Z amplitude are used, providing a similar degree of accuracy and capability to capture the entire surface, however, only big macro wrinkles were investigated in these cases. The overall quality, adhesion to the surface and integrity of the pattern can influence the applicability of DIC systems. It can become a limiting factor near locations that undergo large deformation, i.e.,

folds or wrinkles and subsequent curing steps might be affected by adding speckles to the surface. Utilizing the local curvature, as presented in (Dörr, 2019; Joppich, 2019; Kärger et al., 2020), can result in very exact tracking of the wrinkle formation in terms of occurrence and location, however cannot predict the height.

Thus, the main advantage of comparing 3D scans with the tool is the simultaneous visualization of wrinkles and bridging areas. In general, the method seems to be particularly applicable for the evaluation of draped parts with uncured, unstable semifinished products such as preforms made from prepreg or dry textiles. These



**FIGURE 11** Fiber angle alignment: (A) simulation vs. reference direction (X direction), (B) simulation compared with experimental result, (C) experimental result vs. reference direction (X direction).

**TABLE 1** Measured fiber angle distribution of the raw, undeformed material.

Deviation span	0°–0.5°	0.5°–1°	1°–1.5°	1.5°–2°	2°–3°	>3°
Shares [%]	37.8	33.4	21.0	5.5	2.2	0.1

parts would collapse when removed from the tooling before the final curing/infusion step to obtain the 3D scan. Recent generations of commercial laser scanners enable scanning of shiny surfaces without treatment of the surface, allowing for quick scans (less than a minute) between production steps. Exporting the deviation data (or raw location data) for each measurement, allows for further statistical analysis such as averaging of experimental results to improve comparability.

Analyzing the edge contour in the 3D space to evaluate draping experiments or simulations was not reported in the recent literature, to the authors’ best knowledge. By including information about the Z-direction, the possibility to detect deviations and their magnitude potentially increase. In-plane evaluation of the edge contour might cover up deviations of the part edge for complex 3D parts, as used, e.g., in (Dörr et al., 2017; Joppich, 2019; Han and Chang, 2021a). Thus, a direct comparison of our measured edge contour deviation between simulation and experiments with other literature is challenging due to varying raw material types.

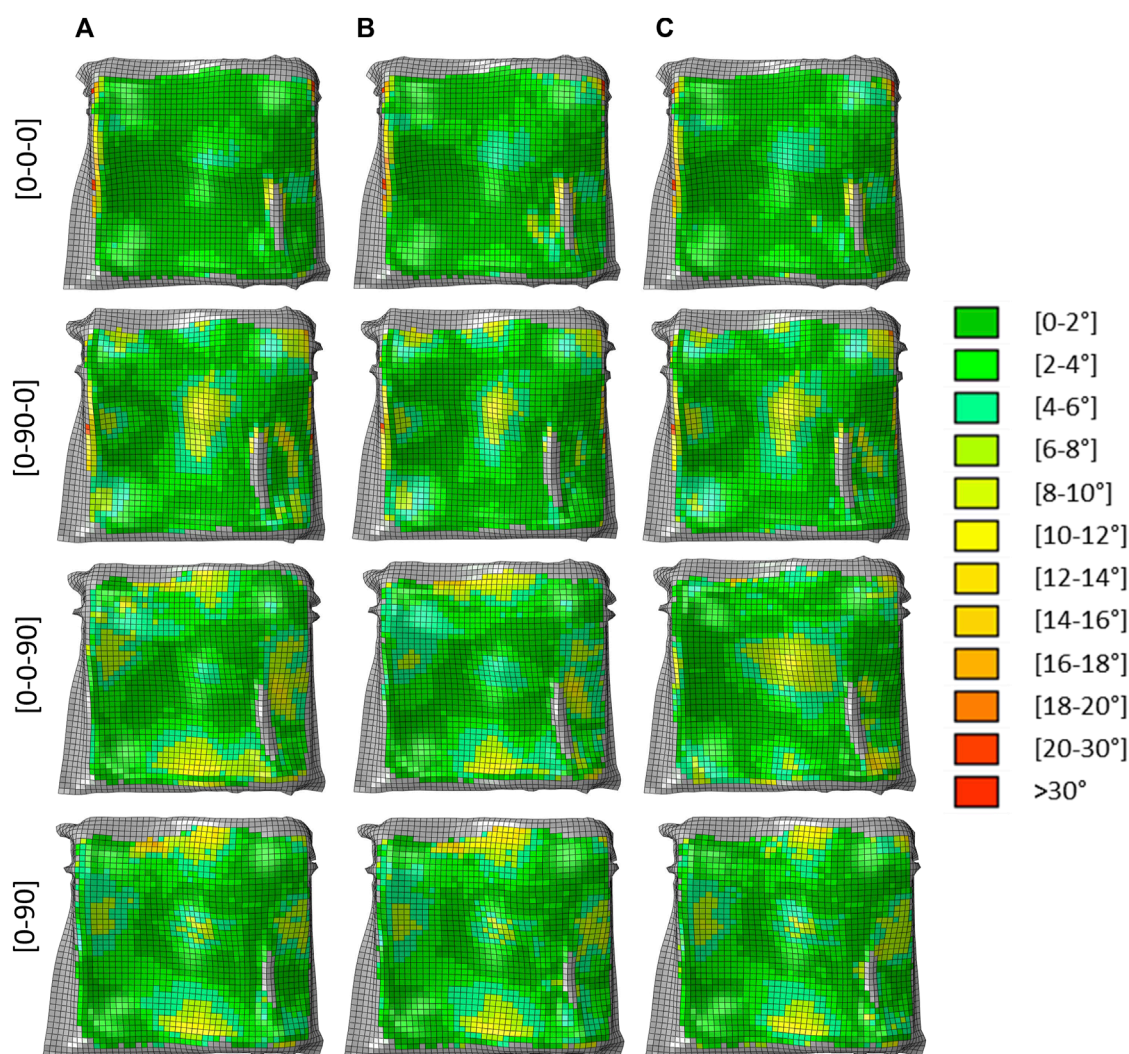
A benchmark study comparing draping simulations for UD thermoplastic materials, conducted with PAM-Form, AniForm, LS-Dyna and Abaqus, reported contour deviations in the range of 8–10 mm (Dörr et al., 2017). Studies using an epoxy prepreg, but with a woven fabric, reported deviations up to 5 mm and 8 mm for a hemisphere and a pyramid, respectively (Chen et al., 2021) and up to 10 mm for a complex egg-box shape (Han and Chang, 2021a; Han and Chang, 2021b). Thus, the presented results (c.f. Figures 7, 10) are in a similar range, despite accounting for the total deviation in 3D and highlight the potential of the Fabric\* material model for unidirectional, uncured prepreg materials. For the validation of forming simulations, it can be stated that using the 3D shaped edge contour allows to investigate the out-of-plane bending properties of the material. Projecting the deviation onto a plane, i.e., only observing the in-plane edge contours, e.g., (Peng and Ding, 2011; Nasri et al., 2019; Chen et al., 2021; Mei et al., 2021), validates mainly the in-plane shear properties.

Visualizing the fiber orientation on the entire 2D surface allows to capture and evaluate the full part geometry at once. The proposed method provides a visualization tool, using the same field of view as the FE simulations. This allows for quick full-field comparisons with a familiar user interface and avoids potential selection bias, that comes with methods that evaluate single predefined points or small patches on the surface as, e.g., in (Harrison et al., 2013; Mei et al., 2021; Rashidi et al., 2021; Bai et al., 2022). The photometric stereo metric method is limited to the top ply but the mapping algorithm could be used for other detection methods as well, e.g., the eddy current method (Bardl et al., 2016).

The method reduces the resolution from the original measurement by averaging values within a defined radius to match the element size of the FE mesh, but comparability is improved. This could be prevented by using finer FE-meshes, which would then increase the computational effort.

A limitation for this procedure is inherent to the measurement method and the geometrical properties of the FScan sensor. The photometric stereo procedure requires the sensor to be perpendicular and within a certain distance from the part surface (Zambal et al., 2015), thus the complexity of the part geometry can be limited by these constraints and the degrees of freedom in robot-movement. Thus, full-surface recording of complex 3D shapes as presented in (Mallach et al., 2017) is probably not possible. This could be prevented by using hand-guided fiber angle measurement systems such as the Apodius Vision System, presented in (Malhan et al., 2021). To prevent or reduce this limitation, multiple individual measurements could be obtained with individual scans and stitched together, assuming ideal alignment. The clear advantage lies in the automated nature of the procedure, which is ideal for repeated scans of identical parts.

Projecting our measured fiber angles onto a global projection plane introduces some uncertainty when the element surfaces are inclined more than 30° (0° would mean that the Element is parallel to the projection plane) (Keller et al., 2022). Areas with higher inclination angles are more prone to be affected by projection distortions. These systemic deviations are visible in Figure 12, where nearly all results show the highest deviations in areas with highest inclination angles. This could be resolved by defining not a single projection plane, but rather multiple regions reasonably parallel to the underneath surface. Alternatively, correction factors could



**FIGURE 12**

Comparison of fiber angle orientations derived from the FE simulations measured against four different experimental layouts [(0-0-0), (0-0-90), (0-90-0), (0-90)] with three experiments per layout (A, B, C).

be determined. However, within the scope of this project a global approach was pursued, and the method will be further improved in upcoming projects.

Comparing the fiber angle measurements in Figure 13 to the literature is again challenging. Typical evaluation methods either focus on a local assessment of absolute fiber orientation or report shear angles. While shear angles provide information about the local distortion of a fabric, they are neither suitable for unidirectional or NCF materials nor do they provide information about how well fibers are aligned with the intended orientation and the loading paths within the component. Reported local deviations in a range from 0°–3.3°, obtained with DIC (Bai et al., 2022), are well aligned with our findings for the (0-0-0) lamina, where up to 65% of the surface showed deviations below 2°. However, an evaluation on local points might be insufficient for a holistic assessment of predicted fiber orientations and might greatly underestimate the potential risk of material failure that can be caused by small, local weak spots. Global evaluations as presented in (Chen et al.,

2016) for a biaxial non-crimp fabric (NCF) reported deviations up to 5°, which is similar to the values for the (0-0-0) layout. Layouts including 90° plies generally show more locations with fiber orientations inaccurately predicted by our simulation. Fiber angle measurements for single ply draping experiments are not included in this study. A preliminary investigation was conducted with single ply experiments and generally less deviation between simulation and experiment, compared to multi-ply experiments, was found. In a representative experiment more than 70% of the surface was within 2° of the predicted fiber angles and approximately 95% of the surface within 4° and larger deviations were exclusively found at the edge or at folds (Keller et al., 2022).

This led to the conclusion that modelling of either the contact interaction including 90° or the in-plane shear properties of the material, using the \*Fabric material model, are critical for the accuracy of the predicted fiber angles and targets for improvement.

The entire data acquisition was reasonably fast. Generating the 3D scans with the laser scanner took approximately 1–2 min and

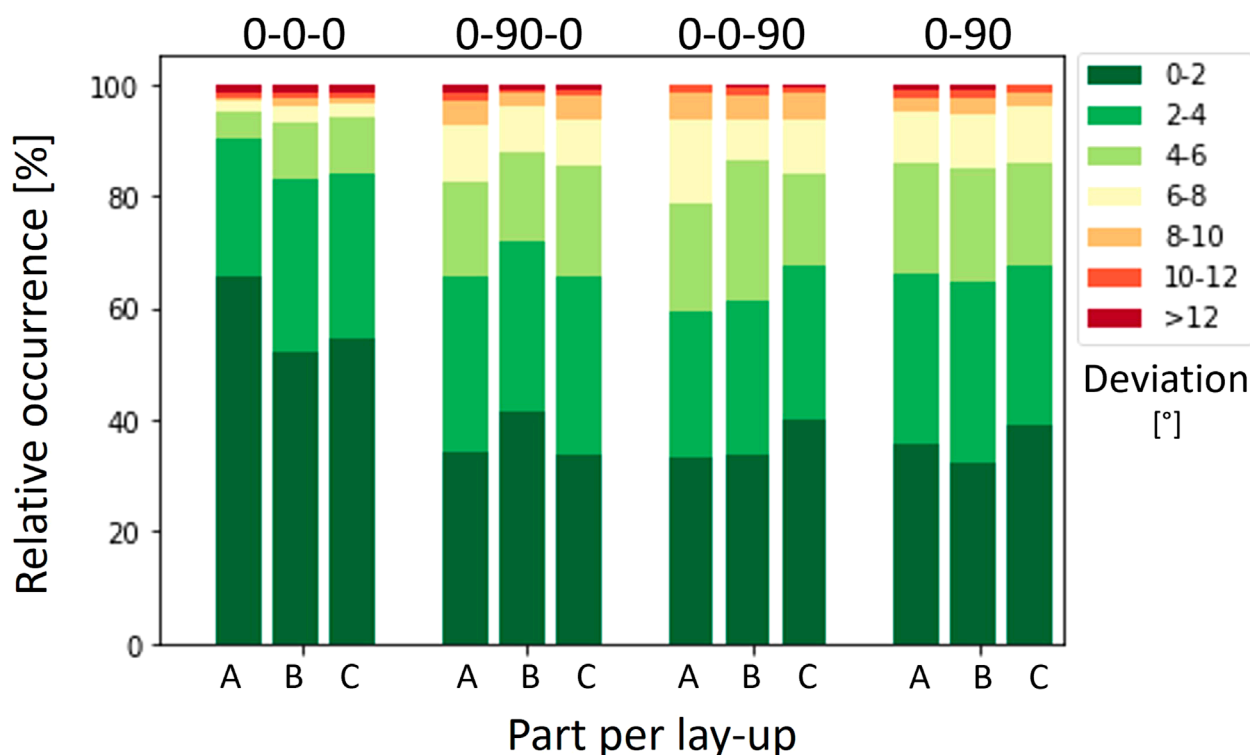


FIGURE 13

Shares for the fiber angle deviation between simulation and experiments for three parts (A, B, C) for four lay-ups, corresponding to Figure 12.

measuring the fiber angles with the FScan took approximately 3–5 min. Both durations depend on the part size and complexity. Increasing the part size increases the duration of manual laser scanning, while increasing complexity increases the duration of the automated fiber angles measurements. Data processing within Geomagic Control X requires manual data alignment and cleaning (local-best-fit with tool region, removing the tool data and contour smoothing) and took 10–15 min per part to obtain images, as shown in Figures 3, 8 for the surface deviation and Figures 6, 9 for the contour deviation. However, it is critical to align the coordinate system of the simulation with the experiment using the scan of the blank tooling. This ensures correct positioning and reduces the time for data processing. Visualizing the FScan Data (Figure 12) was fully automated via python scripts. Only the algorithm to map the measurement data onto the mesh took notable time (30 min at the time the presented results were generated but reduced to 3–5 min in the meantime due to software improvements).

The assessment of deviations from the intended shape and fiber orientation and their classification as tolerable effect or defect depends on their size, number and location within the component and the respective industry. Typically manufacturing effects that are highly disruptive to the load bearing capabilities and the fidelity of the shape, such as folds and fiber bridging are not acceptable. The formation of fiber wrinkles or fiber waviness on the other side, can be within the allowable strength reserve of the component (Thor et al., 2020). The maximum fiber angle deviations should typically be within 3°–5° of the direction specified in the development process for aviation and space industries, to guarantee the components

strength and other anisotropic properties, e.g., thermal expansion. This range might be larger for automotive and nautical applications.

To correctly visualize and, more importantly, quantify these deviations requires a full-field assessment and comparison as proposed in this paper. In the presented case the method was used to gauge the applicability of the Abaqus Fabric\* material model for draping simulations of thin laminas by comparing simulation results with experiments.

Regions where bridging and folds occur, as well as the final part contour were predicted accurately. The fiber angle was predicted within 6° for more than 95% of the surface of the investigated geometry for unidirectional, thin lay-ups. The accuracy drops to less than 80% predicted within 6° for lay-ups containing 0° and 90° plies, emphasizing the need to improve the contact properties in the simulation.

The proposed assessment method provides fast, quantifiable results and can be used to determine the quality during the development or prototyping phase and for a small batch size.

The calibrated material and process model then allows to adjust the tooling geometry and the manufacturing process virtually to reduce the risk of manufacturing defects.

## Data availability statement

The raw data supporting the conclusion of this article will be made available by the authors, without undue reservation. We currently have no means to make this large amount of data publicly available.



## Author contributions

JO and FM carried out the experimental work, the data processing and defined the evaluation methods. SK developed the method and all python scripts necessary for the fiber angle comparison. RH supervised the project. All authors contributed to the article and approved the submitted version.

## Acknowledgments

We thank our funding source, the Austrian Research Promotion Agency (FFG), for supporting us in the project ProSim (866878).

## References

- Alshahrani, H., and Hojjati, M. (2017). Experimental and numerical investigations on formability of out-of-autoclave thermoset prepreg using a double diaphragm process. *Compos. Part A Appl. Sci. Manuf.* 101, 199–214. doi:10.1016/j.compositesa.2017.06.021
- Bai, R., Colmars, J., Chen, B., Naouar, N., and Boisse, P. (2022). The fibrous shell approach for the simulation of composite draping with a relevant orientation of the normals. *Compos. Struct.* 285, 115202. doi:10.1016/j.compstruct.2022.115202
- Bardl, G., Nocke, A., Cherif, C., Pooch, M., Schulze, M., Heuer, H., et al. (2016). Automated detection of yarn orientation in 3D-draped carbon fiber fabrics and preforms from eddy current data. *Compos. Part B Eng.* 96, 312–324. doi:10.1016/j.compositesb.2016.04.040
- Boisse, P., Hamila, N., Vidal-Sallé, E., and Dumont, F. (2011). Simulation of wrinkling during textile composite reinforcement forming. Influence of tensile, in-plane shear and bending stiffnesses. *Compos. Sci. Technol.* 71, 683–692. doi:10.1016/j.compscitech.2011.01.011
- Chen, B., Colmars, J., Naouar, N., and Boisse, P. (2021). A hypoelastic stress resultant shell approach for simulations of textile composite reinforcement forming. *Compos. Part A Appl. Sci. Manuf.* 149, 106558. doi:10.1016/j.compositesa.2021.106558
- Chen, S., McGregor, O. P. L., Endruweit, A., Elsmore, M. T., De Focatiis, D. S. A., Harper, L. T., et al. (2017). Double diaphragm forming simulation for complex composite structures. *Compos. Part A Appl. Sci. Manuf.* 95, 346–358. doi:10.1016/j.compositesa.2017.01.017
- Chen, S., McGregor, O. P. L., Harper, L. T., Endruweit, A., and Warrior, N. A. (2016). Defect formation during preforming of a bi-axial non-crimp fabric with a pillar stitch pattern. *Compos. Part A Appl. Sci. Manuf.* 91, 156–167. doi:10.1016/j.compositesa.2016.09.016
- Dörr, D., Brymerski, W., Ropers, S., Leutz, D., Joppich, T., Kärger, L., et al. (2017). A benchmark study of finite element codes for forming simulation of thermoplastic UD-Tapes. *Procedia CIRP* 66, 101–106. doi:10.1016/j.procir.2017.03.223
- Dörr, D. (2019). *Simulation of the thermoforming process of UD fiber-reinforced thermoplastic tape laminates*. Karlsruhe: KIT Scientific Publishing.
- Han, M. G., and Chang, S. H. (2018). Draping simulation of carbon/epoxy plain weave fabrics with non-orthogonal constitutive model and material behavior analysis of the cured structure. *Compos. Part A Appl. Sci. Manuf.* 110, 172–182. doi:10.1016/j.compositesa.2018.04.022
- Han, M. G., and Chang, S. H. (2021a). Draping simulations of carbon/epoxy fabric prepreps using a non-orthogonal constitutive model considering bending behavior. *Compos. Part A Appl. Sci. Manuf.* 148, 106483. doi:10.1016/j.compositesa.2021.106483
- Han, M. G., and Chang, S. H. (2021b). Simulation of the compressive behaviour of a composite egg-box core with fibre orientation-mapping technique and progressively degraded material properties. *Compos. Part A Appl. Sci. Manuf.* 142, 106272. doi:10.1016/j.compositesa.2021.106272
- Harrison, P., Gomes, R., and Curado-Correia, N. (2013). Press forming a 0/90 cross-ply advanced thermoplastic composite using the double-dome benchmark geometry. *Compos. Part A Appl. Sci. Manuf.* 54, 56–69. doi:10.1016/j.compositesa.2013.06.014
- Huang, J., Boisse, P., Hamila, N., Gnaba, I., Soulat, D., and Wang, P. (2021). Experimental and numerical analysis of textile composite draping on a square box. Influence of the weave pattern. *Compos. Struct.* 267, 113844. doi:10.1016/j.compstruct.2021.113844
- Joppich, T. D. (2019). *Beitrag zum Umformverhalten von PA6/CF Gelegelaminaten im nicht-isothermen Stempelumformprozess*. Karlsruhe: Karlsruher Institut für Technologie KIT.
- Kärger, L., Galkin, S., Dörr, D., and Poppe, C. (2020). Capabilities of macroscopic forming simulation for large-scale forming processes of dry and impregnated textiles. *Procedia Manuf.* 47, 140–147. doi:10.1016/j.promfg.2020.04.155
- Keller, S., Maier, F., and Joachim Osterberger, R. M. (2022). "Hinterhölzl Comparing local fiber angles from draping experiments to simulations," in *Proceedings of the ECCM20, 20th European conference on composite materials* (Lausanne, Switzerland: ECCM). doi:10.5075/epfl-298799\_978-2-9701614-0-0
- Leutz, D. M. (2016). *Forming simulation of AFP material layouts: Material characterization, simulation and validation*. München: Technische Universität München TUM.
- Machado, M., Fischlschweiger, M., and Major, Z. (2016). A rate-dependent non-orthogonal constitutive model for describing shear behaviour of woven reinforced thermoplastic composites. *Compos. Part A Appl. Sci. Manuf.* 80, 194–203. doi:10.1016/j.compositesa.2015.10.028
- Malhan, R. K., Shembekar, A. V., Kabir, A. M., Bhatt, P. M., Shah, B., Zanio, S., et al. (2021). Automated planning for robotic layout of composite prepreg. *Robot. Comput. Integr. Manuf.* 67, 102020. doi:10.1016/j.rcim.2020.102020
- Mallach, A., Härtel, F., Heicie, F., Fuhr, J. P., Middendorf, P., and Gude, M. (2017). Experimental comparison of a macroscopic draping simulation for dry non-crimp fabric preforming on a complex geometry by means of optical measurement. *J. Compos. Mat.* 51, 2363–2375. doi:10.1177/0021998316670477
- Margossian, A. (2017). *Forming of tailored thermoplastic composite blanks: Material characterisation, simulation and validation*. München: Technische Universität München TUM.
- Mei, M., He, Y., Yang, X., and Wei, K. (2021). Analysis and experiment of deformation and draping characteristics in hemisphere preforming for plain woven fabrics. *Int. J. Solids Struct.* 222–223, 111039. doi:10.1016/j.ijsolstr.2021.111039
- Mohammed, U., Lekakou, C., and Bader, M. G. (2000). Experimental studies and analysis of the draping of woven fabrics. *Compos. Part A Appl. Sci. Manuf.* 31, 1409–1420. doi:10.1016/S1359-835X(00)00080-4
- Nasri, M., Garnier, C., Abbassi, F., Labanieh, A. R., Dalverny, O., and Zghal, A. (2019). Hybrid approach for woven fabric modelling based on discrete hypoelastic behaviour and experimental validation. *Compos. Struct.* 209, 992–1004. doi:10.1016/j.compstruct.2018.10.081
- Osterberger, J., and Franz Maier, R. H. (2020). "Process modelling of diaphragm forming with UD semi-finished prepreps," in *Proceedings of the SAMPE europe conference* (Amsterdam, Netherlands: SAMPE), 8.
- Osterberger, J., Maier, F., and Hinterhölzl, R. M. (2022). Application of the Abaqus \*fabric model to approximate the draping behavior of UD prepreps based on suited mechanical characterization. *Front. Mat.* 9, 865477. doi:10.3389/fmats.2022.865477
- Peng, X., and Ding, F. (2011). Validation of a non-orthogonal constitutive model for woven composite fabrics via hemispherical stamping simulation. *Compos. Part A Appl. Sci. Manuf.* 42, 400–407. doi:10.1016/j.compositesa.2010.12.014
- Rashidi, A., Montazerian, H., and Milani, A. S. (2021). Slip-bias extension test: A characterization tool for understanding and modeling the effect of clamping conditions in forming of woven fabrics. *Compos. Struct.* 260, 113529. doi:10.1016/j.compstruct.2020.113529

## Conflict of interest

The authors declare that the research was conducted in the absence of any commercial or financial relationships that could be construed as a potential conflict of interest.

## Publisher's note

All claims expressed in this article are solely those of the authors and do not necessarily represent those of their affiliated organizations, or those of the publisher, the editors and the reviewers. Any product that may be evaluated in this article, or claim that may be made by its manufacturer, is not guaranteed or endorsed by the publisher.



- Schirmaier, F. J., Weidenmann, K. A., Kärger, L., and Henning, F. (2016). Characterisation of the draping behaviour of unidirectional non-crimp fabrics (UD-NCF). *Compos. Part A Appl. Sci. Manuf.* 80, 28–38. doi:10.1016/j.compositesa.2015.10.004
- Schug, A., Kapphan, G., Bardl, G., Hinterhölzl, R., and Drechsler, K. (2018). “Comparison of validation methods for forming simulations,” in *Proceedings of the AIP conference proceedings* (Palermo, Italy: AIP Publishing).
- Thompson, A. J., Belnoue, J. P. H., and Hallett, S. R. (2020). Modelling defect formation in textiles during the double diaphragm forming process. *Compos. Part B Eng.* 202, 108357. doi:10.1016/j.compositesb.2020.108357
- Thor, M., Sause, M. G. R., and Hinterhölzl, R. M. (2020). Mechanisms of origin and classification of out-of-plane fiber waviness in composite materials—a review. *J. Compos. Sci.* 4, 130. doi:10.3390/jcs4030130
- Vanclooster, K., Lomov, S. V., and Verpoest, I. (2009). Experimental validation of forming simulations of fabric reinforced polymers using an unsymmetrical mould configuration. *Compos. Part A Appl. Sci. Manuf.* 40, 530–539. doi:10.1016/j.compositesa.2009.02.005
- Viisainen, J. V., Hosseini, A., and Sutcliffe, M. P. F. (2021). Experimental investigation, using 3D digital image correlation, into the effect of component geometry on the wrinkling behaviour and the wrinkling mechanisms of a biaxial NCF during preforming. *Compos. Part A Appl. Sci. Manuf.* 142, 106248. doi:10.1016/j.compositesa.2020.106248
- Willems, A. (2008). Forming simulation of textile reinforced composite shell structures. PhD Thesis. Leuven, Belgium: katholieke Universiteit Leuven.
- Zambal, S., Palfinger, W., Stöger, M., and Eitzinger, C. (2015). Accurate fibre orientation measurement for carbon fibre surfaces. *Pattern Recognit.* 48, 3324–3332. doi:10.1016/j.patcog.2014.11.009

# Frontiers in Materials

Investigates the discovery and design of materials  
for future application

A multidisciplinary journal that explores the  
breadth of materials science, engineering and  
mechanics - from carbon-based materials to  
smart materials.

## Discover the latest Research Topics

[See more →](#)

### Frontiers

Avenue du Tribunal-Fédéral 34  
1005 Lausanne, Switzerland  
[frontiersin.org](https://frontiersin.org)

### Contact us

+41 (0)21 510 17 00  
[frontiersin.org/about/contact](https://frontiersin.org/about/contact)

